The need for research on solar geoengineering pp. 795, 812, & 815

How the Webb space telescope will revolutionize astronomy p. 806

Chang'e-5 samples show late lunar volcanism p. 887

Science

$15
12 NOVEMBER 2021
science.org
AAAS



EXTREME LIFE SPAN

The genetics of aging in rockfishes pp. 824 & 842



FLEXIBLE.
SENSITIVE.
DEPENDABLE.

CLARIOstar® *Plus*

The CLARIOstar® *Plus* multi-mode microplate reader streamlines assay development and validation by combining monochromator flexibility with best-in-class sensitivity.

- LVF Monochromators™ for highest sensitivity
- EDR technology makes gain adjustment no longer required
- Dedicated detectors for luminescence and red fluorescence
- Best performance in TRF, TR-FRET, FP and AlphaScreen®
- Atmospheric control with gas ramping function
- Made-in-Germany dependability

www.bmglabtech.com

BMG LABTECH

The Microplate Reader Company

©2021 Allrightsreserved.Alllogosandtrademarksarethepropertyof BMGLABTECH



Pushing the Boundaries of Knowledge

As AAAS's first multidisciplinary, open access journal, *Science Advances* publishes research that reflects the selectivity of high impact, innovative research you expect from the *Science* family of journals, published in an open access format to serve a vast and growing global audience. Check out the latest findings or learn how to submit your research: **ScienceAdvances.org**

Science Advances
AAAS

GOLD OPEN ACCESS, DIGITAL, AND FREE TO ALL READERS



On track to enhance innovation in Hungary

New initiatives—national laboratories, science parks, and the University Innovation Ecosystem—are creating a framework for long-term and sustainable cooperation in Hungary. István Szabó, vice president for science and international affairs at Hungary's National Research, Development and Innovation Office (NRDIO), describes ongoing plans and future goals.

On any weekday in the heart of Budapest, which is only about 1.5 kilometers east of the Danube River, you might find István Szabó riding his bicycle to work along Kazinczy Street. "There's a certain connection between cycling and research," he says. "They both take passion, because cyclists and scientists both find joy in what they pursue, while they are aware of all the efforts they must make."

Thinking about this in an even bigger way—something that Szabó tends to do—he delves deeper into his cycling-as-science analogy. Comparing buying a bicycle to purchasing a piece of research equipment with money from a grant, he explains, "You're provided the funding for having a bicycle, but after that you will have to ride that bicycle to reach your goal." Still, it takes more than a bicycle and a passionate cyclist to make the most of that method of transportation, which also demands infrastructure such as bike lanes. The infrastructure of technical innovation lies at the heart of Szabó's role, so he sees opportunities all around him—from cycling to science.

Building a personal infrastructure

Despite his current passion for scientific infrastructure, Szabó more or less stumbled into this profession. "I have to be very honest," he says. "Although I have found the world of research infrastructures amazing from the first moment, it is only now that I can see how important they are and how much I have yet to learn about them." His enthusiasm for the field encouraged him to broaden his knowledge at the highest level. Szabó's engagement with research, development, and innovation (RDI) began in 2011, when he accepted a position managing an information technology (IT) project at Hungary's National Innovation Office.

Along the way, he went back to school and earned his Ph.D. in economics in 2018 at the age of 40. "I was feeling that my knowledge was not complete," Szabó says. "I really wanted to do more for the development of the academic sphere, therefore I decided to study hard and started conducting my own research on research infrastructures to better understand the deeper mechanisms beneath the surface." Now, a few years later, Szabó works with top officials in Hungary and around the world to improve scientific infrastructure.

Setting big goals

Hungary pursues ambitious goals for its RDI infrastructure (https://nkfih.gov.hu/english/top-rife-hungary2021), especially in innovative capabilities. "Like most EU [European Union] countries, Hungary faces the so-called European Paradox," Szabó says, "which basically describes Europe as strong in research or development, but weak in innovation." Szabó is determined to bring on initiatives and support developments to improve this scenario.

"The reason behind this phenomenon is the lack of cooperation between the various sectors, such as business enterprises, higher education institutions, and research institutions," Szabó says. "We have to understand that the innovation ecosystem is based on widespread cooperation, and it is our responsibility to support the partakers of this

IMAGES PROVIDED BY NRDIO

ecosystem in creating and maintaining this cooperation. Therefore, we are currently establishing an infrastructure network to ensure that cooperation happens."

Whereas increasing cooperation in RDI is a main goal, the NRDIO also supports many other objectives. For instance, at present, Hungary invests 1.5% of its gross domestic product in R&D. Although Szabó calls this a nice investment, he adds that Hungary is "eager to increase this to 3% by 2032, which is ambitious." Still, he sees this as an achievable goal, "especially with the measures we are introducing now with the system of national laboratories, which can serve as single points of contact for international partners."

Besides the academic sphere, the private sector also invests a lot in R&D activities. "The businesses in Hungary are spending on R&D," Szabó says. "Also, we see that more and more foreign enterprises are coming to Hungary and bringing their R&D activities here." Szabó points out how these activities contribute to the value chain in science infrastructure. To explain this, he mentions the "smile-curve" concept used in business management theory, in which a graph depicting the value-added versus the stages of production, or the value chain, forms the shape of a smile (the curve is highest on either end of the value chain, at the conception and marketing stages, and lowest in the middle, or manufacturing stage). He says that Hungary is pushing toward the part of the smile curve where the value-added starts to climb.

In terms of scientific and technological innovation, Szabó also envisions a big climb for the country. Currently, Hungary ranks 22nd in innovation among EU countries. By enhancing cooperation among Hungarian sectors in R&D, Szabó and his colleagues aim to improve Hungary's innovation ranking in the EU by 10 places by 2030. "We have a solid strategy for reaching this aim, and in close cooperation with the Ministry for Innovation and Technology, we can provide all parties in RDI with financial and professional support," he says.

First step: Linking education and industry

"We have to build up a diverse system with several different pillars," says Szabó, outlining the government's strategy to reach a higher ranking in the EU.

"First, as mentioned before, the government created a network of national laboratories," he says. The scientific mission of these labs is to invite the most recognized researchers from all over the country to conduct high-quality research. Hungary's system of national laboratories covers many topics: agriculture, artificial intelligence, autonomous systems, biotechnology, climate change, IT, lasers, light, virology, and more. "Each of these national laboratories has a single point of contact, which means that if someone from abroad would approach Hungary about interest in, say laser technology, then they know who to approach," says Szabó.

Second, enhancing Hungary's future innovation potential also depends on the visibility (https://nkfih.gov.hu/openscience) of services, infrastructures, RDI portfolios, and the skills and competence of the academic sector. So, in 2020, Hungary's NRDIO launched the University Innovation Ecosystem program. As was noted at the launch of this program, one of its objectives is to "align the portfolio of RDI services of universities with the specific demand of the business sector. The matchmaking function of the platform makes it easier for businesses to contact and partner with universities."

In addition, to create an even tighter connection between education and industries in science and technology, Hungary is building science parks around some of its universities. In these science parks, Szabó says, "a business enterprise can move in and have the necessary resources to bring its research to maturation."

This industrial–education connection reveals Hungary's focus on creating new generations of scientists. Citing one example of this focus, Szabó says, "We have formed a sort of researcher's life plan, so that each young student already sees what awaits them if they become researchers." He adds, "This means that from the point of entering the university, you can have a dedicated grant scheme that supports your research activities." As these students advance in their education, they can present their work at Hungary's National Scientific Students' Associations Conference.

Second step: Creating cooperation

With challenges in cooperation impeding improvements in R&D innovation in Hungary, many of its programs (https://nkfih.gov.hu/english/forefront) –from R&D investment goals and science parks to national laboratories and educational programs–aim directly at improving the teamwork within and across many related sectors of Hungarian society.

Szabó says that "cooperation between existing laboratories forms a critical mass of researchers and a critical mass of infrastructure, as well." In the near future, he hopes to see just as much cooperation in the RDI-related business sectors. "Building trust between the business sectors can play a key role in actually making sure that innovation happens," he says. "They will see that innovation helps them sell their products much more effectively."

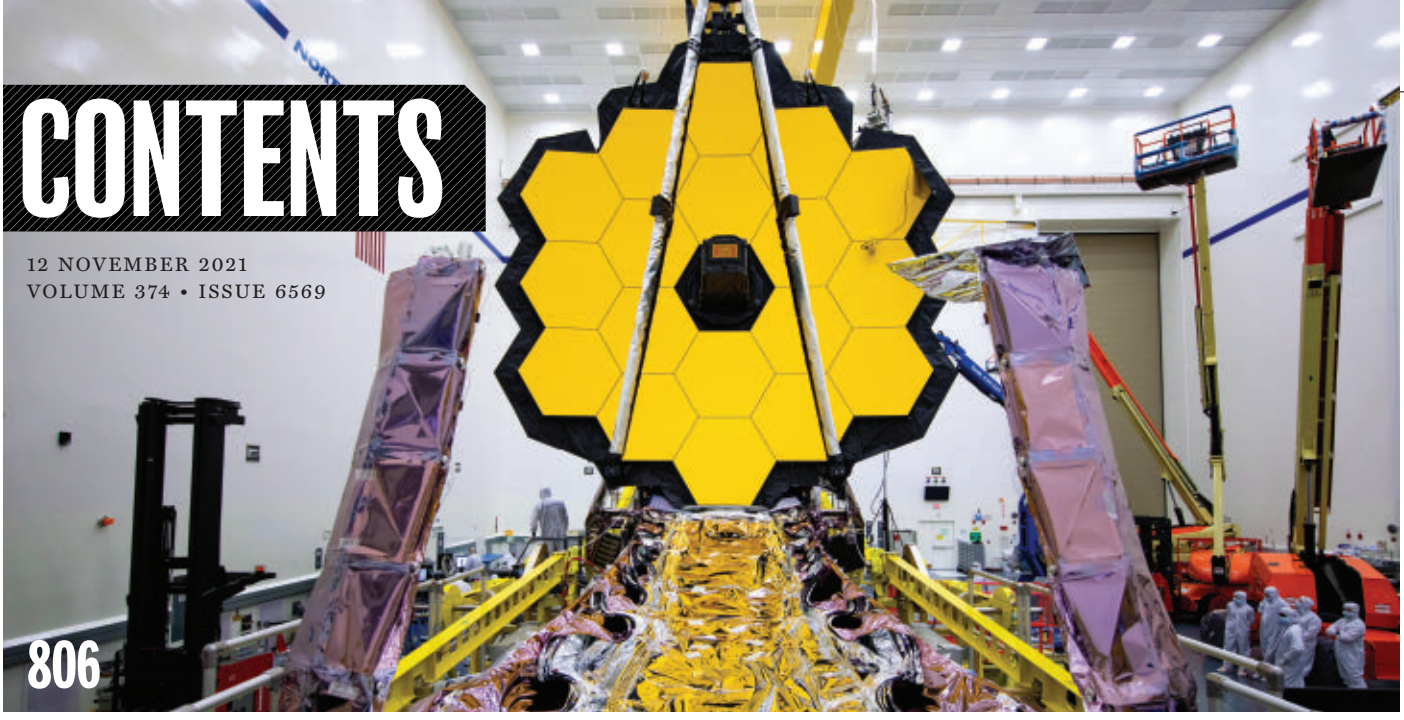
Summing up his thoughts, Szabó says: "We hope these initiatives and programs will enable us to take our innovation ecosystem to a higher level on the value chain. When we reach this goal, the national economy will also enjoy the advantages of all these efforts."

Sponsored by

NATIONAL RESEARCH, DEVELOPMENT AND INNOVATION OFFICE HUNGARY

CONTENTS

12 NOVEMBER 2021
VOLUME 374 • ISSUE 6569



The 6.5-meter-wide, honeycomb mirror of the James Webb Space Telescope, set for launch next month, will gather light from distant galaxies and planets beyond the Solar System.

NEWS

IN BRIEF

796 News at a glance

IN DEPTH

799 Antiviral pills could change pandemic's course
Strong showing for Pfizer protease inhibitor follows success for Merck's molnupiravir
By J. Couzin-Frankel

800 New tool points to mutation behind Delta's infectiousness
"Viruslike particles" open the way to easier study of viral mutations, proteins
By M. Wadman

801 New pledges could keep global warming below 2°C target
But can nations truly realize ambitious goals and provide developing countries with needed financing? *By C. O'Grady*

802 Influential U.S. wish list calls for $11 billion space telescope
Decadal survey says NASA should be frugal and build a series of optical, x-ray, and far-infrared observatories *By D. Clery*

803 Astronomy turns its sights on itself
By J. Mervis

804 AI reveals structures of protein complexes
Software extends protein mapping to complexes that govern the breadth of cell biology *By R. F. Service*
RESEARCH ARTICLE BY I. R. HUMPHREYS *ET AL*. 10.1126/SCIENCE.ABM4805

805 Is the end in sight for famous dark matter claim?
Data cast more doubt on DAMA result as an alternative explanation emerges *By A. Cho*
SCIENCE ADVANCES RESEARCH ARTICLE BY G. ADHIKARI *ET AL*. 10.1126/SCIADV.ABK2699

FEATURES

806 First light machine
At long last, the James Webb Space Telescope is set to launch. It will capture cosmic dawn and bring alien worlds into view *By D. Clery*

810 Telescope name strikes discordant note for many
By D. Clery
PODCAST

INSIGHTS

POLICY FORUMS

812 Toward constructive disagreement about geoengineering
A shared taxonomy of concerns may help
By D. W. Keith
EDITORIAL p. 795; POLICY FORUM p. 815

815 Social science research to inform solar geoengineering
What are the benefits and drawbacks, and for whom? *By J. E. Aldy* et al.
EDITORIAL p. 795; POLICY FORUM p. 812

PERSPECTIVES

819 Cash incentives, ethics, and COVID-19 vaccination
We can pay people to vaccinate, but should we? *By N. S. Jecker*
REPORT p. 879

820 Perovskite retrieved from the lower mantle
The calcium silicate compound was characterized and named as "davemaoite"
By Y. Fei
REPORT p. 891

821 A surprise from the deep
Isotope patterns of methoxyl groups reveal the origin and production potential of methane from coal *By F. Keppler*
REPORT p. 894

823 Autoimmunity in neurodegeneration
A signaling axis in adaptive immunity is a potential target in Lewy body dementia
By M. Krot and A. Rolls
RESEARCH ARTICLE p. 868

824 Long-lived fish in a big pond
The genetic drivers of extreme longevity in Pacific Ocean rockfish are identified *By J. Y. Lu* et al.
RESEARCH ARTICLE p. 842

825 A dynamic duo
Self-assembly of nanofibers facilitates the repair of spinal cord injury in mice
By J. P. Wojciechowski and M. M. Stevens
RESEARCH ARTICLE p. 848

BOOKS *ET AL.*

828 Iterations of evolution
A paleontologist's history of life highlights the recurring role played by geological, climatic, and atmospheric forces
By I. Yanai and M. J. Lercher

829 The politics of epigenetics
Maternal bodies are more than mediators of fetal environments, cautions a historian
By A. Saldaña-Tejeda

PHOTO: NORTHROP GRUMMAN

LETTERS

831 Improving the response to inland flooding
By X. Guo et al.

832 Environmental "nonuse rights" warrant caution
By P. Lucas et al.

832 Protect elephants from tuberculosis
By Y. Shah and S. Paudel

RESEARCH

IN BRIEF

835 From *Science* and other journals

REVIEW

838 Neurodevelopment
Myelin: A gatekeeper of activity-dependent circuit plasticity? *G. Bonetto* et al.
REVIEW SUMMARY; FOR FULL TEXT: DOI.ORG/10.1126/SCIENCE.ABA6905

RESEARCH ARTICLES

839 Disease genomics
Mapping the proteo-genomic convergence of human diseases *M. Pietzner* et al.
RESEARCH ARTICLE SUMMARY; FOR FULL TEXT: DOI.ORG/10.1126/SCIENCE.ABJ1541

840 Plant science
The genetic and epigenetic landscape of the *Arabidopsis* centromeres
M. Naish et al.
RESEARCH ARTICLE SUMMARY; FOR FULL TEXT: DOI.ORG/10.1126/SCIENCE.ABI7489

841 Neuroscience
Tool use and language share syntactic processes and neural patterns in the basal ganglia *S. Thibault* et al.
RESEARCH ARTICLE SUMMARY; FOR FULL TEXT: DOI.ORG/10.1126/SCIENCE.ABE0874

842 Genomics of aging
Origins and evolution of extreme life span in Pacific Ocean rockfishes *S. R. R. Kolora* et al.
PERSPECTIVE p. 824; PODCAST

848 Dynamic bioscaffolds
Bioactive scaffolds with enhanced supramolecular motion promote recovery from spinal cord injury *Z. Álvarez* et al.
PERSPECTIVE p. 825

857 Neuroscience
Stepwise synaptic plasticity events drive the early phase of memory consolidation
A. Goto et al.

863 Spectroscopy
Real-space imaging of anisotropic charge of σ-hole by means of Kelvin probe force microscopy *B. Mallada* et al.

868 Neurodegeneration
$CD4^+$ T cells contribute to neurodegeneration in Lewy body dementia *D. Gate* et al.
PERSPECTIVE p. 823

REPORTS

874 Developmental biology
Symmetry breaking in the female germline cyst *D. Nashchekin* et al.

879 Coronavirus
Monetary incentives increase COVID-19 vaccinations *P. Campos-Mercade* et al.
PERSPECTIVE p. 819

883 Transcription
Structural basis of Integrator-mediated transcription regulation
I. Fianu et al.

887 Lunar geology
Age and composition of young basalts on the Moon, measured from samples returned by Chang'e-5
X. Che et al.

891 Mineralogy
Discovery of davemaoite, $CaSiO_3$-perovskite, as a mineral from the lower mantle
O. Tschauner et al.
PERSPECTIVE p. 820

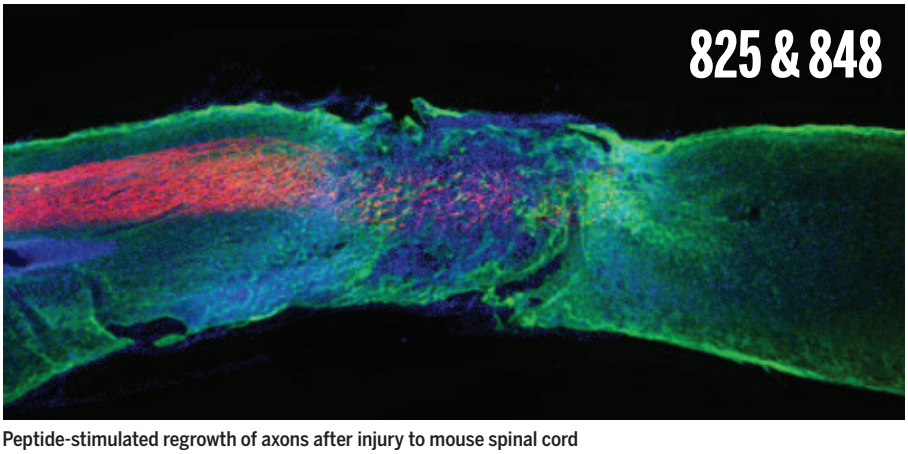
894 Fossil carbon
Methoxyl stable isotopic constraints on the origins and limits of coal-bed methane
M. K. Lloyd et al.
PERSPECTIVE p. 821

DEPARTMENTS

793 Editorial
Self-inflicted wounds
By H. Holden Thorp

795 Editorial
Geoengineering: Symmetric precaution
By Edward A. Parson
POLICY FORUMS pp. 812 & 815

902 Working Life
Out of the fog
By E.A.D.



Peptide-stimulated regrowth of axons after injury to mouse spinal cord

IMAGE: SAMUEL I. STUPP LABORATORY/NORTHWESTERN UNIVERSITY

ON THE COVER

A tiger rockfish (*Sebastes nigrocinctus*) nestled in a cluster of rocks. Tiger rockfish can live as long as 116 years. A genomic analysis of 88 species reveals the genetic underpinnings of rockfish life spans, which range from 11 years for the shortest-lived species (*Sebastes minor*) to >200 years for the ultra-long-lived rougheye rockfish (*Sebastes aleutianus*). See pages 824 and 842.
Photo: Flip Nicklin/ Minden Pictures



Science Staff 794
New Products 898
Science Careers 899

SCIENCE (ISSN 0036-8075) is published weekly on Friday, except last week in December, by the American Association for the Advancement of Science, 1200 New York Avenue, NW, Washington, DC 20005. Periodicals mail postage (publication No. 484460) paid at Washington, DC, and additional mailing offices.

Copyright © 2021 by the American Association for the Advancement of Science. The title SCIENCE is a registered trademark of the AAAS.

Domestic individual membership, including subscription (12 months): $165 ($74 allocated to subscription). Domestic institutional subscription (51 issues): $2148; Foreign postage extra: Air assist delivery: $98. First class, airmail, student, and emeritus rates on request. Canadian rates with GST available upon request, GST #125488122. Publications Mail Agreement Number 1069624. **Printed in the U.S.A.**
Change of address: Allow 4 weeks, giving old and new addresses and 8-digit account number. **Postmaster:** Send change of address to AAAS, P.O. Box 96178, Washington, DC 20090–6178. **Single-copy sales:** $15 each plus shipping and handling available from backissues.science.org; bulk rate on request. **Authorization to reproduce** material for internal or personal use under circumstances not falling within the fair use provisions of the Copyright Act can be obtained through the Copyright Clearance Center (CCC), www.copyright.com. The identification code for *Science* is 0036-8075. *Science* is indexed in the *Reader's Guide to Periodical Literature* and in several specialized indexes.

eppendorf

New epT.I.P.S.®
Box 2.0



Clever and Smart

Time for a fresh reboot

Often copied but unrivaled, the epT.I.P.S.® Box has been in laboratories worldwide since 2002. The fresh new epT.I.P.S Box 2.0 design features a bright white tone, clean lines and a redesigned closure button in typical Eppendorf blue, as well as the bluish-tinted transparent lid with indentations on the sides.

> No slits on the back of boxes to reduce risk of contamination
> Autoclavable up to 100 x for a long lifetime
> Lid with indentations on sides to improve stackability
> Small silicone feet in the bottom of the box reduce risk of slipping



www.eppendorf.com/epTIPS-News

Eppendorf®, the Eppendorf Brand Design, epT.I.P.S.® and PhysioCare Concept® are registered trademarks of Eppendorf AG, Germany.
All rights reserved, including graphics and images. Copyright © 2021 by Eppendorf AG.

EDITORIAL

Self-inflicted wounds

It has been a rough couple of weeks for scientific public relations regarding COVID-19. Missteps by researchers and funding agencies around the origins of severe acute respiratory syndrome coronavirus 2 (SARS-CoV-2) have provided fodder for conspiracy theorists, and caveats about the children's vaccine have provided more ammo for anti-vaxxers. None of these miscues say anything substantive about the science and the conclusion that the virus is almost certainly of zoonotic origin and that the vaccine is safe for children. But clumsy behavior is more eye-catching than the details of research, especially when scientists are so often held to unrealistic standards, expected to be both experts in their fields and skilled communicators.

The latest round of foibles on the origin of SARS-CoV-2 began with the release of an unfunded grant proposal that was submitted in 2018 to the US Defense Advanced Research Projects Agency by the nonprofit EcoHealth Alliance. The proposal featured EcoHealth's president, Peter Daszak, as the principal investigator, and several coronavirus researchers from the University of North Carolina (UNC) at Chapel Hill, the Wuhan Institute of Virology, and Duke–National University of Singapore Medical School. It described experiments to introduce proteolytic cleavage sites into SARS-like coronaviruses. Such a site in SARS-CoV-2 (cleaved by furin) enables the virus to efficiently infect human cells. How the furin cleavage site wound up in the virus is a focus of debate over the origins of the pandemic. Never mind that the experiments, which hardly posed a threat, were not conducted and were proposed by UNC scientists. The researchers failed to get ahead of the story. They should have known that the proposal would arouse interest, especially because the collaborators included scientists at the Wuhan Institute of Virology and US scientists. When the rejected proposal was "leaked," it looked like the scientists were hiding something. This misstep has nothing to do with SARS-CoV-2's origin, but it nevertheless looked suspicious.

Another misstep occurred when the US National Institutes of Health (NIH) sent a letter to Congress chastising EcoHealth for failing to promptly report an "unexpected result" in which a bat coronavirus became more infectious than anticipated in laboratory mice. Nothing about this experiment suggests that the new virus could have become SARS-CoV-2, but the assertion that EcoHealth was late in submitting a report that it knew would be explosive again struck detractors as suspicious. EcoHealth stumbled yet again when earlier this fall a spokesman incorrectly said that the organization had not modified a different coronavirus (one that causes Middle East respiratory syndrome) and then walked back the statement, needlessly provoking suspicion among antiscience forces. Matters were not helped when NIH Director Francis Collins appeared on CNN and struggled to answer questions without seeming to contradict himself. He blamed EcoHealth for not complying with the grant but also said that the experiments didn't meet the standard of problematic gain-of-function research and that NIH didn't fail in monitoring. Collins's performance is understandable: There are details here that are hard to explain in a cable news hit.

> "... science is a messy, human process subject to all features of human frailty."

Miscues like these are not limited to SARS-CoV-2 origins. Last month, when the Vaccines and Related Biological Products Advisory Committee met to advise the US Food and Drug Administration on the Pfizer vaccine for children ages 5 to 11, one member abstained and issued a statement implying that the vaccine was inadequately tested and marginally effective—another scrap to be exploited by anti-vaxxers. Once more, by seeming to contradict themselves, scientists look like they can't get their stories straight and are hiding facts.

These events raise questions about the responsibilities of scientists. These miscues could be honest mistakes or simply people disagreeing. Should scientists be expected to be perfect at communicating and coordinating messages? Scientists have consistently put forward a picture of themselves as highly objective automatons governed solely by their data, when in reality, science is a messy, human process subject to all features of human frailty. Scientists are expected to balance this reality with the fact that their every word and action, when it comes to the pandemic, is under intense scrutiny.

It may seem unfair that scientists are being held to such a high standard. But that is where we find ourselves right now. So, let's strive to be much more thoughtful, because ineptness can cut deep and damaging wounds.

–H. Holden Thorp



PHOTO: CAMERON DAVIDSON

H. Holden Thorp
Editor-in-Chief, *Science* journals.
hthorp@aaas.org;
@hholdenthorp

10.1126/science.abn1244

Science AAAS

Editor-in-Chief Holden Thorp, hthorp@aaas.org

Executive Editor Monica M. Bradford

Editors, Research Valda Vinson, Jake S. Yeston **Editor, Insights** Lisa D. Chong

DEPUTY EDITORS Julia Fahrenkamp-Uppenbrink (UK), Stella M. Hurtley (UK), Phillip D. Szuromi, Sacha Vignieri **SR. EDITORIAL FELLOW** Andrew M. Sugden (UK) **SR. EDITORS** Gemma Alderton (UK), Caroline Ash (UK), Brent Grocholski, Pamela J. Hines, Di Jiang, Priscilla N. Kelly, Marc S. Lavine (Canada), Yevgeniya Nusinovich, Ian S. Osborne (UK), Beverly A. Purnell, L. Bryan Ray, H. Jesse Smith, Keith T. Smith (UK), Jelena Stajic, Peter Stern (UK), Valerie B. Thompson, Brad Wible, Yuen Yiu, Laura M. Zahn **ASSOCIATE EDITORS** Michael A. Funk, Bianca Lopez, Seth Thomas Scanlon (UK), Yury V. Suleymanov **LETTERS EDITOR** Jennifer Sills **LEAD CONTENT PRODUCTION EDITORS** Harry Jach, Lauren Kmec **CONTENT PRODUCTION EDITORS** Amelia Beyna, Jeffrey E. Cook, Chris Filiatreau, Julia Haber-Katris, Nida Masiulis, Abigail Shashikanth, Suzanne M. White **SR. EDITORIAL COORDINATORS** Carolyn Kyle, Beverly Shields **EDITORIAL COORDINATORS** Aneera Dobbins, Joi S. Granger, Jeffrey Hearn, Lisa Johnson, Maryrose Madrid, Ope Martins, Shannon McMahon, Jerry Richardson, Hilary Stewart (UK), Alice Whaley (UK), Anita Wynn **PUBLICATIONS ASSISTANTS** Alexander Kief, Ronmel Navas, Isabel Schnaidt, Brian White **EXECUTIVE ASSISTANT** Jessica Slater **ASI DIRECTOR, OPERATIONS** Janet Clements (UK) **ASI SR. OFFICE ADMINISTRATOR** Jessica Waldock (UK)

News Editor Tim Appenzeller

NEWS MANAGING EDITOR John Travis **INTERNATIONAL EDITOR** Martin Enserink **DEPUTY NEWS EDITORS** Elizabeth Culotta, Lila Guterman, David Grimm, Eric Hand (Europe), David Malakoff **SR. CORRESPONDENTS** Daniel Clery (UK), Jon Cohen, Jeffrey Mervis, Elizabeth Pennisi **ASSOCIATE EDITORS** Jeffrey Brainard, Kelly Servick, Catherine Matacic **NEWS REPORTERS** Adrian Cho, Jennifer Couzin-Frankel, Jocelyn Kaiser, Rodrigo Pérez Ortega (Mexico City), Robert F. Service, Erik Stokstad, Paul Voosen, Meredith Wadman **INTERNS** Menna Ibrahim, Sofia Moutinho, Anil Oza, Alex Viveros **CONTRIBUTING CORRESPONDENTS** Warren Cornwall, Andrew Curry (Berlin), Ann Gibbons, Sam Kean, Eli Kintisch, Kai Kupferschmidt (Berlin), Andrew Lawler, Mitch Leslie, Eliot Marshall, Virginia Morell, Dennis Normile (Tokyo), Elisabeth Pain (Careers), Charles Piller, Michael Price, Tania Rabesandratana (Barcelona), Joshua Sokol, Emily Underwood, Gretchen Vogel (Berlin), Lizzie Wade (Mexico City) **CAREERS** Rachel Bernstein (Editor), Katie Langin (Associate Editor) **COPY EDITORS** Julia Cole (Senior Copy Editor), Morgan Everett, Cyra Master (Copy Chief) **ADMINISTRATIVE SUPPORT** Meagan Weiland

Creative Director Beth Rakouskas

DESIGN MANAGING EDITOR Marcy Atarod **INTERIM GRAPHICS MANAGING EDITOR** Chris Bickel **PHOTOGRAPHY MANAGING EDITOR** William Douthitt **WEB STRATEGY MANAGER** Kara Estelle-Powers **MULTIMEDIA MANAGING PRODUCER** Joel Goldberg **DESIGN EDITOR** Chrystal Smith **DESIGNER** Christina Aycock **GRAPHICS EDITOR** Nirja Desai **INTERACTIVE GRAPHICS EDITOR** Kelly Franklin **SENIOR GRAPHICS SPECIALISTS** Holly Bishop, Nathalie Cary **SENIOR SCIENTIFIC ILLUSTRATOR** Valerie Altounian **SCIENTIFIC ILLUSTRATOR** Ashley Mastin **SENIOR PHOTO EDITOR** Emily Petersen **PHOTO EDITOR** Kaitlyn Dolan **SOCIAL MEDIA STRATEGIST** Jessica Hubbard **SOCIAL MEDIA PRODUCER** Sabrina Jenkins **WEB DESIGNER** Jennie Pajerowski **SENIOR PODCAST PRODUCER** Sarah Crespi **VIDEO PRODUCER** Meagan Cantwell

Chief Executive Officer and Executive Publisher Sudip Parikh

Publisher, Science Family of Journals Bill Moran

DIRECTOR, BUSINESS SYSTEMS AND FINANCIAL ANALYSIS Randy Yi **DIRECTOR, BUSINESS OPERATIONS & ANALYSIS** Eric Knott **DIRECTOR OF ANALYTICS** Enrique Gonzales **MANAGER, BUSINESS OPERATIONS** Jessica Tierney **SENIOR BUSINESS ANALYST** Cory Lipman **FINANCIAL ANALYST** Isacco Fusi **ADVERTISING SYSTEM ADMINISTRATOR** Tina Burks **DIGITAL/PRINT STRATEGY MANAGER** Jason Hillman **SENIOR MANAGER, PUBLISHING AND CONTENT SYSTEMS** Marcus Spiegler **ASSISTANT MANAGER DIGITAL/PRINT** Rebecca Doshi **SENIOR CONTENT AND PUBLISHING SYSTEMS SPECIALIST** Jacob Hedrick **SENIOR CONTENT SPECIALISTS** Steve Forrester, Antoinette Hodal, Lori Murphy **PRODUCTION SPECIALIST** Kristin Wowk **DIGITAL PRODUCTION MANAGER** Lisa Stanford **CONTENT SPECIALIST** Kimberley Oster **ADVERTISING PRODUCTION OPERATIONS MANAGER** Deborah Tompkins **DESIGNER, CUSTOM PUBLISHING** Jeremy Huntsinger **SR. TRAFFIC ASSOCIATE** Christine Hall **SPECIAL PROJECTS ASSOCIATE** Sarah Dhere

ASSOCIATE DIRECTOR, BUSINESS DEVELOPMENT Justin Sawyers **GLOBAL MARKETING MANAGER** Allison Pritchard **DIGITAL MARKETING MANAGER** Aimee Aponte **JOURNALS MARKETING MANAGER** Shawana Arnold **MARKETING ASSOCIATES** Ashley Hylton, Mike Romano, Tori Velasquez, Jenna Voris, Justin Wood **SENIOR DESIGNER** Kim Huynh

DIRECTOR AND SENIOR EDITOR, CUSTOM PUBLISHING Sean Sanders **ASSISTANT EDITOR, CUSTOM PUBLISHING** Jackie Oberst

DIRECTOR, PRODUCT & PUBLISHING DEVELOPMENT Chris Reid **DIRECTOR, BUSINESS STRATEGY AND PORTFOLIO MANAGEMENT** Sarah Whalen **ASSOCIATE DIRECTOR, PRODUCT MANAGMENT** Kris Bishop **PRODUCT DEVELOPMENT MANAGER** Scott Chernoff **PUBLISHING TECHNOLOGY MANAGER** Michael Di Natale **SR. PRODUCT ASSOCIATE** Robert Koepke **PRODUCT ASSOCIATE** Anne Mason **SPJ ASSOCIATE MANAGER** Samantha Bruno Fuller **SPJ ASSOCIATE** Casey Buchta

DIRECTOR, INSTITUTIONAL LICENSING Iquo Edim **MARKETING MANAGER** Kess Knight **BUSINESS DEVELOPMENT MANAGER** Rasmus Andersen **SENIOR INSTITUTIONAL LICENSING MANAGER** Ryan Rexroth **INSTITUTIONAL LICENSING MANAGER** Marco Castellan, Claudia Paulsen-Young **CUSTOMER SUCCESS MANAGER** Judy Lillibridge **SENIOR OPERATIONS ANALYST** Lana Guz **FULFILLMENT COORDINATOR** Melody Stringer

DIRECTOR, GLOBAL SALES Tracy Holmes **US EAST COAST AND MID WEST SALES** Stephanie O'Connor **US MID WEST, MID ATLANTIC AND SOUTH EAST SALES** Chris Hoag **US WEST COAST SALES** Lynne Stickrod **ASSOCIATE DIRECTOR, ROW** Roger Goncalves **SALES REP, ROW** Sarah Lelarge **SALES ADMIN ASSISTANT, ROW** Victoria Glasbey **DIRECTOR OF GLOBAL COLLABORATION AND ACADEMIC PUBLISHING RELATIONS, ASIA** Xiaoying Chu **ASSOCIATE DIRECTOR, INTERNATIONAL COLLABORATION** Grace Yao **SALES MANAGER** Danny Zhao **MARKETING MANAGER** Kilo Lan **ASCA CORPORATION, JAPAN** Yoshimi Toda (Tokyo), Miyuki Tani (Osaka)

DIRECTOR, COPYRIGHT, LICENSING AND SPECIAL PROJECTS Emilie David **RIGHTS AND LICENSING COORDINATOR** Jessica Adams **RIGHTS AND PERMISSIONS ASSOCIATE** Elizabeth Sandler **LICENSING ASSOCIATE** Virginia Warren

---

MAIN HEADQUARTERS
Science/AAAS
1200 New York Ave. NW
Washington, DC 20005

SCIENCE INTERNATIONAL
Clarendon House
Clarendon Road
Cambridge, CB2 8FH, UK

SCIENCE CHINA
Room 1004, Culture Square
No. 59 Zhongguancun St.
Haidian District, Beijing, 100872

SCIENCE JAPAN
ASCA Corporation
Sibaura TY Bldg. 4F, 1-14-5
Shibaura Minato-ku
Tokyo, 108-0073 Japan

EDITORIAL
science_editors@aaas.org

NEWS
science_news@aaas.org

INFORMATION FOR AUTHORS
science.org/authors/
science-information-authors

REPRINTS AND PERMISSIONS
science.org/help/
reprints-and-permissions

MEDIA CONTACTS
scipak@aaas.org

MULTIMEDIA CONTACTS
SciencePodcast@aaas.org
ScienceVideo@aaas.org

INSTITUTIONAL SALES AND SITE LICENSES
science.org/librarian

PRODUCT ADVERTISING & CUSTOM PUBLISHING
advertising.science.org/
products-services
science_advertising@aaas.org

CLASSIFIED ADVERTISING
advertising.science.org/
science-careers
advertise@sciencecareers.org

JOB POSTING CUSTOMER SERVICE
employers.sciencecareers.org
support@sciencecareers.org

MEMBERSHIP AND INDIVIDUAL SUBSCRIPTIONS
science.org/subscriptions

MEMBER BENEFITS
aaas.org/membership/benefits

AAAS BOARD OF DIRECTORS
CHAIR Claire M. Fraser
PRESIDENT Susan G. Amara
PRESIDENT-ELECT Gilda A. Barabino
TREASURER Carolyn N. Ainslie
CHIEF EXECUTIVE OFFICER Sudip Parikh
BOARD Cynthia M. Beall, Rosina M. Bierbaum, Ann Bostrom, Janine Austin Clayton, Laura H. Greene, Kaye Husbands Fealing, Maria M. Klawe, Robert B. Millard, William D. Provine

Science serves as a forum for discussion of important issues related to the advancement of science by publishing material on which a consensus has been reached as well as including the presentation of minority or conflicting points of view. Accordingly, all articles published in *Science*—including editorials, news and comment, and book reviews—are signed and reflect the individual views of the authors and not official points of view adopted by AAAS or the institutions with which the authors are affiliated.

BOARD OF REVIEWING EDITORS (Statistics board members indicated with **(S)**)

Erin Adams, *U. of Chicago*
Takuzo Aida, *U. of Tokyo*
Leslie Aiello, *Wenner-Gren Fdn.*
Deji Akinwande, *UT Austin*
Judith Allen, *U. of Manchester*
Marcella Alsan, *Harvard U.*
Sebastian Amigorena, *Inst. Curie*
James Analytis, *UC Berkeley*
Trevor Archer, *NIEHS, NIH*
Paola Arlotta, *Harvard U.*
David Awschalom, *U. of Chicago*
Delia Baldassarri, *NYU*
Nenad Ban, *ETH Zürich*
Nandita Basu, *U. of Waterloo*
Franz Bauer, *Pontificia U. Católica de Chile*
Ray H. Baughman, *UT Dallas*
Carlo Beenakker, *Leiden U.*
Yasmine Belkaid, *NIAID, NIH*
Philip Benfey, *Duke U.*
Kiros T. Berhane, *Columbia U.*
Joseph J. Berry, *NREL*
Alessandra Biffi, *Harvard Med.*
Chris Bowler, *École Normale Supérieure*
Ian Boyd, *U. of St. Andrews*
Emily Brodsky, *UC Santa Cruz*
Ron Brookmeyer, *UCLA* **(S)**
Christian Büchel, *UKE Hamburg*
Dennis Burton, *Scripps Res.*
Carter Tribley Butts, *UC Irvine*
György Buzsáki, *NYU School of Med.*
Mariana Byndloss, *Vanderbilt U. Med. Ctr.*
Annmarie Carlton, *UC Irvine*
Simon Cauchemez, *Inst. Pasteur*
Ling-Ling Chen, *SIBCB, CAS*
M. Keith Chen, *UCLA*
Zhijian Chen, *UT Southwestern Med. Ctr.*
Ib Chorkendorff, *Denmark TU*
Amander Clark, *UCLA*
James J. Collins, *MIT*
Robert Cook-Deegan, *Arizona State U.*
Virginia Cornish *Columbia U.*
Carolyn Coyne, *Duke U.*
Roberta Croce, *VU Amsterdam*
Ismaila Dabo, *Penn State U.*
Jeff L. Dangl, *UNC*
Chiara Daraio, *Caltech*
Nicolas Dauphas, *U. of Chicago*
Christian Davenport, *U. of Michigan*
Frans de Waal, *Emory U.*
Claude Desplan, *NYU*
Sandra Díaz, *U. Nacional de Córdoba*
Ulrike Diebold *TU Wien*
Stefanie Dimmeler, *Goethe-U. Frankfurt*
Hong Ding, *Inst. of Physics, CAS*
Dennis Discher, *UPenn*
Jennifer A. Doudna, *UC Berkeley*
Ruth Drdla-Schutting, *Med. U. Vienna*
Raissa M. D'Souza, *UC Davis*
Bruce Dunn, *UCLA*
William Dunphy, *Caltech*
Scott Edwards, *Harvard U.*
Todd Ehlers, *U. of Tübingen*
Andrea Encalada, *U. San Francisco de Quito*
Nader Engheta, *UPenn*
Karen Ersche, *U. of Cambridge*
Beate Escher, *UFZ & U. of Tübingen*
Barry Everitt, *U. of Cambridge*
Vanessa Ezenwa, *U. of Georgia*
Michael Feuer, *GWU*
Toren Finkel, *U. of Pitt. Med. Ctr.*
Gwenn Flowers, *Simon Fraser U.*
Peter Fratzl, *Max Planck Inst. Potsdam*
Elaine Fuchs, *Rockefeller U.*
Jay Gallagher, *U. of Wisconsin*
Daniel Geschwind, *UCLA*
Ramon Gonzalez, *U. of South Florida*
Sandra González-Bailón, *UPenn*
Nicolas Gruber, *ETH Zürich*
Hua Guo, *U. of New Mexico*
Taekjip Ha, *Johns Hopkins U.*
Sharon Hammes-Schiffer, *Yale U.*
Wolf-Dietrich Hardt, *ETH Zürich*
Louise Harra, *U. Coll. London*
Carl-Philipp Heisenberg, *IST Austria*
Ykä Helariutta, *U. of Cambridge*
Janet G. Hering, *Eawag*
Christoph Hess, *U. of Basel & U. of Cambridge*
Heather Hickman, *NIAID, NIH*
Hans Hilgenkamp, *U. of Twente*
Kai-Uwe Hinrichs, *U. of Bremen*
Deirdre Hollingsworth, *U. of Oxford*
Randall Hulet, *Rice U.*
Auke Ijspeert, *EPFL*
Akiko Iwasaki, *Yale U.*
Stephen Jackson, *USGS & U. of Arizona*
Erich Jarvis, *Rockefeller U.*
Peter Jonas, *IST Austria*
Matt Kaeberlein, *U. of Wash.*
William Kaelin Jr., *Dana-Farber Cancer Inst.*
Daniel Kammen, *UC Berkeley*
Kisuk Kang, *Seoul Nat. U.*
Sabine Kastner, *Princeton U.*
V. Narry Kim, *Seoul Nat. U.*
Robert Kingston, *Harvard Med.*
Nancy Knowlton, *Smithsonian Institution*
Etienne Koechlin, *École Normale Supérieure*
Alex L. Kolodkin, *Johns Hopkins U.*
Julija Krupic, *U. of Cambridge*
Paul Kubes, *U. of Calgary*
Gabriel Lander, *Scripps Res.* **(S)**
Mitchell A. Lazar, *UPenn*
Wendell Lim, *UCSF*
Luis Liz-Marzán, *CIC biomaGUNE*
Omar Lizardo, *UCLA*
Jonathan Losos, *Wash. U. in St. Louis*
Ke Lu, *Inst. of Metal Res., CAS*
Christian Lüscher, *U. of Geneva*
Jean Lynch-Stieglitz, *Georgia Inst. of Tech.*
David Lyons, *U. of Edinburgh*
Fabienne Mackay, *QIMR Berghofer*
Anne Magurran, *U. of St. Andrews*
Asifa Majid, *U. of York*
Oscar Marín, *King's Coll. London*
Charles Marshall, *UC Berkeley*
Christopher Marx, *U. of Idaho*
David Masopust, *U. of Minnesota*
Geraldine Masson, *CNRS*
Jason Matheny, *Georgetown U.*
Heidi McBride, *McGill U.*
C. Robertson McClung, *Dartmouth*
Rodrigo Medellín, *U. Nacional Autónoma de México*
C. Jessica Metcalf, *Princeton U.*
Baoxia Mi, *UC Berkeley*
Tom Misteli, *NCI, NIH*
Alison Motsinger-Reif, *NIEHS, NIH* **(S)**
Suresh Naidu, *Columbia U.*
Danielle Navarro, *U. of New South Wales*
Daniel Nettle, *Newcastle U.*
Daniel Neumark, *UC Berkeley*
Beatriz Noheda, *U. of Groningen*
Helga Nowotny, *Vienna Sci. & Tech. Fund*
Rachel O'Reilly, *U. of Birmingham*
Pilar Ossorio, *U. of Wisconsin*
Andrew Oswald, *U. of Warwick*
Isabella Pagano, *Istituto Nazionale di Astrofisica*
Elizabeth Levy Paluck, *Princeton U.*
Jane Parker, *Max Planck Inst. Cologne*
Giovanni Parmigiani, *Dana-Farber Cancer Inst.* **(S)**
Daniel Pauly, *U. of British Columbia*
Ana Pêgo, *U. do Porto*
Samuel Pfaff, *Salk Inst.*
Julie Pfeiffer, *UT Southwestern Med. Ctr.*
Philip Phillips, *UIUC*
Matthieu Piel, *Inst. Curie*
Kathrin Plath, *UCLA*
Martin Plenio, *Ulm U.*
Katherine Pollard, *UCSF*
Elvira Poloczanska, *Alfred-Wegener-Inst.*
Julia Pongratz, *Ludwig Maximilians U.*
Philippe Poulin, *CNRS*
Jonathan Pritchard, *Stanford U.*
Lei Stanley Qi, *Stanford U.*
Trevor Robbins, *U. of Cambridge*
Joeri Rogelj, *Imperial Coll. London*
Amy Rosenzweig, *Northwestern U.*
Mike Ryan, *UT Austin*
Miquel Salmeron, *Lawrence Berkeley Nat. Lab*
Nitin Samarth, *Penn State U.*
Erica Ollmann Saphire, *La Jolla Inst.*
Joachim Saur, *U. zu Köln*
Alexander Schier, *Harvard U.*
Wolfram Schlenker, *Columbia U.*
Susannah Scott, *UC Santa Barbara*
Anuj Shah, *U. of Chicago*
Vladimir Shalaev, *Purdue U.*
Jie Shan, *Cornell U.*
Beth Shapiro, *UC Santa Cruz*
Jay Shendure, *U. of Wash.*
Steve Sherwood, *U. of New South Wales*
Brian Shoichet, *UCSF*
Robert Siliciano, *JHU School of Med.*
Lucia Sivilotti, *U. Coll. London*
Alison Smith, *John Innes Ctr.*
Richard Smith, *UNC* **(S)**
Mark Smyth, *QIMR Berghofer*
John Speakman, *U. of Aberdeen*
Tara Spires-Jones, *U. of Edinburgh*
Allan C. Spradling, *Carnegie Institution for Sci.*
V. S. Subrahmanian, *Northwestern U.*
Ira Tabas, *Columbia U.*
Eriko Takano, *U. of Manchester*
Patrick Tan, *Duke-NUS Med. School*
Sarah Teichmann, *Wellcome Sanger Inst.*
Rocio Titiunik, *Princeton U.*
Shubha Tole, *Tata Inst. of Fundamental Res.*
Maria-Elena Torres Padilla, *Helmholtz Zentrum München*
Kimani Toussaint, *Brown U.*
Barbara Treutlein, *ETH Zürich*
Jason Tylianakis, *U. of Canterbury*
Wim van der Putten, *Netherlands Inst. of Ecology*
Ivo Vankelecom, *KU Leuven*
Henrique Veiga-Fernandes, *Champalimaud Fdn.*
Reinhilde Veugelers, *KU Leuven*
Bert Vogelstein, *Johns Hopkins U.*
Julia Von Blume, *Yale School of Med.*
David Wallach, *Weizmann Inst.*
Jane-Ling Wang, *UC Davis* **(S)**
Jessica Ware, *Amer. Mus. of Natural Hist.*
David Waxman, *Fudan U.*
Chris Wikle, *U. of Missouri* **(S)**
Terrie Williams, *UC Santa Cruz*
Ian A. Wilson, *Scripps Res.* **(S)**
Hao Wu, *Harvard U.*
Wei Xie, *Tsinghua U.*
Yu Xie, *Princeton U.*
Jan Zaanen, *Leiden U.*
Kenneth Zaret, *UPenn School of Med.*
Bing Zhu, *Inst. of Biophysics, CAS*
Xiaowei Zhuang, *Harvard U.*
Maria Zuber, *MIT*

EDITORIAL

Geoengineering: Symmetric precaution

As alarm about climate change and calls for action intensify, solar geoengineering (SG) is seeing increased attention and controversy. Views on whether it should or will ever be used diverge, but the evidentiary basis for these views is thin. On such a high-stakes, knowledge-limited issue, one might expect strong support for research, but even research has met opposition. Opponents' objections are grounded in valid concerns but impossible to fully address, as they are framed in ways that make rejecting research an axiom, not a conclusion based on evidence.

Supporters of SG research argue that it can inform future decisions and prepare for likely future calls for deployment. A US National Academies of Sciences, Engineering, and Medicine (NASEM) report earlier this year lent thoughtful support to this view. Opponents raise well-known concerns about SG such as its imperfect climate correction, its time-scale mismatch with greenhouse gases (GHGs), and the potential to over-rely on it or use it recklessly or unjustly. They oppose research based on the same concerns, arguing that usage can never be acceptable so research is superfluous; or that sociopolitical lock-in will drive research toward deployment even if unwarranted. Both support and opposition are often implicit, embedded in debates over additional governance of SG research beyond peer review, program management, and regulatory compliance.

> "...objections are... framed in ways that make rejecting research an axiom..."

At present, potential SG methods and claimed benefits and harms are hypothetical, not demonstrated. The strongest objections to research invoke potential consequences that are indirect, mediated by imprudent or unjust policy decisions. Because the paths from research to these bad outcomes involve political behavior, claims that these "could" happen cannot be fully refuted. Understanding and limiting these risks require the same research and governance-building activities that opponents reject as causing the risks.

To reject an activity based on harms that might follow is to apply extreme precaution. This can be warranted when there is risk of serious, unmitigable harm and the alternative is known to be acceptable. That is not the case here. Rejecting SG research means taking the alternative trajectory of uncertain but potentially severe climate impacts, reduced by whatever emissions cuts, GHG removals, and adaptation are achieved. But these other responses needed to meet prudent climate targets carry their own risks: of falling short and suffering more severe climate change, and of collateral environmental and socioeconomic harms from deployment at the required transformative, even revolutionary, scale.

Suppressing research on SG might reduce risks from its future use, but this is not assured: Rather than preventing use in some future crisis, blocking research might make such use less informed, cruder, and more dangerous. Even if these risks are reduced, this would shift increased risks onto climate change and crash pursuit of other responses. Total climate-related risk may well increase—and be more unjustly distributed, because the largest benefits of SG appear likely to flow to the most vulnerable people and communities.

Yet the concerns that motivate opposition to research are compelling. SG use would be an unprecedented step, affecting climate response, international governance, sustainability, and global justice. Major concerns—about reckless or rivalrous use, or over-reliance weakening emissions cuts—are essential to address, even if they cannot be avoided with certainty. A few directions show promise for doing so. Research should be in public programs, in jurisdictions with cultures of public benefit and research accountability. The NASEM call for a US federal program is sound. Other national programs should be established. Research governance should be somewhat stronger than for less controversial research, including scale limits on field experiments and periodic program reassessments. Exploration of governance needs for larger-scale interventions should begin well before these are considered. Research and governance should seek broad international cooperation—promptly, but not as a precondition to national programs. Broad citizen consultations are needed on overall climate response and the role of SG. These should link to national research and governance programs but not have veto power over specific activities.

Precaution is appropriate, even necessary. But precaution cannot selectively target risks from one climate response while ignoring its linkages to other responses and risks. Suppressing SG research is likely to make the harms and injustices that opponents fear more likely, not less.

–Edward A. Parson

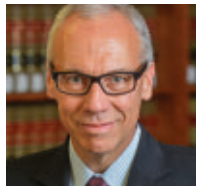


PHOTO: UCLA SCHOOL OF LAW

Edward A. Parson
is Dan and Rae Emmett Professor of Environmental Law and Faculty Director of the Emmett Institute on Climate Change and the Environment at the University of California, Los Angeles, CA, USA.
parson@law.ucla.edu

10.1126/science.abm8462

NEWS

> "The world became one ... to fight this pandemic. This is how I want to see the fight against climate change."
>
> **Climate scientist Nana Ama Browne Klutse** of the University of Ghana, quoted by BBC, about this week's COP26 climate summit.



IN BRIEF

Edited by **Jeffrey Brainard**

CLIMATE SCIENCE

Less deforestation flattens still-alarming carbon emissions curve

A new report finds that carbon emissions from deforestation and other land use changes have decreased over the past decade, partly compensating for increases from burning fossil fuels. Based on updated estimates from satellite data, the report from the Global Carbon Project finds that emissions from sources such as fires, logging, and forest clearing, offset by some reforestation and regrowth of forests and abandoned farm lands, have been decreasing by about 4% a year over the past decade. But current emissions remain too high to appreciably curb warming; at current rates, warming would likely surpass the 1.5°C threshold set in the 2015 Paris agreement within 11 years, the report says. (See p. 801 for updated warming projections based on nations' new greenhouse gas commitments at the global climate summit.) Land use change contributes 10% of global emissions, the report says. It adds that a dip in carbon emissions in 2020 caused by the COVID-19 pandemic was mostly reversed this year as transportation and other activities restarted.

People prepare to plant trees in the Badain Jaran Desert of north-central China to help offset the country's growing fuel emissions.

PHOTO: WANG JIANG/VCG/GETTY IMAGES

Asia eyes switch to renewables

CLIMATE POLICY | The Asian Development Bank last week announced a program to substantially cut carbon emissions from Southeast Asia by helping retire coal-fired power plants and replacing the generating capacity with renewable energy. Unveiled during the COP26 climate change conference in Glasgow, U.K., the Energy Transition Mechanism will be financed by pooling several billion dollars from public, private, and philanthropic sources. Renewable electricity generation is now cheaper than coal, and investors can earn profits by financing the switch. The program aims to cut coal plant generating capacity by 50% in the Philippines, Indonesia, and Vietnam within 10 to 15 years, which could reduce carbon dioxide emissions by 200 million tons per year. The bank expects to extend the program to other countries.

Brazil scientists snub top award

POLITICS | Twenty-one scientists in Brazil who last week received the country's highest scientific honor renounced it days later after President Jair Bolsonaro took back the same award from two fellow researchers whose work is at odds with his policy views. A screening committee had selected 32 scientists to receive the National Order of Scientific Merit, including Marcus Lacerda, lead author of a clinical study that showed the antimalarial drug chloroquine was ineffective against COVID-19 infections, and Adele Benzaken, who was fired from the Ministry of Health in early 2019 after editing a booklet on prevention of sexually transmitted diseases among

transgender men. Without offering an explanation, Bolsonaro on 5 November withdrew Lacerda and Benzaken from the list. The Brazilian Academy of Sciences has asked Bolsonaro to reverse his decision. Scientists were also incensed when Bolsonaro himself was named "grand master" of the order last week, a pro forma recognition that previous presidents of Brazil have also received—even though he has drawn intense criticism for denying and ignoring scientific findings on Amazon deforestation, climate change, the COVID-19 pandemic, and vaccination.

Risky studies of viruses end

BIOMEDICINE | The only experiments funded by the U.S. National Institutes of Health (NIH) that meet the U.S. definition of risky "gain-of-function" (GOF) virus research—and that kicked off controversy 10 years ago—have wound down. In 2011, two studies that modified the H5N1 bird flu to spread more easily in ferrets sparked an uproar from scientists worried about a lab escape. The studies were led by virologists Yoshihiro Kawaoka at the University of Wisconsin, Madison, and Ron Fouchier at Erasmus Medical Center in the Netherlands. The ensuing storm led NIH in 2014 to pause funding of a few especially risky GOF studies. In 2017, the U.S. government adopted a "framework" for evaluating research on "enhanced potential pandemic pathogens" (ePPPs)—risky human pathogens with modifications that could make them more dangerous. Kawaoka's and Fouchier's H5N1 grants were funded again under the new policy in 2019. But Kawaoka's ended in August 2020 and Fouchier's, which was part of a large contract, stopped in March, according to recent updates to federal websites. Kawaoka tells *Science* his work has shifted to pancoronavirus vaccines. Fouchier says he plans to seek funding in Europe to continue the experiments. Debate over U.S. studies of GOF continue: Critics say the ePPP definition is too narrow and should have applied to U.S.-funded coronavirus experiments conducted in China.

HPV jabs ward off cervical cancer

BIOMEDICINE | In girls offered a vaccine against human papillomavirus (HPV) at age 12 or 13, the prevalence of cervical cancer throughout their 20s was 87% lower than in unvaccinated girls, according to a study published online on 3 November in *The Lancet*. The authors examined nearly 28,000 cases of cervical cancer in U.K. women ages 20 to 30 from 2006 to 2019. The HPV vaccine Cervarix, which targets the two strains of HPV that cause most of these cancers, was introduced in the United Kingdom in 2008, and the oldest women in the study were not offered it, forming a comparison group. The United Kingdom recommends giving the vaccine at age 12 to 13, because it is most effective if given before sexual activity begins. But girls offered catch-up doses at ages 14 to 16 and 16 to 18 also saw reductions in cancer prevalence, of 62% and 34%, respectively. A Danish study published last month and a Swedish study that appeared last year reported large reductions in the risk of cervical cancer among women vaccinated as teenagers with a different HPV vaccine, Gardasil-4.

U.S. OKs COVID-19 shots for kids

VACCINES | U.S. regulators last week gave the long-awaited green light for vaccinating younger children against COVID-19, and within hours, the rush to give shots to 5- to 11-year-olds began. On 2 November, advisers to the U.S. Centers for Disease Control and Prevention unanimously recommended Pfizer's vaccine in this age group, saying benefits outweighed risks; CDC Director Rochelle Walensky agreed. The U.S. Food and Drug Administration had given its blessing the previous week. At the CDC advisers' meeting, data presented showed COVID-19's death toll in children was comparable to or

Comparing childhood risks

U.S. regulators have endorsed several childhood vaccines, now widely used, for diseases that killed fewer children than COVID-19 before vaccines.

DISEASE	ANNUAL DEATHS OF CHILDREN BEFORE VACCINES	AGE AT DEATH
Hepatitis A	3 (1990–95)	<20
Varicella (chickenpox)	16 (1990–94)	5–9
Rotavirus (causes diarrhea, vomiting)	20 (1985–91)	<5
COVID-19	66 (October 2020–October 2021)	5–11

CREDITS: (DATA) U.S. CENTERS FOR DISEASE CONTROL AND PREVENTION; (PHOTO) CLIMEWORKS/COVER IMAGES/AP IMAGES



The U.S. government will invest in "air capture" of carbon dioxide, a technology already in use in Iceland.

CLIMATE POLICY

U.S. infrastructure bill bolsters climate response

The $1.2 billion infrastructure bill that President Joe Biden was expected to sign into law this week contains numerous provisions to bolster climate adaptation and accelerate efforts to curb global warming. The law provides $47 billion to prepare the country for worsening fires, floods, and storms. It funds electric car charging stations and mass transit and contains $9.5 billion to develop "clean" hydrogen fuel, produced from low-carbon sources, for industrial use. An additional $3.5 billion will fund four centers to study ways of removing carbon directly from the atmosphere. Last week, the Department of Energy set a goal of making such "air capture" technologies more affordable, with a target cost of $100 per ton of carbon dioxide within 1 decade. Air capture is currently limited to small-scale tests, such as at a plant recently opened by Climeworks in Iceland.

greater than other diseases for which vaccination is now routine. Surveys by the Kaiser Family Foundation suggest about 30% of parents plan to vaccinate their children immediately.

Asian languages' origin pinpointed

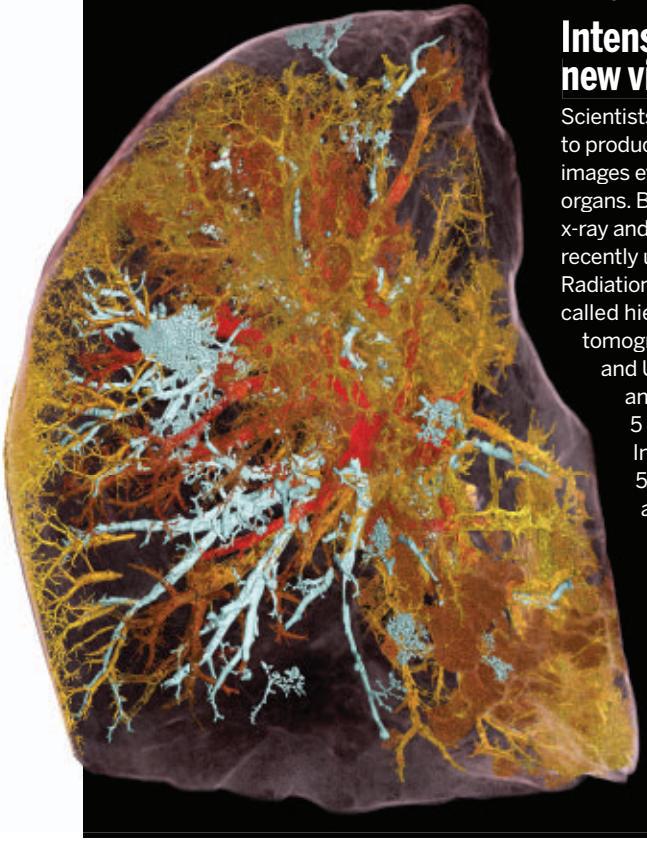
LINGUISTICS | For more than 100 years, linguists have debated when, where, and how a group of languages spoken today across central and eastern Asia, including those in the Japanese, Korean, Tungusic, Mongolic, and Turkic families, emerged. A new study combining linguistic, genetic, and archaeological data suggests these Transeurasian languages share a common origin and spread early with agriculture. Researchers compared ancient DNA from 23 individuals, stretching back to 7500 B.C.E., representing populations across Eurasia, to modern reference genomes to construct a rough family tree. The team mapped those relations onto data from hundreds of archaeological sites as well as etymological similarities in modern languages to puzzle out the evolution of these ancient people's material culture and language. Taken together, the researchers report this week in *Nature*, the evidence indicates the Transeurasian languages originated about 9000 years ago with millet farmers in the West Liao River Valley in present-day northeastern China, then spread and split apart throughout the continent.

Octogenarian earns physics Ph.D.

PHYSICS | Manfred Steiner finally has the degree he always wanted. This fall, the 89-year-old hematologist earned a doctorate in theoretical physics from Brown University. As a young man, Steiner dreamed of pursing physics, but his mother and uncle persuaded him to focus on medicine. He obtained his M.D. in 1955 and a Ph.D. in biochemistry in 1967 before serving on the medical faculty at Brown from 1968 to 1994. Steiner began taking physics courses there in 2000 and successfully defended his thesis in September, the university announced last week. The work describes how the boundary between the two broad classes of quantum particles, bosons and fermions, might be blurred depending on whether the particles are confined to 1D or 2D spaces. In 2020, only 1.2% of recipients of doctorates from U.S. institutions in the physical and earth sciences was over age 45, according to the National Science Foundation's Survey of Earned Doctorates. The median age was 29.6 years.

U.S. drops firm after bad doses

COVID-19 | Emergent BioSolutions announced last week the termination of its $600 million contract with the U.S. government under which the Maryland company would have manufactured millions of doses of a COVID-19 vaccine developed by AstraZeneca. The cancellation comes 8 months after 15 million doses of the Johnson & Johnson COVID-19 vaccine, also being made at Emergent's Baltimore plant, were contaminated with an ingredient of the AstraZeneca vaccine, and production there was temporarily halted. Since then, the company has struggled to meet U.S. Food and Drug Administration requirements for producing either vaccine. Emergent will continue to produce anthrax vaccine for the United States at its Lansing, Michigan, facility, and recently signed a contract to produce a messenger RNA COVID-19 vaccine for the Canadian company Providence Therapeutics at its Winnipeg facility.



IMAGING

Intense x-ray beams offer new views inside organs

Scientists have used an x-ray synchrotron to produce some of the most detailed images ever made of whole human organs. By combining extremely bright x-ray and more laserlike beams from the recently upgraded European Synchrotron Radiation Facility with a scanning method called hierarchical phase contrast tomography, researchers from ESRF and University College London traced anatomical details as small as 5 microns in postmortem organs. In an image of a lung from a 54-year-old (left), blue limns the airways, red traces unobstructed blood vessels, and yellow marks clogged ones. Researchers used the technique to show how COVID-19 damages blood vessels in the lung, ESRF said last week. The synchrotron's x-rays, up to 100 billion times brighter than a conventional hospital x-ray, are too intense to be used to examine living tissue.

PHOTO: PAUL TAFFOREAU

BY THE NUMBERS

78%

Share of U.S. adults who believe or are unsure of at least one of eight false COVID-19 statements tested in a survey. About one-third believe or are unsure about at least half. The false statements include that pregnant women should not get the COVID-19 vaccine and that it has been shown to cause infertility. (Kaiser Family Foundation)

18%

Share of scientific journal articles that showed evidence of plagiarism, according to a meta-analysis. Eight percent exhibited signs of "major" plagiarism, such as reusing ideas and findings. In a 2014 study combining multiple surveys, just 2% of scientists confessed to the practice. (*Scientometrics*)

SCIENCE.ORG/NEWS
Read more news from *Science* online.



A new antiviral dramatically reduced the number of people recently diagnosed with COVID-19 who needed hospitalization.

PHOTO: RORY DOYLE/*THE NEW YORK TIMES*/REDUX PICTURES

COVID-19

Antiviral pills could change pandemic's course

Strong showing for Pfizer protease inhibitor follows success for Merck's molnupiravir

By **Jennifer Couzin-Frankel**

Last week's announcement by drug behemoth Pfizer that its 5-day pill regimen powerfully curbs many early SARS-CoV-2 infections opens a new chapter in the battle against the virus. In a clinical trial that an independent monitoring group halted early because the experimental therapy appeared so effective, it slashed hospitalizations by 89% among those treated within 3 days of symptom onset. If Pfizer's drug candidate passes muster with regulators, it could join molnupiravir, a pill recently developed by Merck & Co. that received approval last week in the United Kingdom, as the first oral medications proved to stop COVID-19 from progressing to severe disease.

Such antivirals, public health experts and scientists say, could help a broad swath of people, including the unvaccinated and those who develop breakthrough infections despite vaccination. If affordable enough—a still unresolved question—the pills could also act as a crucial safety net for low-income countries that have struggled to obtain vaccines and that have more limited hospital resources.

The Pfizer antiviral is a protease inhibitor, a well-studied drug class that targets key enzymes in many viruses and that has already revolutionized the fight against HIV. "This looks like an oral medication that really works," says Oriol Mitjà, a physician-scientist who studies and treats infectious disease in Papua New Guinea and is affiliated with the Germans Trias i Pujol University Hospital.

Although neither company has provided much data publicly, Pfizer's compound appears more effective than molnupiravir, which has a different mechanism. Together, however, the two antivirals could transform the pandemic's course. Although they "can't replace vaccines," says Nahid Bhadelia, an infectious disease doctor at Boston University, they can help "our return to normalcy."

As has been typical for drug and vaccine companies throughout the pandemic, Pfizer initially made only topline clinical results available, and the work has not been peer reviewed. In a press release, the company reported that just three of 389 people, or 0.8%, who took the antiviral within 3 days of testing positive for COVID-19 were hospitalized, compared with 27 out of 385, or 7%, in the placebo group. Six out of 607 who began the antiviral within 5 days, or 1%, were hospitalized, versus 41 out of 612, or 6.7%, on a placebo. Ten patients who got the placebo subsequently died; no one on the Pfizer pill did. Side effects were mild.

All the trial participants were unvaccinated and had at least one medical condition that put them at higher risk of severe COVID-19. The antiviral is also being tested in lower risk people, including those who are vaccinated, and in uninfected people with a household member positive for the virus, to see whether it stops the former from developing COVID-19 symptoms. The company plans to seek authorization in the United States and elsewhere as soon as possible.

Affordable and easily administered COVID-19 treatments are desperately needed. Only one class of therapy for early-stage COVID-19 is authorized in the United States: monoclonal antibodies, which block surface proteins of the coronavirus and slow SARS-CoV-2 from infecting cells. But the price tag (about $2000 per dose, a cost currently paid in the United States by the federal government), scarcity, and the need to infuse or inject them have slowed their use in wealthy countries, let alone developing nations.

Molnupiravir, licensed by Merck from Ridgeback Biotherapeutics, tricks SARS-CoV-2 into incorporating the compound into its genetic information, causing mutations that stop the virus from replicating. The company announced last month that a 5-day regimen cut COVID-19 hospitalization by about 50%. Some scientists worry the drug could cause mutations in people or that, in the long term, widespread use of the drug may create harmful viral variants, but little evidence supports either concern so far. To date, the United Kingdom is green-

lighting it only for people at increased risk of severe COVID-19.

Pfizer's pill works differently, blocking an enzyme central to SARS-CoV-2's replication cycle (see graphic, below). Company scientists designed a version of the compound back in 2003 to inhibit a protease in the coronavirus that causes severe acute respiratory syndrome (SARS), a cousin of SARS-CoV-2. But then the SARS outbreak abated and Pfizer shelved the product. Last year, the company discovered the compound could stop SARS-CoV-2. An early version was tested intravenously, and Pfizer subsequently crafted an easier to deliver tablet.

The treatment also includes a decades-old generic HIV drug called ritonavir that helps stave off enzymes that break down the protease inhibitor. In the trial, patients took six pills a day, two of Pfizer's antiviral and one ritonavir in the morning, and the same regimen at night.

Having more than one oral antiviral for COVID-19 may preserve both drugs' effectiveness. Viruses often evolve resistance to individual medications. But hitting multiple molecular targets in SARS-CoV-2 should make it harder for the pathogen to escape. "Resistance is all a question of probabilities," says Celia Schiffer, a structural biologist at the University of Massachusetts Chan Medical School. When a virus is faced with two different drugs, "it's just much less probable that there would be changes that can evade both simultaneously."

Other protease inhibitors for SARS-CoV-2 are racing through clinical trials. "We need multiple approaches," says Mark Denison, a virologist at Vanderbilt University. "I don't care what your drug is, coronaviruses are capable of developing resistance to it."

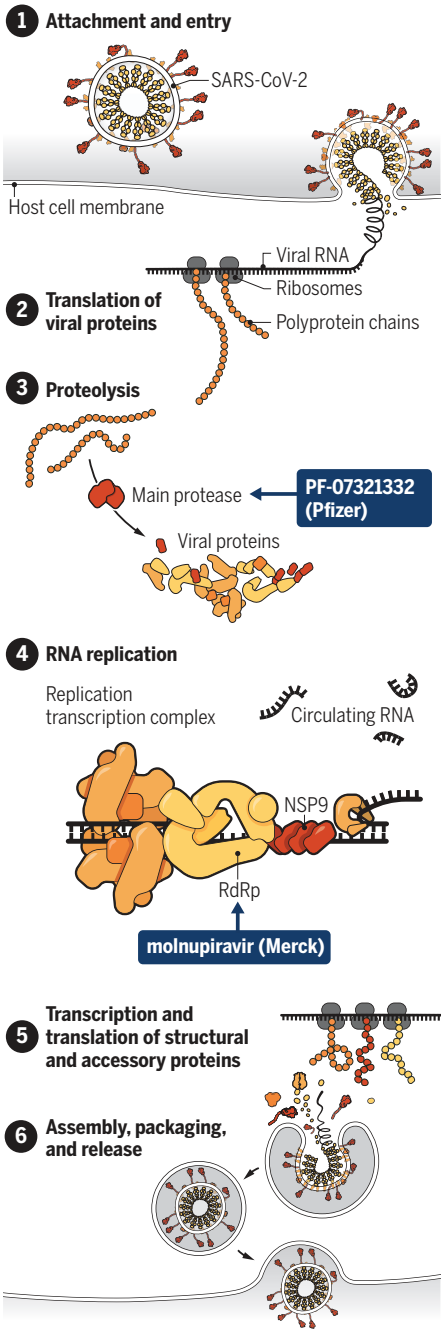
Antiviral treatment also needs to be delivered fast, notes David Ho, a virologist and longtime AIDS physician at Columbia University—within the first week or less of COVID-19 symptoms. After that, the disease often enters "an inflammatory phase, where antiviral intervention makes no difference," he points out. In parts of the United States and some other countries, SARS-CoV-2 testing remains spotty and results can take days to come, which could delay treatment.

There's concern, too, about whether oral antivirals will be accessible to low- and middle-income countries. Merck says its 5-day pill regimen will cost about $700 in the United States, and Pfizer has suggested its pricing will be similar. Both companies, however, are pledging to make their antivirals affordable for countries unable to pay that rate. Merck has granted a royalty-free license to a nonprofit organization, allowing for cheaper manufacturing and distribution, and Pfizer has said it will charge many countries a lower, not-for-profit price.

Mitjà hailed both the Merck and Pfizer results, noting that in his adopted country of Papua New Guinea, only 1% of the population is fully vaccinated against COVID-19 and the disease continues to wreak havoc. For now, he's just hoping the country can get these new antivirals to its population, at a cost it can afford. ■

Two drugs, two targets

As SARS-CoV-2 replicates, Pfizer's pill inhibits a viral protease that creates other proteins needed by the virus. Merck's compound introduces disruptive mutations when the virus copies its genome.



GRAPHIC: V. ALTOUNIAN/*SCIENCE*

COVID-19

New tool points to mutation behind Delta's infectiousness

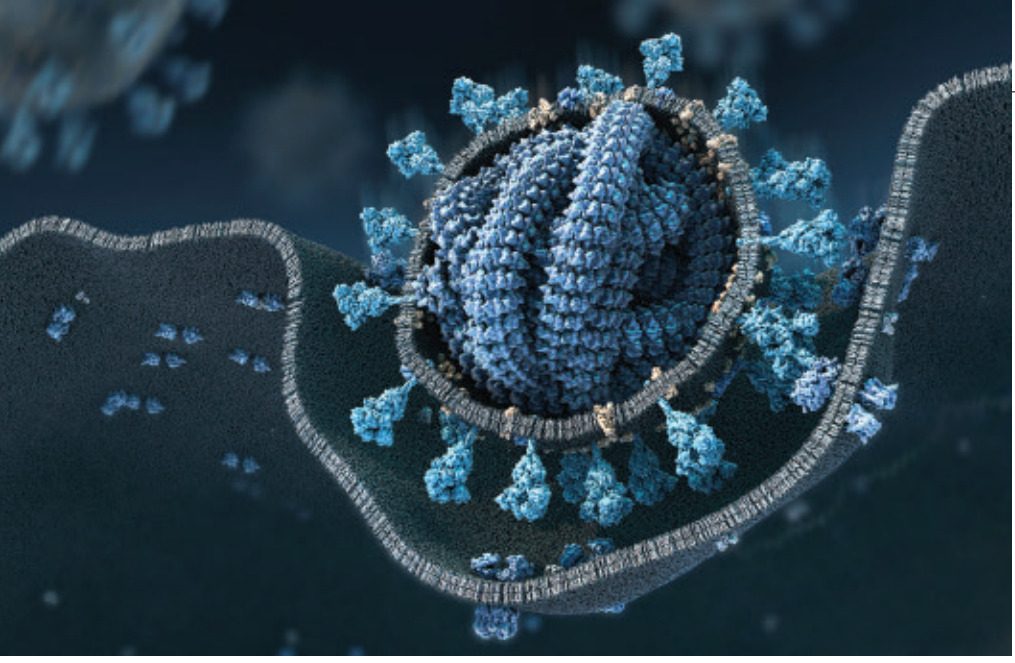
"Viruslike particles" open the way to easier study of viral mutations, proteins

By **Meredith Wadman**

As the world has learned to its cost, the Delta variant of the pandemic coronavirus is more than twice as infectious as previous strains. But just what drives Delta's ability to spread so rapidly hasn't been clear. Now, a new lab strategy that makes it possible to safely study the effects of mutations in SARS-CoV-2 variants has delivered one answer: a little-noticed mutation in Delta that allows the virus to stuff more of its genetic code into host cells, thus boosting the chances that each infected cell will spread the virus to another cell.

That discovery, published last week in *Science*, is "a big deal," says Michael Summers, a structural biologist at the University of Maryland, Baltimore County—and not just because it helps explain Delta's ravages. The new system, developed by Nobel Prize winner Jennifer Doudna of the University of California (UC), Berkeley, and colleagues, is a powerful tool for understanding SARS-CoV-2 variants and exploring how future variants might affect the pandemic, he says. "The system she has developed allows you to look at any mutation and its influence on key parts of viral replication. … That can now be studied in a much easier way by a lot more scientists."

Researchers analyzing how mutations in the coronavirus' genome affect its activity have concentrated on the spike protein, which studs the virus' surface and allows it to invade human cells. That's partly because, short of deliberately mutating the virus and testing it—research that requires high-level biosafety facilities—the best tool for probing individual mutations has been what's called a "pseudovirus," a construct made from a different virus. But those constructs can only express spike, not SARS-CoV-2's other three structural proteins.



A mutation in SARS-CoV-2's nucleocapsid protein (large coil inside virus particle) may help Delta spread.

Doudna and her team made the new tool by tweaking lab constructs called viruslike particles (VLPs), which contain all the virus' structural proteins but lack its genome. From the outside, a SARS-CoV-2 VLP looks exactly like the full-fledged virus. It can bind with cells in a laboratory and invade them. But because it is stripped of the virus' RNA genome, it can't hijack a cell's machinery to replicate and burst out of the host cell to infect more cells. "It's a one-way ticket. It doesn't spread," says Charles Rice, a molecular virologist at Rockefeller University.

Doudna and her colleagues, including co–senior author Melanie Ott, a virologist and director of the Gladstone Institute of Virology, added a new innovation to the VLP system. They inserted a snippet of messenger RNA (mRNA) that causes cells invaded by VLPs to light up. The brighter cells glow, the more mRNA the cells have received from the VLPs.

Next, the researchers tweaked the VLP proteins with mutations. One was R203M, a mutation found in Delta that alters the nucleocapsid protein (N), a molecule tucked inside the virus that plays a key role in viral replication, including packaging and releasing the virus' genetic material. R203M contains a mutational hot spot: a seven–amino acid stretch mutated in most samples of every SARS-CoV-2 variant of interest or concern. R203M is one mutation in this hot spot.

That work "revealed a surprise," Doudna says. "A single amino acid change found in Delta's nucleocapsid protein supercharged the [VLPs] with 10 times more mRNA compared with the original virus!" For VLPs carrying N mutations found in the Alpha and Gamma variants, the figures were 7.5 and 4.2, respectively.

The scientists next tested a real coronavirus engineered to include the R203M mutation, in appropriate lab biosafety conditions. After invading lung cells in the lab, the mutated virus produced 51 times more infectious virus than an original SARS-CoV-2 strain.

In people infected with the coronavirus, a very small proportion of viral particles produced by a cell actually go on to infect another cell, in part because many particles lack a complete viral genome. So mutations that make the viral genome more efficient at putting RNA inside host cells can boost the number of infectious particles produced.

"This mutation that's found in Delta … makes the virus better at making infectious particles and because of that, it spreads more quickly," says co-first author Abdullah Syed, a biomedical engineer at the Gladstone Institute of Data Science and Biotechnology.

The finding has implications for treatments, says Shan Lu, a cell biologist at UC San Diego who studies the N protein. "The field could think more about targeting the nucleocapsid protein to really help control infection and help treat patients." For instance, drugs could be targeted to any host protein found to help Delta's R203M mutation boost the delivery of mRNA to cells.

Scientists are also excited by the new VLP system, which will allow researchers without high-level biosafety labs to study how all four coronavirus structural proteins work. Jasmine Cubuk, a biochemist and biophysicist at Washington University in St. Louis, calls it "a fascinating and a very powerful tool."

Rice cautions the new VLPs are a model system that may not always mimic the real thing. Researchers will still need to work with the real virus in advanced biosafety labs. But he praises the new tool. "It really provides a wonderful system to study coronavirus assembly and also to look for drugs, for inhibitors that interfere with these processes." ■

CREDITS: (ILLUSTRATION) C. BICKEL/*SCIENCE*; (PHOTO) STR/NURPHOTO/GETTY IMAGES

CLIMATE CHANGE

New pledges could keep global warming below 2°C target

But can nations truly realize ambitious goals and provide developing countries with needed financing?

By **Cathleen O'Grady**, *in Glasgow, U.K.*

Nations meeting here at a major climate summit announced new commitments to cutting greenhouse gases that would—if realized—put the world on a path to meeting a key goal of the 2015 Paris agreement. The new pledges unveiled last week include revised commitments from India, China, and 11 other nations, and could keep warming to 1.8°C to 1.9°C this century, two new analyses find. That edges the world closer to the Paris goal of keeping warming "well below" 2°C.

But the new commitments are "not cause for unbounded optimism," cautions University of Melbourne climate scientist Malte Meinshausen, an author of one of the new analyses, released on 4 November by analytics company Climate Resource. Meinshausen worries countries won't follow through. "The world has set its course on roughly the right horizon, but there's still a lot of work to do."

The new warming estimates don't fall far below other recent projections, notes



India, which relies heavily on coal, is among nations that have made fresh pledges to cut emissions.

Zeke Hausfather, a climate scientist at the Breakthrough Institute, an environmental research center. A U.N. report released in October found pledges made to that point would keep warming to about 2°C, whereas a similar International Energy Agency (IEA) analysis projected 2.1°C. So, it's "not very surprising" that new pledges trimmed a few more tenths, Hausfather says.

Shortly before the summit, Meinshausen and his colleagues compiled the pledges that nations had submitted to the United Nations, including both near-term promises to reduce emissions by 2030 and longer term pledges to reach net zero emissions by 2050 to 2070. Some pledges depend on nations receiving financial support, whereas others are unconditional. The researchers fed the promised emissions levels into a climate simulation that generated a range of possible warming outcomes.

The presummit pledges would lead to between 1.5°C and 3.2°C of warming this century, the projections showed, with a 50% chance of staying below 2.1°C. But the new commitments offer a 50% chance of staying below 1.9°C. (The range of possible warming is 1.3°C to 2.7°C.)

In the second analysis, released on 4 November, IEA found that if all current commitments "are met in full and on time," warming could be limited to 1.8°C by 2100.

Joeri Rogelj, a climate scientist at Imperial College London, cautions that even if nations meet their pledges perfectly, there is still a 50% chance of exceeding the 2°C target. He also notes that high-level announcements made at the summit lack crucial detail. India, for example, didn't say whether its commitment to net zero emissions by 2070 applies only to carbon dioxide or to all greenhouse gases.

There's a risk that politicians will use the new projections to justify inaction, Rogelj says. For example, many nations, such as Australia, are still expanding their use of fossil fuels while declaring ambitious climate goals. "There is very low confidence, with the evidence that we have, that those pledges will be implemented," Rogelj says.

Meinshausen adds that developing countries will need financial help from wealthy nations to realize their pledges. "It's not only whether we believe [the pledges]," he says, "but also a question of support."

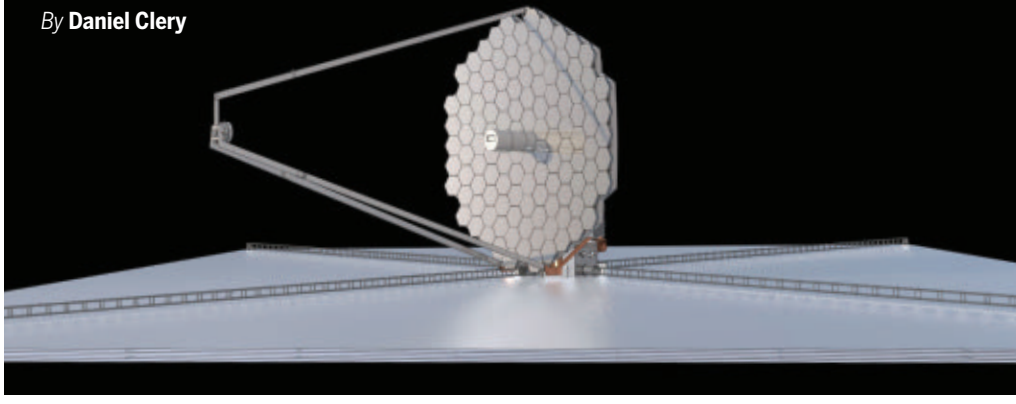
Keeping planetary warming below 1.5°C by the end of the century, the stretch goal of the Paris pact, is now unlikely, analysts say. Still, "We are in a different place now compared to at the end of the Paris agreement," says Corinne Le Quéré, a climate scientist at the University of East Anglia. "No country is going fast enough, but many countries are moving forward." ■

ASTRONOMY

Influential U.S. wish list calls for $11 billion space telescope

Decadal survey says NASA should be frugal and build a series of optical, x-ray, and far-infrared observatories

By **Daniel Clery**



A decadal survey found the 15-meter LUVOIR to be far too pricey; it called for a more modest 6-meter scope.

In 2000, the U.S. astronomy "decadal survey"—a prioritized wish list that guides Congress and funding agencies—said its top priority was the giant, infrared James Webb Space Telescope. Two decades later, astronomers have again put a giant space telescope at the top of their 10-year list. But this time, they hope it will be the first in a series of space observatories working across different wavelengths, from x-rays to the far infrared—"a fleet, not just the flagship," says John O'Meara, chief scientist of the W. M. Keck Observatory.

The Webb telescope, which should finally launch next month (see p. 806), ended up wildly delayed and overbudget, with a cost that has reached $10 billion. It is sometimes called the "telescope that ate astronomy." In the latest survey, released last week, a panel of astronomers kept ambitions for their next great telescope in check. No bigger or costlier than Webb, but sensitive to optical wavelengths so it can search for life on nearby Earth-like exoplanets, it is meant to allow room for other orbiting observatories, reminiscent of the complementary Hubble, Spitzer, Chandra, and Compton space telescopes in the 1990s and 2000s. "It's a rational, balanced plan," says astronomer Wendy Freedman of the University of Chicago.

The survey ranks ground-based facilities with an equally pragmatic eye. It recommends the National Science Foundation (NSF) buy a stake in two enormous optical telescopes that are already in development—the Giant Magellan Telescope (GMT) and the Thirty Meter Telescope (TMT). "It's hard to imagine the scientific community not having access to large telescopes in the coming decades," says survey co-chair Fiona Harrison of the California Institute of Technology.

The report also calls for boosting NSF's grant program, supporting early-career scientists, and providing a bigger budget for operating existing facilities. And it chides universities and funding agencies over their records on diversity and openness to underrepresented groups (see sidebar, p. 803). "There's a lot of talent that is untapped and people who don't feel they have a place in astronomy," O'Meara says. "The committee has charged us with change."

To produce the report, Harrison and co-chair Robert Kennicutt of the University of Arizona led a 20-person steering committee that weighed recommendations from 140 other astronomers in 13 subpanels. Other input came from hundreds of submitted white papers and numerous town hall meetings. The strictures of the COVID-19 pandemic meant almost all deliberations were done virtually, which added a year to the process.

NASA had commissioned studies of four potential cornerstone missions in advance, to give the committee a better sense of their capabilities and costs (*Science*, 14 December 2018, p. 1230). These included a large general purpose optical observatory with a mirror up to 15 meters across, a smaller optical tele-

ILLUSTRATION: C. BICKEL/*SCIENCE*

scope focusing on habitable exoplanets, and observatories sensitive to x-rays and far-infrared light. The survey committee, however, found the missions would be more expensive and take longer than NASA estimated. Even a smaller variant of the large optical telescope known as LUVOIR-B, with an 8-meter mirror, would cost $17 billion and take 20 years to develop. NASA's version of LUVOIR "would have saturated the budget for several decades," Harrison says. "We wouldn't be able to develop the others, and the science really requires multiple wavelength ranges."

The panel found that with just a 6-meter mirror, a telescope like LUVOIR could achieve its most pressing task: figuring out whether a sample of Earth-like planets harbor life. "If you don't find any life you want a robust enough sample to say, yes, life is really rare," Harrison says. The downsizing would keep the cost to $11 billion and allow NASA to develop later x-ray and far-infrared flagships. They too would be scaled down, to about $4 billion each from NASA proposals that were twice as expensive. The teams behind those proposals are disappointed, but can see the logic. "Resources are limited, but this is suggesting a way forward," says Feryal Özel of the University of Arizona, one of the leaders of Lynx, the proposed x-ray observatory.

The committee also recommended that NASA begin a one-per-decade series of medium-size astrophysics missions—telescopes with more targeted goals and smaller suites of instruments. With budgets of $1.5 billion each, these would sit between flagships and the small Explorer mission line of up to $350 million. "You can do powerful things at that scale," Harrison says. And regular missions will allow NASA "to keep the science going while developing the large things."

Astronomy's next big things

The latest U.S. astronomy decadal survey sets priorities for NASA, the National Science Foundation (NSF), and the Department of Energy (DOE).

SPACE-BASED PRIORITIES	
"Great observatories" program	$1.2 billion to mature tech for a series of large missions at different wavelengths
Large optical telescope	First up, in the 2040s: an $11 billion, 6-meter telescope to seek Earth analogs
Probe missions	A series of midsize $1.5 billion missions to maintain scientific diversity

GROUND-BASED PRIORITIES	
U.S. extremely large telescopes	$1.7 billion NSF share of $5.1 billion Giant Magellan and Thirty Meter telescope projects
Stage 4 Cosmic Microwave Background Observatory	$273 million NSF share and $387 million DOE share of telescopes in Chile and Antarctica
Next Generation Very Large Array	$2.5 billion NSF share of $3.2 billion array of 263 radio telescopes spanning North America

The decision to support the ground-based giants, the GMT and the TMT, came after the two projects failed to raise enough money from international partners and private sources to continue to completion (*Science*, 3 September, p. 1066). In 2018, the longtime rivals made a joint pitch to the decadal review, arguing that the two scopes—one in Chile and one in Hawaii—would give U.S. astronomers a view of the entire sky. Europe's Extremely Large Telescope, in contrast, is further along than the U.S.-led projects, but is a single instrument in Chile. The report says NSF should assess the viability of the two projects until 2023 before deciding whether to contribute $1.7 billion to their $5.1 billion combined budgets, buying at least 25% of observing time on the two scopes.

The biggest potential show stopper, Harrison says, is the unresolved issue of where to build the TMT. The start of construction at the project's first choice site, Mauna Kea in Hawaii, has been blocked for 7 years by groups including Native Hawaiians who consider the mountain sacred. Federal support might help break the impasse by bringing another independent assessment of environmental and cultural impacts of building on Mauna Kea. "NSF involvement will allow for a pause and reset of the discussion," says Tyler Trent, a physics graduate student at the University of Arizona and a Native Hawaiian who supports the project.

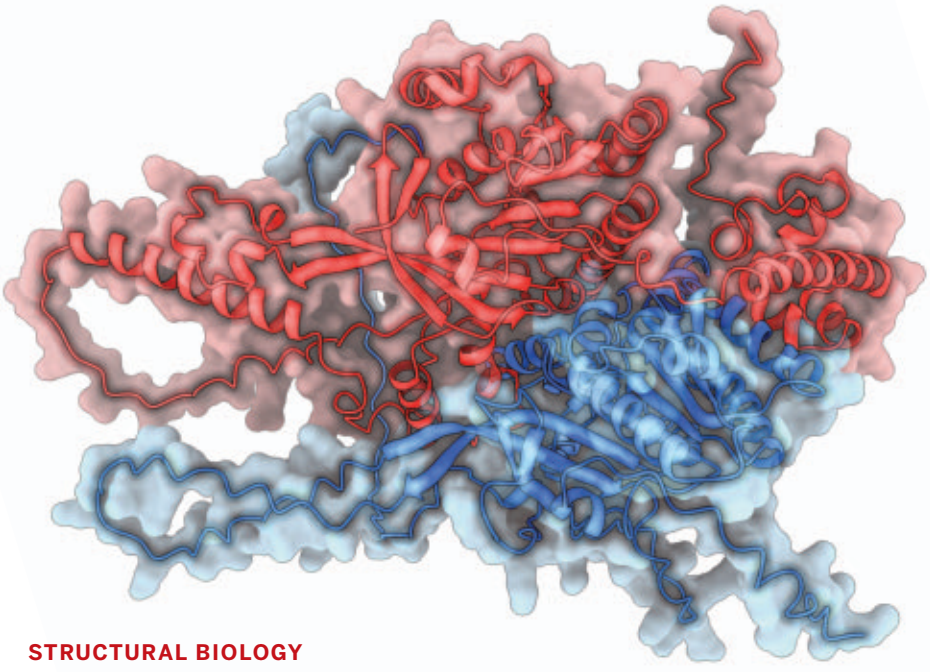
In an unusual step for a report that largely asks for new things and more money, the survey says one NASA mission—an infrared telescope that rides in the bay of a jumbo jet—should end by 2023, consistent with agency plans that have been repeatedly thwarted by Congress. The Stratospheric Observatory for Infrared Astronomy (SOFIA) costs $85 million per year to operate, nearly as much as Hubble. But the survey noted its "modest scientific productivity." Its director, Margaret Meixner, is surprised and says the survey based its conclusion on old data. In recent years, she says, SOFIA has been "really transformed." Others are not convinced. "I'm delighted to see an ending of support for SOFIA," says Garth Illingworth of the University of California, Santa Cruz. Continuing to fund it, "doesn't send a good message." ■

Astronomy turns its sights on itself

The word "underrepresentation" doesn't begin to describe the lack of Black, Latino, and Native American people in astrophysics, says Fiona Harrison, co-chair of U.S. astronomers' latest decadal survey, a 10-year priority-setting exercise (see main story, p. 802). At a total of 4%, "their representation is really nonexistent." In response, Harrison and the steering committee created a panel, the first for a decadal survey, on "the state of the profession and societal impacts." The survey also breaks new ground in telling universities, federal contractors, and funding agencies exactly what they need to do to boost diversity. At the top of the list:

- Collect and disseminate demographic data on who applies for and receives federal grants. Harrison says, "We had a tremendously difficult time" obtaining that information from the National Science Foundation, NASA, and the Department of Energy.
- Expand funding for "bridge" programs that provide additional support for graduate students and that often partner predominantly white and minority-serving institutions.
- Promote people from underrepresented groups who are already in the profession. "The representation of women at the entry level is actually quite good," Harrison says, "but it falls off" as you climb the ranks.
- Improve how undergraduates are taught and mentored to reduce attrition. Students of color interested in majoring in astronomy or physics are three times less likely to earn a degree than their white counterparts.
- Treat harassment and discrimination as forms of scientific misconduct. "This is one of the biggest steps we can take" to reduce the current hostile environment, says co-chair Robert Kennicutt.
- Reward faculty who have a track record of increasing diversity through such mechanisms as additional administrative support and early-career awards.

–Jeffrey Mervis



These two proteins form a complex involved in DNA repair in yeast; artificial intelligence software predicted both proteins' structures.

STRUCTURAL BIOLOGY

AI reveals structures of protein complexes

Software extends protein mapping to complexes that govern the breadth of cell biology

By **Robert F. Service**

The artificial intelligence (AI) revolution in protein structure prediction continues. Only 1 year ago, software programs first succeeded in modeling the 3D shapes of individual proteins as accurately as decades-old experimental techniques can determine them. This summer, researchers used those AI programs to assemble a near-complete catalog of human protein structures. Now, researchers have upped the ante once again, unveiling a combination of programs that can determine which proteins are likely to interact with one another and what the resulting complexes—crucial engines of the cell—look like.

"It's a really cool result," says Michael Snyder, a systems biologist at Stanford University. "Everything in biology works in complexes. So, knowing who works with who is critical." Those relationships were hard to reach with previous techniques. The new ability to predict them, he says, should yield an array of insights into cell biology and possibly reveal new targets for the next generation of therapeutic drugs.

Mapping proteins' shapes down to the atomic scale has until recently required costly and slow experimental techniques, such as x-ray crystallography and nuclear magnetic resonance spectroscopy. Those experimental techniques, if they work at all, typically only produce individual protein structures.

Computer modeling experts have worked for decades to speed things up. Their recent success has depended on deep learning algorithms, which use databases of experimentally solved protein structures to train software programs how to predict structures for proteins based on their amino acid sequences.

Last year, two groups, one from a U.K. company called DeepMind and the other led by David Baker at the University of Washington, Seattle, created rival AI programs that both now churn out predicted protein structures by the thousands (*Science*, 30 July, p. 478). The software also produced structures for a handful of known protein complexes, mostly in bacteria (*Science*, 16 July, p. 262). But in eukaryotes—organisms from yeast to people—the interacting partners are often unknown. Identifying them and predicting how they come together in a complex was too high a bar for the original programs.

Now, both research groups have tweaked their programs so they can solve structures of protein complexes by the hundreds. Online this week in *Science*, Baker and his colleagues use a combination of AI techniques to solve the structures of 712 complexes in eukaryotes.

To find proteins that may form complexes together, the team began by comparing the amino acid sequence of all 6000 yeast proteins to those from 2026 other fungi and 4325 other eukaryotes. The comparisons allowed the researchers to track how those proteins changed over the course of evolution and identify sequences that appeared to change in tandem in different proteins. The researchers reasoned that those proteins might form complexes, and that they changed in step to maintain their interactions. Then the team used its AI program, called RoseTTAFold, along with DeepMind's AlphaFold, which is publicly available, to attempt to solve the 3D structures of each set of candidates. Out of 8.3 million identified coevolving yeast protein pairs, the AI programs identified 1506 proteins that were likely to interact and successfully mapped the 3D structures of 712, or about half.

"These interactions span all processes of eukaryotic cells," says team member Qian Cong, a biomedical informatics expert at the University of Texas Southwestern Medical Center. Among the highlights, Cong and Baker say, are structures for protein complexes that allow cells to repair damage to their DNA, translate RNA into proteins in ribosomes, pull chromosomes apart during cell reproduction, and ferry molecules through the cell membrane.

"It's a great example of the promise" of 3D structures, says DeepMind's John Jumper, one of AlphaFold's lead developers. By revealing precisely how proteins interact with one another, the models should help biologists visualize how previously unknown complexes carry out a multitude of jobs within the cell.

"These models give hypotheses for experimentalists to test," Cong says. And because disrupting these interactions could offer new ways to intervene in a wide variety of diseases, she adds, "it also gives you a lot of potential new drug targets."

More are likely on the way. Last month, Jumper and his colleagues posted a preprint on the bioRxiv server describing a new version of their AI, dubbed AlphaFold-Multimer, which mapped structures of 4433 protein complexes. Analyses within the AI program that gauge the confidence level of each fold suggest the structures were accurate up to 69% of the time. The bottom line, Baker says: "It's really an exciting time for structural biology." ■

ILLUSTRATION: V. ALTOUNIAN/*SCIENCE*

PARTICLE PHYSICS

Is the end in sight for famous dark matter claim?

Data cast more doubt on DAMA result as an alternative explanation emerges

By **Adrian Cho**

The drama of the world's most controversial dark matter claim may have reached its last act, if not its final scene. For 2 decades, physicists with an experiment called DAMA have claimed that particles of dark matter—the unseen stuff whose gravity appears to bind our galaxy—are bumping into atomic nuclei in their subterranean particle detector, even as other dark matter hunts come up empty. Now, physicists with a detector called COSINE-100, designed to mimic DAMA, present the most direct refutation yet of the findings. And in 2020, theorists identified a way in which the DAMA signal could have arisen inadvertently in the team's analysis.

The DAMA team rejects both claims. Rita Bernabei, a physicist at the University of Rome Tor Vergata and DAMA's leader, declined to be interviewed. But she dismissed the new explanation in an email: "We have already demonstrated that the assumptions there reported are untenable and the conclusions are worthless."

The Milky Way is thought to whirl within a vast cloud of dark matter, which could consist of hypothetical weakly interacting massive particles (WIMPs). As the Solar System orbits the galactic center at 225 kilometers per second, Earth presumably plows into a wind of WIMPs. Because our planet also orbits the Sun at 30 kilometers per second, the wind should strengthen slightly when Earth is moving in the same direction as the Sun, in June, and abate when it's moving the opposite way, in December.

DAMA physicists have long claimed to see this yearly cycle in their detector, which now contains 25 10-kilogram crystals of thallium-doped sodium iodide. Each crystal produces a flash of light when a particle pings a nucleus. The DAMA team says that, in a low-energy range that corresponds to WIMPs, the number of collisions has gone up and down each year since observations began in 1995 (*Science*, 3 March 2000, p. 1570).

Other detectors see no such thing. But those experiments use different target materials. So groups have built sodium iodide detectors that can test the DAMA result in an apples-to-apples comparison. One is COSINE, which comprises eight crystals totaling 100 kilograms and has been taking data since 2016 in South Korea's subterranean Yangyang Laboratory. Since 2018, COSINE has improved its sensitivity 100-fold, says Hyun Su Lee, the team's co-spokesperson and a particle physicist at South Korea's Institute for Basic Science. But in 1.7 years of data, they see no sign of WIMPs, the researchers report this week in *Science Advances*.



Dark matter particles should generate flashes of light in the COSINE experiment's sodium iodide crystals. It aims to test a similar experiment's dark matter claim.

There's a caveat. The new COSINE analysis does not look for the annual cycle in the event rate, but simply for an excess number of low-energy events. That tiny signal would appear on top of a much larger background of events caused by ordinary particle radiation from sources both inside and outside the crystals. So the analysis depends on researchers' ability to model the subtle details of those backgrounds, Bernabei notes.

COSINE is not the only experiment testing the DAMA result, however. The ANAIS-112 detector contains nine sodium iodide crystals with a total mass of 112 kilograms and has been taking data in Spain's Canfranc Underground Laboratory since 2017. Three years of data show no annual cycle in low-energy events, ANAIS researchers reported on 27 May in *Physical Review D*. However, the uncertainties were slightly too high to rule out the DAMA signal, says María Luisa Sarsa, a physicist at the University of Zaragoza and ANAIS co-leader.

If the DAMA signal isn't real, "The field of particle physics owes itself to find out what DAMA is seeing," says Reina Maruyama, a nuclear particle physicist at Yale University and co-spokesperson for COSINE. And last year, Dario Buttazzo, a theorist at the Pisa section of Italy's National Institute of Nuclear Physics, and colleagues identified a way in which the DAMA team might have inadvertently created the annual cycle.

DAMA researchers collect data in year-long runs. To make the variation in each run stand out, they subtract the average rate over the year from the event rate measured each day. But if the event rate steadily rises or falls year after year, the subtraction can turn a steady trend into an oscillation, Buttazzo says. For example, if the rate were increasing by 1% every year, DAMA's method would produce a signal that begins each run at −0.5% and ends each run at +0.5%.

"If you do the analysis like DAMA was doing it, and if the background has a particular feature, then you could have such an effect," says Buttazzo, whose group reported its analysis in the *Journal of High Energy Physics* on 21 April 2020. But he cautions that because DAMA hasn't published its data, "we cannot know if this effect is actually there or not."

Still, the COSINE and ANAIS papers suggest the issue could be important. The ANAIS detector's total event rate is decreasing steadily as short-lived radioactive nuclei in the crystals decay away, says María Lucía Martínez Pérez, a physicist at the University of Zaragoza and co-leader of the team. COSINE sees a similar steady decline, Lee says.

Closure could come soon. In weeks, COSINE will release a 3-year annual cycle analysis, Lee says. ANAIS's Sarsa says that by next summer, "We expect to have a high-impact publication with the average rate measured over the year with all 5 years of data." That may be enough data, she says, to bring the curtain down on the DAMA claim. ■

PHOTO: CHANG HYON HA



PACKED WITH PURPOSE
After a sea journey to its launch site in French Guiana, the James Webb Space Telescope was extracted from its shipping container in October. It will remain folded when placed inside the fairing of an Ariane 5 rocket.



FIRST LIGHT MACHINE

At long last, the James Webb Space Telescope is set to launch. It will capture cosmic dawn and bring alien worlds into view *By* **Daniel Clery**

The telescope Galileo Galilei first pointed at the heavens in 1609 had a lens no wider than a slice of cucumber. Yet with that modest tool, he saw the rings of Saturn, the moons of Jupiter—and sparked a scientific revolution that toppled Earth as the center of the cosmos. Astronomy has come a long way since then. But when the James Webb Space Telescope launches in December, with a 6.5-meter mirror that would tower over Galileo himself, it will open views of the universe's first stars and galaxies, probe the atmospheres of planets around other stars—and launch another revolution. "James Webb will blow the lid off everything," says exoplanet hunter Sasha Hinkley of the University of Exeter.

Webb's mirror has more than five times the light-gathering power of the 31-year-old Hubble Space Telescope. Unlike Hubble, Webb will work in the infrared, allowing it to see the heavily "redshifted" light of distant objects and peer through clouds of obscuring dust. It will also be able to sift exoplanet atmospheres for gases whose infrared fingerprints are mostly off-limits to ground-based observatories. "We've never looked at the universe at these wavelengths and these depths and resolution," says Steve Finkelstein of the University of Texas, Austin, who will lead several projects looking at distant galaxies in Webb's first year. "I think we'll be in for some surprises."

More than 1000 teams of astronomers from across the globe applied for time on Webb in its first year, and 286 got lucky. They will task the telescope with a range of inquiries: looking for ice-covered oceans on Uranus's 27 moons, searching for elusive medium-size black holes, and resolving conflicting measurements of the expansion rate of the universe. But broadly speaking, they will use Webb to pursue two overriding themes, at opposite extremes of time and distance: the early universe and nearby planetary systems.

Researchers want to glimpse the universe's gargantuan first stars and study how messy clumps of them evolved into orderly, spiral galaxies. They want to witness the evolution of the giant black holes at the centers of many galaxies and chart their role in clearing a fog of neutral hydrogen gas that filled the early universe. In the nearby universe, Webb is expected to transform our knowledge of how gas and dust around young stars coalesce into planets, what conditions on those worlds are like, and whether they provide a welcoming habitat for life.

It is a dream telescope, and one that has been many years—and $10 billion—in the making. Early on, Webb was expected to launch in 2011 for less than $2 billion. But the complexity of new technologies such as the segmented mirror and the cryocoolers that keep instruments cold enough to see far-infrared wavelengths led to delays and

Just 40 light-years away, the seven known planets of the TRAPPIST-1 system (artist's concept) are Earth-size. The James Webb Space Telescope will probe the composition of their atmospheres.

IMAGES: NASA/JPL-CALTECH; (OPPOSITE PAGE) NASA/CHRIS GUNN

inflated costs. After Congress threatened to cancel the project in 2011, NASA set a new schedule and, for a while, kept to it. But more delays came when prime contractor Northrop Grumman discovered faulty welds, incorrect lubricants, missing bolts, and tears in the telescope's giant sunshield.

Now, all that is fixed, but one last hurdle remains. In September, engineers in California packed Webb up in an environmentally controlled shipping container and sent it by sea to French Guiana, home to Europe's spaceport. On 18 December, Webb will endure the roar and rattle of a 27-minute ride to orbit on a European Ariane 5 rocket, its folded-up mirror just barely fitting inside the fairing.

A month of critical maneuvers will follow as the telescope cruises deeper into space. "It's 30 days of terror," says Garth Illingworth of the University of California, Santa Cruz (UCSC), who was one of the project's early architects. As soon as it's in space, Webb will deploy its solar array and then, 2 hours later, its communications antenna. On day 3, as it passes the Moon, its huge sunshield will begin to unfurl. By day 11, the mirrors will start to unfold and swing into place. Finally, after 29 days, Webb's boosters will make a final burn to put it in orbit around L2, a gravitational balance point 1.5 million kilometers from Earth. Unlike Hubble, Webb will be too far away to be repaired by visiting astronauts. It must work flawlessly straight out of the box.

PLANNING FOR Webb began as far back as 1989, before Hubble had even left the ground. It was originally nicknamed the First Light Machine, recalls Marcia Rieke, an astronomer at the University of Arizona who served on the project's working group in the late 1990s. The goal was to peer back to the universe's infancy.

Ground-based telescopes at the time could barely see halfway back across the 13.8-billion-year history of the universe. Hubble, with no atmosphere to blur its view, could take astronomers much closer to the beginning. In its first "deep-field" exposure, in 1995, it stared at a seemingly empty patch of sky in Ursa Major for 140 hours. Almost every one of the 3000 objects that popped into view was a distant galaxy, shining from times as early as 1.5 billion years after the big bang.

Subsequent exposures went even deeper in time. Astronomers assumed the number of galaxies would fall off sharply at those early times because gravity had not yet pulled clouds of gas into stars, let alone assembled stars into galaxies. But Hubble showed the galaxies were there, albeit in dwindling numbers. In 2016, researchers using Hubble data found a small galaxy, dubbed GN-z11, that dated, astonishingly, from a time when the universe was just 400 million years old. "We had no idea you could see objects at that time," Illingworth says.

At that distance, the expansion of the universe shifts a galaxy's visible light—where stars tend to shine brightest—well into the infrared, which Hubble cannot see. GN-z11 was only visible because it shone brightly in ultraviolet light, seen as visible light after redshifting. Many more early galaxies, invisible to Hubble, may lurk in the infrared band. "It's hard to be sure," Rieke says.

Webb should be able to tell, thanks to its huge mirror and infrared detectors, which are insulated from heat that would degrade their sensitivity. The multilayer fabric sunshield, as big as a tennis court, will create a shadow deep enough to passively chill three of Webb's instruments to −234°C, or 39 K. The cryocooler will refrigerate a fourth instrument, meant to peer further into the infrared, to 7 K.

"We will see the first chemical fingerprints from Earth-sized planets."

Natalie Batalha, University of California, Santa Cruz

Roberto Maiolino, an astronomer at the University of Cambridge, expects Webb to find 10,000 galaxies between cosmic dawn—when the first stars ignited about 200 million years after the big bang—and cosmic noon, the peak of star formation roughly 2 billion years later. The first galaxies probably started out small and disorganized, nucleating around clumps of dark matter, unseen stuff that makes up 85% of the matter of the universe. By compiling a census of early galaxies, Webb will show "how these blobs change to more organized structures," says Rieke, who led the development of Webb's near-infrared camera.

Mapping out how protogalaxies formed might also reveal something about the nature of dark matter, Rieke says. "Finding the first aggregations of stars may tell us more about what was leftover after the big bang," she says. There are other fundamental questions: Did the galaxies grow simply by pulling in more gas, or through a series of mergers, known to spark bursts of star formation in more recent galaxies? "There is so much low-hanging fruit, so many obvious questions … but we didn't have the technical ability to answer them yet," Finkelstein says.

A MAJOR COUP for Webb would be spotting evidence for first-generation stars, known as population III stars, formed from the primordial hydrogen and helium gas leftover from the big bang. Later generations of stars contain heavier elements, forged in stellar furnaces and scattered by supernovae, that radiate energy efficiently. Lacking these radiators, population III stars swell to enormous sizes, and are possibly up to 1000 times as massive as the Sun. Their size means they burn fast and furiously, exhausting their fuel in a few million years.

Webb will almost certainly not be able to see to these stars individually, but a galaxy's spectrum can betray their presence. "If we see a galaxy with a spectrum of only hydrogen and helium, that would be a smoking gun" of population III stars, Maiolino says. The spectrum would also hold clues to the stars' abundance and temperatures, giving astronomers a picture of early star formation and how these fast-burning giants, after exploding in supernovae, delivered the first smattering of heavy elements to the universe.

Those discoveries could also bear on the mystery of what ionized the hydrogen gas that fills the universe, making it transparent to light. Roughly 400,000 years after the big bang, the universe had cooled enough for protons to hook up with electrons. The resulting neutral hydrogen acted as a cosmic fog, absorbing high energy photons. But half a billion years later, the fog began to clear as something split the hydrogen apart again. This "Epoch of Reionization" continued for another half-billion years until all the hydrogen was ionized.

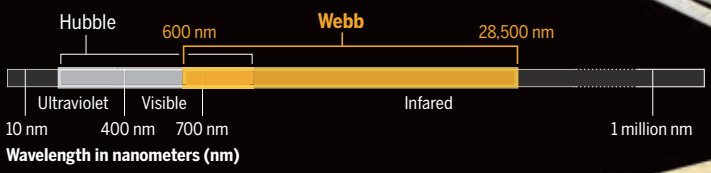
Ultraviolet light from big and hot population III stars is an obvious ionizing source. But were there enough stars to ionize all of space? The small number of early galaxies discovered by Hubble would suggest not, but Webb's more complete census may cement the role of starlight. If not, there is another possibility: the supermassive black holes at the heart of most galaxies. As material sucked into a black hole swirls down the cosmic drain, friction heats it to such enormous temperatures that it shines as a brilliant beacon: a quasar or active galactic nucleus (AGN).

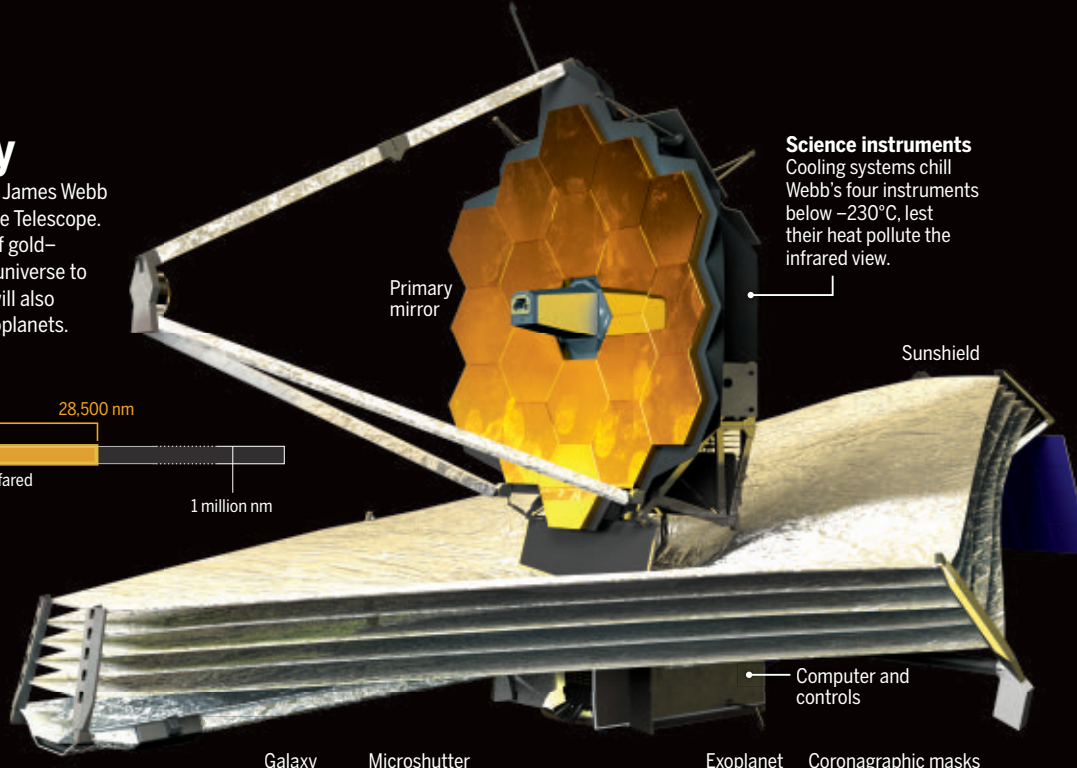
Astronomers have found quasars less than 700 million years after the big bang, but many think they are too few and far between to evenly ionize all of space. Others are more hopeful. The quasars spotted so far are huge, with masses equivalent to 1 billion Suns, which means many smaller ones remain to be discovered, Finkelstein says. "There are probably a lot of 100-million-solar-mass black holes and even more 10-million-solar-mass black holes," he says.

A golden opportunity

On 18 December, NASA will launch the $10 billion James Webb Space Telescope, a successor to the Hubble Space Telescope. The segmented mirror—coated with a thin layer of gold—will work in the infrared, looking back across the universe to gather the light of the first stars and galaxies. It will also bring into view the atmospheres of Earth-size exoplanets.

Graphic by Chris Bickel

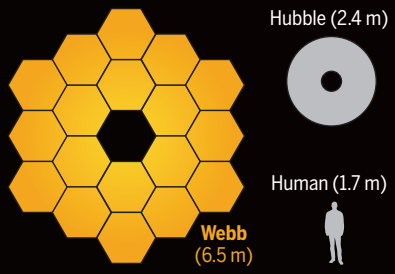




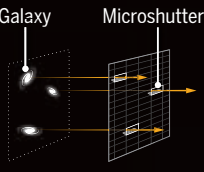
Science instruments
Cooling systems chill Webb's four instruments below −230°C, lest their heat pollute the infrared view.

Honeycomb eye

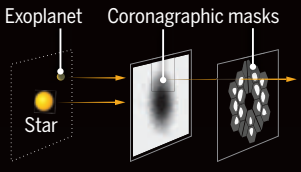
Webb has more than five times the light-gathering power of Hubble.



Multitasking
An array of nearly 250,000 microshutters allows one instrument to analyze light from hundreds of galaxies at once.



Mask mandate
To gather the light of a planet and image it directly, Webb will mask the glare of the star.

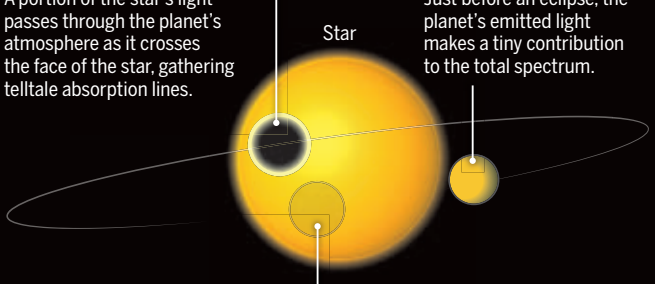


Lighting up a planet

Only a few big, hot exoplanets can be imaged directly. But astronomers can still probe a planet's atmosphere by performing transit spectroscopy, or by comparing light when the star eclipses the planet with light gathered just before.

Transit
A portion of the star's light passes through the planet's atmosphere as it crosses the face of the star, gathering telltale absorption lines.

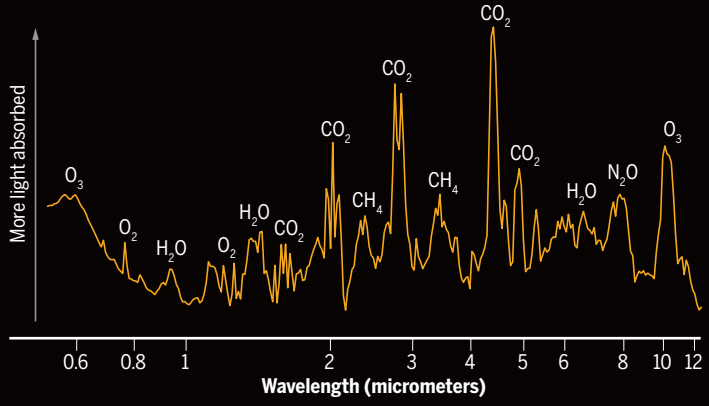
Full face
Just before an eclipse, the planet's emitted light makes a tiny contribution to the total spectrum.



Eclipse
Subtracting an eclipse spectrum from a "full-face" spectrum leaves just the planet's.

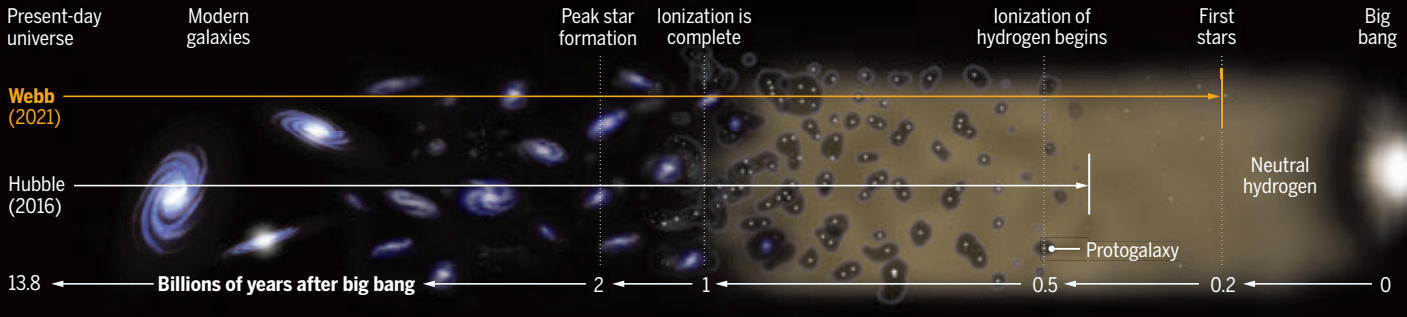
Signs of life

If TRAPPIST-1e, an Earth-size exoplanet 40 light-years away, had an atmosphere like Earth's, its transit spectrum would look like the synthetic one below. Biosignatures like oxygen and ozone are at the edge of detectability. Webb is more likely to sense carbon dioxide and methane, which can have both living and nonliving sources.



Peering into the past

Webb will reach farther out in space and further back in time than Hubble or ground-based telescopes. It could show how galaxies evolved from ungainly clumps to the elegant spirals and ellipses seen today. It should also reveal whether starlight was sufficient to ionize the hydrogen gas that filled the universe, or whether black holes assisted.



DATA: RYAN MACDONALD/CORNELL UNIVERSITY; NASA

"You just have to have the right tools to find them."

If Webb does find the early universe swarming with black holes, astronomers will be forced to reckon with their speedy assembly. Did giant population III stars collapse into black holes, providing "seeds" that merged into supermassive ones? Or did black holes form directly from collapsing clouds of gas after the big bang? "It's hotly debated," Maiolino says.

Besides probing the hectic birth of stars, galaxies, and black holes, Webb will study why the frenzy died down. "Forming stars and galaxies is a party that is over," says Jane Rigby of NASA's Goddard Space Flight Center, who is Webb's project scientist for operations. Astronomers believe some process—supernovae explosions, blasts from AGNs, or stellar winds produced by giant stars—could have blown clouds of gas out of galaxies, starving star formation of its fuel.

One of Webb's four instruments, the Near Infrared Spectrograph (NIRSpec), should be able to see these outflows and trace them to their source. The NIRSpec has an innovative mask with nearly 250,000 slitlike microshutters, each about the width of a human hair, that operators can open to let light through at specific locations. By analyzing light from each slit separately, the NIRSpec can dissect the spectrum of light from multiple points on the sky. It could, for instance, measure redshifts and calculate distances for 100 different distant galaxies, all at once. But it can also focus in on multiple slices of a single galaxy, such as one undergoing a slowdown in star formation. "It will get gorgeous spectra of each distinct region of a galaxy," Rigby says, allowing observers to identify gas clouds and assess their temperatures and movement—along with what seems to be blowing them out. "We've never had that power before," Rigby says.

AFTER 10 YEARS of concept studies and false starts, in 1999 NASA formally greenlighted what was then called the Next Generation Space Telescope. But by then, a new goal had emerged: understanding exoplanets, first discovered in the 1990s.

In the early years, exoplanet discoveries were few—"stamp collecting," says Natalie Batalha of UCSC. But NASA's Kepler mission, launched in 2009, stared at a patch of sky for years on end, continually monitoring 150,000 stars for the telltale dips in brightness that betray the passage, or transit, of an orbiting planet across the star's face. Kepler found thousands of planets, showing exoplanets were not a galactic rarity, but the norm.

Webb isn't aiming to discover lots of new planets; its time is too precious to sit and wait for brightness dips to occur. What it will do is get to know exoplanets better—first by witnessing their formation, something that researchers had previously only theorized about. The Atacama Large Millimeter/submillimeter Array (ALMA), a set of radio telescopes in Chile, has in recent years zoomed in on protoplanetary disks, the swirls of dust and gas around young stars that coalesce into planets. ALMA's images show clear gaps in the disks, suggesting protoplanets are vacuuming up material as they orbit. But ALMA can only see the faint radio emissions from cold dust and gas in the outer parts of the disks—not the planets themselves.

At shorter infrared wavelengths, Webb will see newborn planets, which glow in the infrared. It will be able to dissect the chemical makeup of the planet-forming material and how it varies across the disk. "It's important to know the environment in which the planet is formed," says Isabelle Baraffe, a theorist at Exeter. "It helps to constrain the models."

Webb will also dive into planetary atmospheres. Astronomers using Hubble and an infrared telescope far smaller than Webb, the Spitzer Space Telescope, pioneered the key technique, called transit spectroscopy. During a transit, the planet's atmosphere absorbs a small amount of the starlight, resulting in tiny changes in the star's spectrum. By watching transits, Hubble sensed water vapor in a few exoplanet atmospheres, and Spitzer found methane and carbon monoxide. Webb, sensitive to a large swath of the infrared, should find all those gases and more, including ammonia, acetylene, and hydrogen cyanide. "Webb will blow the door wide open," says Nikole Lewis of Cornell University.

The absorption signatures are strongest when the starlight passes through a thick atmosphere, so Hubble and Spitzer focused on big, puffy planets that orbit close to their

Telescope name strikes discordant note for many

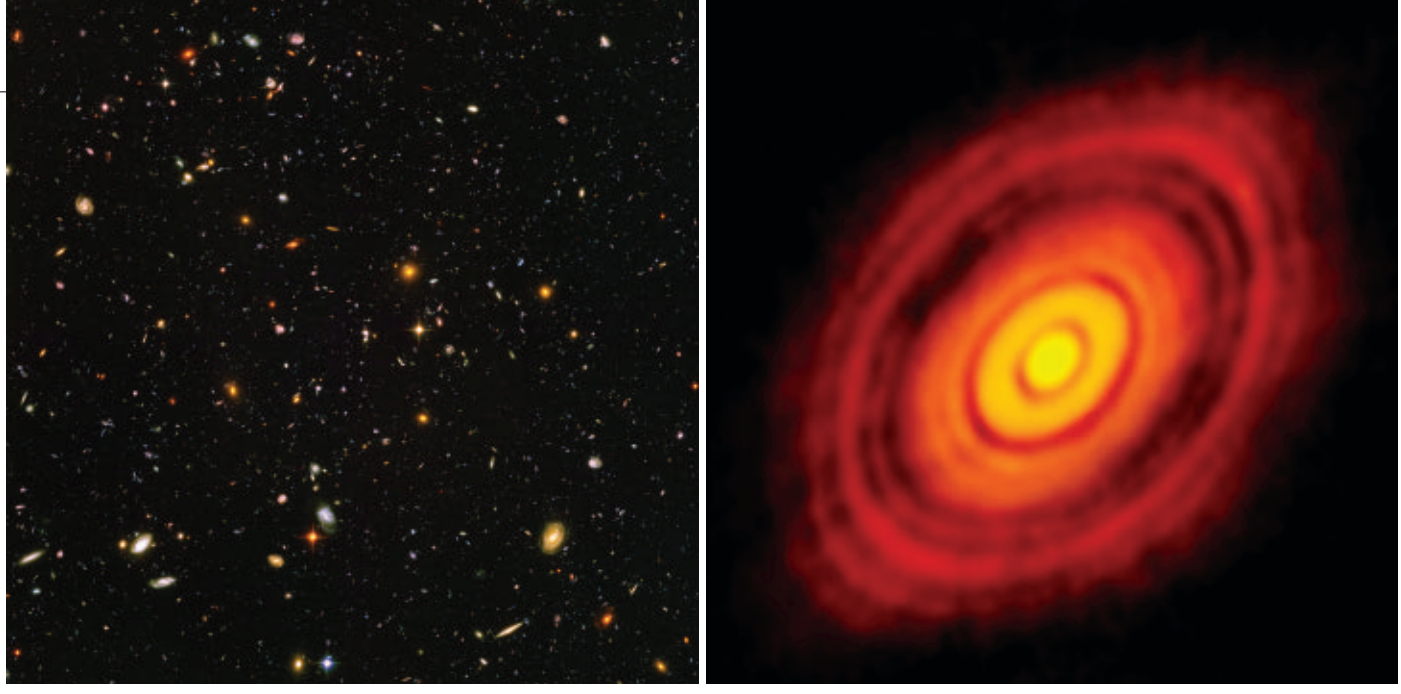
NASA Administrator Sean O'Keefe was trying to humanize what was then known as the Next Generation Space Telescope, when in 2002 he decided to name it after his 1960s predecessor, James Webb. Even at the time the decision raised some eyebrows, because NASA science missions are more typically named after scientists, not bureaucrats. O'Keefe justified his decision by citing Webb's prominent role in the Apollo program and his acknowledged record of championing space science. Now, however, deeper questions have emerged about whether Webb deserves the honor—a debate that is tarnishing the telescope's name just as NASA is trying to celebrate its launch.

Webb, who died in 1992, had a leadership role at the U.S. Department of State in the 1950s during the "lavender scare," a systematic effort—encouraged by prominent members of Congress—that removed hundreds of gay and lesbian people from civil service because of their sexuality. Webb was involved in Senate discussions that initiated the policies, according to historian David Johnson of the University of Southern Florida in his 2004 book *The Lavender Scare: The Cold War Persecution of Gays and Lesbians in the Federal Government*. More recently, astronomer Adrian Lucy of Columbia University found documents in the U.S. National Archives showing Webb was involved in meetings in which the discriminatory policies were discussed and homophobic material was passed on to senators. In 1963, after Webb became NASA administrator, an agency employee was fired on suspicion of being gay.

Earlier this year, four astronomers launched a petition calling for the instrument to be renamed. In their letter to NASA, they wrote: "Webb's legacy of leadership is complicated at best, and at worst, complicit with persecution." The petition drew more than 1200 signatures and included many scientists who will be using the telescope.

In June, NASA began an investigation. The agency's official historian, Brian Odom, and an external expert reviewed archival evidence about Webb's policies and actions. Their findings and conclusions have not been revealed publicly, and in September NASA released only a terse statement from Administrator Bill Nelson: "We have found no evidence at this time that warrants changing the name of the James Webb Space Telescope."

The agency considers the case closed. "It's hard to go back and look at the historical record and see what someone's opinions were, and if NASA has investigated this, we shouldn't second guess that," says Fiona Harrison, an astronomer at the California Institute of Technology who co-chaired a recent astronomy decadal survey. "But I like the idea of honoring scientists." Should a future NASA administrator decide to reverse the decision, there is precedent: In 2018, NASA renamed Swift, a gamma ray telescope—14 years old and going strong—after Neil Gehrels, its principal investigator, who had died the previous year. —*D.C.*



The James Webb Space Telescope will reach deeper in time than Hubble, which captured "deep field" images (left), revealing galaxies that shone 800 million years after the big bang. It will also zoom in on gaps in disks of gas and dust around some young stars, seen in radio telescope images (right), which are thought to mark planetary orbits.

star—so-called hot Jupiters. With its heightened sensitivity, Webb will be able to sniff out molecules in the thinner atmospheres of rocky planets. "We will see the first chemical fingerprints from Earth-sized planets," says Batalha, who has assembled a team of about 60 collaborators to test transit spectroscopy in one of Webb's largest early programs.

Few think Webb will have sharp enough eyes to sense signs of life in an exoplanet's atmosphere, such as oxygen, ozone, or chlorophyll. But it will go a long way toward understanding the variety of atmospheres and how habitable they are. "Webb will give us the demographics of atmospheres," Batalha says. "It's like moving from silent movies in black and white to color TV."

SO INTENSE is the interest in Earth-size planets and their suitability for life that in 2018 NASA launched a "spotter" for Webb: a space mission to identify the best candidates for atmospheric studies—rocky planets around dim red dwarf stars, which do not swamp a planet's light as much as other stars. The Transiting Exoplanet Survey Satellite (TESS) has in its first 3 years found 159 confirmed planets and has another 4500 awaiting confirmation.

A first task for Batalha's team will be to solve a mystery posed by the planetary inventory Kepler and TESS have assembled: The most common exoplanets are a type that doesn't exist in the Solar System, with a mass between that of Earth and Neptune. "We don't really understand what they are," Batalha says. Webb should help. If the mystery planets are smaller versions of Neptune, a gas giant, they should have a thick atmosphere dominated by primordial hydrogen mixed with water, carbon dioxide, and carbon monoxide. If they are rocky bodies—super-Earths—their atmosphere should reflect geological processes, like volcanism, that often spew molecules such as methane or ammonia.

Transiting planets also periodically pass behind their star; Webb will compare the star's light just before and during these eclipses. Prior to the eclipse, the light includes both the star's emissions and the much fainter light from the planet, whereas the eclipse itself blots out the planet's light. By comparing the two signals, astronomers can infer the planet's own glow, which betrays information about temperatures and cloud cover.

The combined light of the star and orbiting planet should change subtly as observers receive light from the planet's dayside, nightside, and varying mixtures of the two. The resulting "phase curve" reveals the dynamics of an atmospheric system: how the atmosphere shuffles heat from the hot dayside to the cooler nightside, which in turn affects winds and cloud movement. "We will also be able to tease out 2D and 3D effects, such as clouds on one side and not the other," Lewis says. "It'll keep us busy for a long time."

Webb will also take pictures of exoplanets directly, with the help of a coronagraph, a mask within the telescope that blocks the overwhelming glare of the star so that the tiny dim planets around it can be seen. The largest telescopes on Earth can only discern the largest planets, more than twice Jupiter's mass, in wide orbits. Furthermore, only young planets have been imaged, ones glowing with the leftover heat of their formation, not just the much dimmer reflected light of the star.

Webb, designed to catch this infrared glow without the blurring interference of Earth's atmosphere, will be able to see smaller planets later in life, orbiting closer to their stars. "Something like Jupiter would be great," Baraffe says; researchers wonder whether the composition and temperature of an alien Jupiter will be anything like the homegrown version. "Will it share general characteristics or be very different because it formed in different conditions?" Baraffe asks. But directly imaging an Earth-like planet and searching for signs of life will have to wait for an even larger and more capable space telescope (*Science*, 14 December 2018, p. 1230).

FOR MANY, the first data from Webb will prompt a shift from one tension to another: from anxiety over its launch and deployment to pressure to make the most of its limited life. Whereas Hubble could be refueled and upgraded by visiting astronauts, extending its life for decades, the clock is ticking for Webb: It's designed to last 5 or 10 years, but beyond that nothing is certain.

The limiting factor is propellant. Webb needs its thrusters to maintain its orbit around L2 and to occasionally dump angular momentum from the reaction wheels that point the telescope and keep the sunshield in position. Without propellant, Webb will drift from L2 and eventually fall into a fatal spin. It won't be able to charge its solar-powered batteries or communicate with Earth. Webb will see no more.

Finkelstein will rue that day, but he is confident he will be plenty busy in the meantime. "I've basically cleared the next decade from my schedule." ■

IMAGES: (LEFT TO RIGHT) NASA/ESA/S. BECKWITH (STSCI) AND THE HUDF TEAM; ALMA (NRAO/ESO/NAOJ)

INSIGHTS

POLICY FORUM



CLIMATE POLICY

Toward constructive disagreement about geoengineering

A shared taxonomy of concerns may help

By **David W. Keith**[1,2]

The divergence of expert opinion about solar geoengineering (SG) may be sharper than in any other area of climate policy. As with other contested technologies, disagreement sometimes conflates divergent scientific and political judgments with divergent normative stances. It is impossible to cleanly disentangle the technical, political, and ethical aspects of the debate. But it is possible to disagree in ways that better serve the public's interests. Disaggregation of judgments about SG may allow experts to disagree more constructively and better serve policy-makers and diverse publics. An organized list of concerns about SG could serve as a tool to encourage disaggregation of complex disagreements while discouraging their conflation into an unhelpful "good versus bad" dichotomy.

SG is defined here as methods that could be used to ameliorate the climate hazards due to long-lived greenhouse gases (GHGs) by modifying the radiative forcing of climate—primarily by reducing the absorbed solar flux. SG is perhaps best defined in relation to other ways of managing climate risk; it is one of four toolboxes: emissions reduction, carbon removal, SG, and adaptation. Tools inside the SG toolbox include space-based shields, stratospheric aerosols, cirrus cloud thinning, marine cloud brightening,

ILLUSTRATION: DAVIDE BONAZZI/SALZMANART

and increasing surface reflectivity (*1*).

There is evidence that some SG technologies could substantially reduce important climate hazards, including changes in water availability or extreme temperatures, over most of the world, with physical harms or risks that are small compared with the aggregated benefits of reduced climate hazards (*1*, *2*). Uncertainty is far too large to justify either a decision to deploy or to renounce deployment, but evidence of SG's potential to reduce human and ecological impacts is arguably sufficient to justify a substantial research effort and sustained policy attention. Of course, many scientists, climate policy experts, and climate advocates would likely disagree with this assessment.

A TAXONOMY OF CONCERNS

A systematic taxonomy of concerns could serve as a step toward more constructive disagreements. I propose an initial catalog, organized into a rough taxonomy with four top-level categories (see the box) ordered by conceptually distinct root causes.

PHYSICAL HARMS OF BENEVOLENT DEPLOYMENT

These concerns arise from side effects of altering radiative forcing, from climate response to that forcing, from accidents, or from incompetence. A benevolent deployment aims at some measure of distributive justice such as a Rawlsian difference principle (greatest benefit to the poorest) or a utilitarian maximization of benefits. Benevolence is a claim about intentions, not outcomes.

Side effects are never generic to SG; they are specific to the methods used to alter radiative fluxes (see the box). No geoengineered radiative forcing can exactly counter the spatial and spectral characteristics of GHG forcing. We may define an intervention as "moderating" a climatic variable when it reduces the local deviation of that variable from its preindustrial value and "exacerbating" when it increases the deviation. Exacerbation is the physical climate risk of SG.

Risk depends on the amount of SG. Reduction in precipitation is, for example, often cited as a risk of SG. Yet increased precipitation is an important climate hazard. Reduced precipitation is only a concern under this definition when SG is large enough to drive precipitation below a reference value so that any additional SG exacerbates the change from that reference. The reference is the climate to which the system is adapted, which may differ from the preindustrial.

The area that sees exacerbation of some climate hazards increases with the amount of SG (*2*), so SG is less able to provide widespread moderation of climate hazards as the amount of SG increases. This is the reason why SG cannot be a substitute for reducing carbon concentrations. The area that sees exacerbation will also be larger—for the same change in global average temperature—for SG methods that are localized as when arctic-only SG shifts tropical rainfall (*3*). This increased disparity of climate changes is a reason why localized deployment of SG may paradoxically increase global governance challenges.

"A serious research program must apply modern risk-assessment tools to the technology and to the institutions proposed for deployment."

Some technologies are particularly prone to errors. We should expect "normal accidents" (*4*) from such technologies even when they are managed with good intent. SG methods will differ in their sensitivity to error. A space-based shield that is only stable with dynamic control might be destroyed with a software error, whereas aerosol injection might be less sensitive to such errors because the 2-year stratospheric lifetime provides opportunity to respond to failures. There has been woefully little effort to assess SG's accident risk. A serious research program must apply modern risk-assessment tools to the technology and to the institutions proposed for deployment.

INJUSTICE

The research, development, and deployment of SG each entail concerns about procedural justice. Any deployment of SG would also entail concerns about distributive justice.

Perhaps the central concern about SG is that deployment, or even the credible possibility of deployment, will slow emissions cuts. This concern—moral hazard, or mitigation inhibition—arises from political links between decisions about SG and emissions cuts in the face of climate risks, not from any physical or technological link between SG and emissions.

SG is fast, cheap, and risky, whereas emissions cuts and carbon removal are—comparatively—expensive and slow because of inertia in the energy system and carbon cycle. Doing a bit less emissions cutting and a bit more SG will tend to provide short-term benefits while imposing long-term costs.

Mitigation inhibition may occur as a collective behavior if the current generation deploys SG while foregoing emissions cuts, reducing their climate risk while increasing risks for the next generation. Even if the current generation's choice conformed to some standard of procedural justice, such a decision could violate intergenerational distributive justice. This is mitigation inhibition as economic free-riding on our grandchildren. Such mitigation inhibition would be bolstered when irrational technological optimism about the effectiveness of SG or of future carbon removal serves as a collective excuse for shortsightedness.

Mitigation inhibition may arise as a violation of procedural justice if a self-interested minority, such as fossil fuel–rich countries or industries, is able to overcome the majority by exaggerating the efficacy of SG.

If the pace of emissions cuts is determined by balancing the cost of faster cuts against future climate risks, then a benevolent policy-maker who expects SG to reduce some risks will delay emissions cuts relative to the rate of mitigation without SG. Mitigation inhibition arises only if emissions cuts are irrationally or unjustly delayed.

Mitigation inhibition couples procedural questions—who makes decisions—and distributive questions about the net distribution of the costs and benefits of emissions cuts and SG.

Independent of the political linkage with emissions cuts, any research and development of SG requires decisions about the conduct and objectives of research, decisions that in turn raise questions of procedural justice. How to resolve disputes between groups such as the Saami council, who oppose SG research, and environmental groups who support research?

Whatever is done about emissions, deployment of SG will require choices, such as the choice to focus the cooling on the tropics or the poles, choices that entail concerns about distributional justice.

CONFLICT

Concerns that SG may induce conflict are rooted in the Cold War salience of weather and climate modification (*5*). Use of weather modification by the United States in the Vietnam war led to a treaty prohibiting hostile use of environmental modification technologies. Conflict could be caused directly by

[1]John F. Kennedy School of Government, Harvard University, Cambridge, MA, USA. [2]John A. Paulson School of Engineering and Applied Sciences, Harvard University, Cambridge, MA, USA. Email: david_keith@harvard.edu

A taxonomy of concerns about solar geoengineering (SG)

Bullet points indicate examples of potential concerns.

PHYSICAL RISKS OF BENEVOLENT DEPLOYMENT

Side effects of perturbing radiative forcing. Physical consequences other than those arising from an idealized reduction in insolation
- Stratospheric sulfates cause ozone loss
- Iodine from sea salt spray increased methane lifetime
- Scattered light alters ecosystems
- Health hazard when aerosols add to particulate matter at surface

Exacerbation of climate changes. SG increases the deviation of a climatic variable in some region from the preindustrial.
- Change in drought frequency
- Increased nitrate contribution to particulate matter ($PM_{2.5}$) due to reduced warming

Accidents
- Termination due to catastrophic failure of deployment system

Incompetence
- Errors in quantities deployed

INJUSTICE

Moral hazard. Unjust reduction in emissions cuts, better termed "mitigation inhibition"

Political exploitation. SG exploited by a group to advance their private interest against the collective interest in emissions cuts
- A petrostate covertly funds civil society groups to exaggerate benefits of SG and lobby for deployment and for slowing emissions cuts
- The industries that will implement SG promote SG

Collective addiction
- Irrational technological optimism serves as a collective excuse for delay

Procedural injustice
- Unilateral deployment

Distributive injustice
- SG is deployed for polar cooling, disproportionally benefitting relatively wealthy mid-latitude countries while doing little to reduce peak temperatures in the tropics.

CONFLICT

Malevolent use
- Weaponization of weather control
- Termination due to destruction of deployment system

Exacerbation of existing conflicts
- Conflict exacerbated by realized or perceived unequal impacts or benefits
- Conflict arises from attribution of weather-related disasters to an SG program
- Conflict arises from perceived illegitimacy of SG deployment

HUMANITY AND NATURE

Earth becomes more of an artifact. Deliberately altering climate—whatever the harms or benefits—makes Earth appear more of an artifact of human political choices.

Slippery slope to enhancement. If SG becomes widely accepted, there will be temptations to use the technology to tailor climate for humanity's benefit rather than to reduce climate changes.
- A combination of increased CO_2 concentrations and SG is used to decrease pole-to-equator gradients and increase biological productivity, nudging the climate toward "equitable" climates.

malevolent deployment or indirectly by deployment that exacerbates existing conflicts.

Despite long-standing concerns about weaponization, there are few or no specific analyses of the military use of SG technologies. Militaries increasingly seek precision weapons, so the long time scale and spatially diffuse climate changes produced by geoengineering appear to lack a credible military use. Perhaps the most plausible military application is weather control. This might be achieved by modulating the radiative forcing with feedback from a weather forecasting system. It would only be possible with methods that can be modulated on synoptic scales (on the order of 1000 km or more), such as marine cloud brightening and cirrus cloud thinning. But this is unproven and, even if possible, might be too diffuse, or easily countered, to have meaningful military application. Beyond weaponization of the system itself, military force might be used against deployment systems to cause or threaten termination shock.

Conflict may be induced if SG deployment sharply exacerbates inequalities, or conflict might arise from instabilities introduced by counter geoengineering (*6*). The likelihood of conflict may also increase if disagreement over deployment of SG distracts political attention from unrelated conflicts.

HUMANITY AND NATURE

If SG was used only to supplement emissions reductions by limiting climatic change, then it can reasonably be seen as a means to limit the human footprint on nature. This use of SG would be anthropogenic but not anthropocentric (*7*). Yet even if SG protects ecosystems by limiting the "climate velocity" (the rate at which species must migrate to find climate conditions suitable to their survival in a warming world), climate being partially controlled by a centralized, high-leverage technocratic process would mark a change in humans' relationship with nature.

Deployment might begin with the goal of limiting environmental change, yet once developed, the temptation may grow to use SG for climate "enhancement." A high-CO_2 climate in which SG reduces pole-to-equator temperature gradients might, for example, provide utilitarian benefits in the form of increased primary productivity and reduced climate extremes. The slippery slope to enhancement is for me a sharper concern than the teleological concerns about the end of nature.

TOWARD MORE CONSTRUCTIVE DISAGREEMENT

An expert can better serve their audience—other experts, policy-makers, or diverse publics—by disaggregating their judgments. They might say that some specific geoengineering proposal "could reduce deaths in heat waves by 30%" while also saying that "research on SG should not proceed because it will be exploited by fossil-rich nations to block emissions cuts" rather than conflating their judgments by saying "geoengineering is risky."

Audiences look to experts because of their knowledge. But expertise in one discipline is not strongly correlated with accurate judgments in other domains (*8*). An expert at predicting heat waves may be no better—and perhaps worse—than an average citizen in predicting political outcomes of deploying SG. Disaggregation allows the audience to weigh expert claims using their own judgment about the expert's accuracy across various domains.

Disaggregation may also help find places where experts agree. Experts who disagree strongly about proceeding with a SG field experiment might nevertheless agree on specific technical judgments, such as the mortality caused by SG aerosols that add to particulate matter pollution or the reduction in mortality from heat waves when SG reduces peak temperatures.

When experts provide an aggregate policy recommendation, they combine their judgment about the likelihood of specific technical and or political outcomes with their personal valuation of those outcomes. This is unhelpful when the audience does not share the expert's valuation. Disaggregation can help avoid conflation of facts and values (*9*).

Support for SG research seems to be stronger in poorer countries (*10*, *11*). It is plausible that this arises from divergent weights given to the outcomes of SG. Residents of poorer and hotter countries may weigh the benefits of short-term cooling more strongly, whereas residents of richer, cooler countries who feel less threat from the immediate impacts of heat may accord more weight to the long-term concerns about SG. There is no value-free resolution to trade-offs between the benefits and harms of SG. What is certain is that experts' valuation of outcomes will likely differ from their audience, and that climate experts are generally more educated, wealthier, and less racially diverse than their audiences. So experts do their audience a disservice by implicitly folding their values into policy recommendations.

How to encourage disaggregation? Experts should strive to delineate areas in which they have expertise from areas in which they do not and should give audiences the opportunity to use their own values. Policy intermediaries such as journalists and opinion-leaders can encourage the distinction between factual judgments and valuation.

A community-based taxonomy of SG concerns could help. Such a taxonomy might be seen as reasonably unbiased if it were maintained by a community using rules adapted from Wikipedia in which substantive statements require pointers to peer-reviewed literature.

Organizations such as the National Association of Science Writers can help by explicitly promoting best practices for reporting on politicly contentious topics. Journalists might better encourage experts to provide narrower answers that are better supported by data in the expert's arena of expertise.

This is not an injunction that experts "stay in their lane." Transdisciplinary research requires collaboration across disciplinary boundaries. Moreover, experts are also citizens and, as citizens, have a right to participate in public policy. But in participating, they have a duty to distinguish statements made on the basis of their expertise from statements they make as citizens.

Nor is this a claim that facts and values can be sharply separated; they cannot. But more careful reporting of expert judgments could help to reduce the role of "cultural cognition" in determining policy preferences (*12*).

Behavioral social science may help untangle interplay between expert judgments, values, and public understanding. Analysis of SG is oversupplied with generic normative claims about governance and undersupplied with detailed empirical research to understand the mental models of relevant groups. Empirical social science could adapt research projects to identify and characterize subjective aspects of expert judgments and anticipate and clarify conflicts that arise from inequitable effects of climate change and geoengineering (*13*).

A coordinated SG research program could support development of community-based taxonomies of SG's benefits and concerns. The program could then use such structures to aid program managers in supporting research that addresses concerns that are both salient and researchable. The program could also encourage development of community-based codes of conduct that include best-practice guidelines for reporting results.

There is no recipe to resolve hard problems at the science-policy interface, but that should not discourage incremental improvements that may allow experts to better serve the public. ■

REFERENCES AND NOTES

1. National Academies of Sciences, Reflecting Sunlight: Recommendations for Solar Geoengineering Research and Research Governance (National Academies of Sciences, 2021).
2. P. Irvine *et al*., *Nat. Clim. Chang.* **9**, 295 (2019).
3. A. Nalam, G. Bala, A. Modak, *Clim. Dyn.* **50**, 3375 (2018).
4. C. Perrow, *Normal Accidents: Living with High-Risk Technologies* (Basic Books, 1984).
5. D. Keith, *Annu. Rev. Energy Environ.* **25**, 245 (2000).
6. A. Parker, J. Horton, D. Keith, *Earths Futur.* **6**, 1058 (2018).
7. L. Thiele, *Glob. Environ. Polit.* **20**, 9 (2020).
8. P. E. Tetlock, *Expert Political Judgment* (Princeton Univ. Press, 2009).
9. R. Keeney, *Value-Focused Thinking: A Path to Creative Decisionmaking* (Harvard Univ. Press, 1996).
10. M. Sugiyama, S. Asayama, T. Kosugi, *Environ. Commun.* **14**, 641 (2020).
11. A. Dannenberg, S. Zitzelsberger, *Nat. Clim. Chang.* **9**, 769 (2019).
12. D. M. Kahan *et al*., *Nat. Clim. Chang.* **2**, 732 (2012).
13. B. Fischhoff, *Behav. Public Policy* **5**, 439 (2021).

ACKNOWLEDGMENTS

D.K. acknowledges support from the Harvard Solar Geoengineering Research Program, for which he serves as Faculty Director. D.K. serves on the advisory group to the Carnegie Climate Governance Initiative and on the board of directors of Carbon Engineering.

10.1126/science.abj1587

CLIMATE POLICY

Social science research to inform solar geoengineering

What are the benefits and drawbacks, and for whom?

By **Joseph E. Aldy[1,2,3,4], Tyler Felgenhauer[5,6], William A. Pizer[2], Massimo Tavoni[7,8], Mariia Belaia[9], Mark E. Borsuk[5,6], Arunabha Ghosh[10], Garth Heutel[3,11], Daniel Heyen[12,13], Joshua Horton[14], David Keith[1,15], Christine Merk[16], Juan Moreno-Cruz[17,18,19,20], Jesse L. Reynolds[21], Katharine Ricke[22,23], Wilfried Rickels[16], Soheil Shayegh[8], Wake Smith[1,24], Simone Tilmes[25], Gernot Wagner[26,27], Jonathan B. Wiener[2,6,28]**

As the prospect of average global warming exceeding 1.5°C becomes increasingly likely, interest in supplementing mitigation and adaptation with solar geoengineering (SG) responses will almost certainly rise. For example stratospheric aerosol injection to cool the planet could offset some of the warming for a given accumulation of atmospheric greenhouse gases (*1*). However, the physical and social science literature on SG remains modest compared with mitigation and adaptation. We outline three research themes for advancing policy-relevant social science related to SG: (i) SG costs, benefits, risks, and uncertainty; (ii) the political economy of SG deployment; and (iii) SG's role in a climate strategy portfolio.

Some concerns have received increased attention in debates over SG and thus illustrate the need for greater social science evidence and understanding. For example, some stakeholders have suggested that undertaking SG research could create a form of moral hazard by deterring emission mitigation efforts, whereas other scholars have challenged this claim. Still other scholars have questioned the ethics of seeking to hide from future generations policy choices that they may wish to consider. And given the evidence of strong free-riding incentives for emission mitigation, it is not clear that there would be much of an additional emission mitigation disincentive from SG. But these questions deserve further study in more realistic models of multiple, heterogeneous actors (*1, 2*).

Further, if a major economy with the technical capacity to implement SG makes a decision about its use, this would have important equity and justice implications, especially for the people living in least developed countries and small island states. These implications take the form of procedural justice—do these peoples have a voice in the decision-making process—as well as the distributive justice of the outcomes associated with a SG intervention decision. Such justice considerations arise regardless of whether the decision is to take or opt against an SG intervention. A critical assessment of the justice implications of SG implementation would enrich the political economy evaluation of government decision-making.

SG is one of several emerging climate engineering technologies. For example, carbon dioxide (CO_2) removal would reverse the flow of greenhouse gases into the atmosphere through large-scale biological and chemical sequestration and industrial direct air capture technologies. In contrast to CO_2 removal, SG faces fewer technological and financial hurdles and would likely influence temperatures more quickly. Indeed, the largest developed and developing nations have the resources and technical means to implement SG interventions in no more than a few years.

Despite the potential for SG to reduce climate change risks, the international community has not addressed SG under the UN Framework Convention on Climate Change. This is mirrored by a dearth of national programs and governance. The limited policy landscape provides an opportunity for new social science research to inform the design of institutions, policy, and governance of SG.

COSTS, BENEFITS, RISK, AND UNCERTAINTY

Policy-makers would gain from assessments of SG's costs and benefits, recognizing uncertainties in quantification, potential indirect costs, and risk-risk trade-offs. The direct costs of implementing SG interventions could be about $5 billion per year (*3*), two to three orders of magnitude less than estimated climate change damages and the costs of ambitious emission mitigation (*4*). These estimates, however, represent direct engineering costs of deploying SG interventions, and more extensive SG assessments can better inform decision-making. This work should be informed by advances in physical science and engineering research on SG deployment, including alternative technologies and design choices, potential small-scale experiments, and the resulting impacts of climate change and SG interventions. For example, building on high spatial resolution, climate change modeling can enable greater precision in estimating benefits and costs and help identify social science data needs where official economic statistics may be limited.

Higher-resolution representation of physical and socioeconomic impacts can also illustrate the distribution of costs and benefits from SG interventions (*5*). Like climate change, SG interventions would impose heterogeneous impacts across the world and over time (*6*), which would have important social welfare, equity and justice, social, and political implications. SG research can build upon and integrate with the growing empirical evidence of climate change impacts on conflicts, migration, health, labor and agricultural productivity.

The outputs of such analyses could be inputs in models with modified social welfare functions that vary in how they weight inequality and justice of outcomes. They can also serve as inputs in models of political economy and international relations. Taking a multi-objective assessment framework to evaluating SG can also guide survey work and laboratory experiments to elicit preferences and trade-offs over SG impacts, risk, inequality, and other considerations. Drawing study participants from developing countries can help address concerns about how integrated assessments reflect the attitudes and preferences of those populations most likely to be affected by climate change.

Integrating science, engineering, and economic analyses can help address uncertainties in the benefits and costs of SG design and deployment decisions, which could vary across geography, altitude, seasonal timing, technique, magnitude of intervention, and other factors. Integrated frameworks that incorporate risk analysis and decision theory can improve the characterization of, and reduce uncertainty about, SG benefits and risks (*1*).

Integrated assessments of SG interventions should also account for the costs of monitoring, attribution, redundancy, evaluation, updating, and any necessary risk management mechanisms. Such analyses can also consider the benefits of learning through a value of information framework. Theoretical and integrated assessment models (IAMs) can illustrate the dimensions of SG deployment with the greatest potential for learning, which in turn could focus future experimentation and measurement.

An SG intervention is not simply reversing climate change. Some climate change impacts, such as ocean acidification, are only to a small extent directly influenced by SG, and SG would occur against the backdrop of recent decades of rapid warming. Moreover, SG may result in unintended, ancillary risks (*7*). A rich array of research tools—models calibrated to real-world observations as well as statistical evaluations—can provide insights on ancillary impacts of SG interventions. For example, studying potential adverse respiratory health outcomes from SG interventions could inform future technical design of SG interventions—e.g., substituting new materials for sulfur particles—and direct evaluations of alternative policy remedies—e.g., improved health care access and treatment. Evaluations of ancillary or unintended impacts could serve as inputs in survey-based research on SG risk communication and political acceptance. SG interventions could also necessitate updating of damage functions used in IAMs, because such damage functions are typically calibrated to temperature as a proxy for climate change (*8*).

POLITICAL ECONOMY OF DEPLOYMENT

Solar geoengineering deployment scholarship has typically focused on either (i) a single, global actor or (ii) a stylized depiction of strategic interactions among possible SG actors. To understand the roles of incentives, institutions, norms, and international relations in SG deployment, the next generation of analyses could build on these to develop more realistic scenarios of SG intervention and political economy dynamics (*1*).

For example, absent strong international governance, a globally coordinated SG regime is unlikely, and decision-making

[1]John F. Kennedy School of Government, Harvard University,Cambridge, MA, USA. [2]Resources for the Future, Washington, DC, USA. [3]National Bureau of Economic Research, Cambridge, MA, USA. [4]Center for Strategic and International Studies, Washington, DC, USA. [5]Pratt School of Engineering, Duke University, Durham, NC, USA. [6]Center on Risk, Duke University, Durham, NC, USA. [7]School of Management, Politecnico di Milano, Milan, Italy. [8]RFF-CMCC European Institute on Economics and the Environment, Centro Euro-Mediterraneo sui Cambiamenti Climatici, Milan, Italy. [9]Forum for Climate Engineering Assessment, American University, Washington, DC, USA. [10]Council on Energy, Environment and Water, New Delhi, India. [11]Department of Economics, Georgia State University, Atlanta, GA, USA. [12]Technische Universität Kaiserslautern, Kaiserslautern, Germany. [13]ETH-Zurich, Zurich, Switzerland. [14]Mossavar-Rahmani Center for Business and Government, Harvard University, Cambridge, MA, USA. [15]John A. Paulson School of Engineering and Applied Sciences, Harvard University, Cambridge, MA, USA. [16]Kiel Institute for the World Economy, Kiel, Germany. [17]School of Environment, Enterprise, and Development, University of Waterloo, Waterloo, Canada. [18]Department of Economics, University of Waterloo, Waterloo, Canada. [19]Balsillie School of International Affairs, Waterloo, Canada. [20]CESifo, Munich, Germany. [21]Independent consultant. [22]School of Global Policy and Strategy, University of California San Diego, San Diego, CA, USA. [23]Scripps Institution of Oceanography, University of California San Diego, San Diego, CA, USA. [24]Yale College, Yale University, New Haven, CT, USA. [25]National Center for Atmospheric Research, Boulder, CO, USA. [26]Robert F. Wagner Graduate School of Public Service, New York University, New York, NY, USA. [27]Department of Environmental Studies, New York University, New York, NY, USA. [28]School of Law, Duke University, Durham, NC, USA. Email: joseph_aldy@hks.harvard.edu

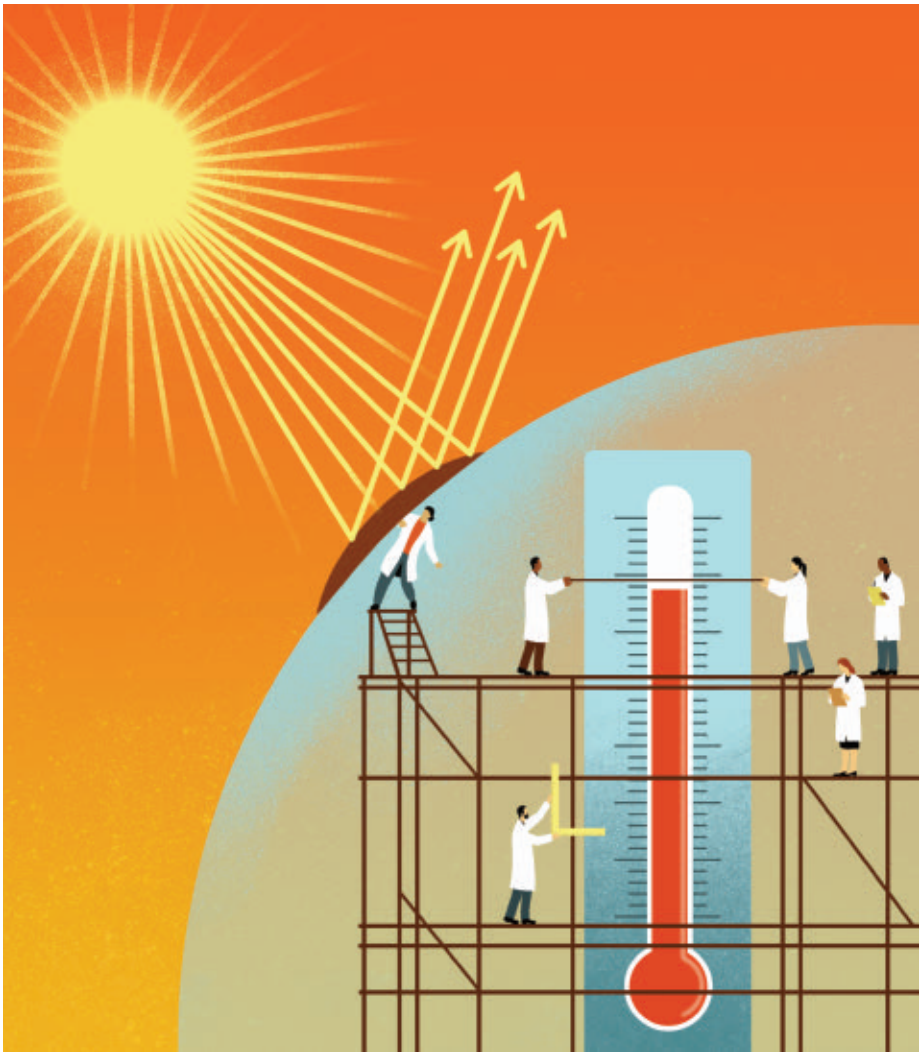


ILLUSTRATION: DAVIDE BONAZZI/SALZMANART

would rest primarily among national governments. Weak global governance, coupled with modest SG engineering costs, has raised concern about "free drivers" unilaterally deploying SG interventions. Social science research can explore the options and incentives for a state (or nonstate) actor to deploy a global SG project or a local intervention (e.g., marine cloud brightening, regional cirrus thinning, or enhancing surface albedo). Such local intervention possibilities raise the prospect that multiple state actors could pursue independent SG strategies without explicit coordination. The atmosphere, however, has nonlocal "teleconnections," so a local intervention's impacts may spill over to other regions, raising governance challenges. Game theory and lab experiments could be used to explore the political, economic, and sociological drivers and inhibitions on a state actor to pursue or refrain from unilateral SG—including the types of events that could trigger unilateral SG deployment.

Inadequate efforts to reduce emissions have also prompted calls for retaliatory measures, such as border tax adjustments. This reaction points to the prospect for countermeasures targeting states that deploy SG by those opposed to such actions (*9*). Might states respond through countergeoengineering or alternative means, such as military interventions or trade sanctions (*10*)? Such responses could influence incentives for deployment, international conflict, and the efficacy, costs, and benefits of SG interventions. This suggests new social science research convening national security experts to understand the theory, models, and evidence that can be drawn from related international problems.

A smaller group of countries could work together for a collectively managed SG intervention. Such a club approach to governance raises additional questions about legitimacy, political organization, and effectiveness. A club could test technologies and governance regimes to build mutual trust and support for SG as a credible climate change response strategy. The emergence, composition, and decision-making of such a club would likely play a key role in determining whether it would enhance confidence in SG as a strategy, or spur greater concern among states outside the club. This suggests a combination of decision- and game-theory tools to explore possible outcomes and equilibria. For example, a club of countries that are simultaneously pursuing ambitious mitigation efforts may be more credible and sustainable than a coalition of mitigation laggards. There may be opportunities to explore clubs in which SG is one element of a broader climate partnership. The prospect of a club could also benefit from study of the procedural justice implications of such institutional design.

Yet another possibility is a mutual restraint agreement. Countries might build the capacity to launch SG and then agree with other SG-capable peers to a mutual agreement to restrain unilateral deployment. This would be akin to an arms control treaty and suggests that legal expertise and experience with such treaties could be leveraged to answer these questions, alongside game theory and lab experiments. For example, the prospect of such a restraint game raises questions about incentives and institutions for such participation and verification to yield a stable outcome.

The incentives and political economy of SG will reflect actors' assessments of the benefits, costs, risks, fairness, equity, and justice. In turn, the institutional design of SG decision-making will also influence the efficacy and related SG outcomes. The need for redundancy and risk management requirements that may emerge through negotiations could likewise affect the returns on SG deployment. The value and risk tradeoffs of SG—evaluated through cost-benefit analysis—would also depend critically on how it may be paired with, or affect, emission mitigation and adaptation.

A PORTFOLIO APPROACH?

Policy-makers have long pursued a portfolio of policies and programs, in lieu of a single policy instrument, to combat climate change. Though initially focused on ways to mitigate emissions—through subsidies, regulatory mandates, carbon pricing, etc.—and more recently advancing ways to enhance resilience to the impacts of a changing climate, future policy portfolios could be broadened to include SG.

Consideration of SG alongside mitigation and adaptation raises important economic, political economy, and decision science questions. Recent analyses have examined scenarios that optimize the mix of strategies—emission mitigation, carbon dioxide removal (CDR), adaptation, and SG—that

minimize the costs of achieving a specific temperature goal (*8*, *11*–*13*). Such an optimized framework illustrates the potentially large benefits of coupling SG with mitigation and adaptation. This work, however, does not address the strategic and behavioral responses that SG projects may entail. Decades of experience with suboptimal and inadequate emission mitigation policies suggest that a more realistic treatment of the factors influencing SG decision-making—and the possibility of suboptimal SG policy—could advance this literature (*14*). For example, how feasible are peak-shaving scenarios—which rely on carefully coordinated timing of emission mitigation, SG, and CDR to limit temperature increases and damages until mitigation efforts realize global net-zero (or lower) emissions—given real-world decision-making processes among multiple actors facing heterogeneous impacts? Moreover, SG research may influence the strategic incentives for investing in other climate change risk reduction technologies.

Exploration of SG options by decision-makers could make climate change more salient for the public and galvanize support for more ambitious emission mitigation (*4*, *15*). Rigorous theoretical analysis, coupled with well-designed surveys and laboratory experiments, could better inform our understanding of how SG deployment would influence emission mitigation. This could be integrated with behavioral decision-making scholarship to explore how political leaders would interpret and act on information about the efficacy of a mitigation+adaptation+SG approach to climate change. The public perception of and engagement in SG research and policy serves as another key element of an SG research agenda (*1*).

Given the uncertainties about climate change and SG, a decision-making under uncertainty framework could guide research on the interactions among climate change strategies. For example, decision-makers may respond to new information that shows climate change is worse than expected by implementing SG and investing in more climate-resilient infrastructure. Constructing models of decision-making that can generate such policy response functions for SG and adaptation has implications for the optimal mitigation strategy, as well as for the estimation of the social cost of carbon. Anticipating SG as an active policy response to knowledge of more severe climate change could preclude the most extreme climate change damages, but could also raise tail risks from SG ancillary impacts. Advancing social science research to characterize these potential risk-risk trade-offs would better inform decision-makers.

Given the persistence of climate change risks even with SG, additional research could explore how learning about the benefits—and shortcomings—of SG could guide future adaptation efforts. For example, ocean acidification will worsen with continued CO_2 emissions even if SG interventions effectively halt the increase in temperatures. Or SG implementation may occur too late to prevent substantial sea level rise, locking in the need to manage coastal retreat worldwide over the coming centuries.

Social science approaches to solar geoengineering

- Interdisciplinary work among social and natural scientists to address the gaps in our SG understanding most relevant for decision-making
- Convening experts on SG and international relations, along with the use of game theory and behavioral experiments and simulations, to better understand the possible evolution of SG strategies and countermoves
- Numerical modeling to integrate the climate and social systems and to understand how multiple interactions "add up" in a consistent framework
- Assessments by sociologists and cultural anthropologists, as well as science and technology studies scholars, to understand how norms and culture evolve as new technologies enter the policy space
- Applications of behavioral science to explore the mental models of relevant decision-makers in government and throughout society with respect to SG and other climate risk reduction strategies

THE WAY FORWARD

In addressing these research themes, we envision contributions from an array of social science disciplines through a mix of approaches (see the box). Effective communication and engagement among the scientific community, decision-makers, and the public on this research could also lead to SG's integration into a broader range of climate change research assessment and synthesis activities (e.g., the Intergovernmental Panel on Climate Change). The governance of social science SG research should also evolve in tandem with broader governance considerations for SG scientific and engineering research.

The evolution of SG social science research should also engage scholars from around the world. The consideration of the justice implications of climate policy can be richer and more credible through a more inclusive approach in undertaking research and the production of evidence. Considering the potential for climate change and SG to have substantial impacts on developing countries, the next generation of SG research should integrate existing scholars and contribute to the training of new scholars in developing countries.

Given the mounting evidence of the economic and social impacts of climate change, the development of new emission mitigation policies and the notable public spending on resilience and adaptation illustrate decision-makers' interest in exploring new ways to combat climate change. Advancing SG social science scholarship—and integrating such research with that undertaken in the physical sciences—can help inform what role SG might or might not play in reducing the risks of climate change. ■

REFERENCES AND NOTES

1. National Academies of Sciences, Engineering, and Medicine, Reflecting Sunlight: Recommendations for Solar Geoengineering Research and Research Governance (National Academies Press, 2021).
2. E. T. Burns *et al*., *Earths Futur*. **4**, 536 (2016).
3. W. Smith, G. Wagner, *Environ. Res. Lett*. **13**, 124001 (2018).
4. J. E. Aldy, R. Zeckhauser, *South. Econ. J*. **87**, 3 (2020).
5. D. Heyen, T. Wiertz, P. J. Irvine, *Clim. Change* **133**, 557 (2015).
6. W. Rickels *et al*., *Energy Econ*. **91**, 104852 (2020).
7. K. Grieger, T. Felgenhauer, O. Renn, J. Wiener, M. Borsuk, *Environ. Syst. Decis*. **39**, 371 (2019).
8. M. Belaia, J.B. Moreno-Cruz, D.W. Keith. *Clim. Chang. Econ*. 2150008 (2021).
9. D. Heyen, J. Horton, J. Moreno-Cruz, *J. Environ. Econ. Manage*. **95**, 153 (2019). https://doi.org/10.1016/j.jeem.2019.03.005
10. A. Parker, J. B. Horton, D. W. Keith, *Earths Futur*. **6**, 1058 (2018).
11. G. Heutel, J. Moreno-Cruz, S. Shayegh, *J. Environ. Econ. Manage*. **87**, 24 (2018).
12. J. Emmerling, M. Tavoni, *Glob. Environ. Change* **53**, 244 (2018).
13. S. Tilmes *et al*., *Earth Syst. Dyn*. **11**, 579 (2020).
14. A. Ghosh, "Environmental Institutions, International Research Programmes, and Lessons for Geoengineering Research" in *Geoengineering our Climate? Ethics, Politics, and Governance*, J. J. Blackstock, S. Low, Eds. (Earthscan-Routledge, 2018).
15. C. Merk, G. Pönitzsch, K. Rehdanz, *Environ. Res. Lett*. **11**, 054009 (2016).

ACKNOWLEDGMENTS

The authors acknowledge Resources for the Future and LAD Climate Fund for sponsoring a series of workshops in 2020 where these ideas were developed. We appreciate many useful intellectual contributions from the workshop participants. J.E.A., T.F., W.A.P., and M.T. acknowledge support from LAD Climate Fund. J.E.A., J.H., and D.K. acknowledge support from the Harvard Solar Geoengineering Research Program. M.E.B., T.F., J.M.-C., W.A.P., and J.B.W. acknowledge support from the National Science Foundation under grant no. SES-1948154. J.L.R. acknowledges support from Open Philanthropy. D.K. serves on the advisory group to the Carnegie Climate Governance Initiative and on the board of directors of Carbon Engineering.

10.1126/science.abj6517



A woman receives a dose of Pfizer-BioNTech COVID-19 vaccine in Skåne County, Sweden.

PHOTO: PETTER ARVIDSON/BILDBYRAN/ZUMA PRESS

ETHICS

Cash incentives, ethics, and COVID-19 vaccination

We can pay people to vaccinate, but should we?

By **Nancy S. Jecker**

Monetary incentives to increase COVID-19 vaccinations are widely used. Do they work? Studies suggest that payments were successfully used to increase vaccination for human papillomavirus in England (*1*), hepatitis B in the United States and United Kingdom (*2*), and tetanus toxoid in Nigeria (*3*). However, little is known about the effect of direct payment or lotteries on COVID-19 vaccination rates. On page 879 of this issue, a new study by Campos-Mercade *et al.* (*4*) shows that monetary incentives changed behavior and increased vaccination in a large group. Yet ethicists hold a range of views about whether we should pay people to vaccinate.

Serbia was the first to adopt payments for COVID-19 vaccinations, announcing a $30 reward (about 5% of the average monthly salary) in May 2021. That same month, vaccinated Hong Kongers became eligible to enter a lottery for a one-bedroom apartment worth $1.4 million and cash prizes totaling $12,890. In July 2021, US President Biden endorsed financial incentives, as did many US states.

Two studies in the United States suggested that using cash to increase COVID-19 vaccination rates might be effective (*5*, *6*), but they relied on self-reports without actually paying people and observing effects. Another US study detected no significant association between lottery announcements and vaccine uptake (*7*). Against this backdrop, Campos-Mercade *et al.* provide much needed insight. They report the results of a randomized controlled trial of unvaccinated people in Sweden (N = 8286) that paid people $24 if they vaccinated within 30 days. They found that vaccination increased 4.2%. No significant group differences emerged based on age, education, race or ethnicity, or income.

Yet questions remain. It is unclear whether participants who vaccinated would have done so eventually, without rewards, or whether paying more would increase vaccination or trigger suspicion and backfire. Research is needed to determine the study's generalizability. Would $24 work in the United States, where 12% of the adult population reported that they would get vaccinated only if required (*8*)? Would it change behavior in sub-Saharan Africa, where 60% of those who would reject the vaccine believe that it is less safe than other vaccines and nearly half think that COVID-19 was planned by foreign actors (*9*)?

WE CAN PAY, BUT SHOULD WE?

Even if it is possible to increase vaccination through cash payments, whether such payments are ethical is a contested issue. Several key issues arise in these debates.

Utility. Arguments defending monetary incentives often appeal to utilitarian principles, claiming that we should use whatever saves the most lives. For example, if education, encouragement, and facilitation fail, a payment-for-risk model is warranted (*10*). One counterargument is that narrowly focusing on saving lives may not be defensible given other urgent goals, like equity. Even if the sole end were saving lives, other means, such as mandates, may yield higher vaccination rates and save more lives.

Liberty. Another defense of monetary incentives puts a premium on minimizing intrusions into people's lives and argues that monetary incentives are the least intrusive method to increase vaccination. One rebuttal is that other measures may work as well and restrict liberty less. For example, conversations with community leaders are less invasive and may work for undocumented immigrants who are concerned about deportation or Catholics who are troubled by fetal cell lines used in vaccine development.

Civic responsibility. Another defense of monetary incentives maintains that they cultivate civic responsibility by rewarding good behavior. A counterargument is that monetary incentives encourage people to do things for money, not to be virtuous citizens. Historically, antivaccinators consistently invoked citizenship to defend their own view, interpreting "good citizenship" to mean honoring diverse views and respecting the bodies of neighbors (*11*).

Equity. Arguments against cash incentives point to unequal effects on different segments of society (*12*). For example, a $100 cash incentive may not feel coercive to prosperous people, yet it might to people who lost jobs during the pandemic. A rejoinder is that it increases equality to pay people who are financially struggling. Yet such a one-time modest payment is unlikely to make a lasting difference in the lives of marginalized people. Another reply is that cash incentives increase equity by reducing infections in hard-hit groups. But this can be done without leveraging economic hardship to increase vaccination.

Exploitation. Opponents of monetary incentives argue that they might be exploitive, "taking advantage of [people] who have lost jobs, experienced food and housing insecurity, or slipped into poverty" (*13*). Although some counter that cash inducements are not exploitive because they encourage a less risky choice (vaccination) (*14*), this misses the mark. What makes a transaction exploitive is

Department of Bioethics and Humanities, University of Washington School of Medicine, Seattle, WA, USA.
Email: nsjecker@uw.edu

not its beneficial or harmful effects, but the nature of the transaction itself. Exploitive transactions use a person's vulnerability to achieve someone else's goals.

Autonomy. Other opponents argue that substituting cash for conversation insults the autonomy of vaccine refusers, signaling that their decisions can be bought. With lotteries, cash awards can manipulate decisions by leveraging cognitive biases, such as "probability neglect," which leads people to irrationally interpret probabilities in their favor (*15*). Defenders of monetary incentives might reply that it is paternalistic to assume that people offered cash cannot decide for themselves. Even if excessive payment or high-stakes lotteries unduly induce people to participate, modest cash awards do not. We also routinely pay people in other settings—for example, for research participation. In reply, safeguarding autonomy calls for mitigating cognitive biases, not manipulating them. Even modest cash awards could unduly induce the least well-off to take part. The purpose of paying research subjects is compensating time and expenses, not inducing participation.

PROCEED WITH CAUTION

Policy-makers considering payment for vaccination should proceed with caution. Cash payments in Sweden may face fewer equity concerns than they do in low-income countries or for countries with meager safety nets and income inequality. In the United States, for example, cash incentives may be more exploitive and manipulative, and race-related differences in wealth could compound this effect for some minorities. Whether monetary incentives for vaccination are ethically sound or morally dubious may depend on the setting to which they are applied. ■

REFERENCES AND NOTES

1. E. Mantzari *et al.*, *Health Psychol.* **34**, 160 (2015).
2. S. Tressler, R. Bhandari, *Open Forum Infect. Dis.* **6**, ofz521 (2019).
3. R. Sato, B. Fintan, *Hum. Vaccin. Immunother.* **16**, 1181 (2020).
4. P. Campos-Mercade *et al.*, *Science* **374**, 879 (2021).
5. L. Vavreck, "$100 as incentive to get a shot? Experiment suggests it can pay off," *New York Times*, 4 May 2021.
6. C. Robertson *et al.*, *J. Law Biosci.* **8**, lsab027 (2021).
7. D. Dave *et al.*, *JAMA Health Forum* **2**, e213117 (2021).
8. L. Hamel *et al.*, KFF Covid-19 vaccine monitor: September 2021, Kaiser Family Foundation, 28 September 2021; https://www.kff.org/coronavirus-covid-19/poll-finding/kff-covid-19-vaccine-monitor-september-2021/.
9. Africa CDC, COVID 19 vaccine perceptions: A 15 country study, February 2021; https://africacdc.org/download/covid-19-vaccine-perceptions-a-15-country-study/.
10. J. Savulescu, J. Pugh, D. Wilkinson, *Nat. Med.* **27**, 1500 (2021).
11. N. Durbach, *Bodily Matters: The Anti-Vaccination Movement in England, 1853–1907* (Duke Univ. Press, 2004).
12. N. S. Jecker, *J. Med. Ethics* 10.1136/medethics-2021-107235 (2021).
13. E. A. Largent, F. G. Miller, *JAMA* **325**, 534 (2021).
14. G. Persad, E. J. Emanuel, *JAMA* **326**, 221 (2021).
15. A. Oza, *Science* **373**, 611 (2021).

10.1126/science.abm6400

GEOLOGY

Perovskite retrieved from the lower mantle

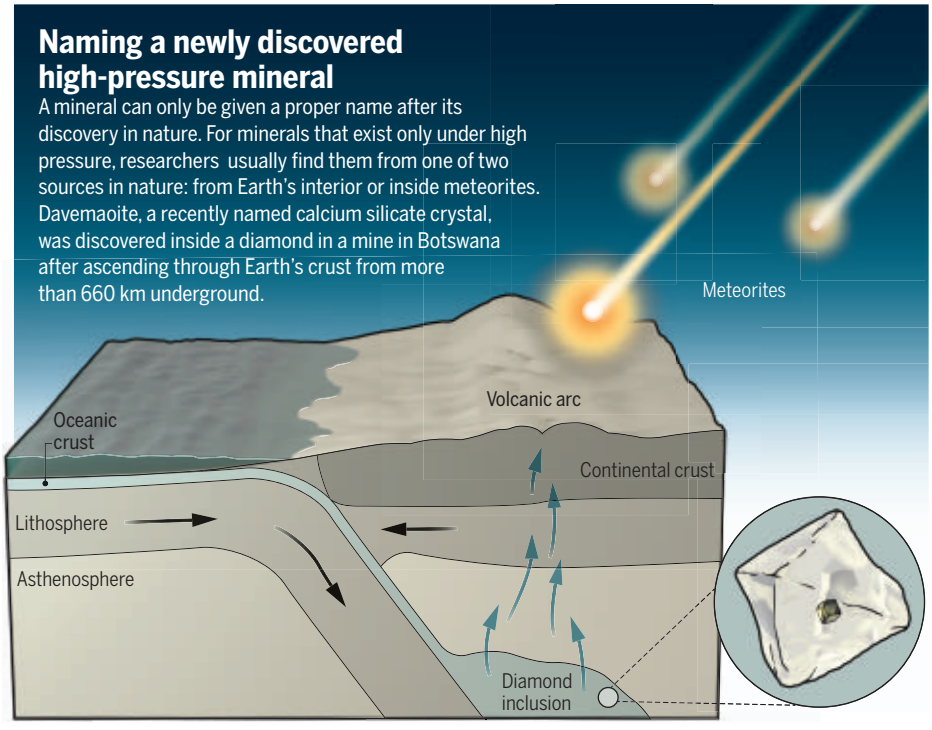
The calcium silicate compound was characterized and named as "davemaoite"

By **Yingwei Fei**

No one has ever successfully retrieved a high-pressure calcium silicate from the lower mantle before. This is because the high-pressure $CaSiO_3$-perovskite is "unquenchable," meaning that it cannot retain its structure after being removed from its high-pressure environment. On page 891 of this issue, Tschauner *et al.* (*1*) report the first-ever silicate obtained from Earth's lower mantle. They have coined the crystalline compound "davemaoite." The sample is a $CaSiO_3$-perovskite trapped inside of a diamond from the lower mantle. The authors provide definitive evidence for a structurally preserved cubic $CaSiO_3$-perovskite by means of synchrotron x-ray diffraction.

The possibility that a high-pressure phase of $CaSiO_3$ might exist in the lower mantle was first suggested in 1967 in a study of $CaSiO_3$-$CaGeO_3$ perovskite-type solid solution (*2*). In 1975, scientists successfully synthesized the $CaSiO_3$- perovskite high-pressure phase with a cubic structure by using a laser-heated diamond anvil cell (*3*). Because of the unquenchable nature of the $CaSiO_3$-perovskite phase, its structure has never been fully refined with single-crystal x-ray diffraction, but powder x-ray diffraction data are broadly consistent with either a cubic perovskite structure (*3*, *4*) or tetragonal symmetry, with very small differences between its long and short axis (*5*, *6*). The natural sample obtained by Tschauner *et al.* shows an x-ray diffraction pattern consistent with that of the synthetic $CaSiO_3$-perovskite high-pressure phase. Named after Dave Mao (also known as Ho-kwang Mao), an experimental geophysicist who contributed to high-pressure research over the past 50 years, davemaoite was approved as a new natural mineral by the Commission of New Minerals, Nomenclature, and Classification of the International Mineralogical Association.

Earth and Planets Laboratory, Carnegie Institution for Science, 5241 Broad Branch Road, NW, Washington DC 20015, USA. Email: yfei@carnegiescience.edu



GRAPHIC: V. ALTOUNIAN/*SCIENCE*

As of today, davemaoite is the first and only high-pressure silicate recovered from the lower mantle. Together with the 2014 discovery of another lower-mantle mineral "bridgmanite," found inside a meteorite and named after physicist Percy Bridgman (*7*), the two form an exclusive club as the only lower-mantle silicate minerals confirmed in nature. The discovery of these high-pressure phases in nature reflects the technological advancement in the characterizations of minerals at the submicrometer scale. Recovery of davemaoite and bridgmanite provides two distinct pathways for obtaining high-pressure phases in nature: through rising mantle rocks from deep interior and through falling meteorites that were highly shocked because of collisions of planetary bodies (see the figure).

The ability of a material to preserve the high-pressure phase in materials depends heavily on what happens once the pressure is removed. Synthetic $CaSiO_3$-perovskite has been observed to revert to glass upon release from high pressure (*3*, *4*); thus, it was considered impossible to retrieve the high-pressure phase from the lower mantle. This expectation was further strengthened by bridgmanite—which has a more stable high-pressure phase than davemaoite—having never been recovered from the lower mantle, only having been found serendipitously in a highly shocked meteorite (*7*).

The high residual pressure of the entrapped davemaoite in the host diamond is likely to have helped preserve the structure by slowing down the retrogression of davemaoite back to its low-pressure phase. Residual pressure in diamond is often observed because of the relative volume difference between the entrapped phase and diamond in responding to their formation condition.

The pressure-temperature-time pathways also play an important role in the survival of the high-pressure phase as the davemaoite made its journey to the surface. Not all davemaoites embedded in deep diamonds can stay as davemaoites, and there have been multiple studies of $CaSiO_3$ inclusions in the diamonds where the high-pressure cubic perovskite phase was nowhere to be found (*8*–*13*). For example, the $CaSiO_3$ sample from a mine in Mato Grasso of Brazil should have formed in its high-pressure phase because it was found alongside hydrous ringwoodite that had remained in the high-pressure phase inside the same super-deep diamond (*8*). However, spectroscopic measurements revealed that the $CaSiO_3$ had reverted to an intermediate-pressure polymorph known as breyite. Another $CaSiO_3$ inclusion, found in a diamond from the Cullinan mine in South Africa (*9*), also did not have sufficient evidence to link it to the synthetic cubic $CaSiO_3$-perovskite phase. In recent years, it has been recognized that breyite is one of most abundant inclusions found in these super-deep diamonds, and its abundance has fueled an ongoing debate on the formation depth of the $CaSiO_3$ inclusions and the survivability of the cubic $CaSiO_3$-perovskite phase (*10*–*13*). The discovery of davemaoite by Tschauner *et al.* demonstrates a viable pathway to recover the cubic $CaSiO_3$-perovskite phase from the lower mantle and opens the door for the recovery of other seemingly "unquenchable" high-pressure phases.

The davemaoite sample recovered by Tschauner *et al.* might have been special because of its very high potassium content. According to chemical composition analysis, the davemaoite sample has more than half of calcium atoms replaced by other elements, such as potassium, iron, and aluminum. In comparison, the unquenchable synthetic $CaSiO_3$-perovskite is usually relatively pure in composition, even when it is synthesized by using natural basalts or peridotites. It is possible for the davemaoite sample to have retained its high-pressure phase because of the substituted calcium atoms, which can be the focus of future experiments. The high potassium content of the davemaoite sample also points toward some chemical heterogeneity in the lower mantle, such as the regional differences in potassium concentration.

The work by Tschauner *et al.* inspires hope in the discovery of other difficult high-pressure phases in nature, either through careful search in deep-origin diamonds or in highly shocked meteorites. The successful retrieval of davemaoite from the lower mantle encourages the ongoing search for bridgmanite from the Earth's lower mantle. Such direct sampling of the inaccessible lower mantle would fill our knowledge gap in chemical composition and heterogeneity of the entire mantle of our planet. ■

REFERENCES AND NOTES

1. O. Tschauner *et al.*, *Science* **374**, 891 (2021).
2. A. E. Ringwood, A. Major, *Earth Planet. Sci. Lett.* **2**, 106 (1967).
3. L. G. Liu, A. E. Ringwood, *Earth Planet. Sci. Lett.* **28**, 209 (1975).
4. H. K. Mao *et al.*, *J. Geophys. Res.* **94** (B12), 17889 (1989).
5. S.-H. Shim, R. Jeanloz, T. S. Duffy, *Geophys. Res. Lett.* **29**, 2166 (2002).
6. H. W. Chen *et al.*, *Am. Mineral.* **103**, 462 (2018).
7. O. Tschauner *et al.*, *Science* **346**, 1100 (2014).
8. D. G. Pearson *et al.*, *Nature* **507**, 221 (2014).
9. F. Nestola *et al.*, *Nature* **555**, 237 (2018).
10. C. Anzolini *et al.*, *Am. Mineral.* **103**, 69 (2018).
11. E. M. Smith *et al.*, *Nature* **560**, 84 (2018).
12. A. B. Woodland, A. V. Girnis, V. K. Bulatov, G. P. Brey, H. E. Höfer, *Eur. J. Mineral.* **32**, 171 (2020).
13. F. E. Brenker, F. Nestola, L. Brenker, L. Peruzzo, J. W. Harris, *Am. Mineral.* **106**, 38 (2021).

10.1126/science.abm4742

GEOCHEMISTRY

A surprise from the deep

Isotope patterns of methoxyl groups reveal the origin and production potential of methane from coal

By **Frank Keppler**[1,2]

In 1885, Simon Zeisel established a method to quantify the content of methoxyl groups in plant tissue (*1*). He certainly could not have envisaged how his work would advance environmental research and our understanding of carbon cycling, particularly with regard to the formation of volatile compounds containing a one-carbon unit—C1 compounds—such as methane, methanol, or chloromethane. These volatile compounds play an important role in atmospheric chemistry and physics. On page 894 of this issue, Lloyd *et al.* (*2*) report the concentration and isotopic patterns of methoxyl groups for humic samples at different stages of coalification—the process by which vegetative matter is converted into coal. They show the involvement of microbes in transforming plant matter in deep-Earth subsurface sediments over geological time scales and establish their contribution to the occurrence of coal-bed methane (CBM) and its limits for exploitation.

Chemically, methoxyl or methoxy defines a methyl group bound to an oxygen atom in an organic molecule (R–OCH). These functional groups, which contribute to biochemical reactions under specific conditions, are ubiquitous in terrestrial plant matter and can constitute up to 7% of wood. Most methoxyl groups in wood are found in lignin as a component of coniferyl or synapyl alcohol (*3*). During humification of plant matter and further maturation processes in sediments, lignite methoxyl content increases up to 10% on a total weight basis because lignin is more stable than other plant components, such as cellulose or starch, which are lost during the initial phase of humification. Further coalification processes under increased temper-

[1]Biogeochemistry Group, Institute of Earth Sciences, Heidelberg University, Heidelberg, Germany.
[2]Heidelberg Center for the Environment (HCE), Heidelberg University, Heidelberg, Germany.
Email: frank.keppler@geow.uni-heidelberg.de

atures and higher pressures in deeper parts of Earth's crust lead to side chain degradation of aromatic compounds and demethylation of the methoxyl groups (*4*, *5*). The loss of methoxyl groups is thus a key stage in the transformation of wood to coal and likely an important source of methane in coal beds. However, whether the mechanism of this process is purely a chemical reaction by thermal decomposition (thermogenic methane) or an enzyme-catalyzed biodegradation by microbes (microbial methane) has been vigorously debated for many years.

Recent evidence supports microbial methanogenesis in coal-bearing marine sediments at depths down to 2.5 km (*6*). Additionally, specific methanogens belonging to the genus *Methermicoccus* can utilize coal methoxyl groups to produce methane (*7*). However, the extent to which methanogens transform methoxyl groups to methane in the deep subsurface is still unknown.

Progress in understanding the key role that plant methoxyl groups play in forming C1 volatiles came about by exploiting the Zeisel reaction (to determine the number of methoxyl groups) and isotope ratio mass spectrometry. This enabled measurement of the ratio of the naturally occurring stable isotopes of carbon (the amount of ^{13}C relative to ^{12}C, expressed as $\delta^{13}C$ values) of the methoxyl groups. The $\delta^{13}C$ values of these groups can be utilized not only to gain deeper insights into the processes that control the formation of C1 volatiles in the environment but also to trace the origin of several atmospheric C1 gases (*8*). In this context, it is important to note that, traditionally, thermogenic methane is considered to contain more ^{13}C than microbial methane, which therefore has more negative $\delta^{13}C$ values (*9*).

Lloyd *et al.* measured both the abundance and isotopic fingerprint of methoxyl groups from organic matter collected from several localities around the globe that represent the major maturity stages, from wood to bituminous coal. They suggest that microorganisms directly metabolize coal structures that fuel methane formation in deep sediments (see the figure). These results are of considerable interest for understanding methane generation from organic carbon of terrestrial deep and surface sediments and the cycling of carbon in the past, present, and future.

The reported carbon isotopic patterns of coal methoxyl groups support the idea that microbial-mediated processes rather than abiotic reactions drive methane formation from plant methoxyl groups on geological time scales of tens of millions of years. It is also important to point out that the results considerably expand the measured range of carbon isotopic signatures for methoxyl groups on Earth, as Lloyd *et al.* reported very positive $\delta^{13}C$ values [up to +27 per mil (‰)], which are usually only observed for organic compounds from extraterrestrial environments, such as meteorites. Thus, when considering the source substrate, these isotopic constraints might elegantly explain why CBM often shows an enrichment in ^{13}C that nevertheless could still be of microbial origin. These results will also alter thinking about the traditional assignment of isotopic patterns of methane sources (*9*) because they offer a straightforward explanation for why microbial methane from coal is often enriched in ^{13}C relative to other microbial methane sources.

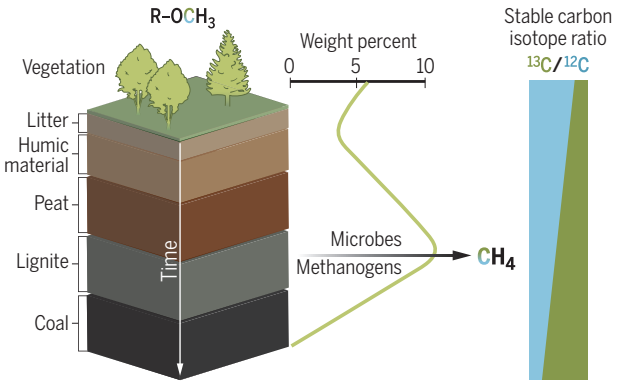
"The reported carbon isotopic patterns of coal methoxyl groups support the idea that microbial-mediated processes rather than abiotic reactions drive methane formation from plant methoxyl groups on geological time scales of tens of millions of years."

Currently, CBM makes up a substantial portion of the world's natural gas resources and may become a transition fuel when moving from a carbon-based to a sustainable green economy. It may displace coal in electricity generation, thereby reducing carbon dioxide emissions and greatly decreasing emissions of particulate matter and other pollutants, such as sulfur. However, CBM production wells often have limited life spans, and thus there are efforts to enhance microbial methanogenesis in coal beds (*10*, *11*). The abundance of methoxyl groups in the lignite and coal samples reported by Lloyd *et al.* not only show that these groups affect the yield of CBM, they limit the potential production of methane from coal by the addition of microbes when almost all methoxyl groups have already been removed during maturation processes. A major known downside of mining activities is that the release of CBM currently accounts for 5 to 10% of the global atmospheric methane budget and thus contributes to global climate change (*12*).

The potent role of methane as a greenhouse gas is also of interest when the findings of Lloyd *et al.* are considered for future carbon cycling and global climate change, given the potential thawing of large permafrost areas that are considered to be one of the tipping elements of the Earth system (*13*). The methoxyl moieties in the vast amounts of organic matter that have accumulated over thousands of years and have been preserved for up to 650,000 years in permafrost (*14*) might be rapidly transformed to methane by methanogens once warmer climates allow their growth and multiplication. If not consumed by degrading microbes, the formed methane might eventually end up in the atmosphere, potentially providing a positive feedback on climate change. ■

The fate of methoxyl groups: From plants to coal

Microbial conversion of methoxyl groups plays an important role in generating methane on geological time scales.



GRAPHIC: N. CARY/*SCIENCE*

REFERENCES AND NOTES

1. S. Zeisel, *Monatsh. Chem.* **6**, 989 (1885).
2. M. K. Lloyd *et al.*, *Science* **374**, 894 (2021).
3. W. Boerjan, J. Ralph, M. Baucher, *Annu. Rev. Plant Biol.* **54**, 519 (2003).
4. P. G. Hatcher, D. J. Clifford, *Org. Geochem.* **27**, 251 (1997).
5. H. Lee, X. Feng, M. Mastalerz, S. J. Feakins, *Org. Geochem.* **136**, 103894 (2019).
6. F. Inagaki *et al.*, *Science* **349**, 420 (2015).
7. D. Mayumi *et al.*, *Science* **354**, 222 (2016).
8. F. Keppler, R. M. Kalin, D. B. Harper, W. C. McRoberts, J. T. G. Hamilton, *Biogeosciences* **1**, 123 (2004).
9. M. J. Whiticar, in *Hydrocarbons, Oils and Lipids: Diversity, Origin, Chemistry and Fate*, H. Wilkes, Ed. (Springer, 2020), pp. 669–746.
10. D. Ritter *et al.*, *Int. J. Coal Geol.* **146**, 28 (2015).
11. D. Strąpoć *et al.*, *Annu. Rev. Earth Planet. Sci.* **39**, 617 (2011).
12. M. Saunois *et al.*, *Earth Syst. Sci. Data* **12**, 1561 (2020).
13. W. Steffen *et al.*, *Proc. Natl. Acad. Sci. U.S.A.* **115**, 8252 (2018).
14. J. B. Murton *et al.*, *Quat. Res.* 10.1017/qua.2021.27(2021).

10.1126/science.abm6027

NEURODEGENERATION

Autoimmunity in neurodegeneration

A signaling axis in adaptive immunity is a potential target in Lewy body dementia

By **Maria Krot**[1,2] *and* **Asya Rolls**[1,2]

Lewy body dementia (LBD) is the second most prevalent form of dementia. In LBD, a neurodegenerative process driven by pathological accumulation of the presynaptic neuronal protein α-synuclein in the central nervous system (CNS) leads to motor and cognitive deficits (*1*). Existing therapies are unable to slow or arrest the progression of LBD. T cells that are reactive to α-synuclein were found in blood samples of LBD patients (*2*), adding to the evidence suggesting that the adaptive immune system is involved in LBD pathogenesis. However, the role of T cells in the neurodegenerative process is still unclear, limiting the potential of therapeutic intervention. On page 868 of this issue, Gate *et al.* (*3*) demonstrate the involvement of inflammatory and autoimmune T helper 17 (T_H17) cells in neurodegeneration in LBD patients. A specific signaling axis that induces T_H17 cell trafficking to the CNS could be a therapeutic target for LBD.

The CNS is an immune-privileged site, confined by barriers that were assumed to isolate it from the systemic immune response. However, it is now clear that the immune system is required for nervous system activity. Because the immune system is much more accessible for manipulation than the brain, immune-modulating drugs could be repurposed to treat nervous system disorders—for example, targeting inhibitory immune checkpoints to unleash the adaptive immune system to treat Alzheimer's disease (*4*).

LBD encompasses two disorders, dementia with Lewy bodies (DLB) and Parkinson's disease dementia (PDD), both characterized by formation of Lewy bodies (abnormal deposits of α-synuclein) in the brain and progressive loss of dopaminergic neurons. Gate *et al.* characterized T cell populations in the cerebrospinal fluid (CSF) of PDD and DLB patients relative to healthy controls using single-cell RNA sequencing (scRNA-seq). In line with previous data showing higher amounts of the pro-inflammatory cytokine interleukin-17A (IL-17A) in the blood of LBD patients (*5*), the authors revealed alterations in a specific memory subset of T_H17 cells in the CSF of LBD patients.

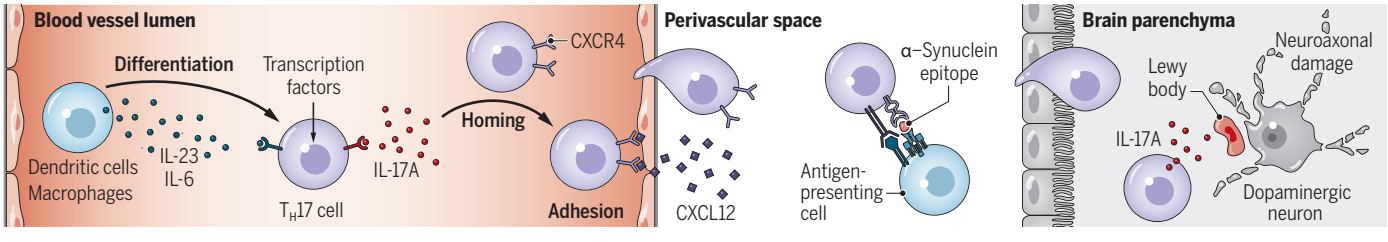
T_H17 cells are a proinflammatory $CD4^+$ T cell population that secretes mainly IL-17A (*6*). T_H17 cells are involved in the pathogenesis of autoimmune diseases such as psoriasis, rheumatoid arthritis, inflammatory bowel disease, and multiple sclerosis (MS) (*7*). In MS, for example, T_H17 cells infiltrate the brain, leading to autoimmunity, neuroinflammation, and neurodegeneration (*6*). Gate *et al.* propose that autoimmunity also plays a role in LBD. They show that T_H17 cells in the CSF of LBD patients are more active, are clonally expanded, and show higher activation levels after stimulation with α-synuclein peptides ex vivo. The presence of α-synuclein-reactive T_H17 cells in the CSF of LBD patients suggests that these cells may home to the LBD brain and induce specific autoimmune proinflammatory responses against α-synuclein deposits, leading to neuronal cell death (see the figure). Indeed, Gate *et al.* confirmed the presence of IL-17A–expressing $CD4^+$ T cells near dopaminergic neurons that were undergoing neurodegeneration. Several therapies are currently available to target T_H17 cells: Monoclonal antibodies that neutralize IL-17A activity treat psoriasis (*7*), or monoclonal antibodies that block cell adhesion molecules required for leukocyte trafficking to the brain are a treatment for MS (*8*).

Although some studies show an increase in T cell infiltration into the LBD brain (*9*), it is not clear what mechanisms regulate the trafficking of these cells. Chemokines, such as C-X-C motif chemokine ligand 12 (CXCL12), play a role in directing C-X-C motif chemokine receptor 4 (CXCR4)–expressing immune cells into the brain (*10*). Gate *et al.* found that T_H17 cells in the CSF of LBD patients highly express CXCR4, suggesting that trafficking of activated T_H17 cells to the LBD brain occurs through CXCR4-CXCL12 signaling. In further support of this, Gate *et al.* found CXCR4-expressing T cells that reside in the perivascular space near CXCL12-expressing cerebrovascular endothelial cells in postmortem PDD brains. Moreover, the CSF concentrations of CXCL12 were increased and positively correlated with neurodegeneration in PDD and DLB patients. Activation of the CXCR4-CXCL12 axis has been implicated in a variety of pathological conditions in the CNS, including neurodegeneration and autoimmunity. For example, expression of CXCL12 is up-regulated in microvessel endothelial cells in MS lesions (*11*). The activation of this pathway may reflect a potential endogenous repair mechanism: It was suggested that increased expression of CXCL12 by reactive vasculature in neurodegenerative lesions signals the initiation of tissue repair by enhancing recruitment of neural progenitor cells (*12*).

[1]Department of Immunology, Rappaport Faculty of Medicine, Technion–Israel Institute of Technology, Haifa, Israel. [2]Department of Neuroscience, Rappaport Faculty of Medicine, Technion–Israel Institute of Technology, Haifa, Israel. Email: rolls@tx.technion.ac.il

Immunotherapy targets in Lewy body dementia

In Lewy body dementia (LBD), a proinflammatory subset of T helper 17 (T_H17) cells recognizes α-synuclein, the major component in Lewy bodies. These T cells express C-X-C motif chemokine receptor 4 (CXCR4) and infiltrate the brain through recognition of C-X-C motif chemokine ligand 12 (CXCL12) produced by endothelial cells. Here, T_H17 cells recognize α-synuclein epitopes and become activated, secreting the inflammatory cytokine interleukin-17A (IL-17A), potentially leading to autoimmune neuroaxonal damage. Targeting T_H17 differentiation or CXCR4-CXCL12–mediated homing to the brain are potential therapeutic strategies for LBD.



GRAPHIC: KELLIE HOLOSKI/*SCIENCE*

The study by Gate *et al.* provides important evidence from human patients for the relevance of this immune pathway as a potential disease-modifying therapeutic target for LBD. As this homing pathway is not specific to the CNS, CXCR4 antagonists have been developed and are effective in treating various immune-related conditions (*13*). Nevertheless, it is worth considering the possibility that these immune cells are part of a corrective response, rather than the cause of damage. Uncovering the functional role of CXCR4$^+$ T_H17 cells in disease etiology will allow the design of treatments to harness the therapeutic potential of an effective immune reaction. Indeed, the concept of autoimmunity is undergoing a revision, because its beneficial role in physiology has become increasingly apparent. A recent theory proposes that autoimmunity is targeted against regulatory and secreting cells, such as β cells in the pancreas, to maintain endocrine regulation (*14*). It will be interesting to consider how this model could be extended to the nervous system and whether autoimmunity is directed more specifically to some types of neurons (e.g., neuropeptide-secreting neurons).

The increasing evidence for the participation of immune mediators in various neurodegenerative conditions, including LBD, Alzheimer's disease, and MS, strengthens the need to understand the neuroimmune dialogue in health and disease. Much of the accumulated evidence comes from animal models and suffers from the limitations of such models and their relevance to humans, highlighting the importance of the Gate *et al.* study. Moreover, because the clinical manifestations of many neurodegenerative diseases appear after substantial damage has already occurred, it is critical to find biomarkers, such as specific immune cells, that define earlier stages of the disease. ■

REFERENCES AND NOTES

1. N. A. Arnaoutoglou, J. T. O'Brien, B. R. Underwood, *Nat. Rev. Neurol.* **15**, 103 (2019).
2. D. Sulzer *et al.*, *Nature* **546**, 656 (2017).
3. D. Gate *et al.*, *Science* **374**, 868 (2021).
4. K. Baruch *et al.*, *Nat. Med.* **22**, 135 (2016).
5. A. Surendranathan *et al.*, *Brain* **141**, 3415 (2018).
6. A. Peters, Y. Lee, V. K. Kuchroo, *Curr. Opin. Immunol.* **23**, 702 (2011).
7. E. Storelli *et al.*, *Front. Neurol.* **10**, 13 (2019).
8. E. Kawamoto, S. Nakahashi, T. Okamoto, H. Imai, M. Shimaoka, *Autoimmune Dis.* 2012, 357101 (2012).
9. H. González, R. Pacheco, *J. Neuroinflammation* **11**, 201 (2014).
10. S. Man *et al.*, *Sci. Transl. Med.* **4**, 119ra14 (2012).
11. T. M. Calderon *et al.*, *J. Neuroimmunol.* **177**, 27 (2006).
12. M. Li, J. S. Hale, J. N. Rich, R. M. Ransohoff, J. D. Lathia, *Trends Neurosci.* **35**, 619 (2012).
13. N. D. Stone *et al.*, *Antimicrob. Agents Chemother.* **51**, 2351 (2007).
14. Y. K. Kohanim, A. Tendler, A. Mayo, N. Friedman, U. Alon, *Immunity* **52**, 872 (2020).

ACKNOWLEDGMENTS

The authors thank S. Schwarzbaum for help with the manuscript.

10.1126/science.abm4739

AGING

Long-lived fish in a big pond

The genetic drivers of extreme longevity in Pacific Ocean rockfish are identified

By **J. Yuyang Lu, Andrei Seluanov, Vera Gorbunova**

Because of competitors, predators, pathogens, and other hazards, most individuals in natural populations die or are killed before they reach advanced age. In such a scenario, natural selection does not act on genes that are expressed at old age, a so-called selection shadow. As a result, genes and pathways that are important for maintaining health at advanced ages are not selected for, making aging an inevitable product of evolution (*1*). However, species have an amazing diversity of life spans, which provide insights into the mechanisms of aging and life span control (*2*). Some species of Pacific rockfish have maximum life spans of up to 150 years and are believed to lack age-associated decline. On page 842 of this issue, Kolora *et al.* (*3*) assembled the genomes of 88 rockfish species to identify genetic drivers of longevity.

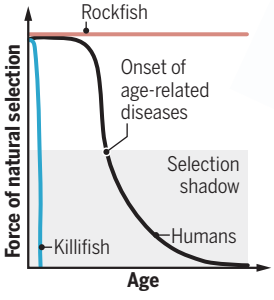
DNA damage accumulates throughout life and has been implicated as a major cause of aging (*4*). To minimize these lesions, a complex network that senses and repairs DNA damage has evolved in various organisms (*5*). Kolora *et al.* reveal that positively selected genes in long-lived rockfish (those that live more than 105 years) are enriched for DNA double-stranded break repair pathways, whereas no gene pathway was enriched in short-lived rockfish (those that live less than 20 years). Longer-lived mammals also maintain DNA better. A study of 18 rodent species with diverse life spans revealed that more robust DNA double-stranded break repair coevolves with longevity (*6*). The difference in DNA repair efficiency was largely due to a more powerful version of a genome maintenance gene, sirtuin 6 (*Sirt6*), in long-lived rodents. The DNA repair genes that are positively selected in the long-lived rockfish also undergo positive selection in the bowhead whale (*7*), whose maximum life span is more than 200 years. Besides DNA repair, genes involved in nutrient sensing show lower evolutionary rates in long-lived rockfish. However, for another vertebrate model in aging research, the short-lived African killifish (which live less than 1 year), the accumulation of deleterious genetic variants, or relaxation of selection, was observed in genes involved in DNA repair and nutrient sensing (*8*). Overall, studies of diverse vertebrate species support DNA repair as a longevity determinant.

Why are DNA repair and other longevity genes positively selected in long-lived rockfish but not in short-lived rockfish and killifish? Living organisms experience DNA damage throughout their life, which can result in the accumulation of mutations and epigenetic changes. Indeed, increased

Evolution of longevity genes in species with different life strategies

Selection pressure

The force of natural selection declines as a function of age in killifish and humans, but not in rockfish.



Longevity genes

Rockfish and killifish show distinct selection patterns of longevity-regulating genes.





	DNA repair	Nutrient sensing pathways	Immunity
ROCKFISH			
Stable environment Low adult mortality	Positive selection (*FEN1*, *WRAP53*, etc.)	Low evolutionary rate (*IGF1*, *FOXO1*, etc.)	Expansion of immunosuppressive genes (butyrophilins)
KILLIFISH			
Changing environment High mortality	Relaxed selection (*MSH2*, *MSH6*, etc.)	Relaxed selection (*mTOR*, *INSR*, etc.)	Loss of immunity genes

FEN1, flap structure-specific endonuclease 1; *FOXO1*, forkhead box O1; *IGF1*, insulin-like growth factor 1; *INSR*, insulin-like growth factor 1 receptor; *MSH*, mutS homolog; *mTOR*, mechanistic target of rapamycin; *WRAP53*, WD repeat containing, antisense to TP53.

GRAPHIC: N. DESAI/*SCIENCE*

genetic mosaicism (whereby cells have different mutational profiles) and transcriptomic heterogeneity were observed in aged mice (*9*). Relaxed selection is manifested as a reduction in the strength of natural selection on particular traits that were formerly important. Short-lived killifish face variable and harsh weather conditions that strongly shape mortality. Thus, genes required for maintenance, such as DNA repair, become less important in short-lived killifish compared with their long-lived counterparts and are under relaxed selection (*8*).

Short-lived rockfish, which are smaller and inhabit shallower waters than long-lived rockfish, might confront more hazards such as competitors, predators, and pathogens. These factors could increase the extrinsic mortality and thus lead to a more relaxed selection in genes with a beneficial role during late life stages, such as DNA repair genes. By contrast, long-lived rockfish are larger in size and inhabit deeper parts of the ocean. Notably, the fecundity of rockfish increases as a function of age, proportional to weight. For instance, 150-year-old yelloweye rockfish can produce more than 1 million offspring per season. In this respect, extra investment in DNA repair can protect the long-lived rockfish from age-associated diseases and substantially increase fecundity at older ages, which would further facilitate the positive selection of DNA repair genes.

Relaxed selection is correlated with genome expansion in killifish, which is mainly attributable to transposable elements (TEs) (*8*). The activity of TEs can promote DNA damage and genome instability that further lead to aging and age-associated diseases (*10*). Furthermore, activation of TEs in humans and mice can drive interferon-induced sterile inflammation, a hallmark of aging in the mouse and human (*11*, *12*). Hence, it will be interesting to see whether TEs are involved in the regulation of longevity in rockfish.

Kolora *et al.* show an expansion of the immunosuppressive butyrophilin gene family in long-lived rockfish, suggesting a tighter control of inflammation. Long-lived rockfish may tolerate the reduced inflammatory function because of a decreased abundance of microbes in the deeper ocean. Inflammaging (increased systemic inflammation with age) has emerged as an important hallmark of aging, and evolutionary strategies that reduce inflammation favor longevity. Indeed, other long-lived animals, such as bats, appear to down-regulate inflammation through diverse mechanisms. For example, the PYHIN family of cytoplasmic DNA sensors is absent in several bat species (*13*).

DNA CpG methylation has been used to build epigenetic clocks to predict chronological age and biological age and to test antiaging interventions (*14*). Kolora *et al.* show that the evolution of different rockfish life histories reshapes the mutational spectrum that drives CpG-to-TpG variants (which can no longer be methylated) in long-lived species. Given the key regulatory roles of the CpG sequence, it is unclear what the genomic distribution of CpG-to-TpG variants in long-lived species is—is it genome-wide or at specific regions? Does it alter gene expression?

The study of Kolora *et al.* presents rockfish as a distinct model that is long-lived while maintaining high fecundity at old age, thereby increasing selection of prolongevity genes. Humans, despite being long-lived, have relatively short reproductive life spans and hence are susceptible to relaxed selection of maintenance pathways at older ages, contributing to age-associated diseases (see the figure). Comparative biology is a fruitful approach to study longevity. Humans live longer than most vertebrates, but long-lived rockfish can offer humans strategies for improvement. Genetic adaptations found in rockfish illustrate that strategies that improve DNA repair and control inflammation may extend life span and health span. The genome assemblies generated by Kolora *et al.* will enable further studies of rockfish as a model of longevity. Yet genomic DNA sequence alone cannot fully explain the aging process. Although the DNA sequence is constant in all cell types of a species, the gene regulatory network of each cell can vary considerably, contributing to dynamic gene expression programs and biological functions. Comparative transcriptomics, proteomics, and metabolomics will reveal further layers of aging and longevity regulation. ■

REFERENCES AND NOTES

1. W. D. Hamilton, *J. Theor. Biol.* **7**, 1 (1964).
2. V. Gorbunova, A. Seluanov, Z. Zhang, V. N. Gladyshev, J. Vijg, *Nat. Rev. Genet.* **15**, 531 (2014).
3. S. R. R. Kolora *et al.*, *Science* **374**, 842 (2021).
4. B. Schumacher, J. Pothof, J. Vijg, J. H. J. Hoeijmakers, *Nature* **592**, 695 (2021).
5. B. Zhao, E. Rothenberg, D. A. Ramsden, M. R. Lieber, *Nat. Rev. Mol. Cell Biol.* **21**, 765 (2020).
6. X. Tian *et al.*, *Cell* **177**, 622 (2019).
7. M. Keane *et al.*, *Cell Rep.* **10**, 112 (2015).
8. R. Cui *et al.*, *Cell* **178**, 385 (2019).
9. Tabula Muris Consortium, *Nature* **583**, 590 (2020).
10. V. Gorbunova *et al.*, *Nature* **596**, 43 (2021).
11. M. Simon *et al.*, *Cell Metab.* **29**, 871 (2019).
12. M. De Cecco *et al.*, *Nature* **566**, 73 (2019).
13. V. Gorbunova, A. Seluanov, B. K. Kennedy, *Cell Metab.* **32**, 31 (2020).
14. S. Horvath, K. Raj, *Nat. Rev. Genet.* **19**, 371 (2018).

Department of Biology, University of Rochester, Rochester, NY, USA. Email: vera.gorbunova@rochester.edu

10.1126/science.abm3392

BIOMATERIALS

A dynamic duo

Self-assembly of nanofibers facilitates the repair of spinal cord injury in mice

By **Jonathan P. Wojciechowski** *and* **Molly M. Stevens**

The extracellular matrix (ECM) is a vital component of all tissues that contributes to the physical and chemical cues that can affect cell fate. The design of materials to encourage the repair of tissue after injury is a long-standing goal of regenerative medicine. Supramolecular polymers based on reversible noncovalent interactions form fibrous materials that can act as simple but tailored ECM mimics. On page 848 of this issue, Álvarez *et al.* (*1*) show that tuning the dynamics of bioactive supramolecular polymers correlates with the degree of regeneration and functional outcome after acute spinal cord injury (SCI) in mice.

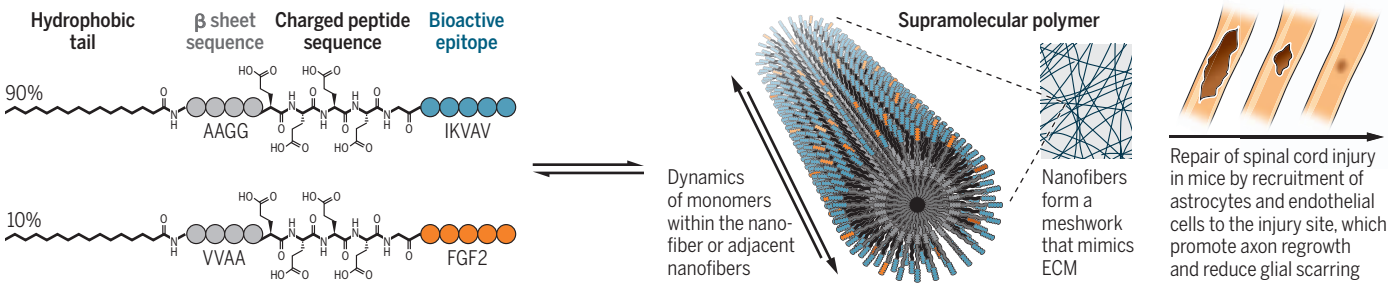
Structurally, the ECM comprises a nanoscale fibrous network composed of a complex and dynamic collection of structural proteins (e.g., collagen, fibronectin, and laminin) along with glycosaminoglycans (e.g., heparin and hyaluronic acid) and signaling proteins (e.g., growth factors and enzymes), which are constantly being remodeled according to interactions with the resident cells. The signals provided by the ECM can have multiple, sometimes opposing, roles on the local tissue environment, beneficially aiding regeneration of damaged tissue or, conversely, negatively amplifying a diseased tissue environment. This is especially true after SCI, where a complex ECM microenvironment of proteins and proteoglycans can inhibit axon regrowth but also act to isolate the injury site, preventing further damage (*2*, *3*). This response contributes to the difficulties in treating SCI, emphasizing the importance of understanding the role of the ECM in tissue environments and of designing synthetic mimics of the ECM to promote regenerative cell behavior (*4*).

Supramolecular polymers are a promising class of materials that are composed of well-defined monomeric subunits, which self-assemble into nanofibers through reversible noncovalent interactions to form a mesh-like network that structurally mim-

Department of Materials, Department of Bioengineering, and Institute of Biomedical Engineering, Imperial College London, London, UK. Email: m.stevens@imperial.ac.uk

Supramolecular polymers in spinal cord injury repair

A mixture of peptide amphiphiles with mismatched β sheet peptide sequences and two different bioactive epitopes, IKVAV (derived from laminin) and fibroblast growth factor 2 (FGF2) peptides, forms a supramolecular polymer with dynamic properties. The nanofibers produce a bioactive meshwork that mimics extracellular matrix (ECM) and promotes repair of spinal cord injury in mice.



ics the ECM. Peptide amphiphiles (PAs) are designer molecules that form supramolecular polymers containing a hydrophobic segment at the amino terminus, a β sheet–like peptide sequence, and a charged solubilizing peptide sequence at the carboxyl terminus (see the figure). The design of the PA allows the incorporation of a bioactive peptide sequence (epitope) at the carboxyl terminus, which is displayed on the outside of the nanofiber (*5*). PAs are injectable; degradable; and, compared with many covalent polymers, display high epitope density (*6*).

PAs functionalized with a laminin-derived peptide (IKVAV) have previously been shown to promote differentiation of neural progenitor cells in vitro and suppress astroglial differentiation (*6*). This was attributed to the availability of the IKVAV epitope, owing to its density on the surface of the PA nanofibers. Later work demonstrated restoration of partial function in a mouse model of SCI (*7*). Álvarez *et al.* add to our understanding of how supramolecular polymers efficiently interact with neural cells and promote regeneration, highlighting the importance of supramolecular assembly dynamics.

Because of their reversible noncovalent bonds, supramolecular polymers exist in an equilibrium between monomeric and aggregated states. Disruption of the β sheet region increases the dynamics of the PAs within the supramolecular structure (*8*). Álvarez *et al.* characterize a library of PAs with a mutated β sheet tetrapeptide sequence by changing the glycine, alanine, and valine content. These mutations affect the organization of the PA within the supramolecular polymer and the equilibrium between the monomer and the supramolecular polymer. They show that IKVAV-presenting PAs with a high degree of dynamics were more effective at promoting neuronal differentiation of neural progenitor cells in vitro. Extending their studies to a severe contusion mouse model of SCI, the authors include a PA displaying a fibroblast growth factor 2 (FGF2) mimetic peptide (YRSRKYSSWYVALKR), a multifunctional growth factor with important roles in adult neurogenesis. The FGF2-presenting PAs are mixed with IKVAV-presenting PAs to make coassembled nanofibers that display both epitopes. They find that the coassemblies of FGF2 PAs with a mismatched β sheet sequence (i.e., VVAA mixed with AAGG) showed higher total axon regrowth compared with controls, reduced glial scarring around the lesion, improved angiogenesis, improved neuronal cell survival, and resulted in higher locomotor recovery.

Further characterization showed that using an FGF2 PA derivative with a mismatched β sheet–forming peptide sequence showed higher degrees of dynamics within the supramolecular polymer. The increased dynamics of the supramolecular polymer may be more effective owing to its interactions with cells, such as through effective integrin clustering or possibly differences in the mechanics perceived by the cells. However, it is currently not possible to attribute the dynamics of the coassemblies to SCI recovery in the mouse models through direct observation. Developing methods to study how bioactive materials interact with biological systems is important to improve understanding of the cell-material interface. Previous work on related supramolecular polymers has shown the importance of characterizing the exchange mechanisms directly using super-resolution microscopy, which has revealed monomer exchange within disordered domains (*9*, *10*). Site-directed spin labeling with electron paramagnetic resonance spectroscopy (SDSL-EPR) was used on related derivatives to characterize the supramolecular dynamics in vitro (*8*). Advances in SDSL-EPR in vivo could be used to characterize the dynamics of these materials in biological environments.

Perhaps a supramolecular systems chemistry approach might be used for kinetic control of the supramolecular polymer (*11*). Additionally, advances in protein structure prediction and understanding of protein structure dynamics may provide opportunities to engineer the dynamics of mimetic materials (*12*). The study of Álvarez *et al.* offers exciting opportunities for kinetically controlled supramolecular polymers, while giving appropriate consideration to the pathway complexity of these self-assembled structures (*13*).

Effectively promoting SCI regeneration will likely require a material with multiple bioactive sequences that mimic other proregenerative circuits in biology. Understanding these systems requires methods to kinetically control the organization of multicomponent supramolecular networks and characterize their composition and behavior (*14*, *15*). These intriguing materials have potential for translation because they originate from well-defined chemical molecules whose degradation products can be identified, aiding in the characterization of the safety profile of the materials. ■

REFERENCES AND NOTES

1. Z. Álvarez *et al.*, *Science* **374**, 848 (2021).
2. C. S. Ahuja *et al.*, *Nat. Rev. Dis. Primers* **3**, 17018 (2017).
3. A. P. Tran, P. M. Warren, J. Silver, *Physiol. Rev.* **98**, 881 (2018).
4. M. M. Stevens, J. H. George, *Science* **310**, 1135 (2005).
5. J. D. Hartgerink, E. Beniash, S. I. Stupp, *Science* **294**, 1684 (2001).
6. G. A. Silva *et al.*, *Science* **303**, 1352 (2004).
7. V. M. Tysseling-Mattiace *et al.*, *J. Neurosci.* **28**, 3814 (2008).
8. J. H. Ortony *et al.*, *Nat. Mater.* **13**, 812 (2014).
9. L. Albertazzi *et al.*, *Science* **344**, 491 (2014).
10. R. M. da Silva *et al.*, *Nat. Commun.* **7**, 11561 (2016).
11. E. Mattia, S. Otto, *Nat. Nanotechnol.* **10**, 111 (2015).
12. J. Jumper *et al.*, *Nature* **596**, 583 (2021).
13. P. K. Hashim *et al.*, *Prog. Polym. Sci.* **105**, 101250 (2020).
14. S. Onogi *et al.*, *Nat. Chem.* **8**, 743 (2016).
15. K. L. Morris *et al.*, *Nat. Commun.* **4**, 1480 (2013).

ACKNOWLEDGMENTS

M.M.S. and J.P.W. are funded by the UK Regenerative Medicine Platform "Acellular / Smart Materials – 3D Architecture" (MR/R015651/1). The authors thank D. J. Peeler, A. T. Speidel, and P. R. A. Chivers for their comments and feedback.

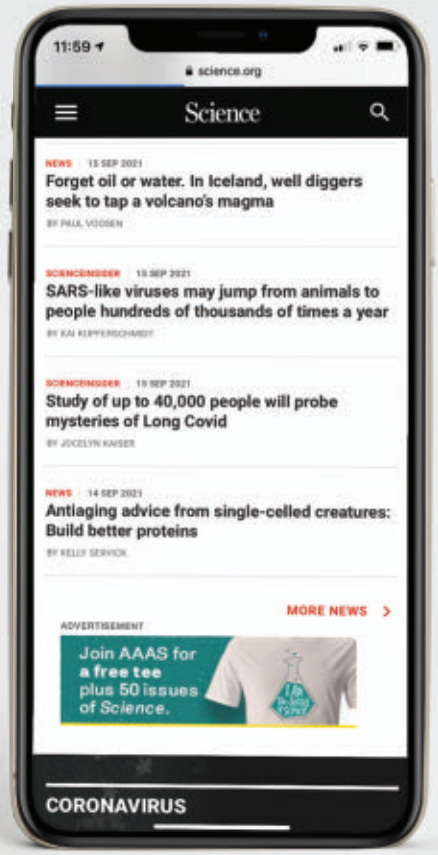
10.1126/science.abm3881

GRAPHIC: KELLIE HOLOSKI/*SCIENCE*

NEWS FROM Science

Up-to-the-minute research and policy news you won't find in print

Visit us online to read all the news coverage that there just wasn't enough room to print in this issue.



Science.org/news



Mammals forage on the banks of a lagoon 145 million years ago in this artist's rendering.

EVOLUTIONARY BIOLOGY

Iterations of evolution

A paleontologist's history of life highlights the recurring role played by geological, climatic, and atmospheric forces

By **Itai Yanai**[1] and **Martin J. Lercher**[2]

With dramatic flair, Henry Gee's sweeping new book, *A (Very) Short History of Life on Earth*, tells the 4-billion-year story of life on this planet and how it has been repeatedly shaped by geological, climatic, and atmospheric forces. Trained as a paleontologist, Gee tells life's history using the framework of the fossil record, offering insights from the related fields of ecology and physiology. Interwoven as it is with geology and climate, life evolves the way Ernest Hemingway said we go broke: "gradually and then suddenly" (*1*).

Life emerged on Earth not long after the planet's aggregation, writes Gee, and faced its first major challenge about 2.4 billion years ago. Until this point, bacteria and archaea had been confined to the oceans, where they evaded the Sun's deadly rays, which were not yet tempered by a protective atmosphere. Bacteria eventually learned to harness sunlight to produce energy, with oxygen as a by-product; but as oxygen levels rose, generations of bacteria and archaea that had evolved in its absence were burned alive.

Later, continental collisions and volcanic eruptions caused waves of extinctions that wiped ancient species from the face of the Earth and propelled previously insignificant lineages into suddenly emptied ecological niches. The book returns often to this theme, reminding readers how creatures that dominated certain periods of Earth's history—the dinosaurs of the Jurassic, for example, or the mammals of the Cenozoic—spent millions of years as minor players before taking center stage. Life, it seems, cannot help but exploit each new crisis it encounters as an opportunity for diversification. In this way, it is akin to the mythical phoenix, which is regularly consumed in a fiery inferno, only to rise again from the ashes.

The main protagonists of Gee's book are vertebrate life-forms. Early vertebrates, which began as fish, evolved jaws, the better to shred other organisms with. Even after they began moving onto land, they still returned to the water to reproduce. Vertebrate embryos, notes Gee, need a liquid medium in which to develop. Thus, the most crucial vertebrate adaptation may have been the egg, which provides a liquid capsule in which life can unfold on dry land.

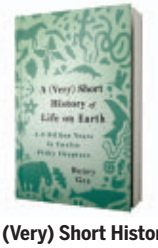
Another amazing early vertebrate adaptation was the development of air sacs, which first arose in dinosaurs and are still found in birds. This adaptation, which enabled a one-way system of air flow, also doubled as an efficient cooling system for internal organs.

As forests became more and more fragmented owing to climate changes linked to continental drift, primates started to venture into the open grasslands, from where the earliest hominins arose 7 million years ago. Their bipedal stance, notes Gee, made them "almost preternaturally maneuverable."

About 2.5 million years ago, *Homo erectus* arose, a territorial savannah predator, deadly thanks to two traits: it was a powerful long-distance runner and a social animal. From this lineage, *Homo sapiens* evolved. Humanity's first attempt at worldwide dispersal failed, shattered by the cold of an ice age 200,000 years ago. Confined to an oasis in what is now the Kalahari Desert, humankind nearly went extinct. We, as a species, are just as fragile as all the others, reminds Gee.

With beautiful exposition, Gee describes the major anatomical, physiological, and behavioral transitions in life's evolution. He largely refrains, however, from discussing the mechanisms and agents of evolution, and he does not offer much evidence from fields other than geology and paleontology. With few references to genes and genomes, the book lacks an appreciation of the mechanisms by which the genes—the ultimate replicators (*2*, *3*)—both constrain morphological change and enable incredible diversifications.

Gee's unbridled excitement also prompts him to sacrifice some precision and downplay some scientific uncertainties in the interest of storytelling. He frequently puts forward matter-of-fact description of topics that are far from settled and weaves in his own "fanciful speculations," freely admitting to these liberties in the endnotes. He advances a conjectural internal anatomy of *Saccorhytus*, a progenitor of vertebrates, for example; speculates about the reproductive strategies of ancient amphibians; and articulates how Stone Age shamans might have performed coming-of-age rituals.



A (Very) Short History of Life on Earth
Henry Gee
St. Martin's Press, 2021. 288 pp.

Some hundreds of million years from now, Earth will become uninhabitable to even the hardiest organisms, spelling the final doom for Earth-evolved life—unless, perhaps, some earthlings manage to escape into space first. Meanwhile, the reader is rewarded with a deeper appreciation of our own place in the grand scheme of life, where even the best-adapted species disappear within a time that is minute on the scale of evolution. ■

The reviewers are at the [1]Institute for Computational Medicine, NYU Langone Health, New York, NY 10016, USA, and [2]Department of Biology and Institute for Computer Science, Heinrich Heine University, 40225 Düsseldorf, Germany. Email: itai.yanai@nyulangone.org

REFERENCES AND NOTES

1. E. Hemingway, *The Sun Also Rises* (Scribner's, 1926).
2. R. Dawkins, *The Selfish Gene* (Oxford Univ. Press, 1976).
3. I. Yanai, M. Lercher, *The Society of Genes* (Harvard Univ. Press, 2016).

10.1126/science.abm0121

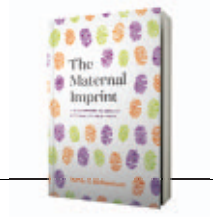
ILLUSTRATION: MARK WITTON

HISTORY OF SCIENCE

The politics of epigenetics

Maternal bodies are more than mediators of fetal environments, cautions a historian

The Maternal Imprint: The Contested Science of Maternal-Fetal Effects
Sarah S. Richardson
University of Chicago Press, 2021. 376 pp.



By **Abril Saldaña-Tejeda**

Filled with research findings and vivid accounts from reproductive biologists, geneticists, epidemiologists, and other scientists immersed in the study of reproduction and heredity, *The Maternal Imprint* offers an outstanding depiction of the mutual constitution of science and society. Cleverly unpacking the complex history of scientific debates on so-called "maternal impressions" (later, "maternal effects") on offspring and future generations, author Sarah Richardson unveils the epistemological origins of concepts we take for granted today—human plasticity, for example, and the biosocial body—and describes how these concepts emerged as artifacts of competing views on sex, heredity, childhood, and other ever-changing social pillars.



Birth weight became the preferred method of tracing maternal effects in the 1960s and 1970s.

At the end of the 19th century, writes Richardson, a German biologist named August Weismann dared to propose that maternal and paternal contributions to heredity were equal, colliding with long-held folk beliefs and scientific premises. Until that time, it was widely believed that a mother's every emotion and experience was imprinted on her offspring during gestation. With this belief came a conception of the female body as a porous, unstable, and irrational entity—ideas that were used to justify the denial of women's political and social rights. Weismann's theory challenged these views, but it also challenged some epistemological premises of the time, as it was based on the idea that scientific knowledge should be formed by deep insights and not merely reflect an accumulation of observations.

Richardson situates turn-of-the-century debates about maternal imprinting in the context of environmentalist approaches to eugenics and the emergence of prenatal culture. At the beginning of the 20th century, she notes, prenatal culturalists homed in on the intrauterine period as being of utmost importance for race improvement, with some using this view to assert women's agential role in the future of humanity. However, the spotlight on women's reproductive bodies was swiftly translated into prescriptions for everyday life, restraining women's autonomy over their own behavior, emotions, and other aspects of their lives. In contrast, adherents to Weismann's theory, many of whom were eugenic scientists, were surprisingly egalitarian, perceiving both parents as equally responsible for the health of future generations.

By the 1930s, the concept of maternal imprinting was generally deemed anti-scientific and superstitious, but another, more flexible, term soon arose to take its place: "maternal effects." As Richardson shows, the fuzziness of the science underlying this notion and its shaky theoretical underpinnings soon became its virtue. Entangled with economic pursuits, including efforts to increase livestock productivity, maternal effects became an enduring term to explain all maternal influences that fell outside cytoplasmic transmission. As they had during debates about maternal imprinting, fetal environments once again took center stage, but this time with an explanatory power that accounted for traits that seemed to be fixed in place over generations.

Birth weight became the favored metric for tracing and studying maternal effects during the 1960s and 1970s, a period when maternal science also became entangled with studies of racial inequality. Richardson illuminates the complex debates that framed the maternal body as the mediator of all sorts of social ills, including the biosocial inscription of racism on the bodies of generations to come, and explores their technical and epistemological underpinnings. She critically explores the science of fetal programming and the study of methylation as it relates to intergenerational epigenetic effects. Using a series of studies on the effects of hardship (i.e., hunger, trauma) on pregnant mothers and their offspring, Richardson rightly points to the potentiality and limitations of grand epigenetic claims based on limited human samples and technologies, a phenomenon she calls "cryptic causality."

In the book's closing chapters, Richardson illustrates the social and political implications of scientifically assigning women's reproductive bodies the enormous task of ensuring a healthy future for humankind and invites readers to reflect on the stigmatizing and deterministic discourse that often accompanies studies of maternal intrauterine effects. The book is an epistemological provocation, a reminder that science is a political enterprise, and an invitation to produce knowledge that empowers women instead of knowledge that makes them solely responsible for our collective future. ■

The reviewer is at the Department of Philosophy, University of Guanajuato, Guanajuato, Mexico.
Email: abrilsaldana@ugto.mx

10.1126/science.abm3722

PHOTO: RYANJLANE/ISTOCK.COM

Your Legacy to Science

AN ESTATE GIFT TO THE
AMERICAN ASSOCIATION FOR THE ADVANCEMENT OF SCIENCE





Since 1848, our founding year, the American Association for the Advancement of Science (AAAS) has been deeply committed to advancing science, engineering and innovation around the world for the benefit of all people.

By making AAAS a beneficiary of your will, trust, retirement plan or life insurance policy, you become a member of our 1848 Society, joining Thomas Edison, Alexander Graham Bell and the many distinguished individuals whose vision led to the creation of AAAS and our world-renowned journal, *Science*, so many years ago.

Unlike many of its peers, *Science* is not for-profit. Your estate gift would provide long-term financial stability and durable annual income that will support operations and competitive innovation for years to come. **This support is vital.**

"As a teacher and instructor, I bear responsibility for the younger generations. If you have extra resources, concentrate them on organizations, like AAAS, that are doing work for all."

—Prof. Elisabeth Ervin-Blankenheim, 1848 Society member

If you intend to include AAAS in your estate plans, provide this information to your lawyer or financial adviser:

Legal Name: American Association for the Advancement of Science
Federal Tax ID Number: 53-0196568
Address: 1200 New York Avenue, NW, Washington, DC 20005

If you would like more information on making an estate gift to AAAS, cut out and return the form below or send an email to philanthropy@aaas.org. Additional details are also available online at **www.aaas.org/1848Society**.

1848 SOCIETY
AAAS

cut here ✂

Yes, I would like more information about joining the AAAS 1848 Society.

PLEASE CONTACT ME AT:

Name: _____

Address: _____

City: _____ State: _____ Zip code: _____ Country: _____

Email: _____ Phone: _____

RETURN THIS FORM TO:
AAAS Office of Philanthropy and Strategic Partnerships • 1200 New York Avenue, NW • Washington, DC 20005 USA



Rescuers evacuate stranded people in the waterlogged urban area of Weihui City in central China's Henan Province, 27 July 2021, after a heavy rainfall.

PHOTO: LI JIANAN/XINHUA/GETTY IMAGES

Edited by **Jennifer Sills**

Improving the response to inland flooding

Extreme precipitation across China, Europe, and the United States led to unprecedented flood disasters this year, with hundreds of people killed and billions of dollars in losses. Thousand-year flood events in China and Europe and a 100-year flood event in the United States devastated inland regions not typically subject to extreme floods (*1*). The flooding in China, largely in Henan province, affected more than 14 million people, killing over 300 and inundating 16 million hectares of crops with direct economic losses of US$20.69 billion and indirect costs magnitudes greater (*2*). While climate change has been viewed as the primary culprit of these disasters (*3*, *4*), these inland regions' extreme lack of preparedness for such flooding events compounded the losses (*5*).

The damages and human cost of the flooding this summer resulted in part from human choices and activities. In Henan, the meteorological observatory issued no fewer than seven red alerts calling for staying at home before the flooding occurred (*6*), but the warnings were not taken seriously by municipality government or citizens (*7*). Metro passengers, as well as those trapped in the flooded Jingguang tunnel, did not know how to proceed in the face of such an emergency, resulting in 14 and 6 lives lost, respectively (*2*). The loss of green spaces, compounded by outdated and poorly maintained drainage systems, increased the region's flood risk (*6*).

In Europe, the situation was similar, with the European Flood Awareness System sending more than 25 early warnings to public authorities across the affected river basins, none of which led to meaningful action on the ground (*8*). In New York City, the death toll was not the greatest in coastal areas, but rather inland where flooding basements and subway lines, according to Mayor Bill de Blasio, were "catching people unaware" (*9*). Across all three flood events, lack of communication and cooperation between emergency management agencies within cities and between upstream and downstream river system authorities created further difficulties.

Transformative climate adaptation based on lessons from previous disasters can help mitigate future impacts as formerly safe regions increasingly face unprecedented conditions (*4*). Improving monitoring, forecasting, and warning systems by weather and hydrological agencies—or leveraging climate services already provided by insurance companies—can greatly reduce risks (*10*). Enhancing flood drainage systems and applying nature-based solutions such as protecting green spaces and lakes can reduce waterlogging in cities (*11*). Strengthening water infrastructure on medium and small rivers is also necessary to control floodwaters (*12*). Establishing a coordination mechanism for multiple departments and river basins will allow meteorological, transportation, communication, and emergency authorities to respond more promptly to hazards. Designing detailed emergency plans will help evacuate people more quickly, and improving public awareness will decrease casualties. Implementing a reward and punishment system to stimulate government agencies to react swiftly to combat flooding is also critical for disaster prevention and mitigation. Lastly, flood maps should be developed and distributed so that policy-makers, planners, and citizens better understand flood risk.

Xiaona Guo[1], Annah Zhu[2], Qiang Li[3], Ruishan Chen[1]*
[1]Shanghai Jiaotong University, Shanghai 200040, China. [2]Wageningen University, 6706KN Wageningen, Netherlands. [3]Henan University, Kaifeng 475000, China.
*Corresponding author.
Email: chenrsh04@gmail.com

REFERENCES AND NOTES

1. J. Sclafani, R. Falconer, "Deadly Northeast floods: More than 40 killed by Hurricane Ida's remnants," *Axios* (2021).
2. Henan Provincial Government, "Henan held its 10th news release conference on flood control and disaster relief," *The State Council Information*

Office of the People's Republic of China (2021); www.scio.gov.cn/xwfbh/gssxwfbh/xwfbh/henan/Document/1710343/1710343.htm [in Chinese].
3. D. Carrington, "Climate crisis made deadly German floods 'up to nine times more likely,'" *The Guardian* (2021).
4. L. Shi, S. Moser, *Science* **372**, eabc8054 (2021).
5. K. Bradsher, S. Lee Myers, "How record rain and officials' mistakes led to drownings on a subway," *The New York Times* (2021).
6. S. Feng, "Rethinking Zhengzhou after the flood retreat: How did this 'natural disaster' happen?," *China Business News* (2021); www.yicai.com/news/101125402.html [in Chinese].
7. J. Chen, "The examination and advice of Zhengzhou 7.20 flood to solve 17 world-class problems," *Kunlunce* (2021); www.kunlunce.com/e/wap/show2021.php?classid=183&id=154143 [in Chinese].
8. K. Mathiesen *et al.*, "Europe's floods: How a modern warning system was overwhelmed," *Politico* (2021).
9. J. McKinley *et al.*, "The storm warnings were dire. Why couldn't New York be protected?," *The New York Times* (2021).
10. W. Cornwall, *Science*, 10.1126/science.abl5271 (2021).
11. J. Du, "In Gorakhpur, India, citizens use nature to prevent floods," World Resources Institute (2019); www.wri.org/insights/gorakhpur-india-citizens-use-nature-prevent-floods.
12. W. R. Travis, *Climatic Change* **98**, 1 (2009).

10.1126/science.abm7149

Environmental "nonuse rights" warrant caution

In their Policy Forum "Allow 'nonuse rights' to conserve natural resources" (27 August, p. 958), B. Leonard *et al.* argue that conservation—not just extractive activities—should be a valid form of land use and that such "nonuse rights" should be granted to natural resources to enable their conservation through trading in environmental markets. We offer a cautionary tale from Australia's water markets, where nonuse rights appear useful but offer limited environmental benefits. These limitations arise from both rent-seeking behavior and regulatory capture, through which decision-making in the public interest is co-opted by vested interests (*1*).

Nonuse rights for water in Australia's one-million-square-kilometer Murray-Darling Basin were introduced in 2012 to protect water-dependent downstream ecosystems from overextraction (*2*). A combination of open-tender water trading (where owners sell to the highest bidder) and reverse auctions (where owners bid to one buyer) allowed the transfer of entitlements between users and the purchase and retirement of entitlements by governments. The measures were implemented with the intention of returning water to the basin for environmental purposes while ensuring that remaining rights to extract water flowed to their most profitable use. Murray-Darling Basin water markets are now seen as among the world's most successful (*3*) in terms of trading volumes, which is most likely true (*4*).



Efforts to conserve Australia's Murray-Darling Basin have been undermined by commercial interests.

However, the legitimacy of environmental allocations remains contested, and the effectiveness of the cap-and-trade approach built into market design has been undermined (*2*, *5*). Sustained lobbying from irrigation representatives has led to water purchases for the environment shifting from open tenders to particular sellers—usually large-scale water rights holders—being invited for "targeted" purchases of water. One purchase, shrouded in commercial confidentiality, totaled A$78.9 million, more than 25% above market rate, and the nature of the water entitlement acquired is not exclusively secured for the environmental flow (*1*).

Regulatory reform and improved market design in the Murray-Darling Basin could, in principle, address some of these issues. The question is whether reforms that allow private conservation actors to purchase and retire water entitlements would improve environmental outcomes without negatively affecting legitimate objectives of social and economic wellbeing. The answer is likely no. Few, if any, conservation organizations, not-for-profit actors, or First Nations peoples or groups are likely to have the capacity to outbid commercial water users. Moreover, the retirement of water entitlements that governments have made available for consumptive use could undermine the aspirations of First Nations people and the viability of rural communities. Markets dominated by commercial users or a small number of large conservation nongovernmental organizations can also prioritize tangible ecosystem goods at the expense of intangible ecological and cultural services (*6*).

To include nonuse forms of value, decision-makers must deliberate with stakeholders who have noncommercial interests in the resource area, which includes First Nations' cultural, social, and economic interests. Environmental markets can be better served if they are underpinned by democratic processes, such as thorough public deliberation, so stakeholders perceive them to be legitimate and equitable (*4*). Nonuse rights are no exception.

Patrick Lucas[1]*, Megan C. Evans[1], Stewart Lockie[3], Katie Moon[1,2]
[1]School of Business, University of New South Wales, Canberra, ACT 2600, Australia. [2]Centre for Ecosystem Science, School of Biological, Earth, and Environmental Sciences, University of New South Wales, Sydney, NSW 2052, Australia. [3]The Cairns Institute, James Cook University, Cairns, QLD 4878, Australia.
*Corresponding author.
Email: p.austin.lucas@gmail.com

REFERENCES AND NOTES
1. R. Q. Grafton, J. Williams, *Int. J. Water Resour. Dev.* **36**, 484 (2020).
2. Y. Chen, M. J. Colloff, A. Lukasiewicz, J. Pittock, *Mar. Freshw. Res.* **72**, 601 (2021).
3. B. Richter, "Water markets can support an improved water future" (2016); https://blogs.worldbank.org/water/water-markets-can-support-improved-water-future.
4. S. Lockie, *Failure or Reform? Market-Based Policy Instruments for Sustainable Agriculture and Resource Management* (Routledge/Taylor & Francis Group, ed. 1, 2020).
5. J. Williams, R. Q. Grafton, *Australasian J. Water Resour.* **23**, 78 (2019).
6. K. Moon, D. Marsh, C. Cvitanovic, *Conserv. Lett.* **14**, e12767 (2021).

10.1126/science.abm4324

Protect elephants from tuberculosis

Both African elephants (*Loxodonta africana*) and Asian elephants (*Elephas maximus*) are Endangered (*1*, *2*). About 415,000 African elephants, including both savanna and forest elephants, remain on the African continent (*3*); fewer than 48,000 Asian elephants remain globally (*4*). Poaching for the

PHOTO: IGNACIO PALACIOS/GETTY IMAGES

ivory is the main cause of rapid decline in population of African elephants (*3*), whereas the survival of Asian elephants is also threatened by habitat fragmentation and human-elephant conflict (*5*). In addition to these challenges, tuberculosis (TB) has emerged as a potential threat to both African and Asian elephants.

TB in elephants is mostly caused by *Mycobacterium tuberculosis*, a human form of TB that can be fatal in elephants (*6*), and by *M. bovis*, a form of TB that infects bovine species (*7*). TB has been widely reported in captive elephants globally (*7*). In some countries, captive elephants are treated with anti-TB drugs, but there are no tools to confirm whether the TB treatment is successful. The elephants' thick skin makes taking x-rays difficult (*7*). Captive elephants in range countries intermingle with wild elephants in protected areas during grazing in pasture, elephant rides, and other activities, providing an opportunity for TB transmission at the captive-wild interface.

Since 2014, *M. tuberculosis* infection has been reported in five wild Asian elephants from Sri Lanka and India (*7*). More recently, TB has been confirmed in free-ranging African elephants in Kruger National Park in South Africa, one of which was infected with *M. tuberculosis* (*6*) and two of which were infected by *M. bovis* (*8*). The bovine TB cases could be evidence of spillover transmission, given that it has been reported in more than 24 wildlife species in the park (*9*). The long-term effects of TB in elephant populations remain unknown, but in African buffaloes, bovine TB affects both survival and fecundity in adults and has reduced the rate of population growth (*10*).

Surveillance and monitoring of TB in wild elephants are challenging (*11*), and the currently available methods for diagnosing TB in captive elephants are difficult to use in wild elephants due to challenges in sample collection. Given the multiple potential routes for transmission and the negative effects seen in other species, it is imperative to design early diagnostic tools and to increase the surveillance of TB in these species using serological, bacteriological, and molecular techniques. Genomic studies of the TB isolates in elephants can clarify transmission patterns and sources of infection of TB in elephants. To help conserve these endangered elephant species, we must minimize the threats they face.

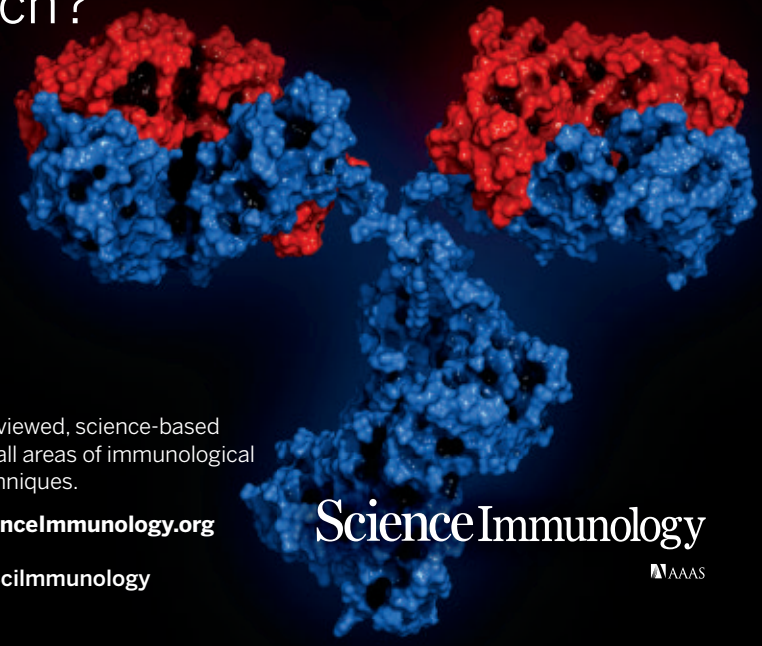
Yogendra Shah[1]* and Sarad Paudel[2]
[1]National Zoonoses and Food Hygiene Research Center, Kathmandu, Nepal. [2]Department of Pathobiology and Diagnostic Investigation, College of Veterinary Medicine, Michigan State University, East Lansing, MI 48824, USA.
*Corresponding author.
Email: yogendra.90@gmail.com

REFERENCES AND NOTES

1. K. S. Gobush *et al.*, *Loxodonta africana* (amended version of 2021 assessment) (The IUCN Red List of Threatened Species, 2021); www.iucnredlist.org/species/181008073/204401095.
2. C. Williams *et al.*, *Elephas maximus* (The IUCN Red List of Threatened Species, 2020); www.iucnredlist.org/species/7140/45818198.
3. C. R. Thouless *et al.*, in *Occasional Paper Series of the IUCN Species Survival Commission, No. 60*, IUCN/SSC Africa Elephant Specialist Group, Ed. (IUCN, Gland, Switzerland, 2016).
4. P. Fernando, J. Pastorini, *Gajah* **35**, 15 (2011).
5. R. Sukumar, *Int. Zoo Yearbook* **40**, 1 (2006).
6. M. A. Miller *et al.*, *Front. Vet. Sci.* **6**, 18 (2019).
7. S. Paudel, S. Sreevatsan, *Tuberculosis* **123**, 101962 (2020).
8. M. A. Miller *et al.*, *Emerg. Infect. Dis.* **27**, 990 (2021).
9. N. Bernitz *et al.*, *Front. Vet. Sci.* **8**, 588697 (2021).
10. A. E. Jolles *et al.*, *Ecology* **86**, 2258 (2005).
11. S. Paudel *et al.*, *Science*, **363**, 356 (2019).

10.1126/science.abm5609

Antibodies Recognize Antigens...
How will you get **recognized** for your immunology research?



Science Immunology publishes original, peer-reviewed, science-based research articles that report critical advances in all areas of immunological research, including important new tools and techniques.

Submit your research today. Learn more at: **ScienceImmunology.org**

@ScienceImmunology @SciImmunology

ScienceImmunology
AAAS

CALL FOR PAPERS

SPJ
SCIENCE PARTNER JOURNALS



Energy Material Advances

Energy Material Advances is an online-only, Open Access journal published in affiliation with **Beijing Institute of Technology (BIT)** and distributed by the **American Association for the Advancement of Science (AAAS)**. The journal publishes, research articles, review articles, short communications, perspectives, and editorials. *Energy Material Advances* covers multiple fields from cutting-edge material to energy science, investigating theoretical, technological as well as engineering aspects.

Submit your research to *Energy Material Advances* today!

Learn more at **spj.sciencemag.org/energymatadv**

The Science Partner Journal (SPJ) program was established by the American Association for the Advancement of Science (AAAS), the nonprofit publisher of the *Science* family of journals. The SPJ program features high-quality, online-only, Open Access publications produced in collaboration with international research institutions, foundations, funders and societies. Through these collaborations, AAAS furthers its mission to communicate science broadly and for the benefit of all people by providing top-tier international research organizations with the technology, visibility, and publishing expertise that AAAS is uniquely positioned to offer as the world's largest general science membership society.

Visit us at: **spj.sciencemag.org**

@SPJournals **@SPJournals**

OPEN ACCESS

ARTICLE PROCESSING CHARGES WAIVED UNTIL JULY 2023

RESEARCH

IN *SCIENCE* JOURNALS

Edited by **Michael Funk**



PHOTO: NASA

LUNAR GEOLOGY

Sample return shows late lunar volcanism

Measuring physical samples of Solar System bodies in the laboratory provides more information than is possible from remote sensing alone. In December 2020, the Chang'e-5 mission landed on the Moon, collected samples, and then returned them to Earth. Che *et al.* analyzed two fragments of volcanic lunar basalt collected by Chang'e-5. Radiometric dating using lead isotopes indicated that the rocks formed from magma that erupted about 2 billion years ago, later than other volcanic lunar samples. The abundance of extinct radioactive elements in the rock is too low for radioactive heating to have produced the magma. Another, thus far unknown, source must have been responsible for the late lunar volcanism. —KTS *Science*, abl7957, this issue p. 887

Samples of lunar basalt returned by the Chang'e-5 lander provide evidence for late volcanism on the Moon.

NEUROSCIENCE

Where and when of memory consolidation

Episodic memory is initially encoded in the hippocampus and later transferred to other brain regions for long-term storage. Synaptic plasticity underlies learning and plays a critical role in memory consolidation. However, it remains largely unknown where and when synaptic plasticity occurs and how it shapes the neuronal representation. Goto *et al*. developed a new tool for controlling early structural long-term potentiation (sLTP). By selectively manipulating sLTP, the authors showed that the local circuitry in hippocampal area CA1 is required for memory formation shortly after the encoding event. The local circuitry is also important for offline memory consolidation within 24 hours. The anterior cingulate cortex, another brain region directly connected with area CA1, is crucial for memory consolidation during sleep on the second night. —PRS

Science, abj9195, this issue p. 857

TRANSCRIPTION

How Integrator ends transcription early

Transcription is the central process that activates the genetic information in cells, but our understanding of how gene transcription is regulated is incomplete. The so-called Integrator can stop the transcribing enzyme RNA polymerase II at the beginning of genes, but how such down-regulation of transcription occurs is unclear. Fianu *et al*. present the three-dimensional structure of Integrator bound to the transcribing polymerase complex, providing molecular and mechanistic insights into how Integrator mediates transcription regulation. —DJ

Science, abk0154, this issue p. 883

CORONAVIRUS

Valuing vaccination

Using money as a motivation for the public to get vaccinated is controversial and has had mixed results in studies, few of which have been randomized trials. To test the effect of money as an incentive to obtain a vaccine, Campos-Mercade *et al*. set up a study in Sweden in 2021, when various age groups were first made eligible to receive the severe acute respiratory coronavirus 2 vaccine (see the Perspective by Jecker). The effect of a small cash reward, around US $24, was compared with the effect of several behavioral nudges. The outcome of this preregistered, randomized clinical trial was that money had the power to increase participation by about 4 percentage points. Nudging and reminding didn't seem to be deleterious and even had a small positive effect. Of course, the question of whether it is ethical to pay people to be vaccinated needs to be addressed. —CA

Science, abm0475, this issue p. 879; see also abm6400, p. 819

SPECTROSCOPY

Resolution of the σ-hole

Anisotropic distribution of charges on atoms plays an important role in intermolecular interactions, yet direct experimental imaging remains a long-standing challenge. A good example is the σ-hole, an anisotropic charge distribution on a halogen atom covalently linked

to carbon atoms. The σ-hole gives rise to the halogen-bonding mechanism, which is well known in supramolecular chemistry despite its existence being confirmed only indirectly. Mallada *et al.* developed Kelvin probe force microscopy with a specifically functionalized tip and report direct real-space visualization of the σ-hole, revealing its strong anisotropic charge distribution. The authors show that this technique, which relies entirely on electrostatic interactions, may be a powerful tool with which to study anisotropic atomic charge distributions. —YS

Science, abk1479, this issue p. 863

DENDRITIC CELLS

Infected lungs call for backup

Resident dendritic cells (DCs) within the lung epithelium are positioned to rapidly detect invading pathogens and initiate an adaptive immune response. They can also be expanded through recruitment of blood-derived progenitors. In a mouse model of influenza virus infection, Cabeza-Cabrerizo *et al.* showed that expression of the chemokine receptor CCR2 is required for recruitment of DC progenitors (pre-DCs) to the lungs and subsequent positioning at foci of infection. Using mice with conditional deletion of CCR2 in the DC lineage, they found that pre-DC recruitment is necessary for effective T cell responses and protection against reinfection. These results demonstrate that expansion of the homeostatic lung DC network by circulating pre-DCs is essential for immunity against respiratory viruses. —CO

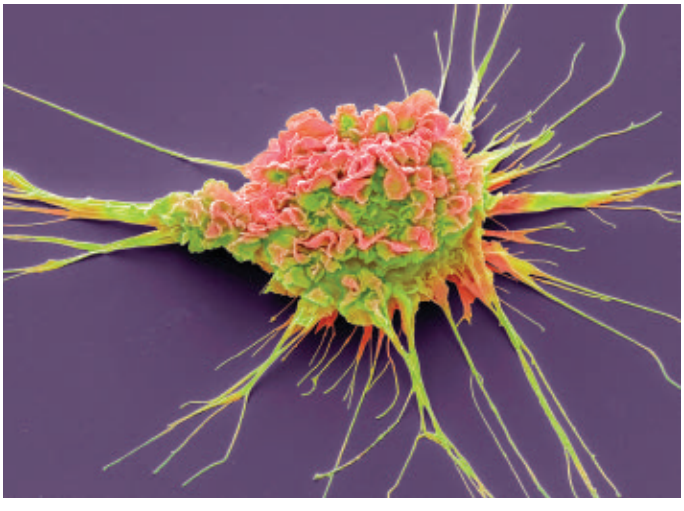
Sci. Immunol. **6**, eabi9331 (2021).

PHYSICS

Dark matter declines to reveal itself

Astrophysicists hold that our universe is dominated by mysterious "dark" matter and energy that puzzle outsiders and which, in truth, are not yet well understood even though their existence is supported by many lines of evidence. Several new fundamental particles have been proposed as candidates for dark matter, but there are few claims of definitive signals. An exception is the claim by the DAMA collaboration of a statistically significant annual modulation in their event rate, consistent with weakly interacting massive particles, but this result had seemed inconsistent with other direct search experiments. Adhikari *et al.* analyzed data from a different collaboration, COSINE-100, which appears to exclude the DAMA result. Dark matter thus remains elusive. —WSW

Sci. Adv. 10.1126/sciadv.abk2699 (2021).



Dendritic cells, seen here in a colored scanning electron microscope image, help detect and respond to pathogens in the lungs.



IN OTHER JOURNALS

Edited by **Caroline Ash** *and* **Jesse Smith**

MACROECOLOGY

Biotic interactions limit range edges

Species ranges are strongly influenced by climate, but species interactions can also limit ranges and constrain range shifts with climate change. Paquette and Hargreaves used a meta-analysis of 338 studies of range limits from 654 taxa to test a long-standing hypothesis that abiotic factors are more important at cooler, more stressful range edges (high latitudes and elevations), and biotic interactions limit more biodiverse warm edges. The authors found that species interactions were more important at warm than at cool range edges. Climate affects both warm and cool range edges; however, incorporating information about competition, predation, and parasitism is especially important for predicting changes in warm range edges. —BEL

Ecol. Lett. **24**, 2427 (2021).

PLANT SCIENCE

Light directs leaf shape

Coordinated patterns of cell division followed by cell expansion combine to define the shape of a plant leaf. A wide, flat leaf shape maximizes light capture and gas exchange. Phototropins in the leaf perceive blue and ultraviolet light direction and, through auxins, locate signals for stems to grow toward the light and for leaves to flatten to maximize light reception. Legris *et al.* defined the signaling cascades initiated by phototropins that direct whether an *Arabidopsis* leaf will be flat or curly. The phototropins have their effect rather late in leaf development,

PHOTOS: (LEFT TO RIGHT) STEVE GSCHMEISSNER/SCIENCE SOURCE; ZUMA PRESS, INC./ALAMY STOCK PHOTO



DEVELOPMENT

Contacts determine cell fate

During embryonic development, differentiation processes transform a ball of homogeneous cells into multicellular complexity. A neuronal cell acquires its unique identity because of its neighbors within the early embryo. Studies have suggested that the size of the contact areas and the strengths of the signals work in concert to direct this transformation. Williaume *et al.* attempted a quantitative understanding of this process in the development of the sea squirt, a protochordate model animal. When sea squirt embryos grow to 32 cells, two cells adopt a neuronal fate. The authors found that the strength of the instructional signal that directs the cells to become a neuron is proportional to the area of cell-cell contact. Cells convert the resulting gradual signal into a bimodal gene expression output, which is fine-tuned by inhibitory signals from the cells' other neighbors. —DJ

Dev Cell. 10.1016/j.devcel.2021.09.025 (2021).

Development of the protochordate sea squirt *Ciona* reveals how cell fate is directed by a cell's neighbors.

after the cell division phase has ended and while new cells are enlarging. Asymmetric signaling cascades subsequently prime the developing leaf with differing sensitivities to light on its shady side versus the side exposed to light. —PJH

Plant Physiol. 10.1093/plphys/kiab410 (2021).

MECHANICAL BONDS

Clipped in place

In rotaxanes, bulky end groups on a molecular axle keep a threaded ring from sliding off. Peris *et al.* now report a distinct type of interlocked compound, which they call a clippane. The building block is a tweezer-shaped molecule in which a polycyclic aromatic spacer connects two arms capped by polycyclic aromatics perpendicular to the spacer. Two tweezer molecules can interlock at right angles as the arms form, but bulky tert-butyl substituents then prevent them from sliding back apart. The clippanes were characterized in crystalline, solution, and gas phases and were stable up to 100°C. —JSY

Angew. Chem. Int. Ed. 10.1002/anie.202112513 (2021).

LUNAR FORMATION

Did Theia impact Earth twice?

Geophysical and geochemical evidence indicates that the Moon formed from debris ejected by a giant impact between Earth and a protoplanet, referred to as Theia, which was mostly accreted into Earth. Simulations support this model if the impact velocity is close to the minimum possible, the mutual escape velocity, but this requires fine tuning. Asphaug *et al.* propose that Theia collided with Earth twice, first in a grazing "hit-and-run" that left both objects intact but modified their orbits, and then, less than a million years later, in a giant impact that destroyed Theia and formed the Moon. They argue that a range of initial velocities for the first collision produced a second collision at the escape velocity. —KTS

Planet. Sci. J. 10.3847/PSJ/ac19b2 (2021).

SCIENTIFIC WORKFORCE

Exacerbated inequalities in publishing

During the initial pandemic lockdowns, academics submitted scientific manuscripts at an increased rate. Squazzoni *et al.* analyzed data on more than 5 million authors and referees related to submitted manuscripts for Elsevier journals between February and May of 2018–2020 as a way of investigating the demographics behind the increased submissions. Results revealed an unsurprising gender pattern, with women submitting fewer manuscripts than men. Unfortunately, more junior cohorts of women, likely women without permanent positions who are competing for tenure, promotion, and grants, experienced the lowest rates of submission. Perhaps most upsetting is the finding that women took on a greater service responsibility for journals. Collectively, these data contribute to a growing number of studies suggesting that the pandemic exacerbated cumulative advantages for men. —MMc

PLoS ONE 10.1371/journal.pone.0257919 (2021).

NEUROSCIENCE

Spiny neurons are diverse

The striatum is the major input nucleus for the basal ganglia. Striatal information processing is dependent on cell-type-specific circuits. Medium spiny neurons account for most striatal neurons and are traditionally classified as direct- or indirect-pathway neurons. However, this traditional model does not do justice to the complexity and diversity of these cells. He *et al.* used single-nucleus RNA sequencing and fluorescence in situ hybridization to characterize the transcriptional and anatomical diversity of rhesus monkey striatal medium spiny neurons. The authors identified five distinct subtypes in the dorsal striatum, whereas the ventral striatum contained at least four distinct neuronal subtypes, including the known D1 and D2 subtypes. These neuronal subtypes provide a framework for studying cell-type-specific functions during sophisticated primate behaviors. —PRS

Curr. Biol. 10.1016/j.cub.2021.10.015 (2021).

ALSO IN *SCIENCE* JOURNALS

Edited by **Michael Funk**

NEURODEVELOPMENT

Insulation for circuit regulation

Lipid-rich myelin, which wraps around and insulates neuronal axons, improves the speed and efficiency of signal propagation. Myelination is not universally applied in the central nervous system, and even axons within the same circuit can vary in the amount of myelination they carry. Bonetto *et al*. reviewed what is known about how such variability can affect computational functions in brain circuits. Myelin plasticity may be one mechanism linking experiential learning to modified brain connections. Whether you are learning to juggle or learning to read, changes in myelination may tune the circuits underlying those skills. —PJH

Science, aba6905, this issue p. 838

DISEASE GENOMICS

Detangling gene-disease connections

Many diseases are at least partially due to genetic causes that are not always understood or targetable with specific treatments. To provide insight into the biology of various human diseases as well as potential leads for therapeutic development, Pietzner *et al*. undertook detailed, genome-wide proteogenomic mapping. The authors analyzed thousands of connections between potential disease-associated mutations, specific proteins, and medical conditions, thereby providing a detailed map for use by future researchers. They also supplied some examples in which they applied their approach to medical contexts as varied as connective tissue disorders, gallstones, and COVID-19 infections, sometimes even identifying single genes that play roles in multiple clinical scenarios. —YN

Science, abj1541, this issue p. 839

PLANT SCIENCE

A closer look at centromeres

Centromeres are key for anchoring chromosomes to the mitotic spindle, but they have been difficult to sequence because they can contain many repeating DNA elements. These repeats, however, carry regularly spaced, distinctive sequence markers because of sequence heterogeneity between the mostly, but not completely, identical DNA sequence repeats. Such differences aid sequence assembly. Naish *et al*. used ultra-long-read DNA sequencing to establish a reference assembly that resolves all five centromeres in the small mustard plant *Arabidopsis*. Their view into the subtly homogenized world of centromeres reveals retrotransposons that interrupt centromere organization and repressive DNA methylation that excludes centromeres from meiotic crossover repair. Thus, *Arabidopsis* centromeres evolve under the opposing forces of sequence homogenization and retrotransposon disruption. —PJH

Science, abi7489, this issue p. 840

NEUROSCIENCE

Common basis for language and tool use

Tool use and language are hallmarks of human evolution. Because of the similarity between the motor processes for tool use and those supporting language, it has been hypothesized that syntax and tool use may share brain resources. Using functional magnetic resonance imaging and multivariate pattern analysis, Thibault *et al*. found that small portions of the basal ganglia in the human brain act as common neural substrates for both tool use and syntax in language. In a behavioral experiment, they showed that learning a novel task that involves the use of a tool also improves performance in a complex language task. These results further support the hypothesis of a co-evolution of tool use and language. —PRS

Science, abe0874, this issue p. 841

NEURODEGENERATION

Autoimmunity in Lewy body dementia

Lewy body dementia (LBD) is a brain disease that leads to progressive decline in thinking, movement, and independent function. It results from the buildup of microscopic deposits called Lewy bodies, which develop from the aggregation of a misfolded protein called α-synuclein. Gate *et al*. observed immune cells known as T cells in the brains of LBD patients (see the Perspective by Krot and Rolls). Genomics analysis revealed that T cells traffic to the LBD brain and are associated with neuronal damage. When stimulated with α-synuclein, LBD patient T cells secrete an inflammatory protein known to damage neurons. These findings suggest an unexpected detrimental role of the immune system in LBD. —SMH

Science, abf7266, this issue p. 868; see also abm4739, p. 823

GENOMICS OF AGING

A fishy tale of long and short life span

Fish have wide variations in life span even within closely related species. One such example are the rockfish species found along North Pacific coasts, which have life spans ranging from 11 to more than 200 years. Kolora *et al*. sequenced and performed a genomic analysis of 88 rockfish species, including long-read sequencing of the genomes of six species (see the Perspective by Lu *et al*.). From this analysis, the authors unmasked the genetic drivers of longevity evolution, including immunity and DNA repair–related pathways. Copy number expansion in the butyrophilin gene family was shown to be positively associated with life span, and population historical dynamics and life histories correlated differently between long- and short-lived species. These results support the idea that inflammation may modulate the aging process in these fish. —LMZ

Science, abg5332, this issue p. 842; see also abm3392, p. 824

DYNAMIC BIOSCAFFOLDS

Fibril motion improves peptide signaling

Artificial scaffolds that bear the peptide-signaling sequences of proteins for tissue regeneration often have limited effectiveness. Álvarez *et al*. synthesized supramolecular peptide fibril scaffolds bearing two peptide sequences that promote nerve regeneration, one that reduces glial scarring and another that promotes blood vessel formation (see the Perspective by Wojciechowski and Stevens). In a mouse model of paralyzing human spinal cord injury, mutations in a tetrapeptide domain outside of the signaling regions improved recovery by promoting intense supramolecular motion within the fibrils. The mutation with the most intense dynamics resulted in corticospinal axon regrowth and myelination, functional revascularization, and motor neuron survival. —PDS

Science, abh3602, this issue p. 848 see also abm3881, p. 825

MINERALOGY

Lower mantle "garbage can"

Calcium silicate perovskite has finally been identified in a natural sample and now has the mineral name davemaoite. Tschauner *et al*. discovered the type mineral trapped at high pressure and

temperature as a diamond inclusion (see the Perspective by Fei). Structural and chemical analysis of the mineral showed that it can host a wide variety of elements, not unlike fitting bulky objects into a garbage can. Specifically, it has a large amount of trapped potassium. Davemaoite can thus host three of the major heat-producing elements (uranium and thorium were previously shown experimentally) affecting heat generation in Earth's lower mantle. —BG

Science, abl8568, this issue p. 891; see also abm4742, p. 820

DEVELOPMENTAL BIOLOGY

Specifying one oocyte from many

In many animals, only one cell from a cyst of germ cells is selected to become the oocyte. Using fruit flies as a model, Nashchekin *et al*. identified the microtubule minus end-binding protein Patronin/CAMSAP as a key factor for specifying oocyte fate. Patronin amplifies an initial asymmetry provided by the fusome to form a noncentrosomal microtubule network focused on one cell, along which dynein transports oocyte fate determinants. This mechanism for selecting a single oocyte may be shared in other organisms. —BAP

Science, abj3125, this issue p. 874

FOSSIL CARBON

Coaling in the deep

Despite our current reliance on fossil carbon for energy, the biogeochemical reactions that produce coal and natural gas aren't entirely understood. Lloyd *et al*. tested the chemistry and isotope composition in samples ranging from wood to hard, mature coal (see the Perspective by Keppler). Methyoxyl groups in this organic material, a potential source of methane, declined with maturity, whereas the carbon-13 fraction increased gradually. The most plausible explanation for this observed pattern is biological demethylation under substrate-limited conditions. These results help us understand the processes that form coal and natural gas on geologic time scales. —MAF

Science, abg0241, this issue p. 894; see also abm6027, p. 821

NEUROSCIENCE

Curbing neonatal seizures with KCC2

Neonatal seizures are often associated with reduced levels of KCC2, a potassium/chloride cotransporter involved in inhibitory neurotransmission. Sullivan *et al*. identified KCC2 as a potential target for treating neonatal seizures resistant to the first-line seizure medication phenobarbital. Administering the drug CLP290 to acutely enhance KCC2 activity in mice decreased the number and duration of seizures and restored the antiseizure efficacy of phenobarbital. These effects depended on KCC2 abundance and the phosphorylation of a particular serine residue within KCC2. —LKF

Sci. Signal. **14**, eabg2648 (2021).

PAIN

Itching to block OSM

Inflammatory skin diseases are often associated with the development of chronic itch. Although inflammation-related cytokines have been shown to modulate the activity of peripheral itch-selective neurons, the involvement of inflammatory mediators in the pathophysiology of chronic itch remains unclear. Tseng and Hoon discovered that the cytokine oncostatin M (OSM) plays a major role in itch. OSM is up-regulated in immune cells during skin diseases associated with itch. In vitro, OSM modulated itch neurons' excitability and sensitivity to pruritogens. In vivo data showed that OSM depletion or inhibition reduced itch behavior in a rodent model of dermatitis, suggesting that targeting OSM could be effective in reducing itch associated with inflammatory conditions. —MM

Sci. Transl. Med. **13**, eabe3037 (2021).

REVIEW SUMMARY

NEURODEVELOPMENT

Myelin: A gatekeeper of activity-dependent circuit plasticity?

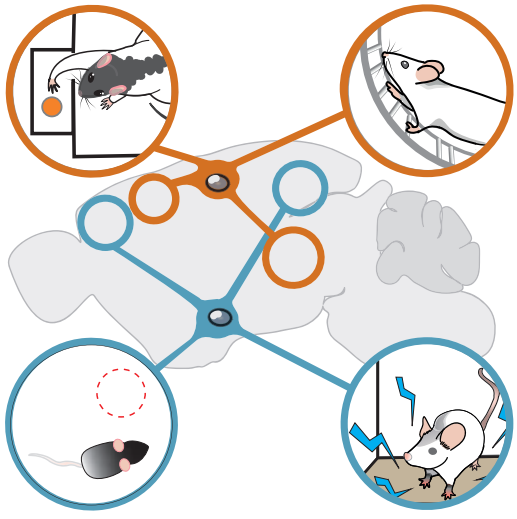
Giulia Bonetto, David Belin*, Ragnhildur Thóra Káradóttir*

BACKGROUND: Myelin, produced by oligodendrocytes, supports the rapid and synchronized transfer of information across the central nervous system (CNS). Earlier views of myelin as inert and immutable have been reformed with the discovery that myelin changes throughout the life span with experience or the acquisition of new skills, adapting the function of neuronal circuits like those underlying learning and memory. We discuss the functional implications of myelin changes, capitalizing on previous reviews of mechanisms of myelin plasticity to assess how such changes might be linked to circuit function underlying learning and memory.

In the CNS, there remains a substantial proportion of unmyelinated or partially myelinated axons, which can potentially become myelinated during the life span. This offers a dynamic range for activity-dependent structural plasticity, whereby newly generated oligodendrocytes myelinate these axons and axonal segments, or existing oligodendrocytes alter myelin internodes in response to neuronal activity. Neuronal activity seems to promote oligodendrocyte precursor cells (OPCs), evenly distributed throughout the adult brain, to differentiate into new myelinating oligodendrocytes and to alter the internodal length and thickness of existing myelin, as well as increasing lactate release from oligodendrocytes via myelin to fuel conduction. Computational models indicate that neuronal activity–dependent myelin alterations can promote neural phase synchronization, which is needed for learning and memory. Myelin plasticity therefore represents a mechanism by which experience and associated learning may modify brain connections, presumably by shaping the computation of neuronal circuits via alterations in the timing of neuronal signal transmission.

ADVANCES: The few studies that have directly investigated the role of myelin plasticity in learning and memory have provided evidence that brain plasticity in the form of de novo myelin formation may play a role in the encoding (learning) and storage (memory) of information. Collectively these studies reveal that OPC proliferation is fast, almost immediate, upon initiation of training in a behavioral task, driving change at a speed similar to that of structural synaptic plasticity. However, new oligodendrocytes and new myelin do not appear until days or weeks later. These dynamic changes do not seem to be universal nor to follow the ongoing constitutive myelination program. Instead, they differ in brain regions and timing depending on the task, the performance of which relies on distinct and/or interacting memory processes, including prefrontal cortex–dependent short-term/working memory, hippocampus-dependent spatial memory, dorsal striatum–dependent procedural memory, or amygdala-dependent Pavlovian and emotional memory. As a result, it appears that although the proliferation of oligodendrocytes seems nonspecific to the function and underlying neural substrate that is being recruited to the task, the pattern of myelination is indeed memory system–dependent.

The functional role of OPC differentiation, as these cells form new oligodendrocytes at different times during learning and memory formation, can be causally interrogated in transgenic mouse models that use inducible OPC-specific Cre lines to genetically delete transcription factors needed for this process. Preventing OPC differentiation into new myelinating oligodendrocytes affects memory across an array of behavioral tasks, including prefrontal cortex– and hippocampus-dependent spatial navigation (in the Morris water maze), contextual fear conditioning, and motor cortex/dorsal striatum–dependent skill learning. Despite differences in study designs that preclude direct comparison, collectively the results of these studies converge on one overarching picture: The time at which the deficit emerges after blockade of OPC differentiation seems to coincide with the time when multiple brain regions coordinate functionally to mediate long-term storage of a memory.



Myelin plasticity underpins learning and memory. Stylized diagram of myelinating oligodendrocytes connecting different types of long-term memory, including spatial memory, Pavlovian fear memory, and motor skills, assessed in specific behavioral paradigms (clockwise from top left: single-pellet forelimb reach, complex wheel, contextual fear, Morris water maze) and underpinned by distinct neural systems, representing how oligodendrocyte and myelin changes in the brain are involved in the modification of circuit functions underlying learning and behavior.

OUTLOOK: Various studies demonstrate that suppression of adult oligodendrogenesis differentially impairs memory across memory/neural systems. Collectively, they support the conclusion that myelin plasticity could support systems-wide memory consolidation, a mechanism underlying long-term memory. Together with the evidence that dysfunctional myelin or altered myelination during development impairs learning and adaptive behavior, this body of data suggests that even small changes in myelin across the life span can have an impact on circuit- and systems-level mechanisms involved in cognition and behavior. Myelin might have a broader function than previously assumed: Dysfunctional or maladaptive myelination may contribute to neurodegenerative and neuropsychiatric disorders, which have hitherto been considered to have a neuronal basis. A deeper knowledge of the functional role of myelin plasticity may unlock alternative therapeutic approaches. Collectively, this calls for further investigation of the functional role of myelin plasticity. ■

The list of author affiliations is available in the full article online.
*Corresponding author. Email: rk385@cam.ac.uk (R.T.K.); bdb26@cam.ac.uk (D.B.)
Cite this article as G. Bonetto *et al.*, *Science* **374**, eaba6905 (2021). DOI: 10.1126/science.aba6905

READ THE FULL ARTICLE AT
https://doi.org/10.1126/science.aba6905

REVIEW

NEURODEVELOPMENT

Myelin: A gatekeeper of activity-dependent circuit plasticity?

Giulia Bonetto[1], David Belin[2]*, Ragnhildur Thóra Káradóttir[1,3]*

The brain is responsive to an ever-changing environment, enabling the organism to learn and change behavior accordingly. Efforts to understand the underpinnings of this plasticity have almost exclusively focused on the functional and underlying structural changes that neurons undergo at neurochemical synapses. What has received comparatively little attention is the involvement of activity-dependent myelination in such plasticity and the functional output of circuits controlling behavior. The traditionally held view of myelin as a passive insulator of axons is changing to one of lifelong changes in myelin, modulated by neuronal activity and experience. We review the nascent evidence of the functional role of myelin plasticity in strengthening circuit functions that underlie learning and behavior.

More than half of the human brain is white matter, which supports rapid and synchronized transfer of information across the many gray-matter areas of the central nervous system (CNS). The function of white matter depends on oligodendrocytes. These specialized glial cells wrap a lipid-rich membrane, myelin, around axons in the CNS, increasing the speed of the action potential and providing axons with energy for impulse propagation (*1*) required for maintaining high impulse frequency (*2*). Changes in myelin within a tract or brain region can affect the function of neural circuits, such as those involved in emotion, cognition, motivation, and associated behavior, by fine-tuning and reducing the failure rate of information transfer between different areas in the brain's gray matter.

Although the essential function of myelin has long been recognized in white-matter diseases such as multiple sclerosis, where myelin loss leads to both motor and cognitive dysfunction (*1*, *3*), it remains widely viewed as a passive insulator. However, evidence indicates that myelination in mammals is a protracted dynamic process involved in CNS function and development (*4*, *5*). Myelination in humans begins during the last trimester and extends into late adulthood (*4*) and varies between individuals, potentially affecting personality traits (*6*).

Human postmortem histological observations suggest that myelination of axonal tracts linking brain regions is synchronized with the functional maturation of the neural circuits they form (*4*). Likewise, magnetic resonance imaging (MRI) studies have revealed that the maturation of sensorimotor or language-related white-matter tracts in humans is associated with the development of these basic skills in childhood, whereas the maturation of frontoparietal (*7*, *8*) and frontostriatal (*9*) white-matter pathways coincides with protracted development of executive functions and behavioral control during adolescence and early adulthood.

Evidence is accumulating that myelination is not confined to the developmental period; rather, it now appears that myelin turns over and its patterns change throughout the lifespan, which may relate to experience-dependent changes in the function of neural circuits. Here, we focus on the functional implications of myelin changes, capitalizing on previous reviews of mechanisms of myelin plasticity (*4*, *5*) to assess how these might be linked to circuit function underlying learning and memory.

Myelin: From conduction to circuit function

Myelin increases the speed of propagation and the temporal resolution of the action potential by effectively decreasing the capacitance of the axonal membrane, as well as increasing its resistance by reducing current leak across the membrane. Myelin therefore extends the membrane electrical length constant and reduces the action potential propagation failure rate. Between myelin segments, axons have exposed patches of membrane rich in voltage-gated sodium channels, known as the nodes of Ranvier (Fig. 1A), that allow the action potential to propagate from node to node (*10*, *11*). Myelin also enhances the fidelity of information transmission by virtue of its biophysical properties (*10*, *12*) and by facilitating metabolic support from oligodendrocytes to axons (*2*).

Six biophysical variables can affect the speed and/or fidelity of action potential propagation: axon diameter (*13*), myelin thickness (*12*, *14*), internode length (*15*), periaxonal space (*12*), paranodal tightness (*12*), and nodal geometry (*16*) (Fig. 1A). In the mammalian CNS, these biophysical parameters differ along and between axons, even in the same tract or area. For instance, conduction velocity varies along the length of retinal ganglion cell axons, with a difference between the optic nerve and optic tract (*17*). Moreover, axons within the same circuit, tract, and area can be unmyelinated, partially myelinated, or fully myelinated along their length (Fig. 1B). For example, up to 70% of axons in the corpus callosum, one of the main white-matter tracts connecting the two brain hemispheres, remain unmyelinated (*18*), and some myelinated axons in the cortex can exhibit a partial myelin pattern (*19*). Some axons in the auditory circuit have progressively shorter myelin internodes, particularly at the point where they enter the gray matter (Fig. 1B) (*20*). This heterogeneity implies that the velocity and fidelity of conduction can vary within and between neural circuits, suggesting a role for myelin in the temporal precision of computations in functional circuits (Fig. 1C).

Oligodendrocytes, via myelin, also provide ion homeostasis and metabolic support to the axon (*21*). This support can be adapted according to demand; for example, increased neuronal firing rate increases siphoning of potassium (*22*, *23*) and lactate release (*24*). This can affect conduction fidelity and helps to maintain high-frequency firing rates (*2*, *22*, *24*). Dysregulation of oligodendrocyte metabolic support (*2*) or ion homeostasis (*22*, *25*) can alter circuit synchronization and function.

Myelin may therefore have a more sophisticated role in circuit function. For instance, differential myelination of olivocerebellar and thalamocortical axons regulates the conduction velocity of individual axons within these tracts and contributes to the synchronized activity of populations of cerebellar Purkinje cells and cortical neurons onto which these fibers synapse (*26*, *27*). Moreover, the number and length of myelin internodes have been shown to underlie coincidence detection in the auditory system, in which distinct patterns of myelination in cochlear neuron collateral branches correlate with differential conduction velocity, tuned to allow for temporal summation of inputs arising from both ears (*28*). Failure to provide energy to axons by oligodendrocytes results in impairment of auditory input synchrony and temporal summation in the auditory cortex (*2*). Dysregulations in myelination, ion homeostasis, or energy provision alter neuronal firing rate and synchronization as well as the associated function of the related circuits (*2*, *23*, *29*).

Emerging from these studies is a potential functional role for oligodendrocytes in modulating the velocity and fidelity of conduction

[1]Wellcome–Medical Research Council Cambridge Stem Cell Institute and Department of Veterinary Medicine, University of Cambridge, Cambridge, UK. [2]Department of Psychology, University of Cambridge, Cambridge, UK. [3]Department of Physiology, Biomedical Centre, Faculty of Medicine, University of Iceland, Reykjavik, Iceland.
*Corresponding author. Email: rk385@cam.ac.uk (R.T.K.); bdb26@cam.ac.uk (D.B.)

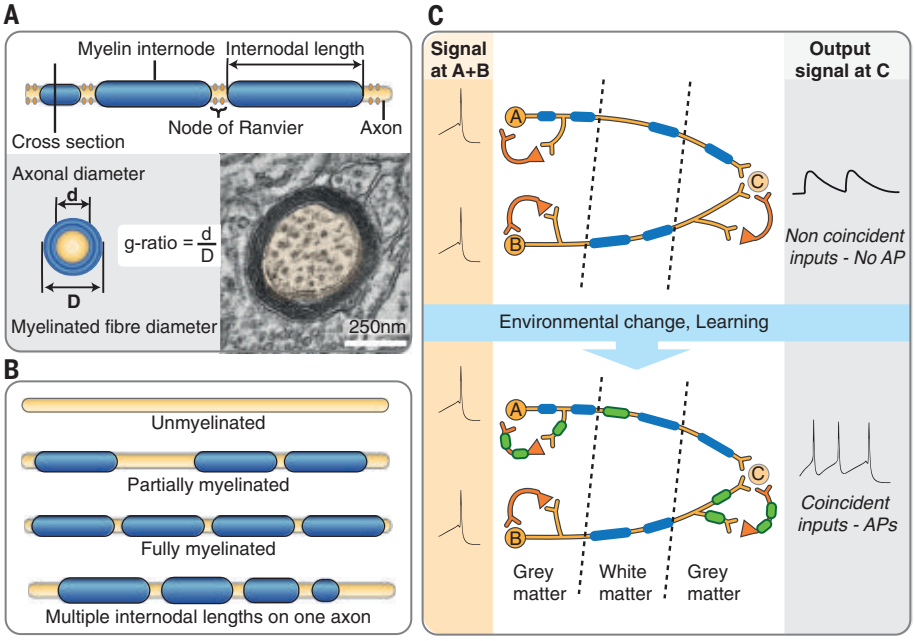


Fig. 1. Myelin parameters and action potential propagation. (**A**) Axons in the central nervous system (CNS) have multiple myelin sheaths along their lengths, each originating from a different oligodendrocyte. Some key parameters of myelin shown to alter conduction velocity are internodal length, myelin thickness (usually expressed as a g-ratio), and nodal geometry (nodes have a high density of voltage-gated sodium channels, shown as orange ellipses). Electron micrograph image is a cross section of a myelinated axon (yellow), showing multiple myelin wraps. (**B**) Axons in the CNS can be unmyelinated, partially myelinated, fully myelinated, or fully myelinated with different patterns of progressively shorter internodal length and larger nodal distances. Along a single axon and between axons, there are different patterns of myelination, providing differences in myelin patterns within and between neuronal circuits. (**C**) Schematic diagram of a neural circuit, depicting yellow projection neurons (A, B, and C) and orange interneurons. In the naïve circuit, myelination promotes action potential propagation, but despite neurons A+B simultaneously firing action potentials, inputs arrive asynchronously at postsynaptic neuron C because of different conduction velocities. During learning or experience, myelin changes along the circuit may modulate conduction velocity to allow synchronous spike arrival at neuron C. [EM image by S. Timmler; illustrations by K. Evans]

along and between axons, so as to regulate the synchronization of inputs in neuronal circuits involving several brain regions by facilitating coincidence of activity onto specific postsynaptic neurons (Fig. 1C). This may affect activity- or timing-dependent synaptic plasticity (*30*), a mechanism suggested to be needed for memory formation (*31*). Thus, mechanisms influencing timing should be considered when designing models of neural networks. Such attempts with models that take active modulation of conduction velocity into account have demonstrated that spike-time arrival, phase differences of oscillatory brain activity, and neural phase synchronization are all sensitive to small changes in myelin parameters (Fig. 1) (*32*, *33*). Although computational models for the role of oligodendrocyte metabolic support and ion homeostasis in activity-dependent circuit plasticity are lacking, existing models indicate that neuronal activity–dependent alterations in myelination alone can promote neural phase synchronization (*33*) relevant for memory formation. Myelin plasticity may therefore provide mechanisms through which experience and associated learning may modify brain connections, presumably by shaping the computation of neural circuits via alterations in the timing of neuronal signal transmission.

Oligodendrocyte lineage structural and functional cellular plasticity

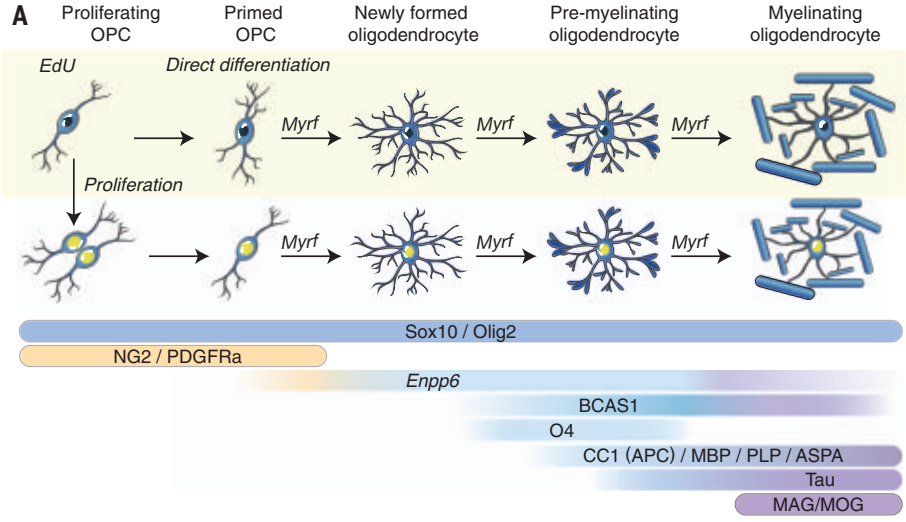
Oligodendrocyte lineage cells display two forms of plasticity: short-term functional and long-term structural plasticity. This, in addition to the heterogeneity in the extent to which axons in the CNS are myelinated (Fig. 1B), offers a wide variety of ways for dynamic myelin changes to fine-tune neural circuits.

The strongest experimental evidence is for structural plasticity in the form of myelin plasticity, involving both oligodendrocytes and the oligodendrocyte precursor cells (OPCs) from which they differentiate, in a multistep process (Fig. 2). OPCs are the main proliferative cells in the adult CNS (*34*) and are evenly distributed throughout it (*34*, *35*), but their function has not been fully elucidated. Throughout life, OPCs differentiate into new myelinating oligodendrocytes in a mechanism that can be bidirectionally modulated by changes in neuronal activity. When neuronal activity is enhanced in vivo pharmacologically in the optic nerve (*36*), or with optogenetic (*37*) or chemogenetic stimulation (*38*) of cortical neurons in the adult motor or somatosensory cortex, the result is an increase in OPC proliferation, differentiation, and myelination in the stimulated area. Conversely, decreasing neuronal activity by means of pharmacological manipulations (*36*) or directly with chemogenetics (*38*) decreases OPC differentiation and myelination in mice. Although identifying the exact mechanisms that underlie these activity-dependent changes warrants further work in vivo, evidence from in vitro experiments implicates mechanisms similar to those involved in synaptic plasticity, including the reliance on growth factors, such as brain-derived neurotrophic factor (BDNF) or neuregulin, and concurrent activation of glutamate receptors on OPCs (*39*). In addition to myelin plasticity, OPCs also phagocytose axons/presynapses (*40*), indicating that OPCs may have more versatile structural plasticity than previously anticipated.

It is unclear whether intermediary oligodendrocytes can affect neuronal function (Fig. 2), although results from behavioral studies indicate that this may be a possibility (*41*, *42*). This could be mediated by secreted factors that induce nodal clustering on unmyelinated axons, leading to accelerated conduction velocity (*43*).

Myelin plasticity is not restricted to activity-dependent differentiation of OPCs into new myelinating oligodendrocytes (Fig. 2B). Longitudinal in vivo imaging of myelin in mice has revealed that established myelin undergoes turnover and quantifiable structural plasticity, where oligodendrocytes modify internodal length (*44*, *45*), alter the length of the nodes of Ranvier (*46*), and remove or add new myelin internodes (*46*). These changes, as well as alterations in the thickness of the myelin sheath (shown by g-ratio measurements from electron micrographs) (Figs. 1A and 2A) (*37*, *38*), can all be influenced by changes in neuronal activity and experience. Thus, myelin structural plasticity continuously alters myelin patterns in neural circuits throughout life.

Oligodendrocyte lineage cells can also display short-term plasticity (Fig. 2B). OPCs can shed the NG2 protein, which can interact with glutamate receptors at neuronal synapses and influence neuronal synaptic plasticity (*47*). Myelinating oligodendrocytes can alter action potential propagation speed by regulating potassium levels in the periaxonal space (*48*) and changing the expression and distribution of molecules involved in metabolic support of the axon, potentially relevant in setting its maximum firing rate (*2*, *24*). Plasticity displayed by



B

	OPC	Newly formed oligodendrocyte	Myelinating oligodendrocyte
Long-term Structural Plasticity	• Direct differentiation to oligodendrocytes (EdU^-) • Proliferation then differentiation to oligodendrocytes (EdU+) • Pruning of axon/pre-synapses	• Potentially, secrete factors that induce clustering of nodal proteins on unmyelinated axons	• Modifications of myelin internodal length • Removal/addition of myelin internodes • Secrete factors that induce clustering of nodes
Short-term Functional Plasticity	• Shed NG2 protein (impacts synaptic plasticity)	• Potential role in circuit function (yet to be determined)	• Regulate potassium levels (impacting firing rate) • Metabolic support to maintain fast neuronal firing rate

Fig. 2. From OPCs to myelinating oligodendrocytes. (**A**) Oligodendrocyte precursor cells (OPCs) differentiate into myelinating oligodendrocytes in a multistep process dependent on the transcription factor *Myrf*. Cell markers for each lineage stage and their approximate onsets/offsets are shown below the lineage progression diagram. Emerging evidence suggests that OPCs can enter a primed state, mostly likely in G_1 phase arrest. These cells and newly differentiated cells, marked by high *Enpp6* expression, are present in the brain and are ready to rapidly differentiate further into premyelinating, and then myelinating, oligodendrocytes. Only proliferating OPCs incorporate EdU (yellow nuclei), which fate-maps OPC differentiation into myelinating oligodendrocytes. Cells already past the proliferative stage are not marked by EdU. (**B**) Table illustrating the forms of plasticity displayed by oligodendrocyte lineage cells with implications for circuit plasticity, divided into long-term structural and short-term functional plasticity. Abbreviations: EdU, ethynyl-2′-deoxyuridine; Myrf, myelin regulatory factor; Sox10, SRY-box transcription factor 10; Olig2, oligodendrocyte transcription factor 2; NG2, neuron-glial antigen 2; PDGFRa, platelet-derived growth factor receptor–α; *Enpp6*, ectonucleotide pyrophosphatase/phosphodiesterase 6; BCAS1, brain-enriched myelin-associated protein 1; CC1, anti-adenomatous polyposis coli clone CC1; ASPA, aspartoacylase; MBP, myelin basic protein; PLP, proteolipid protein 1; MAG, myelin-associated glycoprotein; MOG, myelin oligodendrocyte glycoprotein. [Illustrations by K. Evans]

oligodendrocyte lineage cells seems to be affected by neuronal activity (*24*, *37*, *38*, *47*), consistent with neuronal activity playing a regulatory function in myelin modulation, particularly in adulthood (*36*–*39*, *49*). However, the role of myelin plasticity in brain functions such as learning and memory is only now being investigated.

Myelin plasticity in learning and memory

Our understanding of myelin function is changing. Whereas it had been thought to provide inert structural support, it is now being viewed as a plastic and dynamic actor of adaptive (and maladaptive) behavior, especially through its role in memory, defined here as a change in circuit function caused by an experience leading to a behavioral change and learning (*50*).

MRI studies have revealed that when humans learn new motor skills (e.g., juggling, playing the piano) or cognitive skills (e.g., learning to read), structural changes occur in the white-matter tracts related to the fine-tuning of circuits (*51*). A caveat of these studies is that the nature of white-matter changes detected by structural MRI techniques (such as fractional anisotropy, an indication of white-matter microstructure) is unclear, although it is assumed that these changes are myelin-related (*52*). Nonetheless, consistent with the human data, rats that undergo motor learning tasks show an increase in fractional anisotropy on MRI scans, which is associated with increased optical density of myelin basic protein (MBP) staining in the white matter subjacent to the motor cortex (*53*). Such studies provide some validation of the outcomes of MRI analyses and support the hypothesis that changes in myelin accompany learning and/or memory.

Studies capitalizing on the many advantages of transgenic mice have sparked the notion that de novo myelin formation may be a form of brain plasticity similar to synapse formation, which is generally accepted to be a mechanism for learning, even though direct experimental evidence has been difficult to provide (*54*). The evidence that new oligodendrocytes are formed during the acquisition of a new motor skill in mice, and the subsequent demonstration that preventing OPC differentiation into new myelinating oligodendrocytes impairs behavioral performance in a wide array of tasks (Fig. 3A) (*41*, *55*–*57*), further supports the hypothesis that myelin is causally involved in learning and/or memory.

OPC proliferation in learning and memory

Cross-sectional studies in mice consistently report that OPC proliferation is fast, almost immediate, upon initiation of training in a behavioral task (Fig. 3) (*42*, *55*, *56*). In some studies, the first time point tested was days or weeks after training, making it difficult to draw any firm conclusions about the exact time course of OPC proliferation across tasks and memory systems (Fig. 3B). Longitudinal in vivo experiments indicate that OPC proliferation may reflect a homeostatic response to a loss of OPCs (*35*). In fact, the overall number of OPCs does not change during motor skill learning (*58*) and proliferation seems to be preceded by OPC differentiation into premyelinating oligodendrocytes (*42*) (Figs. 2A and 3B). These premyelinating oligodendrocytes are not labeled by the proliferation marker ethynyl-2′-deoxyuridine (EdU) (*42*), and as the majority of OPCs directly differentiate after learning a new motor skill, this indicates the presence of primed OPCs (*59*, *60*) equipped to directly differentiate, without proliferating first (Fig. 2A), upon changes in neuronal activity. This structural plasticity occurs at a speed similar to that of structural synaptic plasticity (*61*). However, despite evidence for fast OPC proliferation and early differentiation, detectable changes in oligodendrogenesis (identified as $CC1^+$/ EdU^+ cells; Fig. 2A) do not appear until days or weeks later (Fig. 3B) (*41*, *42*), even though myelination can be a rapid process [at least in the developing zebrafish (*62*)]. Hence, oligodendrogenesis detected using this method may indicate a second round of OPC differentiation.

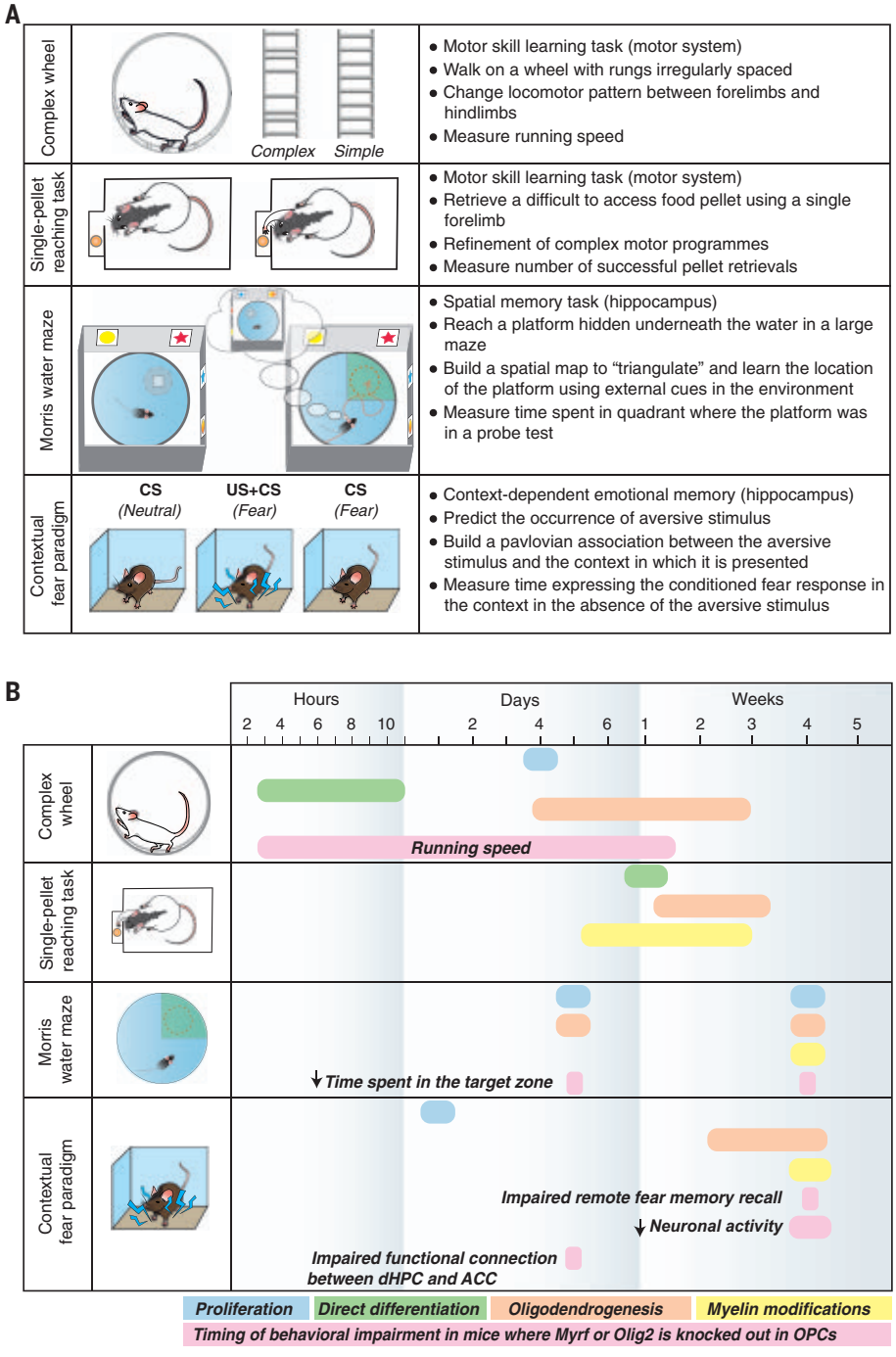


Fig. 3. Oligodendrogenesis dynamics across behavioral paradigms. (**A**) An introduction to the four behavioral paradigms in which oligodendrogenesis and the role of de novo myelination have been investigated. (**B**) Schematic diagram of the dynamics of OPC proliferation (blue), direct OPC differentiation (green), oligodendrogenesis (orange), myelin modifications (yellow), and the timing of behavioral impairments after genetic arrest of OPC differentiation into new myelinating oligodendrocytes (pink). Respective methods of analysis: cFos immunolabelg or in vivo calcium imaging (neuronal activity); EdU labeling (proliferation); CC1 or ASPA immunolabeling (differentiation); transgenic mouse model NG2-mGFP (longitudinal visualization of OPC proliferation and differentiation); electron microscopy quantification of myelinated axons or fractional anisotropy quantification, or tau-mGFP transgenic mouse models to identify myelinating oligodendrocytes by genetically fate-mapping OPC differentiation or MOG-mGFP for longitudinal visualization of the appearance of fully myelinating oligodendrocytes (myelination). [Illustrations by K. Evans]

Oligodendrogenesis dynamics in learning and memory

Overall, the systematic assessment of oligodendrogenesis dynamics over the course of learning behavioral tasks reveals differences that are suggestive of some circuit specificity. These tasks test different types of memory (Fig. 3) underpinned by partly overlapping but dissociable neural circuits on which the task-related memory relies, including prefrontal cortex–dependent short-term/working memory, hippocampus-dependent spatial memory, dorsal striatum–dependent procedural memory (*63*), or amygdala- and hippocampus-dependent Pavlovian and emotional memory (*64*). Oligodendrogenesis dynamics differ in brain regions and timing, depending on the task (Fig. 3B) (*42*, *55*, *56*, *58*). Although further research is warranted to understand the reasons for these differences, oligodendrogenesis dynamics can be useful in deciphering the potential role of specific activity–dependent myelin plasticity in task-relevant circuits.

Although oligodendrogenesis (e.g., $CC1^+/EdU^+$ cells) is a useful surrogate, it has some limitations and may wrongly estimate the extent of de novo myelination. First, this approach does not detect oligodendrocytes generated from direct differentiation of OPCs, which can occur early in the learning process (Fig. 2) (*42*). Second, increases in newly formed oligodendrocyte numbers do not necessarily translate into increased myelination, as high numbers of oligodendrocytes can be detected in demyelinating lesions that fail to remyelinate (*65*). Third, newly formed oligodendrocytes often die (*35*, *66*), with only ~20% becoming stable myelinating oligodendrocytes (*45*). Nonetheless, quantification of myelinating oligodendrocytes, using either electron microscopic analysis (Fig. 1A) (*55*, *56*) or transgenic mice that enable specific labeling of newly formed myelinating oligodendrocytes (*56*) [e.g., using a promoter only expressed in myelinating oligodendrocytes (i.e., *Tau* or *MOG*; Fig. 2A) to drive membrane-bound green fluorescent protein (mGFP) expression], has corroborated that increased myelination occurs in some regions undergoing oligodendrogenesis, even if only days or weeks after the first OPC differentiation. A longitudinal in vivo imaging study in mice, in which terminally myelinating oligodendrocytes were visualized rather than OPC differentiation, revealed a biphasic process taking place in the upper layer of the motor cortex during motor skill learning. The number of new myelinating oligodendrocytes decreased during the learning period, and later increased, eventually exceeding the number of cells displayed by nontrained controls 2 weeks after learning (*58*). The percentage increase in new myelinating oligodendrocytes detected after training was comparable to that of the change in the number of synapses in the same brain

region after learning the same skill (*61*). The delayed appearance of myelinating oligodendrocytes indicates a pause in the constitutive myelination program during learning, before myelinating oligodendrocytes appear.

Conceivably, in the first hours of learning, OPCs proliferate and either enter a primed state or start differentiation, as identified with *Enpp6* expression (Fig. 2A) (*42*), but pause differentiation (*58*) until they have integrated the activity-dependent instructions that determine which axons should undergo myelination (e.g., those within the circuit underlying learning). This could indicate a switch from a constitutive to an activity-dependent targeted myelination program (*39*). Indeed, knocking out BDNF receptors in OPCs, needed for activity-dependent myelination, results in memory impairment in an object recognition task (*67*). Alternatively, the pause in myelination may indicate a switch from myelination of excitatory neurons to myelination of interneurons (*46*). Thus, even though the proliferation of oligodendrocytes seems nonspecific to the function (and underlying neural substrate) that is being recruited in tasks, the pattern of myelination is indeed task- and memory system–dependent.

Gray- and white-matter myelin plasticity

The heterogeneity in oligodendrogenesis timing (Fig. 3B) across brain regions involved in behavioral tasks may reflect differences in myelination between gray and white matter. For example, in mice learning the Morris water maze (*55*), oligodendrogenesis is first detected in specific gray-matter regions before being detected in white matter, whereas myelination is detected at the same time in white and gray matter in mice learning to run on a complex wheel (Fig. 3) (*42*). White-matter myelination predominantly affects long-distance connections between brain regions, likely involved in macrocircuit function (cooperation between different brain regions). Gray-matter myelination, predominantly of interneurons and excitatory connections within a restricted brain region, is potentially involved in microcircuit function. Myelination of short-range axons in the gray matter is considered unlikely to have a meaningful effect on conduction velocity. However, electrophysiological recordings indicate that myelination of short-range interneurons induces physiologically relevant changes in conduction velocity (*68*). Moreover, the dispersed myelin pattern in the gray matter may be optimized for spatiotemporal integration of impulses (*69*), and the pattern of myelin in the gray matter seems to have functional relevance (*58*). Modeling of biophysical properties of myelin indicates that these changes could modulate input synchronization within the microcircuit (*20*, *32*, *33*). Alternatively, gray-matter myelin may predominantly serve to provide metabolic support to the axon to fuel increased neuronal activity, facilitating repetitive fast firing rates (*2*, *24*). The exact role of gray-matter myelination remains to be determined, but it seems to affect microcircuit function.

The differences in timing of oligodendrogenesis between regions may also reflect differences in the type of neurons becoming myelinated. Myelination of neuronal subtypes is differently regulated by neuronal activity (*37*, *70*). Oligodendrocytes can be biased toward certain neuronal subtypes (*71*), although with a change in circuit function they are capable of switching between them (*46*). Hence, the differences in the region and timing of oligodendrogenesis may reflect, and allow the interrogation of, a hierarchy of functional involvement in local- and systems-level circuit plasticity underlying behavior.

Functional implications of oligodendrogenesis for memory

Causal interrogation of the functional role of OPC differentiation into newly formed oligodendrocytes can be achieved by preventing it at any time in transgenic mouse models that use inducible OPC-specific Cre lines to genetically delete one of the transcription factors *Myrf* or *Olig2* (*57*, *72*). This prevents ongoing differentiation into new oligodendrocytes and de novo myelination without influencing preexisting myelin (*41*, *57*, *72*). Despite lacking control over localization (all oligodendrocyte formation is prevented throughout the CNS after tamoxifen administration), this approach offers an opportunity to causally establish the role of myelin plasticity in brain function. For example, it is possible to interrogate the involvement of de novo myelination in either learning or memory consolidation (in carefully designed behavioral experiments) by altering the timing of tamoxifen administration to occur before, during, or after training. Preventing OPC differentiation into new myelinating oligodendrocytes consistently impairs memory across a wide array of behavioral tasks (*41*, *55*–*57*), although differences between study designs make direct comparisons difficult. Nonetheless, the varying times at which the deficits emerge (Fig. 3B) seem to coincide with the requirements for systems-level consolidation of memory (i.e., the functional coordination of multiple brain regions mediating the long-term storage of a memory) (*73*).

Oligodendrogenesis in motor circuit plasticity

The link between myelin and motor function is well established. Motor defects are one of the main phenotypes of dysfunctional myelination; conversely, transgenic animals in which myelin or myelination has been enhanced show enhanced behavioral outcomes in a range of motor skill tasks (*74*, *75*). Mice in which oligodendrogenesis is blocked do not appear to exhibit nonspecific motor deficits in running ability, but begin to show behavioral impairments in learning to run on the complex wheel within 2.5 hours (*41*), which aligns with early OPC differentiation in white matter (Fig. 3B) (*42*). However, early differentiation in the motor cortex occurs a few hours later, and oligodendrogenesis ($CC1^+$/ EdU^+) only appears in both white and cortical gray matter 4 days after introduction to the task (Fig. 3B). In another motor task, the single-pellet reaching task, oligodendrogenesis in the upper layer of the cortex occurs comparatively later (Fig. 3B) (*58*).

How behavioral impairments can precede oligodendrogenesis is unclear. This may indicate a previously unknown role for primed OPCs or premyelinating oligodendrocytes in circuit function (Fig. 2), or instead may indicate that direct differentiation to newly myelinating oligodendrocytes occurred elsewhere in the underlying neural circuit extrinsic to the brain regions investigated. These studies have focused on the motor cortex and the underlying white matter, presumably because when the motor cortex (*76*) or the corpus callosum (*77*) are removed, motor skill learning and/or memory are impaired. However, motor skill learning is not confined to these regions; other regions of the motor circuit are also involved (e.g., striatum, thalamus, and/or cerebellum) (*78*). Some evidence suggests that the cerebellum is needed for early skill training, whereas the motor cortex is needed for long-term retention of a motor skill (*79*, *80*). It is possible that oligodendrogenesis, and presumably myelination, may occur at different times elsewhere in this distributed neural circuit, aiding mice to develop a strategy to run efficiently on a complex wheel. Once mice have developed a strategy, it is transferrable to other complex wheels without alteration in oligodendrogenesis, so that impairing OPC differentiation then no longer impairs running speed (*41*, *42*). Hence, the capacity for OPCs to differentiate is necessary for developing a locomotor skill, although it remains to be elucidated where in the underlying distributed brain regions these changes need to occur, and whether premyelinating oligodendrocytes are involved in learning (Fig. 2B).

Oligodendrogenesis in memory consolidation

The synchronized timing of gray and white matter oligodendrogenesis in motor skill learning is in contrast to the differential trajectories of oligodendrogenesis observed in hippocampus-dependent spatial memory (*81*), as measured in the Morris water maze (*55*). In spatial memory, oligodendrogenesis is first detected during learning in cortical and subcortical areas, at the first probe test that ensures that navigation relies on spatial memory and not on an egocentric wayfinding strategy (Fig. 3A) (*82*).

In the white matter connecting these brain regions, oligodendrogenesis is, in contrast, only detected 4 weeks after learning.

Oligodendrogenesis has been reported to take place with a delay of 4 weeks from the probe test (Fig. 3) (*56*), in another form of hippocampus-dependent memory: contextual Pavlovian fear memory (*83*). Mice that cannot produce new oligodendrocytes display deficits in remote, but not recent, recall of contextual fear memory, in line with the delayed engagement of oligodendrogenesis (*56*). However, newly formed myelinating oligodendrocytes (detected by genetic fate mapping of OPC differentiation into $mGFP^+$ myelinating oligodendrocytes) are observed in the total absence of any EdU^+ oligodendrocytes in the dorsal hippocampus 1 week after initiation of conditioning in this task (Fig. 3B). This suggests early direct OPC differentiation to myelinating oligodendrocytes that is not followed by later oligodendrogenesis in the hippocampus during early consolidation of the fear memory. This observation needs further investigation but highlights the potential for temporal differences in oligodendrogenesis dynamics between brain regions and indicates that fast direct differentiation of OPCs into newly myelinating oligodendrocytes may occur in some task-dependent regions.

The varied temporal distribution of oligodendrogenesis (Fig. 3B) may indicate a general difference in myelin plasticity in encoding and systems-dependent consolidation of a memory (*84*, *85*). Indeed, in spatial and contextual fear memory, the memory initially encoded in the hippocampus requires functional coupling with cortical regions (*86*) to be consolidated, a process mediated by the interplay between cortical oscillations and hippocampal sharp wave ripples (*87*). In mice that cannot produce new oligodendrocytes, deficits in recall of a contextual fear memory are preceded by alterations in systems-level coupling between cortical oscillations and hippocampal sharp wave ripples (*55*), although in control mice, oligodendrogenesis is not detected until weeks later. Potentially, the early direct differentiation to myelinating oligodendrocytes detected in the hippocampus (*56*), or oligodendrocyte-mediated axonal nodal clustering (Fig. 2) (*43*), may be sufficient to support early consolidation of learning and initiate the systems-level changes necessary for long-term changes in behavioral responses, although not needed for recent recall. Blocking oligodendrogenesis impairs task-evoked changes in neuronal calcium spikes in the medial prefrontal cortex and reduces expression of the immediate early gene *cFos*, a marker of cellular activity (*88*), in brain regions involved in Pavlovian fear memory (*56*), such as the hippocampus and amygdala (*89*), at the time of remote recall. This is in line with the temporal nature of the behavioral deficits in recall observed in mice in which new oligodendrogenesis is blocked. Together, these data suggest an involvement of myelin plasticity in the systems-level consolidation mechanisms underlying long-term contextual fear memory.

Likewise, no differences in oligodendrogenesis were detected in the hippocampus at the time of probe test after spatial navigation training in the Morris water maze, supporting the view that myelin plasticity in this circuit is more relevant for systems-level consolidation of spatial memory than for learning. Indeed, inhibition of new myelinating oligodendrogenesis by knocking out the transcription factors *Myrf* or *Olig2* in adult OPCs before (*57*), during, or immediately after (*55*) training did not affect learning but impaired the consolidation of recent and remote spatial memory. Moreover, spatial memory (*57*) and neuronal *cFos* (*56*) activity can be enhanced by promoting OPC differentiation into myelinating oligodendrocytes. However, *Myrf* deletion from OPCs after a memory has been consolidated does not result in behavioral deficits, which shows that knocking out *Myrf* does not inherently prevent spatial memory retrieval (*41*, *55*) and that further production of myelin is unnecessary to maintain a memory that has already been consolidated.

We have gained only a limited understanding of the role of myelin plasticity in learning and memory, and of the location of myelin changes in circuits underlying memory. Nonetheless, these studies collectively support the conclusion that myelin plasticity could be a mechanism for systems-level memory consolidation, which in turn could aid retrieval.

Beyond task-related circuit plasticity

The studies summarized above suggest that suppression of adult oligodendrogenesis differentially impairs learning and memory across different systems, and that myelin might have a broader function than previously thought (*41*, *55*, *56*, *58*). A series of studies indicate that myelin dysfunction substantially affects neuronal firing rate (*29*, *90*), jitter (*91*), latency of action potential (*2*, *91*), synchrony (*2*, *92*), synaptic mechanisms (*29*, *90*), and eventually neural circuit function (*2*, *29*). Together with the evidence that dysfunctional myelin or altered myelination during development impairs learning and adaptive behavior (*74*, *93*–*96*), this body of data suggests that even small changes in myelin across the life span can affect the circuit- and systems-level mechanisms involved in cognition and behavior. Deficits in myelin formation and maintenance have been suggested to contribute to multiple CNS disorders involving alterations of learning and memory that have hitherto been considered to have a neuronal basis, such as schizophrenia, addiction, depression, and dementia (*97*, *98*).

Summary and future directions

We have highlighted experimental evidence for myelin plasticity shaping the circuits and systems involved in learning and memory. This nascent field introduces alternative mechanisms of brain plasticity that may underlie memory. Whether myelin plasticity provides a mechanism for the generation of memory engrams (the specific collection of neurons underlying a specific memory) (*84*) warrants further research.

Seminal work on the basic regulatory mechanisms of myelination (*99*) has led to the emergence of experimental tools that allow manipulation of new myelin formation and can be used to investigate the role of myelin in learning and memory. However, efforts should be made to bring together the expertise of myelin biology with behavioral neuroscience and experimental psychology, so as to frame hypotheses about circuit function in well-defined psychological and neural systems.

The timing of some behavioral impairments after *Myrf* deletion in OPCs warrants investigation of the roles of different oligodendrocyte stages on neural circuit function. Additionally, experimental approaches more refined than the global inhibition of ongoing myelination in the CNS are needed to dissect the functional role of de novo myelination in different brain regions or in the white-matter tracts connecting them. Most studies to date have used fate mapping of EdU^+ OPCs, using $EdU^+/CC1^+$ oligodendrocytes as a surrogate marker for new myelination. However, not all OPCs proliferate before differentiation (Fig. 2). Experimental tools such as genetic fate mapping of OPC differentiation into myelinating oligodendrocytes, along with EdU fate mapping, provide an improved approach for identifying fully myelinating oligodendrocytes and thereby establish where, when, and how learning- and memory-related myelination occurs.

The next steps would be to determine the mechanisms of myelination, and, in the gray matter, how the myelin pattern is established and which neurons are becoming myelinated: projection neurons, interneurons, or both? What determines when and how OPCs proliferate, differentiate, and myelinate axons, and how does learning-associated myelination affect ongoing lifelong myelination in the underlying circuits? Do premyelinating oligodendrocytes affect neuronal function? Further evaluation of the functional role of myelin in the CNS is needed to disentangle the contributions of metabolism, ion homeostasis, and myelin-dependent biophysical properties of the axons to circuit function. Future research will need to combine myelin biology with in vivo neurophysiology to establish the causal relationship between myelin and circuit function.

Beyond the promise of a better understanding of the cellular- and neural-systems basis

of learning and memory, a deeper knowledge of the functional role of myelin plasticity may unlock alternative therapeutic approaches for neurodegenerative diseases and neuropsychiatric disorders. Although little is known about the role of oligodendrocytes and myelin in these diseases, the development of new methods (*98*, *100*) to determine their contributions could lead to a new understanding of these conditions. The advancement of remyelination strategies promoting OPC differentiation into new myelinating oligodendrocytes may offer avenues to remediate cognitive deficits (including memory) or aberrant functional engagement of brain circuits in psychiatric diseases. These possibilities call for further investigation of the functional role of myelin plasticity.

REFERENCES AND NOTES

1. K.-A. Nave, Myelination and support of axonal integrity by glia. *Nature* **468**, 244–252 (2010). doi: 10.1038/nature09614; pmid: 21068833
2. S. Moore *et al*., A role of oligodendrocytes in information processing. *Nat. Commun.* **11**, 5497 (2020). doi: 10.1038/s41467-020-19152-7; pmid: 33127910
3. R. J. M. Franklin, C. Ffrench-Constant, Regenerating CNS myelin - from mechanisms to experimental medicines. *Nat. Rev. Neurosci.* **18**, 753–769 (2017). doi: 10.1038/nrn.2017.136; pmid: 29142295
4. O. de Faria Jr., E. A. C. Pama, K. Evans, A. Luzhynskaya, R. T. Káradóttir, Neuroglial interactions underpinning myelin plasticity. *Dev. Neurobiol.* **78**, 93–107 (2018). doi: 10.1002/dneu.22539
5. S. E. Pease-Raissi, J. R. Chan, Building a (w)rapport between neurons and oligodendroglia: Reciprocal interactions underlying adaptive myelination. *Neuron* **109**, 1258–1273 (2021). doi: 10.1016/j.neuron.2021.02.003; pmid: 33621477
6. G. Ziegler *et al*., Compulsivity and impulsivity traits linked to attenuated developmental frontostriatal myelination trajectories. *Nat. Neurosci.* **22**, 992–999 (2019). doi: 10.1038/s41593-019-0394-3; pmid: 31086316
7. Z. Nagy, H. Westerberg, T. Klingberg, Maturation of white matter is associated with the development of cognitive functions during childhood. *J. Cogn. Neurosci.* **16**, 1227–1233 (2004). doi: 10.1162/0898929041920441; pmid: 15453975
8. B. D. Peters *et al*., Age-related differences in white matter tract microstructure are associated with cognitive performance from childhood to adulthood. *Biol. Psychiatry* **75**, 248–256 (2014). doi: 10.1016/j.biopsych.2013.05.020; pmid: 23830668
9. F. Darki, T. Klingberg, The role of fronto-parietal and fronto-striatal networks in the development of working memory: A longitudinal study. *Cereb. Cortex* **25**, 1587–1595 (2015). doi: 10.1093/cercor/bht352; pmid: 24414278
10. P. Alcami, A. El Hady, Axonal Computations. *Front. Cell. Neurosci.* **13**, 413 (2019). doi: 10.3389/fncel.2019.00413; pmid: 31619963
11. Z. Chorghay, R. T. Káradóttir, E. S. Ruthazer, White Matter Plasticity Keeps the Brain in Tune: Axons Conduct While Glia Wrap. *Front. Cell. Neurosci.* **12**, 428 (2018). doi: 10.3389/fncel.2018.00428; pmid: 30519159
12. C. C. H. Cohen *et al*., Saltatory Conduction along Myelinated Axons Involves a Periaxonal Nanocircuit. *Cell* **180**, 311–322.e15 (2020). doi: 10.1016/j.cell.2019.11.039; pmid: 31883793
13. W. A. Rushton, A theory of the effects of fibre size in medullated nerve. *J. Physiol.* **115**, 101–122 (1951). doi: 10.1113/jphysiol.1951.sp004655; pmid: 14889433
14. S. G. Waxman, M. V. Bennett, Relative conduction velocities of small myelinated and non-myelinated fibres in the central nervous system. *Nat. New Biol.* **238**, 217–219 (1972). doi: 10.1038/newbio238217a0; pmid: 4506206
15. M. H. Brill, S. G. Waxman, J. W. Moore, R. W. Joyner, Conduction velocity and spike configuration in myelinated fibres: Computed dependence on internode distance. *J. Neurol. Neurosurg. Psychiatry* **40**, 769–774 (1977). doi: 10.1136/jnnp.40.8.769; pmid: 925697
16. I. L. Arancibia-Cárcamo *et al*., Node of Ranvier length as a potential regulator of myelinated axon conduction speed. *eLife* **6**, e23329 (2017). doi: 10.7554/eLife.23329; pmid: 28130923
17. G. E. Baker, M. P. Stryker, Retinofugal fibres change conduction velocity and diameter between the optic nerve and tract in ferrets. *Nature* **344**, 342–345 (1990). doi: 10.1038/344342a0; pmid: 2314474
18. R. R. Sturrock, Myelination of the mouse corpus callosum. *Neuropathol. Appl. Neurobiol.* **6**, 415–420 (1980). doi: 10.1111/j.1365-2990.1980.tb00219.x; pmid: 7453945
19. G. S. Tomassy *et al*., Distinct profiles of myelin distribution along single axons of pyramidal neurons in the neocortex. *Science* **344**, 319–324 (2014). doi: 10.1126/science.1249766; pmid: 24744380
20. M. C. Ford *et al*., Tuning of Ranvier node and internode properties in myelinated axons to adjust action potential timing. *Nat. Commun.* **6**, 8073 (2015). doi: 10.1038/ncomms9073; pmid: 26305015
21. C. Stadelmann, S. Timmler, A. Barrantes-Freer, M. Simons, Myelin in the Central Nervous System: Structure, Function, and Pathology. *Physiol. Rev.* **99**, 1381–1431 (2019). doi: 10.1152/physrev.00031.2018; pmid: 31066630
22. V. A. Larson *et al*., Oligodendrocytes control potassium accumulation in white matter and seizure susceptibility. *eLife* **7**, e34829 (2018). doi: 10.7554/eLife.34829; pmid: 29596047
23. Y. Yamazaki *et al*., Oligodendrocytes: Facilitating axonal conduction by more than myelination. *Neuroscientist* **16**, 11–18 (2010). doi: 10.1177/1073858409334425; pmid: 19429890
24. A. S. Saab *et al*., Oligodendroglial NMDA Receptors Regulate Glucose Import and Axonal Energy Metabolism. *Neuron* **91**, 119–132 (2016). doi: 10.1016/j.neuron.2016.05.016; pmid: 27292539
25. L. Schirmer *et al*., Oligodendrocyte-encoded Kir4.1 function is required for axonal integrity. *eLife* **7**, e36428 (2018). doi: 10.7554/eLife.36428; pmid: 30204081
26. M. Salami, C. Itami, T. Tsumoto, F. Kimura, Change of conduction velocity by regional myelination yields constant latency irrespective of distance between thalamus and cortex. *Proc. Natl. Acad. Sci. U.S.A.* **100**, 6174–6179 (2003). doi: 10.1073/pnas.0937380100; pmid: 12719546
27. E. J. Lang, J. Rosenbluth, Role of myelination in the development of a uniform olivocerebellar conduction time. *J. Neurophysiol.* **89**, 2259–2270 (2003). doi: 10.1152/jn.00922.2002; pmid: 12611949
28. A. H. Seidl, E. W. Rubel, Systematic and differential myelination of axon collaterals in the mammalian auditory brainstem. *Glia* **64**, 487–494 (2016). doi: 10.1002/glia.22941; pmid: 26556176
29. N. Benamer, M. Vidal, M. Balia, M. C. Angulo, Myelination of parvalbumin interneurons shapes the function of cortical sensory inhibitory circuits. *Nat. Commun.* **11**, 5151 (2020). doi: 10.1038/s41467-020-18984-7; pmid: 33051462
30. Y. Dan, M. M. Poo, Spike timing-dependent plasticity of neural circuits. *Neuron* **44**, 23–30 (2004). doi: 10.1016/j.neuron.2004.09.007; pmid: 15450157
31. S. J. Martin, P. D. Grimwood, R. G. Morris, Synaptic plasticity and memory: An evaluation of the hypothesis. *Annu. Rev. Neurosci.* **23**, 649–711 (2000). doi: 10.1146/annurev.neuro.23.1.649; pmid: 10845078
32. S. Pajevic, P. J. Basser, R. D. Fields, Role of myelin plasticity in oscillations and synchrony of neuronal activity. *Neuroscience* **276**, 135–147 (2014). doi: 10.1016/j.neuroscience.2013.11.007; pmid: 24291730
33. R. Noori *et al*., Activity-dependent myelination: A glial mechanism of oscillatory self-organization in large-scale brain networks. *Proc. Natl. Acad. Sci. U.S.A.* **117**, 13227–13237 (2020). doi: 10.1073/pnas.1916646117; pmid: 32482855
34. M. R. Dawson, A. Polito, J. M. Levine, R. Reynolds, NG2-expressing glial progenitor cells: An abundant and widespread population of cycling cells in the adult rat CNS. *Mol. Cell. Neurosci.* **24**, 476–488 (2003). doi: 10.1016/S1044-7431(03)00210-0; pmid: 14572468
35. E. G. Hughes, S. H. Kang, M. Fukaya, D. E. Bergles, Oligodendrocyte progenitors balance growth with self-repulsion to achieve homeostasis in the adult brain. *Nat. Neurosci.* **16**, 668–676 (2013). doi: 10.1038/nn.3390; pmid: 23624515
36. C. Demerens *et al*., Induction of myelination in the central nervous system by electrical activity. *Proc. Natl. Acad. Sci. U.S.A.* **93**, 9887–9892 (1996). doi: 10.1073/pnas.93.18.9887; pmid: 8790426
37. E. M. Gibson *et al*., Neuronal activity promotes oligodendrogenesis and adaptive myelination in the mammalian brain. *Science* **344**, 1252304 (2014). doi: 10.1126/science.1252304; pmid: 24727982
38. S. Mitew *et al*., Pharmacogenetic stimulation of neuronal activity increases myelination in an axon-specific manner. *Nat. Commun.* **9**, 306 (2018). doi: 10.1038/s41467-017-02719-2; pmid: 29358753
39. I. Lundgaard *et al*., Neuregulin and BDNF induce a switch to NMDA receptor-dependent myelination by oligodendrocytes. *PLOS Biol.* **11**, e1001743 (2013). doi: 10.1371/journal.pbio.1001743; pmid: 24391468
40. J. Buchanan *et al*., Oligodendrocyte precursor cells prune axons in the mouse neocortex. bioRxiv [preprint]. 29 May 2021. pmid: 446047
41. I. A. McKenzie *et al*., Motor skill learning requires active central myelination. *Science* **346**, 318–322 (2014). doi: 10.1126/science.1254960; pmid: 25324381
42. L. Xiao *et al*., Rapid production of new oligodendrocytes is required in the earliest stages of motor-skill learning. *Nat. Neurosci.* **19**, 1210–1217 (2016). doi: 10.1038/nn.4351; pmid: 27455109
43. S. A. Freeman *et al*., Acceleration of conduction velocity linked to clustering of nodal components precedes myelination. *Proc. Natl. Acad. Sci. U.S.A.* **112**, E321–E328 (2015). doi: 10.1073/pnas.1419099112; pmid: 25561543
44. R. A. Hill, A. M. Li, J. Grutzendler, Lifelong cortical myelin plasticity and age-related degeneration in the live mammalian brain. *Nat. Neurosci.* **21**, 683–695 (2018). doi: 10.1038/s41593-018-0120-6; pmid: 29556031
45. E. G. Hughes, J. L. Orthmann-Murphy, A. J. Langseth, D. E. Bergles, Myelin remodeling through experience-dependent oligodendrogenesis in the adult somatosensory cortex. *Nat. Neurosci.* **21**, 696–706 (2018). doi: 10.1038/s41593-018-0121-5; pmid: 29556025
46. S. M. Yang, K. Michel, V. Jokhi, E. Nedivi, P. Arlotta, Neuron class–specific responses govern adaptive remodeling of myelination in the neocortex. *Science* **370**, eabd2109 (2020). doi: 10.1126/science.abd2109
47. D. Sakry *et al*., Oligodendrocyte precursor cells modulate the neuronal network by activity-dependent ectodomain cleavage of glial NG2. *PLOS Biol.* **12**, e1001993 (2014). doi: 10.1371/journal.pbio.1001993; pmid: 25387269
48. Y. Yamazaki *et al*., Short- and long-term functional plasticity of white matter induced by oligodendrocyte depolarization in the hippocampus. *Glia* **62**, 1299–1312 (2014). doi: 10.1002/glia.22681; pmid: 24756966
49. B. Stevens, S. Tanner, R. D. Fields, Control of myelination by specific patterns of neural impulses. *J. Neurosci.* **18**, 9303–9311 (1998). doi: 10.1523/JNEUROSCI.18-22-09303.1998; pmid: 9801369
50. H. Okano, T. Hirano, E. Balaban, Learning and memory. *Proc. Natl. Acad. Sci. U.S.A.* **97**, 12403–12404 (2000). doi: 10.1073/pnas.210381897; pmid: 11035781
51. J. Scholz, M. C. Klein, T. E. Behrens, H. Johansen-Berg, Training induces changes in white-matter architecture. *Nat. Neurosci.* **12**, 1370–1371 (2009). doi: 10.1038/nn.2412; pmid: 19820707
52. K. B. Walhovd, H. Johansen-Berg, R. T. Káradóttir, Unraveling the secrets of white matter—Bridging the gap between cellular, animal and human imaging studies. *Neuroscience* **276**, 2–13 (2014). doi: 10.1016/j.neuroscience.2014.06.058; pmid: 25003711
53. C. Sampaio-Baptista *et al*., Motor skill learning induces changes in white matter microstructure and myelination. *J. Neurosci.* **33**, 19499–19503 (2013). doi: 10.1523/JNEUROSCI.3048-13.2013; pmid: 24336716
54. N. E. Ziv, E. Ahissar, New tricks and old spines. *Nature* **462**, 859–861 (2009). doi: 10.1038/462859a; pmid: 20016588
55. P. E. Steadman *et al*., Disruption of Oligodendrogenesis Impairs Memory Consolidation in Adult Mice. *Neuron* **105**, 150–164.e6 (2020). doi: 10.1016/j.neuron.2019.10.013; pmid: 31753579
56. S. Pan, S. R. Mayoral, H. S. Choi, J. R. Chan, M. A. Kheirbek, Preservation of a remote fear memory requires new myelin formation. *Nat. Neurosci.* **23**, 487–499 (2020). doi: 10.1038/s41593-019-0582-1; pmid: 32042175
57. F. Wang *et al*., Myelin degeneration and diminished myelin renewal contribute to age-related deficits in memory. *Nat. Neurosci.* **23**, 481–486 (2020). doi: 10.1038/s41593-020-0588-8; pmid: 32042174
58. C. M. Bacmeister *et al*., Motor learning promotes remyelination via new and surviving oligodendrocytes.

Nat. Neurosci. **23**, 819–831 (2020). doi: 10.1038/s41593-020-0637-3; pmid: 32424285
59. S. O. Spitzer *et al*., Oligodendrocyte Progenitor Cells Become Regionally Diverse and Heterogeneous with Age. *Neuron* **101**, 459–471.e5 (2019). doi: 10.1016/j.neuron.2018.12.020; pmid: 30654924
60. Y. Kamen, H. Pivonkova, K. A. Evans, R. T. Káradóttir, A matter of state: Diversity in oligodendrocyte lineage cells. *Neuroscientist* 1073858420987208 (2021). doi: 10.1177/1073858420987208; pmid: 33567971
61. T. Xu *et al*., Rapid formation and selective stabilization of synapses for enduring motor memories. *Nature* **462**, 915–919 (2009). doi: 10.1038/nature08389; pmid: 19946267
62. T. Czopka, C. Ffrench-Constant, D. A. Lyons, Individual oligodendrocytes have only a few hours in which to generate new myelin sheaths in vivo. *Dev. Cell* **25**, 599–609 (2013). doi: 10.1016/j.devcel.2013.05.013; pmid: 23806617
63. R. J. McDonald, N. M. White, A triple dissociation of memory systems: Hippocampus, amygdala, and dorsal striatum. *Behav. Neurosci.* **107**, 3–22 (1993). doi: 10.1037/0735-7044.107.1.3; pmid: 8447956
64. A. J. Gruber, R. J. McDonald, Context, emotion, and the strategic pursuit of goals: Interactions among multiple brain systems controlling motivated behavior. *Front. Behav. Neurosci.* **6**, 50 (2012). doi: 10.3389/fnbeh.2012.00050; pmid: 22876225
65. H. O. Gautier *et al*., Neuronal activity regulates remyelination via glutamate signalling to oligodendrocyte progenitors. *Nat. Commun.* **6**, 8518 (2015). doi: 10.1038/ncomms9518; pmid: 26439639
66. B. D. Trapp, A. Nishiyama, D. Cheng, W. Macklin, Differentiation and death of premyelinating oligodendrocytes in developing rodent brain. *J. Cell Biol.* **137**, 459–468 (1997). doi: 10.1083/jcb.137.2.459; pmid: 9128255
67. A. C. Geraghty *et al*., Loss of Adaptive Myelination Contributes to Methotrexate Chemotherapy-Related Cognitive Impairment. *Neuron* **103**, 250–265.e8 (2019). doi: 10.1016/j.neuron.2019.04.032; pmid: 31122677
68. K. D. Micheva, M. Kiraly, M. M. Perez, D. V. Madison, Conduction Velocity Along the Local Axons of Parvalbumin Interneurons Correlates With the Degree of Axonal Myelination. *Cereb. Cortex* **31**, 3374–3392 (2021). doi: 10.1093/cercor/bhab018; pmid: 33704414
69. M. Deschênes, P. Landry, Axonal branch diameter and spacing of nodes in the terminal arborization of identified thalamic and cortical neurons. *Brain Res.* **191**, 538–544 (1980). doi: 10.1016/0006-8993(80)91302-5; pmid: 7378769
70. S. Koudelka *et al*., Individual Neuronal Subtypes Exhibit Diversity in CNS Myelination Mediated by Synaptic Vesicle Release. *Curr. Biol.* **26**, 1447–1455 (2016). doi: 10.1016/j.cub.2016.03.070; pmid: 27161502
71. M. Zonouzi *et al*., Individual Oligodendrocytes Show Bias for Inhibitory Axons in the Neocortex. *Cell Rep.* **27**, 2799–2808.e3 (2019). doi: 10.1016/j.celrep.2019.05.018; pmid: 31167127
72. B. Emery *et al*., Myelin gene regulatory factor is a critical transcriptional regulator required for CNS myelination. *Cell* **138**, 172–185 (2009). doi: 10.1016/j.cell.2009.04.031; pmid: 19596243
73. L. R. Squire, L. Genzel, J. T. Wixted, R. G. Morris, Memory consolidation. *Cold Spring Harb. Perspect. Biol.* **7**, a021766 (2015). doi: 10.1101/cshperspect.a021766; pmid: 26238360
74. E. A. Gould *et al*., Mild myelin disruption elicits early alteration in behavior and proliferation in the subventricular zone. *eLife* **7**, e34783 (2018). doi: 10.7554/eLife.34783; pmid: 29436368
75. M. A. Jeffries *et al*., ERK1/2 Activation in Preexisting Oligodendrocytes of Adult Mice Drives New Myelin Synthesis and Enhanced CNS Function. *J. Neurosci.* **36**, 9186–9200 (2016). doi: 10.1523/JNEUROSCI.1444-16.2016; pmid: 27581459
76. R. Kawai *et al*., Motor cortex is required for learning but not for executing a motor skill. *Neuron* **86**, 800–812 (2015). doi: 10.1016/j.neuron.2015.03.024; pmid: 25892304
77. P. M. Schalomon, D. Wahlsten, Wheel running behavior is impaired by both surgical section and genetic absence of the mouse corpus callosum. *Brain Res. Bull.* **57**, 27–33 (2002). doi: 10.1016/S0361-9230(01)00633-5; pmid: 11827734
78. A. E. Papale, B. M. Hooks, Circuit changes in motor cortex during motor skill learning. *Neuroscience* **368**, 283–297 (2018). doi: 10.1016/j.neuroscience.2017.09.010; pmid: 28918262
79. D. Spampinato, P. Celnik, Temporal dynamics of cerebellar and motor cortex physiological processes during motor skill learning. *Sci. Rep.* **7**, 40715 (2017). doi: 10.1038/srep40715; pmid: 28091578
80. J. M. Galea, A. Vazquez, N. Pasricha, J. J. de Xivry, P. Celnik, Dissociating the roles of the cerebellum and motor cortex during adaptive learning: The motor cortex retains what the cerebellum learns. *Cereb. Cortex* **21**, 1761–1770 (2011). doi: 10.1093/cercor/bhq246; pmid: 21139077
81. R. G. Morris, P. Garrud, J. N. Rawlins, J. O'Keefe, Place navigation impaired in rats with hippocampal lesions. *Nature* **297**, 681–683 (1982). doi: 10.1038/297681a0; pmid: 7088155
82. C. V. Vorhees, M. T. Williams, Assessing spatial learning and memory in rodents. *ILAR J.* **55**, 310–332 (2014). doi: 10.1093/ilar/ilu013; pmid: 25225309
83. P. Tovote, J. P. Fadok, A. Lüthi, Neuronal circuits for fear and anxiety. *Nat. Rev. Neurosci.* **16**, 317–331 (2015). doi: 10.1038/nrn3945; pmid: 25991441
84. T. Kitamura *et al*., Engrams and circuits crucial for systems consolidation of a memory. *Science* **356**, 73–78 (2017). doi: 10.1126/science.aam6808; pmid: 28386011
85. T. Abel, K. M. Lattal, Molecular mechanisms of memory acquisition, consolidation and retrieval. *Curr. Opin. Neurobiol.* **11**, 180–187 (2001). doi: 10.1016/S0959-4388(00)00194-X; pmid: 11301237
86. G. Buzsáki, The hippocampo-neocortical dialogue. *Cereb. Cortex* **6**, 81–92 (1996). doi: 10.1093/cercor/6.2.81; pmid: 8670641
87. G. Girardeau, M. Zugaro, Hippocampal ripples and memory consolidation. *Curr. Opin. Neurobiol.* **21**, 452–459 (2011). doi: 10.1016/j.conb.2011.02.005; pmid: 21371881
88. R. J. Smeyne *et al*., fos-lacZ transgenic mice: Mapping sites of gene induction in the central nervous system. *Neuron* **8**, 13–23 (1992). doi: 10.1016/0896-6273(92)90105-M; pmid: 1730004
89. S. Campeau *et al*., Induction of the c-fos proto-oncogene in rat amygdala during unconditioned and conditioned fear. *Brain Res.* **565**, 349–352 (1991). doi: 10.1016/0006-8993(91)91669-R; pmid: 1842702
90. T. Barron, J. Saifetiarova, M. A. Bhat, J. H. Kim, Myelination of Purkinje axons is critical for resilient synaptic transmission in the deep cerebellar nucleus. *Sci. Rep.* **8**, 1022 (2018). doi: 10.1038/s41598-018-19314-0; pmid: 29348594
91. J. H. Kim, R. Renden, H. von Gersdorff, Dysmyelination of auditory afferent axons increases the jitter of action potential timing during high-frequency firing. *J. Neurosci.* **33**, 9402–9407 (2013). doi: 10.1523/JNEUROSCI.3389-12.2013; pmid: 23719808
92. S. E. Kim, K. Turkington, C. Kushmerick, J. H. Kim, Central dysmyelination reduces the temporal fidelity of synaptic transmission and the reliability of postsynaptic firing during high-frequency stimulation. *J. Neurophysiol.* **110**, 1621–1630 (2013). doi: 10.1152/jn.00117.2013; pmid: 23843435
93. M. Makinodan, K. M. Rosen, S. Ito, G. Corfas, A critical period for social experience-dependent oligodendrocyte maturation and myelination. *Science* **337**, 1357–1360 (2012). doi: 10.1126/science.1220845; pmid: 22984073
94. J. Liu *et al*., Clemastine Enhances Myelination in the Prefrontal Cortex and Rescues Behavioral Changes in Socially Isolated Mice. *J. Neurosci.* **36**, 957–962 (2016). doi: 10.1523/JNEUROSCI.3608-15.2016; pmid: 26791223
95. M. Swire, Y. Kotelevtsev, D. J. Webb, D. A. Lyons, C. Ffrench-Constant, Endothelin signalling mediates experience-dependent myelination in the CNS. *eLife* **8**, e49493 (2019). doi: 10.7554/eLife.49493; pmid: 31657718
96. A. Teissier *et al*., Early-life stress impairs postnatal oligodendrogenesis and adult emotional behaviour through activity-dependent mechanisms. *Mol. Psychiatry* **25**, 1159–1174 (2020). doi: 10.1038/s41380-019-0493-2; pmid: 31439936
97. D. Koshiyama *et al*., White matter microstructural alterations across four major psychiatric disorders: Mega-analysis study in 2937 individuals. *Mol. Psychiatry* **25**, 883–895 (2020). doi: 10.1038/s41380-019-0553-7; pmid: 31780770
98. B. Zhao *et al*., Common genetic variation influencing human white matter microstructure. *Science* **372**, eabf3736 (2021). doi: 10.1126/science.abf3736; pmid: 34140357
99. B. Emery, Regulation of oligodendrocyte differentiation and myelination. *Science* **330**, 779–782 (2010). doi: 10.1126/science.1190927; pmid: 21051629
100. R. Schurr, A. A. Mezer, The glial framework reveals white-matter fiber architecture in human and primate brains. *Science* **374**, 762 (2021).

ACKNOWLEDGMENTS

We thank K. A. Evans for illustrations, S. Timmler for the electron micrograph image, and B. Everitt, T. Robbins, D. Rowitch, S. Crisp, A. Vanhaesebrouck, H. Pivonkova, S. Hall, K. Evans, and Y. Kamen for comments on the manuscript. **Funding:** Supported by the European Research Council (ERC: the European Union's Horizon 2020 research and innovation program grant agreement 771411; R.T.K., G.B.); the Paul G. Allen Frontiers Group (Allen Distinguished Investigator program #12076, R.T.K.); the UK Multiple Sclerosis Society (Centre of Excellence Award #132, R.T.K.); the Lister Institute of Preventive Medicine (a research prize, R.T.K.); and the Medical Research Council (grant MR/N02530X/1, D.B.). The funders had no role in the decision to publish, nor in the preparation of the manuscript. **Competing interests:** The authors have no competing interest to declare.

10.1126/science.aba6905

RESEARCH ARTICLE SUMMARY

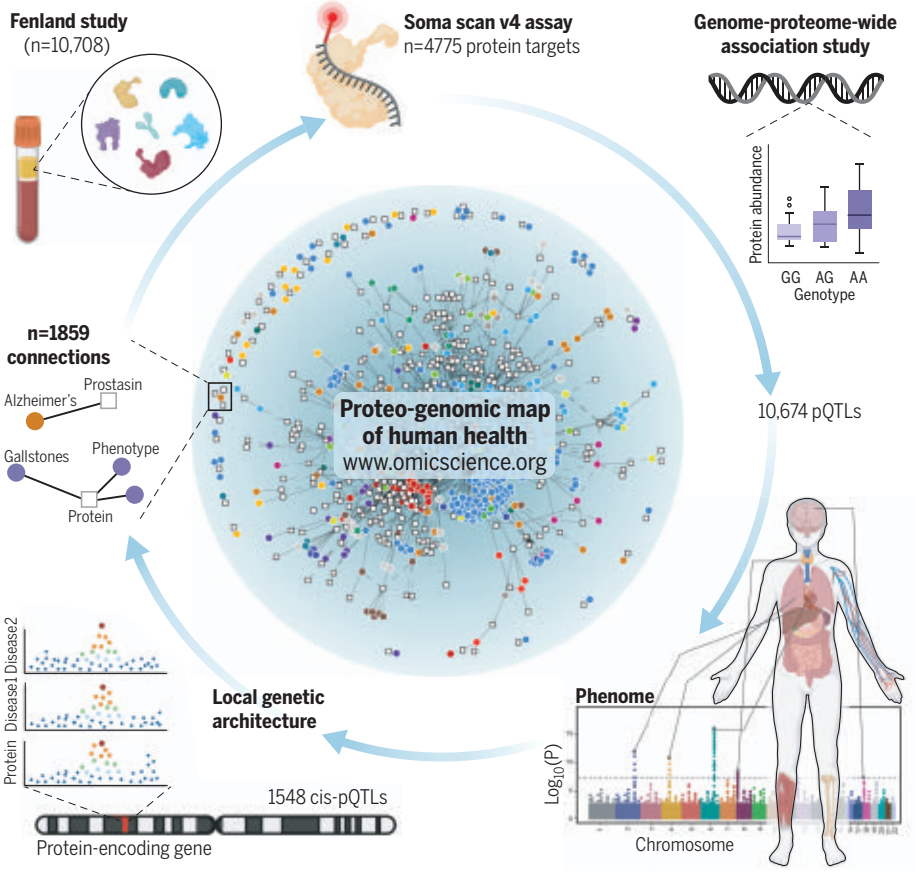
DISEASE GENOMICS

Mapping the proteo-genomic convergence of human diseases

Maik Pietzner†, Eleanor Wheeler†, Julia Carrasco-Zanini, Adrian Cortes, Mine Koprulu, Maria A. Wörheide, Erin Oerton, James Cook, Isobel D. Stewart, Nicola D. Kerrison, Jian'an Luan, Johannes Raffler, Matthias Arnold, Wiebke Arlt, Stephen O'Rahilly, Gabi Kastenmüller, Eric R. Gamazon, Aroon D. Hingorani, Robert A. Scott, Nicholas J. Wareham, Claudia Langenberg*

INTRODUCTION: Proteins are essential functional units of the human body and represent the largest class of drug targets.

RATIONALE: Broad-capture proteomics has the potential to identify causal disease genes, mechanisms, and candidate drug targets through systematically integrating knowledge about genetic signals that are shared among the protein-encoding gene, the resulting protein abundance or function, and common complex diseases. Although technological advances now enable such enquiry at scale, the genetic architecture of most proteins and its relevance for human health remains unknown. We performed a genome-proteome–wide association study including 4775 protein targets measured in plasma from 10,708 European-descent individuals (mean age 48.6 years, 53.3% women). We used the identified protein–quantitative trait loci (pQTLs) to create a proteo-genomic map of human health based on shared, colocalized genetic architecture tested across thousands of phenotypes at protein-encoding loci (cis-pQTLs).



Summary of the study design (outer circle) to construct a proteo-genomic map (inner circle) of human health. Connections between protein-encoding genes, proteins, diseases, and phenotypes were drawn for all examples with strong evidence of a shared genetic signal based on statistical colocalization (posterior probability > 80%). Parts of the figure were generated using BioRender.com.

RESULTS: We identified 10,674 genetic variant–protein target associations ($P < 1.004 \times 10^{-11}$) distributed across 2548 genomic regions (1097 unreported) and covering 3892 distinct protein targets. Of 1538 protein targets with at least one cis-pQTL, we found that half share a genetic signal with gene expression in at least one of 49 tissues; alternative splicing events account for about one-fifth of those, demonstrating the utility of plasma proteomics as a means to infer tissue effects. We demonstrated that cis-pQTLs helped to prioritize candidate causal genes at 558 established risk loci for 537 collated phenotypes. For one-fourth of these (24.6%), this included genes not reported or different from those prioritized by gene expression QTLs, including *PRSS8* (encoding prostasin) for Alzheimer's disease or *RSPO1* (encoding R-spondin–1) for endometrial cancer. We created a cis-anchored proteo-genomic map of human health including 1859 gene-protein-phenotype connections comprising 412 proteins and 506 curated traits. The map highlighted strong cross-disease biological convergence. For example, the genetic signal at *EFEMP1* (EGF-containing fibulin-like extracellular matrix protein 1) was shared across diverse connective tissue disorders consistent with abnormal elastic fiber morphology of the *Efemp1* knockout mouse. Integration of diverse "omic" layers identified a supersaturated bile to promote cholesterol crystallization and gallstone formation as the mode of action at *SULT2A1*. We developed an approach to classify pQTLs by integrating ontology mapping with a data-derived protein network. This showed that 39% (n = 2302) of trans-pQTLs (i.e., those distant from the protein-encoding gene) were protein- or pathway-specific and identified established risk loci, such as rs738409 (*PNPLA3*), an established liver fibrosis locus, to act on several proteins that are all part of a specific protein community. We developed an interactive web resource (www.omicscience.org/apps/pgwas) to facilitate rapid access and interrogation to our results.

CONCLUSION: Genetically anchored plasma proteomics identifies shared etiologies across diseases, enables prioritization of drug targets, and provides a systems biology context for gene-to-phenotype and protein-to-phenotype connections. ■

The list of author affiliations is available in the full article online.
***Corresponding author. Email: claudia.langenberg@mrc-epid.cam.ac.uk**
†These authors contributed equally to this work.
Cite this article as M. Pietzner *et al.*, *Science* 374, eabj1541 (2021). DOI: 10.1126/science.abj1541

READ THE FULL ARTICLE AT
https://doi.org/10.1126/science.abj1541

RESEARCH ARTICLE

DISEASE GENOMICS

Mapping the proteo-genomic convergence of human diseases

Maik Pietzner[1,2]†, Eleanor Wheeler[1]†, Julia Carrasco-Zanini[1], Adrian Cortes[3], Mine Koprulu[1], Maria A. Wörheide[4], Erin Oerton[1], James Cook[1], Isobel D. Stewart[1], Nicola D. Kerrison[1], Jian'an Luan[1], Johannes Raffler[4,5], Matthias Arnold[4,6], Wiebke Arlt[7], Stephen O'Rahilly[8], Gabi Kastenmüller[4,9], Eric R. Gamazon[10,11], Aroon D. Hingorani[12,13,14], Robert A. Scott[3], Nicholas J. Wareham[1,13], Claudia Langenberg[1,2,13]*

Characterization of the genetic regulation of proteins is essential for understanding disease etiology and developing therapies. We identified 10,674 genetic associations for 3892 plasma proteins to create a cis-anchored gene-protein-disease map of 1859 connections that highlights strong cross-disease biological convergence. This proteo-genomic map provides a framework to connect etiologically related diseases, to provide biological context for new or emerging disorders, and to integrate different biological domains to establish mechanisms for known gene-disease links. Our results identify proteo-genomic connections within and between diseases and establish the value of cis-protein variants for annotation of likely causal disease genes at loci identified in genome-wide association studies, thereby addressing a major barrier to experimental validation and clinical translation of genetic discoveries.

Proteins are the central layer of information transfer from the genome to the phenome, and recent studies have started to elucidate how natural sequence variation in the human genome affects protein concentrations measured from readily available biofluids such as blood (*1*–*6*). Investigation of the clinical consequences of these so-called protein–quantitative trait loci (pQTLs) can help to better explain disease mechanisms and provide insights into the shared genetic architecture across diseases within a translational framework that puts humans as the model organism at the center (*2*, *4*). This approach is now pursued at scale by pharmaceutical companies for the discovery of drug targets or repurposing opportunities (*7*, *8*). Earlier studies have used bespoke panels (*3*, *6*, *9*) or larger proteomic platforms (*1*, *2*, *4*, *5*) to characterize the genetic architecture of proteins, and their results have shown how these strategies can provide insight into the pathogenesis of specific diseases. Less attention has been given to (i) providing a framework to assess the protein specificity of genetic variation residing outside (trans) the protein-encoding gene; (ii) understanding the clinical relevance of pQTLs for proteins detected in plasma but not known to be actively secreted (*7*); (iii) classifying thousands of proteins according to their genetic architecture as explained by cis variants, specific trans variants, or unspecific trans variants; (iv) demonstrating the specific utility of pQTLs for the prioritization of candidate genes at established risk loci; and (v) systematically mapping shared gene-protein-disease signals to uncover connections among thousands of considered diseases and other phenotypes.

Profiling thousands of proteins circulating in blood at population scale is currently possible only with the use of large libraries of affinity reagents—antibodies or short oligonucleotides called aptamers—because gold-standard methods such as mass spectrometry lack throughput. We previously provided a detailed comparison of 871 overlapping proteins measured in 485 individuals (*10*) using the two most comprehensive platforms, the aptamer-based SomaScan v4 assay and the antibody-based Olink proximity extension assay. We demonstrated that the majority of pQTLs are consistent across platforms (64%), in line with smaller-scale efforts (*4*), but also highlighted the need to triangulate pQTLs with gene expression and phenotypic information to derive tangible biological hypotheses. Here, we present a genome-proteome–wide association study targeting 4775 distinct proteins measured from plasma samples of 10,708 generally healthy European-descent individuals who were participants in the Fenland study (table S1) (*11*). We identified 10,674 variant-protein associations and developed a framework to systematically identify protein- and pathway-specific pQTLs augmenting current ontology-based classifications in a data-driven manner. We found that half of all pQTLs close to the protein-encoding gene—cis-pQTLs—colocalize with gene expression or splicing QTLs in various tissues, allowing us to derive functional insights within tissues by integrating genetics with plasma proteomics. Moreover, cis-pQTLs have the specific ability to prioritize candidate causal genes at established genetic risk loci. By means of phenome-wide colocalization screens, we generated a proteo-genomic map of human health covering 1859 gene-protein-phenotype triplets, which provides insights into the shared etiology across diseases and the identification of pathophysiological pathways through cross-domain integration.

Genetic associations for protein targets

We performed a genome-proteome–wide association analysis by testing 10.2 million genotyped or imputed autosomal and X-chromosomal genetic variants with minor allele frequency (MAF) of >1% among 10,708 participants in the Fenland study measuring 4775 distinct proteins (*12*). We identified 2584 genomic regions (1543 within ±500 kb of the protein-encoding genes, i.e., cis) associated with at least one of 3892 protein targets at $P < 1.004 \times 10^{-11}$. Of these regions, 1097 covered variants that have not previously been reported to be associated with plasma proteins (*1*–*6*, *9*) ($r^2 < 0.1$), of which 64% (867 of 1356 pQTLs) available in (*4*) replicated ($P < 0.05$, directionally consistent). Further, 61% of pQTLs (488 of 797; table S2) replicated using the complementary Olink technique (see supplementary materials), with a higher proportion of replication for variants in cis (81.2%) relative to trans (44.2%). Most regions (79.3%, $n = 2050$) were associated with a single protein target, but we observed pleiotropy (≥2 protein targets) at the remaining regions, including association with up to five (16.1%, $n = 418$), 6 to 20 (3.4%, $n = 88$), or 21 to 50 (0.7%, $n = 19$) associated protein targets, and substantial pleiotropy at eight regions (*CFH*, *ARF4-ARHGEF3*, *C4A-CFB*, *BCHE*, *VTN*, *CFD*, *ABO*, *GCKR*) associated with 59 to 1539 protein targets (Fig. 1). The 194 pleiotropic regions harboring a cis-pQTL identified master regulators of the plasma proteome, including glycosyltransferases such as the histo-blood

[1]MRC Epidemiology Unit, Institute of Metabolic Science, University of Cambridge School of Clinical Medicine, Cambridge CB2 0QQ, UK. [2]Computational Medicine, Berlin Institute of Health at Charité–Universitätsmedizin Berlin, 10117 Berlin, Germany. [3]GlaxoSmithKline, Stevenage SG1 2NY, UK. [4]Institute of Computational Biology, Helmholtz Zentrum München, German Research Center for Environmental Health, 85764 Neuherberg, Germany. [5]Institut für Digitale Medizin, Universitätsklinikum Augsburg, 86156 Augsburg, Germany. [6]Department of Psychiatry and Behavioral Sciences, Duke University, Durham, NC 27710, USA. [7]Institute of Metabolism and Systems Research, University of Birmingham, Birmingham B15 2TT, UK. [8]MRC Metabolic Diseases Unit, Wellcome Trust–Medical Research Council Institute of Metabolic Science, University of Cambridge, Cambridge CB2 0QQ, UK. [9]German Centre for Diabetes Research (DZD), 85764 Neuherberg, Germany. [10]Vanderbilt Genetics Institute, Vanderbilt University Medical Center, Nashville, TN 37203, USA. [11]Clare Hall, University of Cambridge, Cambridge CB3 9AL, UK. [12]UCL British Heart Foundation Research Accelerator, Institute of Cardiovascular Science, University College London, London WC1E 6BT, UK. [13]Health Data Research UK, Gibbs Building, London NW1 2BE, UK. [14]Institute of Health Informatics, University College London, London NW1 2DA, UK.

***Corresponding author. Email: claudia.langenberg@mrc-epid.cam.ac.uk**

†These authors contributed equally to this work.

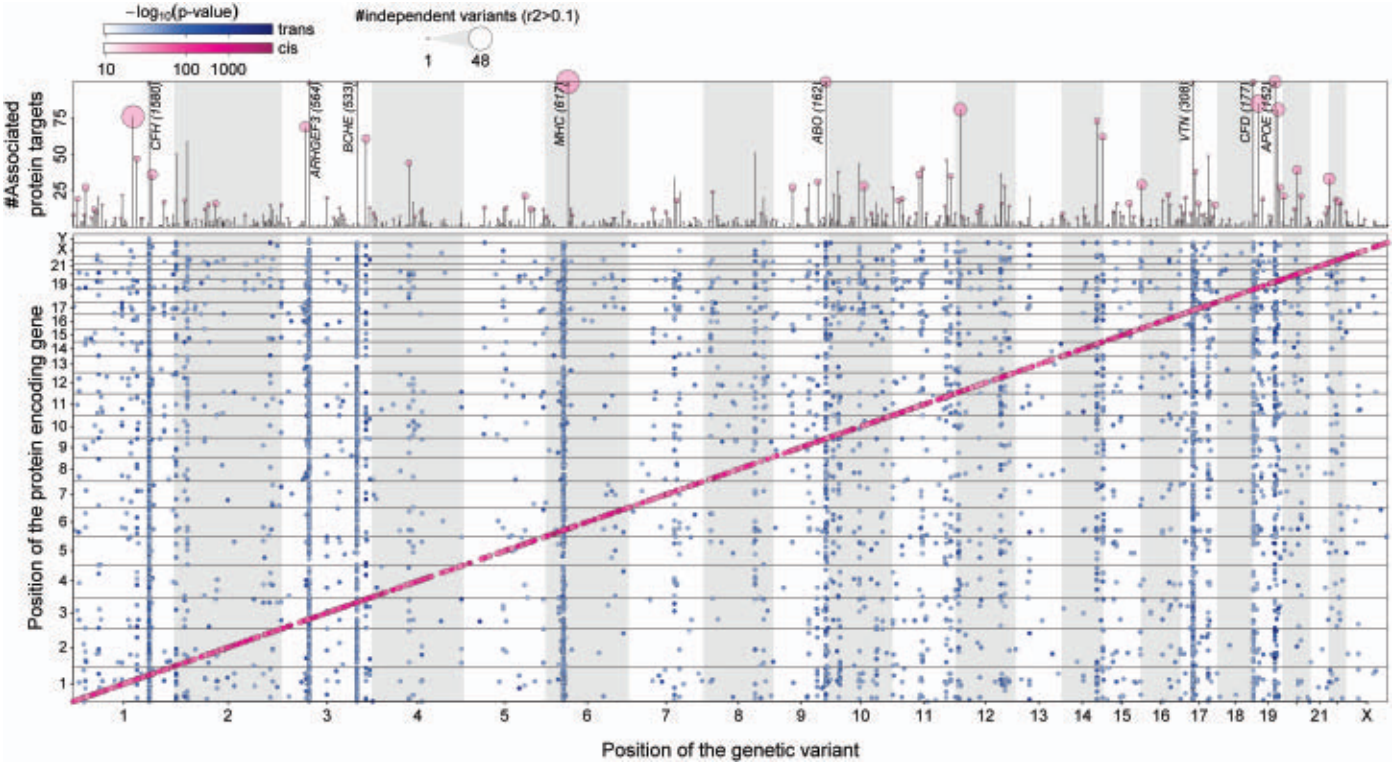


Fig. 1. Regional sentinel genetic variants associated ($P < 1.004 \times 10^{-11}$) with at least one protein target in up to 10,708 participants from the Fenland Study. The lower panel maps the genomic locations of the genetic variants against the genomic locations of the protein-encoding genes. Genetic variants close to the protein-encoding gene (±500 kb) are highlighted in pink (cis-pQTLs); all others are shown in blue (trans-pQTLs). Darker shades indicate more significant *P* values. The upper panel shows the number of associated protein targets for each genomic region (vertical line), with circles above representing the number of approximately independent genetic variants ($r^2 < 0.1$), such that larger circles indicate more genetic variants in the region.

group ABO system transferase (*ABO*), key metabolic enzymes such as glucokinase regulatory protein (*GCKR*), or lipid mediators such as apolipoprotein E, establishing a network-like structure of the circulating proteome (*1*).

Of the 3892 protein targets, 26.8% (n = 1046) had pQTLs in both cis and trans, 13.4% (n = 523) in cis only, and 59.6% (n = 2323) in trans only, among a total of 8328 sentinel variant-protein target associations (Fig. 1 and tables S2 and S3). We identified another 2346 secondary pQTLs at those loci by means of an adapted stepwise conditional analysis (median, 1; range, 1 to 13), indicating widespread allelic heterogeneity in cis (68.8%) and trans (31.2%). The majority of the 5442 distinct variants were located in introns (~44%) or were in high linkage disequilibrium (LD) ($r^2 > 0.6$) with a missense variant (~21%), with similar distributions across cis- and trans-pQTLs (fig. S1). We observed 663 cis-pQTLs with direct consequences for the structure of the protein target (protein-altering variants, PAVs), including important substructures such as disulfide bonds (4.2%), α helices (3.1%), and β strands (2.6%) (fig. S1). Such variants are predicted to affect correct folding of protein targets, including diminished secretion or reduced half-life in the bloodstream, rather than expression of the protein-encoding gene (*13*). For example, we observed an enrichment of PAVs among actively secreted proteins (*14*) (39.6% versus 33.7%, P = 0.04, χ^2 test), possibly indicating modulation of common posttranslational modifications such as glycosylation.

An integrated classification system for pathway-specific pQTLs

We integrated a data-driven protein network with ontology mapping [Gene Ontology (GO) terms; Fig. 2, A and B, and fig. S2] to distinguish pathway-specific pQTLs from those exerting effects on multiple unrelated targets (see supplementary materials) (*15*). We successfully assigned 40.8% (n = 1790 in cis, n = 423 in trans) of the 5442 genetic variants as protein-specific and 5.9% (n = 236 in cis, n = 86 in trans) as pathway-specific on the basis of converging evidence from the network and ontology mapping, and another 16.5% (n = 498 in cis, n = 402 in trans) to be likely pathway-specific based on either source. In total, 1802 protein targets had at least one (likely) specific pQTL in cis (n = 1385) or trans (n = 417). We classified 648 variants that would have been missed by ontology mapping as protein community–specific through our data-driven network approach. One example is rs738408 (*PNPLA3*), a non-alcoholic fatty liver disease variant (*16*) associated with 22 of 70 aptamers from the same protein community (Fig. 2C). *PNPLA3* encodes patatin-like phospholipase domain–containing protein 3 (PNPLA3), and rs738408 tags the missense variant rs738409 (I148M), which renders PNPLA3 resistant to ubiquitylation-mediated degradation and results in subsequent accumulation on hepatic lipid droplets, which in turn causes fatty liver disease (*17*). The associated protein targets included multiple metabolic and detoxification enzymes highly expressed in the liver, such as alcohol dehydrogenases, arginosuccinate lyase, bile salt sulfotransferase, or aminoacylase-1. Our results support the hypothesis that these enzymes might appear in plasma of otherwise healthy individuals only as a result of lipid overload–induced lysis of hepatocytes. The putative liver damage–specific effect, anchored on the *PNPLA3* trans-pQTL, makes those protein targets potential biomarker candidates, as opposed to the tissue-unspecific proteins currently used to identify fatty liver disease or liver injury in the clinic (*18*).

Contribution of cis and trans genetic architecture

We observed three major categories of protein targets based on the contribution of genetic

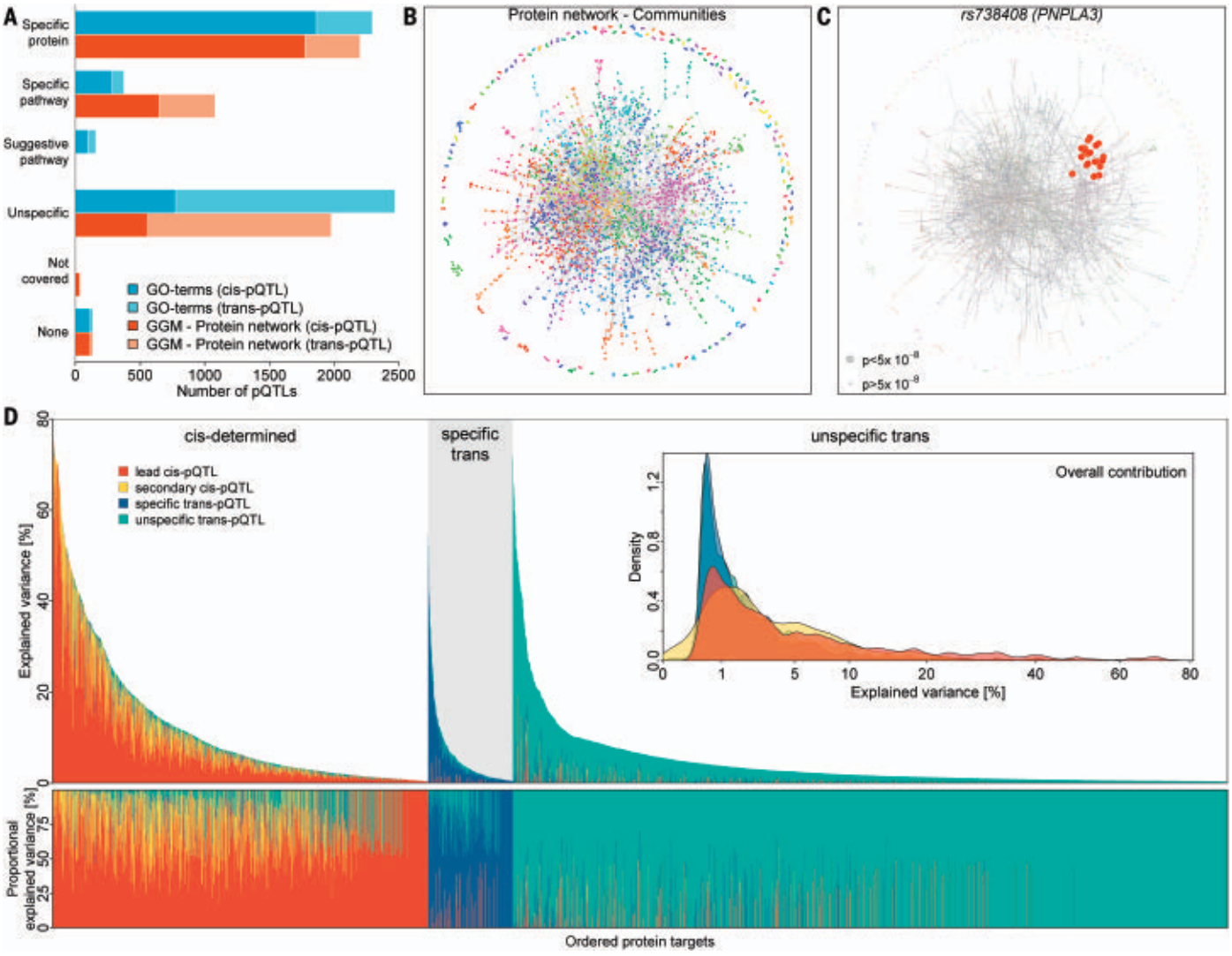


Fig. 2. Classification of protein quantitative trait loci (pQTLs, cis and trans) and subsequent partition of the explained variance in plasma abundances of protein targets. (**A**) Bar chart of pQTL classification based on GO term mapping (blue) or community mapping in a protein network derived by Gaussian graphical modeling (GGM; orange) of associated protein targets. Darker shades indicate cis-pQTLs and lighter colors trans-pQTLs. (**B**) Data-driven protein network colored according to 191 identified protein communities. (**C**) A community-specific pQTL (*PNPLA3*) that was not captured by GO term mapping. Gene annotation was as reported in the supplementary materials. (**D**) Absolute (top) and relative (bottom) explained variance in plasma abundances of protein targets by identified pQTLs. Coloring indicates contribution of the lead cis-pQTL (orange), secondary cis-pQTLs (yellow), protein- or pathway-specific trans-pQTLs (blue), and unspecific trans-pQTLs (green). Protein targets have been grouped by underlying genetic architecture as mostly explained by cis-pQTLs ("cis-determined"), mostly explained by specific trans-pQTLs ("specific trans"), and mostly explained by unspecific trans-pQTLs ("unspecific trans"). The inset displays the overall distribution of explained variance by each of the four categories. The variance explained was computed using linear regression models. See fig. S3 for a graphical display of effect size distributions.

variation to plasma concentrations (Fig. 2D, fig. S3, and table S3). For about one-third of the protein targets (n = 1249), >50% of genetic variance was explained by one or more cis-pQTLs, whereas for 7.2% of the targets (n = 282), protein- or pathway-specific trans-pQTLs accounted for most of the genetic variation; this left two-thirds of the targets (n = 2361) mainly explained by unspecific trans-pQTLs (*12*). Overall, we observed a median genetic contribution of 2.7% [interquartile range (IQR), 1.0% to 7.6%], reaching values above 70% for proteins such as vitronectin (rs704, MAF = 47.3%) or sialic acid–binding Ig-like lectin 9 (rs2075803, MAF = 44.1%) which were often driven by only a single common cis-pQTL. PAVs, which affect the binding epitope of the protein target, are the likely explanation for such strong and isolated genetic effects. Although more than two-thirds of the protein targets with at least one cis-pQTL were unrelated to PAVs, we found that 158 of the protein targets (32.9%) linked to a PAV ($r^2 > 0.6$) shared a genetic signal with at least one disease or risk factor (see below). This suggests that the conformation and possibly the function of the protein target, rather than the plasma abundance of the protein target, might be more relevant as mediators of downstream phenotypic consequences, and that aptamers are able to detect such probably dysfunctional proteins.

Our approach to identify protein-/pathway-specific trans-pQTLs allowed us to uncover biologically relevant information, which was otherwise hidden by strong and unspecific trans-pQTLs that possibly interfere with the measurement technique rather than the biology of the protein target. For example, rs704, a missense variant within *VTN* that associated with a higher fraction of single-chain vitronectin with altered binding properties (*19*, *20*) explained 72% of the variance in MICOS complex

subunit MIC10 (MOS1), far outperforming the contribution of the specific trans-pQTL rs398041972 (0.7%). rs398041972 resides about 1 Mb upstream of *TMEM11*, encoding transmembrane protein 11, a physical interaction partner of MOS1 as part of the MICOS complex (*21*). In general, we observed that the median contribution of specific trans-pQTLs to the variance in plasma concentrations was 1.1% (IQR, 0.6% to 2.6%) across 687 protein targets, reaching values as high as 38.3% for catenin β-1 via two trans-pQTLs (rs1392446 and rs35024584) within the same region for which we prioritized *CDH6* as a candidate causal gene. *CDH6* encodes cadherin 6, which physically interacts with catenin β-1 (*22*). We systematically tested for an enrichment of putative protein interaction partners among the 20 closest genes at each specific trans locus and observed a factor of 1.53 enrichment ($P = 1.8 \times 10^{-10}$, χ^2 test) of first- and second-degree neighbors from the STRING network (*23*), highlighting the ability of our classification system to identify biologically meaningful trans-pQTLs.

Shared genetic architecture with gene expression and splicing

We integrated plasma pQTL results with both gene expression and splicing QTL data (eQTL and sQTL, respectively) from the GTEx version 8 release (*24*) using statistical colocalization [posterior probability (PP) > 80%] for all 1584 protein targets with at least one cis-pQTL (*12*). There was strong evidence that half (50.1%) of these had a shared signal with gene expression in at least one tissue, with a median of 4.5 tissues (IQR, 2 to 12; Fig. 3A), vastly expanding our previous knowledge of gene expression contribution across tissues (*4*, *9*). The majority of cis-pQTLs ($n = 584$, 73.4%) showed plasma protein and gene expression effects in the same direction in all tissues (Fig. 3A), but 26.6% ($n = 212$) showed evidence of at least one pair with opposite effects, including 108 where the protein effect was opposite to the direction observed for gene expression across all tissues with evidence for colocalization. For example, the A-allele of the lead cis-pQTL rs2295621 for immunoglobulin superfamily member 8 (*IGSF8*) was inversely associated with plasma abundance of the protein target ($\beta = -0.19$, $P < 1.65 \times 10^{-32}$) but positively associated with expression of the corresponding mRNA across 33 tissues (table S4). Uncoupling of gene and protein expression, even within the same cell, is a frequently described phenomenon, and possible mechanisms include differential translation, protein degradation, contextual confounders such as time and developmental state, or protein-level buffering (*25*). For 145 protein targets, we identified strong evidence of a tissue-specific contribution to plasma abundances based on a single tissue strongly outweighing all others (Fig. 3A and table S4). These included known tissue-specific examples such as vitamin K–dependent protein C in liver tissue, but also less obvious ones, such as hepatitis A virus cellular receptor 1 (or TIM-1), an entry receptor for multiple human viruses, for which the cis-pQTL and cis-eQTL specifically colocalized in tissue from the transverse colon. To maximize power for the most closely aligned tissue compartment,

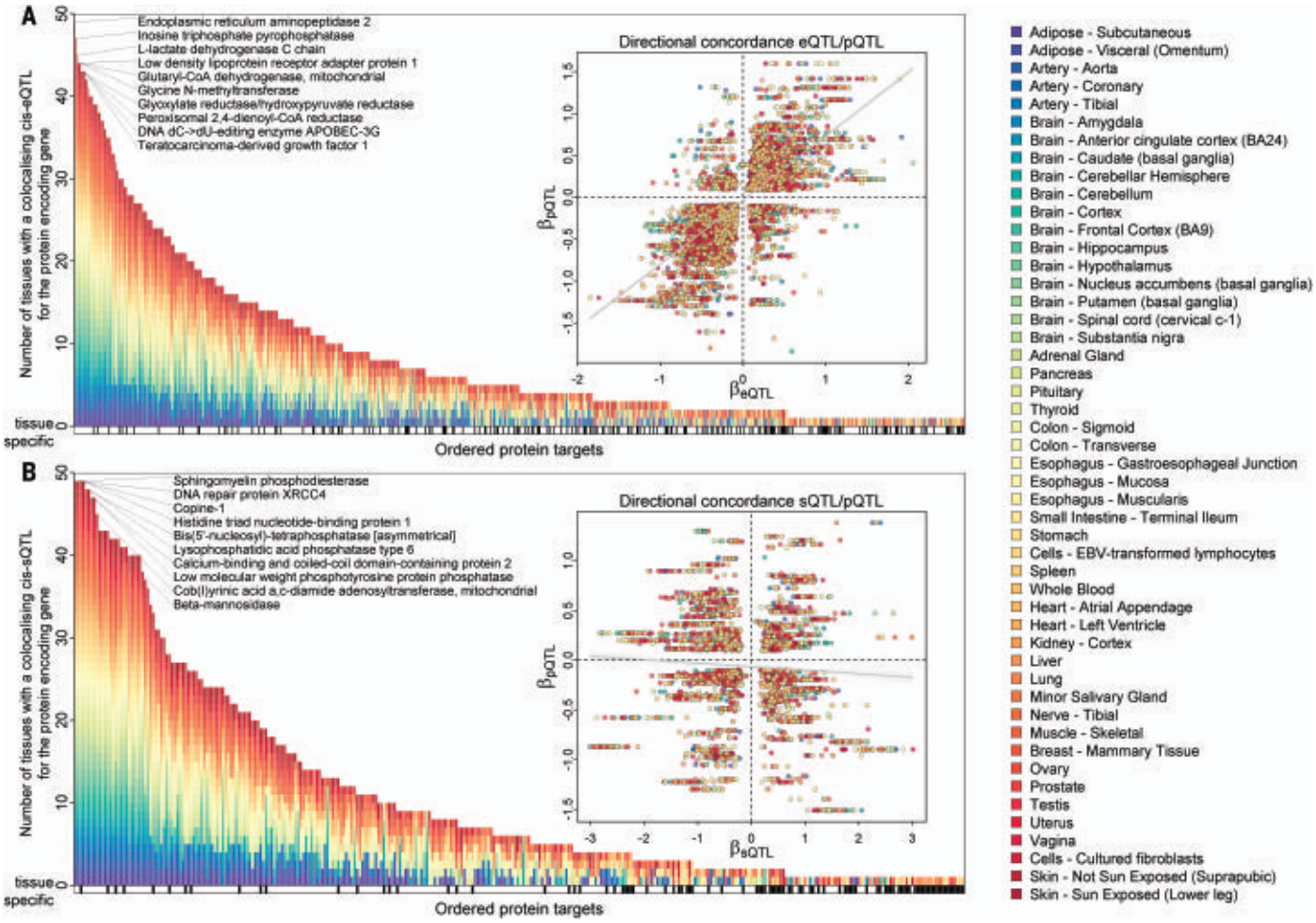


Fig. 3. Integration of gene and splicing quantitative trait loci (eQTLs and sQTLs). (**A**) Protein targets ordered by the number of tissues for which at least one of the cis-pQTLs was also a cis-eQTL as determined by statistical colocalization (posterior probability >80% for a shared signal). Protein targets for which the eQTL showed evidence for a tissue-specific effect are indicated by black vertical lines underneath. (**B**) Same as (A) but considering cis-sQTLs.

whole blood, we integrated gene expression data from the eQTLGen consortium (*26*), which confirmed 140 cis-eQTL/pQTL pairs and revealed another 38 cis-eQTL/pQTL pairs not seen in the GTEx resource, including immune cell–specific mediators of the inflammatory response such as leukocyte immunoglobulin-like receptor subfamily A member 3 (table S4).

To obtain insights beyond the average readout across all transcript species, we examined alternative splicing as a source of protein target variation (*12*). One-fifth (20.1%) of cis signals were shared with a cis-sQTL in at least one tissue (median, 6 tissues; IQR, 2 to 15) (Fig. 3B); 84 of these were not seen with eQTL data, which suggests that the pQTL-relevant transcript isoform was masked from the bulk of assayed transcripts. In contrast to the eQTL colocalization, we did not observe an overall pattern of aligning effect directions (Fig. 3B). This might be best explained by the intron-usage quantification of splicing events within GTEx version 8, which does not allow straightforward mapping of the eventually transcribed isoforms, and the expression of an alternative protein isoform with less affinity to the SOMAmer reagent. The latter may have accounted for the 90 protein target examples where the colocalizing cis-sQTL explained more than 10% of the variance in plasma concentrations (table S4) and emphasizes the ability of splicing QTLs to determine the underlying sources of variation in plasma abundances of protein targets. In summary, our results demonstrate that proteins measured in plasma can be used as proxies for tissue processes when anchored on a shared genetic variation with tissue-specific gene expression or alternative splicing data.

cis-pQTLs enable identification of candidate causal genes at GWAS loci

We used the inherent biological specificity of cis-pQTLs to systematically identify candidate causal genes for genome-wide significant variants reported in the genome-wide association studies (GWAS) catalog as of 25 January 2021 ($P < 5 \times 10^{-8}$) by assessing 558 cis-regions for which the pQTL was in strong LD ($r^2 > 0.8$) with at least one variant for 537 collated traits and diseases (Fig. 4 and table S5) (see supplementary materials) (*12*). For one-fourth of these (24.6%), we annotated a gene different from the reported or mapped gene, and for another 79 cis-regions (14.2%), our predicted causal gene was reported as part of a longer list of potential causal genes.

Among the genes we identified are candidates with strong biological plausibility, such as *AGRP*, encoding Agouti-related protein, a neuropeptide involved in appetite regulation (*27*), suggesting a possible mechanism for measures of body fat distribution associated at this locus. Another example was *NSF*, encoding *N*-ethylmaleimide–sensitive factor (NSF), which may be involved in the fusion of vesicles with membranes, enabling the release of

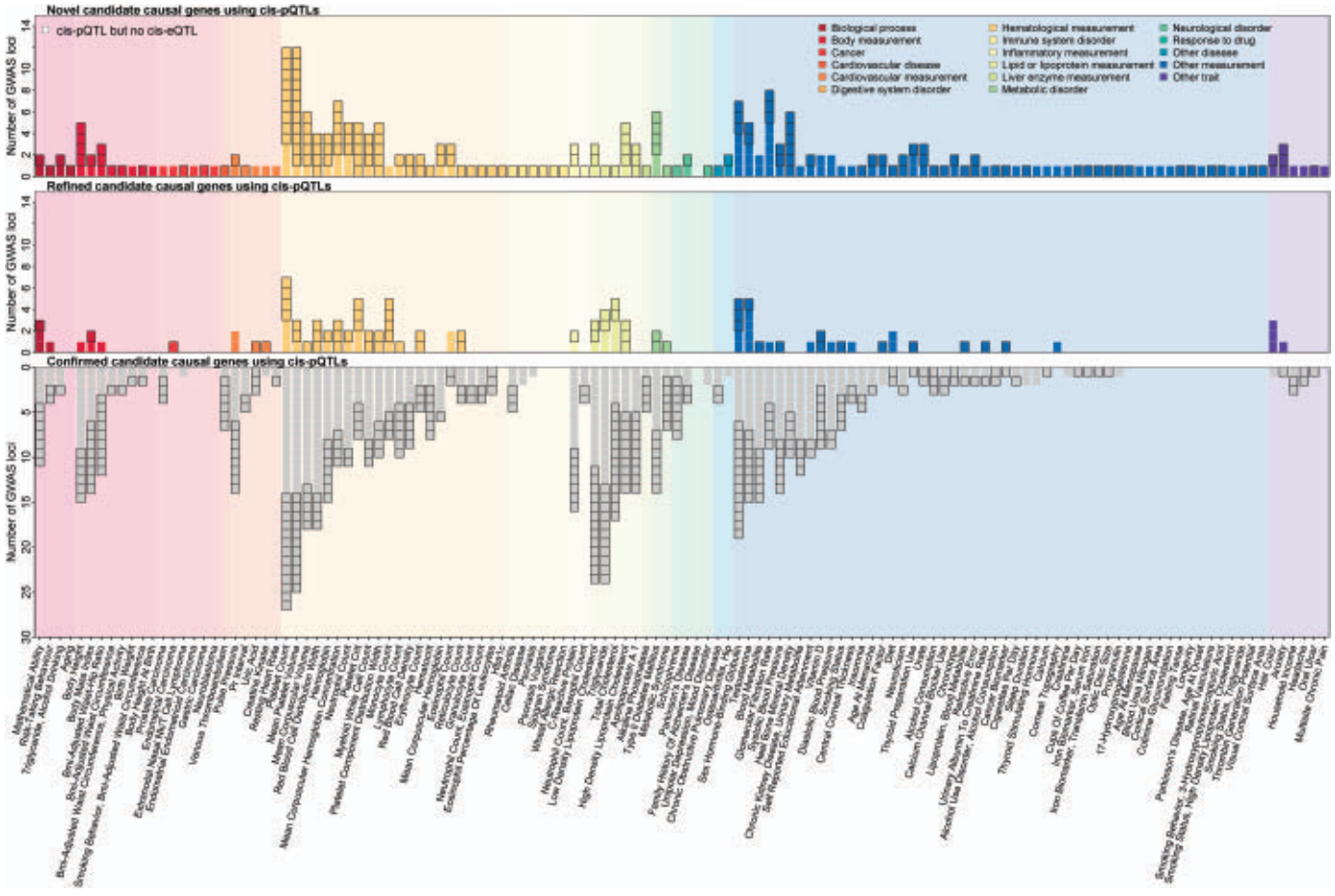


Fig. 4. Causal gene assignment for associations reported in the GWAS catalog using identified cis-pQTLs. Each panel displays the number of loci that have been reported in the GWAS catalog for a curated phenotype and were identified as protein quantitative trait in close proximity (±500 kb) to the protein-encoding gene (cis-pQTL) in the current study. Mapping of GWAS loci and cis-pQTLs was done using the LD between the reported variants ($r^2 > 0.8$). The upper panel displays the number of GWAS loci for which cis-pQTLs provided candidate causal genes. The middle panel displays the number of GWAS loci for which cis-pQTLs refined the list of candidate causal genes at the locus. The lower panel displays the number of GWAS loci with confirmative evidence from cis-pQTLs for already assigned candidate causal genes. Examples where gene prioritization was facilitated through pQTL but not gene expression QTL (eQTL) evidence are highlighted by a border around the box. Colors represent broad trait categories.

neurotransmitters into the extracellular space (28); this locus was previously identified for Parkinson's disease (table S5).

We further assigned *PRSS8* as a candidate causal gene at the *KAT8* locus for Alzheimer's disease (AD), supported by strong LD (r^2 = 0.96) and a high posterior probability of a shared genetic signal (98%) between the lead cis-pQTL (rs368991827, MAF = 27.8%) and the common *KAT8* intronic variant (rs59735493) that has been reported for AD (fig. S4). *PRSS8* codes for prostasin, and we estimated a 13% reduction in AD risk [odds ratio, 0.87; 95% confidence interval (CI), 0.82 to 0.91; $P = 3.8 \times 10^{-8}$] for each 1 SD higher normalized plasma abundance of prostasin. The locus has been identified by multiple GWAS efforts (29), yet prioritization strategies have failed to provide conclusive evidence for a causal gene (30). Prostasin is a serine protease highly expressed in epithelial tissue, which regulates sodium channels (31) and represses TLR4-mediated inflammation in human and mouse models of inflammatory bowel disease (32), a mechanism that might also be relevant to TLR4-mediated neuroinflammation in AD (33).

We observed multiple examples in which our cis-pQTL mapping identified biologically plausible candidate genes that were not implicated by cis-eQTL mapping (Fig. 4). For example, we assigned *RSPO1* as a candidate causal gene at the eQTL-supported *CDCA8* locus for endometrial cancer (34). The intergenic variant rs113998067 is the lead signal for endometrial cancer and was a secondary cis-pQTL for R-spondin–1, encoded by *RSPO1*. Statistical colocalization confirmed a highly likely shared signal (PP = 98.2%) (fig. S5). Accordingly, we estimated a 91% increased risk for endometrial cancer per 1 SD higher plasma abundance of R-spondin–1 (odds ratio, 1.91; 95% CI, 1.52 to 2.41; $P = 3.6 \times 10^{-8}$). R-spondin–1 is a secreted activator protein that acts as an agonist for the canonical Wnt signaling pathway (35), playing a regulatory role as an adult stem cell growth factor. Work in mouse models (36), however, suggests that R-spondin–1 up-regulates the expression of estrogen receptor–α independent of Wnt/β-catenin signaling and might therefore amplify estrogen-mediated endometrial cancer risk (36). We note that the effect estimate for rs113998067 did not differ by sex (P = 0.12), and knockout models in male and female mice have shown abnormal development of testes and ovaries, respectively (37, 38), possibly indicating a wider impact on diseases of reproductive tissues.

A map of proteo-genomic connections across the phenome

We systematically assessed the sharedness of gene-protein-disease triplets through phenome-wide colocalization of cis-pQTL regions (see supplementary materials) (12) to identify and create a genetically anchored map of proteins involved in the etiology of common complex diseases, which could represent potential druggable targets. We identified 1859 gene-protein-trait triplets (network edges, Fig. 5 and fig. S6) comprising 412 protein targets and 506 curated phenotypes (fig. S7 and table S6). The mapping of these shared gene-protein-phenome connections highlights a large number of insights, as discussed below, while confirming previously established connections for known pleiotropic loci [e.g., GCKR (n = 197 traits), α-1-antitrypsin (n = 79 traits), or apolipoprotein A-V (n = 64 traits)] and established disease genes [e.g., roto-oncogene tyrosine protein kinase receptor RET (*RET*) and Hirschsprung's disease (39), or C-C motif chemokine 21 (*CCL21*) and rheumatoid arthritis (40)].

The map highlights 10 diseases for which we identified five or more colocalizing cis-pQTLs, including coronary artery disease (n = 12), hyperlipidemia indicated by lipid-lowering medication (n = 8), ulcerative colitis (n = 7), Alzheimer's disease (n = 6), and type 2 diabetes (n = 5). Statistical power was greatest for the detection of shared genetic architecture for traits for which measures were available in the largest number of people, in line with a median of 2 colocalizing cis-pQTLs (IQR, 2 to 4; maximum 32 for mean platelet volume) for blood cell parameters and biomarkers available in large-scale biobanks. For 104 of 191 curated phenotypes with at least three colocalizing protein targets, we observed significant enrichment of pathways [false discovery rate (q value) < 5%; table S7]. These reflected the known biology of the corresponding clinical entities, such as "wound healing" for platelet count, "skeletal system development" for height, "cholesterol metabolism" for coronary artery disease, or "response to virus" for Crohn's disease, as well as yet less understood ones such as "Toll-like receptor signaling" for hypothyroidism, for which two of the genes (*IRF3* and *TLR3*) have already been shown to confer virus-induced disease onset in mouse models (41).

The proteo-genomic map provides a new framework to (i) connect etiologically related diseases, (ii) provide biological context for new or emerging disorders such as COVID-19, and (iii) integrate information from different biological domains to establish mechanisms for known gene-disease links. For each of these scenarios, we provide selected examples to highlight the scientific opportunities arising from this map, both below and on the related open resource platform (www.omicscience.org).

Potential candidate genes for COVID-19 outcomes

We integrated GWAS summary statistics in our map for four different outcome definitions related to COVID-19, ranging from susceptibility to COVID-19 to severe cases requiring hospitalization (42). These GWAS differed substantially in the number of included cases (5101 to 38,984), and we observed that results were sensitive to the choice of outcome. We replicated the previously reported candidate genes *ABO* and *OAS1* (43) (fig. S8), both of which showed consistent evidence across these different outcome definitions. For *ABO*, the lead cis-pQTL (rs576125, MAF = 33.5%) also colocalized with pulmonary embolism (Fig. 5), a common complication of severe COVID-19 (44) potentially attributable to altered abundances of proteins involved in the coagulation cascade (15). We further observed suggestive evidence for *NSF* (for the risk of COVID-19 hospitalization) and *BCAT2* (for severe COVID-19), each of which shared a genetic signal with only one of these four outcomes and therefore will require external validation of their possible role in COVID-19 or associated pathologies.

Integrating multiple OMICs layers elucidates a disease mechanism for gallstones

We identified a signal at *SULT2A1*, a known gallstone locus (45), to be shared between bile salt sulfotransferase (SULT2A1) and the risk of cholelithiasis (odds ratio per 1 SD higher normalized protein abundance, 2.12; 95% CI, 1.66 to 2.70; $P = 2.1 \times 10^{-37}$) as well as cholecystectomy (odds ratio, 2.09; 95% CI, 1.86 to 2.34; $P = 7.8 \times 10^{-38}$). Multitrait colocalization (46) further identified that the signal was also shared with mRNA expression of *SULT2A1* in the liver, plasma concentrations of multiple sulfated steroids (47) including sulfate conjugates of androgen and pregnenolone metabolites, and bile acids. The high posterior probability (PP = 99%) was largely explained (63%) by rs212100, a variant in high LD (r^2 = 0.90) with the lead cis-pQTL at this locus (Fig. 6A and fig. S9). The consistent positive effect directions across all physiological entities, and in particular sulfated steroids and primary bile acid metabolites, suggest higher SULT2A1 activity as the mode of action. The concurrent inverse association with lower plasma concentrations of the secondary bile acid glycolithocholate indicates diminished formation of lithocholic acid, an essential detergent to solubilize fats, including cholesterol (48). Our vertical integration of diverse biology entities points to a supersaturated bile that promotes cholesterol crystallization and gallstone formation as a causal mechanism at a locus for which the mode of action has only been vaguely hypothesized (45).

Convergence of soft tissue disorders through FBLN3

A protein target connected to a very large number (n = 37) of diseases and other phenotypes was FBLN3 (extracellular matrix glycoprotein encoded by *EFEMP1*), which showed

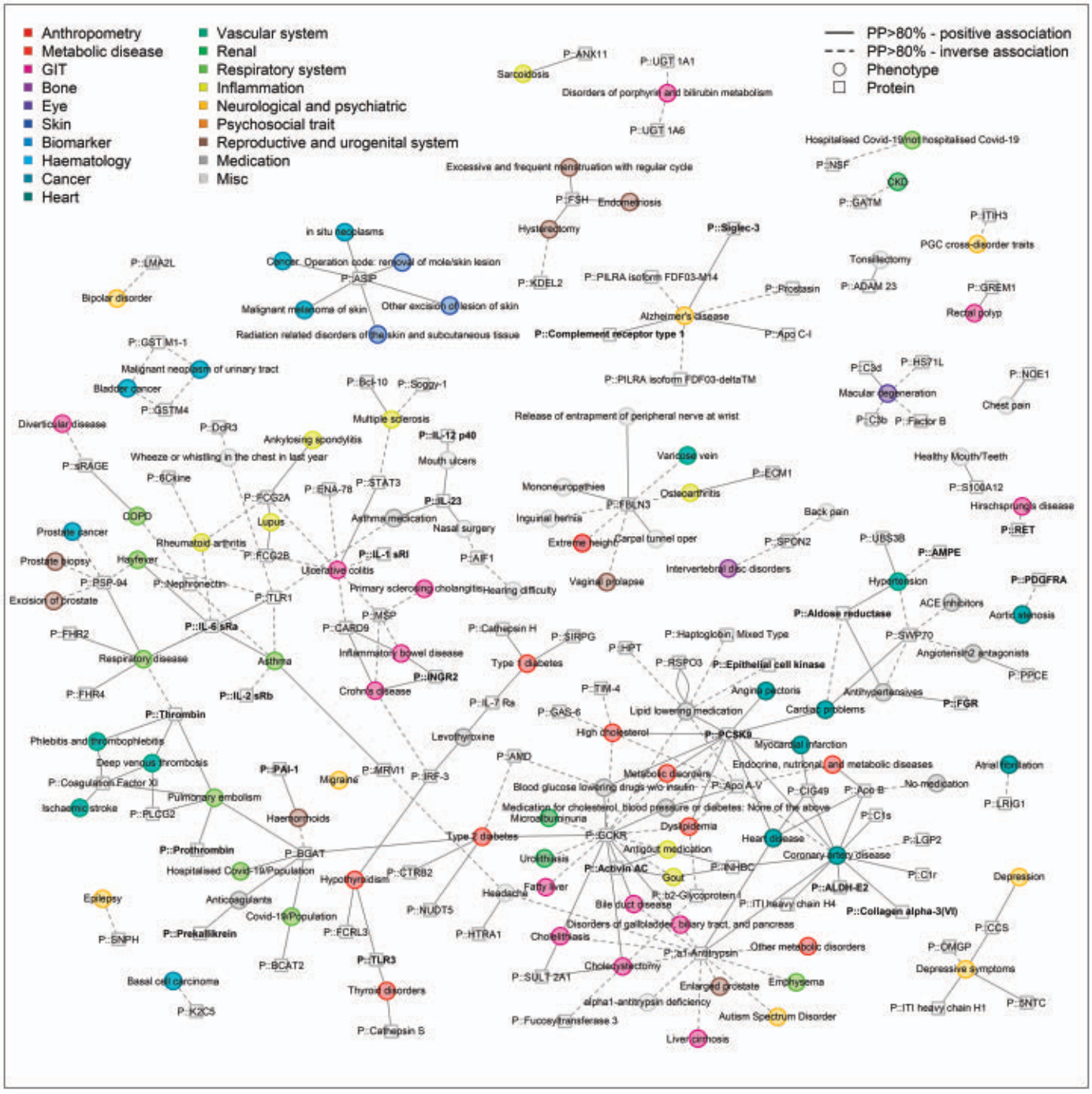


Fig. 5. Network representation of phenome-wide colocalization analysis for protein-encoding loci. This figure is restricted to connections between proteins and binary endpoints, mainly diseases, to increase visibility and show shared etiology. Only protein targets and phenotypes with at least one connection are included. Effect directions are indicated by the line type (solid = higher protein abundance, increased risk; dashed = higher protein abundance, reduced risk). Colors indicate categories of phenotypes. The entire network is composed of 412 protein targets (squares) and 506 phenotypes (circles) as nodes, which are connected (n = 1859 edges) if there is evidence of a shared genetic signal (posterior probability >80%) and is shown in fig. S6. See www.omicscience.org/apps/pgwas for an interactive version of the figure.

gene-protein convergence of diverse connective tissue disorders as well as gene expression of *EFEMP1* in subcutaneous adipose tissue, with high confidence in the lead cis-pQTL (rs3791679, MAF = 23.4%) being the causal variant in multitrait colocalization (Fig. 6B and fig. S10). The common A-allele of rs3791679 was associated with lower plasma abundance of FBLN3 and increased risk for a range of connective or soft tissue abnormalities, including hernias, varicose veins, vaginal prolapse, and hypermobility, several of which have previously been reported in individual GWAS but have not been connected (*49*–*54*). This spectrum of human clinical features suggests that lower plasma levels of A-allele carriers result in altered elastic fiber morphology and/or lower content, in line with evidence from *Efemp1*

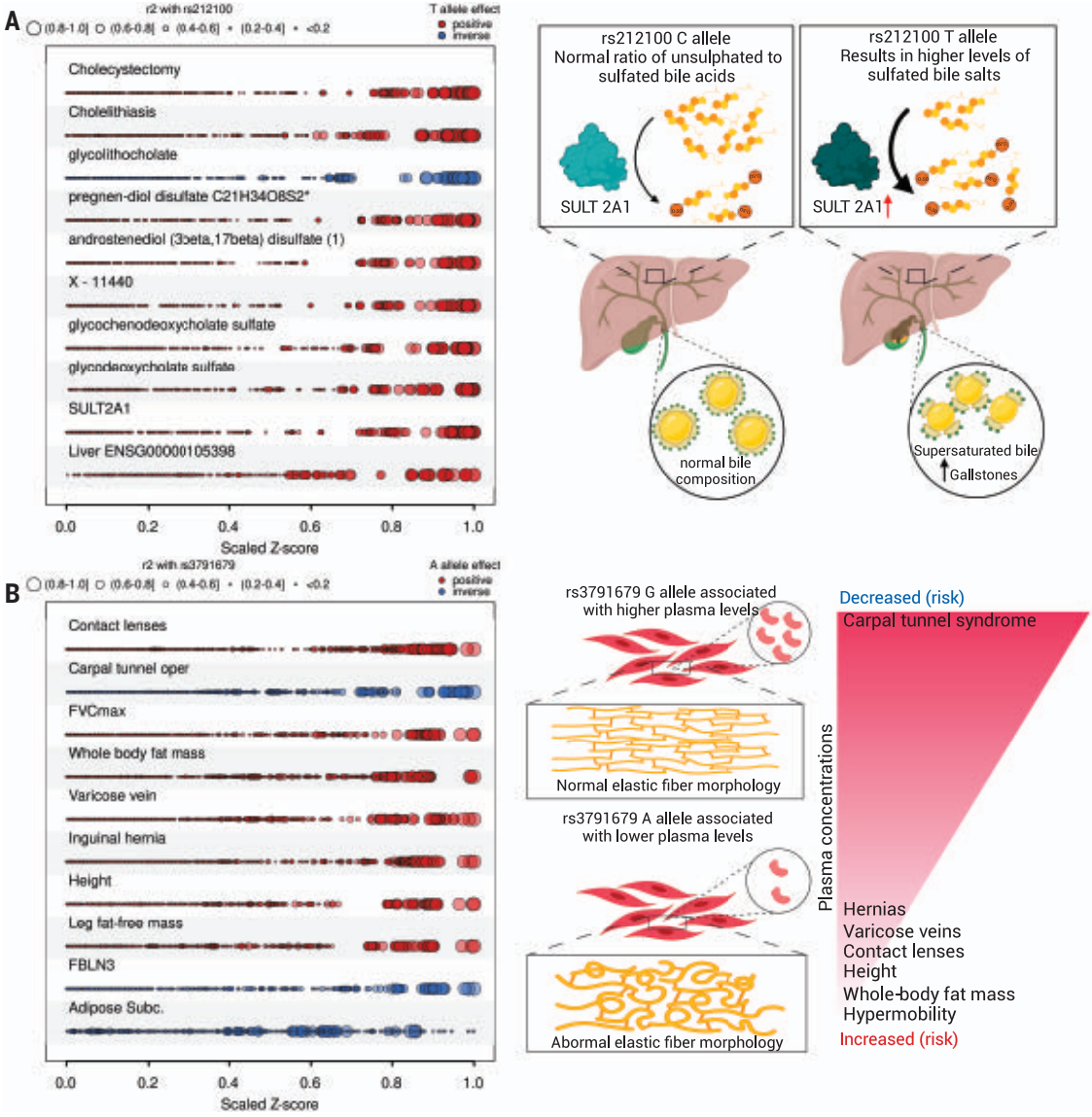


Fig. 6. Selected phenotypic examples from the proteo-genomic map. (**A**) Plot visualizing convergence of genetic variants at the *SULT2A1* locus in relation to the LD with the candidate gene variant identified by multitrait colocalization. Z-scores from GWAS for each annotated trait have been scaled by the absolute maximum, and dot size is proportional to the LD (r^2). Colors indicate the direction of effect aligned to the risk-increasing allele (red, positive; blue, inverse). The scheme on the right depicts the suggested mode of action by which higher SULT2A1 activity translates to higher risk of gallstones. (**B**) Same as (A), but for diseases and other phenotypes colocalizing at the *EFEMP1* locus. The scheme on the right depicts a proposed mechanism by which altered secretion of FBLN3 leads to the observed phenotypes. See figs. S9 and S10 for stacked regional association plots for (A) and (B).

knockout mice that display abnormal elastic fiber morphology, develop different types of hernias, and exhibit pelvic organ prolapse (*55*). FBLN3 is part of the extracellular matrix and widely expressed, but its function is incompletely understood (*56*). We provide insights about its role in the etiology of a large number of connective tissue disorders, including a potential explanation for the established link between carpal tunnel syndrome and shorter stature (*51*). Mutations in *EFEMP1* cause a rare eye disease called Doyne honeycomb retinal dystrophy (DHRD) (*57*), characterized by visual disturbances and drusenoid deposits due to accumulating intracellular FBLN3. We observed sharedness of the signal at this protein locus with vision-related phenotypes, including use of contact lenses (myopia) and decreased optic disc area, a risk factor for open-angle glaucoma (*50*), with lower protein concentrations associated with greater risk, as also observed in patients with DHRD.

Differential effect sizes of cis-pQTLs by sex and age

We systematically tested differences in the genetic associations of all protein targets included in the proteo-genomic map (N = 412) by age or sex. We identified a total of 14 protein targets that showed evidence for significant ($P < 5.9 \times 10^{-5}$) effect modification of the cis-pQTL by sex (N = 10) or age (N = 8), including four common to both (table S8). This included biologically plausible candidates, such as annexin II, where the cis-pQTL showed a stronger effect in women, albeit with a strong significant effect in either sex (women, $\beta = -0.86$, $P < 1.7 \times 10^{-467}$; men, $\beta = -0.64$, $P < 2.5 \times 10^{-231}$). This finding is in line with evidence of isoform expression of the protein-encoding gene *ANXA2* in male and female reproductive tissues, including prostate (PP = 81.9%)

and vagina (PP = 87.4%), and a possible role of the locus in puberty timing (*58*, *59*).

We noted that most of the identified cis-pQTLs showed age- and sex-differential and not dimorphic effects (*60*) and were linked to missense variation (inhibin C, vitronectin, Siglec 9, GCKR, SOD3, CPA4, and PILRA) or alternative splicing events (annexin II, BGAT, and CO8G) with very strong overall effects, enabling the detection of even small effect differences between strata more easily (*61*). In general, our results are concordant with the few sex-specific effects of molecular QTLs reported so far (*62*, *63*) and show that systematic efforts for both molecular QTLs and disease GWAS are needed to better understand the mechanisms underlying such differences. Crucially, investigating the relevance of these genetic differences for phenotypic expression depends on the availability of sex-specific GWAS results across the human phenome.

Druggable targets and repurposing opportunities

We systematically identified druggable proteins in the proteo-genomic map by linking the protein-encoding gene to the druggable genome (*64*) and identified 60 protein targets linked to at least one phenotype, including 22 protein targets linked to a disease (table S9). We replicated established examples, such as the interleukin-6 receptor for rheumatoid arthritis or thrombin for deep venous thrombosis (Fig. 5). We also identified 31 candidates with potential repurposing opportunities for one to eight diseases (for a total of 32 different indications), following a search and prioritization strategy in Open Targets (*65*).

Webserver

To enable customized and in-depth exploration of high-priority protein targets—that is, those with at least one cis-pQTL—we created an interactive online resource (www.omicscience.org/apps/pgwas). The webserver provides intuitive representations of genetic findings and enables the look-up of summary statistics for individual single-nucleotide polymorphisms (SNPs), genes, and whole genomic regions across all protein targets. To interactively assess specificity and to identify pleotropic cis-pQTLs that present strong trans-like association profiles, we generated an interactive heatmap of genetic associations of all cis-pQTLs across all high-priority candidate proteins. We further provide detailed annotations of the protein targets, including links to external databases such as UniProt or Reactome, information on currently available drugs, characterization of associated SNPs, as well as results from our colocalization analysis with eQTLs, sQTLs, diseases, and other phenotypes. An interactive version of the proteo-genomic map allows a deep dive into proteins or phenotypes of particular interest to explore cross-disease connections within subnetworks.

Discussion

The promise of proteomic technologies and their integration with genomic data lies in their application to rare and common human diseases. Although previous studies had started to exploit the phenotypic consequences of pQTLs, they mainly focused on identifying and describing the genetic architecture of proteins measured by specific platforms (*1*–*6*, *9*). We performed a systematic integration of the phenome and created a proteo-genomic map of human health that identifies many potential causal disease genes and highlights genetically driven connections across diverse human conditions. The traditional classification of diseases relies on the aggregation of symptoms commonly presenting together and, with the exception of Mendelian disorders, is rarely based on shared etiology (*66*). Our network anchors the convergence of diseases in their shared genetic etiology, as shown for FBLN3, providing mechanistic understanding and a starting point for the identification of treatment strategies targeting underlying genetic causes.

Uncertainty in assigning causal genes and variants remains a major limitation for experimental validation and clinical translation of results from the plethora of hypothesis-free genetic association studies. We show how cis-pQTLs identify causal candidate genes at established disease risk loci, including COVID-19, providing immediate hypotheses for experimental follow-up for a large number of disease genes.

The uncertain specificity of genetic variation affecting protein content outside of the protein-encoding region, trans-pQTLs, restricts the discovery of de novo biological insights in protein regulation and instrumentation of such variants for genetic prediction, such as with polygenic scores. We show how data-driven network clustering augments ontology-based classification approaches and identifies biologically plausible examples, such as for *PNLPA3* and a community of liver-derived protein targets.

Genetic variation found for proteins circulating in blood raises the question of transferability to disease-relevant tissue processes. We show that for about half of the protein targets with a cis-pQTL, this can be linked to gene expression in various tissues and provide examples, such as for SULT2A1, that illustrate how multidomain integration can identify tissue-specific mechanism. In its most simple form, such cis-pQTLs determine the basal rate of protein production within cells and are more or less constantly released into plasma as a result of natural cell turnover (*67*). Integration of genetic information allowed us to separate out such enclosed effects from other mechanisms, leading to higher cell turnover or leakage, such as for SULT2A1 and the liver-specific effect of the *PNPLA3* variant. Although this provides a strategy to point to relevant tissues, overlapping data for tissue-specific gene and protein expression is required to quantify the contribution of various tissues to the plasma proteome.

To accelerate the use and translational potential of our findings, we generated an open-access interactive web resource that enables the scientific community to easily and rapidly capitalize on these results for future research across clinical specialties. We demonstrate for multiple examples how this resource can be used to put gene-phenotype findings into a systems biological context.

Although our study is distinguished by its comprehensive discovery and characterization of pQTLs in cis and trans along with a systematic integration of the phenome, it does have limitations. First, the nature of the technology used to measure protein concentrations is designed to maximize discovery by generating a large library of affinity reagents, which rely on a preserved shape of the target protein and hence might miss genetic effects specific to a particular isoform of the protein (*10*). The semiquantitative nature of the assay makes risk estimates based on Mendelian randomization studies challenging. A thorough discussion of assay differences can be found in our previous work (*10*), and we observed consistent cis-pQTLs for the highlighted examples, including RSPO1, SULT2A1, and FBLN3, as measured with Olink. Second, our study cohort consisted of predominantly healthy middle-aged participants of European descent, and replication of our results in ethnically diverse populations is warranted, in particular for the discovery of drug targets. Further work would also be required to investigate possible modifying effects of phenotypic characteristics on gene-protein associations, such as by sex, age, or behavioral factors. Third, our study concentrated on the common spectrum of variation in the genome. Investigation of rare variation is likely to identify pQTLs with larger effect sizes and possibly more severe phenotypic consequences. Finally, our proteo-genomic map is limited to publicly available GWAS summary statistics; additional insights will result from the inclusion of further data for additional phenotypes (in particular, cancers) and understudied diseases.

Methods summary

Detailed materials and methods are provided in the supplementary materials (*12*). We performed a genome-proteome–wide association study among 10,708 participants of European descent in the Fenland study (table S1) on 10.2 million genetic variants and plasma abundances of 4775 distinct protein targets measured in plasma using established workflows (*15*). Protein targets were measured using the SomaScan v4 assay employing 4979 single-stranded oligonucleotides (aptamers) with specific binding affinities to 4775 unique protein targets (*68*, *69*).

We used the term "protein target" to refer to proteins targeted by at least one aptamer. We define significant genetic variant–protein target associations (pQTLs) at a stringent Bonferroni threshold ($P < 1.004 \times 10^{-11}$) and performed approximate conditional analysis to detect secondary signals for each genomic region identified by distance-based clumping of association statistics. We defined cross-aptamer regions using a combined approach of multi-trait colocalization (*46*) and LD-clumping. We classified pQTLs as protein- or pathway-specific by assessing pQTL specificity across the entire proteome ($P < 5 \times 10^{-8}$) while testing whether associated protein targets were captured by a common GO term or a protein community in a data-driven protein network. We computed the variance explained in plasma abundances of protein targets by cis-pQTLs (within ±500 kb of the protein-encoding gene) or trans-pQTLs according to different specificity categories using linear regression models. We used statistical colocalization (*70*) to test for a shared genetic signal between expression or alternative splicing of the protein-encoding gene and the cis-pQTL in one of at least 49 tissues of the GTEx v8 project (*24*). We systematically cross-referenced established genetic risk loci for common complex diseases and phenotypes with pQTLs by identifying cis-pQTLs or strong proxies ($r^2 > 0.8$) in the GWAS catalog (www.ebi.ac.uk/gwas/). We finally performed phenome-wide colocalization screens at 1548 protein-encoding loci using publicly available (*71*) as well as in-house–curated genome-wide association statistics for thousands of phenotypes. We applied stringent priors and conservative filters to derive high-confidence protein-phenotype links. We used basic functions of R (v.3.6.0), the R package *igraph*, and the BioRender web application (https://biorender.com/) to create figures. The Fenland study was approved by the National Health Service (NHS) Health Research Authority Research Ethics Committee (NRES Committee–East of England Cambridge Central, ref. 04/Q0108/19), and all participants provided written informed consent.

REFERENCES AND NOTES

1. V. Emilsson *et al*., Co-regulatory networks of human serum proteins link genetics to disease. *Science* **361**, 769–773 (2018). doi: 10.1126/science.aaq1327; pmid: 30072576
2. K. Suhre *et al*., Connecting genetic risk to disease end points through the human blood plasma proteome. *Nat. Commun.* **8**, 14357 (2017). doi: 10.1038/ncomms14357; pmid: 28240269
3. L. Folkersen *et al*., Mapping of 79 loci for 83 plasma protein biomarkers in cardiovascular disease. *PLOS Genet.* **13**, e1006706 (2017). doi: 10.1371/journal.pgen.1006706; pmid: 28369058
4. B. B. Sun *et al*., Genomic atlas of the human plasma proteome. *Nature* **558**, 73–79 (2018). doi: 10.1038/s41586-018-0175-2; pmid: 29875488
5. C. Yao *et al*., Genome-wide mapping of plasma protein QTLs identifies putatively causal genes and pathways for cardiovascular disease. *Nat. Commun.* **9**, 3268 (2018). doi: 10.1038/s41467-018-05512-x; pmid: 30111768
6. A. Gilly *et al*., Whole-genome sequencing analysis of the cardiometabolic proteome. *Nat. Commun.* **11**, 6336 (2020). doi: 10.1038/s41467-020-20079-2; pmid: 33303764
7. K. Suhre, M. I. McCarthy, J. M. Schwenk, Genetics meets proteomics: Perspectives for large population-based studies. *Nat. Rev. Genet.* **22**, 19–37 (2021). doi: 10.1038/s41576-020-0268-2; pmid: 32860016
8. J. Zheng *et al*., Phenome-wide Mendelian randomization mapping the influence of the plasma proteome on complex diseases. *Nat. Genet.* **52**, 1122–1131 (2020). doi: 10.1038/s41588-020-0682-6; pmid: 32895551
9. L. Folkersen *et al*., Genomic and drug target evaluation of 90 cardiovascular proteins in 30,931 individuals. *Nat. Metab.* **2**, 1135–1148 (2020). doi: 10.1038/s42255-020-00287-2; pmid: 33067605
10. M. Pietzner *et al*., Cross-platform proteomics to advance genetic prioritisation strategies. bioRxiv [preprint]. 19 March 2021. doi: 10.1101/2021.03.18.435919; pmid: 435919
11. T. Lindsay *et al*., Descriptive epidemiology of physical activity energy expenditure in UK adults (The Fenland study). *Int. J. Behav. Nutr. Phys. Act.* **16**, 126 (2019). doi: 10.1186/s12966-019-0882-6; pmid: 31818302
12. Associated code is available on GitHub. doi: 10.5281/zenodo.5385532
13. M. Narayan, Disulfide bonds: Protein folding and subcellular protein trafficking. *FEBS J.* **279**, 2272–2282 (2012). doi: 10.1111/j.1742-4658.2012.08636.x; pmid: 22594874
14. M. Uhlén *et al*., The human secretome. *Sci. Signal.* **12**, eaaz0274 (2019). doi: doi:
15. M. Pietzner *et al*., Genetic architecture of host proteins involved in SARS-CoV-2 infection. *Nat. Commun.* **11**, 6397 (2020). doi: 10.1038/s41467-020-19996-z; pmid: 33328453
16. M. Eslam, L. Valenti, S. Romeo, Genetics and epigenetics of NAFLD and NASH: Clinical impact. *J. Hepatol.* **68**, 268–279 (2018). doi: 10.1016/j.jhep.2017.09.003; pmid: 29122391
17. S. BasuRay, Y. Wang, E. Smagris, J. C. Cohen, H. H. Hobbs, Accumulation of PNPLA3 on lipid droplets is the basis of associated hepatic steatosis. *Proc. Natl. Acad. Sci. U.S.A.* **116**, 9521–9526 (2019). doi: 10.1073/pnas.1901974116; pmid: 31019090
18. P. N. Newsome *et al*., Guidelines on the management of abnormal liver blood tests. *Gut* **67**, 6–19 (2018). doi: 10.1136/gutjnl-2017-314924; pmid: 29122851
19. D. M. Tollefsen, C. J. Weigel, M. H. Kabeer, The presence of methionine or threonine at position 381 in vitronectin is correlated with proteolytic cleavage at arginine 379. *J. Biol. Chem.* **265**, 9778–9781 (1990). doi: 10.1016/S0021-9258(19)38738-1; pmid: 1693616
20. D. I. Leavesley *et al*., Vitronectin—Master controller or micromanager? *IUBMB Life* **65**, 807–818 (2013). pmid: 24030926
21. V. Guarani *et al*., QIL1 is a novel mitochondrial protein required for MICOS complex stability and cristae morphology. *eLife* **4**, e06265 (2015). doi: 10.7554/eLife.06265; pmid: 25997101
22. P. B. Maguire *et al*., Proteomic Analysis Reveals a Strong Association of β-Catenin With Cadherin Adherens Junctions in Resting Human Platelets. *Proteomics* **18**, e1700419 (2018). doi: 10.1002/pmic.201700419; pmid: 29510447
23. D. Szklarczyk *et al*., STRING v11: Protein-protein association networks with increased coverage, supporting functional discovery in genome-wide experimental datasets. *Nucleic Acids Res.* **47**, D607–D613 (2019). doi: 10.1093/nar/gky1131; pmid: 30476243
24. GTEx Consortium, The GTEx Consortium atlas of genetic regulatory effects across human tissues. *Science* **369**, 1318–1330 (2020). doi: 10.1126/science.aaz1776; pmid: 32913098
25. C. Buccitelli, M. Selbach, mRNAs, proteins and the emerging principles of gene expression control. *Nat. Rev. Genet.* **21**, 630–644 (2020). doi: 10.1038/s41576-020-0258-4; pmid: 32709985
26. U. Võsa *et al*., Unraveling the polygenic architecture of complex traits using blood eQTL metaanalysis. bioRxiv 447367 [preprint]. 19 October 2018. doi: 10.1101/447367; pmid: 447367
27. S. M. Sternson, D. Atasoy, Agouti-related protein neuron circuits that regulate appetite. *Neuroendocrinology* **100**, 95–102 (2014). doi: 10.1159/000369072; pmid: 25402352
28. R. W. Baker, F. M. Hughson, Chaperoning SNARE assembly and disassembly. *Nat. Rev. Mol. Cell Biol.* **17**, 465–479 (2016). doi: 10.1038/nrm.2016.65; pmid: 27301672
29. I. E. Jansen *et al*., Genome-wide meta-analysis identifies new loci and functional pathways influencing Alzheimer's disease risk. *Nat. Genet.* **51**, 404–413 (2019). doi: 10.1038/s41588-018-0311-9; pmid: 30617256
30. J. Schwartzentruber *et al*., Genome-wide meta-analysis, fine-mapping and integrative prioritization implicate new Alzheimer's disease risk genes. *Nat. Genet.* **53**, 392–402 (2021). doi: 10.1038/s41588-020-00776-w; pmid: 33589840
31. S. Aggarwal, P. K. Dabla, S. Arora, Prostasin: An Epithelial Sodium Channel Regulator. *J. Biomark.* **2013**, 179864 (2013). doi: 10.1155/2013/179864; pmid: 26317012
32. Y. Sugitani *et al*., Sodium absorption stimulator prostasin (PRSS8) has an anti-inflammatory effect via downregulation of TLR4 signaling in inflammatory bowel disease. *J. Gastroenterol.* **55**, 408–417 (2020). doi: 10.1007/s00535-019-01660-z; pmid: 31916038
33. M. Calvo-Rodriguez, C. García-Rodríguez, C. Villalobos, L. Núñez, Role of Toll Like Receptor 4 in Alzheimer's Disease. *Front. Immunol.* **11**, 1588 (2020). doi: 10.3389/fimmu.2020.01588; pmid: 32983082
34. T. A. O'Mara *et al*., Identification of nine new susceptibility loci for endometrial cancer. *Nat. Commun.* **9**, 3166 (2018). doi: 10.1038/s41467-018-05427-7; pmid: 30093612
35. M. E. Binnerts *et al*., R-Spondin1 regulates Wnt signaling by inhibiting internalization of LRP6. *Proc. Natl. Acad. Sci. U.S.A.* **104**, 14700–14705 (2007). doi: 10.1073/pnas.0702305104; pmid: 17804805
36. A. Geng *et al*., A novel function of R-spondin1 in regulating estrogen receptor expression independent of Wnt/β-catenin signaling. *eLife* **9**, e56434 (2020). doi: 10.7554/eLife.56434; pmid: 32749219
37. A.-A. Chassot *et al*., WNT4 and RSPO1 together are required for cell proliferation in the early mouse gonad. *Development* **139**, 4461–4472 (2012). doi: 10.1242/dev.078972; pmid: 23095882
38. A.-A. Chassot *et al*., Activation of beta-catenin signaling by Rspo1 controls differentiation of the mammalian ovary. *Hum. Mol. Genet.* **17**, 1264–1277 (2008). doi: 10.1093/hmg/ddn016; pmid: 18250098
39. P. Edery *et al*., Mutations of the RET proto-oncogene in Hirschsprung's disease. *Nature* **367**, 378–380 (1994). doi: 10.1038/367378a0; pmid: 8114939
40. E. A. Stahl *et al*., Genome-wide association study meta-analysis identifies seven new rheumatoid arthritis risk loci. *Nat. Genet.* **42**, 508–514 (2010). doi: 10.1038/ng.582; pmid: 20453842
41. N. Harii *et al*., Thyrocytes express a functional toll-like receptor 3: Overexpression can be induced by viral infection and reversed by phenylmethimazole and is associated with Hashimoto's autoimmune thyroiditis. *Mol. Endocrinol.* **19**, 1231–1250 (2005). doi: 10.1210/me.2004-0100; pmid: 15661832
42. COVID-19 Host Genetics Initiative, Mapping the human genetic architecture of COVID-19. *Nature* 10.1038/s41586-021-03767-x (2021). doi: 10.1038/s41586-021-03767-x
43. S. Zhou *et al*., A Neanderthal OAS1 isoform protects individuals of European ancestry against COVID-19 susceptibility and severity. *Nat. Med.* **27**, 659–667 (2021). doi: 10.1038/s41591-021-01281-1; pmid: 33633408
44. M. B. Whyte, P. A. Kelly, E. Gonzalez, R. Arya, L. N. Roberts, Pulmonary embolism in hospitalised patients with COVID-19. *Thromb. Res.* **195**, 95–99 (2020). doi: 10.1016/j.thromres.2020.07.025; pmid: 32682004
45. A. D. Joshi *et al*., Four Susceptibility Loci for Gallstone Disease Identified in a Meta-analysis of Genome-Wide Association Studies. *Gastroenterology* **151**, 351–363.e28 (2016). doi: 10.1053/j.gastro.2016.04.007; pmid: 27094239
46. C. N. Foley *et al*., A fast and efficient colocalization algorithm for identifying shared genetic risk factors across multiple traits. *Nat. Commun.* **12**, 764 (2021). doi: 10.1038/s41467-020-20885-8; pmid: 33536417
47. S.-Y. Y. Shin *et al*., An atlas of genetic influences on human blood metabolites. *Nat. Genet.* **46**, 543–550 (2014). doi: 10.1038/ng.2982; pmid: 24816252
48. F. Lammert *et al*., Gallstones. *Nat. Rev. Dis. Primers* **2**, 16024 (2016). doi: 10.1038/nrdp.2016.24; pmid: 27121416
49. A. R. Wood *et al*., Defining the role of common variation in the genomic and biological architecture of adult human height. *Nat. Genet.* **46**, 1173–1186 (2014). doi: 10.1038/ng.3097; pmid: 25282103
50. H. Springelkamp *et al*., New insights into the genetics of primary open-angle glaucoma based on meta-analyses of intraocular pressure and optic disc characteristics. *Hum. Mol. Genet.* **26**, 438–453 (2017). pmid: 28073927
51. A. Wiberg *et al*., A genome-wide association analysis identifies 16 novel susceptibility loci for carpal tunnel syndrome. *Nat. Commun.* **10**, 1030 (2019). doi: 10.1038/s41467-019-08993-6; pmid: 30833571
52. E. Jorgenson *et al*., A genome-wide association study identifies four novel susceptibility loci underlying inguinal hernia.

Nat. Commun. **6**, 10130 (2015). doi: 10.1038/ncomms10130; pmid: 26686553
53. N. Shrine *et al*., New genetic signals for lung function highlight pathways and chronic obstructive pulmonary disease associations across multiple ancestries. *Nat. Genet.* **51**, 481–493 (2019). doi: 10.1038/s41588-018-0321-7; pmid: 30804560
54. J. K. Pickrell *et al*., Detection and interpretation of shared genetic influences on 42 human traits. *Nat. Genet.* **48**, 709–717 (2016). doi: 10.1038/ng.3570; pmid: 27182965
55. P. J. McLaughlin *et al*., Lack of fibulin-3 causes early aging and herniation, but not macular degeneration in mice. *Hum. Mol. Genet.* **16**, 3059–3070 (2007). doi: 10.1093/hmg/ddm264; pmid: 17872905
56. I. Livingstone, V. N. Uversky, D. Furniss, A. Wiberg, The Pathophysiological Significance of Fibulin-3. *Biomolecules* **10**, 1294 (2020). doi: 10.3390/biom10091294; pmid: 32911658
57. L. Y. Marmorstein *et al*., Aberrant accumulation of EFEMP1 underlies drusen formation in Malattia Leventinese and age-related macular degeneration. *Proc. Natl. Acad. Sci. U.S.A.* **99**, 13067–13072 (2002). doi: 10.1073/pnas.202491599; pmid: 12242346
58. B. Hollis *et al*., Genomic analysis of male puberty timing highlights shared genetic basis with hair colour and lifespan. *Nat. Commun.* **11**, 1536 (2020). doi: 10.1038/s41467-020-14451-5; pmid: 32210231
59. F. R. Day *et al*., Genomic analyses identify hundreds of variants associated with age at menarche and support a role for puberty timing in cancer risk. *Nat. Genet.* **49**, 834–841 (2017). doi: 10.1038/ng.3841
60. E. A. Khramtsova, L. K. Davis, B. E. Stranger, The role of sex in the genomics of human complex traits. *Nat. Rev. Genet.* **20**, 173–190 (2019). doi: 10.1038/s41576-018-0083-1; pmid: 30581192
61. H. Aschard, A perspective on interaction effects in genetic association studies. *Genet. Epidemiol.* **40**, 678–688 (2016). doi: 10.1002/gepi.21989; pmid: 27390122
62. M. Oliva *et al*., The impact of sex on gene expression across human tissues. *Science* **369,** eaba3066 (2020). doi: 10.1126/science.aba3066
63. K. Mittelstrass *et al*., Discovery of sexual dimorphisms in metabolic and genetic biomarkers. *PLOS Genet.* **7**, e1002215 (2011). doi: 10.1371/journal.pgen.1002215; pmid: 21852955
64. C. Finan *et al*., The druggable genome and support for target identification and validation in drug development. *Sci. Transl. Med.* **9**, eaag1166 (2017). doi: 10.1126/scitranslmed.aag1166; pmid: 28356508
65. D. Ochoa *et al*., Open Targets Platform: Supporting systematic drug-target identification and prioritisation. *Nucleic Acids Res.* **49**, D1302–D1310 (2021). doi: 10.1093/nar/gkaa1027; pmid: 33196847
66. I. Kola, J. Bell, A call to reform the taxonomy of human disease. *Nat. Rev. Drug Discov.* **10**, 641–642 (2011). doi: 10.1038/nrd3534; pmid: 21878965
67. R. Sender, R. Milo, The distribution of cellular turnover in the human body. *Nat. Med.* **27**, 45–48 (2021). doi: 10.1038/s41591-020-01182-9; pmid: 33432173
68. S. A. Williams *et al*., Plasma protein patterns as comprehensive indicators of health. *Nat. Med.* **25**, 1851–1857 (2019). doi: 10.1038/s41591-019-0665-2; pmid: 31792462
69. L. Gold *et al*., Aptamer-based multiplexed proteomic technology for biomarker discovery. *PLOS ONE* **5**, e15004 (2010). doi: 10.1371/journal.pone.0015004; pmid: 21165148
70. C. Giambartolomei *et al*., Bayesian test for colocalisation between pairs of genetic association studies using summary statistics. *PLOS Genet.* **10**, e1004383 (2014). doi: 10.1371/journal.pgen.1004383; pmid: 24830394
71. B. Elsworth *et al*., The MRC IEU OpenGWAS data infrastructure. bioRxiv 244293 [preprint]. 10 August 2020.doi: 10.1101/2020.08.10.244293; pmid: 244293

ACKNOWLEDGMENTS

We are grateful to all Fenland volunteers and to the General Practitioners and practice staff for assistance with recruitment. We thank the Fenland Study Investigators, Fenland Study Co-ordination team and the Epidemiology Field, Data and Laboratory teams. Proteomic measurements were supported and governed by a collaboration agreement between the University of Cambridge and SomaLogic. This research has been conducted using the UK Biobank Resource (application no. 20361 and 44448). **Funding:** The Fenland Study (10.22025/2017.10.101.00001) is funded by the Medical Research Council (MC_UU_12015/1). We further acknowledge support for genomics from the Medical Research Council (MC_PC_13046). This work was supported in part by the UKRI/NIHR Strategic Priorities Award in Multimorbidity Research for the Multimorbidity Mechanism and Therapeutics Research Collaborative (MR/V033867/1); NIH awards R35HG010718, R01HG011138, R01GM140287, and NIH/NIA AG068026 (E.R.G.); National Institute on Aging grants U01 AG061359, RF1 AG057452, and RF1 AG059093 (M.A.W., M.A., and G.K.); a 4-year Wellcome Trust PhD Studentship and the Cambridge Trust (J.C.-Z.); a Gates Fellowship (M.K.); and the Medical Research Council (MC_UU_00006/1 - Etiology and Mechanisms) (C.L., E.W., M.P., J.L., E.O., I.S., N.K., and N.J.W.). **Author contributions:** Conceptualization: C.L., M.P., E.W.; data curation/software: E.O., N.D.K., J.L., M.A.W., J.R.; formal analysis: M.P., E.W., J.C.-Z., A.C., M.K., I.D.S., J.C.; methodology: R.A.S., E.R.G.; visualization: M.P., J.C.-Z., M.K., C.L.; funding acquisition: C.L., N.J.W.; project administration: C.L., N.J.W.; supervision: C.L., R.A.S., G.K.; writing–original draft: M.P., C.L., E.W., J.C.-Z., M.K.; writing–review and editing: E.O., J.C., I.D.S., A.D.H., N.D.K., M.A., W.A., S.O., N.J.W. **Competing interests:** R.A.S. and A.C. are current employees and/or stockholders of GlaxoSmithKline. E.R.G. receives an honorarium from the journal *Circulation Research* of the American Heart Association as a member of the Editorial Board. S.O. has received remuneration for consultancy services provided to Pfizer Inc., Astra Zeneca, ERX Pharmaceuticals, GSK, Third Rock Ventures, and LG Life Sciences. All other authors declare that they have no competing interests. **Data and materials availability:** Data from the Fenland cohort can be requested by bona fide researchers for specified scientific purposes via the study website (www.mrc-epid.cam.ac.uk/research/studies/fenland/information-for-researchers/). Summary statistics can be obtained from www.omicscience.org/apps/pgwas. Publicly available summary statistics for look-up and colocalization of pQTLs were obtained from https://gwas.mrcieu.ac.uk/ and www.ebi.ac.uk/gwas/. Associated code and scripts for the analysis are available on GitHub (https://github.com/MRC-Epid/pGWAS_discovery) and have been permanently archived using Zenodo (*12*).

SUPPLEMENTARY MATERIALS

science.org/doi/10.1126/science.abj1541
Materials and Methods
Figs. S1 to S10
Tables S1 to S9
References (*72*–*81*)
MDAR Reproducibility Checklist

23 April 2021; accepted 29 September 2021
Published online 14 October 2021
10.1126/science.abj1541

Science
JOURNALS AAAS



Publish your research in the *Science* family of journals

The *Science* family of journals (*Science, Science Advances, Science Immunology, Science Robotics, Science Signaling*, and *Science Translational Medicine)* are among the most highly-regarded journals in the world for quality and selectivity. Our peer-reviewed journals are committed to publishing cutting-edge research, incisive scientific commentary, and insights on what's important to the scientific world at the highest standards.

Submit your research today!

Learn more at **Science.org/journals**

RESEARCH ARTICLE SUMMARY

PLANT SCIENCE

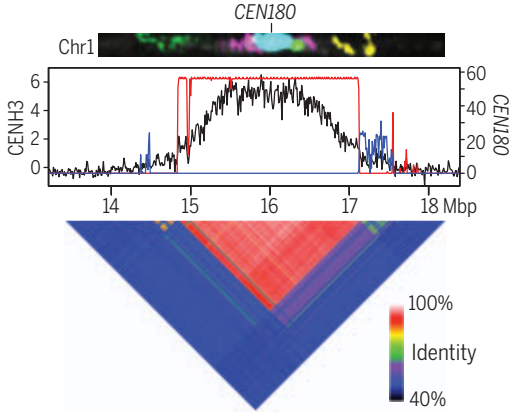
The genetic and epigenetic landscape of the *Arabidopsis* centromeres

Matthew Naish†, Michael Alonge†, Piotr Wlodzimierz†, Andrew J. Tock, Bradley W. Abramson, Anna Schmücker, Terezie Mandáková, Bhagyshree Jamge, Christophe Lambing, Pallas Kuo, Natasha Yelina, Nolan Hartwick, Kelly Colt, Lisa M. Smith, Jurriaan Ton, Tetsuji Kakutani, Robert A. Martienssen, Korbinian Schneeberger, Martin A. Lysak, Frédéric Berger, Alexandros Bousios, Todd P. Michael, Michael C. Schatz*, Ian R. Henderson*

INTRODUCTION: The centromeres of eukaryotic chromosomes assemble the multiprotein kinetochore complex and thereby position attachment to the spindle microtubules, allowing chromosome segregation during cell division. The key function of the centromere is to load nucleosomes containing the CENTROMERE SPECIFIC HISTONE H3 (CENH3) histone variant [also known as centromere protein A (CENPA)], which directs kinetochore formation. Despite their conserved function during chromosome segregation, centromeres show radically diverse organization between species at the sequence level, ranging from single nucleosomes to megabase-scale satellite repeat arrays, which is termed the centromere paradox. Centromeric satellite repeats are variable in sequence composition and length when compared between species and show a high capacity for evolutionary change, both at the levels of primary sequence and array position along the chromosome. However, the genetic and epigenetic features that contribute to centromere function and evolution are incompletely understood, in part because of the challenges of centromere sequence assembly and functional genomics of highly repetitive sequences. New long-read DNA sequencing technologies can now resolve these complex repeat arrays, revealing insights into centromere architecture and chromatin organization.

RATIONALE: *Arabidopsis thaliana* is a model plant species; its genome was first sequenced in 2000, yet the centromeres, telomeres, and ribosomal DNA repeats have remained unassembled, owing to their high repetition and similarity. Genomic repeats are difficult to assemble from fragmented sequencing reads, with longer, high-identity repeats being the most challenging to correctly assemble. As sequencing reads have become longer and more accurate, eukaryotic de novo genome assemblies have captured an increasingly complete picture of the repetitive component of the genome, including the centromeres. For example, Oxford Nanopore Technologies (ONT) reads have become longer and more accurate, now reaching >100 kilo–base pairs (kbp) in length with 95 to 99% modal accuracy. PacBio high-fidelity (HiFi) reads, although shorter (~15 kbp), are >99% accurate. Using ONT and HiFi reads, it is possible to bridge across interspersed unique marker sequences and accurately assemble centromere sequences. In this study, we used long-read DNA sequencing to generate a genome assembly of the *A. thaliana* accession Columbia (Col-CEN) that resolves all five centromeres. We use the Col-CEN assembly to derive insights into the chromatin and recombination landscapes within the *Arabidopsis* centromeres and how these regions evolve.

RESULTS: The Col-CEN assembly reveals that the *Arabidopsis* centromeres consist of megabase-scale tandemly repeated satellite arrays, which support high CENH3 (the centromere-specific histone variant that recruits kinetochores) occupancy and are densely DNA methylated. We show patterns of higher-order repetition within centromeres and that many satellite variants are private to each chromosome, which has implications for the recombination pathways acting in the centromeres. CENH3 preferentially occupies the satellites with the least amount of divergence and that show higher-order repetition. The *Arabidopsis* centromeres are mainly composed of satellite repeats that are ~178 bp in length, termed the *CEN180* satellites. *Arabidopsis* centromeres have also been invaded by *ATHILA* long terminal repeat–class retrotransposons, which disrupt the genetic and epigenetic organization of the centromeres. Using chromatin immunoprecipitation sequencing (ChIP-seq) and immunofluorescence, we demonstrate that the centromeres show a hybrid chromatin state that is distinct from euchromatin and heterochromatin. We show that crossover recombination is suppressed within the centromeres, yet low levels of meiotic double-strand breaks occur, which are regulated by DNA methylation. Together, our Col-CEN assembly reveals the genetic and epigenetic landscapes within the *Arabidopsis* centromeres.



Assembly of the *Arabidopsis* centromeres. The structure of *Arabidopsis* centromere 1 is shown by fluorescence in situ hybridization (top) [upper-arm bacterial artificial chromosomes (BACs) (green), *ATHILA* (purple), *CEN180* (blue), the telomeric repeat (green), and bottom-arm BACs (yellow)] and a long-read genome assembly (middle). The density of centromeric histone CENH3 binding measured by ChIP-seq is shown (black), alongside the frequency of *CEN180* centromere satellite repeats. Red and blue represent forward- and reverse-strand satellites, respectively. The heatmap (bottom) shows patterns of sequence identity across the centromere between nonoverlapping 5-kbp windows. Chr, chromosome 1.

CONCLUSION: Our Col-CEN assembly and functional genomics analysis have implications for understanding centromere sequence evolution in eukaryotes. We propose that a recombination-based homogenization process, occurring between allelic or nonallelic locations on the same chromosome, maintains the *CEN180* library close to the consensus optimal for CENH3 recruitment. The advantage conferred to *ATHILA* retrotransposons by integration within the centromeres is presently unclear. They may be engaged in centromere drive, supporting the hypothesis that centromere satellite homogenization acts as a mechanism to purge driving elements. Each *Arabidopsis* centromere appears to represent different stages in cycles of satellite homogenization and *ATHILA*-driven diversification. These opposing forces provide both a capacity for homeostasis and a capacity for change during centromere evolution. In the future, assembly of centromeres from multiple *Arabidopsis* accessions and closely related species may further clarify how centromeres form and the evolutionary dynamics of *CEN180* and *ATHILA* repeats. ■

The list of author affiliations is available in the full article online.
***Corresponding author. Email: mschatz@cs.jhu.edu (M.C.S.); irh25@cam.ac.uk (I.R.H.)**
†These authors contributed equally to this work.
Cite this article as M. Naish *et al.*, *Science* 374, eabi7489 (2021). DOI: 10.1126/science.abi7489

READ THE FULL ARTICLE AT
https://doi.org/10.1126/science.abi7489

RESEARCH ARTICLE

PLANT SCIENCE

The genetic and epigenetic landscape of the *Arabidopsis* centromeres

Matthew Naish[1]†, Michael Alonge[2]†, Piotr Wlodzimierz[1]†, Andrew J. Tock[1], Bradley W. Abramson[3], Anna Schmücker[4], Terezie Mandáková[5], Bhagyshree Jamge[4], Christophe Lambing[1], Pallas Kuo[1], Natasha Yelina[1], Nolan Hartwick[3], Kelly Colt[3], Lisa M. Smith[6], Jurriaan Ton[6], Tetsuji Kakutani[7], Robert A. Martienssen[8], Korbinian Schneeberger[9,10], Martin A. Lysak[5], Frédéric Berger[4], Alexandros Bousios[11], Todd P. Michael[3], Michael C. Schatz[2]*, Ian R. Henderson[1]*

Centromeres attach chromosomes to spindle microtubules during cell division and, despite this conserved role, show paradoxically rapid evolution and are typified by complex repeats. We used long-read sequencing to generate the Col-CEN *Arabidopsis thaliana* genome assembly that resolves all five centromeres. The centromeres consist of megabase-scale tandemly repeated satellite arrays, which support CENTROMERE SPECIFIC HISTONE H3 (CENH3) occupancy and are densely DNA methylated, with satellite variants private to each chromosome. CENH3 preferentially occupies satellites that show the least amount of divergence and occur in higher-order repeats. The centromeres are invaded by *ATHILA* retrotransposons, which disrupt genetic and epigenetic organization. Centromeric crossover recombination is suppressed, yet low levels of meiotic DNA double-strand breaks occur that are regulated by DNA methylation. We propose that *Arabidopsis* centromeres are evolving through cycles of satellite homogenization and retrotransposon-driven diversification.

Despite their conserved function during chromosome segregation, centromeres show diverse organization between species, ranging from single nucleosomes to megabase-scale tandem repeat arrays (*1*). Centromere "satellite" repeat monomers are commonly ~100 to 200 base pairs (bp) long, with each repeat capable of hosting a CENTROMERE SPECIFIC HISTONE H3 (CENH3) [also known as centromere protein A (CENPA)] variant nucleosome (*1*, *2*). CENH3 nucleosomes ultimately assemble the kinetochore and position spindle attachment on the chromosome, allowing segregation during cell division (*3*). Satellites are highly variable in sequence composition and length when compared between species (*2*). The library of centromere repeats present within a genome often shows concerted evolution, yet they have the capacity to change rapidly in structure and sequence within and between species (*1*, *2*, *4*). However, the genetic and epigenetic features that contribute to centromere evolution are incompletely understood, in large part because of the challenges of centromere sequence assembly and functional genomics of highly repetitive sequences.

Genomic repeats, especially long or high-similarity repeats, are notoriously difficult to assemble from fragmented sequencing reads (*5*). As sequencing reads have become longer and more accurate, eukaryotic de novo genome assemblies have captured an increasingly complete picture of repetitive elements. Oxford Nanopore Technologies (ONT) long reads have become substantially longer and more accurate (>100 kbp with 95 to 99% modal accuracy), owing to improved DNA extraction and library preparation, together with advanced machine learning–based base calling. Additionally, PacBio high-fidelity (HiFi) reads, although shorter (~15 kbp), are highly accurate (>99%). Using these technologies with new computational methods, researchers have assembled a complete telomere-to-telomere representation of a human genome, including the centromere satellite arrays (*6*–*8*). This work revealed that ONT and HiFi reads are sufficient to span interspersed unique marker sequences in human centromeres and other complex repeats, suggesting that truly complete genome assemblies for diverse eukaryotes are on the horizon.

Arabidopsis thaliana is a major model plant species; its genome was sequenced in 2000, yet the centromeres, telomeres, and ribosomal DNA repeats have remained unassembled, owing to their high repetition and similarity (*9*). The *Arabidopsis* centromeres contain millions of base pairs of the *CEN180* satellite, which support CENH3 loading (*10*–*14*). We used long-read ONT sequencing, followed by polishing with high-accuracy PacBio HiFi reads, to establish the Col-CEN reference assembly, which wholly resolves all five *Arabidopsis* centromeres from the Columbia (Col-0) accession. The assembly contains a library of 66,131 *CEN180* satellites, with each chromosome possessing mostly private satellite variants. Chromosome-specific higher-order *CEN180* repetition is prevalent within the centromeres. We identified *ATHILA* retrotransposons that have invaded the satellite arrays and interrupt the genetic and epigenetic organization of the centromeres. By analyzing SPO11-1-oligonucleotide data from mutant lines, we demonstrate that DNA methylation epigenetically silences initiation of meiotic DNA double-strand breaks (DSBs) within the centromeres. Our data suggest that satellite homogenization and retrotransposon invasion are driving cycles of centromere evolution in *Arabidopsis*.

Complete assembly of the *Arabidopsis* centromeres

We collected Col-0 genomic ONT and HiFi sequencing data comprising a total of 73.6 Gbp (~56×, >50 kbp) and 14.6 Gbp (111.3×, 15.6 kbp mean read length), respectively. These data yielded an improved assembly of the Col-0 genome (Col-CEN v1.2), where chromosomes 1, 3, and 5 are wholly resolved from telomere to telomere, and chromosomes 2 and 4 are complete apart from the short-arm 45*S* ribosomal DNA (rDNA) clusters and adjacent telomeres (Fig. 1). After telomere patching and repeat-aware polishing with ONT, HiFi, and Illumina reads (*15*), the Col-CEN assembly has a quality value of 45.99 and 51.71 inside and outside of the centromeres, equivalent to approximately one error per 40,000 and 148,000 bases, respectively (figs. S1 and S2A and table S1). Additionally, Hi-C and Bionano optical maps validate the large-scale structural accuracy of the assembly (fig. S2). The Col-CEN assembly is highly concordant with TAIR10, showing no large structural differences within the chromosome arms (Fig. 1B). Of the Col-0 bacterial artificial chromosome (BAC) contigs, 97.5% align to both TAIR10 and Col-CEN with high coverage and identity (>95%), and 99.9% of TAIR10 gene annotations are represented in Col-CEN.

Col-CEN reconstructs all five centromeres spanning 12.6 Mbp of new sequence, 120.0 and 97.6 kbp of 45*S* rDNA in the chromosome 2 and 4 nucleolar organizer regions (NORs), and

[1]Department of Plant Sciences, Downing Street, University of Cambridge, Cambridge CB2 3EA, UK. [2]Department of Computer Science, Johns Hopkins University, Baltimore, MD, USA. [3]The Plant Molecular and Cellular Biology Laboratory, Salk Institute for Biological Studies, La Jolla, CA, USA. [4]Gregor Mendel Institute (GMI), Austrian Academy of Sciences, Vienna BioCenter (VBC), Dr. Bohr-Gasse 3, 1030 Vienna, Austria. [5]Central European Institute of Technology (CEITEC), Masaryk University, Kamenice 5, Brno 625 00, Czech Republic. [6]School of Biosciences and Institute for Sustainable Food, University of Sheffield, Sheffield S10 2TN, UK. [7]Department of Biological Sciences, University of Tokyo, Tokyo, Japan. [8]Howard Hughes Medical Institute, Cold Spring Harbor Laboratory, Cold Spring Harbor, NY, USA. [9]Faculty of Biology, LMU Munich, Großhaderner Str. 2, 82152 Planegg-Martinsried, Germany. [10]Department of Chromosome Biology, Max Planck Institute for Plant Breeding Research, Carl-von-Linné-Weg 10, 50829 Cologne, Germany. [11]School of Life Sciences, University of Sussex, Brighton BN1 9RH, UK.
***Corresponding author. Email: mschatz@cs.jhu.edu (M.C.S.); irh25@cam.ac.uk (I.R.H.)**
†These authors contributed equally to this work.

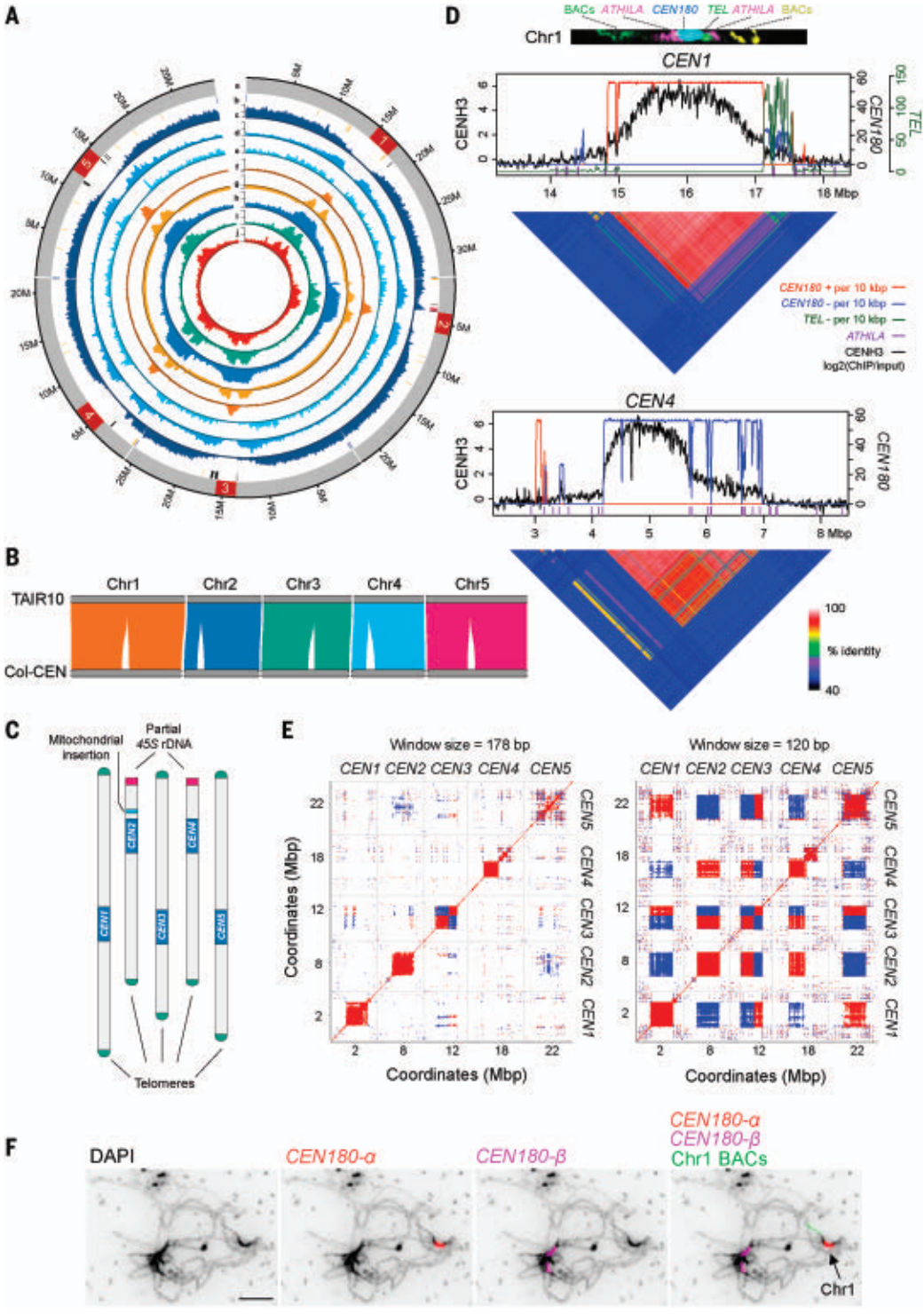


Fig. 1. Complete assembly of the *Arabidopsis* centromeres. (**A**) Circos plot of the Col-CEN assembly. Quantitative tracks (labeled c to j) are aggregated in 100-kbp bins, and independent *y*-axis labels are given as (low value, mid value, high value, measurement unit) as follows: (a) chromosome with centromeres shown in red; (b) telomeres (blue), 45*S* rDNA (yellow), 5*S* rDNA (black), and the mitochondrial insertion (pink); (c) genes (0, 25, 51, gene number); (d) transposable elements (0, 84, 167, transposable element number); (e) Col×Ler F_2 crossovers (0, 7, 14, crossover number); (f) CENH3 [−0.5, 0, 3, $\log_2$(ChIP/input)]; (g) H3K9me2 [−0.6, 0, 2, $\log_2$(ChIP/input)]; (h) CG methylation (0, 47, 95, %); (i) CHG methylation (0, 28, 56, %); and (j) CHH methylation (0, 7, 13, %). (**B**) Syntenic alignments between the TAIR10 and Col-CEN assemblies. (**C**) Col-CEN ideogram with annotated chromosome landmarks (not drawn to scale). (**D**) CENH3 $\log_2$(ChIP/input) (black) plotted over centromeres 1 and 4 (*10*). *CEN180* per 10-kbp plotted for forward (red) or reverse (blue) strand orientations. *ATHILA* are indicated by purple *x*-axis ticks. Heatmaps show pairwise sequence identity between all nonoverlapping 5-kbp regions. A FISH-stained chromosome 1 at pachytene is shown at the top, probed with upper-arm BACs (green), *ATHILA* (purple), *CEN180* (blue), the telomeric repeat (green), and bottom-arm BACs (yellow). (**E**) Dot plots comparing the five centromeres using a search window of 120 or 178 bp. Red and blue indicate forward- and reverse-strand similarity, respectively. (**F**) Pachytene-stage chromosomes stained with 4′,6-diamidino-2-phenylindole (DAPI) (black) and *CEN180*-α (red), *CEN180*-β (purple), and chromosome 1 BAC (green) FISH probes. The scale bar represents 10 μM.

the complete telomeres of the eight chromosome arms without subtelomeric NORs (Fig. 1, A to C; and figs. S1 to S3). We found several instances of apparently genuine variation between the Col-0 strains used to generate TAIR10 and Col-CEN (fig. S4 and tables S2 and S3). For example, a thionin gene cluster shows a deletion in Col-CEN relative to TAIR10 (fig. S4). In total, 27 TAIR10 genes are missing from Col-CEN owing to presence or absence variation, and 13 are present in multiple copies (tables S2 and S3). To comprehensively account for variation between Col-0 strains, we aligned ONT, HiFi, and Illumina reads to the Col-CEN assembly and called variants, providing a database of potential allelic differences, including heterozygous variants (https://github.com/schatzlab/Col-CEN). This revealed only 41 and 37 structural variant calls from ONT and HiFi data genome-wide, respectively, consistent with very low heterozygosity.

We confirmed chromosome landmarks flanking centromere 1 using fluorescence in situ hybridization (FISH), which included labeling a telomeric-repeat cluster located adjacent to the centromere (Fig. 1D and fig. S5). To validate centromere structure, we performed in silico

digestion with AscI and NotI and compared the predicted fragments with published physical maps, which validated Col-CEN (fig. S6) (*16*). We also examined our Bionano optical data across the centromeres (fig. S7). The optical contigs are consistent with the structure of Col-CEN *CEN180* arrays, although the low density of centromeric labeling sites prevents full resolution by optical fragments alone (fig. S7).

The centromeres are characterized by a 178-bp satellite repeat (*CEN180*), arranged head to tail and organized into higher-order repeats (Figs. 1D and 2 and fig. S8). We validated the structural and base-level accuracy of the centromeres using techniques from the human Telomere-to-Telomere (T2T) Consortium (*6*, *8*) and observed even long-read coverage across the centromeres with few loci showing plausible alternate base signals (fig. S1B). We observed relatively few missing *k*-mers that are found in the assembly but not in Illumina short reads, which are diagnostic of residual consensus errors that remain after polishing (fig. S1B) (*17*). We observed that unique marker sequences are frequent, with a maximum distance between consecutive markers of 41,765 bp within the centromeres, suggesting that our reads can confidently span these markers and assemble reliably (fig. S1C). The five centromeres are relatively distinct at the sequence level, with each exhibiting chromosome-specific repeats (Figs. 1E and 2 and tables S4 and S5). Using the Col-CEN sequence, we designed *CEN180* variant FISH probes to label specific centromere arrays (Fig. 1F and fig. S5). For example, the *CEN180*-α, *CEN180*-γ, and *CEN180*-δ probes specifically label arrays within centromere 1 (Fig. 1F and fig. S5), providing cytogenetic validation for chromosome-specific satellites.

The *Arabidopsis CEN180* satellite repeat library

We performed de novo searches for tandem repeats to define the centromere satellite library (table S4). We identified 66,131 *CEN180* satellites in total, with between 11,848 and 15,613 copies per chromosome (Fig. 2, fig. S9, and table S4). The *CEN180* repeats form large tandem arrays, with the satellites within each centromere found predominantly on the same strand, except for centromere 3, which is formed of two blocks on opposite strands (Fig. 1D and fig. S8). The distribution of repeat monomer length is constrained around 178 bp (Fig. 2A and fig. S9). We aligned all *CEN180* sequences to derive a genome-wide consensus and calculated nucleotide frequencies at each alignment position to generate a position probability matrix (PPM). Each satellite was compared with the PPM to calculate a "variant distance" by summation of disagreeing nucleotide probabilities. Substantial sequence variation was observed between satellites and the PPM, with a mean variant distance of 20.2 (Fig. 2A). Each centromere contains essentially private libraries of *CEN180* monomers, with only 0.3% sharing an identical copy on a different chromosome (Fig. 1E and table S4). By contrast, there is a high degree of *CEN180* repetition within chromosomes, with 57.1 to 69.0% showing one or more duplicates (table S4). We also observed a minor class of *CEN160* repeats found on chromosome 1 (1289 repeats, mean length of 158.2 bp) (*14*).

We aligned CENH3 chromatin immunoprecipitation sequencing (ChIP-seq) data to the Col-CEN assembly and observed, on average, 12.9-fold $\log_2$(ChIP/input) enrichment within the *CEN180* arrays, compared with the chromosome arms (Fig. 1D and fig. S8) (*10*). CENH3 ChIP-seq enrichment is generally highest within the interior of the main *CEN180* arrays (Fig. 1D and fig. S8). We observed a negative relationship between CENH3 ChIP-seq enrichment and *CEN180* variant distance (Fig. 2, D and E), consistent with the idea that CENH3 nucleosomes prefer to occupy satellites that are closer to the genome-wide consensus. In this respect, centromere 4 is noteworthy because it consists of two distinct *CEN180* arrays, with the right array showing higher variant distances and lower CENH3 enrichment (Figs. 1D and 2D and fig. S8). Together, these data are consistent with the possibility that satellite divergence leads to loss of CENH3 binding, or vice versa.

To define *CEN180* higher-order repeats, monomers were considered the same if they shared five or fewer pairwise variants. Consecutive repeats of at least two monomers below this variant threshold were identified, yielding 2,408,653 higher-order repeats (Fig. 2D and table S5). Like the *CEN180* monomer sequences, higher-order repeats are largely chromosome specific (table S5). The mean number of *CEN180* monomers per higher-order repeat was 2.41 (equivalent to 429 bp) (Fig. 2B and table S5), and 95.4% of *CEN180* were monomers of at least one larger repeat unit. Higher-order repeat block sizes show a negative exponential distribution, and the largest block was formed of 60 monomers (equivalent to 10,689 bp) (Fig. 2B). Many higher-order repeats are in close proximity (26% are <100 kbp apart), although they are dispersed throughout the length of the centromeres. For example, the average distance between higher-order repeats was 380 kbp and the maximum was 2365 kbp (Fig. 2B and table S5). We also observed that higher-order repeats further apart showed a higher level of variants between the blocks (variants per monomer) (Fig. 2F), consistent with the idea that satellite homogenization is more effective over repeats that are physically closer. Genome-wide, the *CEN180* quantile with highest CENH3 occupancy correlates with higher-order repetition and increased CG DNA methylation (Fig. 2, D, E, and G). However, an exception to these trends is centromere 5, which has 6.8 to 13.4% of higher-order repeats compared with the other centromeres yet recruits comparable CENH3 (Fig. 2G and table S5).

Invasion of the *Arabidopsis* centromeres by *ATHILA* retrotransposons

In addition to reduced *CEN180* higher-order repetition, centromere 5 is also disrupted by breaks in the satellite array (Fig. 2G and fig. S8). Most of the main satellite arrays are *CEN180* (92.8%), with only 111 interspersed sequences >1 kbp. Within these breaks, we identified 53 intact and 20 fragmented *ATHILA* long terminal repeat (LTR) retrotransposons of the *GYPSY* superfamily (Fig. 3, A to C, and table S6) (*18*). The intact *ATHILA* have a mean length of 11.05 kbp, and most have similar and paired LTRs, target site duplications, primer binding sites, polypurine tracts, and *GYPSY* open reading frames (Fig. 3C and table S6). LTR comparisons indicate that the centromeric *ATHILA* are young, with, on average, 98.7% LTR sequence identity, which was significantly higher than that for *ATHILA* located outside the centromeres (96.9%, $n = 58$, Wilcox test, $P = 4.89 \times 10^{-8}$) (Fig. 3D and fig. S10). We also identified 12 *ATHILA* solo LTRs, consistent with postintegration intra-element homologous recombination (table S6). We observed six instances where centromeric *ATHILA* loci were duplicated on the same chromosome and located between 8.9 and 538.5 kbp apart, consistent with the idea that transposons are copied postintegration, potentially by the same mechanism that generates *CEN180* higher-order repeats. For example, a pair of adjacent *ATHILA5* and *ATHILA6A* elements within centromere 5 has been duplicated within a higher-order repeat (fig. S11). The duplicated elements share target site duplications and flanking sequences and show high identity between copies (99.5 and 99.6%) (fig. S11 and table S6). By contrast, the surrounding *CEN180* show higher divergence and copy number variation between the higher-order repeats (94.3 to 97.3% identity) (fig. S11). This indicates an increased rate of *CEN180* sequence change compared with that of the *ATHILA*, after duplication.

We analyzed centromeric *ATHILA* for CENH3 ChIP-seq enrichment and observed a decrease relative to the surrounding *CEN180*, yet higher levels than in *ATHILA* located outside of the centromere (Fig. 3E). The *ATHILA* show greater histone H3 lysine 9 dimethylation (H3K9me2) enrichment compared with all *CEN180* (Fig. 3E). We used our ONT reads to profile DNA methylation over the *ATHILA* and observed dense methylation, with higher CHG-context methylation (where H is A, T, or C) than the

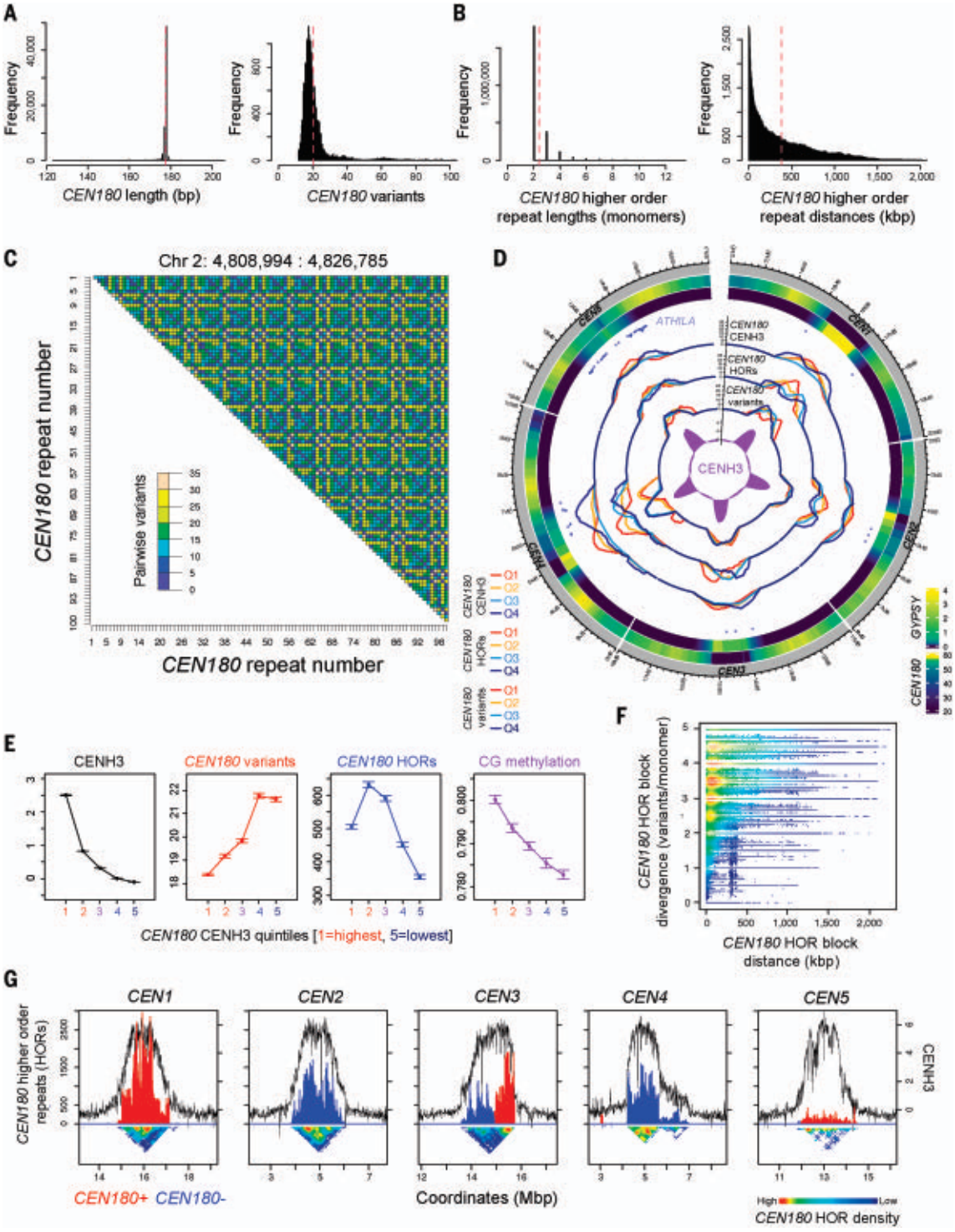


Fig. 2. The *Arabidopsis CEN180* satellite repeat library. (**A**) Histograms of *CEN180* monomer lengths (bp), and variant distances relative to the genome-wide consensus. Red dashed lines indicate mean values. (**B**) Same as for (A) but showing widths of *CEN180* higher-order repeat blocks (monomers) and the distance between higher-order repeats (kbp). (**C**) Heatmap of a representative region within centromere 2, shaded according to pairwise variants between *CEN180*. (**D**) Circos plot showing (i) *GYPSY* density; (ii) *CEN180* density; (iii) centromeric *ATHILA* "rainfall"; (iv) *CEN180* density grouped by decreasing CENH3 $\log_2$(ChIP/input) (red, high; navy, low); (v) *CEN180* density grouped by decreasing higher-order repetition (red, high; navy, low); (vi) *CEN180* grouped by decreasing variant distance (red, high; navy, low); and (vii) CENH3 $\log_2$(ChIP/input) (purple) across the centromeres. (**E**) *CEN180* were divided into quintiles according to CENH3 $\log_2$(ChIP/input) and mean values with 95% confidence intervals plotted. The same groups were analyzed for *CEN180* variant distance (red), higher-order repetition (blue), and CG-context DNA methylation (purple). (**F**) Plot of the distance between pairs of higher-order repeats (kbp) and divergence (variants per monomer) between the higher-order repeats. (**G**) Plots of CENH3 $\log_2$(ChIP/input) (black) across the centromeres compared with *CEN180* higher-order repetition on forward (red) or reverse (blue) strands. The heatmap beneath is shaded according to higher-order repeat density.

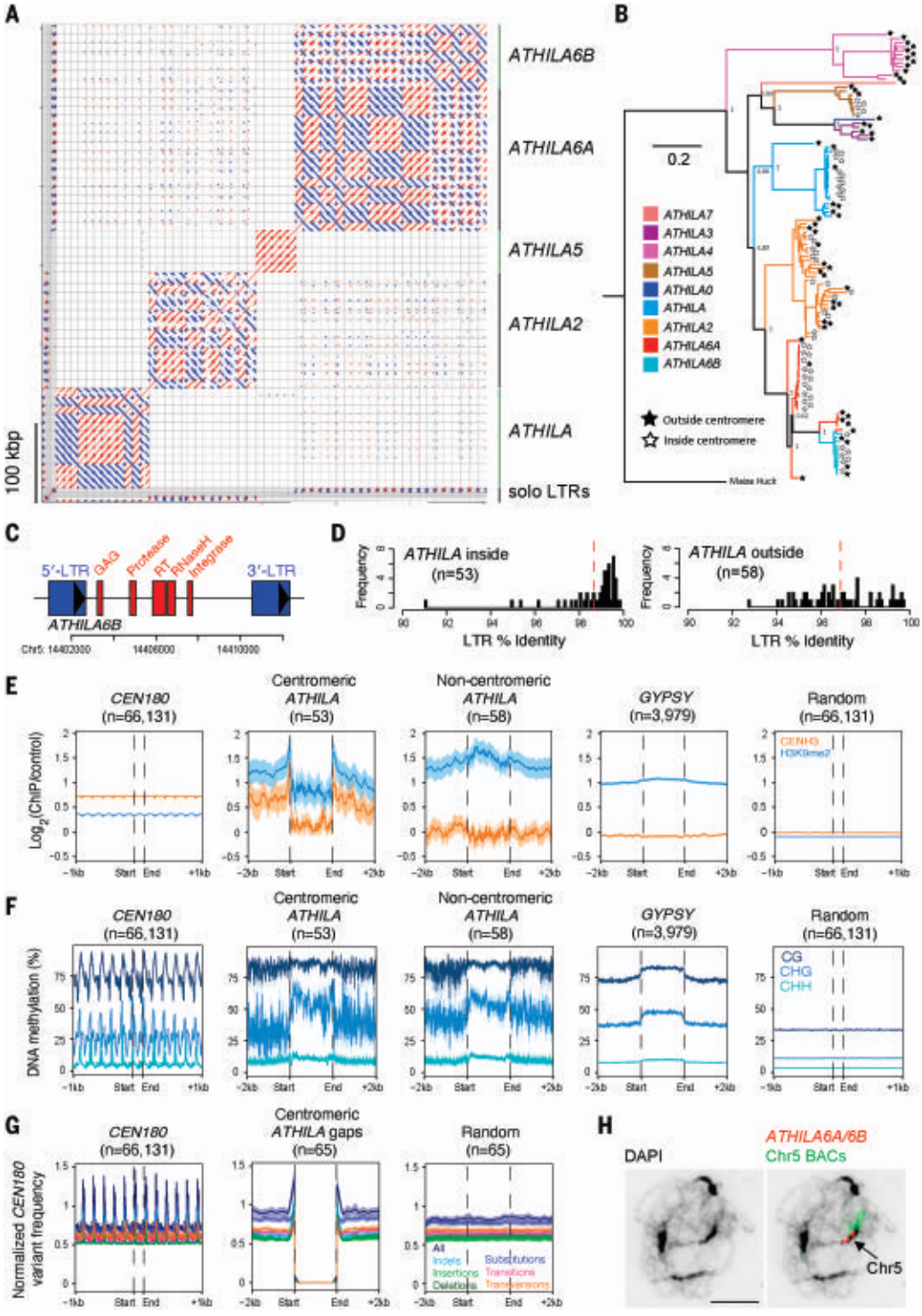


Fig. 3. Invasion of the *Arabidopsis* centromeres by *ATHILA* retrotransposons. (**A**) Dot plot of centromeric *ATHILA* using a 50-bp search window. Red and blue indicate forward- and reverse-strand similarity, respectively. *ATHILA* subfamilies and solo LTRs are indicated. (**B**) Maximum likelihood phylogenetic tree of 111 intact *ATHILA* elements, color coded according to subfamily. Stars at the branch tips indicate *ATHILA* inside (white) or outside (black) the centromeres. (**C**) An annotated map of an *ATHILA6B* with LTRs (blue) and core protein domains (red) highlighted. (**D**) Histograms of LTR sequence identity for centromeric *ATHILA* elements (n = 53) compared with *ATHILA* outside of the centromeres (n = 58). Red dashed lines indicate mean values. (**E**) Metaprofiles of CENH3 (orange) and H3K9me2 (blue) ChIP-seq signals around *CEN180* (n = 66,131), centromeric intact *ATHILA* (n = 53), *ATHILA* located outside the centromeres (n = 58), *GYPSY* retrotransposons (n = 3979), and random positions (n = 66,131). Shaded ribbons represent 95% confidence intervals for windowed mean values. (**F**) Same as for (E) but analyzing ONT-derived percentage of DNA methylation in CG (dark blue), CHG (blue), and CHH (light blue) contexts. (**G**) Metaprofiles of *CEN180* sequence edits (insertions, deletions, and substitutions relative to the *CEN180* consensus), normalized by *CEN180* presence, in positions surrounding *CEN180* gaps containing *ATHILA* (n = 65) or random positions (n = 65). All edits (dark blue), substitutions (blue), indels (light blue), insertions (light green), deletions (dark green), transitions (pink), and transversions (orange) are shown. Shaded ribbons represent 95% confidence intervals for windowed mean values. (**H**) Pachytene-stage chromosome spread stained with DAPI (black), an *ATHILA6A/6B GAG* FISH probe (red), and chromosome 5–specific BACs (green). The scale bar represents 10 μM.

surrounding *CEN180* (Fig. 3F). Hence, *ATHILA* elements are distinct from the *CEN180* satellites at the chromatin level. We profiled *CEN180* variants around centromeric *ATHILA* loci (n = 65) and observed increased satellite divergence in the flanking regions (Fig. 3G), reminiscent of *Nasonia PSR* tandem repeat divergence at the junction with a *NATE* retrotransposon (*19*). This indicates that *ATHILA* insertion was mutagenic on the surrounding satellites or that transposon insertion influenced the subsequent divergence or homogenization of the adjacent *CEN180*. We also used FISH to cytogenetically validate the presence of *ATHILA6A/6B* and *ATHILA2* subfamilies within the centromeres (Fig. 3H and fig. S5). Together, these data show that *ATHILA* insertions interrupt the genetic and epigenetic organization of the *Arabidopsis CEN180* arrays.

Epigenetic organization and meiotic recombination within the centromeres

To assess genetic and epigenetic features of the centromeres, we analyzed all of the chromosome arms along their telomere-centromere axes using a proportional scale (Fig. 4A). Centromere midpoints were defined as the point of maximum CENH3 ChIP-seq enrichment (fig. S12). As expected, *CEN180* satellites are highly

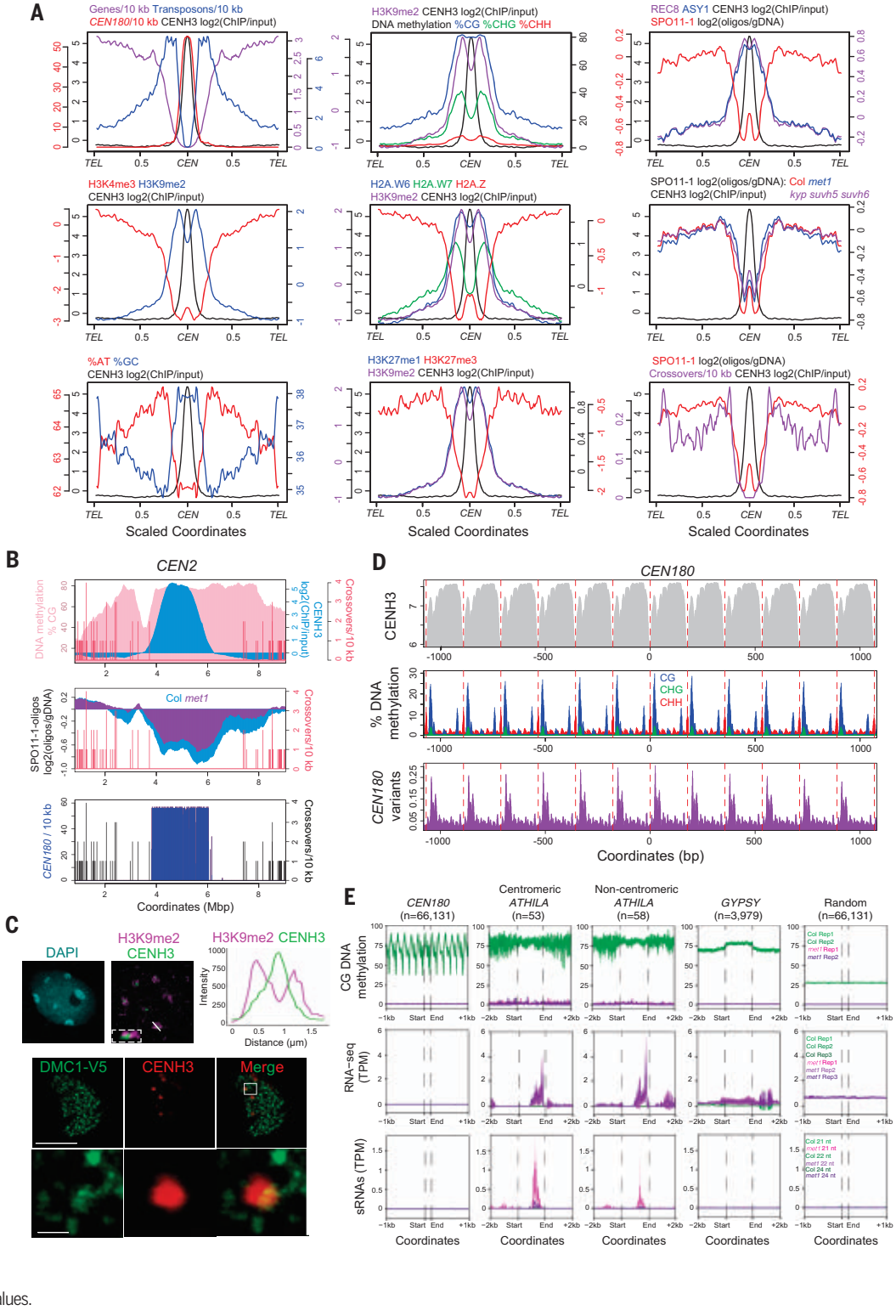


Fig. 4. Epigenetic organization and meiotic recombination within the centromeres. (**A**) Quantification of genomic features plotted along chromosome arms that were proportionally scaled between telomeres (*TEL*) and centromere midpoints (*CEN*) [defined by maximum CENH3 ChIP-seq $\log_2$(ChIP/input) enrichment]. Data analyzed were gene, transposon, and *CEN180* density; CENH3, H3K4me3, H3K9me2, H2A.W6, H2A.W7, H2A.Z, H3K27me1, H3K27me3, REC8, and ASY1 $\log_2$ (ChIP/input); and percentage of AT/GC base composition, DNA methylation, SPO11-1-oligonucleotides (in wild type and *met1*), and crossovers (table S7). (**B**) Plot quantifying crossovers (red), percentage of CG DNA methylation (pink), CENH3 (blue), SPO11-1-oligonucleotides in wild type and *met1*, and *CEN180* density along centromere 2. (**C**) An interphase nucleus immunostained for H3K9me2 (magenta) and CENH3-GFP (green) is shown at the top. The white line indicates the confocal section used for the intensity plot shown on the right; the region outlined by the white dashed line shows a magnified image of a centromere. The scale bar represents 5 μM. At the bottom is a male meiocyte (early prophase I) immunostained for CENH3 (red) and V5-DMC1 (green). The region outlined by the white line indicates the magnified region shown in the lower row of images. Scale bars are 10 μM (upper) and 1 μM (lower). (**D**) Plots of CENH3 ChIP enrichment (gray), DNA methylation in CG (blue), CHG (green) and CHH (red) contexts, and *CEN180* variants (purple), averaged over windows centered on *CEN180* starts. The red dashed lines show 178-bp increments. (**E**) Metaprofiles of CG-context DNA methylation, RNA-seq, and siRNA-seq in wild type (green) or *met1* (pink and purple) (*29*) around *CEN180* (n = 66,131), centromeric intact *ATHILA* (n = 53), *ATHILA* located outside the centromeres (n = 58), *GYPSY* (n = 3979), and random positions (n = 66,131). Shaded ribbons represent 95% confidence intervals for windowed mean values.

enriched in proximity to centromeres, and these regions are relatively GC-rich compared with the AT-rich chromosome arms (Fig. 4A). Gene density drops as the centromeres are approached, whereas transposon density increases, until they are replaced by *CEN180* (Fig. 4A). Gene and transposon densities are tracked closely by H3K4me3 and H3K9me2 ChIP-seq enrichment, respectively (Fig. 4A). H3K9me2 enrichment is observed within the centromere, although there is a reduction in the center coincident with CENH3 enrichment (Fig. 4A), consistent with reduced H3 occupancy caused by CENH3 replacement. A slight increase in H3K4me3 enrichment is observed within the centromeres, relative to the flanking pericentromeres (Fig. 4A).

Using our ONT reads with the DeepSignal-plant algorithm (*20*), we observed dense DNA methylation across the centromeres in CG, CHG, and CHH contexts (Fig. 4, A and B). However, CHG DNA methylation shows relatively

reduced centromeric frequency compared with CG methylation (Fig. 4A). This may reflect centromeric depletion of H3K9me2 (Fig. 4A), a histone modification that maintains DNA methylation in non-CG contexts (*21*). To further investigate the DNA methylation environment associated with CENH3 deposition, we performed ChIP using either H3K9me2 or CENH3 antibodies and sequenced the immunopurified DNA with ONT. We analyzed methylation frequency in reads that aligned to the centromeres and observed dense CG methylation in both read sets but depletion of CHG and CHH methylation in the CENH3 reads relative to H3K9me2 (fig. S13). This further supports that H3 replacement by CENH3 causes a decrease in non-CG methylation maintenance within the *Arabidopsis* centromeres.

To investigate genetic control of centromeric DNA methylation, we analyzed bisulfite sequencing (BS-seq) data from wild type and eight mutants defective in CG and non-CG DNA methylation maintenance (fig. S14) (*21*, *22*). Centromeric non-CG methylation is eliminated in *drm1 drm2 cmt2 cmt3* mutants and reduced in *kyp suvh5 suvh6* mutants, whereas CG methylation is intact in these backgrounds (fig. S14) (*21*, *22*). By contrast, both CG and non-CG methylation in the centromeres are reduced in *ddm1* and *met1* mutants (fig. S14) (*22*). Hence, centromeric CG-context methylation is relatively high compared with non-CG, and non-CG methylation shows an unexpected dependence on CG maintenance pathways.

We observed pericentromeric ChIP-seq enrichment of the heterochromatic marks H2A.W6, H2A.W7, and H3K27me1, which are relatively depleted within the centromeres (Fig. 4A) (*23*, *24*). The polycomb-group modification H3K27me3 is low in the centromeres and found largely in the chromosome arms (Fig. 4A). Enrichment of the euchromatic histone variant H2A.Z is low in the centromeres, but, like H3K4me3, shows a slight increase in the centromeres relative to the pericentromeres (Fig. 4A), suggesting that the centromeres have a distinct chromatin state relative to neighboring heterochromatin. We performed immunofluorescent staining of *Arabidopsis* nuclei for CENH3-GFP (GFP, green fluorescent protein) and euchromatic and heterochromatic histone modifications (Fig. 4C and figs. S15 and S16). Quantification of fluorescence intensity confirmed that heterochromatic marks are relatively depleted where CENH3-GFP is enriched (Fig. 4C and fig. S16). Hence, the *Arabidopsis* centromeres show depletion of heterochromatic and enrichment of euchromatic marks relative to the pericentromeres, consistent with a hybrid chromatin state.

Meiotic recombination, including unequal crossover and gene conversion, has been proposed to mediate centromere evolution (*4*, *25*). We mapped 2080 meiotic crossovers from Col×Ler F_2 sequencing data against the Col-CEN assembly (resolved, on average, to 1047 kbp) (fig. S17). As expected, crossovers were suppressed in proximity to the centromeres (Fig. 4, A and B, and fig. S17). We observed high centromeric ChIP-seq enrichment of REC8-cohesin and ASY1, which are components of the meiotic chromosome axis (Fig. 4A) (*26*, *27*). To investigate the potential for meiotic DSB formation within the centromeres, we aligned SPO11-1-oligonucleotides from wild type (*28*). Overall, SPO11-1-oligonucleotides are low within the centromeres, although we observed an increase relative to the pericentromeres, reminiscent of H3K4me3 and H2A.Z ChIP-seq enrichment (Fig. 4A). To investigate the role of DNA methylation, we mapped SPO11-1-oligonucleotides from the CG DNA methylation mutant *met1-3* (*28*), which showed a gain of DSBs within the centromeres (Fig. 4, A and B). We immunostained meiocytes in early prophase I for CENH3 and V5-DMC1, which is a marker of meiotic interhomolog recombination (Fig. 4C and figs. S18 and S19). DMC1-V5 foci were observed along the chromosomes and adjacent to the surface of CENH3 foci, but not within them (Fig. 4C). Hence, despite suppression of crossovers, we observe evidence for low levels of meiotic recombination initiation within the centromeres, which is influenced by DNA methylation.

CENH3 nucleosomes show a phased pattern of enrichment with the *CEN180*, with relative depletion in spacer regions at the satellite edges (Fig. 4D). CENH3 spacer regions also associate with increased DNA methylation and *CEN180* variants (Fig. 4D), consistent with the possibility that CENH3-nucleosomes influence epigenetic modification and satellite divergence. We analyzed chromatin and transcription around *CEN180* and *ATHILA* at the fine scale and compared wild type with the DNA methylation mutant *met1-3*. In *met1-3*, CG-context DNA methylation is lost in both *ATHILA* and *CEN180* repeats (Fig. 4E and fig. S20) (*29*). However, *met1* RNA sequencing (RNA-seq) and small interfering RNA sequencing (siRNA-seq) signals show increased expression of *ATHILA* transcripts, but not *CEN180* (Fig. 4E and fig. S20) (*29*). The greatest RNA and siRNA expression increases in *met1-3* are observed in the *ATHILA* internal 3′ regions (Fig. 4E and fig. S20), which correspond to transcriptionally silent information (TSI) transcripts and epigenetically activated siRNA (easiRNA) populations (*30*, *31*). This further indicates that epigenetic regulation of the *CEN180* repeats is distinct from that of the *ATHILA* elements.

Discussion

Leveraging advances in sequencing technology and genome assembly, we have generated the Col-CEN reference genome, which resolves the centromere satellite arrays. By profiling chromatin and recombination within the centromeres, we demonstrate that Col-CEN enables biological insights from existing functional genomics data. Using ONT long reads, we have also resolved patterns of DNA methylation within the centromeres, highlighting the potential of complete reference assemblies for understanding epigenetic regulation of repeats. The Col-0 centromeres contain interspersed unique sequences that facilitate assembly with modern sequencing reads. However, similar to the human T2T Consortium, the Col-CEN assembly required extensive manual processes to polish and curate repetitive loci (*8*, *15*, *32*). We anticipate that as complete genome assembly becomes more automated, researchers will be able to compare centromere sequences across populations and species, ultimately revealing how centromere diversity and evolution affect genome function.

In the centromeres, extensive variation is observed among the *CEN180*, and most monomer sequences are private to each centromere. This is consistent with the model that satellite homogenization occurs primarily within chromosomes. The negative correlation between *CEN180* divergence and CENH3 occupancy suggests that centromeric chromatin may promote recombination pathways that lead to homogenization, including DSB formation and repair through homologous recombination. For example, interhomolog strand invasion and noncrossover repair during meiosis, using allelic or nonallelic templates, have the potential to cause *CEN180* gene conversion and structural change (fig. S21). Similarly, repair and recombination using a sister chromatid may also contribute to *CEN180* change, which could occur during mitosis or meiosis (fig. S21). We note that *CEN180* higher-order repeats are, on average, 432 bp long, which is within the size range of *Arabidopsis* gene conversions (*33*), although we also observe large (10 to 100 kbp) intra-centromere duplications, for which the origin is less clear. We observe a proximity effect on divergence between *CEN180* higher-order repeats, with repeat blocks that are further apart showing greater differences. These patterns are reminiscent of human centromeric higher-order repeats, although duplicated blocks of α-satellites are longer and occur over greater physical distances (*6*, *34*, *35*). Because meiotic crossover repair is suppressed within the centromeres, consistent with patterns across eukaryotes (*25*, *36*), we do not consider unequal crossover to be a major pathway driving *Arabidopsis* centromere evolution. However, we propose that a recombination-based homogenization process, occurring between allelic or nonallelic locations on the same chromosome, maintains the *CEN180* library close to

the consensus that is optimal for CENH3 recruitment (fig. S21).

Aside from homogenizing recombination within the *CEN180*, the centromeres have experienced invasion by *ATHILA* retrotransposons. The ability of *ATHILA* to insert within the centromeres is likely determined by their integrase protein. The Tal1 *COPIA* element from *Arabidopsis lyrata* also shows an insertion bias into *CEN180* when expressed in *A. thaliana (37)*, despite satellite sequences varying between these species (*38*), indicating that epigenetic information may be important for targeting. Most of the centromeric *ATHILA* elements appear young, based on high LTR identity, and possess many features required for transposition, although the centromeres show differences in the frequency of *ATHILA* insertions, with centromeres 4 and 5 being the most invaded. Compared with *CEN180*, centromeric *ATHILA* have distinct chromatin profiles and are associated with increased satellite divergence in adjacent regions. Therefore, *ATHILA* elements represent a potentially disruptive influence on the genetic and epigenetic organization of the centromeres. However, transposons are widespread in the centromeres of diverse eukaryotes and can directly contribute to repeat evolution (e.g., mammalian CENP-B is derived from a Pogo DNA transposase) (*39*). Therefore, *ATHILA* elements may also beneficially contribute to centromere integrity and stability in *Arabidopsis*.

The advantage conferred to *ATHILA* by integration within the centromeres is presently unclear, although we speculate that they may be engaged in centromere drive (*40*). Haig-Grafen scrambling through recombination has been proposed as a defense against drive elements within the centromeres (*41*). For example, maize meiotic gene conversion can eliminate centromeric *CRM2* retrotransposons (*25*). Therefore, centromere satellite homogenization may serve as a mechanism to purge *ATHILA*, although in some cases this results in transposon duplication (fig. S22). The presence of *ATHILA* solo LTRs is also consistent with homologous recombination acting on the retrotransposons after integration (fig. S22). Centromere 5 and the diverged *CEN180* array in centromere 4 show both high *ATHILA* density and reduced *CEN180* higher-order repetition. This indicates that *ATHILA* may inhibit *CEN180* homogenization or that loss of homogenization facilitates *ATHILA* insertion. We propose that each *Arabidopsis* centromere represents a different stage in cycles of satellite homogenization and *ATHILA*-driven diversification. These opposing forces provide a dual capacity for homeostasis and change during centromere evolution. Assembly of centromeres from multiple *Arabidopsis* accessions, and closely related species, has the potential to reveal new insights into centromere formation and the evolutionary dynamics of *CEN180* and *ATHILA* repeats.

Methods summary

Genomic DNA was extracted from *A. thaliana* Col-0 plants and used for ONT and PacBio HiFi long-read sequencing and Bionano optical mapping. ONT reads were used to establish a draft assembly, which was then scaffolded and polished with HiFi reads to generate the Col-CEN v1.2 assembly. ONT reads were used to analyze DNA methylation with the DeepSignal-plant algorithm (*20*). *CEN180* monomers, higher-order repeats, and *ATHILA* retrotransposons were identified de novo using custom pipelines. Short-read datasets (table S7) were aligned to Col-CEN to map chromatin and recombination distributions, using standard methods. Cytogenetic analysis of the centromeres was performed using FISH and immunofluorescence staining. A full description of all experimental and computational methods can be found in the supplementary materials.

REFERENCES AND NOTES

1. H. S. Malik, S. Henikoff, Major evolutionary transitions in centromere complexity. *Cell* **138**, 1067–1082 (2009). doi: 10.1016/j.cell.2009.08.036; pmid: 19766562
2. D. P. Melters *et al*., Comparative analysis of tandem repeats from hundreds of species reveals unique insights into centromere evolution. *Genome Biol.* **14**, R10 (2013). doi: 10.1186/gb-2013-14-1-r10; pmid: 23363705
3. K. L. McKinley, I. M. Cheeseman, The molecular basis for centromere identity and function. *Nat. Rev. Mol. Cell Biol.* **17**, 16–29 (2016). doi: 10.1038/nrm.2015.5; pmid: 26601620
4. M. K. Rudd, G. A. Wray, H. F. Willard, The evolutionary dynamics of α-satellite. *Genome Res.* **16**, 88–96 (2006). doi: 10.1101/gr.3810906; pmid: 16344556
5. M. Jain *et al*., Nanopore sequencing and assembly of a human genome with ultra-long reads. *Nat. Biotechnol.* **36**, 338–345 (2018). doi: 10.1038/nbt.4060; pmid: 29431738
6. K. H. Miga *et al*., Telomere-to-telomere assembly of a complete human X chromosome. *Nature* **585**, 79–84 (2020). doi: 10.1038/s41586-020-2547-7; pmid: 32663838
7. G. A. Logsdon *et al*., The structure, function and evolution of a complete human chromosome 8. *Nature* **593**, 101–107 (2021). doi: 10.1038/s41586-021-03420-7; pmid: 33828295
8. S. Nurk *et al*., The complete sequence of a human genome. *bioRxiv* 2021.05.26.445798 [Preprint] (2021). doi: 10.1101/2021.05.26.445798
9. Arabidopsis Genome Initiative, Analysis of the genome sequence of the flowering plant *Arabidopsis thaliana*. *Nature* **408**, 796–815 (2000). doi: 10.1038/35048692; pmid: 11130711
10. S. Maheshwari, T. Ishii, C. T. Brown, A. Houben, L. Comai, Centromere location in *Arabidopsis* is unaltered by extreme divergence in CENH3 protein sequence. *Genome Res.* **27**, 471–478 (2017). doi: 10.1101/gr.214619.116; pmid: 28223399
11. G. P. Copenhaver *et al*., Genetic definition and sequence analysis of *Arabidopsis* centromeres. *Science* **286**, 2468–2474 (1999). doi: 10.1126/science.286.5449.2468; pmid: 10617454
12. P. B. Talbert, R. Masuelli, A. P. Tyagi, L. Comai, S. Henikoff, Centromeric localization and adaptive evolution of an *Arabidopsis* histone H3 variant. *Plant Cell* **14**, 1053–1066 (2002). doi: 10.1105/tpc.010425; pmid: 12034896
13. J. M. Martinez-Zapater, M. A. Estelle, C. R. Somerville, A highly repeated DNA sequence in *Arabidopsis thaliana*. *Mol. Gen. Genet.* **204**, 417–423 (1986). doi: 10.1007/BF00331018
14. E. K. Round, S. K. Flowers, E. J. Richards, *Arabidopsis thaliana* centromere regions: Genetic map positions and repetitive DNA structure. *Genome Res.* **7**, 1045–1053 (1997). doi: 10.1101/gr.7.11.1045; pmid: 9371740
15. A. M. McCartney *et al*., Chasing perfection: validation and polishing strategies for telomere-to-telomere genome assemblies. *bioRxiv* 2021.07.02.450803 [Preprint] (2021). doi: 10.1101/2021.07.02.450803
16. T. Hosouchi, N. Kumekawa, H. Tsuruoka, H. Kotani, Physical map-based sizes of the centromeric regions of *Arabidopsis thaliana* chromosomes 1, 2, and 3. *DNA Res.* **9**, 117–121 (2002). doi: 10.1093/dnares/9.4.117; pmid: 12240833
17. A. Rhie, B. P. Walenz, S. Koren, A. M. Phillippy, Merqury: Reference-free quality, completeness, and phasing assessment for genome assemblies. *Genome Biol.* **21**, 245 (2020). doi: 10.1186/s13059-020-02134-9; pmid: 32928274
18. D. A. Wright, D. F. Voytas, *Athila4* of *Arabidopsis* and *Calypso* of soybean define a lineage of endogenous plant retroviruses. *Genome Res.* **12**, 122–131 (2002). doi: 10.1101/gr.196001; pmid: 11779837
19. B. F. McAllister, J. H. Werren, Evolution of tandemly repeated sequences: What happens at the end of an array? *J. Mol. Evol.* **48**, 469–481 (1999). doi: 10.1007/PL00006491; pmid: 10079285
20. P. Ni *et al*., Genome-wide detection of cytosine methylations in plant from nanopore sequencing data using deep learning. *bioRxiv* 2021.02.07.430077 [Preprint] (2021). doi: 10.1101/2021.02.07.430077
21. H. Stroud *et al*., Non-CG methylation patterns shape the epigenetic landscape in *Arabidopsis*. *Nat. Struct. Mol. Biol.* **21**, 64–72 (2014). doi: 10.1038/nsmb.2735; pmid: 24336224
22. H. Stroud, M. V. C. Greenberg, S. Feng, Y. V. Bernatavichute, S. E. Jacobsen, Comprehensive analysis of silencing mutants reveals complex regulation of the *Arabidopsis* methylome. *Cell* **152**, 352–364 (2013). doi: 10.1016/j.cell.2012.10.054; pmid: 23313553
23. Y. Jacob *et al*., ATXR5 and ATXR6 are H3K27 monomethyltransferases required for chromatin structure and gene silencing. *Nat. Struct. Mol. Biol.* **16**, 763–768 (2009). doi: 10.1038/nsmb.1611; pmid: 19503079
24. R. Yelagandula *et al*., The histone variant H2A.W defines heterochromatin and promotes chromatin condensation in *Arabidopsis*. *Cell* **158**, 98–109 (2014). doi: 10.1016/j.cell.2014.06.006; pmid: 24995981
25. J. Shi *et al*., Widespread gene conversion in centromere cores. *PLOS Biol.* **8**, e1000327 (2010). doi: 10.1371/journal.pbio.1000327; pmid: 20231874
26. C. Lambing *et al*., Interacting genomic landscapes of REC8-cohesin, chromatin, and meiotic recombination in *Arabidopsis*. *Plant Cell* **32**, 1218–1239 (2020). doi: 10.1105/tpc.19.00866; pmid: 32024691
27. C. Lambing, P. C. Kuo, A. J. Tock, S. D. Topp, I. R. Henderson, ASY1 acts as a dosage-dependent antagonist of telomere-led recombination and mediates crossover interference in *Arabidopsis*. *Proc. Natl. Acad. Sci. U.S.A.* **117**, 13647–13658 (2020). doi: 10.1073/pnas.1921055117; pmid: 32499315
28. K. Choi *et al*., Nucleosomes and DNA methylation shape meiotic DSB frequency in *Arabidopsis thaliana* transposons and gene regulatory regions. *Genome Res.* **28**, 532–546 (2018). doi: 10.1101/gr.225599.117; pmid: 29530928
29. M. Rigal *et al*., Epigenome confrontation triggers immediate reprogramming of DNA methylation and transposon silencing in *Arabidopsis thaliana* F1 epihybrids. *Proc. Natl. Acad. Sci. U.S.A.* **113**, E2083–E2092 (2016). doi: 10.1073/pnas.1600672113; pmid: 27001853
30. A. Steimer *et al*., Endogenous targets of transcriptional gene silencing in *Arabidopsis*. *Plant Cell* **12**, 1165–1178 (2000). doi: 10.1105/tpc.12.7.1165; pmid: 10899982
31. S. C. Lee *et al*., *Arabidopsis* retrotransposon virus-like particles and their regulation by epigenetically activated small RNA. *Genome Res.* **30**, 576–588 (2020). doi: 10.1101/gr.259044.119; pmid: 32303559
32. A. Rhie *et al*., Towards complete and error-free genome assemblies of all vertebrate species. *Nature* **592**, 737–746 (2021). doi: 10.1038/s41586-021-03451-0; pmid: 33911273
33. E. Wijnker *et al*., The genomic landscape of meiotic crossovers and gene conversions in *Arabidopsis thaliana*. *eLife* **2**, e01426 (2013). doi: 10.7554/eLife.01426; pmid: 24347547
34. S. J. Durfy, H. F. Willard, Patterns of intra- and interarray sequence variation in alpha satellite from the human X chromosome: Evidence for short-range homogenization of tandemly repeated DNA sequences. *Genomics* **5**, 810–821 (1989). doi: 10.1016/0888-7543(89)90123-7; pmid: 2591964
35. N. Altemose *et al*., Complete genomic and epigenetic maps of human centromeres. *bioRxiv* 2021.07.12.452052 [Preprint] (2021). doi: 10.1101/2021.07.12.452052
36. M. M. Mahtani, H. F. Willard, Physical and genetic mapping of the human X chromosome centromere: Repression of recombination. *Genome Res.* **8**, 100–110 (1998). doi: 10.1101/gr.8.2.100; pmid: 9477338

37. S. Tsukahara *et al*., Centromere-targeted de novo integrations of an LTR retrotransposon of *Arabidopsis lyrata*. *Genes Dev.* **26**, 705–713 (2012). doi: 10.1101/gad.183871.111; pmid: 22431508
38. A. Kawabe, S. Nasuda, Structure and genomic organization of centromeric repeats in *Arabidopsis* species. *Mol. Genet. Genomics* **272**, 593–602 (2005). doi: 10.1007/s00438-004-1081-x; pmid: 15586291
39. S. J. Klein, R. J. O'Neill, Transposable elements: Genome innovation, chromosome diversity, and centromere conflict. *Chromosome Res.* **26**, 5–23 (2018). doi: 10.1007/s10577-017-9569-5; pmid: 29332159
40. H. S. Malik, The centromere-drive hypothesis: A simple basis for centromere complexity. *Prog. Mol. Subcell. Biol.* **48**, 33–52 (2009). doi: 10.1007/978-3-642-00182-6_2; pmid: 19521811
41. D. Haig, A. Grafen, Genetic scrambling as a defence against meiotic drive. *J. Theor. Biol.* **153**, 531–558 (1991). doi: 10.1016/S0022-5193(05)80155-9; pmid: 1806752

ACKNOWLEDGMENTS

This paper is dedicated to Simon Chan. We thank I. Thompson for *ATHILA* analysis, S. Henikoff for the generous gift of CENH3 antibodies, A. Shumate for help with gene Liftoff interpretation, B. Fischer for advice on high–molecular weight DNA isolation, and M. Pouch for assistance designing FISH probes. **Funding:** This work was supported by BBSRC grants BB/S006842/1, BB/S020012/1, and BB/V003984/1 to I.R.H.; European Research Council Consolidator Award ERC-2015-CoG-681987 "SynthHotSpot" to I.R.H.; Marie Curie International Training Network "MEICOM" to I.R.H.; Human Frontier Science Program award RGP0025/2021 to T.K., M.C.S., and I.R.H.; US National Institutes of Health grant S10OD028632-01; US National Science Foundation grants DBI-1350041 and IOS-1732253 to M.C.S.; Royal Society awards UF160222 and RGF/R1/180006 to A.B.; the Czech Science Foundation grant no. 21-03909S to M.A.L.; the Gregor Mendel Institute to F.B.; grants Fonds zur Förderung der wissenschaftlichen Forschung (FWF) P26887, P28320, P30802, P32054, and TAI304 to F.B. and chromatin dynamics W1238 to A.S. and B.J.; Leverhulme Trust Research Leadership grant RL-2012-042 to J.T.; and grants from the Howard Hughes Medical Institute and US National Institutes of Health (RO1GM067014) to R.A.M. **Author contributions:** M.N. sequenced DNA; performed genome assembly and analysis, ChIP-seq, and DNA methylation analysis; and wrote the manuscript. M.A. performed genome assembly, polishing, validation, annotation, and analysis and wrote the manuscript. P.W. performed satellite repeat annotation and genome analysis and wrote the manuscript. A.J.T. performed short-read alignment and genome analysis and wrote the manuscript. B.W.A. sequenced DNA, performed optical mapping, and contributed to the assembly. A.S. performed chromatin immunofluorescence analysis. B.J. provided ChIP-seq data. C.L. and P.K. performed immunocytology. N.Y. generated the DMC1 epitope-tagged line. N.H. and K.C. sequenced DNA and contributed to the assembly. L.M.S., J.T., and K.S. performed PacBio sequencing. T.K. and R.A.M. provided intellectual input. T.M. and M.A.L. performed FISH. F.B. supervised ChIP-seq and immunofluorescence analysis and wrote the manuscript. A.B. performed *ATHILA* annotation and genome analysis and wrote the manuscript. T.P.M. supervised DNA sequencing and genome assembly and analysis and wrote the manuscript. M.C.S. supervised genome assembly, validation, annotation, and analysis and wrote the manuscript. I.R.H. supervised DNA sequencing, genome assembly, validation, annotation, and analysis and wrote the manuscript. **Competing interests:** The authors have no competing interests. **Data and materials availability:** The ONT sequencing reads used for assembly are available for download at ArrayExpress accession E-MTAB-10272 (www.ebi.ac.uk/arrayexpress/). The PacBio HiFi reads are available for download at European Nucleotide Archive accession number PRJEB46164 (www.ebi.ac.uk/ena/browser/view/PRJEB46164). All data, code and materials are available in the manuscript or the supplementary materials and at https://github.com/schatzlab/Col-CEN.

SUPPLEMENTARY MATERIALS

science.org/doi/10.1126/science.abi7489
Materials and Methods
Figs. S1 to S22
Tables S1 to S8
References (*42*–*94*)
MDAR Reproducibility Checklist

31 March 2021; resubmitted 5 August 2021
Accepted 27 September 2021
10.1126/science.abi7489



AAAS.ORG/COMMUNITY







AAAS' Member Community is a one-stop destination for scientists and STEM enthusiasts alike. It's "Where Science Gets Social": a community where facts matter, ideas are big and there's always a reason to come hang out, share, discuss and explore.

Member COMMUNITY
AAAS

AMERICAN ASSOCIATION FOR THE ADVANCEMENT OF SCIENCE

RESEARCH ARTICLE SUMMARY

NEUROSCIENCE

Tool use and language share syntactic processes and neural patterns in the basal ganglia

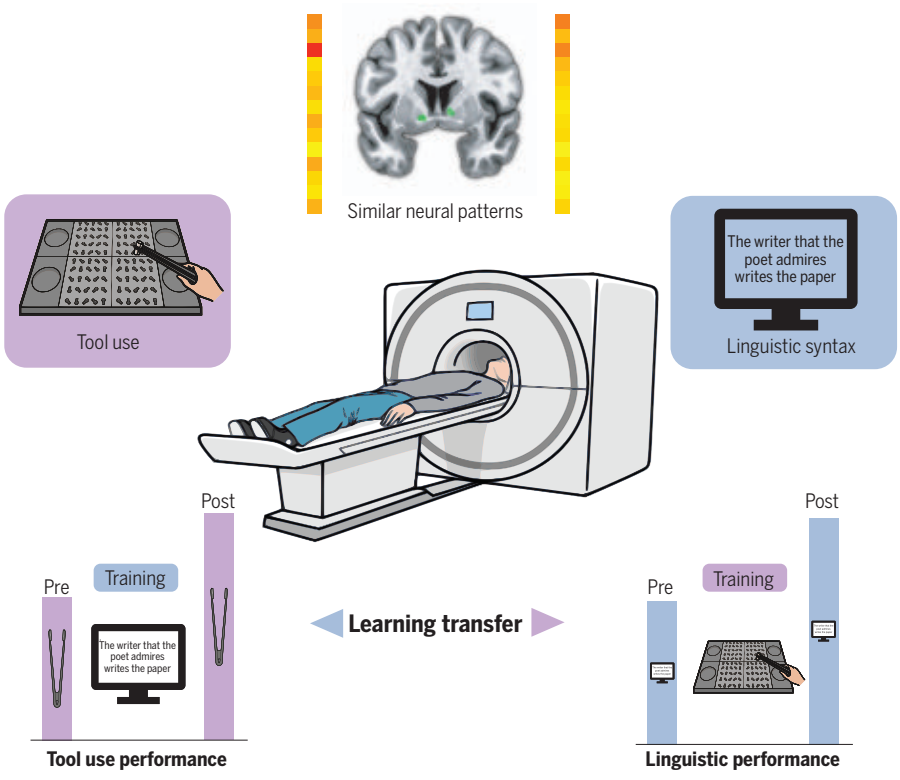
Simon Thibault*, Raphaël Py, Angelo Mattia Gervasi, Romeo Salemme, Eric Koun, Martin Lövden, Véronique Boulenger†, Alice C. Roy†, Claudio Brozzoli*†

INTRODUCTION: Tool use is a hallmark of human evolution. Beyond its sensorimotor components, the complexity of which has been extensively investigated, tool use affects cognition from a different perspective. Indeed, tool use requires integrating an external object as a body part and embedding its functional structure in the motor program. This adds a hierarchical level into the motor plan of manual actions, subtly modifying the relationship between interdependent subcomponents. Embedded structures also exist in language, and syntax is the cognitive function handling these linguistic hierarchies. One example is center-embedded object-relative clauses: "The poet *[that the scientist admires]* reads the paper." Accordingly, researchers have advanced a role for syntax in action and the existence of similarities between the processes underlying tool use and language, so that shared neural resources for a common cognitive function could be at stake.

RATIONALE: We first tested the existence of shared neural substrates for tool use and syntax in language. Second, we tested the prediction that training one ability should affect performance in the other. In a first experiment, we measured participants' brain activity with functional magnetic resonance imaging during tool use or, as a control, manual actions. In separate runs, the same participants performed a linguistic task on complex syntactic structures. We looked for common activations between tool use and the linguistic task, predicting similar patterns of activity if they rely on common neural resources. In further behavioral experiments, we tested whether motor training with the tool selectively improves syntactic performance in language and if syntactic training in language, in turn, selectively improves motor performance with the tool.

RESULTS: Tool-use planning and complex syntax processing (i.e., object relatives) elicited neural activity anatomically colocalized within the basal ganglia. A control experiment ruled out verbal working memory and manual (i.e., without a tool) control processes as an underlying component of this overlap. Multivariate analyses revealed similar spatial distributions of neural patterns prompted by tool-use planning and object-relative processing. This agrees with the recruitment of the same neural resources by both abilities and with the existence of a supramodal syntactic function. The shared neurofunctional resources were moreover reflected behaviorally by cross-domain learning transfer. Indeed, tool-use training significantly improved linguistic performance with complex syntactic structures. No learning transfer was observed on language syntactic abilities if participants trained without the tool. The reverse was also true: Syntactic training with complex sentences improved motor performance with the tool more than motor performance in a task without the tool and matched for sensorimotor difficulty. No learning transfer was observed on tool use if participants trained with simpler syntactic structures in language.

CONCLUSION: These findings reveal the existence of a supramodal syntactic function that is shared between language and motor processes. As a consequence, training tool-use abilities improves linguistic syntax and, reciprocally, training linguistic syntax abilities improves tool use. The neural mechanisms allowing for boosting performance in one domain by training syntax in the other may involve priming processes through preactivation of common neural resources, as well as short-term plasticity within the shared network. Our findings point to the basal ganglia as the neural site of supramodal syntax that handles embedded structures in either domain and also support longstanding theories of the coevolution of tool use and language in humans. ■



Tool use and language share syntactic processes. Functional magnetic resonance imaging revealed that tool use and syntax in language elicit similar patterns of brain activation within the basal ganglia. This indicates common neural resources for the two abilities. Indeed, learning transfer occurs across the two domains: Tool-use motor training improves syntactic processing in language and, reciprocally, linguistic training with syntactic structures improves tool use.

The list of author affiliations is available in the full article online.
*Corresponding author. Email: simon.thibault@inserm.fr (S.T.); claudio.brozzoli@inserm.fr (C.B.)
†These authors contributed equally to this work.
Cite this article as S. Thibault *et al.*, *Science* **374**, eabe0874 (2021). DOI: 10.1126/science.abe0874

READ THE FULL ARTICLE AT
https://doi.org/10.1126/science.abe0874

RESEARCH ARTICLE

NEUROSCIENCE

Tool use and language share syntactic processes and neural patterns in the basal ganglia

Simon Thibault[1,2]*, Raphaël Py[1,2], Angelo Mattia Gervasi[1], Romeo Salemme[1], Eric Koun[1], Martin Lövden[3,4], Véronique Boulenger[2,5]†, Alice C. Roy[2,5]†, Claudio Brozzoli[1,2,3]*†

Does tool use share syntactic processes with language? Acting with a tool is thought to add a hierarchical level into the motor plan. In the linguistic domain, syntax is the cognitive function handling interdependent elements. Using functional magnetic resonance imaging, we detected common neurofunctional substrates in the basal ganglia subserving both tool use and syntax in language. The two abilities elicited similar patterns of neural activity, indicating the existence of shared functional resources. Manual actions and verbal working memory did not contribute to this common network. Consistent with the existence of shared neural resources, we observed bidirectional behavioral enhancement of tool use and syntactic skills in language so that training one function improves performance in the other. This reveals supramodal syntactic processes for tool use and language.

Tool use is a highly sophisticated skill, and its sensory (*1*) and motor components (*2*) have been extensively studied across disciplines. Tool use has been suggested to add a further hierarchical level to the motor plan (*3*–*5*). Interdependent elements and hierarchies are common in language, and decades of research have pointed to syntax as the cognitive function handling complex linguistic structures (*6*). Does tool use share syntactic processes with language? A wide range of cognitive processes exploit activity in sensorimotor regions (*7*–*13*). We posit that syntactic processes are also grounded in sensorimotor structures.

Center-embedded object-relative sentences (*14*–*16*) provide a paradigmatic example of complex linguistic structures (Table 1A). Embedded clauses split interdependent elements and add further dependencies in the sentence. However, by handling hierarchical sequential elements, syntactic processes allow us to understand such complex structures. Studies suggest that action and language share syntactic processes (*17*–*21*). Actions indeed involve hierarchies of interdependent subcomponents within an entire motor sequence (*22*–*25*). Dexterous tool use in particular implies incorporating an external object (*1*). The functional combination of the body and the external object to perform an action (*3*) embeds a further level into the manual motor program (*26*). Goal-directed movements feature several subcomponents integrated in the action sequence (*27*) such as reaching, grasping, lifting, rotating, and placing an object. This sequence provides an example of complex motor structures with several elements whose relationship needs to be subtly rearranged when the tool is embedded in the motor program (*28*, *29*). An individual's tool-use dexterity in such a motor task predicts linguistic production skills in a syntactically constrained task (*30*). Neuroimaging supports the behavioral link between tool use and language. Syntactic processing managing linguistic hierarchical structures indeed relies on activity within the left inferior frontal gyrus (lIFG) (*6*, *14*–*16*) and basal ganglia (BG) (*21*, *31*, *32*), especially within the striatum (*33*, *34*). Similarly, activity in a parietofrontal network as well as in the BG supports skillful tool use (*35*, *38*). Brain imaging studies have therefore described partially overlapping neural networks for syntax (*15*, *21*, *33*) and tool use (*35*–*38*). However, these lines of research have so far diverged, and the anatomo-functional overlap between tool use and syntax remains anecdotal. Here, we tested the hypothesis that tool use and syntax share neural resources and, as a consequence, that the two abilities affect one another at the behavioral level.

Anatomical overlap of tool use and syntactic activity in the BG

Using functional magnetic resonance imaging (fMRI), we first mapped the brain regions where tool use and syntactic processes overlap. To isolate the syntactic network, 20 participants solved a task requiring them to process center-embedded relative clauses (*14*, *15*) (Experiment 1, Fig. 1A). The protocol consisted of the presentation of sentences relying on the same

[1]Integrative Multisensory Perception Action & Cognition Team (ImpAct), Centre de Recherche en Neurosciences de Lyon, INSERM U1028, CNRS UMR5292, Lyon, 69000, France. [2]University of Lyon, Lyon 69000, France. [3]Aging Research Center (ARC), Department of Neurobiology, Care Sciences and Society, Karolinska Institutet, 17177 Stockholm, Sweden. [4]Department of Psychology, University of Gothenburg, 40530 Gothenburg, Sweden. [5]Dynamics of Language laboratory, CNRS UMR5596, Lyon, France.
***Corresponding author. Email: simon.thibault@inserm.fr (S.T.); claudio.brozzoli@inserm.fr (C.B.)**
†These authors contributed equally to this work.

Table 1. Comprehension of sentences in a two-alternative forced choice (2-AFC) task. (**A**) Syntactic structures presented during the sentence-encoding phase. (**B**) Test affirmation for the 2-AFC task (two true and two false possible probes for each encoded sentence). CC, coordinated clauses; SRCs, subject-relative clauses; ORCs, object-relative clauses.

(A) Sentence encoding

CCs	SRCs	ORCs
"L'écrivain admire le poète et écrit le papier" "The writer admires the poet and writes the paper" (canonical subject-object order)	"L'écrivain qui admire le poète écrit le papier" "The writer that admires the poet writes the paper" (subject-object order compatible with the canonical order)	"L'écrivain que le poète admire écrit le papier" "The writer that the poet admires writes the paper" (noncanonical subject-object order)

(B) Test affirmation (one selected of four)

"L'écrivain admire le poète" "The writer admires the poet" (CC = true, SRC = true, ORC = false)	"Le poète admire l'écrivain" "The poet admires the writer" (CC = false, SRC = false, ORC = true)
"Le poète écrit le papier" "The poet writes the paper" (CC = false, SRC = false, ORC = false)	"L'écrivain écrit le papier" "The writer writes the paper" (CC = true, SRC = true, ORC = true)

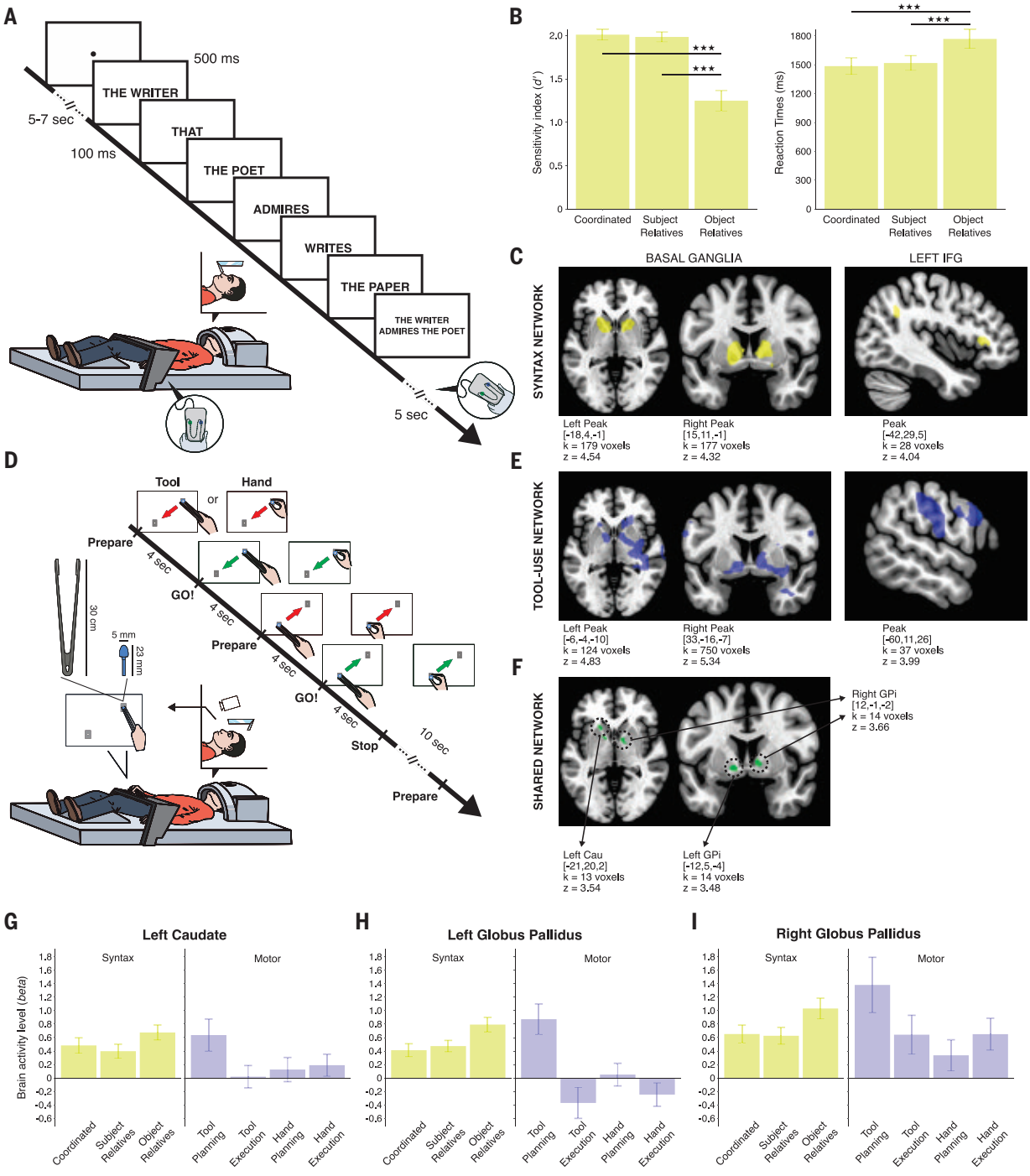


Fig. 1. Experiment 1: Overlap of syntax and tool-use planning activity. (**A**) Setup and experimental design of the syntactic task. (**B**) *d'* (left graph) and RTs (right graph) for the syntactic comprehension of the three sentence structures. Both the one-way rmANOVA on *d'* and the LMM on RTs showed a significant main effect of *Sentence* (*d'*: $F_{(1.6,30.6)} = 40.04$; $P < 0.001$; $\eta_G^2 = 0.49$; RTs: $\chi^2_{(2)} = 25.21$, $P < 0.001$). Error bars show SEs. ***$P < 0.001$, Tukey's post hoc test. (**C**) Statistical maps thresholded at $P < 0.001$, uncorrected, for syntax (object relatives compared with the two other sentence types). (**D**) Setup and experimental design of tool-use and free-hand motor tasks. (**E**) Statistical maps thresholded at $P < 0.001$, uncorrected, for tool-use planning. (**F**) Joint neuronal activity for syntax and tool-use planning in the BG, thresholded at $P < 0.001$, uncorrected. (**G** to **I**) Average brain activity level in each cluster significantly activated by both tasks. The highest activations were found for tool-use planning (blue) and object-relative clauses (yellow) in the motor and syntactic tasks, respectively.

content words but featuring three different syntactic structures: a coordinated clause (e.g., "The writer admires the poet and writes the paper"), a subject-relative clause (e.g., "The writer that admires the poet writes the paper"), or an object-relative clause (e.g., "The writer that the poet admires writes the paper"; Table 1A). Each sentence was followed by a test affirmation (e.g., "The poet admires the writer"; Table 1B), which the participants had to judge as true or false with respect to the immediately preceding sentence. The participants succeeded

in this task (Fig. 1B), revealing, as expected, the worst sensitivity index (d') scores and the longest reaction times (RTs) for the object relatives (mean ± SEM: d' = 1.25 ± 0.12; RTs = 1769 ± 97 ms) compared with both subject relatives (d' = 1.98 ± 0.06; RTs = 1519 ± 76 ms; P < 0.001, Tukey's post hoc test) and coordinated clauses (d' = 2.01 ± 0.06; RTs = 1487 ± 87 ms; P < 0.001). No difference was found between coordinated and subject-relative clauses (P > 0.74). This pattern reflects the increased syntactic complexity of the object relatives with respect to the two other conditions (*14*). We assessed the functional syntactic network by contrasting brain activity elicited during the presentation of the object relatives with that elicited during the presentation of the two other types of clauses. This window of interest targeted the processes underlying syntactic encoding of the sentence material rather than processes engaged in sentence reorganization to answer the affirmation test (*15*). The syntactic network consisted of activity in a parietofrontal ensemble of cortical areas (table S1A) as well as subcortically within the BG [familywise error–corrected P (P_{FWE}) < 0.05 at the cluster level], encompassing the bilateral caudate nuclei, internal globus pallidus (GPi), and putamen. Frontal activity was observed within the lIFG (P < 0.001, uncorrected) in a cluster localized in Broca's area (Fig. 1C).

To identify the overlap between the syntactic and tool-use networks, we required the same participants to use a pair of 30-cm-long pliers, or their free right hand in different trials, to move a peg from one side of a board to the other (Fig. 1D and movies S1 and S2). We recorded their brain activity while they prepared and executed the movement with the tool or their free hand. The planning phase engages processes necessary for the organization of the components of the subsequent action (*24*) and is not influenced by the visual differences present during overt movement execution. We therefore isolated the activity specifically related to the preparation of movements with the tool and subtracted the activity related to preparation of manual movements and to movement execution with the tool and the hand (see the supplementary text for contrasts defined to investigate planning and execution of free-hand actions and tool-use execution). Tool-use planning involved a network encompassing parietal and prefrontal areas (table S1B) as well as the BG (P_{FWE} < 0.05 at the cluster level), including the bilateral caudate nuclei, GPi, and putamen (Fig. 1E). A frontal region within the lIFG (P < 0.001, uncorrected) located in the ventral premotor cortex, an area more posterior than the area identified in the syntactic task, was also activated. The syntactic and tool-use planning networks thus anatomically overlapped within the BG, sharing significant activations of the left caudate nucleus (lCau) and bilateral GPi (Fig. 1, F to I and table S1C). Even though syntax and tool-use planning both relied on the lIFG, the respective clusters of activation did not overlap (even at a lenient threshold P < 0.005, uncorrected). We used a stringent contrast for tool-use planning; nonetheless, we sought potential overlap between free-hand planning and syntax at the whole-brain level but did not find any significant cluster of shared activation (see the supplementary text for the free-hand planning neural activity). Although syntax has been disentangled from working memory resources (*15*), the latter might still support the processing of complex syntactic structures. To rule out such a contribution of working memory to the overlap between tool-use planning and syntactic networks, we measured brain activity in the same participants while they performed two verbal n-back tasks with two levels of difficulty (see fig. S1 and the supplementary text for behavioral results). Working memory mainly recruited a network involving the bilateral inferior parietal lobes (angular gyri), the left middle frontal gyrus, and the left caudate (fig. S2 and table S2). The working memory brain map did not significantly overlap with the tool-use planning network.

Common neurocognitive resources for tool-use planning and syntax in the BG

Does the neural overlap of activity subserving tool-use planning and syntax within the BG reflect common cognitive processes? If so, then the same neural resources should be recruited across conditions. Accordingly, brain activities underlying tool-use planning and syntactic encoding during object-relative sentences may show representational similarity in their respective spatial distribution within the overlapping clusters.

We therefore studied the representational similarity of brain activity patterns (*39*) across the two motor conditions, tool-use and free-hand planning, and the two most complex linguistic conditions, object and subject relatives. Considering the overlapping voxels revealed by the conjunction analysis (n = 41), we tested two models, including the similarity expected between conditions of the same domain (tool use and free hand for the motor domain and object and subject relatives for the linguistic domain). The first model tested the hypothesis of cross-domain similarity between activity patterns for tool-use planning and object relatives. The second control model instead tested for cross-domain similarity between free-hand planning and object relatives. The model assessing the representational similarity between tool-use planning and object relatives was significant (Pearson's r mean = 0.25 ± 0.08; Fisher's z mean = 0.29 ± 0.10; $t_{(19)}$ = 3.00; P = 0.007 Bonferroni-corrected, Cohen's d = 0.66). By contrast, the second model testing for a similarity between free-hand planning and object-relative clauses did not yield a good fit for the data (Pearson's r mean = 0.14 ± 0.09; Fisher's z mean = 0.19 ± 0.11; $t_{(19)}$ = 1.63; P = 0.12, Bonferroni corrected). To test for the specificity of the similarity between tool-use and object-relative patterns, we extracted the patterns elicited by the verbal working memory tasks (3-back and 1-back) on the same voxels and entered them into our models instead of the syntactic patterns. This did not reveal any significant similarity with either tool-use or free-hand planning (t < 1.36; P > 0.18, Bonferroni corrected; see the supplementary text).

We further investigated whether the reported significant similarity allows a classifier trained on the motor patterns (tool-use and free-hand) to coherently predict those elicited by object relatives. A successful cross-domain classification would corroborate the evidence for common neural resources shared by the two abilities. We applied a classification-based multivoxel pattern analysis (MVPA) on the patterns of activity extracted from the overlapping voxels identified with the conjunction analysis (n = 41). A support vector machine (SVM) classifier was trained on the motor data (tool-use planning versus free-hand planning) and tested cross-domain on the object-relative data using a leave-one-subject-out procedure. We assessed the accuracy of the classifier as the proportion of object-relative neural patterns classified as tool-use patterns. An accuracy of 0.5 indicates that the classifier performed at chance. An accuracy significantly above chance level means that object-relative patterns were classified more as tool-use than as free-hand patterns, whereas accuracy values significantly below 0.5 indicate the opposite. Object-relative patterns were significantly classified as tool-use rather than free-hand planning patterns (accuracy = 0.87, P = 0.003). When tested cross-domain on the working memory neural patterns (3-back) within the same voxels, the accuracy of the same classifier was not significantly different from chance level (accuracy = 0.64, P = 0.15; see the supplementary text).

As a further step, we computed voxelwise Pearson's correlation scores between activity levels supporting tool-use planning and successful comprehension of object relatives (*40*). These correlation scores were compared with correlation scores found between free-hand planning and object-relative processing. We compared the difference between the two observed Pearson's r values with an empirical null distribution of differences obtained after 10,000 permutations. The observed correlation between patterns for tool-use planning and object-relative comprehension was significantly larger than that between free-hand planning and object relatives, both for the lGPi and rGPi (lGPi: Pearson's r difference = 0.61;

P = 0.03 and rGPi: Pearson's r difference = 0.79; P = 0.007; Fig. 2, A to F, and supplementary text). The difference was not significant for the lCau (Pearson's r difference = −0.08; P = 0.64).

Overall, these findings establish that tool use and syntax rely on neural activity within common anatomical territories in the BG. The activity independently elicited by the two tasks displays similar spatial distribution, which is consistent with common neural resources. It has been documented that when two functions share neural resources and cognitive processes, learning transfer occurs (*41*): Training a specific ability can therefore benefit an untrained one (*41*, *42*). Therefore, we predicted cross-domain learning transfer between tool use and syntactic skills in language.

Learning transfer from tool use to syntactic skills in language

In Experiment 2, we tested whether tool-use training improves syntactic skills in language. We used the same syntactic task as in Experiment 1 to measure syntactic skills in 26 naïve, healthy adults before and after tool-use training (Fig. 3A). The specificity of tool use was controlled for by testing a distinct group (n = 26) undergoing an identical training regime but with the free hand. A third passive control group (n = 26) was also included to quantify potential test-retest effects. These participants were assessed in the same syntactic task before and after watching natural documentary videos for an equivalent amount of time as the two active groups engaged in motor training. The three groups were comparable in terms of relevant sociodemographic characteristics (see the supplementary text).

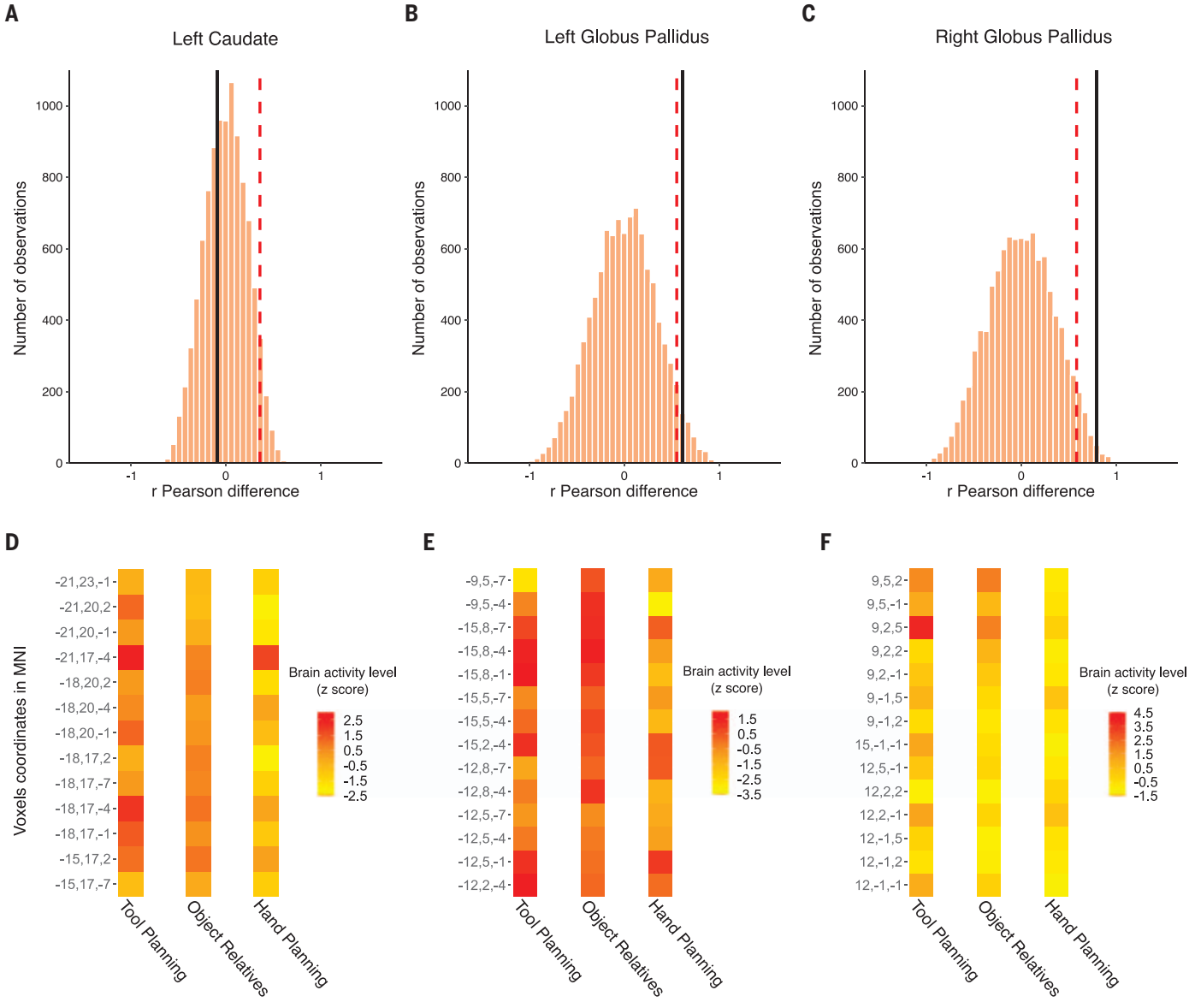


Fig. 2. Experiment 1: Functional link between tool-use planning and syntax in the BG. (**A** to **C**) Distribution, after 10,000 permutations, of differences of Pearson's r computed for the correlations between patterns of brain activity for object-relative clauses and those for motor planning of tool use and free hand separately for the lCau (A), lGPi (B), and rGPi (C). Larger positive differences indicate stronger similarity between tool-use planning and object-relative processing compared with free-hand planning and object-relative processing. The black line indicates the observed difference, and the red dotted line indicates the P-value threshold set at 0.05. (**D** to **F**) Spatial distribution of neural activity for tool-use planning, object-relative planning, and free-hand planning in the BG. Each single colored square represents a single voxel for the lCau (D), lGPi (E), and rGPi (F).

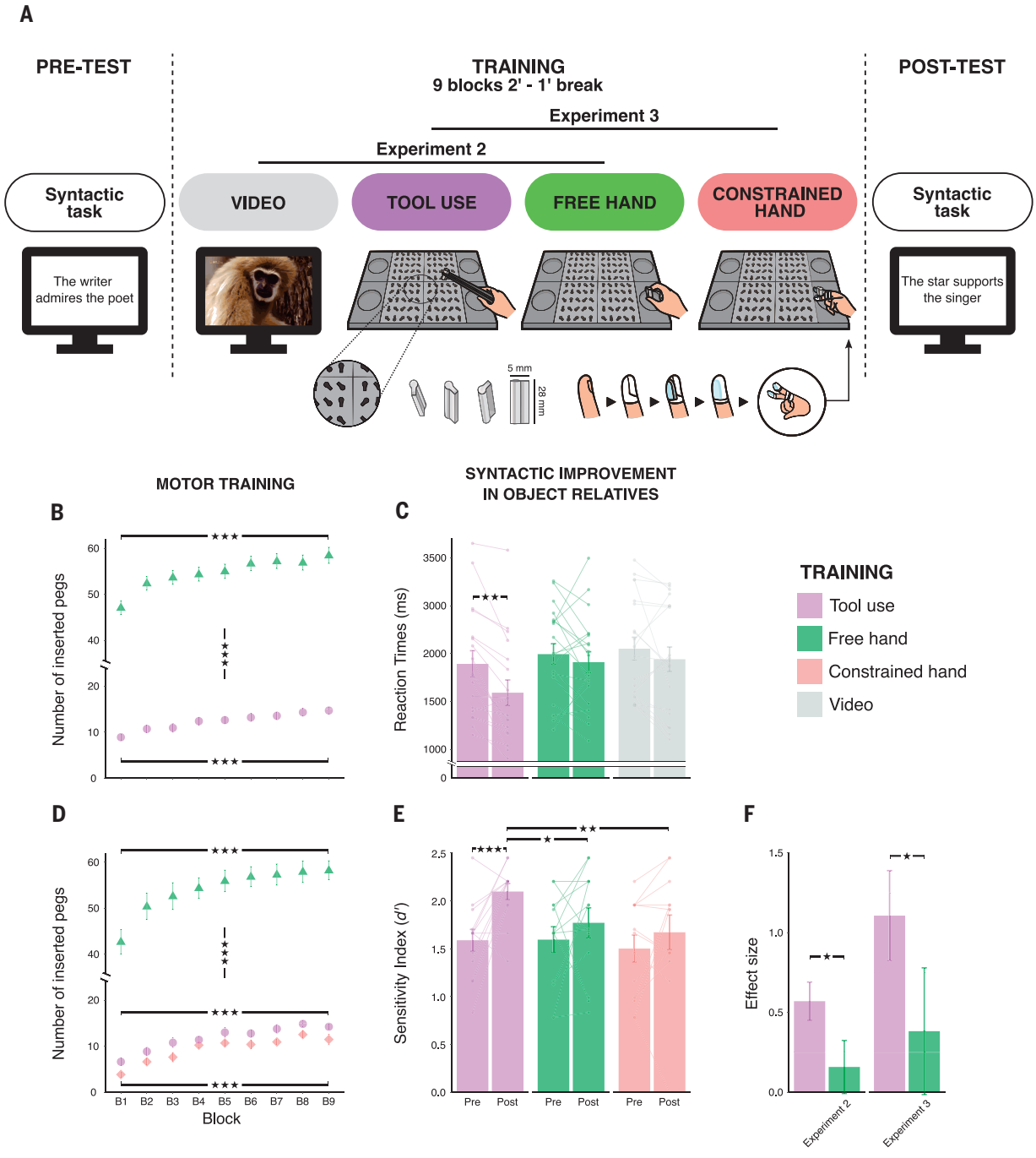


Fig. 3. Experiments 2 and 3: Cross-domain learning transfer from tool use to syntactic skills in language. (**A**) Timeline of training and syntactic pretests and posttests. Different groups were trained either to use a tool (purple inset) or the free hand (green inset) to grab and enter key-shaped pegs into grooved holes or they passively watched videos (gray inset). In Experiment 3, training difficulty was controlled with a further manual training condition (red inset) with increased sensorimotor constraints mimicking those present during tool use. (**B**) Motor improvement during tool-use training (purple) and free-hand training (green) in Experiment 2. (**C**) In Experiment 2, participants with high initial syntactic skills improved for object relatives in the syntactic task after training with the tool (purple bars) but not after free-hand training (green bars) or passive video watching (gray bars). Connected dots across pretest and posttest represent individual data. (**D**) Motor improvement during tool-use training (purple), free-hand training (green), and constrained-hand training (red) in Experiment 3. (**E**) In Experiment 3, after tool use, the participants improved for object relatives in the syntactic task (purple bars) but not after training with the free hand (green bars) or with the hand mimicking similar sensorimotor constraints as the tool. Red bars indicate significant *Training* × *Time* × *Sentence* interaction of the three-way rmANOVA ($F_{(3.1,56.4)}$ = 2.81; P = 0.04; η_G^2 = 0.03). (**F**) Effect size of the improvements in Experiments 2 and 3. Two-way *Training* × *Experiment* rmANOVA: There was a significant main effect of *Training* ($F_{(1,60)}$ = 5.37; P = 0.02; η_G^2 = 0.082), a nonsignificant effect of *Experiment* ($F_{(1,60)}$ = 2.8; P = 0.11), and no interaction ($F_{(1,60)}$ = 0.51; P = 0.58). ***P < 0.001; **P < 0.01; *P < 0.05.

To assess the learning transfer to the syntactic task, we ensured that the participants significantly improved in their respective motor training (Fig. 3B and supplementary text) and then analyzed the impact of tool-use training compared with both free-hand training and passive video watching on performance in the syntactic task. We accounted for potential interindividual differences in the initial syntactic level by including pretest performance (d') as a covariate in a three-way *Training* × *Time* × *Sentence* analysis of covariance (ANCOVA) run on RTs [see the supplementary text for the corresponding analysis without the continuous factor]. The improvement in syntax depended on the type of training and the participants' initial level of syntactic performance ($F_{(2,72)} = 3.99$; $P = 0.02$; $\eta_G^2 = 0.009$). Because participants with lower scores before training are more prone to contextual improvements with task repetition (*43*), we specifically examined the training-dependent effects separating participants with low from those with high initial syntactic skills. We set a d' threshold based on the performance in the pretest session, defined as the sample median minus 1 SD (threshold $d' > 1.38$). Participants with lower syntactic skills (tool-use group: $n = 8$; free-hand group: $n = 6$; video group: $n = 6$) significantly improved with all sentence structures at posttest and this was independent of training (see the supplementary text). This test-retest amelioration, potentially linked to more contextual aspects of the task such as motor and response selection, may hide potential selective effects of training. In the participants showing higher initial syntactic skills (tool-use group: $n = 18$, free-hand group: $n = 20$, video group: $n = 20$), tool-use training significantly improved syntactic performance compared with both free-hand training and passive video watching [significant *Training* × *Time* × *Sentence* interaction of the linear mixed model (LMM): $\chi^2_{(4)} = 13.6$, $P = 0.009$; Fig. 3C]. After tool use, the participants were significantly faster in correctly processing object relatives than before (pretest RTs = 1892 ± 137 ms versus posttest RTs = 1591 ± 133 ms, $P < 0.001$, Tukey's post hoc test). By contrast, performance for object relatives did not significantly change for the two control groups (free hand: pretest RTs = 1994 ± 109 ms versus posttest RTs = 1910 ± 109 ms, $P = 0.17$; video: pretest RTs = 2051 ± 119 ms versus posttest RTs = 1940 ± 128 ms, $P = 0.10$). Comprehension of object relatives was indistinguishable across the three groups before training ($P > 0.63$). A significant improvement was found for simpler syntactic structures, namely coordinated and subject-relative clauses; nevertheless, these improvements were equivalent among the three groups (fig. S3, C and D, and supplementary text).

Training to use a tool improved syntactic abilities in a linguistic task. This effect depended on the individuals' initial syntactic level and was found in those participants showing better syntactic skills before training. To corroborate this finding, we performed an additional experiment (Experiment 3) in which we included a sample of 39 naïve participants showing high syntactic scores in the pretest session. As an independent criterion for inclusion in this new sample of participants, we adopted the threshold of syntactic performance before training identified in Experiment 2 ($d' > 1.38$). To rule out the sensorimotor difficulty of the tool-use task as a factor contributing to learning transfer, we added a training condition in which we reduced the degrees of freedom of free-hand movements to mimic those imposed by the tool. To rule out the sensorimotor difficulty of the tool-use task as a factor contributing to learning transfer, we introduced sensorimotor constraints in free-hand motor training (see the supplementary text). Tactile feedback was furthermore hampered (Fig. 3A). These changes were meant to provide a good simulation of pliers' sensorimotor constraints and difficulty. Two groups underwent either tool-use or free-hand training as in Experiment 2 to replicate our findings in an independent sample of participants with high syntactic skills. The third group was assigned to the control training condition with the constrained hand. Syntactic skills were measured in the three groups as in the previous assessments before and after motor training.

First, we reaffirmed that tool-use training selectively improved comprehension of object relatives [Fig. 3E; pretest $d' = 1.59 \pm 0.11$; posttest $d' = 2.1 \pm 0.08$; $P < 0.001$, Tukey's post hoc test; significant *Training* × *Time* × *Sentence* interaction of the three-way repeated-measures ANOVA (rmANOVA): $F_{(3.1,56.4)} = 2.81$; $P = 0.04$; $\eta_G^2 = 0.03$]. Second, neither free-hand training (pretest $d' = 1.59 \pm 0.14$; posttest $d' = 1.77 \pm 0.16$; $P = 0.10$) nor constrained-hand training (pretest $d' = 1.50 \pm 0.14$; posttest $d' = 1.67 \pm 0.18$; $P = 0.12$) enhanced the performance for object relatives in a statistically significant way. After training, the tool-use group significantly outperformed both the free-hand ($P = 0.04$) and constrained-hand ($P = 0.005$) groups in the comprehension of object relatives. A difference between groups was observed for simpler syntactic structures (fig. S3, C and D, and supplementary text). Furthermore, the magnitude of transfer was consistent with the syntactic improvement observed in Experiment 2 (Fig. 3F and supplementary text).

Learning transfer from syntactic training in language to tool use

Consistent with the previous conclusion, shared neurofunctional resources between tool use and language also predict the reverse learning transfer: Training syntactic processes with complex sentences should improve tool use. In the single-blind Experiment 4, we tested this prediction by measuring tool-use performance in 48 naïve, healthy adults before and after syntactic training in language (Fig. 4A). Participants were randomly assigned to train with either object- or subject-relative clauses. Before and after syntactic training, we measured the number of pegs entered with the tool in an adapted version of the motor task devised in the previous Experiments 2 and 3. The experimenter was blinded with respect to the type of syntactic training to which the participant was assigned. The two groups were comparable in terms of relevant sociodemographic characteristics (see the supplementary text). Given the shared syntactic processes recruited by complex linguistic structures and tool use, we expected the participants to perform better with the tool after training with object relatives rather than with subject relatives.

Both groups improved in processing relative sentences during training (Fig. 4, B and C). During pretest, the two groups improved similarly. In posttest, participants who trained with object relatives were able to enter significantly more pegs with the tool compared with those trained with subject relatives (significant *Time* × *Block* × *Training* interaction of the LMM $\chi^2_{(3)} = 9.88$, $P = 0.01$; Fig. 4D). Participants who trained with object relatives kept improving significantly with the tool (inserted pegs for block 4 pretest = 12.9 ± 0.6 versus block 3 posttest = 15.9 ± 0.6 and block 4 posttest = 15.7 ± 0.7, $P < 0.001$; no difference compared with block 1 posttest = 13.0 ± 0.7 and block 2 posttest = 14.3 ± 0.6, $P > 0.30$; Fig. 4D). By contrast, at no point after training with subject relatives did participants' motor performance differ from their best score before training (inserted pegs for block 4 pretest = 12.8 ± 0.8 versus block 1 posttest = 12.6 ± 0.77 or block 2 posttest = 13.8 ± 0.7 or block 3 posttest = 13.1 ± 0.9 or block 4 posttest = 14.0 ± 0.8, $P > 0.54$). We calculated the slope of the regression line modeling individual motor performance along the blocks before and after training separately (see the methods). The slope was used to indicate motor improvement. A positive slope indicates that motor performance with the tool improved along the blocks, whereas a negative or horizontal slope means no improvement. A two-way *Training* × *Time* rmANOVA revealed a significant interaction (Fig. 4E; $F_{(1,46)} = 4.57$; $P = 0.03$; $\eta_G^2 = 0.05$). The motor progression of the two groups was indistinguishable before training (subject-relative group $\beta = 1.18 \pm 0.20$ versus the object-relative group $\beta = 0.92 \pm 0.21$, $P = 0.91$). After training, the object-relative group further improved ($\beta = 0.95 \pm 0.21$), as demonstrated by

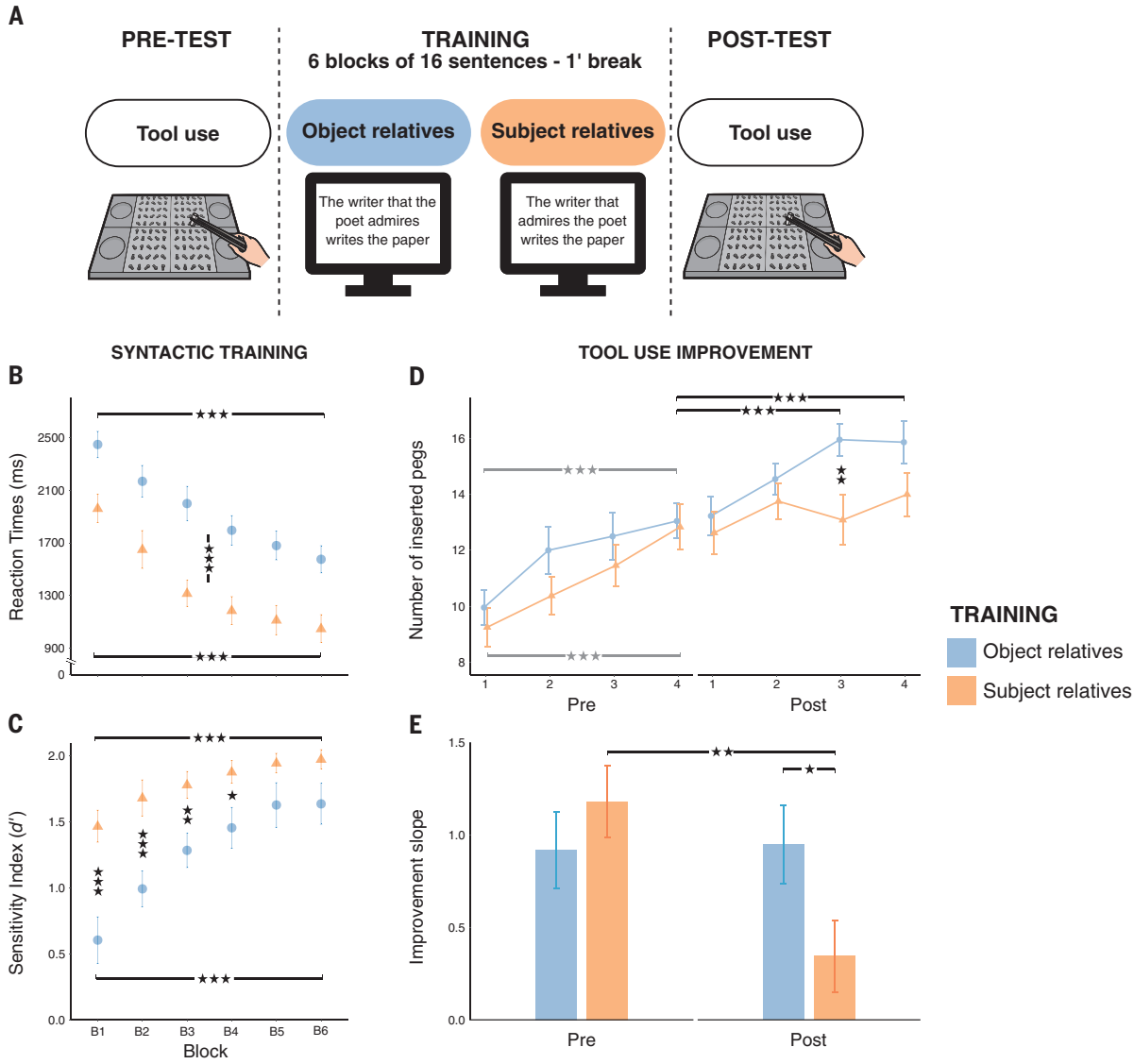


Fig. 4. Experiment 4: Cross-domain learning transfer from syntax in language to tool use. (**A**) Timeline of syntactic training and motor pretests and posttests with the tool. Different groups were tested in entering pegs as fast as possible with the tool before and after training either with object-relative clauses (blue) or subject-relative clauses (orange). (**B** and **C**) Linguistic progress in RTs (B) and *d'* (C) during syntactic training. (**D**) Motor performance assessed as the number of pegs inserted with the tool equally improved in pretest for the two groups. In posttest, only the group trained with object relatives (blue) kept improving, whereas the group trained with subject relatives (orange) did not (significant *Training* × *Time* × *Sentence* interaction of LMM: $\chi^2_{(3)} = 9.88$, $P = 0.01$). (**E**) Motor improvement quantified with the slope of the regression line along the progression from the first to the fourth block of tool use before (pretest) and after (posttest) training with syntactic structures in language. ***$P < 0.001$; **$P < 0.01$; *$P < 0.05$.

the significant difference between the observed slope and a horizontal line ($t_{(23)} = 4.47$, $P < 0.001$, Bonferroni corrected, Cohen's d = 0.91) and by the comparison with the subject-relative group ($\beta = 0.35 \pm 0.20$, $P = 0.03$). After training, this latter group stopped improving ($P = 0.005$ compared with before training and $t_{(23)} = 1.76$, $P = 0.18$ compared with a flat line). An additional Experiment 5 showed that the motor improvement observed after linguistic training with object relatives is specific to tool use. Indeed, after the object-relative training, the participants inserted more pegs with the tool than with the constrained hand (fig. S4 and supplementary text).

Discussion

Our findings provide major new insights into the neurocognitive links between tool use and syntax in language, as well as into the principles underpinning cross-domain transfer. First, tool use and syntax rely on brain activity of anatomically overlapping neural networks, particularly in striatal structures (lCau) and the GPi. This overlap excluded working memory processes or unspecific difficulty as underlying components. Second, tool use and syntax elicited similar activity patterns, consistent with common neural processes for both tasks.

These findings bolster the hypothesis of a supramodal syntactic function serving both action and language (*20*, *25*), which is consistent with the documented role of the dorsal striatum in processing complex hierarchical structures in both the motor (*24*) and linguistic (*33*) domains. The dorsal striatum supports a wide range of procedural learning processes across several species (*44*–*46*) and tasks (*24*, *47*). This part of the procedural system is involved

in syntactic training (*47*) and in the implementation of grammatical rules (*21*, *33*). Furthermore, it acts as a parser of actions to chunk motor sequences (*24*, *48*). Accurate and efficient tool use requires embedding an external object into the motor sequence and thus relies more on the striatum than on manual actions to parse the motor primitives (*4*). During dexterous tool use, hand movements integrate the functional structure of the tool to maintain an efficient interaction with the action target. The sensorimotor transformations imposed by the tool (*28*) constitute the additional level embedded in the manual motor program. Parsing and hierarchy handling also support syntactic comprehension of center-embedded object relatives (*21*, *33*, *34*). These functional similarities are reflected by the neural overlap that we revealed between tool use and syntax. However, the complexity of the hierarchies to be handled might not be strictly commensurate. It is worth noting that this overlap was found in the BG but not within the left IFG. In keeping with its documented involvement in both tool use (*35*) and language (*15*), the lIFG was recruited by both functions yet in two separately clustered regions. This occurred more posteriorly in the ventral premotor cortex for tool use and more anteriorly in Broca's area for syntactic comprehension, in accordance with the cytoarchitectonic and functional specialization of the lIFG for motor and linguistic processing, respectively (*49*, *50*).

These results explain the cross-domain learning transfer from tool use to syntactic skills in language and from linguistic syntax training to skilled tool use. Learning transfer arises provided that trained and untrained tasks rely on overlapping neural networks and shared cognitive processes (*41*). Transfer effects have been demonstrated from trained to untrained tasks belonging to the same domain: perception (*51*), motor (*52*), or cognitive control (*41*–*43*). Crucially, we extended to different cognitive domains the principle of transfer that had so far been limited to a single domain (*41*, *42*, *51*, *52*). Thus, the transfer holds true even when different cognitive domains such as action and language are involved. If trained and untrained tasks do not share common neurocognitive resources, then transfer might be tempered or absent. Indeed, training with subject-relative structures did not improve motor performance with the tool, and free-hand training failed to induce benefits to syntax in the comprehension of complex structures. Furthermore, the benefits induced by tool use over language were not based on the mere additional sensorimotor complexity of the action executed with the tool compared with the free hand. After training with a hand configuration that involved similar sensorimotor constraints imposed by the tool, the participants did not show any advantage in processing complex syntactic structures compared with the participants training with the free hand. The learning transfer between tool use and syntactic processes in language occurs bidirectionally. This finding unambiguously indicates that the two abilities rely on a common cognitive component, namely a supramodal syntax. It also suggests that the neural resources underlying the shared function can be similarly mobilized by either of the two abilities to improve the other.

What drives this cross-domain transfer? Preactivation of common resources and fast plasticity within shared circuitries can underlie the reciprocal boosting of behavioral performance in tool use and syntax processing in language. Training may act as a functional prime for the subsequent task: Training-dependent neuronal responses are elicited by tool use or sentence processing, thus yielding neuronal adaptation and more efficient activity (*53*). This in turn facilitates the subsequent behavioral performance for the untrained task relying on the same neural assemblies (*54*, *55*). Alternatively, cross-domain transfer may rely on fast plastic changes within common circuitries. Short motor training (i.e., <2 hours) triggers rapid functional (*44*) and local structural changes, which are accompanied by improvements in behavioral performance (*56*). The untrained task may benefit from such plastic changes and recruit new resources within the shared territories. These results raise the question of whether learning transfer can generalize to other linguistic tasks and if an optimal training duration could maximize the benefits. In the theoretical framework of the expansion-renormalization hypothesis (*57*), a thrilling opportunity would be to take advantage of the temporal dynamics of plastic changes, for instance, by testing syntax while new neural resources are locally and temporarily available during the course of tool-use training.

Overall, our findings reignite the hypothesis of a coevolution of tool use and language (*58*–*60*). Longstanding theories have claimed a motor origin of language during evolution (*25*, *61*). The advent and refinement of tool use may have offered the neural niche for the coevolution of new cognitive skills serving both motor and communicative aims (*5*, *58*, *62*, *63*). According to this hypothesis, the role of tool use has been twofold. On the one hand, the sophistication of tool use and tool making has put forward the need for cognitive functions to efficiently chunk, temporally parse, and deal with hierarchies of sequences (*60*). On the other hand, tool use and tool making posed evolutionary pressure for communication, allowing better social transmission of knowledge (*63*). Functions responding to demands of the motor system would therefore have met communicative needs and progressively been exapted and recycled for language (*62*, *64*). Such a coevolution scenario has involved a large brain network, from parietal (*58*, *60*) to frontal regions (*60*, *65*) and including the BG (*66*). Here, we provide central human evidence pointing to the BG in particular as the neural niche for a supramodal syntactic function serving both action and language. Our findings show that the motor system can be exploited to promote other cognitive functions that partly share the same neurocognitive foundations.

Materials and Methods

Participants

A total of 244 participants were included in the study, which consisted of five different experiments. None of the participants took part in more than one experiment. All participants were healthy, right-handed, French native speakers with normal or corrected-to-normal vision and no known motor, linguistic, or neurological disorders. They gave their written informed consent before experiment acquisition. All procedures agreed with the Helsinki declaration and were approved by an ethical committee (46/17_2, OUEST IV).

Experiment 1

The fMRI acquisition in Experiment 1 included 24 participants who received a compensation of 110 euros. Four participants were excluded: two did not fulfill the pre-set familiarization performance requirements before any neuroimaging acquisition, one dropped out after the inclusion phase, and one was removed from analyses because of substantial head movements (several runs with movements >1.5 mm). Data from 20 participants with the following sociodemographic characteristics and manual preference were analyzed: 10 males and 10 females; mean age ± SD: 24 ± 4 years; mean score on the Edinburgh handedness inventory (*67*): 0.93 ± 0.09; higher education level (the number of years of education after a high school degree): 3 ± 2 years.

Experiment 2

In this experiment, 85 participants were recruited and paid 10 euros for their participation. Six participants performed the experiment but were excluded from analysis because of performance below chance level in at least one sentence condition and one was excluded for having incorrectly used the right hand to deliver the button press. Data from 78 participants with the following characteristics were analyzed: 27 males and 51 females; mean age: 23 ± 3 years; mean Edinburgh score: 0.9 ± 0.12; higher education level: 4 ± 1 years.

Experiment 3

In this experiment, 46 participants were recruited and paid 15 euros for their participation. The threshold of $d' > 1.38$ in pretest, as

identified in Experiment 2, was applied as an independent criterion for inclusion. Data from two participants were excluded because of an error in the sensitivity index calculation at pretest; four others were excluded for sensitivity index below the threshold and one other for having inverted the response keys during the task. Data from 39 participants with the following characteristics were analyzed: 11 males and 28 females; mean age: 24 ± 5 years old; mean Edinburgh score: 0.87 ± 0.11; higher education level: 3 ± 1 years.

Experiment 4

In this experiment, 48 participants were recruited and paid 40 euros for their participation. The group had the following characteristics: 24 males and 24 females; mean age: 27 ± 5 years old; mean Edinburgh score: 0.88 ± 0.1; higher education level: 5 ± 2 years.

Experiment 5

In this experiment, 41 participants were recruited and paid 45 euros for their participation. Data from one participant were excluded because of a technical problem. Overall, data from 40 participants were analyzed. The group had the following characteristics: 13 males and 27 females; mean age: 27 ± 6 years old; mean Edinburgh score: 0.92 ± 0.1; higher education level: 4 ± 2 years.

Tasks

Syntactic task

A two-alternative forced choice task (2-AFC) allowed us to assess syntactic abilities to process sentences composed of the same content words but featuring different structures: coordinated clauses, center-embedded subject-relative clauses, or center-embedded object-relative clauses. Table 1A offers examples for each condition, and the entire material is available in table S3. The content words included in the sentences were controlled for word frequency and number of syllables from the Lexique 3.80 database (*68*), as well as for the gender of the subjects and objects of the described action. Each sentence was presented using rapid serial visual presentation (RSVP) in six consecutive segments displayed in the middle of the screen for 500 ms, interspaced by a 100-ms blank screen. This presentation mode was chosen on the basis of previous work using comprehension tasks of visually presented sentences (*14*, *15*) to avoid idiosyncratic reading strategies and/or saccadic eye movements. After presentation of the final segment of each sentence, a test affirmation was displayed on the screen (Table 1B) until the participant answered or for a maximum of 5 s. The participants were instructed to respond as quickly and correctly as possible through a button press with their left hand as to whether the affirmation was true or false with respect to the preceding sentence. The button-response association was counterbalanced across the participants.

In the fMRI Experiment 1, a total of 48 trials were presented in a randomized order during the run and consisted of the presentation of sentences featuring the three different syntactic structures in equal proportion (n = 16 each): coordinated clauses, subject-relative clauses, and object-relative clauses. The intertrial period was jittered between 5 and 7 s. The sentences were visible through the mirror oriented toward the screen placed on the back of the scanner bore.

For behavioral Experiments 2 and 3, outside of the scanner, the total number of trials in each experiment was 72, with 24 trials per each syntactic structure. The intertrial period was jittered between 2.5 and 3.5 s, and a 1-min rest period was added halfway through the block. The scripts controlling the presentation and recording participants' answers were programmed in *Psychtoolbox-3* (PTB-3) running on MATLAB (The MathWorks, Natick, MA, USA).

Verbal working memory task

In Experiment 1, to disentangle the potential contribution of working memory processes to syntactic brain activity, the participants also performed an n-back task with four words of equal length and frequency (Lexique 3.80). Two 1-back and two 3-back runs were acquired. Words were presented with a RSVP in the center of the screen for 1500 ms. The intertrial period varied between 1 and 4 s at 1-s steps, consistent with effective published protocols (*69*). The participants were required to press a button with their left index finger if a target word appearing on the screen matched the preceding word (1-back) or the one presented two steps earlier (3-back). Each run included 76 trials with 19 targets. The word stream was made visible using the same apparatus as for the syntactic task. Similar to this latter task, the verbal working memory task scripts were programmed onto PTB-3 running on MATLAB.

fMRI tool-use task

The participants were required to use a pair of 30-cm-long pliers held with their right hand to move a peg (Fig. 1D) on a plastic board (Quercetti, Torino, Italy) between two fixed visual landmarks separated by an approximate 9-cm distance (see movies S1 and S2). To begin a trial, the participants, in a resting position, had to wait for a pure tone signal delivered through an MRI-compatible device aimed to actively reduce MRI noise (Optoacoustics OptoACTIVE two-way noise cancellation communication system, Mazor, Israel). A single presentation of the pure tone warned the participant to prepare to move, and the double presentation of this tone presented 4 s later indicated the "Go" for the action. This sequence was repeated twice to pace the requested movements: grasping the peg to displace it from the first to the second location and then grasping it again to move it back to its initial position. The whole sequence (4-s planning, 4-s execution, 4-s planning, 4-s execution, and 10-s rest) was repeated 15 times in a single run. If a peg fell, then the participant had to indicate the missed sequence by pressing a button with the left index finger and then grab a new peg from the left side of the plastic board. The few missed trials (<0.5%) were modeled separately. In a distinct run, the same task was performed with the free hand and served as a control to highlight the tool-specific neural network. The motor task device was placed in front of the participant at a reachable distance and made visible with a double mirror mounted onto the head coil. The participants' right upper arm was strapped to the trunk to limit elbow and shoulder movements. The scripts controlling the audio sequence of instructions in the scanner were delivered with Presentation software (NBS, Berkeley, CA, USA).

Motor training

Tool-use training was similar to the tool-use task design for fMRI acquisitions. As previously described, the participants were required to insert pegs on a board using the same 30-cm-long pliers with their right hand. Training was performed with grooved, key-shaped pegs (Grooved Pegboard Test, Lafayette Instruments, model 32025[2]), which need to be meticulously oriented to fit the target hole. In total, four boards were placed in front of the participant with a plastic box containing the pegs located in front of the boards. The training consisted of inserting as many pegs as possible during nine blocks of 2 min interspersed with 1-min rest. The motor performance was indexed by the total number of correctly inserted pegs. A between-subjects design across Experiments 2 and 3 tested the hypothesis that syntactic skills improved in the group of participants training with the tool compared with three control groups of participants. One control condition consisted of the same motor training but performed with the right bare hand (i.e., free-hand training) to control for unspecific effects of motor training over the untrained task (Experiments 2 and 3). The second control condition was a passive control for potential test-retest effects in the absence of any motor task. The participants assigned to this condition were required to watch soundless nature documentary videos (Experiment 2) following the same procedure as for both tool-use and free-hand motor training, namely nine blocks of 2-min videos interspersed with 1-min rest (with a gray screen).

In Experiment 3, we replicated the acquisition with tool-use and free-hand training in

new samples of participants and added a third training condition to control for the sensorimotor difficulty of tool-use training. From a sensorimotor point of view, training with the tool was more difficult than free-hand training. Indeed, the tool reduces sensory feedback while handling the pegs. In addition, the motor constraints introduced by the tool hinder the potential easing contribution of the fingers available in the free-hand condition. Proof of the difficulty is the reduced number of pegs inserted by the participants training with the tool compared with the free hand in Experiment 2. To rule out the sensorimotor difficulty of the task as a factor contributing to learning transfer, we introduced additional sensorimotor constraints in the free-hand motor training to mimic those imposed by the tool. To this end, we instructed participants to grab and enter pegs using a pinch formed by their middle and index fingers. Beside the fingers used to perform the grip, two further changes were applied to reduce the degrees of freedom of manual movements toward those characterizing tool use. The degrees of freedom of the hand are estimated to exceed 20 [~27 (*70*)]: 4 df for each finger except for the thumb (3 df for flexion/extension and 1 df for abduction/adduction); 5 df for the thumb; and 6 df for translation and rotation of the wrist. The degrees of freedom of tool use on the other hand approximate 7: 1 df for abduction/adduction of pliers and 6 df for wrist translation and rotation. Participants were asked to cross their index and middle fingers (index underneath), which were strapped together at the level of the proximal phalanx with dermo-compatible tape and Velcro. This prevented independent flexion or extension of the fingers (~−3 df). This constraint resulted in a pliers-like configuration with the middle finger's inner side over the index fingernail, and participants were explicitly required to use these two fingers without the contribution of the thumb, the ring finger, and the little finger (~13 fewer df). Second, we hindered somatosensory feedback of participants' index and middle fingers with a layer of flat Velcro between two layers of dermo-compatible tape attached on each fingertip (Fig. 3A, red inset). This constrained hand condition ensured lack of direct sensory feedback, as experienced with the tool, as well as the inability to adjust peg orientation by simply slipping it between the middle and index fingers (therefore reducing the impact of the 6 df of flexion/extension). Accordingly, the participants had to rely more on wrist rotations to insert the pegs and had hindered sensory feedback, similar to the experience during tool use.

Motor test

The motor training was adjusted into a motor test to enable the measurement of a change in tool-use motor performance after syntactic training in Experiment 4. Participants were asked to use the tool with their right hand to enter as many pegs as possible during four blocks of 2 min interspersed with 1-min rest. This test was performed before and after linguistic training. The motor performance was indexed by the number of correctly inserted pegs per block. In Experiment 5, a similar adjustment allowed us to measure the motor performance with the constrained hand before and after linguistic training and compare it with changes in tool use performance. For the constrained-hand condition, the participants' right hand featured the same constraints as described above for the constrained-hand training. To avoid any difference in the motor baseline between the tool-use and constrained-hand groups and therefore ensure the reliability of the comparison, participants could start to train with object relatives only after they reached a threshold of eight pegs inserted in a block of 2 min. Such a threshold was based on the data of Experiment 3 showing similar performance for the tool-use and the constrained-hand tasks around the fourth block of the motor training (on average, 10.8 pegs with an SD of 2.4 pegs). The 2-min block was repeated up to a limit of six blocks to reach the eight-peg criterion. All participants reached this threshold before the sixth block (i.e., 1.6 blocks on average and 4 blocks maximum for the slowest participants). Once we ensured a comparable level of pretest performance, after the linguistic training, the participants performed four blocks of 2 min with 1-min rest (posttest).

Syntactic training

To evaluate the effect of linguistic training on tool use in Experiment 4, the syntactic task used in Experiments 1 to 3 was adapted into a training protocol. Training was composed of 96 trials, split in six blocks of 16 sentences each. Blocks were interspersed with 1-min rest periods. Participants were allowed a maximum of 5 s to respond to the test affirmation presented after each sentence by pressing one of two buttons with their left hand. Once they answered, a coherent feedback appeared for 1.5 s: a green checkmark for correct answers and a red "X" for incorrect answers. At the end of each block, the accuracy and average RT were displayed so that participants were made aware of their progress in performance (as in the motor training in Experiments 2 and 3). Using a single-blind procedure, participants were assigned to one of two groups, one that was trained with subject-relative clauses and the other with object-relative clauses. Participants were reminded to try to improve their accuracy and RT performance at each block. Task scripts were programmed onto PTB-3 running on MATLAB. In Experiment 5, all participants underwent the same training with only object-relative clauses following the same procedure as for Experiment 4.

Procedures

Experiment 1: fMRI

The experiment consisted of an inclusion session to familiarize participants with the tasks and ensure that the individual level of performance met the inclusion criteria. Short versions of the syntactic, verbal working memory, and motor tasks were conducted. The requirements to be included in the fMRI session were at least 16 successes in the syntactic task (over 24 trials), with four successes for the most complex condition (object-relative clauses over eight trials). For the 3-back task, the participants were required to correctly identify at least three targets out of eight among a total of 32 trials, without performing more than six false alarms. For the 1-back task, one block of 16 trials was performed, with the same requirements. This was meant to maximize the number of correct and analyzable trials in each task during the neuroimaging acquisition. The motor task for inclusion comprised two blocks of tool-use movements and two blocks of free-hand movements. In each block, the participants were instructed to insert 10 pegs as quickly as possible on the two first lines of the grooved pegboard test. To be included in the experiment, they had to perform the two tool-use blocks in <5 min on average and the two free-hand blocks with an average of <1 min. After inclusion, the participants performed two different fMRI sessions separated by 2 days. Each session consisted of an anatomical acquisition (T1-weighted), followed by motor (tool use and free hand) and linguistic runs in a counterbalanced order. The participants were tested in the working memory and syntactic tasks during the same session. Two additional linguistic tasks assessing phonological and semantic processing were performed in the other session; these results will be presented in a separate report. The session order was counterbalanced across participants.

Functional and anatomical MRIs were acquired with a Siemens Prisma 3T scanner (Siemens Medical Systems, Erlangen, Germany) with a gradient echo EPI sequence, with TE = 30 ms and TR = 2400 ms. Volumes were acquired with 44 interleaved slices of 3-mm thickness (3 × 3 × 3.3 mm voxel size) aligned to the AC-PC plane. Overall, 171 volumes were acquired for each motor block, 305 for the syntactic task and 140 for the working memory task. T1-weighted images were acquired with a 1-mm isotropic voxel and a generalized autocalibrating partial parallel acquisition (GRAPPA) acceleration factor of 2 (TE = 3.8 ms, TR = 3000 ms).

Experiments 2 to 5: Behavioral acquisition

In Experiment 2, after a short familiarization with five trials, participants performed the syntactic test before and after their respective training. A first group (n = 26) trained with the tool. As controls, two additional groups either trained with the free hand (n = 26) or simply watched videos (n = 26). The linguistic material selected in the pretest was always different from that presented in the posttest.

In Experiment 3, three groups of 13 participants were included, and each underwent one of three different motor training: tool-use, free-hand, or constrained-hand training.

In Experiment 4, 48 participants were included and equally divided into two different groups (n = 24 each) with a single-blind procedure by experimenter A. Each group underwent one of two different syntactic training, with object-relative clauses or with subject-relative clauses. Regardless of the group, before and after the syntactic training, participants performed the motor test with the tool. To avoid potential observational bias, experimenter B supervised the motor test acquisition, whereas experimenter A gave instructions for the syntactic training. Experimenter B was blinded with respect to which syntactic training condition each participant had been assigned to.

In Experiment 5, 40 participants were included and divided into two different groups (n = 20 each) tested on their ability to insert pegs with the tool or with the constrained hand before and after a syntactic training with object relatives.

Analyses

Experiment 1: fMRI analyses

Preprocessing. fMRI data were analyzed with statistical parametric mapping (SPM12; Wellcome Trust Centre for Neuroimaging). Functional data were preprocessed using a standard procedure consisting of spatial realignment, slice timing, and coregistration of anatomical to mean functional images. Data were then spatially normalized into the MNI (Montreal Neurological Institute) stereotactic space with a resampling to 3 × 3 × 3 mm. As a last step, data were spatially smoothed using a three-dimensional (3D) Gaussian kernel with a full-width at half-maximum of 8 mm and temporally high-pass filtered with a cutoff at 1/128 Hz.

Univariate analyses. At the first level, each participant's hemodynamic responses were modeled with a boxcar function. Each motor block was designed with planning, execution, rest, and, as regressors of no interest, missed trials and head movements. Both directions of the movements (back and forth) were taken into consideration. For the syntactic task, we modeled the coordinated, subject-relative, and object-relative clauses during sentence presentation (i.e., syntactic encoding) and test affirmation separately. This last part contains participants' RTs, incorrect responses, and head movements, which were entered as regressors of no interest in the model. For the working memory task, hits, false alarms, correct rejections, miss trials, and head movements were considered. At the second level, we conducted within-subjects ANOVAs to identify the general network underlying each assessed function. We computed the interaction contrast highlighting the specific tool-use planning neural network with respect to free-hand planning and the overall execution network as follows:

$$\text{tool-use planning network} = [(\text{tool-use}_{\text{planning}} - \text{free-hand}_{\text{planning}}) - (\text{tool-use}_{\text{execution}} - \text{free-hand}_{\text{execution}})].$$

To assess the specific syntactic neural network, we contrasted the activity in the encoding phase for object relative clauses with that in the encoding phase for both coordinated and subject relative clauses, for correct trials only, as follows:

$$\text{syntax network} = [2\ \text{object-relative clauses} - (\text{coordinated clauses} + \text{subject-relative clauses})].$$

For working memory, we computed the difference between hits in the 3-back and 1-back tasks as follows:

$$\text{working memory network} = \text{hits}_{\text{3-back}} - \text{hits}_{\text{1-back}}.$$

These contrasts were then entered into conjunction analyses [minimum statistic compared with conjunction-null hypothesis (*71*)], allowing us to assess the anatomical overlap between the different processes: tool-use planning network ∩ syntax network and, as a control, tool-use planning network ∩ working memory network.

As further control for the specificity of the shared functional activation between tool-use planning and syntax, we computed the hand planning network as follows:

$$\text{free-hand planning network} = [(\text{free-hand}_{\text{planning}} - \text{tool-use}_{\text{planning}}) - (\text{free-hand}_{\text{execution}} - \text{tool-use}_{\text{execution}})],$$

and the conjunction free-hand planning network ∩ syntax network was assessed.

To investigate the network activated during action execution, we computed both of the following:

$$\text{tool-use execution network} = [(\text{tool-use}_{\text{execution}} - \text{free-hand}_{\text{execution}}) - (\text{tool-use}_{\text{planning}} - \text{free-hand}_{\text{planning}})]$$

and

$$\text{free-hand execution network} = [(\text{free-hand}_{\text{execution}} - \text{tool-use}_{\text{execution}}) - (\text{free-hand}_{\text{planning}} - \text{tool-use}_{\text{planning}})]$$

and then further studied the conjunctions tool-use execution network ∩ syntax network and free-hand execution network ∩ syntax network.

To guarantee the reliability of the results, for each analysis, we reported each cluster at the whole-brain level containing >10 contiguous voxels (> 270 mm^3) with a P value below the 0.001 threshold uncorrected for multiple comparisons. Furthermore, each motor contrast was submitted to an exclusive mask defined at 0.05 uncorrected for multiple comparisons aiming to rule out the contribution of the interaction second component (i.e., for tool-use planning network, the contribution hand execution > tool execution was masked). This mask was also used for the conjunction analyses. Clusters passing the FWE correction for multiple comparisons at the cluster level were highlighted.

Multivariate analyses. We then assessed our prediction of shared cognitive processes within the overlapping territories between tool-use planning and syntax. We tested whether the brain activity level during tool-use planning, compared with free-hand planning, presented stronger pattern similarity with brain activity levels associated with object-relative clauses.

For the first series of analyses, we used the CoSMoMVPA toolbox (*72*) to extract, for each participant, the nonsmoothed parameter estimates (beta) from each voxel of the overlapping clusters for both tool-use and free-hand planning. We did the same for object- and subject-relative clauses. This produced for each participant four vectors of parameter estimates (i.e., one per condition) composed of all significant voxels (n = 41) evidenced by the conjunction analysis. We then performed a representational similarity analysis. For each participant, the four individual vectors were entered in a 4 × 4 similarity matrix in which each node represented the correlation (Pearson's r) between the activity patterns of two conditions. Higher correlation scores indicated better similarity. The obtained matrix was symmetrical with respect to the diagonal, containing six nodes of interest corresponding to all pairwise comparisons between nonidentical conditions. The similarity matrix obtained for each individual was then compared with hypothesis-driven models aiming to predict the data. A correlation between the observed similarity matrix and the model was computed as a measure of fit of the model: The higher the correlation coefficient, the better the fit of the model. Each individual correlation score

was Fisher's *z*-transformed before any statistical analysis and tested with a unilateral-sample *t* test against zero with a Bonferroni correction applied to correct *P* values for multiple comparisons.

We tested two models, both of which included within-domain similarity between the two motor conditions and between the two most complex syntactic conditions. Crucially, the two models differed regarding the tested cross-domain similarity. The first model, represented by matrix 1 (Table 2), tested the cross-domain similarity between tool-use planning and object-relative clauses, whereas the second control model, represented by matrix 2 (Table 3), tested the cross-domain similarity between free-hand planning and object-relative clauses.

To assess the specificity of the similarity between syntax and tool-use patterns, the same analysis was also run on working memory patterns as a control. In other words, we tested for possible cross-domain similarities between 3-back and tool-use patterns. To do so, we entered in the matrices of the models described above activity patterns elicited during 1-back and 3-back tasks instead of object- and subject-relative patterns, respectively.

We further tested whether the similarity between patterns could be exploited to accurately predict the activity elicited by complex syntactic structures from that elicited by tool use. A classification-based MVPA using a leave-one-subject-out procedure was run with the CoSMoMVPA toolbox. Data from the 41 significant voxels in the BG identified in the conjunction analysis were used as features for the classification. More specifically, an SVM classifier was trained on the nonsmoothed t-maps derived from motor activations (tool-use planning versus baseline and free-hand planning versus baseline) and then tested cross-domain on the activation elicited by object relatives against baseline. We normalized each feature using the toolbox built-in function. At each iteration, the classifier trained on motor data from all subjects but one, iteratively left out. The classifier was then tested cross-domain on the object-relative data of all subjects (n = 20 tests per iteration). This resulted in an average accuracy score for each iteration. The overall average score across all iterations was tested for significance after performing 10,000 permutations of neural patterns across subjects to estimate a null distribution. The *P* values were calculated to test whether the observed difference was significantly and positively different from chance level (accuracy = 0.5). The same procedure was subsequently used with the 3-back task to control for syntactic specificity, namely the SVM classifier was trained on the motor data and tested on the 3-back data.

Table 2. Matrix of similarity 1.

	Tp	Fp	SRC	ORC
Tp	1	1	0	1
Fp	1	1	0	0
SRC	0	0	1	1
ORC	1	0	1	1

Tp and Fp, tool-use planning and free-hand planning, respectively. Additionally, each node was defined by 1 or 0, with 1 representing the similarity between a pair of vectors and 0 representing a dissimilarity.

Table 3. Matrix of similarity 2.

	Tp	Fp	SRC	ORC
Tp	1	1	0	0
Fp	1	1	0	1
SRC	0	0	1	1
ORC	0	1	1	1

Abbreviations are as in Table 2.

Cluster-based voxelwise correlations. We studied in more detail the similarity between patterns of activity underlying tool-use planning and object-relative clauses in each cluster by computing voxelwise correlations (*40*). As a control, we calculated the same voxelwise correlations also between patterns of activity underlying free-hand planning and object-relative clauses in each cluster separately. To this aim, averaged contrast estimates (betas) were computed from the nonsmoothed images for each voxel for both tool-use planning and object relatives. This produced two vectors of betas per cluster, one for tool-use planning and one for object relatives. The correlation between the two vectors of the same cluster was assessed as a measure of the similarity of the spatial distribution of brain activity: A higher correlation coefficient indicates strong similarity. We repeated the same procedure to calculate the correlation between patterns of activity corresponding to free-hand planning and object relatives. This procedure resulted in two Pearson's correlation scores, one for the relationship between tool-use planning and object-relative clauses and a second for the relationship between free-hand planning and object-relative clauses. For comparison, the second score was subtracted from the first one, giving an observed difference in correlations. Statistical inference was allowed by comparing the observed difference to an empirical null distribution of differences obtained after 10,000 permutations across the features of the two motor conditions. The *P* values were calculated to test whether the observed difference was significantly positive.

Experiments 1 to 5: Behavioral data preprocessing

For the syntactic and verbal working memory tasks, RTs (i.e., the time interval from the display of the test affirmation or target word, respectively, to participant's response) and sensitivity index (d') were measured to index performance. In the working memory task, to complement our analyses, we also studied the proportion of hits and false alarms. Trials with RTs deviating from the mean ± 2.5 SDs were removed from analysis. This represented in total 1.4% of the trials across all experiments. Statistics on these data were run in R-studio with built-in statistical functions and the *afex* package (*73*). The statistical models performed for each experiment are presented below. For all analyses, Tukey's post hoc comparisons were performed to further explore significant interactions. All results are reported as the mean ± SEM.

Experiment 1: Behavior statistics

For the syntactic task, we performed rmANOVA on d' and LMMs on RTs. The one-way ANOVA was performed with the within-subjects factor *Sentence* (coordinated clauses versus subject-relative clauses versus object-relative clauses). The LMM performed on RTs included the same within-subject factor, with *Subjects* and *Sentence* as random factors.

To account for differences in performance between the 1-back and 3-back working memory tasks, paired-sample *t* tests were performed on d', the proportion of hits and proportion of false alarms. RTs were assessed through LMM analysis with *Difficulty* (1-back versus 3-back) as within-subject factor, *Subjects* and *Difficulty* were added as random factors.

Experiments 2 and 3: Statistics

To assess the progress in performance during motor training in each behavioral experiment, rmANOVAs on the number of inserted pegs were conducted with *Block* (nine blocks) as the within-subjects factor and *Training* (tool use versus free hand in Experiment 2 and tool use versus free hand versus constrained hand in Experiment 3) as the between-subjects factor. To identify performance differences between training conditions, the total number of pegs inserted across the nine blocks was assessed, in Experiment 2 by a two-sample *t* test (*Training*: tool use versus free hand) and in Experiment 3 with a one-way rmANOVA (*Training*: tool use versus free hand versus constrained hand).

We accounted for possible effects of participants' initial syntactic skills on the improvement in the posttest. This was done by conducting an ANCOVA on the RTs, entering the initial syntactic performance measured by the d' as a covariate, *Sentence* and *Time* as within-subject factors, and *Training* as

a between-subjects factor. Next, syntactic performance was analyzed through a LMM on RTs with *Training* (tool use versus free hand versus video in Experiment 2 and tool use versus free hand versus constrained hand in Experiment 3) as the between-subjects factor and *Sentence* (coordinated clauses versus subject-relative clauses versus object-relative clauses) and *Time* (pretest versus posttest) as within-subjects factors. *Subjects*, *Sentence*, and *Time* were added to account for random effects. rmANOVA was run on *d′*, with *Training* (tool use versus free hand versus video in Experiment 2 and tool use versus free hand versus constrained hand in Experiment 3) as the between-subjects factor and *Sentence* (coordinated clauses versus subject-relative clauses versus object-relative clauses) and *Time* (pretest versus posttest) as within-subjects factors.

To quantify the robustness of the syntactic benefits after tool-use training across Experiments 2 and 3, we finally computed the effect size of the pretest-to-posttest improvement in the syntactic task (*41*, *43*). This was done by calculating the difference between pretest and posttest performance divided by the pooled SD in the pretest (for the entire sample of participants). The effect size in the object relative clauses condition was then analyzed in an rmANOVA with *Training* (tool use versus free hand) and *Experiment* (Experiment 2 versus Experiment 3) as between-subjects factors.

Experiments 4 and 5: Statistics

In Experiment 4, to assess the progress in performance during syntactic training, an rmANOVA on *d′* and an LMM on RTs were conducted. The rmANOVA was performed with *Block* (six blocks) as the within-subjects factor and *Training* (object-relative clauses versus subject-relative clauses) as the between-subjects factor. The LMM performed on RTs included the same within-subject factor, with *Subjects* and *Block* as random factors.

Next, motor performance with the tool was analyzed through an LMM on the total number of inserted pegs with *Training* (object-relative clauses versus subject-relative clauses) as the between-subjects factor and *Time* (pretest versus posttest) and *Block* (four blocks) as within-subjects factors. *Subjects*, *Time*, and *Block* were added to account for random effects.

Finally, to corroborate our results, motor performance was analyzed using an rmANOVA on the individual improvement slope (β) with *Training* (object-relative clauses versus subject-relative clauses) as the between-subjects factor and *Time* (pretest versus posttest) as the within-subjects factor. Improvement slope was obtained by performing a linear regression over the number of inserted pegs for each participant before and after syntactic training separately. Slopes were also compared against zero with one-sample *t* tests for object relatives and subject relatives separately. No difference against zero predicted no improvement (i.e., flat slope), whereas a significant difference predicted a change in performance, as indexed by a positive (i.e., increased performance) or negative (i.e., decreased performance) slope. Bonferroni correction was applied to correct *P* values for multiple comparisons.

In Experiment 5, similar models to Experiment 4 were applied. To assess the progress in performance during syntactic training, we conducted an rmANOVA on *d′* and an LMM on RTs. The rmANOVA was performed with *Block* (six blocks) as the within-subjects factor and *Motor Test* (tool versus constrained hand) as the between-subjects factor. The LMM performed on RTs included the same within-subject factor, with *Subjects* and *Block* as random factors. To evaluate motor performance, an rmANOVA was performed on the number of pegs inserted in pretest and posttest. For pretest, we considered the number of pegs inserted in the last block, namely when the participants reached the required motor threshold (eight pegs). Conversely, for posttest, we calculated the mean across the four blocks performed. The rmANOVA was performed with *Time* (pretest versus posttest) as the within-subjects factor and *Motor Test* (tool versus constrained hand) as the between-subjects factor. An rmANOVA was also conducted by considering only the posttest performance across the four blocks performed. The rmANOVA included *Block* (four blocks) as the within-subjects factor and *Motor Test* (tool versus constrained hand) as the between-subjects factor. To corroborate the effects found in the Experiment 4, paired-sample *t* tests were performed between the last pretest block (i.e., when the threshold was reached) and each of the posttest blocks separately for the tool-use and constrained-hand conditions. Two-sample *t* tests were additionally conducted to compare the number of pegs inserted between the two motor conditions for each posttest block. Bonferroni correction was applied to account for multiple comparisons. As in Experiment 4, we analyzed the improvement slope (β). This was obtained by performing a linear regression over the number of inserted pegs for each participant after syntactic training. Slopes were also compared against zero with one-sample *t* tests for tool use and constrained hand separately. Bonferroni's correction was applied to correct *P* values for multiple comparisons.

REFERENCES AND NOTES

1. L. E. Miller *et al*., Sensing with tools extends somatosensory processing beyond the body. *Nature* **561**, 239–242 (2018). doi: 10.1038/s41586-018-0460-0; pmid: 30209365
2. S. H. Johnson-Frey, The neural bases of complex tool use in humans. *Trends Cogn. Sci.* **8**, 71–78 (2004). doi: 10.1016/j.tics.2003.12.002; pmid: 15588811
3. P. M. Greenfield, Language, tools and brain: The ontogeny and phylogeny of hierarchically organized sequential behavior. *Behav. Brain Sci.* **14**, 531–551 (1991). doi: 10.1017/S0140525X00071235
4. K. Pastra, Y. Aloimonos, The minimalist grammar of action. *Philos. Trans. R. Soc. Lond. B Biol. Sci.* **367**, 103–117 (2012). doi: 10.1098/rstb.2011.0123; pmid: 22106430
5. J. Steele, P. F. Ferrari, L. Fogassi, From action to language: Comparative perspectives on primate tool use, gesture and the evolution of human language. *Philos. Trans. R. Soc. Lond. B Biol. Sci.* **367**, 4–9 (2012). doi: 10.1098/rstb.2011.0295; pmid: 22106422
6. M. Ben-Shachar, T. Hendler, I. Kahn, D. Ben-Bashat, Y. Grodzinsky, The neural reality of syntactic transformations: Evidence from functional magnetic resonance imaging. *Psychol. Sci.* **14**, 433–440 (2003). doi: 10.1111/1467-9280.01459; pmid: 12930473
7. L. W. Barsalou, Grounded cognition. *Annu. Rev. Psychol.* **59**, 617–645 (2008). doi: 10.1146/annurev.psych.59.103006.093639; pmid: 17705682
8. F. Pulvermüller, L. Fadiga, Active perception: Sensorimotor circuits as a cortical basis for language. *Nat. Rev. Neurosci.* **11**, 351–360 (2010). doi: 10.1038/nrn2811; pmid: 20383203
9. L. Craighero, L. Fadiga, G. Rizzolatti, C. Umiltà, Action for perception: A motor-visual attentional effect. *J. Exp. Psychol. Hum. Percept. Perform.* **25**, 1673–1692 (1999). doi: 10.1037/0096-1523.25.6.1673; pmid: 10641315
10. C. Brozzoli *et al*., Touch perception reveals the dominance of spatial over digital representation of numbers. *Proc. Natl. Acad. Sci. U.S.A.* **105**, 5644–5648 (2008). doi: 10.1073/pnas.0708414105; pmid: 18385382
11. M. H. Fischer, A. D. Castel, M. D. Dodd, J. Pratt, Perceiving numbers causes spatial shifts of attention. *Nat. Neurosci.* **6**, 555–556 (2003). doi: 10.1038/nn1066; pmid: 12754517
12. O. Hauk, I. Johnsrude, F. Pulvermüller, Somatotopic representation of action words in human motor and premotor cortex. *Neuron* **41**, 301–307 (2004). doi: 10.1016/S0896-6273(03)00838-9; pmid: 14741110
13. S. M. Wilson, A. P. Saygin, M. I. Sereno, M. Iacoboni, Listening to speech activates motor areas involved in speech production. *Nat. Neurosci.* **7**, 701–702 (2004). doi: 10.1038/nn1263; pmid: 15184903
14. M. A. Just, P. A. Carpenter, T. A. Keller, W. F. Eddy, K. R. Thulborn, Brain activation modulated by sentence comprehension. *Science* **274**, 114–116 (1996). doi: 10.1126/science.274.5284.114; pmid: 8810246
15. M. Makuuchi, J. Bahlmann, A. Anwander, A. D. Friederici, Segregating the core computational faculty of human language from working memory. *Proc. Natl. Acad. Sci. U.S.A.* **106**, 8362–8367 (2009). doi: 10.1073/pnas.0810928106; pmid: 19416819
16. A. Santi, Y. Grodzinsky, Working memory and syntax interact in Broca's area. *Neuroimage* **37**, 8–17 (2007). doi: 10.1016/j.neuroimage.2007.04.047; pmid: 17560794
17. P. Fazio *et al*., Encoding of human action in Broca's area. *Brain* **132**, 1980–1988 (2009). doi: 10.1093/brain/awp118; pmid: 19443630
18. A. C. Roy *et al*., Syntax at hand: Common syntactic structures for actions and language. *PLOS ONE* **8**, e72677 (2013). doi: 10.1371/journal.pone.0072677; pmid: 23991140
19. F. Vargha-Khadem, K. Watkins, K. Alcock, P. Fletcher, R. Passingham, Praxic and nonverbal cognitive deficits in a large family with a genetically transmitted speech and language disorder. *Proc. Natl. Acad. Sci. U.S.A.* **92**, 930–933 (1995). doi: 10.1073/pnas.92.3.930; pmid: 7846081
20. F. Pulvermüller, The syntax of action. *Trends Cogn. Sci.* **18**, 219–220 (2014). doi: 10.1016/j.tics.2014.01.001; pmid: 24582824
21. M. T. Ullman, A neurocognitive perspective on language: The declarative/procedural model. *Nat. Rev. Neurosci.* **2**, 717–726 (2001). doi: 10.1038/35094573; pmid: 11584309
22. E. Koechlin, T. Jubault, Broca's Area and the Hierarchical Organization of Human Behavior, Broca's area and the hierarchical organization of human behavior. *Neuron* **50**, 963–974 (2006). doi: 10.1016/j.neuron.2006.05.017; pmid: 16772176
23. L. Maffongelli *et al*., Distinct brain signatures of content and structure violation during action observation. *Neuropsychologia* **75**, 30–39 (2015). doi: 10.1016/j.neuropsychologia.2015.05.020; pmid: 26004058
24. M. J. D. Martins, R. Bianco, D. Sammler, A. Villringer, Recursion in action: An fMRI study on the generation of new hierarchical levels in motor sequences. *Hum. Brain Mapp.* **40**, 2623–2638 (2019). doi: 10.1002/hbm.24549; pmid: 30834624
25. A. C. Roy, M. A. Arbib, *The Syntactic Motor System* (John Benjamins Publishing, 2005).

26. L. Cardinali *et al*., Tool-use induces morphological updating of the body schema. *Curr. Biol.* **19**, R478–R479 (2009). doi: 10.1016/j.cub.2009.06.048; pmid: 19549491
27. M. Jeannerod, Visuomotor channels: Their integration in goal-directed prehension. *Hum. Mov. Sci.* **18**, 201–218 (1999). doi: 10.1016/S0167-9457(99)00008-1
28. L. Cardinali, C. Brozzoli, L. Finos, A. C. Roy, A. Farnè, The rules of tool incorporation: Tool morpho-functional & sensori-motor constraints. *Cognition* **149**, 1–5 (2016). doi: 10.1016/j.cognition.2016.01.001; pmid: 26774102
29. Y. Itaguchi, K. Fukuzawa, Hand-use and tool-use in grasping control. *Exp. Brain Res.* **232**, 3613–3622 (2014). doi: 10.1007/s00221-014-4053-3; pmid: 25081103
30. C. Brozzoli, A. C. Roy, L. H. Lidborg, M. Lövdén, Language as a tool: Motor proficiency using a tool predicts individual linguistic abilities. *Front. Psychol.* **10**, 1639 (2019). doi: 10.3389/fpsyg.2019.01639; pmid: 31379674
31. M. P. Alexander, M. A. Naeser, C. L. Palumbo, Correlations of subcortical CT lesion sites and aphasia profiles. *Brain* **110**, 961–991 (1987). doi: 10.1093/brain/110.4.961; pmid: 3651803
32. M. Grossman *et al*., Grammatical and resource components of sentence processing in Parkinson's disease: An fMRI study. *Neurology* **60**, 775–781 (2003). doi: 10.1212/01.WNL.0000044398.73241.13; pmid: 12629232
33. A. Moro *et al*., Syntax and the brain: Disentangling grammar by selective anomalies. *Neuroimage* **13**, 110–118 (2001). doi: 10.1006/nimg.2000.0668; pmid: 11133314
34. M. Teichmann *et al*., A cortical-subcortical syntax pathway linking Broca's area and the striatum. *Hum. Brain Mapp.* **36**, 2270–2283 (2015). doi: 10.1002/hbm.22769; pmid: 25682763
35. M.-L. Brandi, A. Wohlschläger, C. Sorg, J. Hermsdörfer, The neural correlates of planning and executing actual tool use. *J. Neurosci.* **34**, 13183–13194 (2014). doi: 10.1523/JNEUROSCI.0597-14.2014; pmid: 25253863
36. F. E. Garcea, L. J. Buxbaum, Gesturing tool use and tool transport actions modulates inferior parietal functional connectivity with the dorsal and ventral object processing pathways. *Hum. Brain Mapp.* **40**, 2867–2883 (2019). doi: 10.1002/hbm.24565; pmid: 30900321
37. S. H. Johnson-Frey, R. Newman-Norlund, S. T. Grafton, A distributed left hemisphere network active during planning of everyday tool use skills. *Cereb. Cortex* **15**, 681–695 (2005). doi: 10.1093/cercor/bhh169; pmid: 15342430
38. S. Obayashi *et al*., Functional brain mapping of monkey tool use. *Neuroimage* **14**, 853–861 (2001). doi: 10.1006/nimg.2001.0878; pmid: 11554804
39. J. Diedrichsen, N. Kriegeskorte, Representational models: A common framework for understanding encoding, pattern-component, and representational-similarity analysis. *PLOS Comput. Biol.* **13**, e1005508 (2017). doi: 10.1371/journal.pcbi.1005508; pmid: 28437426
40. M. V. Peelen, A. J. Wiggett, P. E. Downing, Patterns of fMRI activity dissociate overlapping functional brain areas that respond to biological motion. *Neuron* **49**, 815–822 (2006). doi: 10.1016/j.neuron.2006.02.004; pmid: 16543130
41. E. Dahlin, A. S. Neely, A. Larsson, L. Bäckman, L. Nyberg, Transfer of learning after updating training mediated by the striatum. *Science* **320**, 1510–1512 (2008). doi: 10.1126/science.1155466; pmid: 18556560
42. S. M. Jaeggi, M. Buschkuehl, J. Jonides, W. J. Perrig, Improving fluid intelligence with training on working memory. *Proc. Natl. Acad. Sci. U.S.A.* **105**, 6829–6833 (2008). doi: 10.1073/pnas.0801268105; pmid: 18443283
43. S. M. Jaeggi, M. Buschkuehl, J. Jonides, P. Shah, Short- and long-term benefits of cognitive training. *Proc. Natl. Acad. Sci. U.S.A.* **108**, 10081–10086 (2011). doi: 10.1073/pnas.1103228108; pmid: 21670271
44. S. Lehéricy *et al*., Distinct basal ganglia territories are engaged in early and advanced motor sequence learning. *Proc. Natl. Acad. Sci. U.S.A.* **102**, 12566–12571 (2005). doi: 10.1073/pnas.0502762102; pmid: 16107540
45. H. Makino, E. J. Hwang, N. G. Hedrick, T. Komiyama, Circuit mechanisms of sensorimotor learning. *Neuron* **92**, 705–721 (2016). doi: 10.1016/j.neuron.2016.10.029; pmid: 27883902
46. H. H. Yin *et al*., Dynamic reorganization of striatal circuits during the acquisition and consolidation of a skill. *Nat. Neurosci.* **12**, 333–341 (2009). doi: 10.1038/nn.2261; pmid: 19198605
47. K. M. Tagarelli, K. F. Shattuck, P. E. Turkeltaub, M. T. Ullman, Language learning in the adult brain: A neuroanatomical meta-analysis of lexical and grammatical learning. *Neuroimage* **193**, 178–200 (2019). doi: 10.1016/j.neuroimage.2019.02.061; pmid: 30826361
48. A. M. Graybiel, S. T. Grafton, The striatum: Where skills and habits meet. *Cold Spring Harb. Perspect. Biol.* **7**, a021691 (2015). doi: 10.1101/cshperspect.a021691; pmid: 26238359
49. K. Amunts *et al*., Broca's region: Novel organizational principles and multiple receptor mapping. *PLOS Biol.* **8**, e1000489 (2010). doi: 10.1371/journal.pbio.1000489; pmid: 20877713
50. G. Papitto, A. D. Friederici, E. Zaccarella, The topographical organization of motor processing: An ALE meta-analysis on six action domains and the relevance of Broca's region. *Neuroimage* **206**, 116321 (2020). doi: 10.1016/j.neuroimage.2019.116321; pmid: 31678500
51. D. Muret *et al*., Touch improvement at the hand transfers to the face. *Curr. Biol.* **24**, R736–R737 (2014). doi: 10.1016/j.cub.2014.07.021; pmid: 25137581
52. S. Vyas *et al*., Neural population dynamics underlying motor learning transfer. *Neuron* **97**, 1177–1186.e3 (2018). doi: 10.1016/j.neuron.2018.01.040; pmid: 29456026
53. K. Grill-Spector, R. Henson, A. Martin, Repetition and the brain: Neural models of stimulus-specific effects. *Trends Cogn. Sci.* **10**, 14–23 (2006). doi: 10.1016/j.tics.2005.11.006; pmid: 16321563
54. V. Boulenger *et al*., Cross-talk between language processes and overt motor behavior in the first 200 msec of processing. *J. Cogn. Neurosci.* **18**, 1607–1615 (2006). doi: 10.1162/jocn.2006.18.10.1607; pmid: 17014366
55. R. N. A. Henson, Neuroimaging studies of priming. *Prog. Neurobiol.* **70**, 53–81 (2003). doi: 10.1016/S0301-0082(03)00086-8; pmid: 12927334
56. T. Xu *et al*., Rapid formation and selective stabilization of synapses for enduring motor memories. *Nature* **462**, 915–919 (2009). doi: 10.1038/nature08389; pmid: 19946267
57. E. Wenger, C. Brozzoli, U. Lindenberger, M. Lövdén, Expansion and renormalization of human brain structure during skill acquisition. *Trends Cogn. Sci.* **21**, 930–939 (2017). doi: 10.1016/j.tics.2017.09.008; pmid: 29149999
58. A. Iriki, M. Taoka, Triadic (ecological, neural, cognitive) niche construction: A scenario of human brain evolution extrapolating tool use and language from the control of reaching actions. *Philos. Trans. R. Soc. Lond. B Biol. Sci.* **367**, 10–23 (2012). doi: 10.1098/rstb.2011.0190; pmid: 22106423
59. M. S. Ponce de León *et al*., The primitive brain of early *Homo*. *Science* **372**, 165–171 (2021). doi: 10.1126/science.aaz0032; pmid: 33833119
60. D. Stout, T. Chaminade, Stone tools, language and the brain in human evolution. *Philos. Trans. R. Soc. Lond. B Biol. Sci.* **367**, 75–87 (2012). doi: 10.1098/rstb.2011.0099; pmid: 22106428
61. G. Rizzolatti, M. A. Arbib, Language within our grasp. *Trends Neurosci.* **21**, 188–194 (1998). doi: 10.1016/s0166-2236(98)01260-0; pmid: 9610880
62. S. Dehaene, L. Cohen, Cultural recycling of cortical maps. *Neuron* **56**, 384–398 (2007). doi: 10.1016/j.neuron.2007.10.004; pmid: 17964253
63. T. J. H. Morgan *et al*., Experimental evidence for the co-evolution of hominin tool-making teaching and language. *Nat. Commun.* **6**, 6029 (2015). doi: 10.1038/ncomms7029; pmid: 25585382
64. M. L. Anderson, Précis of after phrenology: Neural reuse and the interactive brain. *Behav. Brain Sci.* **39**, e120 (2016). pmid: 26077688
65. W. D. Hopkins *et al*., Motor skill for tool-use is associated with asymmetries in Broca's area and the motor hand area of the precentral gyrus in chimpanzees (*Pan troglodytes*). *Behav. Brain Res.* **318**, 71–81 (2017). doi: 10.1016/j.bbr.2016.10.048; pmid: 27816558
66. P. Lieberman, The evolution of language and thought. *J. Anthropol. Sci.* **94**, 127–146 (2016). pmid: 26963222
67. R. C. Oldfield, The assessment and analysis of handedness: The Edinburgh inventory. *Neuropsychologia* **9**, 97–113 (1971). doi: 10.1016/0028-3932(71)90067-4; pmid: 5146491
68. B. New, C. Pallier, M. Brysbaert, L. Ferrand, Lexique 2: A new French lexical database. *Behav. Res. Methods Instrum. Comput.* **36**, 516–524 (2004). doi: 10.3758/BF03195598; pmid: 15641440
69. J. R. Reynolds, R. West, T. Braver, Distinct neural circuits support transient and sustained processes in prospective memory and working memory. *Cereb. Cortex* **19**, 1208–1221 (2009). doi: 10.1093/cercor/bhn164; pmid: 18854581
70. L. A. Jones, S. J. Lederman, *Human Hand Function* (Oxford Univ. Press, 2006).
71. T. Nichols, M. Brett, J. Andersson, T. Wager, J. B. Poline, Valid conjunction inference with the minimum statistic. *Neuroimage* **25**, 653–660 (2005). doi: 10.1016/j.neuroimage.2004.12.005; pmid: 15808966
72. N. N. Oosterhof, A. C. Connolly, J. V. Haxby, CoSMoMVPA: Multi-modal multivariate pattern analysis of neuroimaging data in matlab/GNU octave. *Front. Neuroinform.* **10**, 27 (2016). doi: 10.3389/fninf.2016.00027; pmid: 27499741
73. H. Singmann, B. Bolker, J. Westfall, F. Aust, S. M. Ben-Shachar, "afex: Analysis of factorial experiments (R Package Version 0.27-2, 2020); https://CRAN.R-project.org/package=afex.

ACKNOWLEDGMENTS

We thank E. Wenger, A. Farnè, and E. Macaluso for precious advice; E. Blini for help with parts of the statistical analyses; F. Lamberton and D. Ibarrola for help with fMRI acquisitions and settings; F. Leconte for graphic contribution to the figures; F. Volland for realization of parts of the setup; the research assistants for helping with the acquisitions; Quercetti for kindly providing the peg-board games used in the scanner; and S. Alouche, J.-L. Borach, and C. Farge for administrative support. **Funding:** C.B. is supported by Swedish Research Council grants 2015-01717 and Agence Nationale de le Recherche grant ANR-JC (ANR-16-CE28-0008-01). M.L. is supported by Swedish Research Council grant 2018-01047. A.C.R. is supported by ANR-16-CE28-0015. A.C.R. and V.B. are supported by LabEx ASLAN grants ANR-10-LABX-0081 and ANR-11-IDEX-0007. **Author contributions:** Conceptualization and methodology: S.T., M.L., V.B., A.C.R., and C.B. Software, validation and formal analyses: S.T., R.S., E.K., C.B.; Material and set-up: S.T., R.S., and E.K.; Investigation and data curation: S.T., R.P., A.M.G., and C.B.; Original draft preparation and visualization: S.T., V.B., A.C.R., and C.B.; Writing - review and editing: all authors. **Competing interests:** The authors declare no competing interests. **Data and materials availability:** Data, materials, and codes for analyses are available at https://osf.io/mw3pf/.

SUPPLEMENTARY MATERIALS

science.org/doi/10.1126/science.abe0874
Supplementary Text
Figs. S1 to S4
Tables S1 to S3
References (*74*, *75*)
Movies S1 and S2
MDAR Reproducibility Checklist

4 August 2020; resubmitted 4 May 2021
Accepted 24 September 2021
10.1126/science.abe0874

RESEARCH ARTICLES

GENOMICS OF AGING

Origins and evolution of extreme life span in Pacific Ocean rockfishes

Sree Rohit Raj Kolora[1]†, Gregory L. Owens[1,2]†, Juan Manuel Vazquez[1], Alexander Stubbs[1], Kamalakar Chatla[1], Conner Jainese[3], Katelin Seeto[3], Merit McCrea[3], Michael W. Sandel[4], Juliana A. Vianna[5], Katherine Maslenikov[6], Doris Bachtrog[1], James W. Orr[6], Milton Love[3], Peter H. Sudmant[1,7]*

Pacific Ocean rockfishes (genus *Sebastes*) exhibit extreme variation in life span, with some species being among the most long-lived extant vertebrates. We de novo assembled the genomes of 88 rockfish species and from these identified repeated signatures of positive selection in DNA repair pathways in long-lived taxa and 137 longevity-associated genes with direct effects on life span through insulin signaling and with pleiotropic effects through size and environmental adaptations. A genome-wide screen of structural variation reveals copy number expansions in the immune modulatory butyrophilin gene family in long-lived species. The evolution of different rockfish life histories is coupled to genetic diversity and reshapes the mutational spectrum driving segregating CpG→TpG variants in long-lived species. These analyses highlight the genetic innovations that underlie life history trait adaptations and, in turn, how they shape genomic diversity.

Decades of theoretical work on the evolution of aging have demonstrated that senescence is a "theoretically inevitable" consequence of the increased selective impact of genes that influence early-life survival and fecundity compared with genes that act late in life (*1*). Nonetheless, across vertebrates alone, life span varies by more than three orders of magnitude, ranging from the 5-week life cycle of the pygmy goby (*2*) to the ~400-year life span of the Greenland shark (*3*), highlighting exceptional diversity of this trait across species. Understanding evolutionary transitions in life span can highlight diverse genetic mechanisms of life-span control and the subsequent impacts of life-history shifts on patterns of genetic diversity.

Across organisms, aging is accompanied by several molecular hallmarks including genome instability, loss of protein homeostasis, and mitochondrial dysfunction, among others (*4*). Vertebrates in particular also exhibit a number of distinct hallmarks of aging that are directly linked to human disease and health span, such as immunosenescence, inflammation, and stem cell exhaustion (*5*). Thus, understanding the underpinnings of life-span variation across vertebrate taxa can provide critical insights into the maintenance of human health and vigor in old age.

Rockfishes (genus *Sebastes*) of the Pacific Ocean exhibit life spans ranging from 11 years (*Sebastes minor*) to >200 years (rougheye rockfish, *Sebastes aleutianus*) (*6*) (Fig. 1A). This phenotype exhibits a relatively uniform distribution across the more than 75 different species of this clade for which detailed longevity information is available (fig. S1). Rockfishes are thus distinctive in that while some species are among the longest-lived vertebrates known to exist, life span can widely range even among closely related taxa. More than 120 different species of rockfish are found throughout the northeast and northwest Pacific Ocean (*7*) (Fig. 1B). This abundance of species with vastly differing life histories represents an example of repeated, recent adaptations that have reshaped longevity phenotypes.

Results

Sequencing and assembly of 102 rockfish genomes

To dissect the genetic underpinnings of life-span variation and adaptation, we sequenced and de novo assembled the genomes of 102 rockfish individuals encompassing 88 different species, including 79 members of the *Sebastes* clade and nine closely related outgroup taxa (figs. S1 and S2). Long-read Pacific Biosciences genome assemblies were generated for six *Sebastes* species and the outgroup *Sebastolobus alascanus* [mean contig N50: 6.1 million base pairs (Mbp)] (Fig. 1C). Five of these *Sebastes* genomes were scaffolded with long-range Hi-C data, resulting in chromosome-scale assemblies (mean scaffold N50: 34.1 Mbp) (Fig. 1C, table S1, and fig. S3). High-coverage Illumina-based assemblies were generated for 71 additional *Sebastes* species (mean contig N50: 73.8 kilobase pairs). Genome completeness [assessed by BUSCO scores (*8*)] ranged from an average of 97.9% for long-read–based genomes to 91.2% for Illumina-based assemblies, and the majority (five of seven) of the long-read–based genomes reached QV40 base quality (average QV39 for all seven) (fig. S4). Transcriptomes were generated from brain and eye tissue for eight species, including six individuals for which we generated long-read–based genome assemblies to assist in gene annotation. In total, we identified ~25,000 protein-coding genes on average across the seven long-read genome assemblies (table S3). Together, these genome assemblies encompass the majority of species represented in the *Sebastes* genus and almost all representatives for which detailed life-span information has been cataloged, including a chromosome-level assembly of the ultra-long-lived *S. aleutianus*.

We established the phylogenetic relationships and speciation times among rockfish species by constructing an ultrametric species phylogeny [see supplementary methods (*9*)] (Fig. 1A). The topology of this tree is consistent with previous phylogenetic analyses of rockfishes (*7*, *10*). The varied placement of long-lived taxa in the tree suggests repeated life span–related evolution (Fig. 1A), which is supported by character mapping analysis that shows multiple independent gains of long life span (fig. S7).

Repeated signatures of positive selection in DNA repair pathways in long-lived taxa

We next sought to determine the genetic underpinnings of life span in Pacific rockfishes. We used a branch-site model test of codon evolution to identify candidates of positive selection in the longest-lived (≥105 years) and shortest-lived (≤20 years) species (life span decile tails, n = 7 species), identifying 772 and 873 genes, respectively. Most of these positively selected genes (PSGs) were lineage specific, although ~12 to 15% of genes (127 and 118, respectively) were present in two or more species, representing either selection on the ancestral branch or convergent evolution. Additionally, 180 PSGs were found in both long- and short-lived individuals, highlighting that many of these genes may be under selection for other traits. Whereas no pathways were enriched in PSGs in short-lived species after multiple testing correction, PSGs in long-lived species were enriched for DNA double-stranded break repair pathways (Fig. 2A and table S5).

[1]Department of Integrative Biology, University of California, Berkeley, CA, USA. [2]Department of Biology, University of Victoria, Victoria, BC, Canada. [3]Marine Sciences Institute, University of California, Santa Barbara, CA, USA. [4]Department of Biological and Environmental Sciences, University of West Alabama, Livingston, AL, USA. [5]Departamento de Ecosistemas y Medio Ambiente, Pontificia Universidad Católica de Chile, Santiago, Chile. [6]School of Aquatic and Fishery Sciences and Burke Museum of Natural History and Culture, University of Washington, Seattle, WA, USA. [7]Center for Computational Biology, University of California, Berkeley, CA, USA.
*Corresponding author. Email: psudmant@berkeley.edu
†These authors contributed equally to this work.

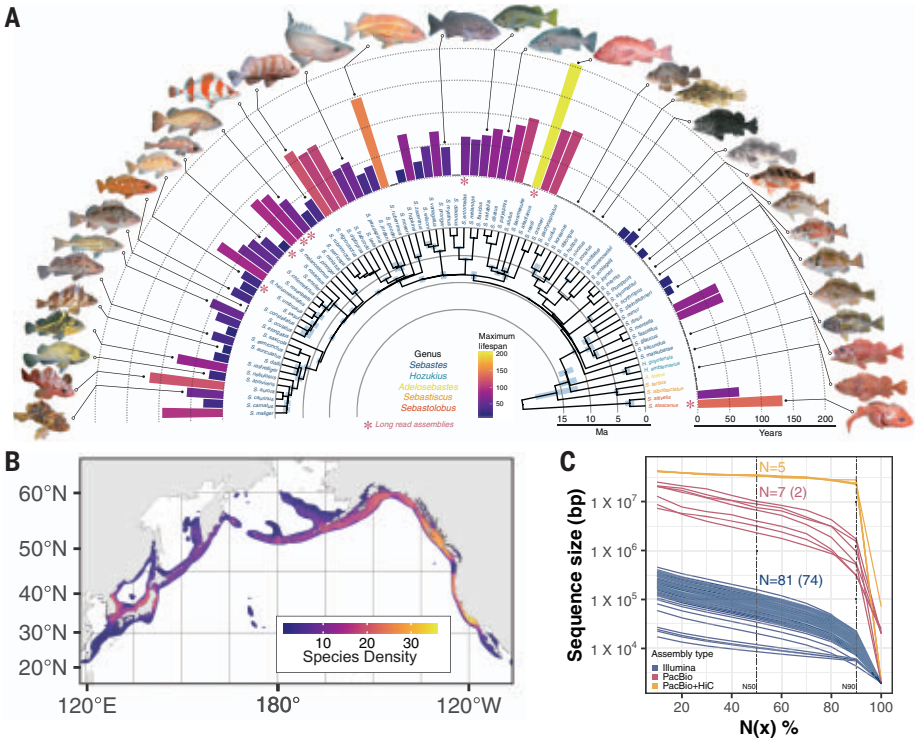


Fig. 1. Genome assemblies and relationships among rockfish species. (**A**) Ultrametric tree of the rockfish species sequenced in this study and their associated maximum life spans along with representative images (node timing confidence intervals in light blue) created using IQ-TREE, ASTRAL (Accurate Species Tree Algorithm), and BPPR. Asterisks indicate individuals for which long-read sequencing-based genomes were assembled. (**B**) The density of rockfish species (heatmap colors) throughout the Pacific Ocean. (**C**) Genome assembly statistics for 81 species, blue and pink represent N(x) contig lengths, while orange indicates N(x) scaffold lengths.

The enrichment in DNA replication, repair, and maintenance is driven by 16 genes (Fig. 2B), five of which exhibit selective signatures in more than one species. These include genes in pathways associated with life span across organisms, such as telomere maintenance (e.g., *WRAP53* and *DCLRE1B*) and base excision repair (e.g., *FEN1*). Intriguingly, adaptive signatures in *DCLRE1B* and *FEN1* have been identified in the bowhead whale and giant tortoise, respectively (*11*, *12*). MCM6, a core member of the DNA replication helicase machinery, exhibits signatures of positive selection in *S. ruberrimus* and *S. nigrocinctus*. These signatures of selection suggest that repeated transitions in life span in rockfishes are likely enabled by parallel evolution of different genes in shared critical DNA maintenance pathways.

Genes associated with life-span adaptations through direct and pleiotropic effects

We next examined the role of evolution in convergent genes and pathways on rockfish life span by comparing the relative evolutionary rates of genes across the phylogeny (*13*). This approach allowed us to identify genes with evolutionary rates that are correlated, either positively or negatively, with life span (Fig. 2C and table S14). Although these correlations do not prove causation, they can guide insights in experimentally intractable systems, such as rockfishes. At a q-value cutoff of 0.05, we discovered 91 genes significantly associated with life span, including candidates with roles in cell growth and proliferation (e.g., *NRG1*), DNA repair (e.g., *BRIP1*), and suppression of apoptosis (e.g., *TNFRSF6B*) (Fig. 2D and fig. S9). However, life span in rockfishes is correlated with body size and environmental factors, such as depth (*14*). Thus, some of these genes associated with life span may act by influencing growth and size or may facilitate adaptations to environments that promote longevity.

To identify genes associated with rockfish longevity, independent of other factors, we constructed a linear model using the two most predictive variables for life span, size at maturity and maximum depth (Fig. 2E). This model described 59% of the variation in life span (Fig. 2F), which is comparable to simple models of life span and body size in mammals (*15*). Using the residuals of this model as phenotypes, we identified 56 genes associated with life span independent of size at maturity or depth (Fig. 2D and table S14). These genes were overrepresented for insulin and glucose signaling (hypergeometric test, $P = 1.8 \times 10^{-6}$) (Fig. 2G and fig. S10), including genes with roles in life-span extension across many organisms (*5*). The rate of evolution for most of these genes was negatively correlated with life span, emphasizing the importance of nutrient-sensing maintenance in long-lived species. We also identified genes associated with reproductive aging in mice (*16*), the antiviral innate immunity factor *TRAF3IP3* (*17*), and the tumor suppressor *DYRK2* (*18*).

Of the 91 genes associated with life span, before correcting for size and depth, only 10 overlapped with those identified as associated with the life-span residual, suggesting that the majority (n = 81) of the genes we identified in *Sebastes* act indirectly by influencing size or facilitating adaptations to depth. To parse the axes along which these life span–associated genes act, we correlated their relative evolutionary rates with either the growth-associated component of life span in our linear model (S, size), the depth-associated component of life span (D), or the residual of the model (R) (Fig. 2H). The size axis was associated with the most genes (n = 33, $S > 0.5$) in comparison to depth or the residual (n = 18, $D > 0.5$; n = 17, $R > 0.5$), which is in line with the importance of growth- and size-related pathways underlying differences in life span among different organisms (*19*). Pathways enriched along this axis included mTOR signaling DNA and telomere maintenance, and cancer (Fig. 2I). Genes and pathways along the D axis reflect environmental adaptations such as lipid metabolism and synthesis. The R axis was enriched for insulin signaling and protein homeostasis, with ribosome assembly pathways along the DR axis. Apoptosis genes were more closely clustered with the R axis intermediate to S and D, and antigen processing and presentation genes were also clustered along the SD axis. Together, these results suggest that the genetic basis of longevity in rockfish species may be due to the combined effect of genes acting directly on life span alongside genes affecting ecological and growth phenotypes that pleiotropically influence life span.

Expansion of the immune modulatory butyrophilin gene family in long-lived species

Gene duplications and structural rearrangements can drive evolutionary innovations (*20*, *21*). To identify copy number changes associated with variation in life span, we performed a genome-wide screen using windowed read-depth–based copy estimates across chromosomes. Controlling for phylogenetic signal, we found an enrichment for positive associations between life span and copy number,

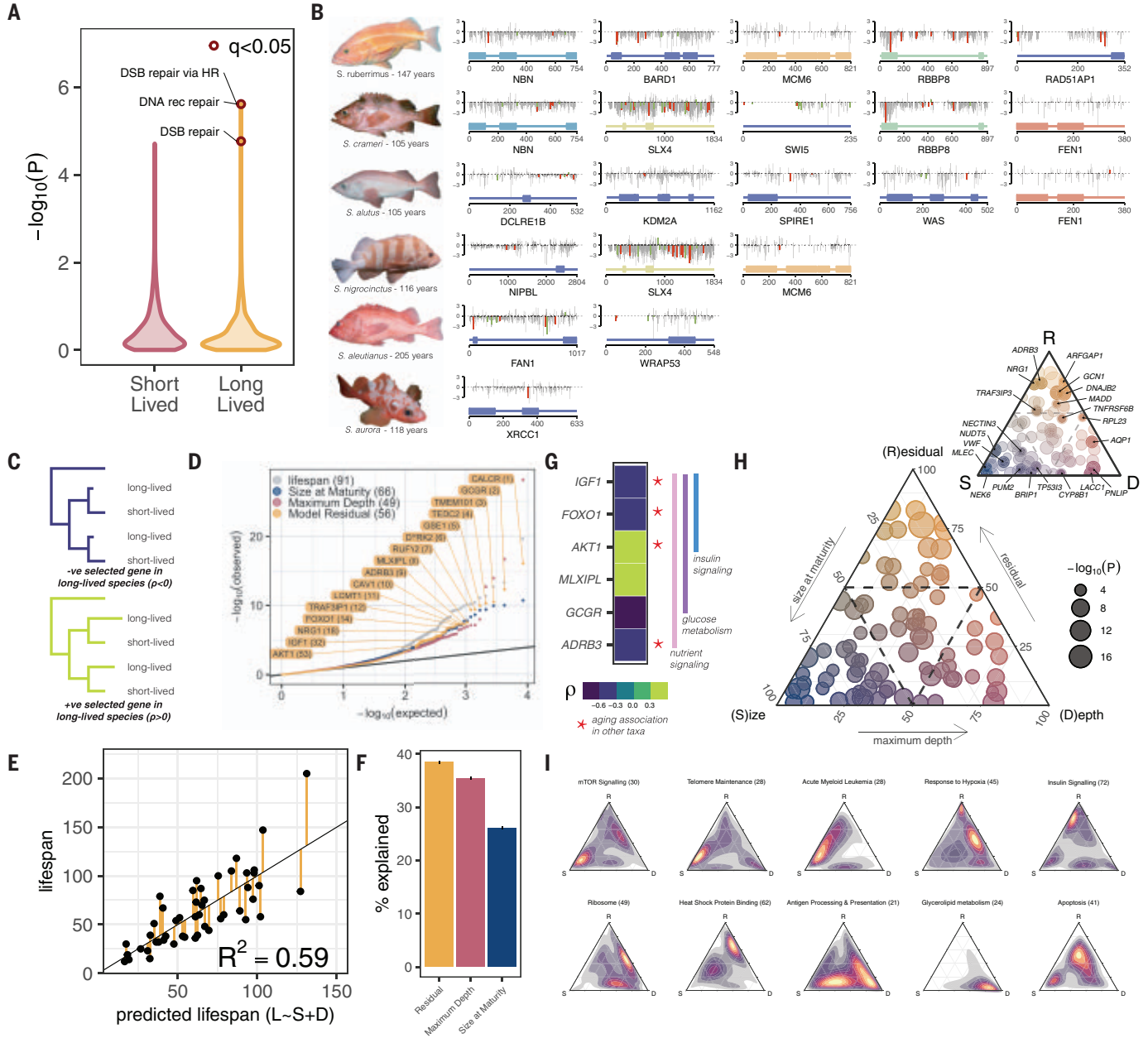


Fig. 2. Genetic underpinnings of life-span adaptations. (**A**) Distribution of pathway enrichment *P* values for genes under positive selection in short- and long-lived species. DSB, double-strand break; HR, homologous recombination; rec, recombination. (**B**) Schematics of the 16 DNA replication, repair, or maintenance genes exhibiting positive selection in long-lived rockfishes. Domain structure (bottom), gray lines indicate putative functional consequence of rockfish amino acid compared with human (PROVEAN score). Red and green bars indicate mutations distinct from all non-long-lived taxa colored by SIFT score – tolerated (green) / damaging (red). (**C**) Schematic representation of relative evolutionary rate test and (**D**) *P* value distribution of genes from relative evolutionary rate test (RERconverge) of correlation between evolutionary rate and individual traits. Life span and the individual components of a predictive linear model of life span (E) are used as traits. Gene names are highlighted for the top 12 genes associated with the linear model residual as a trait in addition to four other significant gene candidates previously associated with aging (full gene list in table S14). (**E**) Linear regression model between maximum life span and predicted life span based on body size and depth for different species. (**F**) Proportion of variation in life span explained by size, depth, and the residual from the linear model. (**G**) Relative evolutionary rates of six genes involved in glucose, insulin, and nutrient signaling, four of which have been associated with aging in other taxa (table S14). (**H**) Ternary plot of 91 life span–associated genes plotted as a function of the relative importance along linear model axes, with dashed line at 50% (inset with gene labels) and (**I**) heatmaps of pathway enrichment along axes.

regardless of whether we used a short- or long-lived species reference (χ^2, $P < 1 \times 10^{-15}$). The greatest cluster of positive associations was on chromosome 1 (Fig. 3A); it extended for almost 250 kb and overlapped nine genes (Fig. 3B) ranging from zero to seven copies among different species (Fig. 3C). These nine genes included six members of the butyrophilin gene family (*BTN* and *BTNL* genes) (Fig. 3D), a family of immune regulators associated with human inflammatory diseases (*22*). Using our linear model, we found that this signature is primarily driven by the depth-associated component of life span (Fig. 2H and fig. S15). Mutations in *BTNL2* cause sarcoidosis in humans

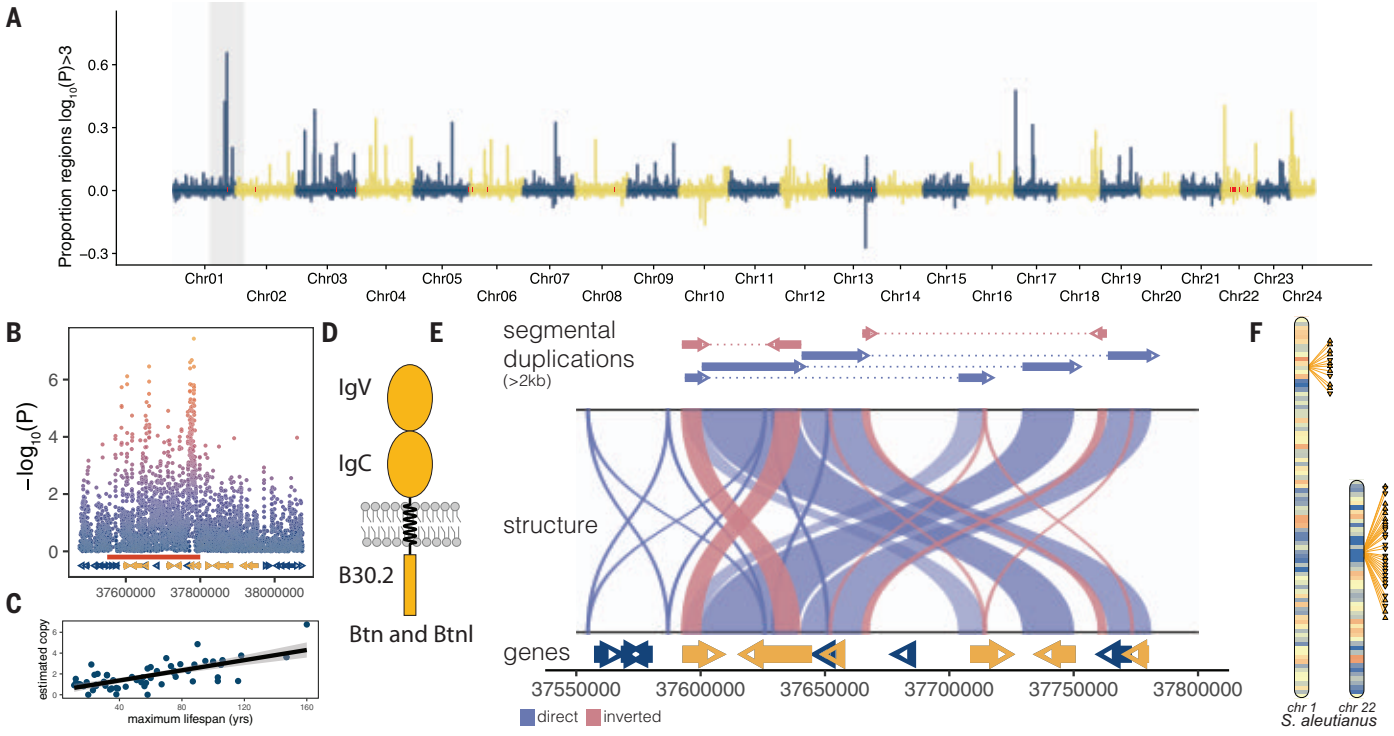


Fig. 3. Life span–associated butyrophilin gene duplications. (**A**) Miami plot of proportion of 100-bp regions with significant phylogenetic least squares linear model (PGLS) correlations between read-depth inferred copy number and life span (10-kb windows) across the *S. aleutianus* reference genome. (**B**) Manhattan plot of ~250-kb chromosome 1 butyrophilin locus and (**C**) copy number association. Butyrophilin genes shown in orange. (**D**) Protein structural organization of *BTN* and *BTNL* gene family members. IgV, immunoglobulin V domain; IgC; immunoglobulin C domain. (**E**) Genome structure of the butyrophilin locus in the *S. aleutianus* genome assembly. Segmental duplications are highlighted above a self-alignment of the locus to show the underlying duplication architecture with genes below. (**F**) Karyotypes of chromosomes 1 and 22 in *S. aleutianus* (color indicates gene density) highlighting the two butyrophilin gene family clusters in *Sebastes* species.

(*23*), and variants in *BTN3A2* have been associated with human life span (*24*).

Butyrophilins are members of the B7 immunoglobulin superfamily and in response to inflammatory stimuli inhibit cytokine secretion and production in T cells, thus serving an immunosuppressive function. We resolved the underlying segmental duplication (SD) architecture of the life span–associated butyrophilin duplication in the *S. aleutianus* genome (Fig. 3E), identifying 22 large (>1 kb, >90% identity) SD blocks across the locus. The majority of the locus is contained in three pairs of large adjacent SDs in direct orientation, which together encompass 163 kb. Two large, high-identity (>95%) inverted duplications add additional complexity to the locus. While the copy number of *BTN* and *BTNL* genes at this locus correlates significantly (Fig. 3C) with life span in rockfishes, we identified *BTN* and *BTNL* copies not associated with life span as well, largely localized to two clusters on chromosomes 1 and 22 (Fig. 3F). Among our six *Sebastes* reference genome assemblies, the total number of *BTN* and *BNTL* genes ranges from 18 to 36, highlighting expansion of this gene family across taxa. Teleost fishes exhibit diverse immune defense strategies, and gene expansions of the major histocompatibility complex I locus have occurred numerous times (*25*). Here, a distinct class of immunoregulatory genes in rockfishes may have facilitated adaptations to extreme life span.

Life-history transitions are tightly coupled to patterns of genetic diversity

To assess genetic diversity across the *Sebastes* clade, we performed variant calling on samples mapped to each of their respective genome assemblies. We identified a >13-fold range in heterozygosity among *Sebastes* species (π = 2.9×10^{-4} to 3.8×10^{-3} per base pair) (Fig. 4A) and a 20-fold range when the outgroup taxa were also considered. These levels of diversity correspond to a range in effective population size (N_e) of 7.2×10^4 to 9.6×10^5 in the *Sebastes* clade, assuming a mutation rate of 1×10^{-9}.

We applied multiple sequentially Markovian coalescent (MSMC) analysis (*26*) to dissect the demographic histories underlying these differences in diversity. We grouped MSMC trajectories by life-span quartile and compared the mean N_e over the last 10^6 generations (Fig. 4B). While we observed a wide range of different demographic trajectories, short-lived species exhibited increases in N_e over the past ~10^6 generations. Note that the short-lived African killifish exhibits reduced life span linked to severe population bottlenecks (*27*). However, rockfish life span was significantly negatively correlated with N_e as a function of maximum life span [phylogenetic generalized least squares (PGLS) P = 0.005] (Fig. 4C).

Body mass is strongly positively correlated with both census population sizes and life spans across terrestrial vertebrates (*28*, *29*). In rockfishes too, size is correlated with life span (Fig. 2E), and, indeed, size is a better predictor of N_e than life span (PGLS $P = 6.6 \times 10^{-5}$) (Fig. 4D). These results suggest that life-history transitions to shortened life and smaller body size are potentially adaptive, in contrast to the drift-driven transitions observed in killifish. These results also underscore the inherent genetic vulnerability of larger long-lived marine fish species, which are often the targets of commercial fisheries (*30*).

Shifts in life span reshape the mutational spectrum of segregating genetic variation

Long-lived, larger, terrestrial vertebrates with smaller N_e often exhibit low rates of fecundity,

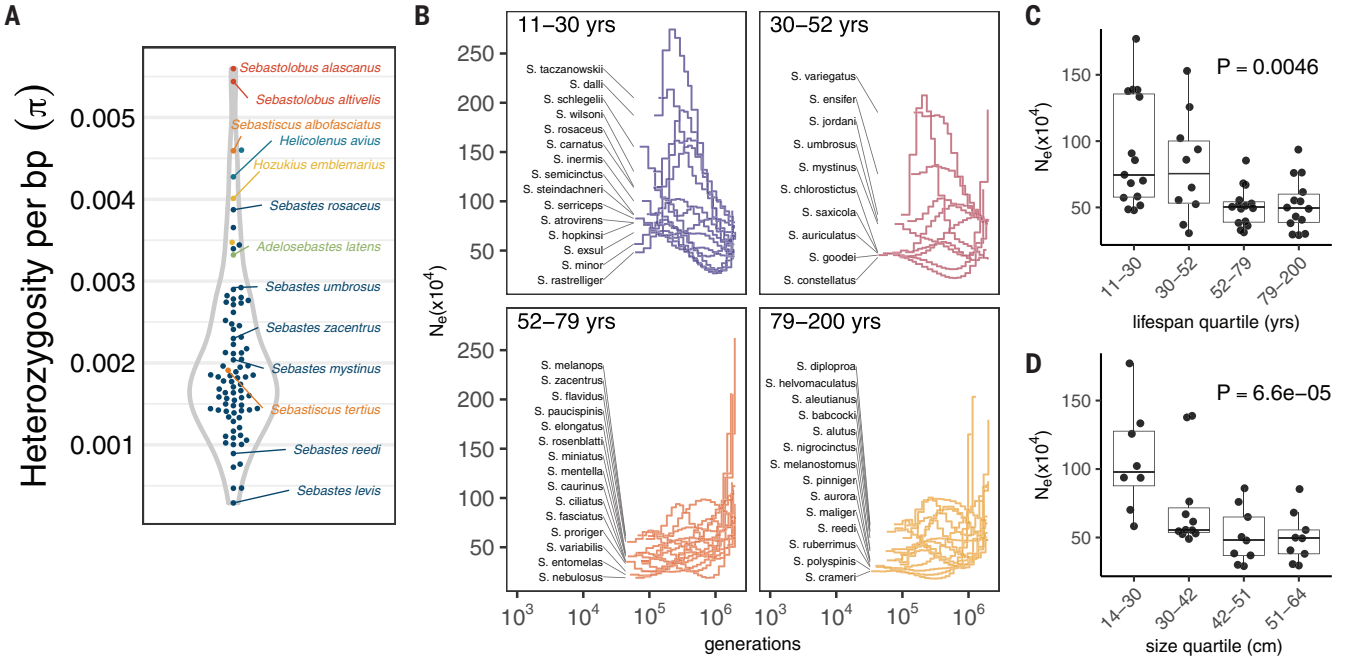
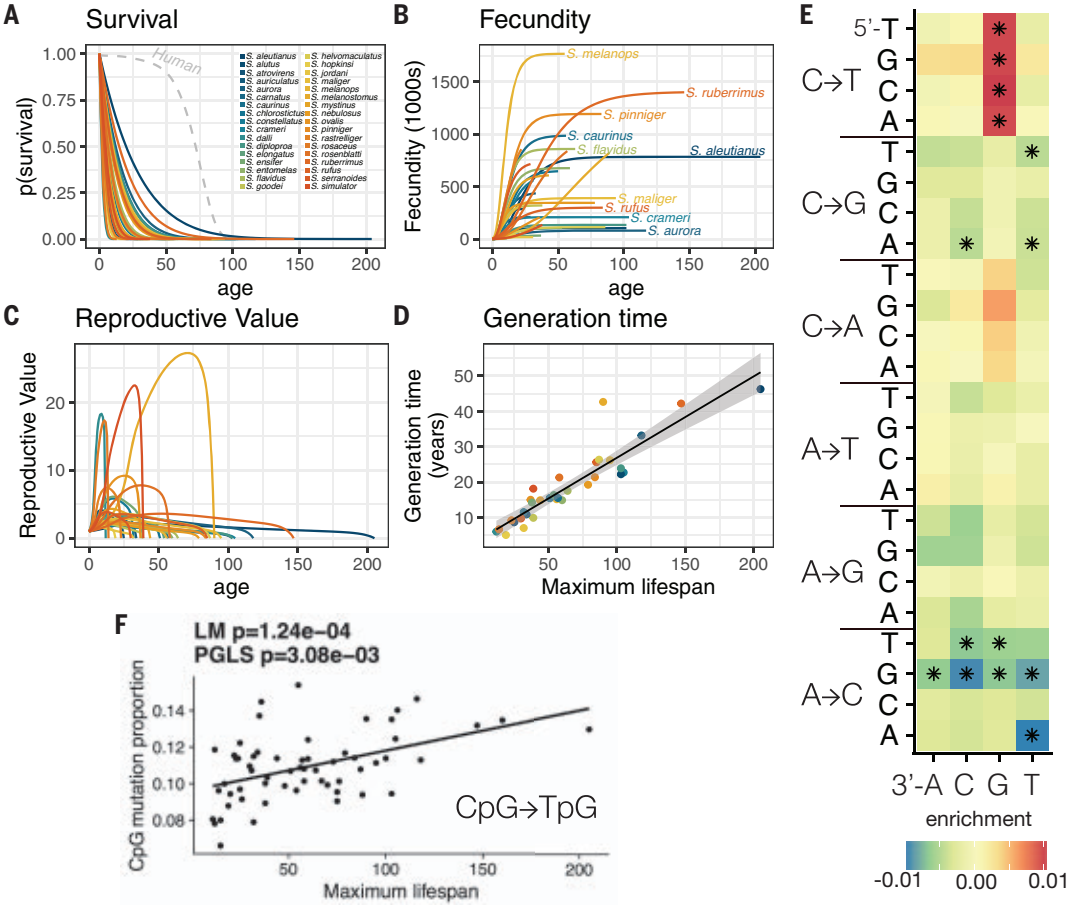


Fig. 4. Life-history transitions are associated with patterns of diversity. (**A**) Nucleotide diversity across 88 different species. (**B**) MSMC-based estimates of effective population sizes grouped by life span quartile over the last ~10^6 generations and averaged N_e grouped by (**C**) life-span quartile or (**D**) grouped by size quartile. Box and whisker plots indicate the median and interquartile range (IQR) with tails at the minimum and maximum values within 1.5 × IQR. *P* values from PGLS linear model.

Fig. 5. Shifts in life-history traits reshape the mutational spectrum of segregating genetic variation. (**A**) Survival curves for 34 rockfish species. Humans, shown for comparison, exhibit maximum life spans similar to those of many rockfish species but different survival curves (type I versus type III survival). (**B**) Rockfish fecundity (births per season) plotted as a function of age. (**C**) Reproductive value plotted as a function of age. (**D**) Generation times estimated from survival and fecundity plotted as a function of life span. (**E**) Association of segregating single-nucleotide variant mutation types with life span across all trinucleotide contexts. Asterisks indicate age-associated mutational profiles significant after multiple testing correction ($q < 0.05$). (**F**) The proportion of segregating CpG→TpG mutations as a function of maximum life span. LM, linear regression model.



increased maturation times, and higher survival of offspring (*31*). Long-lived rockfish species also exhibit extremely long maturation times stretching to more than a decade (*3*). We modeled survival, maturation, and fecundity in 34 different rockfish species for which detailed information could be ascertained to understand the evolutionary trade-offs driving rockfish life histories (Fig. 5, A to D, and tables S15 to S17). Similar to other marine fishes, rockfishes exhibit a "type III" survivorship curve, with high mortality at young ages and very few individuals surviving to old age (*32*) (Fig. 5A). However, fecundity increases rapidly as a function of age, proportional to size (Fig. 5B), and thus aging imparts minimal declines in their reproductive values (Fig. 5C). In extreme cases, such as in yelloweye rockfish (*S. ruberrimus)*, 150-year-old individuals can produce more than one million offspring per season. Even compared with other marine fishes, which exhibit nonlinear scaling in reproductive output with size (*33*), older, larger rockfish have significantly higher reproductive output per unit weight (Wilcoxon $P = 6.3 \times 10^{-6}$) (fig. S20).

The disproportionate reproductive output of older fish results in generation times that span from 5 to 45 years across different species (Fig. 5D and table S17). We find that these differences in generation time and life span are associated with reduced nucleotide substitution rates (resulting in shortened phylogenetic branch lengths) in longer-lived species, as observed in terrestrial mammals (fig. S21) (*34*). Generation time can also influence the mutational spectrum, with certain classes of mutations being more likely to occur in older parents (*35*, *36*). We thus classified species-specific segregating single-nucleotide variants by mutation type and trinucleotide context (fig. S22). Correlations between mutation types and life span (Fig. 5E) were seen with enrichments of CpG→TpG mutations; longer-lived species exhibited a significantly increased proportion of CpG transitions in all *CG→*TG contexts (PGLS $P = 1 \times 10^{-4}$) (Fig. 5F). CpG→TpG transitions are characteristic of spontaneous methylated cytosine deamination, a mutational signature that occurs independent of DNA replication (*37*) and is the dominant age-associated mutational profile of human tumors (*38*).

In humans, a reduced proportion of CpG variants in European populations has been hypothesized to have been driven by shortened generation times (*39*), which, if due to similar processes in fish, may be consistent with our findings. A number of mutational signatures were also at reduced frequency across long-lived rockfish species, including A→C and C→G transversions (Fig. 5E), however it is unclear what the underlying mutational mechanism of this signature might be. Together, these results indicate that shifts in life histories can in turn reshape patterns of segregating genetic diversity.

Discussion

The vast diversity of life histories in Pacific Ocean rockfishes presents an opportunity to dissect the genetic adaptations that shape life-history transitions in vertebrates. Our results highlight selective signatures in pathways underlying "hallmarks of aging" (*4*) that are conserved across all eukaryotes (e.g., DNA damage and nutrient-sensing pathways) as well as in vertebrate-specific hallmarks such as immunity and inflammation (*5*). Chronic inflammation ("inflammaging") in particular has emerged as a key therapeutic target in humans, and our results identify a specific gene family, the butyrophilins, that may play a role in modulating life span in rockfishes. We also find that the genetic adaptations that enable extreme longevity in rockfishes do so both directly, by influencing insulin signaling and other key pathways, as well as indirectly, by influencing size and adaptations to depth. Further, our results indicate that such life-history transitions themselves reshape patterns of genetic diversity. Long-lived rockfish species exhibit reduced genetic diversity in contrast to short-lived species, and the mutational spectrum of segregating genetic variation is also altered by life span. Indeed, the disproportionately higher reproductive output in older, larger rockfishes is likely directly linked to their extreme longevity. Our work further highlights the utility of genus-wide genome assembly efforts to answer questions that have thus far been limited to representative species from broad taxonomic groups (e.g., vertebrates). The advent of additional complete genome assemblies from vertebrates will advance our understanding of the generality of our findings across evolutionary and physical scales.

REFERENCES AND NOTES

1. B. Charlesworth, *Genetics* **156**, 927–931 (2000).
2. M. Depczynski, D. R. Bellwood, *Curr. Biol.* **15**, R288–R289 (2005).
3. J. Nielsen *et al*., *Science* **353**, 702–704 (2016).
4. C. López-Otín, M. A. Blasco, L. Partridge, M. Serrano, G. Kroemer, *Cell* **153**, 1194–1217 (2013).
5. P. P. Singh, B. A. Demmitt, R. D. Nath, A. Brunet, *Cell* **177**, 200–220 (2019).
6. M. S. Love, M. Yoklavich, L. Thorsteinson, *The Rockfishes of the Northeast Pacific* (Univ. of California Press, ed. 1, 2002).
7. D. L. Rabosky *et al*., *Nature* **559**, 392–395 (2018).
8. M. Seppey, M. Manni, E. M. Zdobnov, in *Gene Prediction: Methods and Protocols*, M. Kollmar, Ed. (Methods in Molecular Biology, Springer, 2019), pp. 227–245.
9. Materials and methods are available as supplementary materials.
10. J. R. Hyde, R. D. Vetter, *Mol. Phylogenet. Evol.* **44**, 790–811 (2007).
11. M. Keane *et al*., *Cell Rep.* **10**, 112–122 (2015).
12. V. Quesada *et al*., *Nat. Ecol. Evol.* **3**, 87–95 (2019).
13. A. Kowalczyk *et al*., *Bioinformatics* **35**, 4815–4817 (2019).
14. M. Mangel, H. K. Kindsvater, M. B. Bonsall, *Evolution* **61**, 1208–1224 (2007).
15. S. N. Austad, K. E. Fischer, *J. Gerontol.* **46**, B47–B53 (1991).
16. T. Umehara *et al*., *Aging Cell* **16**, 1288–1299 (2017).
17. M. Deng *et al*., *Nat. Commun.* **11**, 2193 (2020).
18. V. Tandon, L. de la Vega, S. Banerjee, *J. Biol. Chem.* **296**, 100233 (2021).
19. D. E. Promislow, *J. Gerontol.* **48**, B115–B123 (1993).
20. M. Todesco *et al*., *Nature* **584**, 602–607 (2020).
21. P. H. Sudmant *et al*., *Science* **349**, aab3761 (2015).
22. H. A. Arnett, J. L. Viney, *Nat. Rev. Immunol.* **14**, 559–569 (2014).
23. R. Valentonyte *et al*., *Nat. Genet.* **37**, 357–364 (2005).
24. K. M. Wright *et al*., *G3* **9**, 2863–2878 (2019).
25. M. Malmstrøm *et al*., *Nat. Genet.* **48**, 1204–1210 (2016).
26. S. Schiffels, R. Durbin, *Nat. Genet.* **46**, 919–925 (2014).
27. R. Cui *et al*., *Cell* **178**, 385–399.e20 (2019).
28. S. I. Nikolaev *et al*., *Proc. Natl. Acad. Sci. U.S.A.* **104**, 20443–20448 (2007).
29. K. Popadin, L. V. Polishchuk, L. Mamirova, D. Knorre, K. Gunbin, *Proc. Natl. Acad. Sci. U.S.A.* **104**, 13390–13395 (2007).
30. J. Rolland, D. Schluter, J. Romiguier, *Mol. Biol. Evol.* **37**, 2192–2196 (2020).
31. E. R. Pianka, *Am. Nat.* **104**, 592–597 (1970).
32. E. S. Deevey Jr., *Q. Rev. Biol.* **22**, 283–314 (1947).
33. D. R. Barneche, D. R. Robertson, C. R. White, D. J. Marshall, *Science* **360**, 642–645 (2018).
34. M. A. W. Sayres, C. Venditti, M. Pagel, K. D. Makova, *Evolution* **65**, 2800–2815 (2011).
35. A. P. Martin, S. R. Palumbi, *Proc. Natl. Acad. Sci. U.S.A.* **90**, 4087–4091 (1993).
36. H. Jónsson *et al*., *Nature* **549**, 519–522 (2017).
37. L. Ségurel, M. J. Wyman, M. Przeworski, *Annu. Rev. Genomics Hum. Genet.* **15**, 47–70 (2014).
38. J. G. Tate *et al*., *Nucleic Acids Res.* **47**, D941–D947 (2019).
39. K. Harris, J. K. Pritchard, *eLife* **6**, e24284 (2017).
40. G. Owens, R. Kolora, P. Sudmant, sudmantlab/rockfishgenomeproject: RGP_codebase_v1.3, version 1.3, Zenodo (2021); https://doi.org/10.5281/zenodo.5535007.

ACKNOWLEDGMENTS

We acknowledge L. Smith and A. Bentley of the University of Kansas Biodiversity Institute and M. Miya at Chiba Natural History Museum and Institute for their assistance in sample acquisition. We thank the National Oceanic and Atmospheric Administration's Alaska Fisheries Science Center, RACE Division, for specimens collected during resource assessment surveys. Fish image credits: Kyoto University, Fish Collection; SWFSC ROV Team; R. R. Lauth, Alaska Fisheries Science Center; D. E. Stevenson, Alaska Fisheries Science Center; J.W.O.; J. Nichols; C. Grossman; D. Karimoto; P. Ridings; K. Lee; M. Chamberlain; M. Guimaraes; and S. Geitler. We also thank M. Slatkin for helpful discussions. **Funding:** National Institute of General Medical Sciences grant R35GM142916 to P.H.S. **Author contributions:** P.H.S. conceptualized and designed the experiment. A.S., C.J., K.S., J.A.V., K.M., M.M., M.W.S., J.W.O., and M.L. coordinated sample collection efforts. S.R.R.K., G.L.O., J.M.V., and P.H.S. performed all analyses. K.C. and D.B. performed Hi-C experiments for genome assembly. P.H.S., G.L.O., S.R.R.K., and M.L. wrote the manuscript. **Competing interests:** The authors declare no competing interests. **Data and materials availability:** All sequencing data have been deposited in the European Nucleotide Archive under accession PRJEB42258. Complete methods are described in the supplementary materials (*9*), and all code required to recapitulate analyses, including BUSCO gene alignments and gene trees, has been posted at Zenodo (*40*).

SUPPLEMENTARY MATERIALS

science.org/doi/10.1126/science.abg5332
Materials and Methods
Figs. S1 to S23
Tables S1 to S17
References (*41*–*84*)
MDAR Reproducibility Checklist

12 November 2021; resubmitted 27 May 2021
Accepted 7 October 2021
10.1126/science.abg5332

DYNAMIC BIOSCAFFOLDS

Bioactive scaffolds with enhanced supramolecular motion promote recovery from spinal cord injury

Z. Álvarez[1,2], A. N. Kolberg-Edelbrock[1,3], I. R. Sasselli[1,4]†, J. A. Ortega[1,5], R. Qiu[1,4], Z. Syrgiannis[1,4], P. A. Mirau[6], F. Chen[1], S. M. Chin[1,4], S. Weigand[7], E. Kiskinis[1,5], S. I. Stupp[1,2,3,4,8]*

The signaling of cells by scaffolds of synthetic molecules that mimic proteins is known to be effective in the regeneration of tissues. Here, we describe peptide amphiphile supramolecular polymers containing two distinct signals and test them in a mouse model of severe spinal cord injury. One signal activates the transmembrane receptor β1-integrin and a second one activates the basic fibroblast growth factor 2 receptor. By mutating the peptide sequence of the amphiphilic monomers in nonbioactive domains, we intensified the motions of molecules within scaffold fibrils. This resulted in notable differences in vascular growth, axonal regeneration, myelination, survival of motor neurons, reduced gliosis, and functional recovery. We hypothesize that the signaling of cells by ensembles of molecules could be optimized by tuning their internal motions.

Pharmacological signaling of cells usually proceeds through the strong binding of small organic molecules to proteins that activate or inhibit particular responses. An emerging signaling strategy is to use nanostructures that target specific cells to deliver a therapeutic cargo or materials functioning as bioactive scaffolds in the extracellular space. Cell-signaling materials that trigger the regeneration of tissues mimic the fibrillar components of natural extracellular matrices (ECMs) (*1*). Mechanobiology has been an important part of the science behind this idea on the basis of the discovery that stiffness and viscoelasticity of materials can mediate multiple aspects of cell behavior (*2*).

Less-developed aspects of this field are the molecular design of materials bearing signals for receptors and the connections between such signals and the motions of molecules within artificial scaffolds. Bioactive signals have been incorporated into covalent polymers (*3*) and more recently in supramolecular polymers (*4*). A commonly investigated signal has been the peptide RGDS, present in extracellular fibrils, such as fibronectin, that promote cellular adhesion. Supramolecular polymers, which form by noncovalent association among monomers, have potential advantages for regenerative signaling because of the easy tunability of signal density, their ability to architecturally mimic the high-persistence length of natural ECM fibrils, and their rapid biodegradation after they serve their function (*5*).

Here, we report a supramolecular scaffold of nanoscale fibrils that integrates two different orthogonal biological signals—the laminin signal IKVAV known to promote differentiation of neural stem cells into neurons and to extend axons (*1*) and the fibroblast growth factor 2 (FGF-2) mimetic peptide YRSRKYSSWYVALKR, which activates the receptor FGFR1 to promote cell proliferation and survival (*6*). The two signals were placed at the termini of two different peptides with alkyl tails, known as peptide amphiphiles (PAs), that copolymerize noncovalently in aqueous media to form supramolecular fibrils. It was previously shown that the IKVAV signal on PA supramolecular polymers could restore partial function after a mild compression injury in a mouse model of spinal cord injury (SCI) (*7*). Fibril-forming PA molecules that display biological signals at one terminus contain peptide domains between the bioactive moiety and the alkyl tail that can be modified to tune mechanical properties (*8*, *9*).

We therefore investigated different domains that alter the physical properties of a potential scaffold therapy to restore functional recovery in vivo after hind limb paralysis in a murine model of severe SCI. The development of SCI therapies that avoid permanent paralysis in humans after traumatic injuries remains a major challenge given the inability of damaged axons to regenerate in the adult central nervous system (CNS) (*10*, *11*). We found that keeping both biological signals at the same density while slightly mutating the tetrapeptide sequence of these domains could markedly change the biological responses of cells in vitro as well as the functional recovery from SCI in mice in vivo.

Supramolecular polymer synthesis and characterization

To investigate nanofiber-shaped supramolecular polymers with different physical properties that display the same two signals, we synthesized a library of different IKVAV PAs in which the tetrapeptide domain controlling physical behavior has different sequences of the amino acids V, A, and G (IKVAV PA1 to PA8) (see Fig. 1A, fig. S1, and table S1 for the list of PAs used and their peptide sequences). These amino acids were selected because they affect the propensity of molecules within the fibrils to form β sheets, which have high intermolecular cohesion as a result of their hydrogen bond density. These interactions in turn result in suppressed mobility of PA molecules within the fibril. For example, V_2A_2 (PA1) has a high propensity to form β sheet structure because of its valine content, whereas A_2G_2 (PA2) is potentially a less-ordered segment without secondary structure (Fig. 1A). The rest of the sequences were selected as potential candidates for an intermediate level of motion. All IKVAV PAs utilized the sequence E_4G, which spaces this segment from the bioactive signal and provides high solubility in water (*12*).

Cryo–transmission electron microscopy (cryo-TEM) revealed that all IKVAV PAs formed nanofibers after supramolecular polymerization in water (Fig. 1B). Furthermore, synchrotron solution small-angle x-ray scattering (SAXS) confirmed the formation of filaments, revealing a slope in the range of –1 to –1.7 in the Guinier region except for that of PA5, which suggests a mixture of filaments and spherical micelles (slope = –0.2) (Fig. 1D). We also compared the physical behavior of the various assemblies in the library using coarse-grained molecular dynamic (CG-MD) simulations using the MARTINI force field (*13*) (fig. S2 and supplementary materials). These simulations predicted that molecules within the various IKVAV PA fibers had different degrees of internal dynamics (Fig. 1B). Differences in the ability of the molecules to change positions internally over appreciable distances (on the order of nanometers) were suggested by the simulations, which yielded values of the parameter defined as the root mean square fluctuation (RMSF), which is a measure of the average displacement of a PA molecule during the last 5 μs of the simulation (Fig. 1C). These simulations indicate that molecules in PA2 fibers do in fact have a high degree of internal motion, including PA5, which only contains G residues. Wide-angle x-ray scattering (WAXS) also revealed the

[1]Simpson Querrey Institute for BioNanotechnology, Northwestern University, Chicago, IL 60611, USA. [2]Department of Medicine, Northwestern University, Chicago, IL 60611, USA. [3]Department of Biomedical Engineering, Northwestern University, Evanston, IL 60208, USA. [4]Department of Chemistry, Northwestern University, Evanston, IL 60208, USA. [5]The Ken & Ruth Davee Department of Neurology, Department of Physiology, Feinberg School of Medicine, Northwestern University, Chicago, IL 60611, USA. [6]Materials and Manufacturing Directorate, Nanostructured and Biological Materials Branch, Air Force Research Laboratories, Wright-Patterson AFB, OH 45433, USA. [7]DuPont-Northwestern-Dow Collaborative Access Team Synchrotron Research Center, Northwestern University, DND-CAT, Argonne, IL 60439, USA. [8]Department of Materials Science and Engineering, Northwestern University, Evanston, IL 60208, USA.
*Corresponding author. Email: s-stupp@northwestern.edu
†Present address: Center for Cooperative Research in Biomaterials (CIC biomaGUNE), Basque Research and Technology Alliance (BRTA), Donostia, San Sebastián, 20014, Spain.

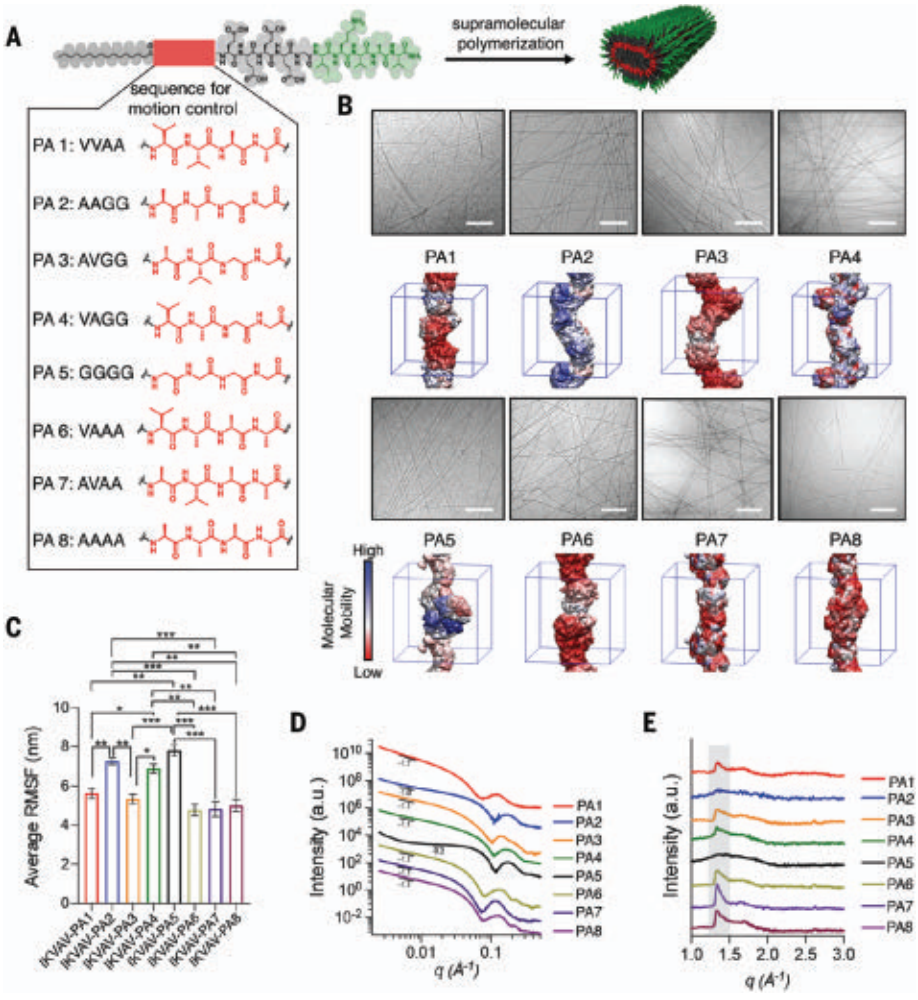


Fig. 1. Library of investigated IKVAV PA molecules. (**A**) Specific chemical structures of IKVAV PA molecules used and molecular graphics representation of a supramolecular nanofiber displaying the IKVAV bioactive signal. (**B**) Cryo-TEM micrographs of IKVAV PAs in the library and their corresponding color-coded representations of RMSF values for single IKVAV PA filaments. (**C**) Bar graphs of the average RMSF values of the different IKVAV PA molecules. Error bars correspond to three independent simulations. *P < 0.05; **P < 0.01; ***P < 0.001; one-way analysis of variance (ANOVA) with Bonferroni. (**D** and **E**) SAXS patterns (D) and WAXS profiles (E) of the different IKVAV PA nanofibers. The scattering intensities were offset vertically for clarity; the Bragg peak corresponding to the β sheet spacing around 1.35 Å is framed in a gray box. a.u., arbitrary units. Scale bars, 200 nm.

presence of internal order (β sheet Bragg peak with a d-spacing of 4.65 Å) in all the IKVAV PAs except for those with low RMSF values (PA2 and PA5) (Fig. 1E).

To probe differences in dynamics among the IKVAV PAs, we performed fluorescence depolarization (FD) measurements by encapsulating 1,6-diphenyl-1,3,5-hexatriene (DPH) within PA nanofibers to measure the microviscosity of the inner hydrophobic core. As expected, PA2 and PA5 had the lowest anisotropy values (0.21 and 0.18, respectively), indicating that they formed the most dynamic supramolecular assemblies; PA4 had intermediate dynamics (0.30); and the remaining PAs had less-intense supramolecular motion (0.40 to 0.37) (Fig. 2A). We also measured molecular dynamics in the IKVAV epitope using transverse-relaxation nuclear magnetic resonance (T2-NMR) spectroscopy. These experiments obtained the relaxation rate for the methylene protons attached to the ε carbon ($H_ε$) of the K residue in the IKVAV sequence [observed at 2.69 to 2.99 parts per million (ppm)] (figs. S3 to S10 and table S2). IKVAV PA1 showed the highest relaxation rate (a low degree of motion), whereas IKVAV PA2 and PA5 had the lowest relaxation rates in the IKVAV PA library (^{1}H-R_2 = 2.7 ± 0.1 and 2.6 ± 0.003 s^{-1}, respectively, consistent with greater motion) (Fig. 2B, figs. S3 to S10, and table S2). Consistent with FD results, IKVAV PA4 revealed an intermediate level of supramolecular motion, between that of PA1 and PA2 (or PA5). Collectively, the simulations as well as the FD, WAXS, and T2-NMR measurements are consistent with three levels of supramolecular motion in the library of molecules investigated.

Supramolecular motion and in vitro bioactivity

We performed in vitro experiments to determine whether the IKVAV signal was equally bioactive in the library of IKVAV PAs. To establish the bioactivity of IKVAV PAs, neural progenitor cells derived from human embryonic stem cells [human neural progenitor cells (hNPCs)] were treated either with the different IKVAV PA fibers in solution or the recombinant protein laminin (Fig. 2C). PA filaments associate closely with cells and can activate receptors when their surfaces display signals (*14*).

We first investigated the activation of the transmembrane receptor β1-INTEGRIN (ITGB1), known to be expressed in the presence of IKVAV PAs and laminin (*15*–*17*), using the active form–specific antibody HUTS4 and also verified activation of the receptor's intracellular signaling pathway. Fluorescence confocal microscopy and Western blot (WB) analysis showed that IKVAV PA2 and PA5 induced significantly higher concentrations of active ITGB1 and the downstream effectors integrin-linked kinase (ILK) and phospho-focal adhesion kinase (p-FAK) relative to the rest of the IKVAV PAs, the IKVAV peptide, and laminin or ornithine coatings as controls (Fig. 2, D and E, and figs. S11 and S12). We observed an intermediate level of activation with PA4 that correlated with its intermediate supramolecular motion relative to the rest of the PAs in the library. As expected, PAs displaying the VVIAK scrambled sequence resulted in minimal cellular activation of ITGB1 (figs. S12 and S13). Furthermore, pretreatment with an ITGB1 antibody blocked the attachment of hNPCs on all IKVAV PAs, which suggests that an IKVAV-ITGB1 interaction mediated this process (fig. S14).

Although hNPCs up-regulated the neuronal form of β-TUBULIN (TUJ-1$^+$) when treated with IKVAV PAs, this induction (which reflects neuronal differentiation commitment) was higher for IKVAV PA2 and PA5 (20.5 ± 1% and 20.7 ± 1.2%, respectively), the two most dynamic supramolecular fibrils (Fig. 2, F to H, and fig. S15). The other IKVAV PAs, with the exception of IKVAV PA4 that showed an intermediate neuronal differentiation commitment (PA4: 14 ± 1.2%), had a lower percentage of induction of TUJ-1$^+$ neuronal cells (PA1: 8.2 ± 0.7%; PA3: 7.5 ± 0.6%; PA6: 7.9 ± 1.3%; PA7: 7.4 ± 0.6%; and PA8: 7.5 ± 0.5%). By using

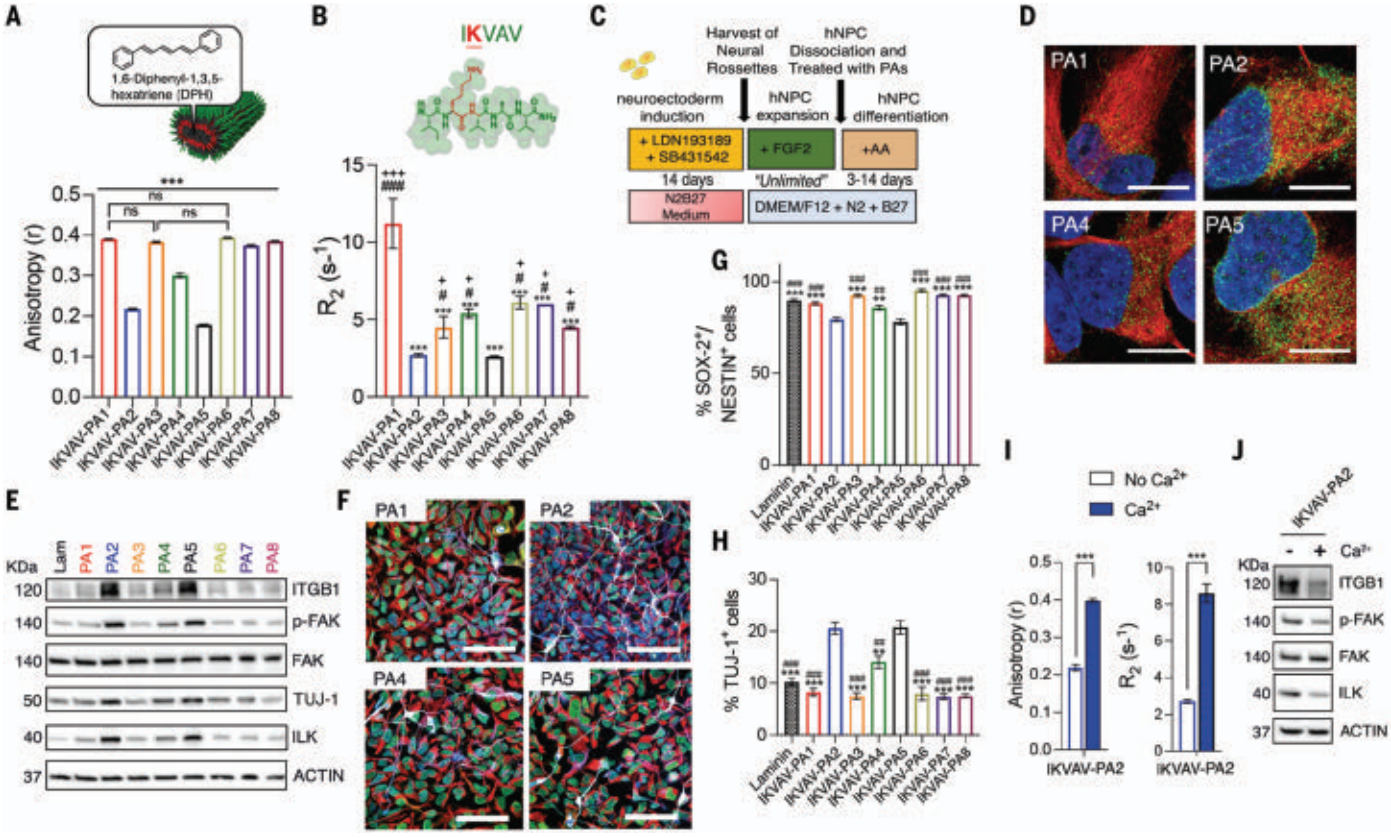


Fig. 2. Effect of supramolecular motion on hNPCs signaling in vitro. (**A**) (Top) Molecular graphics representation of an IKVAV PA nanofiber indicating the chemical structure and location of DPH used as a probe in fluorescence depolarization measurements. (Bottom) Bar graph of fluorescence anisotropy of IKVAV PA solutions. Error bars correspond to three independent experiments. n.s., not significant; ***$P < 0.0001$; one-way ANOVA with Bonferroni. (**B**) (Top) Chemical structure of the IKVAV peptide sequence, highlighting the K residue probed by NMR. (Bottom) Bar graph of the K relaxation time for the different IKVAV PAs investigated. Error bars correspond to three runs per condition. ***$P < 0.0001$ versus IKVAV PA1; $^{\#}P < 0.05$, $^{\#\#\#}P < 0.0001$ versus IKVAV PA2; and $^{+}P < 0.05$, $^{+++}P < 0.0001$ versus IKVAV PA5; one-way ANOVA with Bonferroni. (**C**) Differentiation conditions used for hNPCs. DMEM, Dulbecco's minimum essential medium. (**D**) Representative micrographs of hNPCs treated with IKVAV PA1, PA2, PA4, and PA5. NESTIN indicates the stem cells in red, ITGB1 indicates the receptors in green, and 4′,6-diamidino-2-phenylindole (DAPI) indicates the nuclei in blue. (**E**) WB results of ITGB1, p-FAK, FAK, ILK, and TUJ-1 in hNPCs treated with laminin (Lam) and the various IKVAV PAs. (**F**) Representative confocal micrographs of hNPCs treated with IKVAV PA1, PA2, PA4, and PA5. NESTIN indicates stem cells (red), SOX-2 indicates stem cells (green), TUJ-1 indicates neurons (white), and DAPI indicates nuclei (blue). (**G** and **H**) Bar graphs of the percentage of SOX-2^+ and NESTIN$^+$ stem cells (G) and TUJ-1^+ neuronal cells (H) treated with the various IKVAV PAs. Error bars correspond to three independent differentiations. **$P < 0.01$, ***$P < 0.001$ versus IKVAV PA2 and $^{\#\#}P < 0.01$, $^{\#\#\#}P < 0.001$ versus IKVAV PA5; one-way ANOVA with Bonferroni. (**I**) Fluorescence anisotropy (left) and K residue relaxation times (right) obtained for IKVAV PA2 nanofibers in the absence (no Ca^{2+}) or presence (Ca^{2+}) of calcium ions. ***$P < 0.001$; Student's t test. (**J**) WB results of ITGB1, p-FAK, FAK, and ILK in hNPCs treated with IKVAV PA2 in the absence (−) or presence (+) of Ca^{2+}. Scale bars, 10 μm (D) and 100 μm (F).

puromycin-based protein synthesis analysis [the surface sensing of translation (SUnSET) technique], we verified that all of the conditions showed similar protein translation levels, so the observed differences were not linked to a metabolic effect (fig. S16).

We also performed in vitro experiments in which hNPCs were treated with the most bioactive IKVAV PAs (PA2 and PA5) mixed with 5 mM $CaCl_2$, which is known to electrostatically cross-link negatively charged PA fibers (*18*, *19*). The addition of Ca^{2+} suppressed supramolecular motion, which was confirmed by FD and T2-NMR experiments (Fig. 2I and fig. S17). When supramolecular motion was decreased by adding Ca^{2+} ions to the media, the activation of ITGB1 and its downstream intracellular pathway (ILK and p-FAK–FAK) also decreased (Fig. 2J and fig. S18). These results showed a strong positive correlation between dynamics and in vitro bioactivity, as mutations were introduced in the tetrapeptide amino acid sequence in the nonbioactive domain of IKVAV PAs.

SCI model: Axon regrowth and formation of glial scar

We then proceeded to test the ability of dual-signal fibrils to enhance functional recovery after SCI in vivo. Given the low level of in vitro bioactivity observed for IKVAV PA1, PA3, PA4, PA6, PA7, and PA8, we did not to use these PAs in combination with the FGF2 PAs. We also needed nanofibers that display both signals simultaneously, so the binary systems had to be miscible and form hydrogels with similar mechanical properties upon contact with physiological fluids once injected at the site of the injury. Only IKVAV PA2 was both miscible and could form hydrogels with similar mechanical properties when mixed with either FGF2 PA1 or FGF2 PA2, particularly at a molar ratio of 90:10 (Fig. 3, A to C; fig. S19; and table S3). Furthermore, both FGF2 PAs alone formed highly aggregated short fibers that further contributed

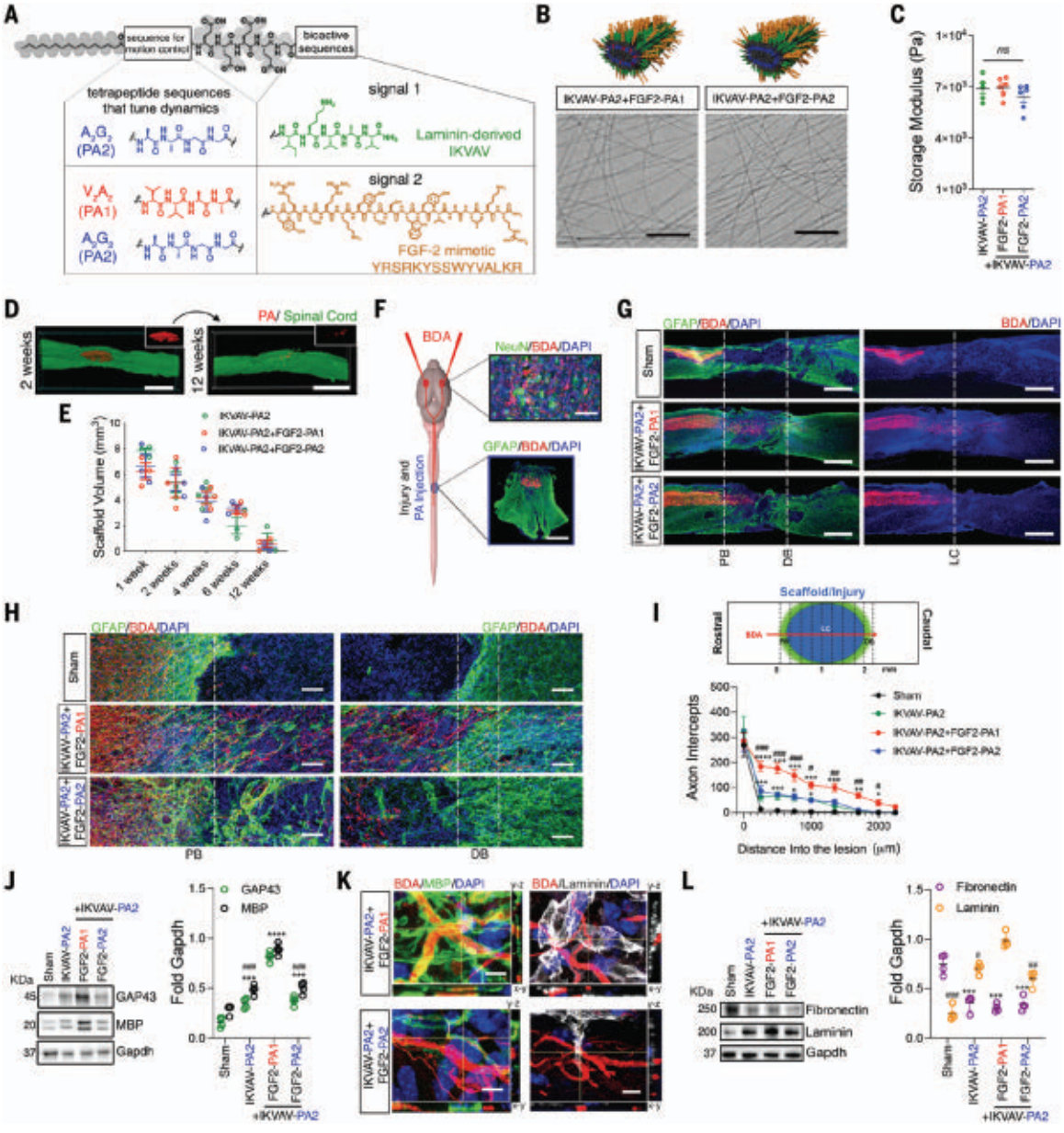


Fig. 3. Two chemically different PA scaffolds with two identical bioactive sequences reveal differences in growth of corticospinal axons after SCI. (**A**) Chemical structures of the two PA molecules used. (**B**) (Top) Molecular graphics representation of a supramolecular nanofiber displaying two bioactive signals. (Bottom) Cryo-TEM micrographs of IKVAV PA2 coassembled with FGF2 PAs (FGF2 PA1 and FGF2 PA2). (**C**) Storage modulus of IKVAV PA2 (green) and their respective coassemblies with FGF2 PAs (FGF2 PA1, red; FGF2 PA2, blue). (**D**) Fluorescent micrographs of spinal cords (green) injected with IKVAV PA2 + FGF2 PA1 (red) covalently labeled with Alexa 647. (**E**) Dot plot of PA scaffold volume as a function of time after implantation. (**F**) (Left) Schematic illustration showing the site of BDA and PA injections. (Right) Fluorescent micrographs of the brain cortex (top)—stained for NeuN, neurons (green); BDA, labeled neurons (red); and DAPI, nuclei (blue)—and transverse spinal cord section (bottom)—stained for GFAP, astrocytes (green); BDA, labeled descending axons (red); and DAPI, nuclei (blue). (**G**) Fluorescent micrographs of longitudinal spinal cord sections in sham, IKVAV PA2 + FGF2 PA1, and IKVAV PA2 + FGF2 PA2 groups. GFAP indicates astrocytes (green), BDA indicates labeled axons (red), and DAPI indicates nuclei (blue); vertical white dashed lines indicate the proximal border (PB), the distal border (DB), and the central part of the lesion (LC). (**H**) Representative magnified images of those shown in (G). (**I**) (Top) Schematic lesion site and vertical lines used to count the number of axons crossing at each location indicated. (Bottom) Plot of the number of crossing axons. Error bars correspond to six animals per group. $^{*}P < 0.05$, $^{**}P < 0.01$, $^{***}P < 0.001$ versus sham and $^{\#}P < 0.05$, $^{\#\#}P < 0.01$, $^{\#\#\#}P < 0.001$ versus IKVAV PA2 and IKVAV PA2 + FGF2 PA2 groups; repeated measures of two-way ANOVA with Bonferroni. (**J**) WB results (left) and dot plot of the normalized values for GAP43 and MBP protein in sham, IKVAV PA2, IKVAV PA2 + FGF2 PA1, and IKVAV PA2 + FGF2 PA2 (right). $^{**}P < 0.01$, $^{***}P < 0.001$ versus sham and $^{\#\#\#}P < 0.001$ versus IKVAV PA2 + FGF2 PA1 group; one-way ANOVA with Bonferroni. (**K**) Representative three-dimensional fluorescent micrographs of BDA-labeled axon regrowth (red) and myelin basic protein (MBP) (green) (left) and laminin (white) (right). (**L**) WB results (left) and dot plot of the normalized values for laminin and fibronectin expression in conditions described in (J) (right). $^{***}P < 0.001$ versus sham and $^{\#}P < 0.05$, $^{\#\#}P < 0.01$, $^{\#\#\#}P < 0.001$ versus IKVAV PA2 + FGF2 PA1 group; one-way ANOVA with Bonferroni. Gapdh, glyceraldehyde-3-phosphate dehydrogenase. Data points in (E) correspond to three animals per group and to four animals per group in (J) and (L). Scale bars, 1500 μm [(D) and (G)], 25 μm [(F) top], 200 μm [(F) bottom], 100 μm (H), and 2 μm (K).

to immiscibility with other IKVAV PAs, such as PA1, PA4, or PA5 (figs. S20 and S21).

The miscible and gel-forming binary systems with similar mechanical properties—IKVAV PA2 with either FGF2 PA1 or FGF2 PA2—were taken forward to in vivo experiments (Fig. 3A and fig. S22; for full characterization of these systems, see supplementary text). We injected saline solutions of 90:10 molar ratio of IKVAV PA2 coassembled with either FGF2 PA1 or with FGF2 PA2 into the spinal cord of mice 24 hours after a severe contusion in an established murine model of SCI (see supporting information for specific details of the animal model protocol) (*20*). IKVAV PA2, which was the most bioactive single signal system, was used as a control in all in vivo experiments. All PA solutions gelled in situ when delivered into the spinal cord and localized into the damaged area. To track and quantify the bioactive scaffold's biodegradation as a function of time, the PA molecules were fluorescently labeled with Alexa 647 dye. We then injected the fluorescent materials into the spinal cord 24 hours after injury and measured their volume at 1, 2, 4, 6, and 12 weeks by fully reconstructing spinal cords using spinning disk confocal microscopy (Fig. 3D and supplementary materials). The soft materials biodegraded gradually within a period of 1 to 12 weeks after implantation, and we did not observe any differences in biodegradation rate among the three experimental materials (Fig. 3E and fig. S23).

We performed bilateral injections of biotinylated dextran amine (BDA) administered 10 weeks after the injury into the sensorimotor cortex to trace the corticospinal tracts (CSTs), which mediate voluntary motor function (Fig. 3F) (*21*). We evaluated anterogradely labeled CST axon regrowth 12 weeks after injury in all PA and sham (injected with saline solution only) groups. This process required quantification of the number of labeled axons that regrew to the proximal lesion border and beyond. We also injected IKVAV PA1 and PA fibers lacking any bioactive signals on their surfaces (backbone PA) as controls (see fig. S24 and table S1 for the peptide sequence).

In mice injected with saline solution, we hardly observed any regrown axons within the lesion, whereas we observed some regrowth of axons for IKVAV PA1, in which fibers exhibited low mobility (Fig. 3G and fig. S25; see supplementary text for additional PA controls). By contrast, in mice injected with IKVAV PA2 alone or coassembled with FGF2 PA2 (which shares the same A_2G_2 nonbioactive domain as that in IKVAV PA2), we only observed a modest but increased axon regrowth compared with that seen in the sham condition. However, injections of IKVAV PA2 coassembled with FGF2 PA1 (which includes the V_2A_2 nonbioactive domain instead of A_2G_2) led to robust corticospinal axon regrowth across the lesion site, even surpassing its distal border (Fig. 3, G and H, and fig. S26). In this group, the total axon regrowth within the lesion was twofold greater than that in the group using the coassembly of IKVAV PA2 and FGF2 PA2 and 50-fold greater than in the sham group (Fig. 3I). Serotonin axons (5HT), which may also play a role in locomotor function, also regrew within the lesion core with a similar trend as that observed with CST (fig. S27).

We hypothesize that the CST and 5HT axon regrowth observed could be in part the result of the absence of a substantial astrocytic scar, which is a strong barrier for axonal regeneration (*11*). In the sham and backbone PA groups, this barrier was revealed as a dense population of reactive astrocytes expressing high levels of glial fibrillary acidic protein (GFAP) at the borders of the injury, whereas in all bioactive PA groups, the glial scar was less dense (Fig. 3H and figs. S25 and S26). In agreement with these results, WB analysis showed a higher level of growth-associated protein 43 (GAP-43), which resides in the growth cone of regenerating axons, only in the most bioactive coassembly (IKVAV PA2 + FGF2 PA1) (Fig. 3J).

Finally, we determined whether PA scaffolds could induce remyelination of corticospinal axons 3 months after injury and found high levels of myelin basic protein (MBP) within the lesion, particularly wrapping the regrown axons in IKVAV PA2 + FGF2 PA1 (Fig. 3, J and K). Moreover, in this condition, we observed many growing axons within the lesion to be in contact with high levels of laminin and low levels of fibronectin, indicative of a reduced fibrotic core (Fig. 3, K and L, and fig. S26). Our histological and biochemical observations suggested that physical differences between the two supramolecular coassemblies bearing two bioactive signals could greatly enhance neuroregenerative outcomes after injury.

SCI model: Angiogenesis, cell survival, and functional recovery

We next explored the effect of both dual-signal coassemblies on angiogenesis at the site of injury, which is important for a fully anatomical and functional regeneration. Relative to uninjured tissue sections, the transverse spinal cord sections of sham mice revealed a substantial degree of tissue degeneration extending rostro-caudally >2.0 mm away from the center of the lesion. In this case, a significant decrease in vascular area fraction, vascular length, and branching was observed compared with that observed in the uninjured control (Fig. 4, A and B). We assessed the existence of a functional vessel network by transcardially injecting a glucose solution containing 1,1′-dioctadecyl-3,3,3′,3′-tetramethylindocarbocyanine perchlorate (DiI), a lipophilic carbocyanine dye that incorporates into endothelial cell membranes (Fig. 4A) (*22*). In groups treated with PA scaffolds, there was high preservation of the ventral tissue structure, revealing the maintenance of a functional blood vessel network. However, we again observed that treatment with the most bioactive coassembly led to an increase in vascular area fraction, vascular length, and branching, especially in the dorsal region (Fig. 4, A and B, and fig. S28). These parameters did not differ significantly between the IKVAV PA2 alone and the less bioactive coassembly group (IKVAV PA2 + FGF2 PA2), which implies that the mimetic FGF2 angiogenic signal was not functioning optimally in IKVAV PA2 + FGF2 PA2.

To determine the origin of the blood vessels within the lesion, the thymidine analog 5′-bromo-2′-deoxyuridine (BrdU) was intraperitoneally injected during the first week after injury, and we observed newly formed blood vessels within the lesion of the most bioactive coassembly group 12 weeks after injury. This was confirmed by a significant increase in the number of double positive $BrdU^+$ and $CD31^+$ cells relative to samples for all other groups (Fig. 4, C and D, and fig. S29) as well as by WB analysis (Fig. 4E). The IKVAV PA2 + FGF2 PA2 coassembly and IKVAV PA2 alone led to a very modest but significantly increased blood vessel formation compared with that observed in the sham group.

We also assessed the effect of both dual-signal coassemblies on neuronal survival, maintenance of spinal circuitry, and local function. Native FGF-2 has previously been associated with an increase in neuronal viability after SCI (*23*). Transverse spinal cord sections of the most bioactive coassembly group showed $NeuN^+$ neurons near the newly generated vessels in the dorsal region similar to the uninjured control group (Fig. 5A). Furthermore, neurons ($NeuN^+$ cells) that were also $ChAT^+$ (motor neurons) were only found in the ventral horn when PAs were utilized, showing a significantly higher number in the most bioactive system relative to other groups (Fig. 5, B and C). The lack of any double positive $BrdU^+$ and $NeuN^+$ neurons within the lesion in any of the groups suggested the absence of local neurogenesis.

We investigated whether the observed axonal regeneration, angiogenesis, and local neuronal cell survival led to behavioral improvement in injured animals. For this purpose, we obtained Basso mouse scale (BMS) open field locomotor scores and locomotor recovery by footprint analysis in all groups during the 12 weeks after injury (Fig. 5D and fig. S30). At 1 week after injury and thereafter, all PA groups demonstrated significant and sustained behavioral improvement compared with that of the sham group. Notably, 3 weeks after

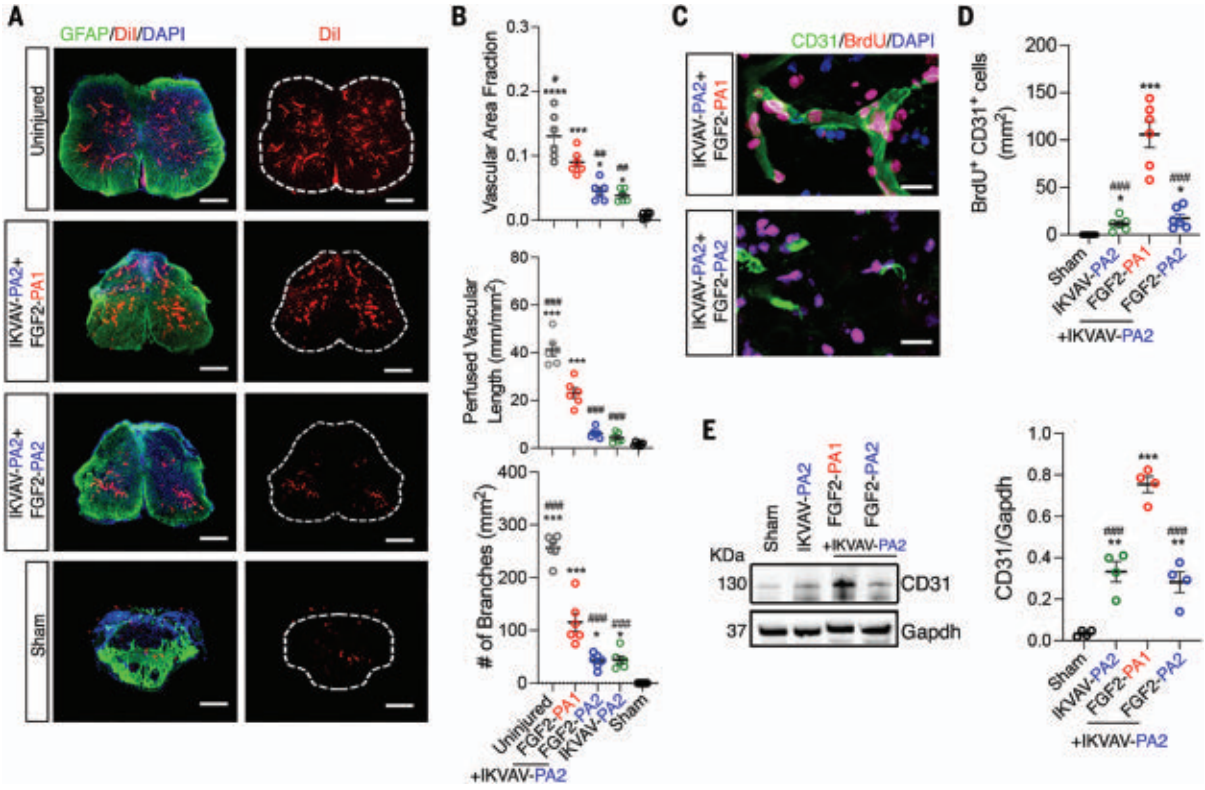


Fig. 4. Two chemically different PA scaffolds with two identical bioactive sequences reveal differences in angiogenesis. (**A**) Fluorescent micrographs of transverse spinal cord sections in uninjured, IKVAV PA2 + FGF2 PA1, IKVAV PA2 + FGF2 PA2, and sham groups. GFAP indicates astrocytes (green), DiI indicates labeled blood vessels (red), and DAPI indicates nuclei (blue). (**B**) Dot plots of the vascular area fraction, perfused vascular length, and number of branches in the transverse sections of groups in (A). $^{*}P < 0.05$, $^{***}P < 0.0001$ versus sham and $^{\#\#}P < 0.001$, $^{\#\#\#}P < 0.0001$ versus IKVAV PA2 + FGF2 PA1 group; one-way ANOVA with Bonferroni. (**C**) Fluorescent images of BrdU^{+} and CD31^{+} cells in the center of the lesion in animals injected with IKVAV PA2 + FGF2 PA1 and IKVAV PA2 + FGF2 PA2. CD31 indicates blood vessels (green), BrdU indicates newly generated cells (red), and DAPI indicates nuclei (blue). (**D**) Dot plot of the number of BrdU^{+} and CD31^{+} cells per square millimeter in groups treated with IKVAV PA2 alone, IKVAV PA2 + FGF2 PA1, IKVAV PA2 + FGF2 PA2, and saline (sham). $^{*}P < 0.05$, $^{***}P < 0.001$ versus sham and $^{\#\#\#}P < 0.0001$ versus IKVAV PA2 + FGF2 PA1 group; one-way ANOVA with Bonferroni. (**E**) WB results (left) and dot plot of the normalized values for CD31 protein (right). $^{**}P < 0.001$, $^{***}P < 0.0001$ versus sham and $^{\#\#\#}P < 0.001$ versus IKVAV PA2 + FGF2 PA1 group; one-way ANOVA with Bonferroni. Data points in (B) and (D) correspond to six animals per group and to four animals per group in (E). Scale bars, 200 μm (A) and 25 μm (C).

injury, mice treated with the most bioactive coassembly showed a significant functional recovery (5.9 ± 0.5) compared with that observed in mice injected with IKVAV PA2 + FGF2 PA2 and IKVAV PA2 alone (4.4 ± 0.5 and 4.3 ± 0.5, respectively) (Fig. 5D). Quantification of footprints revealed significantly larger stride lengths and widths in mice treated with the most bioactive coassembly relative to those of other groups (fig. S30). Collectively, these data suggest that the neuronal cell survival and functional recovery that we observed in dual-signal systems are unexpectedly linked to the differences in the chemical composition of their respective nonbioactive tetrapeptides.

In vitro results on human endothelial and neural progenitor cells

On the basis of the results described above, we next investigated the bioactivity of the FGF2 signal in vitro in both coassemblies using human umbilical vein vascular endothelial cells (HUVECs). As mentioned previously, native FGF-2 enhances endothelial cell proliferation and network formation (*24*), and we found that within 48 hours of culturing HUVECs on the most bioactive coassembly or FGF2 protein, there was extensive branching and formation of vessel-like capillary networks (Fig. 6, A and B, and fig. S31; see also supplementary materials for methodology used). We also performed WB analysis to verify whether the observed in vitro bioactivity of the FGF2 PA1 coassembled with the IKVAV PA2 was linked to the FGF-2 intracellular signaling pathway. HUVECs treated with the most bioactive coassembly or native FGF-2 revealed high levels of p-FGFR1 and the downstream proteins phospho–extracellular signal–regulated kinase 1 (p-ERK1) and p-ERK2 (p-ERK1/2), which activate the proliferation and migration of endothelial cells (Fig. 6C) (*6*, *25*). As expected, systems containing the scrambled FGF2 mimetic sequence did not reveal any bioactivity (figs. S31 and S32).

To establish the simultaneous bioactivity of the IKVAV and FGF2 signals in both coassemblies, we assessed the effects of these molecules on hNPC proliferation in vitro by quantifying the double positive EdU^{+} and SOX-2^{+} as well as the induction of ITGB1 and p-FGFR1 (Fig. 6, D to F, and fig. S33; see also supplementary text for more information). These experiments suggest that the FGF2 signal in the less bioactive coassembly is largely nonfunctional, whereas the IKVAV signal remains operative in both. These results are consistent with our observations in the SCI experiments.

Physical experiments and computer simulations on supramolecular motion

We investigated what might be the physical reasons for the loss of in vitro and in vivo bioactivity when the tetrapeptide that follows the

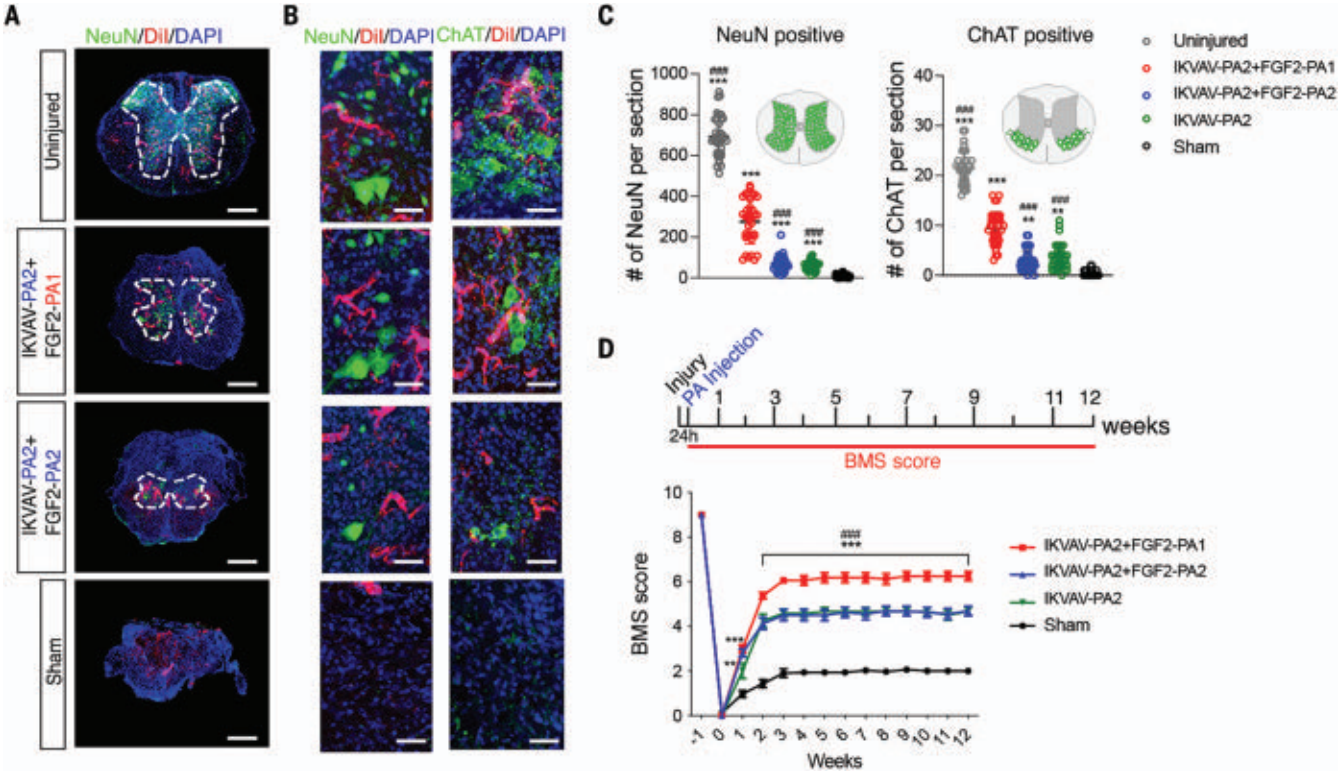


Fig. 5. Two chemically different PA scaffolds with two identical bioactive sequences reveal differences in neuronal survival and functional recovery. (**A**) Fluorescent micrographs of transverse spinal cord sections corresponding to uninjured, IKVAV PA2 + FGF2 PA1, IKVAV PA2 + FGF2 PA2, and sham groups. NeuN indicates neurons (green), DiI indicates labeled blood vessels (red), and DAPI indicates nuclei (blue); dashed lines indicate the gray matter (horn). (**B**) High-magnification images of the ventral horn area for slices in (A). On the left, NeuN indicates neurons (green), DiI indicates labeled blood vessels (red), and DAPI indicates nuclei (blue); on the right, ChAT indicates motor neurons (green), DiI indicates labeled blood vessels (red), and DAPI indicates nuclei (blue). (**C**) Dot plots showing the number of $NeuN^+$ (left) and $ChAT^+$ (right) cells per transverse section. Data points correspond to a total of 48 sections; eight sections per animal and six animals per group. $^{**}P < 0.01$, $^{***}P < 0.001$ versus sham and $^{\#\#\#}P < 0.001$ versus IKVAV PA2 + FGF2 PA1 group; one-way ANOVA with Bonferroni. (**D**) Experimental time line of in vivo experiments (top) and BMS for locomotion (bottom). Error bars correspond to 38 animals per group. $^{**}P < 0.001$, $^{***}P < 0.0001$ all PA groups versus sham and $^{\#\#\#}P < 0.0001$ versus IKVAV PA2 + FGF2 PA2 and IKVAV PA2 groups; repeated measures of two-way ANOVA with Bonferroni. Scale bars, 200 μm (A) and 20 μm (B).

alkyl tail was mutated from V_2A_2 to A_2G_2 in the FGF2 PAs. Differences in dynamics between FGF2 PA molecules in the two coassemblies were studied with T2-NMR spectroscopy and FD (Fig. 6, G to I). We measured the relaxation rates of the aromatic protons in Y and W amino acids, which are only present in the FGF2 mimetic signal (*26*, *27*). The rates were slower in the most bioactive coassembly, indicating greater supramolecular motion in the signaling peptide (^{1}H-R_2 = 49.3 ± 11 s^{-1} versus 80.9 ± 18.9 s^{-1} for the less bioactive coassembly) (Fig. 6, G and H, and fig. S34). We also carried out FD experiments on the two coassemblies using FGF2 PA molecules that were covalently labeled with a Cy3 dye (based on cryo-TEM images, the dye did not disrupt the supramolecular assemblies; fig. S35). A lower anisotropy was found in the most bioactive coassembly, indicating a higher mobility of the FGF2 signal molecules within the nanofibers (Fig. 6I).

CG-MD simulations supported the T2-NMR and FD results above by yielding higher RMSF values for FGF2 PA molecules in the most bioactive coassembly. The simulations also revealed that FGF2 PA molecules form clusters in both coassemblies (slightly larger in the most bioactive system) with a distribution of mobilities (RMSF values) (Fig. 6J, fig. S36, and supplementary materials). The decrease in bioactivity in one of the systems could be attributed to differences in the extent of coassembly between the two PA molecules bearing signals. However, one-dimensional proton nuclear magnetic resonance (1D ^{1}H-NMR), diffusion ordered spectroscopy (DOSY), and T2-NMR (*28*, *29*) of methylene units in alkyl tails indicate the occurrence of coassembly in both systems (figs. S37 to S39, table S4, and supplementary text).

The results obtained on greater degrees of motion in FGF2 PA1 molecules were counterintuitive because the tetrapeptide V_2A_2 (present in FGF2 PA1) had the least mobility in systems containing only IKVAV PA. The lower mobility in FGF2 PA2 molecules in the coassembly with IKVAV PA2 was likely the result of greater interactions through hydrogen bonding and side chain contacts among the identical tetrapeptides present in both molecules. By contrast, two dissimilar tetrapeptides are present in the two molecules of the highly bioactive IKVAV PA2 + FGF2 PA1 coassembly, which would not favor a strong interaction between both types of molecules and lead to higher degrees of supramolecular motion.

The evidence for a strong interaction between IKVAV PA2 and FGF2 PA2 and less motion is the essentially invariant circular dichroism (CD) spectrum when FGF2 PA2 is added to IKVAV PA2. However, the CD spectrum was modified when the less interactive FGF2 PA1 was added to IKVAV PA2, suggesting a disruption of secondary structure (fig. S40).

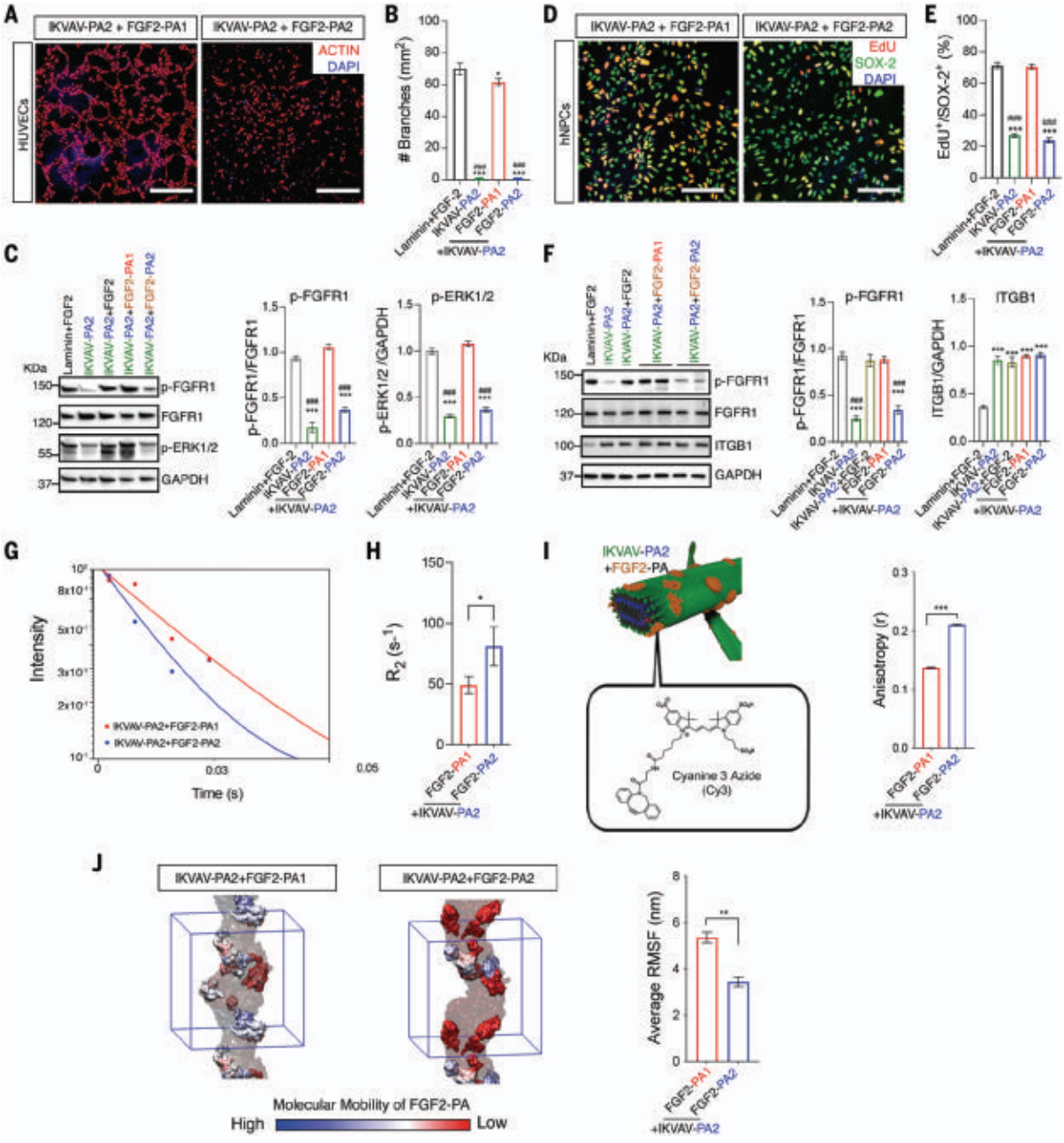


Fig. 6. Validating cell-signaling differences in vitro between two PA scaffolds exhibiting different supramolecular motion. (**A**) Confocal micrographs of HUVECs treated with IKVAV PA2 + FGF2 PA1 and IKVAV PA2 + FGF2 PA2. ACTIN indicates cytoskeleton (red) and DAPI indicates nuclei (blue). (**B**) Bar graph of the number of branches in HUVECs treated with laminin + FGF-2, IKVAV PA2 alone, IKVAV PA2 + FGF2 PA1, and IKVAV PA2 + FGF2 PA2. (**C**) WB results (left) and bar graphs of the normalized values for active FGFR1 (p-FGFR1) versus total FGFR1 (FGFR1) and active ERK1/2 (p-ERK1/2) using the conditions in (B) (right). (**D**) Confocal micrographs of hNPCs on coatings of IKVAV PA2 + FGF2 PA1 and IKVAV PA2 + FGF2 PA2. EDU indicates proliferative marker (red), SOX-2 indicates neural stem cell marker (green), and DAPI indicates nuclei (blue). (**E**) Bar graph of the percentage of EDU$^+$ and SOX-2$^+$ cells on the various coatings. (**F**) WB results (left) and bar graphs of the normalized values for active FGFR1 (p-FGFR1) versus total FGFR1 (FGFR1) and β1-INTEGRIN (ITGB1) (right). (**G**) ^{1}H-NMR spin-spin relaxation time of the aromatic protons in Y and W amino acids in the FGF2 mimetic signal at 6.81 ppm (solid lines are single linear best fits). (**H**) Bar graph of the aromatic relaxation times measured in (G). Error bars correspond to three runs per condition. $^*P < 0.05$; Student's t test. (**I**) Bar graph of fluorescence anisotropy of FGF2 PAs chemically modified with Cy3 dye. Error bars correspond to three independent experiments. $^{***}P < 0.001$; Student's t test. (**J**) Color-coded representation of RMSF values in clusters of FGF2 PAs (left) and the corresponding bar graph (right). IKVAV PA2 molecules are shown in transparent gray, ions and water molecules are removed for clarity, and the simulation box is shown in blue. Error bars correspond to five independent simulations. $^{**}P < 0.01$; Student's t test. Error bars in (B) and (E) correspond to three independent experiments and in (C) and (F) correspond to four independent experiments per condition. $^{***}P < 0.0001$ versus laminin + FGF2 and $^{\#\#\#}P < 0.0001$ versus IKVAV PA2 + FGF2 PA1; one-way ANOVA with Bonferroni. Scale bars, 200 μm (A) and 100 μm (D).

Thus, the greater motion detected by NMR for FGF2 PA1 molecules must indicate freer translational motion of its clusters within the fibrils or vertical motion of the signaling clusters in and out of the fibrils. Although we have gathered substantial evidence for the correlation between supramolecular motion and bioactivity of fibrillar scaffolds used here to promote SCI recovery, we could not directly link this physical phenomenon to our in vivo observations with techniques currently available.

Discussion

Our work demonstrates that bioactive scaffolds that physically and computationally reveal greater supramolecular motion lead to greater functional recovery from SCI in the murine model. In one-dimensional scaffolds of noncovalently polymerized bioactive molecules, we expected polyvalency effects to help cluster receptors for effective signaling. We also expected that the internal structure of the supramolecular scaffolds could limit free motion and favorably orient signals toward receptors perpendicular to their fibrillar axis. However, the unexpected finding in this work is that the intensity of molecular motions within the bioactive fibrils, as measured on the bench, correlated with enhanced axonal regrowth, neuronal survival, blood vessel regeneration, and functional recovery from SCI. A direct link between the motion and the recovery will require techniques not currently available that could precisely detect supramolecular motion in vivo with high resolution.

However, the computer simulations and experimental data do suggest that translation on the scale of nanometers within or vertically out of the assemblies to reach receptor sites might enhance bioactivity. That is, a highly agile and physically plastic supramolecular scaffold could be more effective at signaling receptors in cell membranes undergoing rapid shape fluctuations. An alternative hypothesis for the cause of the recovery could be broadly more-favorable interactions of the molecularly dynamic scaffolds with the protein milieu of the ECM. In the context of our correlative findings between supramolecular motion and bioactivity, it is intriguing to ask why there is such a prevalence of intrinsically disordered proteins in biological systems (*30*), and one wonders whether the added motion of disordered protein domains, in analogy to our bioactive and dynamic supramolecular fibrils, provides greater capacity to signal efficiently in the biological environment. We conclude that our observations suggest great opportunities in the structural design of dynamics to optimize the bioactivity of therapeutic supramolecular polymers.

REFERENCES AND NOTES

1. G. A. Silva *et al*., *Science* **303**, 1352–1355 (2004).
2. D. E. Discher, D. J. Mooney, P. W. Zandstra, *Science* **324**, 1673–1677 (2009).
3. B. K. Brandley, R. L. Schnaar, *Anal. Biochem.* **172**, 270–278 (1988).
4. J. D. Hartgerink, E. Beniash, S. I. Stupp, *Science* **294**, 1684–1688 (2001).
5. T. Aida, E. W. Meijer, S. I. Stupp, *Science* **335**, 813–817 (2012).
6. C. M. Rubert Pérez, Z. Álvarez, F. Chen, T. Aytun, S. I. Stupp, *ACS Biomater. Sci. Eng.* **3**, 2166–2175 (2017).
7. V. M. Tysseling-Mattiace *et al*., *J. Neurosci.* **28**, 3814–3823 (2008).
8. S. Sur, C. J. Newcomb, M. J. Webber, S. I. Stupp, *Biomaterials* **34**, 4749–4757 (2013).
9. J. H. Ortony *et al*., *Nat. Mater.* **13**, 812–816 (2014).
10. C. S. Ahuja *et al*., *Nat. Rev. Dis. Primers* **3**, 17018 (2017).
11. A. P. Tran, P. M. Warren, J. Silver, *Physiol. Rev.* **98**, 881–917 (2018).
12. J. E. Goldberger, E. J. Berns, R. Bitton, C. J. Newcomb, S. I. Stupp, *Angew. Chem. Int. Ed.* **50**, 6292–6295 (2011).
13. O.-S. Lee, V. Cho, G. C. Schatz, *Nano Lett.* **12**, 4907–4913 (2012).
14. A. N. Edelbrock *et al*., *Nano Lett.* **18**, 6237–6247 (2018).
15. L. Yap, H. G. Tay, M. T. X. Nguyen, M. S. Tjin, K. Tryggvason, *Trends Cell Biol.* **29**, 987–1000 (2019).
16. L. Pan *et al*., *PLOS ONE* **9**, e104335 (2014).
17. W. L. Lei *et al*., *Cell Res.* **22**, 954–972 (2012).
18. J. C. Stendahl, M. S. Rao, M. O. Guler, S. I. Stupp, *Adv. Funct. Mater.* **16**, 499–508 (2006).
19. M. A. Greenfield, J. R. Hoffman, M. O. de la Cruz, S. I. Stupp, *Langmuir* **26**, 3641–3647 (2010).
20. O. G. Bhalala, L. Pan, H. North, T. McGuire, J. A. Kessler, *Bio. Protoc.* **3**, e866 (2013).
21. M. A. Anderson *et al*., *Nature* **561**, 396–400 (2018).
22. Y. Li *et al*., *Nat. Protoc.* **3**, 1703–1708 (2008).
23. M. Kasai, T. Jikoh, H. Fukumitsu, S. Furukawa, *J. Neurotrauma* **31**, 1584–1598 (2014).
24. M. Murakami, T. Sakurai, *WIREs Syst. Biol. Med.* **4**, 615–629 (2012).
25. R. Goetz, M. Mohammadi, *Nat. Rev. Mol. Cell Biol.* **14**, 166–180 (2013).
26. D. F. Gauto *et al*., *J. Am. Chem. Soc.* **141**, 11183–11195 (2019).
27. Y. Toyama *et al*., *Nat. Commun.* **8**, 14523 (2017).
28. K. H. Gardner, L. E. Kay, *Annu. Rev. Biophys. Biomol. Struct.* **27**, 357–406 (1998).
29. M. Kainosho *et al*., *Nature* **440**, 52–57 (2006).
30. P. E. Wright, H. J. Dyson, *Nat. Rev. Mol. Cell Biol.* **16**, 18–29 (2015).

ACKNOWLEDGMENTS

The authors are grateful to M. Karver, E. Testa, and S. Biswas of the Peptide Synthesis Core Facility of the Simpson Querrey Institute for BioNanotechnology at Northwestern University for their assistance and key insights into the synthesis and purification of the PAs. We also thank the laboratory of J. A. Kessler for the initial training of Z.A., A.N.K.-E., and F.C. on the SCI model. We thank M. Seniw for the preparation of graphic illustrations shown in the figures. The authors would also like to thank C. Rubert-Perez, L. C. Palmer, and K. Sato for their initial help with the FGF2 PA materials, especially for helpful discussions about materials characterization and CD results. **Funding:** The experimental work and simulations were supported by the Louis A. Simpson and Kimberly K. Querrey Center for Regenerative Nanomedicine at the Simpson Querrey Institute for BioNanotechnology (S.I.S.). Work on NMR analysis was supported by the Air Force Research Laboratory under agreement no. FA8650-15-2-5518. Part of the biological experiments reported here was supported by the National Institute on Neurological Disorders and Stroke (NINDS) and the National Institute on Aging (NIA) R01NS104219 (E.K.), NIH/NINDS grants R21NS107761 and R21NS107761-01A1 (E.K.), the Les Turner ALS Foundation (E.K.), and the New York Stem Cell Foundation (E.K.). We thank the Paralyzed Veterans of America (PVA) Research Foundation PVA17RF0008 (Z.A.), the National Science Foundation (A.N.K.-E. and S.M.C.), and the French Muscular Dystrophy Association (J.A.O.) for graduate and postdoctoral fellowships. We thank the Peptide Synthesis Core and the Analytical Bionanotechnology Equipment Core at the Simpson Querrey Institute for Bionanotechnology for biological and chemical analyses. These facilities have support from the Soft and Hybrid Nanotechnology Experimental (SHyNE) Resource (NSF ECCS – 1542205). Imaging work was performed at the Center for Advanced Microscopy, and CD measurements were performed at the Northwestern University Keck Biophysics facility. Both of these facilities are generously supported by NCI CCSG P30 CA060553 awarded to the Robert H. Lurie Comprehensive Cancer Center. Spinning disk confocal microscopy was performed on an Andor XDI revolution microscope, purchased through the support of NCRR 1S10 RR031680-01. Multiphoton microscopy was performed on a Nikon A1R multiphoton microscope, acquired with support from NIH 1S10OD010398-01. Tissue processing was performed at the Pathology Core Facility supported by NCI CA060553 awarded to the Robert H. Lurie Comprehensive Cancer Center. Electron microscopy experiments were performed at the Electron Probe Instrumentation Center (EPIC) and the BioCryo facility of Northwestern University's NUANCE Center, both of which have received support from the SHyNE Resource (NSF ECCS-1542205); the MRSEC program (NSF DMR-1720139) at the Materials Research Center; the International Institute for Nanotechnology (IIN); the Keck Foundation; and the State of Illinois, through the IIN. NMR and Fourier transform infrared spectroscopy characterization in this work made use of IMSERC at Northwestern University, which has received support from the SHyNE Resource (NSF ECCS-1542205), the State of Illinois, and IIN. Portions of this work were performed at the DuPont-Northwestern-Dow Collaborative Access Team (DND-CAT) located at Sector 5 of the Advanced Photon Source (APS). DND-CAT is supported by Northwestern University, The Dow Chemical Company, and DuPont de Nemours, Inc. This research used resources of the Advanced Photon Source, a US Department of Energy (DOE) Office of Science User Facility operated for the DOE Office of Science by Argonne National Laboratory under contract no. DE-AC02-06CH11357. E.K. is a Les Turner ALS Research Center Investigator and a New York Stem Cell Foundation–Robertson Investigator. **Authors contributions:** Z.A. designed the materials, performed in vitro and in vivo experiments, analyzed data, and wrote the manuscript. A.N.K.-E. prepared all the materials, performed some of the materials characterization, and conducted in vivo experiments. I.R.S. performed some of the materials characterization, carried out the computational simulations, analyzed the simulated data, and took part in discussions. J.A.O. carried out hNPCs in vitro experiments and took part in discussions. R.Q. performed some of the materials characterization and analysis. Z.S. and P.A.M. carried out the NMR experiments and analyzed the data. F.C. assisted during the in vivo experiments. S.M.C. acquired cryo-TEM imaging. S.W. carried out experiments at Argonne National Laboratory. E.K. supervised hNPCs in vitro studies and took part in discussions. S.I.S. supervised the research and wrote the manuscript. All authors helped to edit and approved the final version of the manuscript. **Competing interests:** Z.A. and S.I.S. are inventors on a pending patent pertaining to this work (Supramolecular Motion in Bioactive Scaffolds Promotes Recovery from Spinal Cord Injury). The authors declare no other competing interests. **Data and materials availability:** All data needed to evaluate the conclusions in the paper are present either in the main text or the supplementary materials.

SUPPLEMENTARY MATERIALS

science.org/doi/10.1126/science.abh3602
Materials and Methods
Supplementary Text
Figs. S1 to S40
Tables S1 to S4
References (*31*–*50*)

3 March 2021; resubmitted 16 July 2021
Accepted 23 September 2021
10.1126/science.abh3602

NEUROSCIENCE

Stepwise synaptic plasticity events drive the early phase of memory consolidation

Akihiro Goto[1,2], Ayaka Bota[1,2,3], Ken Miya[2,4,5], Jingbo Wang[1], Suzune Tsukamoto[1], Xinzhi Jiang[1], Daichi Hirai[2], Masanori Murayama[2,6], Tomoki Matsuda[7], Thomas J. McHugh[2,6], Takeharu Nagai[7], Yasunori Hayashi[1,2,8]*

Memories are initially encoded in the hippocampus but subsequently consolidated to the cortex. Although synaptic plasticity is key to these processes, its precise spatiotemporal profile remains poorly understood. Using optogenetics to selectively erase long-term potentiation (LTP) within a defined temporal window, we found that distinct phases of synaptic plasticity play differential roles. The first wave acts locally in the hippocampus to confer context specificity. The second wave, during sleep on the same day, organizes these neurons into synchronously firing assemblies. Finally, LTP in the anterior cingulate cortex during sleep on the second day is required for further stabilization of the memory. This demonstrates the precise localization, timing, and characteristic contributions of the plasticity events that underlie the early phase of memory consolidation.

The current prevailing view of episodic memory is that it is initially encoded in the hippocampus and subsequently transferred to other regions, including the cerebral cortex, for long-term storage in a process termed memory consolidation (*1*, *2*). It has been proposed that synaptic plasticity may underlie learning, which is assumed to play a critical role in memory consolidation (*3*, *4*). However, it remains largely unknown where and when synaptic plasticity occurs, along with the more complex question of how synaptic plasticity shapes neuronal representation. This is due primarily to a lack of appropriate experimental techniques to detect and modify synaptic plasticity in a precise spatiotemporal manner. We thus developed an optogenetic method to selectively erase long-term potentiation (LTP) without affecting basal transmission or precluding future plasticity events.

Optical erasure of sLTP

Previous studies have demonstrated that the early phase of LTP is associated with rapid polymerization of actin within dendritic spines, which acts to enlarge their structure [structural LTP (sLTP)](*5*). At the same time, cofilin (CFL), an F-actin side-binding protein, accumulates at the bottom of the spine head (*6*). CFL exerts differential effects on F-actin depending on its density on the filament (*7*, *8*). At low density, CFL twists and severs F-actin, leading to its disassembly. By contrast, when CFL binds F-actin at a high stoichiometric ratio, it forms cofilactin, thus stabilizing F-actin. We previously demonstrated that sLTP induction promotes CFL-actin interaction, consistent with the formation of cofilactin (*6*). Therefore, we hypothesized that inactivating CFL would lead to destabilization of the cofilactin structure within the dendritic spine, thereby permitting selective erasure of sLTP.

To test this, we employed the genetically encoded photosensitizer protein SuperNova (SN), which allows for chromophore-assisted light inactivation (CALI) of specific molecules in living cells. Upon illumination at specific wavelengths, SN generates reactive oxygen species that inactivate the proteins to which it is fused (*9*, *10*). In nonneuronal cells expressing a fusion protein of CFL with SN (CFL-SN), induction of CALI by light illumination inhibited the actin-dependent motility of lamellipodia, consistent with the inactivation of CFL (fig. S1) (*9*, *11*). We then coexpressed CFL-SN with CFL–green fluorescent protein (GFP) in CA1 pyramidal neurons in hippocampal slice cultures, together with DsRed2 as a volume filler. Owing to the cooperativity of CFL binding to F-actin, we predicted that CALI of CFL-SN would also lead to dissociation of CFL-GFP from F-actin. Upon induction of sLTP by two-photon uncaging of MNI (4-methoxy-7-nitroindolinyl)-glutamate at single dendritic spines, we observed a rapid accumulation of CFL-GFP, overshooting the increase in volume (*6*) (Fig. 1, A and B). By inducing CALI 10 min after sLTP induction, both the enrichment of CFL-GFP and the increase in spine volume were reversed.

sLTP is accompanied by decreased actin turnover within dendritic spines (*12*). To establish whether the enriched CFL and resulting cofilactin formation are involved in this process, we tested whether CALI of CFL-SN can restore actin turnover using photoactivatable GFP (PAGFP)–fused actin (*12*). Photoactivation of PAGFP-actin at the tip of dendritic spines revealed actin turnover within the body of the dendritic spine, which slowed after the induction of sLTP (Fig. 1C). However, when CALI was performed after sLTP induction, actin turnover was restored and spine volumes returned to baseline levels. Overall, these results are consistent with the idea that cofilactin structure maintains the increase in spine volume after sLTP induction, and that CALI of CFL-SN can efficiently reverse sLTP by destabilizing this structure and restoring actin turnover (fig. S2).

Time window of optical erasure of sLTP

To understand the temporal window of effectiveness, CALI was triggered at multiple time points after sLTP induction. Light illumination of spines expressing CFL-SN 10 min after LTP led to a decrease in spine enlargement compared with spines expressing an unfused SN (Fig. 1, D and E). Similarly, 30 min after sLTP induction, CALI remained effective in reducing spine volume. However, this effect was not evident after 50 min (Fig. 1F) (*6*). CALI applied to spines 1 min before sLTP had no effect on its subsequent expression (Fig. 1F). Moreover, CALI triggered in spines where sLTP had not been induced had no effect on spine volume regardless of its original size (Fig. 1, D and E, and fig. S3). Reinduction of sLTP in the same spine after CALI was still possible, indicating that the procedure does not cause permanent damage, but only temporarily disrupts the spine-associated plasticity machinery (Fig. 1E and fig. S4).

Electrically recorded LTP can also be optically erased

To test whether CALI of CFL-SN could erase electrically recorded LTP, field excitatory postsynaptic potentials (fEPSPs) were recorded in the CA1 stratum radiatum of hippocampal slices from CaMKIIα-Cre mice infected with AAV_2-EF1α-DIO-CFL-SN (fig. S5A). LTP was induced by high-frequency stimulation (HFS) and CALI was triggered 10 min later. fEPSPs were specifically decreased in the LTP pathway, but not in the control pathway or in slices expressing unfused SN (fig. S5B). Subsequent HFS produced a sustained potentiation of the fEPSPs, indicating that CALI selectively erased the existing LTP without interfering with any future plasticity events. When CALI was conducted either 1 min before or 50 min after LTP induction, it did not have any impact on potentiation (fig. S5, B and C). Because both *N*-methyl-d-aspartate receptor- and metabotropic glutamate receptor-dependent long–term depression (LTD) share CFL as a

[1]Department of Pharmacology, Kyoto University Graduate School of Medicine, Kyoto 606-8501, Japan. [2]RIKEN Brain Science Institute, Wako, Saitama 351-0198, Japan. [3]Graduate School of Science and Engineering, Saitama University, Saitama 338-8570, Japan. [4]Department of Molecular Neurobiology, Faculty of Medicine, University of Tsukuba, Tsukuba, Ibaraki 305-8575, Japan. [5]Graduate School of Comprehensive Human Sciences, University of Tsukuba, Tsukuba, Ibaraki 305-8575, Japan. [6]RIKEN Center for Brain Science, Wako, Saitama 351-0198, Japan. [7]SANKEN (The Institute of Scientific and Industrial Research), Osaka University, Mihogaoka 8-1, Ibaraki, Osaka 567-0047, Japan. [8]Brain and Body System Science Institute, Saitama University, Saitama 338-8570, Japan.
*Corresponding author. Email: yhayashi-tky@umin.ac.jp

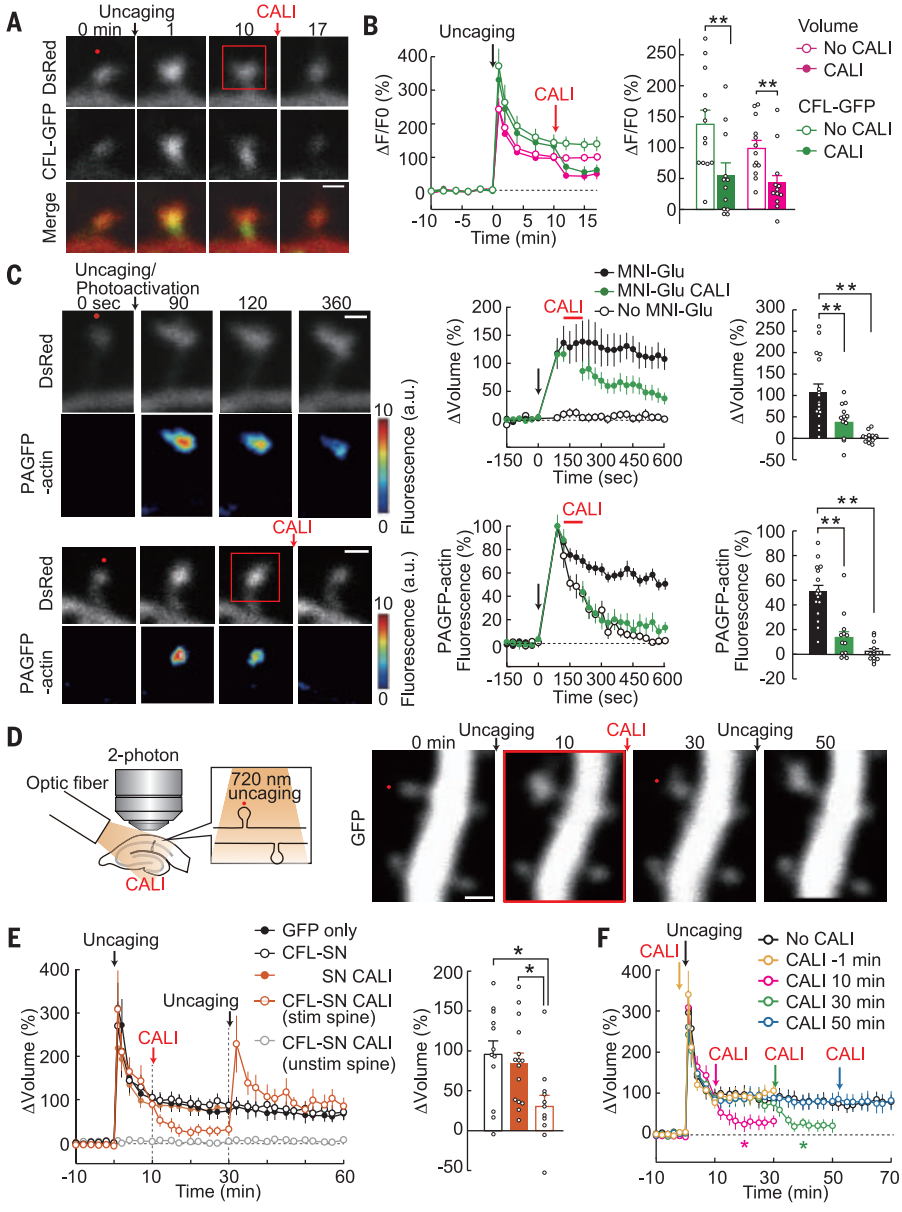


Fig. 1. Optical erasure of sLTP. (**A**) DsRed2 (top) and CFL-GFP (bottom) images. Persistent enlargement of the spine was induced with two-photon (2P) uncaging of MNI-glutamate in single dendritic spines in hippocampal slice cultures, which expressed CFL-SN, CFL-GFP, and DsRed2. The red dot in the DsRed2 image indicates the uncaging spot. A 559-nm laser was irradiated within the square region to induce CALI in the stimulated spine. Scale bar, 1 μm. (**B**) Time courses of changes in spine volume and the amount of CFL-GFP relative to the averaged baseline fluorescence intensity from spines without illumination (n = 13) and spines with 593-nm illumination 10 min after sLTP induction (n = 12) (left). Summary of changes in the intensity of CFL-GFP and spine volume 5 min after CALI (right). Wilcoxon signed-rank test, P = 0.0098 (volume), P = 0.0043 (CFL-GFP). (**C**) Images of DsRed2 and PAGFP-actin in spines. Red dots in the DsRed2 images indicate uncaging and photoactivation points. 559-nm light was illuminated within the square region around the spine head. The fluorescence of PAGFP after photoactivation was normalized to 100%. With MNI-glutamate without CALI (n = 15), with MNI-glutamate and CALI (n = 14), without MNI-glutamate and CALI (n = 13). Averaged spine volume 600 s after uncaging and photoactivation are shown as bar graphs. One-way analysis of variance (ANOVA) test followed by Tukey-Kramer post hoc test (versus MNI-Glu). ΔVolume; P = 0.0027 (MNI-Glu CALI), P = 0 (No MNI-Glu), $F_{2,41}$ = 15.05. Fluorescence; P = 0.0001 (MNI-Glu CALI), P = 0 (No MNI-Glu), $F_{2,41}$ = 17.72. Scale bars, 1 μm. a.u., arbitrary units. (**D**) Field illumination of neurons expressing CFL-SN and GFP in hippocampal slice cultures (left). To induce CALI, a 593-nm laser (0.8W/cm^2, 60 sec, 2-mm diameter spot) was illuminated using an optic fiber. GFP images of a representative neuron expressing CFL-SN and GFP (right). Red dots indicate two-photon uncaging spots. A 593-nm laser was irradiated 10 min after LTP induction. Scale bar, 1 μm. (**E**) Summary of effect of CALI of CFL-SN on sLTP. Spine volume was quantified by measuring the total GFP fluorescence intensity relative to the baseline intensity. Neurons expressing GFP only without CALI (GFP only, n = 12), CFL-SN and GFP without CALI (CFL-SN No CALI, n = 12), SN and GFP with CALI (SN CALI, n = 15), CFL-SN and GFP with CALI (CFL-SN CALI, both glutamate stimulated and unstimulated adjacent spines, n = 12). Averaged spine volume 7 min after CALI are shown as bar graphs. One-way ANOVA test followed by Tukey-Kramer post hoc test. P = 0.0119 (CFL-SN versus CFL-SN CALI), P = 0.0335 (SN CALI versus CFL-SN CALI), $F_{2,36}$ = 5.34. (**F**) Effect of CALI of CFL-SN on sLTP at various time points before and after induction. CALI was conducted 1 min before sLTP induction or 10, 30, and 50 min after induction. Wilcoxon signed-rank test, 10 min after CALI of each CALI group versus control (No CALI), P = 0.1811 (CALI 1 min, n = 12), P = 0.0221 (CALI 10 min, n = 12), P = 0.0306 (CALI 30 min, n = 10), P = 0.9732 (CALI 50 min, n = 13). Means ± SEMs are shown; significance is indicated in the figures as follows: *: P < 0.05; **: P < 0.01.

common downstream mediator (*13*, *14*), it was necessary to characterize the effects of CALI on LTD. However, we observed no effect on low-frequency stimulation–induced LTD (fig. S5D).

Optical erasure of LTP impairs context-specific memory within a specific time window

Next, we tested whether we could erase memories in intact animals. CFL-SN was expressed bilaterally in dorsal CA1 of the hippocampus by injecting AAV$_2$-EF1α-DIO-CFL-SN in CaMKIIα-Cre mice, and optic fibers were implanted above the area of injection (Fig. 2A). Memory was assessed using an inhibitory avoidance (IA) learning paradigm. In this task, mice were placed in the lit side of a partitioned chamber. They typically crossed over to the dark side within 30 s of the door opening, where they received a foot shock (Fig. 2B). Although naïve animals (no virus injection or illumination) showed a prolonged crossover latency to the dark side on day 2, mice expressing CFL-SN that underwent CALI 2 min after the shock had significantly shorter latencies, indicating that memory formation was disrupted (Fig. 2C). The same mice were able to form the memory after they were shocked on day 2 without CALI and tested on day 3, ruling out any nonspecific interference with neuronal function. Animals expressing either CFL-GFP or unfused SN formed memories as normal even in the presence of illumination. Likewise, animals expressing CFL-SN

in the absence of illumination also formed a robust memory, ruling out the possibility that overexpression of CFL-SN contributes to the observed effects.

CALI was triggered at various time points after the shock. Memory was significantly impaired when CALI was conducted within 20 min after the shock (Fig. 2D). However, memory was not impaired when the light was delivered either 1 min before the animals were placed in the IA chamber or 1 hour after the shock.

To test the context specificity of the impaired memory, we prepared two IA contexts that differed in size, floor texture, visual cues, illumination color, and odor (Fig. 2E). Mice were first trained in context A without CALI. Two hours later, mice were placed in context B where they displayed a short crossover latency, indicating that they could sufficiently distinguish context B from context A (Fig. 2E). After crossover, the mice were shocked and CALI was subsequently conducted. The next day, when returned to context B, mice that underwent CALI displayed shorter crossover latencies, indicating that the memory for context B was erased. However, when placed in context A, the same mice had crossover latencies similar to those of the control mice that did not receive CALI, demonstrating that context-specific memories can be selectively impaired.

Optical erasure of LTP during sleep also impairs memory

Hippocampal neuronal activity patterns associated with memory formation are subsequently replayed offline while animals are stationary or asleep, a process thought to underlie memory consolidation (*15*–*20*). However, it remains unknown whether such activity induces additional LTP in the brain; if it does, it is also unknown when and where this occurs. To establish whether additional LTP is induced offline (offline LTP) locally in the hippocampus during extended periods after learning, we illuminated the hippocampus every 20 min (the temporal resolution of the CFL-SN system) after the mice were returned to the home cage, starting 2 hours after the shock and continuing for 8 hours. We found that the memory was totally erased (Fig. 3A). When the same group of mice were shocked on day 2 and tested on day 3, the animals exhibited normal memory, ruling out nonspecific tissue damage. To further narrow down the time window of LTP, light was delivered either in the first or second 4-hour period. The memory was still erased, though to a lesser extent in both time windows. Because local hippocampal LTP was still contributing to memory formation in the home cage up to 8 hours after the shock, we next tested whether offline LTP extends over days. We illuminated the hippocampus only on day 2, but observed no degradation of memory (Fig. 3B), suggesting that offline LTP extends more than 2 hours after learning, but consolidation is restricted to a single day locally within the hippocampus.

Hippocampal replay occurs during both wakefulness and sleep, and it has been suggested that events in these states may serve differential roles (*19*). We analyzed the state-dependent contribution of these processes relative to the memory consolidation process. electroencephalography (EEG) and electromyography (EMG) data were analyzed online

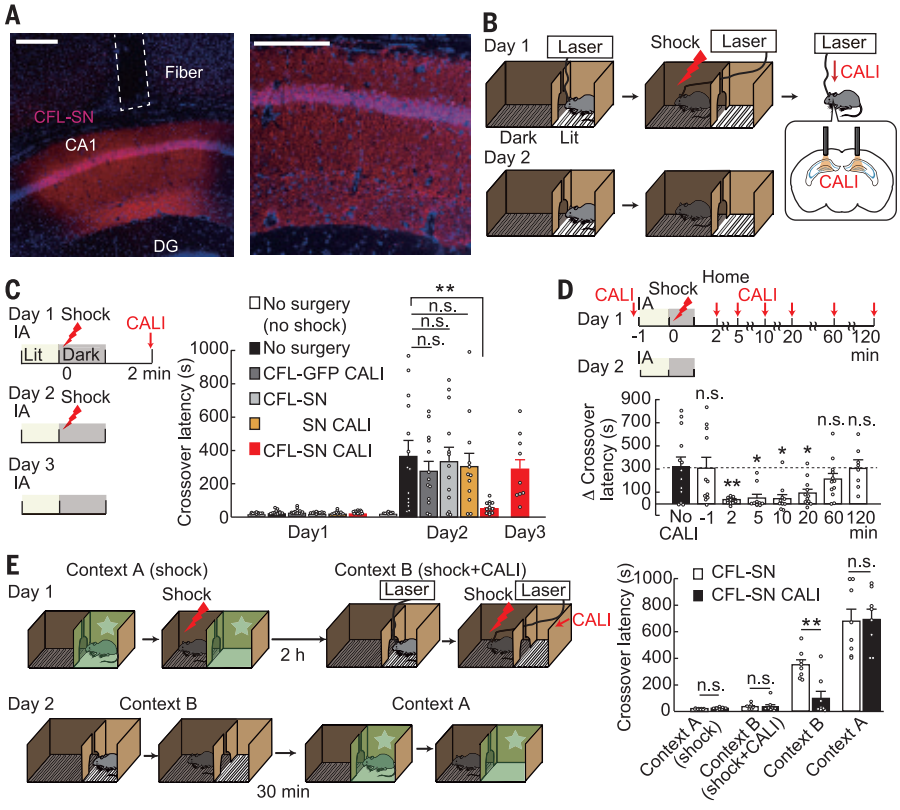


Fig. 2. Optical erasure of memory by CALI. (**A**) Distribution of CFL-SN expressed by AAV vector in dorsal CA1 pyramidal neurons (immunostained); the optical fiber tract is indicated by a dashed line in the cortex. An AAV viral vector carrying EF1α-DIO-CFL-SN was injected bilaterally into the dorsal CA1 of CaMKIIα-Cre transgenic mice. DG, Dentate gyrus. Scale bars, 300 μm. (**B**) Experimental protocol for inhibitory avoidance testing. (**C**) Erasure of memory by CALI of CFL-SN. Bar graph shows the average crossover latency in inhibitory avoidance test. Mice without virus injection or shock (no shock, n = 10), mice without virus injection but shocked (No surgery, n = 14), mice expressing CFL-GFP, shocked and illuminated (CFL-GFP CALI, n = 13), mice expressing CFL-SN, shocked but not illuminated (CFL-SN, n = 12), mice expressing SN, shocked and illuminated (SN CALI, n = 12), mice expressing CFL-SN and illuminated (CFL-SN CALI, n = 13). A subset of the last group was shocked again on day 2 but without illumination and tested on day 3 (CFL-SN CALI, n = 9). All groups except the no shock group on day 2 were statistically analyzed using one-way ANOVA tests followed by Tukey-Kramer post hoc tests (versus no surgery). P = 0.885 (CFL-GFP CALI), P = 0.998 (CFL-SN), P = 0.986 (SN CALI), P = 0.0156 (CFL-SN CALI), $F_{4,60}$ = 3.26. (**D**) Time-window of the effect of CALI of CFL-SN. CALI of CFL-SN was carried out at various time points before and after shock. Mice without CALI (n = 10), CALI 1 min before shock (n = 10), CALI 2 min (n = 10), 5 min (n = 10), 10 min (n = 10), 20 min (n = 10), 60 min (n = 10), and 120 min (n = 10) after shock. One-way ANOVA test followed by Tukey-Kramer post hoc test (versus noCALI group). P = 1, P = 0.0042, P = 0.0171, P = 0.0103, P = 0.0478, P = 0.797, P = 1 (the order is the same as in the figure), $F_{7,82}$ = 5.36. (**E**) Context selectivity of the effect of CALI. The IA test was carried out in two distinct contexts: A and B. CALI was induced 2 min after shock in context B but not in context A. Summary of crossover latency in each context with CALI (n = 8) and without CALI (n = 8). Wilcoxon signed-rank test, P = 0.1105 (Context A+shock), P = 0.314 (Context B+shock+CALI), P = 0.004 (Context B), P = 0.9591 (Context A). Means ± SEMs are shown; significance is indicated in the figures as follows: *: P < 0.05; **: P < 0.01; n.s., not significant.

to automatically determine the behavioral state of the animal (*21*), and CALI was triggered separately during either awake or sleep periods that extended for at least 20 min (Fig. 3C and fig. S6). When CALI was conducted during sleep, memory was impaired (Fig. 3D). However, when it was restricted to awake periods, no impact was evident. Further, when CALI was specifically performed during sleep periods but only on day 2, it no longer impaired memory formation (Fig. 3D). Our intervention used a similar total number of illuminations across conditions (Fig. 3E) and did not alter the patterns or periods of the sleep and wake states (fig. S7).

Differential roles of online and offline LTP on the formation of hippocampal representation

So far we have demonstrated that two forms of hippocampal LTP are required for memory formation: online LTP that takes place during or immediately after the event and offline LTP that takes place during the subsequent sleep period. We next sought to establish whether these two forms of LTP have differential impacts on hippocampal representations. We imaged Ca^{2+}-responses in hippocampal excitatory neurons of active mice using a head-mounted miniaturized fluorescence microscope (*22*). AAV_9-CAG-DIO-CFL-SN-P2A-GCaMP6f was injected into the dorsal hippocampus of CaMKIIα-Cre mice, after which a gradient index (GRIN) lens was implanted directly above the injection site (Fig. 4A). On day 1, neuronal activity was recorded when the mice were exposed to the IA chamber without shock (Fig. 4B). On day 2, mice were reexposed to the same chamber and shocked after entering the dark side. In one group of mice, light was illuminated through the lens 2 min after the shock to erase online LTP (online CALI group). To limit the effect on the local circuit, we induced CALI unilaterally on the observed side (fig. S8). In a second group, light was illuminated every 20 min—starting 2 hours after the IA test for a total of 8 hours—to erase offline LTP (offline CALI group), whereas control groups were shocked but did not receive illumination (shock noCALI group). On day 3, all three groups were reexposed to the IA test chamber and neuronal activity was recorded. We compared the firing of individual neurons in the habituation chamber and in the IA test chamber by defining a selectivity score for each cell (see methods; Fig. 4, C to E; and fig. S9A).

CA1 neurons in animals that did not receive the shock showed modest selectivity for the test chamber compared with the habituation chamber at similar levels on both day 1 and 2 (fig. S9 and Fig. 4D). By contrast, in animals that received shock (shock noCALI group), neurons fired significantly more in the test chamber than in the habituation chamber on day 3 compared with day 1, resulting in an increase in overall selectivity (fig. S9 and Fig. 4, C to E). When online LTP was erased 2 min after the shock (shock+online CALI group), increased selectivity failed to emerge. By contrast, erasure of offline LTP did not impair the increased selectivity (shock+offline CALI group).

To dissect the impact of offline LTP on the hippocampal synaptic circuit, we analyzed the population Ca^{2+} dynamics using principal component analysis (PCA) (*23*) (Fig. 4F). In the shock-only mice, after IA learning we observed that activity repeatedly deviated from the trajectories of day 1. In epochs where these deviations were observed, Ca^{2+} signals increased in multiple cells shared between the epochs (Fig. 4G), indicating that they reflect the recurring synchronous activity of specific sets of neurons. We confirmed that synchronous events occurred primarily when the deviations were observed and that the number of synchronous events increased after the shock, though the mean firing rate did not change between days 1 and 3 (Fig. 4H). The deviation in PCA, as well as the increase in synchronous events, were not evident when either online LTP or offline LTP were erased (Fig. 4, F and H, and fig. S10C), indicating the importance of both forms of LTP for synchronous activity after learning. Before door opening on day 3, synchronous firing was observed broadly around the center of the chamber, whereas after door opening, it was most pronounced adjacent to the door (Fig. 4I and fig. S10, A and B). This suggests that such assembly activity may reflect recall of the training episode. CALI eliminated such

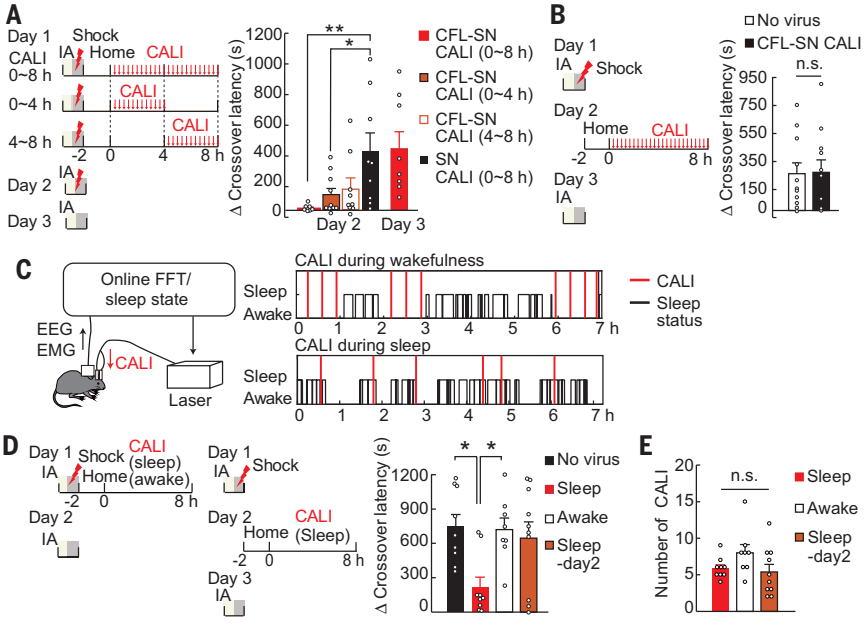


Fig. 3. Offline LTP in the hippocampus during sleep is required for memory. (**A**) Repeated CALI in the home cage erased memory. Light was delivered while animals were in the home cage every 20 min for 8 hours, either 2 hours after shock (n = 8), the first 4 hours (n = 10), or the second 4 hours (n = 9). Animals only expressing SN were illuminated and used as a control (n = 9). Animals received 8 hour repeated illumination, and shock was given again on day 2 without CALI; memory was then retested on day 3 (n = 8). One-way ANOVA test followed by the Tukey-Kramer post hoc test (versus SN CALI). P = 0.0079 (0 to 8 h), P = 0.0425 (0 to 4 h), P = 0.1153 (4 to 8 h), $F_{3,32}$ = 4.53. (**B**) Same as in (A) except that CALI was conducted the next day and memory was tested on day 3 (CFLSN-CALI, n = 11). Control mice did not express CFL-SN (No virus, n = 10). Wilcoxon signed-rank test, P = 0.843. (**C**) Automatic detection of behavioral state. EEG and EMG were recorded and analyzed online using a fast Fourier transform (FFT) every 4 sec. Light was illuminated during sleep or wake periods lasting for ≥20 min. Examples of sleep states and light illumination (red line) are shown on the right. (**D**) CALI of CFL-SN erases memory during sleep on the same day, but not the next day. Light was illuminated either during sleep (Sleep, n = 9) or wake (Awake, n = 8) periods commencing 2 hours after shock, and mice were returned to the IA box again on day 2. Control mice did not undergo CALI (No virus, n = 9). The experimental group (Sleep-day 2, n = 10) received light during sleep on the next day and were returned to the IA box on day 3. One-way ANOVA test followed by Tukey-Kramer post hoc test (versus Sleep), P = 0.0135 (No virus), P = 0.0251 (Awake), $F_{3,32}$ = 4.59. (**E**) Average number of CALI was not different among Sleep, Awake, and Sleep-day 2 groups. One-way ANOVA test, P = 0.1449. Means ± SEMs are shown; significance is indicated in the figures as follows: *: P < 0.05; **: P < 0.01; n.s., not significant.

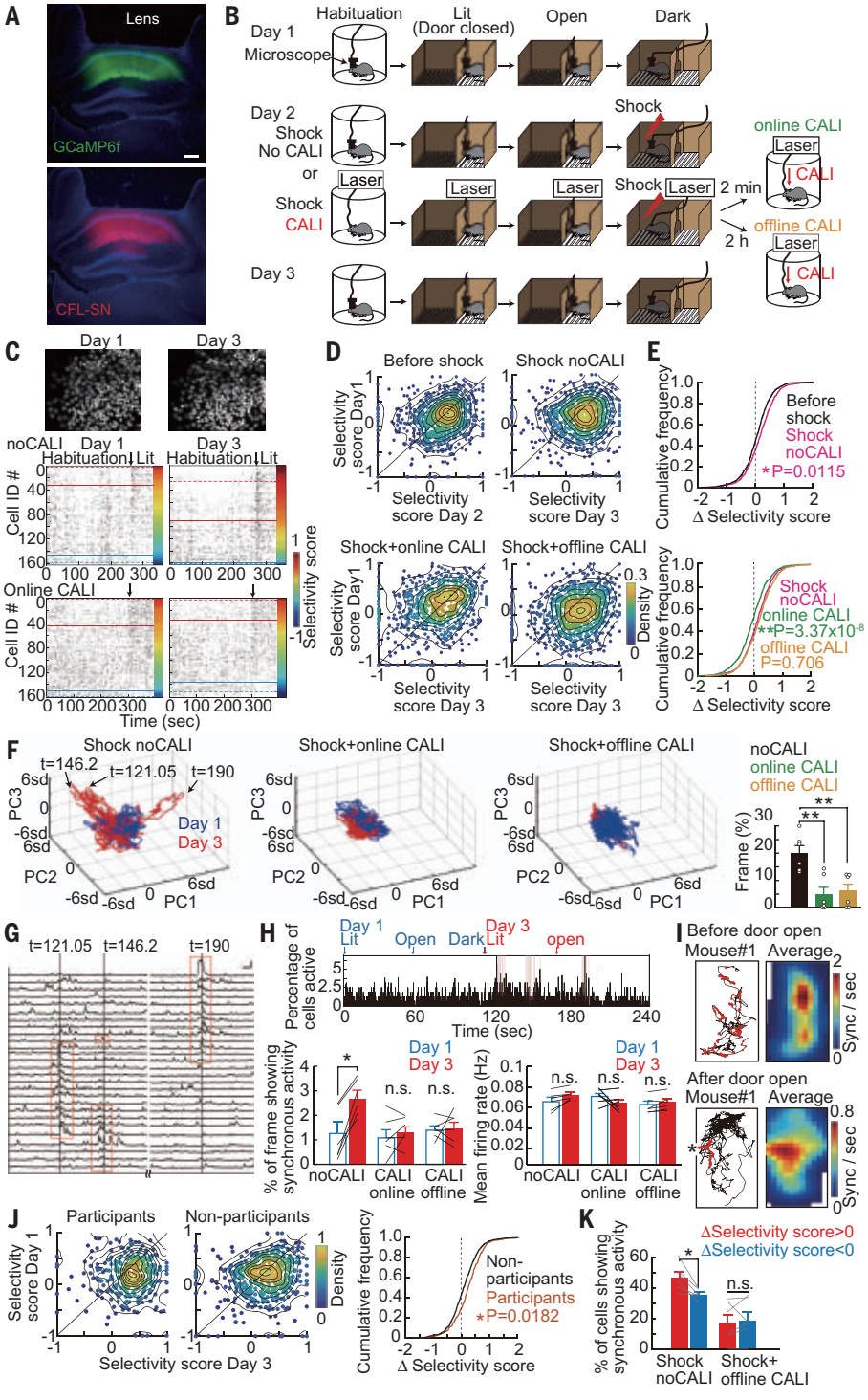


Fig. 4. Hippocampal online LTP and offline LTP have distinct roles in memory engram formation. (**A**) Expression of CFL-SN and GCaMP6f by AAV_9-CAG-DIO-CFL-SN-P2A-GCaMP6f in CA1 pyramidal neurons. (**B**) Experimental protocol of Ca^{2+} imaging during IA testing and CALI. (**C**) Images of detected cells on day 1 (before shock) and on day 3 (after shock) from a Shock noCALI mouse. Raster plot of representative cells commonly active on day 1 and day 3. Ca^{2+} events (>2 events) are plotted per sec and cells are sorted in order of selectivity score on each day. Red and blue horizontal lines indicate selectivity scores of 0.4 and -0.4, and dotted lines indicate scores of 0.8 and -0.8. Shock noCALI (top) and Shock+online CALI (bottom) mice. Raw values are shown in fig. S9B. (**D**). Selectivity score of cells on day 1 versus day 2 (Before shock, 852 cells, *n* = 6 mice) or on day 1 versus day 3 (Shock noCALI, 776 cells, *n* = 6 mice, Shock+CALI online, 763 cells, *n* = 6 mice, Shock+CALI offline, 935 cell, *n* = 6 mice) are shown. Density of plot is displayed in pseudocolor, with contours depicted as black lines. (**E**) Same data as in (D) but differences in selectivity scores are plotted in cumulative histograms. Kolmogorov-Smirnov test: No shock versus Shock noCALI (top), and with respect to control (Shock noCALI) (bottom). (**F**) Principal component analysis (PCA) of concatenated Ca^{2+} traces of day 1 and day 3 data from a mouse shocked on day 2 without CALI (left). Population trajectories were projected onto the first three principal components. Arrows indicate time points with high deviation on day 3. 6sd denotes 6 times standard deviation (SD) of PCA score on day 1. Similar PCA analysis from a mouse shocked on day 2 that underwent CALI 2 min after shock to cancel online LTP (Shock+online CALI, middle), and a mouse shocked on day 2 that underwent CALI in the home cage to cancel offline LTP (Shock+offline CALI, right). The bar graph displays the average percentage of frames that showed PCA scores on day 3 that had >3 SD of the PCA score on day 1. One-way ANOVA test followed by Tukey-Kramer post hoc test (versus Shock noCALI, *n* = 6 mice). $P = 0.0028$ (Shock+online CALI, *n* = 6 mice), $P = 0.0058$ (Shock+offline CALI, *n* = 6 mice), $F_{2,15} = 10.04$. (**G**) Sample traces of neurons from a Shock noCALI mouse in (F). (t = 121.05, 146.2, and 190). Red rectangles indicate activation at those time points. Scale: 50% ΔF/F, 5 s. (**H**) Percentage of cells active on day 1 and day 3 (top). The red area indicates frames where high deviation was observed in (F). Percent of frame showing synchronous activity (bottom left) and mean firing rate (bottom right) on day 1 and day 3. Paired t-test, $*P < 0.05$. (noCALI, *n* = 6 mice, CALI 2 min, *n* = 6 mice, CALI Sleep, *n* = 6 mice). (**I**) Synchronous firing is selectively seen near the door to the dark side. Trajectory (black line) and location where high deviation was observed in PCA analysis (red dots) from a representative shock-only mouse on day 3, before and after the door opened (left). Heat map of average synchronous activity rate in lit chamber on day 3 (right). The number of synchronous activities detected by PCA analysis in each bin was pooled from 6 mice and divided by total their occupancy time in each bin. The asterisk indicates door location. (**J**) Selectivity score from cells that participated in synchronous activity were increased after shock, but no increase was observed for those that did not participate in synchronous activity. Cells that were activated (>4 SD of basal Ca^{2+} signal) at least once in the frame when high deviation was observed by PCA analysis were classified as participants. (Participant, *n* = 309, nonparticipant *n* = 467 from 6 mice). Kolmogorov-Smirnov test. (**K**) Percent of cells showing synchronous activity in the group of cells showing a higher selectivity score after shock (red bar, cells below the diagonal line in Fig. 4D) and that in the group of cells showing lower selectivity score after shock (blue bar, cells beyond the diagonal line). Paired t-test, $P = 0.014$, *n* = 6 mice (noCALI), $P = 0.669$, *n* = 6 mice (offline CALI). Means ± SEMs are shown; significance is indicated in the figures as follows: *: $P < 0.05$; **: $P < 0.01$; n.s., not significant.

accumulation (fig. S10, A and B). We then classified neurons in the noCALI group into two classes based on their participation in synchronous events using PCA analysis, then separately calculated selectivity scores (Fig. 4J). Cells that participated in synchronous activity at least once displayed a higher selectivity score after learning (day 3) than before (day 1), although those that did not exhibited a significant reduction in the degree to which the selectivity score was modulated by learning. We then classified the cells into two groups based on the changes in selectivity score before and after shock (Fig. 4K). In noCALI animals, cells that showed an increase in selectivity score after shock were more likely to participate in synchronous activity than those that showed a decrease. In offline CALI animals, the fraction of cells participating in synchronous activity was overall lower than that of noCALI animals and was comparable between cells showing an increase in selectivity score after shock and those showing a decrease. These results are indicative of a causal relationship between selectivity score and synchronous activity, which can be erased by offline CALI.

Erasure of LTP in ACC during sleep on the following day impairs memory

Finally, we attempted to better understand the process of memory transfer to the cortex by focusing on the anterior cingulate cortex (ACC), which is activated during recall of remote memory (*24*–*26*). CFL-SN was expressed in ACC excitatory neurons using AAV_2-EF1α-DIO-CFL-SN in CaMKIIα-Cre mice, and optical fibers were bilaterally implanted above ACC (Fig. 5). First, we explored the time window of synaptic plasticity within the ACC. In contrast to CALI in the hippocampus, CALI in the ACC that was triggered either 2 min after shock (Fig. 5) or every 20 min for 8 hours (commencing 2 hours after shock) did not impair memory expression (Fig. 5). By contrast, when CALI was induced every 20 min for 8 hours on day 2 and memory was assessed on day 3, we observed a robust erasure of the memory (Fig. 5). However, this was not the case when the manipulation was performed on day 25 (Fig. 5). When illumination in the ACC was restricted to either sleep or awake periods on day 2, memory could be effectively erased only during sleep (Fig. 5), demonstrating that plasticity in the ACC occurs 1 day after learning and most likely reflects the mechanism by which memories are transferred from the hippocampus to the ACC.

We developed a versatile optogenetic method allowing for the selective optical erasure of LTP in a spatially and temporally restricted manner. It effectively erases established LTP, without altering basal transmission or interfering with future LTP. This is different from other genetic or pharmacological approaches, where temporal or cell-type specificities are difficult to attain (*27*, *28*). Although other tools exist that can erase LTP, such as AS-PARac, PA-AIP, and eosin-tagged AMPA receptor antibody (*29*–*31*), our method is able to erase the early phase of LTP. This differs from AS-PARac, which is aimed at the late protein synthesis phase of LTP, as it has a much wider temporal window of intervention than PA-AIP (~1 min). It is also purely genetically encoded, unlike the eosin-tagged antibody, making it an effective method for in vivo manipulation of memories.

We found that hippocampal LTP occurs as two distinct temporal processes: online immediately after learning and offline during periods of sleep. These two processes have distinct roles: Online LTP establishes the selectivity of neuronal firing to the shock context, as previously reported (*32*), and offline LTP is predominantly responsible for the recruitment of those neurons into repeated bouts of synchronized firing. Synchronized activity was observed when animals looked into the dark side of the chamber but did not enter, possibly reflecting recall of the shock context. Our results indicate that this synchronous activity induces further LTP in neurons, which serves to stabilize the nascent memory engram encoding the abstract features encompassing an episode.

After the two waves of LTP in the hippocampus, a third wave of extra-hippocampal LTP takes place during sleep the next day in the ACC; this is required for systems consolidation. On the other hand, LTP in the hippocampus is no longer required for memory recall. Our data are consistent with a recent study that demonstrated the rapid generation of immature engram cells after training in the prefrontal cortex (*33*). They proposed that a memory engram can be formed as early as after 1 day in the ACC, but remains silent. Subsequent consolidation is required to become a fully mature engram (*2*, *33*). The density of dendritic spines consistently remains unchanged in ACC after one day but subsequently increases, possibly reflecting the maturation process, and is required for memory consolidation (*34*). In our study, the reversal of ACC plasticity on day 2 had already impaired memory 24 hours later, suggesting that even at this early point in systems consolidation, cortical circuits can play a role in memory recall. The discrepancy between our study and that of Kitamura *et al.* (*33*) is not clear at this point, but it may be due to differences in the method of inactivation (tetanus toxin to block output versus CFL-SN to erase LTP while leaving basal activity intact).

Synaptic plasticity in ACC during sleep is also most likely mediated by replay, with the high-frequency oscillatory activity that occurs across hippocampal–cortical networks thought to be key in promoting the strengthening of synaptic connections (*35*). Reinforcing the coordination between hippocampal sharp wave

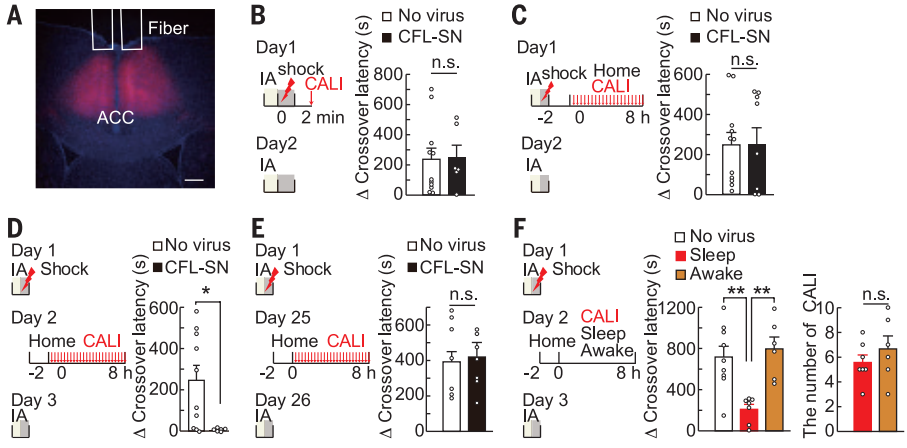


Fig. 5. ACC has an LTP time window distinct from that of the hippocampus. (**A**) Expression of CFL-SN in ACC neurons. Scale bar, 200 μm. (**B** to **E**) Effect of CALI in ACC 2 after shock. (B) 2 min, (C) 2 to 8 hours, (D) 1 day, and (E) 25 days after. Memory was erased only when CALI was performed 1 day later (2 min after; No virus, n = 11; CFLSN-CALI, n = 6. 2 to 8 hours; No virus, n = 11; CFLSN-CALI, n = 8, 1 day after; No virus, n = 10; CFLSN-CALI, n = 6. 25 days after; No virus, n = 7; CFLSN-CALI, n = 7). All experiments were done during the light cycle. Wilcoxon signed-rank tests, P = 0.81 (B), P = 0.90 (C), P = 0.025 (D), P = 0.70 (E). (**F**) Offline LTP during sleep on next day in ACC is required for memory formation. 26 hours after shock, light was illuminated either during sleep or during wake for 8 hours. All experiments were done during the dark cycle. One-way ANOVA test followed by Tukey-Kramer post hoc test with respect to sleep (n = 10), P = 0.0029 (No virus, n = 9), P = 0.0019 (awake, n = 8), $F_{2,19}$= 10.37. Average number of CALI trials did not differ between sleep CALI and awake CALI groups. Wilcoxon signed-rank test, P = 0.43. Means ± SEMs are shown; significance is indicated in the figures as follows: *: P < 0.05; **: P < 0.01; n.s., not significant.

ripples and cortical waves by electrical stimulation resulted in enhanced recall performance, whereas disruption of coupling resulted in memory impairment (*36*, *37*). Likewise, disruption of replay during sleep (*17*) has been shown to impair performance in memory-dependent tasks; however, the exact nature of the mechanisms responsible for inducing plasticity in ACC remains to be elucidated.

In conclusion, we show clear evidence that the early phase of systems consolidation is composed of multiple steps of synaptic plasticity; presumably each undergoes synaptic consolidation. Further application of the introduced optogenetic tool, possibly with color variants of SN (*38*), will allow for a more comprehensive temporal dissection of synaptic plasticity events across multiple neuronal structures and populations, thus providing a much clearer picture of memory consolidation. Although this tool was not directly shown as working for sLTP in vivo associated with learning, it may enable identification of spines that undergo synaptic plasticity during memory consolidation through combination with in vivo imaging.

REFERENCES AND NOTES

1. M. Sakaguchi, Y. Hayashi, *Mol. Brain* **5**, 32 (2012).
2. S. Tonegawa, M. D. Morrissey, T. Kitamura, *Nat. Rev. Neurosci.* **19**, 485–498 (2018).
3. J. Z. Tsien, P. T. Huerta, S. Tonegawa, *Cell* **87**, 1327–1338 (1996).
4. P. W. Frankland, C. O'Brien, M. Ohno, A. Kirkwood, A. J. Silva, *Nature* **411**, 309–313 (2001).
5. K. Okamoto, T. Nagai, A. Miyawaki, Y. Hayashi, *Nat. Neurosci.* **7**, 1104–1112 (2004).
6. M. Bosch *et al.*, *Neuron* **82**, 444–459 (2014).
7. E. Andrianantoandro, T. D. Pollard, *Mol. Cell* **24**, 13–23 (2006).
8. J. R. Bamburg, A. McGough, S. Ono, *Trends Cell Biol.* **9**, 364–370 (1999).
9. K. Takemoto *et al.*, *Sci. Rep.* **3**, 2629 (2013).
10. K. Kim *et al.*, *Neuron* **87**, 813–826 (2015).
11. E. A. Vitriol, A. L. Wise, M. E. Berginski, J. R. Bamburg, J. Q. Zheng, *Mol. Biol. Cell* **24**, 2238–2247 (2013).
12. N. Honkura, M. Matsuzaki, J. Noguchi, G. C. Ellis-Davies, H. Kasai, *Neuron* **57**, 719–729 (2008).
13. Q. Zhou, K. J. Homma, M. M. Poo, *Neuron* **44**, 749–757 (2004).
14. Z. Zhou, J. Hu, M. Passafaro, W. Xie, Z. Jia, *J. Neurosci.* **31**, 819–833 (2011).
15. M. A. Wilson, B. L. McNaughton, *Science* **265**, 676–679 (1994).
16. D. Nakayama *et al.*, *J. Neurosci.* **35**, 819–830 (2015).
17. G. Girardeau, K. Benchenane, S. I. Wiener, G. Buzsáki, M. B. Zugaro, *Nat. Neurosci.* **12**, 1222–1223 (2009).
18. L. A. Atherton, D. Dupret, J. R. Mellor, *Trends Neurosci.* **38**, 560–570 (2015).
19. Z. Chen, M. A. Wilson, *Trends Neurosci.* **40**, 260–275 (2017).
20. K. Ghandour *et al.*, *Nat. Commun.* **10**, 2637 (2019).
21. D. Miyamoto *et al.*, *Science* **352**, 1315–1318 (2016).
22. Y. Ziv *et al.*, *Nat. Neurosci.* **16**, 264–266 (2013).
23. P. Rajasethupathy *et al.*, *Nature* **526**, 653–659 (2015).
24. B. Bontempi, C. Laurent-Demir, C. Destrade, R. Jaffard, *Nature* **400**, 671–675 (1999).
25. P. W. Frankland, B. Bontempi, L. E. Talton, L. Kaczmarek, A. J. Silva, *Science* **304**, 881–883 (2004).
26. Y. Zhang, H. Fukushima, S. Kida, *Mol. Brain* **4**, 4 (2011).
27. G. Riedel *et al.*, *Nat. Neurosci.* **2**, 898–905 (1999).
28. E. Shimizu, Y. P. Tang, C. Rampon, J. Z. Tsien, *Science* **290**, 1170–1174 (2000).
29. A. Hayashi-Takagi *et al.*, *Nature* **525**, 333–338 (2015).
30. H. Murakoshi, H. Wang, R. Yasuda, *Nature* **472**, 100–104 (2011).
31. K. Takemoto *et al.*, *Nat. Biotechnol.* **35**, 38–47 (2017).
32. K. Z. Tanaka *et al.*, *Science* **361**, 392–397 (2018).
33. T. Kitamura *et al.*, *Science* **356**, 73–78 (2017).
34. G. Vetere *et al.*, *Proc. Natl. Acad. Sci. U.S.A.* **108**, 8456–8460 (2011).
35. K. Takehara-Nishiuchi, *Brain Neurosci. Adv.* **4**, 2398212820925580 (2020).
36. N. Maingret, G. Girardeau, R. Todorova, M. Goutierre, M. Zugaro, *Nat. Neurosci.* **19**, 959–964 (2016).
37. F. Xia *et al.*, *eLife* **6**, e27868 (2017).
38. Y. D. Riani, T. Matsuda, K. Takemoto, T. Nagai, *BMC Biol.* **16**, 50 (2018).

ACKNOWLEDGMENTS

We thank K. Okamoto and M. Bosch for their contribution in the conceptualization of this work; P. Frankland, S. Kida, S. Middleton and T. Toyoizumi for comments; T. Manabe for help in setting up field recording; Y. Nishiyama for help in PCA analysis; and I. Nakahara (Neuro Programming Research) for writing the custom MATLAB program used in the sleep experiment. **Funding:** Grant-in-Aid for Scientific Research JP21650080, JP16H01292, JP16H01438, JP16H02455, JP17K19631, JP18H05434, and JP19H01010 from the MEXT, Japan, was given to Y.H. Grant-in-Aid for Scientific Research JP19H05233 was given to T.J.M. Grant-in-Aid for Scientific Research JP15K06728, JP17H05949, JP18K14818, and JP20K15901 from MEXT, Japan, was given to A.G. Grant-in-Aid for JSPS Research Fellow supported A.G. Grant-in-Aid for Scientific Research JP18H05410 from MEXT, Japan, was given to T.N. The Uehara Memorial Foundation supported Y.H., and the Naito Foundation supported Y.H. and T.N. Research Foundation for Opto-Science and Technology, Novartis Foundation, and the Takeda Science Foundation supported Y.H.; Y.H. also received HFSP Research Grant RGP0022/2013. JST CREST JPMJCR20E4 was given to Y.H. and T.M. JST Presto JPMJPR0165 was given to T.N. Inamori Grants from the Inamori Foundation were given to T.N. **Author contributions:** Conceptualization: A.G. and Y.H. Methodology: A.G., D.H., M.M., T.M., T.N., and Y.H. Investigation: A.G., A.B., K.M., J.W., S.T., X.J., and Y.H. Visualization: A.G. and Y.H. Funding acquisition: A.G., T.M., T.N., and Y.H. Project administration: Y.H. and T.J.M. Writing – original draft: A.G. and Y.H. Writing – review and editing: T.J.M. **Competing interests:** Y.H. is partly supported by Fujitsu Laboratories and Dwango. **Data and materials availability:** All data are available in the main text or in the supplementary materials. The gene for SuperNova is available from Addgene as SuperNova/pRSETB (#53234).

SUPPLEMENTARY MATERIALS

science.org/doi/10.1126/science.abj9195
Materials and Methods
Figs. S1 to S10
References (*39*, *40*)
MDAR Reproducibility Checklist

10 June 2021; accepted 24 September 2021
10.1126/science.abj9195

SPECTROSCOPY

Real-space imaging of anisotropic charge of σ-hole by means of Kelvin probe force microscopy

B. Mallada[1,2,3]†, A. Gallardo[2,4]†, M. Lamanec[3,5]†, B. de la Torre[1,2], V. Špirko[5,6], P. Hobza[5,7]*, P. Jelinek[1,2]*

An anisotropic charge distribution on individual atoms, such as σ-holes, may strongly affect the material and structural properties of systems. However, the spatial resolution of such anisotropic charge distributions on an atom represents a long-standing experimental challenge. In particular, the existence of the σ-hole on halogen atoms has been demonstrated only indirectly through the determination of the crystal structures of organic molecules containing halogens or with theoretical calculations, consequently calling for its direct experimental visualization. We show that Kelvin probe force microscopy with a properly functionalized probe can image the anisotropic charge of the σ-hole and the quadrupolar charge of a carbon monoxide molecule. This opens a new way to characterize biological and chemical systems in which anisotropic atomic charges play a decisive role.

The observation of molecular structures with the unusual atomic arrangement of possessing two adjacent halogens or a pair of halogen atoms and electron donor motifs (oxygen, nitrogen, sulfur, ...), found in different crystals in the second half of the 20th century (*1*–*4*), represented a long-standing puzzle in supramolecular chemistry. Both halogens and electron donors are electronegative elements that carry a negative charge. Thus, close contacts of these atoms should theoretically cause highly repulsive electrostatic interaction. Counterintuitively, such atoms are frequently found to form intermolecular bonds, called latter halogen bonds, that stabilize the molecular crystal structure. An elegant solution offered by Auffinger *et al.* (*5*), Clark *et al.* (*6*), and Politzer *et al.* (*7*, *8*) showed that the formation of a covalent bond between certain halogen atoms (chlorine, bromine, and iodine) and a more electronegative atom (such as carbon) gives rise to a so-called σ-hole that has an anisotropic charge distribution on the halogen atom. Thus, a physical observable corresponding electrostatic potential around the halogen atom is not uniform (as considered within all empirical force fields) but exhibits an electropositive distal to covalently bound carbon

[1]Regional Centre of Advanced Technologies and Materials, Czech Advanced Technology and Research Institute (CATRIN), Palacký University Olomouc, 78371 Olomouc, Czech Republic. [2]Institute of Physics, Academy of Sciences of the Czech Republic, Prague, Czech Republic. [3]Department of Physical Chemistry, Palacký University Olomouc, tr. 17. listopadu 12, 771 46 Olomouc, Czech Republic. [4]Department of Condensed Matter Physics, Faculty of Mathematics and Physics, Charles University, V Holešovičkách 2, 180 00 Prague, Czech Republic. [5]Institute of Organic Chemistry and Biochemistry, Czech Academy of Sciences, Flemingovo Náměstí 542/2, 16000 Prague, Czech Republic. [6]Department of Chemical Physics and Optics, Faculty of Mathematics and Physics, Charles University in Prague, Ke Karlovu 3, 12116 Prague, Czech Republic. [7]IT4Innovations, VŠB-Technical University of Ostrava, 17. listopadu 2172/15, 70800 Ostrava-Poruba, Czech Republic.
***Corresponding author. Email: pavel.hobza@uochb.cas.cz (P.H.); jelinekp@fzu.cz (P.J.)**
†These authors contributed equally to this work.

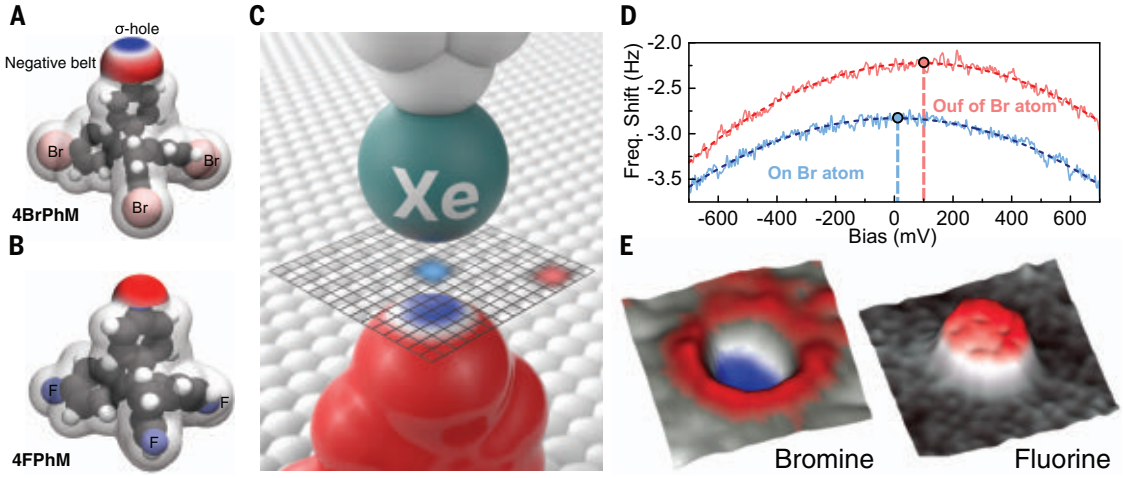


Fig. 1. Schematic view of the KPFM measurements to image a σ-hole. (**A** and **B**) Models of 4BrPhM and 4FPhM molecules, including corresponding electrostatic potential map on outermost Br/F atom. They reveal the presence of the σ-hole on a Br atom, and there is an isotropic negative charge on the F atom. (**C**) Schematic view of the acquisition method of the KPFM measurement with a functionalized Xe-tip on a 2D grid. (**D**) Corresponding $\Delta f(V)$ parabolas acquired in the central part (blue) of the 2D grid and on the periphery (red). Vertical dashed lines indicate the value of V_{LCPD} for the given $\Delta f(V)$ parabola, which forms the 2D KPFM image. (**E**) 3D representation of the KPFM images (V_{LCPD} maps) acquired with an Xe-tip over bromide and fluoride atoms of 4BrPhM and 4FPhM molecules. Blue indicates low values of V_{LCPD}, and red indicates high values of V_{LCPD}.

crown surrounded by an electronegative belt (Fig. 1A).

Consequently, halogen bonding is attributed to attractive electrostatic interaction between a halogen's electropositive σ-hole and an electronegative belt of the other halogen or an electronegative atom with negative charge. The International Union of Pure and Applied Chemistry (IUPAC) definition of a halogen bond (*9*) states that a halogen bond "occurs when there is evidence of a net attractive interaction between an electrophilic region associated with a halogen atom in a molecular entity and a nucleophilic region in another, or the same, molecular entity." Stability of the σ-hole bonding is comparable with that of hydrogen-bonded complexes, and attraction in both types of noncovalent complexes was originally assigned to electrostatic interaction. Although this scenario is basically true for H-bonded complexes, in the case of halogen-bonded systems, the importance of dispersion interaction (*10*) was highlighted. The importance of the dispersion interaction is not surprising because close contact takes place between two heavy atoms with high polarizability in halogen-bonded complexes.

The concept of halogen bonding was later generalized to a σ-hole bonding concept. In particular, the halogen (group 17), chalcogen (group 16), pnicogen (group 15), tetrel (group 14), and aerogen bonding (group 18) were established according to the name of the electronegative atom bearing the positive σ-hole. The existence of a σ-hole in atoms of the mentioned groups of elements has a common origin in the unequal occupation of valence orbitals.

The σ-hole bonding plays a key role in supramolecular chemistry (*11*), including the engineering of molecular crystals or in biological macromolecular systems (*5*). Despite its relevance and intensive research devoted to σ-hole bonding, the existence of the σ-hole itself was confirmed only indirectly with quantum calculations (*5*–*8*) or crystal structures of complexes containing σ-hole donors and electron acceptors (*11*–*15*). However, a direct visualization of this entity allowing for the resolution of its peculiar shape has thus far been missing.

The cause of the σ-hole is the anisotropic distribution of the atomic charge on a halogen atom. The imaging of anisotropic atomic charge represents an unfulfilled challenge for experimental techniques, including scanning probe microscopy (SPM), electron microscopy, and diffraction methods. Thus, we sought a technique in which the imaging mechanism relies on the electrostatic force to facilitate the visualization of the anisotropic charge distribution on a halogen atom with a sub-ångstrom spatial resolution. We show that real-space visualization of the σ-hole can be achieved through Kelvin probe force microscopy (KPFM) under ultrahigh vacuum (UHV) conditions (*16*, *17*) with unprecedented spatial resolution.

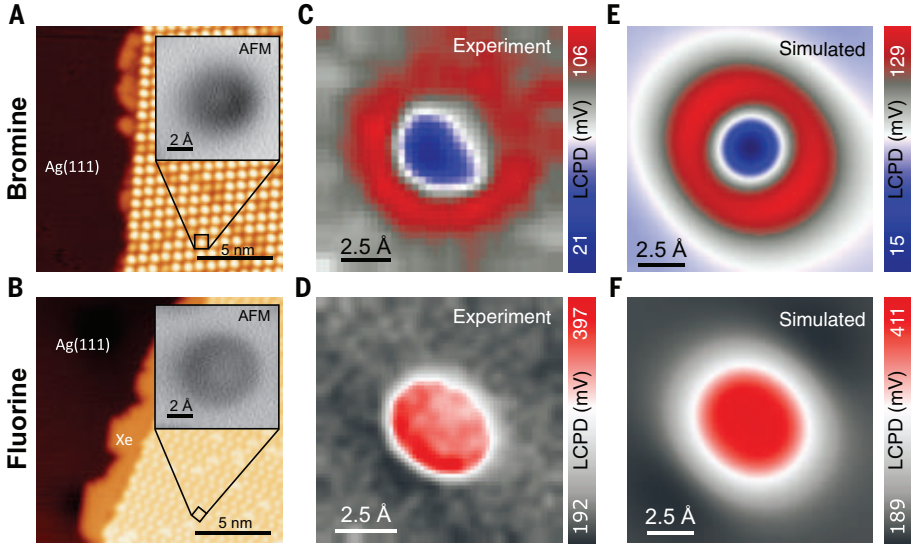


Fig. 2. KPFM imaging of 4BrPhM and 4FPhM molecules with an Xe-tip. (**A** and **B**) STM images of a molecular self-assembled submonolayer of 4BrPhM and 4FPhM molecules on an Ag(111) surface. (Insets) AFM images acquired on a single molecule with a Xe tip at the minima of the frequency shift. (**C** and **D**) Experimental KPFM images obtained with a functionalized Xe tip over bromide and fluoride atoms of single 4BrPhM and 4FPhM molecules. (**E** and **F**) Calculated KPFM images with a functionalized Xe tip of single 4BrPhM and 4FPhM molecules. Blue indicates low values of V_{LCPD} and red indicates high values of V_{LCPD}).

KPFM belongs to a family of SPM techniques that routinely provide real-space atomic resolution of surfaces. In the KPFM technique, the variation of the frequency shift Δf of an oscillating probe on applied bias voltage V with the quadratic form $\Delta f \sim V^2$ is recorded (*18*). The vertex of the Kelvin parabola $\Delta f(V)$ determines the difference between work functions of tip and sample, also called the contact potential difference V_{CPD}. Moreover, the spatial variation of the contact potential difference V_{CPD} across the surface allows the mapping of local variation of surface dipole on the sample (V_{LCPD}) (*17*). Recent developments of the KPFM technique operating in UHV conditions made it possible to reach true atomic resolution on surfaces (*19*, *20*) to image intramolecular charge distribution (*21*), to control single-electron charge states (*22*), to resolve bond polarity (*23*), or to discriminate charge (*24*).

The atomic contrast in KPFM images originates from a microscopic electrostatic force between static (ρ_0) and polarized charge densities ($\delta\rho$) located on frontier atoms from the tip apex and sample when an external bias is applied (*17*). There are two dominant components of this force: the interaction between the polarized charge on the apex $\delta\rho_t$, which is linearly proportional to the applied bias voltage (V), and the static charge on sample ρ_s^0. The second term consists of the electrostatic interaction between the polarized charge on the sample $\delta\rho_s$ and the static charge on tip ρ_t^0. Consequently, these two components cause local variation of the contact potential difference V_{LCPD} (a detailed description of the mechanism is provided in the supplementary materials), thus providing atomic-scale contrast.

Results

Consequently, KPFM appears to be the tool of choice for imaging anisotropic charge distribution within a single atom, such as the σ-hole. To test this hypothesis, we deliberately chose tetrakis(4-bromophenyl) methane (4BrPhM) and tetrakis(4-fluorophenyl) methane (4FPhM) compounds (Fig. 1, A and B).The skeleton arrangement of these compounds facilitates a tripodal configuration once deposited onto a surface with a single bromine-fluor atom oriented outward from the surface (fig. S1). This arrangement facilitated direct inspection of the σ-hole on a halogen atom by the front-most atom of a scanning probe, (Fig. 1C). Deposition of the molecules in low coverage (less than 1 monolayer) on the Ag(111) surface held at room temperature under UHV conditions led to the formation of well-ordered, self-assembled molecular arrangements in a rectangular formation (Fig. 2, A and B). Bromine atoms of the 4BrPhM molecule have a substantial positive σ-hole (Fig. 1A), and fluorine atoms possess an isotropic negative charge (Fig. 1B). This enabled us to perform comparative measurements on similar systems with and without the presence of the σ-hole.

Shown in Fig. 2, C and D, is a substantial contrast between two-dimensional (2D) constant-height KPFM maps acquired over Br and F front-most atoms of the molecular compounds with an Xe-decorated tip. In the case of the 4FPhM molecule, we observed a monotonous elliptical increase of the V_{LCPD} signal over the fluorine atom. In comparison, the KPFM image over the 4BrPhM molecule featured a notable ring-like shape. The 2D KPFM maps were recorded in the attractive tip-sample interaction regime near the minimum of the Δf-z curve (fig. S2) to avoid undesired topographic cross-talk (fig. S3 and supplementary text) or the effect of lateral bending of the functionalized probe due to repulsive forces (*25*) that could cause image distortions. Evolution of the contrast of the KPFM image of the σ-hole on the front-most Br atom with the tip-sample distance is shown in fig. S4.

Discussion

To confirm the origin of the anisotropic contrast observed experimentally on the Br atom, we carried out KPFM simulations using static ρ_0 and polarized $\delta\rho$ charges of Br and F-terminated molecules and Xe-tip models obtained from density functional theory (DFT) calculations (fig. S5). Simulated KPFM images that are perfectly matched to the experimental maps are shown in Fig. 2, E and F. Our theoretical model allowed us to decompose the two leading contributions: the electrostatic interaction of the polarized charge on tip $\delta\rho_t$ with the static charge on the molecule and the counterpart term of the electrostatic interaction between the polarized charge on molecule $\delta\rho_s$ with the ρ_t^0 static charge of the tip (fig. S5). We found that the anisotropic contrast obtained on the Br-terminated molecule can be rationalized from a variation of the microscopic electrostatic interaction between atomic-scale charges of tip and sample. On the periphery of the Br atom, the positive shift of V_{CPD} is given by the electrostatic interaction of the spherical polarized charge, $\delta\rho_t$ of the Xe-tip apex, with the belt of negative charge surrounding the positive σ-hole. By contrast, in the central part, the electrostatic interaction with the positive crown of the σ-hole turned the V_{LCPD} value with respect to that on the peripheral region. In the case of the 4FPhM molecule, both terms provided a trivial contrast with a positive shift of the V_{LCPD} over the atom. The term corresponding to the static charge ρ_s^0 on the molecule revealed an elliptical shape originating from neighbor positively charged hydrogen atoms in the underlying phenyl group of the 4FPhM molecule. Therefore, the shape of the feature presented in the KPFM image provided additional information about the internal arrangement of the molecule on the surface.

We deliberately used a single Xe atom to functionalize the tip apex instead of the more commonly used carbon monoxide (CO). As discussed above, the Xe tip allowed us to optimize the imaging conditions of the σ-hole because static charge density ρ_0 on the apex of the CO-tip had a strong quadrupolar character (Fig. 3A), and the charge on the Xe tip was highly spherical (fig. S5). This choice eliminated spurious spatial variation of the V_{LCPD} signal, which did not belong directly to the σ-hole. In particular, a component of the microscopic electrostatic interaction between static charge ρ_t^0 of the tip and polarized charge on sample $\delta\rho_s$ needs to be abolished. In the case of the Xe-tip, the spatial variation of the local V_{CPD} was dominated by the component that includes the interaction of a spherically polarized charge on the Xe atom $\delta\rho_t$ with the anisotropic electrostatic field of the σ-hole. This

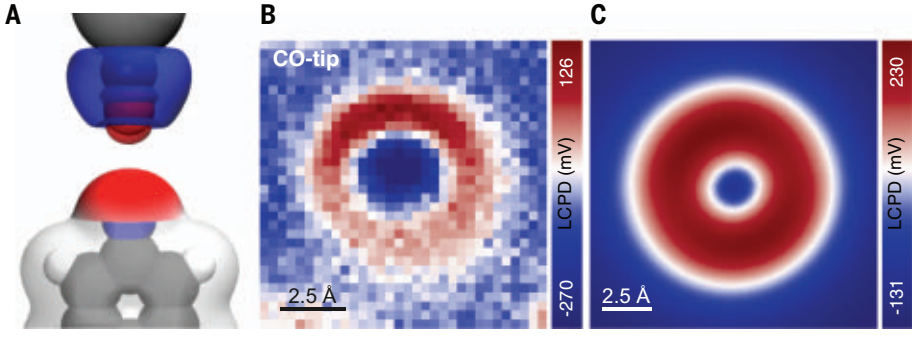


Fig. 3. KPFM imaging of a 4FPhM molecule with a CO tip. (**A**) Schematic view of a CO tip above a 4FPhM molecule with a superimposed calculated differential charge density of the CO tip, revealing (top) a quadrupole charge of a CO-tip model and (bottom) calculated electrostatic potential of 4FPhM molecule showing an isotropic negative charge on the frontier fluorine atom in 4FPhM. (**B**) Experimental KPFM image acquired over the frontier fluorine atom with a CO tip. (**C**) Simulated KPFM image of a 4FPhM molecule with a CO tip. Blue indicates low values of V_{LCPD}, and red indicates high values of V_{LCPD}).

enabled a direct mapping of the spatial charge distribution of the σ-hole by means of the KPFM technique.

Thus, it is instructive to look at the KPFM images acquired with the CO tip on the 4FPhM molecule as well. Despite the frontier fluorine atom of the 4FPhM molecule having an isotropic charge distribution, the experimental KPFM image (Fig. 3B) features a nontrivial ringlike shape with lower values of the V_{LCPD} signal on the center of the fluorine atom. Our KPFM simulation using a CO-tip (Fig. 3C) coincided qualitatively with the experimental counterpart. From a detailed analysis of the electrostatic components (fig. S6), we found that the contrast arose from the interaction of the spherical polarized charge $\delta\rho_s$ on a fluorine atom with the static quadrupole charge on a CO tip, composed of a negative crown of density on an oxygen atom surrounded by a positive charge belt (Fig. 3A). Thus, the KPFM features resolved on the 4FPhM molecule reflected the quadrupolar charge distribution of the CO tip. Thus, from the spatial variation of the V_{LCPD} signal, we could determine the sign of the quadrupole of the CO molecule on the tip. The shift of V_{LCPD} toward lower values in the central part of the KPFM image was caused by the negative charge crown of the quadrupole charge localized at oxygen (Fig. 3A). The enhanced V_{LCPD} value on the periphery reflects the positively charged belt of the quadrupole charge of the CO molecule. This reverse shift of V_{LCPD} with respect to the previous case of the σ-hole was caused by our inspection of the anisotropic charge on the tip instead of the sample. A detailed explanation of the origin and sign of V_{LCPD} shift is available in the supplementary materials.

Alternatively, some works reported subatomic features in noncontact atomic force microscopy (nc-AFM) (*26*) images with CO functionalized tips (*27*). However, the origin of such contrast and their interpretation of the physical meaning are under debate (*28*, *29*). Additionally, nc-AFM has demonstrated unprecedented chemical resolution of single molecules (*30*) or their charge distribution (*31*). Thus, we were intrigued by the possibility of imaging the σ-hole by means of nc-AFM with functionalized tips (*27*).

A series of high-resolution nc-AFM images acquired at a wide range of tip-sample distances are shown in fig. S7 with a CO tip and Xe tip, respectively. At the onset of the atomic contrast in nc-AFM mode, the tip-sample interaction was dominated by an attractive dispersion. The resulting AFM contrast for both 4FPhM and 4BrPhM molecules had a similar spherical character that lacks any subatomic feature. Also, in close tip-sample distances, the AFM contrast remained similar for both molecular compounds, featuring a bright spot in the center caused by the Pauli repulsion. Thus, we found that the AFM images did not reveal any signature of the σ-hole in the whole range of tip-sample distances covering both an attractive and repulsive interaction regime.

To understand in detail this experimental observation, we performed theoretical analysis of the nc-AFM images with a CO tip using the probe particle SPM model (*25*). Shown in figs. S8 and S9 are lateral cross sections of different force components of the interaction energy acting between the CO tip and the outermost F and Br atoms of the 4FPhM and 4BrPhM molecules, respectively. The calculated AFM images showed similar atomic contrast, ruling out the possibility to image the σ-hole with a CO tip. From the analysis, we inferred that the AFM contrast was dominated by dispersive and Pauli interaction, both of which have a highly spherical character. On the other hand, the electrostatic interaction possesses an anisotropic character caused by the presence of both a σ-hole on the Br atom and a quadrupolar charge distribution on the apex of the CO-tip (Fig. 3A). Nevertheless, the magnitude of the electrostatic interaction was about one order smaller than the competing dispersion and Pauli interactions, which made the σ-hole hard to image in the AFM technique. From this analysis, we could conclude that the resolution of anisotropic atomic charges requires a technique such as KPFM, whose contrast mechanism is mastered by the electrostatic interaction that maps the charge distribution on the forefront atoms.

Next, we investigated the influence of the σ-hole on the noncovalent intermolecular interaction energies. The nc-AFM technique provided the distinctive possibility to explore interaction energies between individual atoms and molecules placed on the tip apex and sample by means of site-specific force spectroscopies (*32*–*35*). Apart from a quantitative evaluation of the interaction energies between well-defined entities, the nc-AFM technique also gave an invaluable opportunity to benchmark the accuracy of different theoretical methods to describe these weak noncovalent interactions (*34*–*36*).

Tip functionalization offered an opportunity to explore distinct scenarios of the interaction mechanisms with molecular complexes. The Xe tip has a positive net charge and large polarizability, but the CO tip possesses a quadrupolar charge (O and C carry negative and positive net charge, respectively) and a relatively small polarizability. Their interaction energies are shown in Fig. 4, with the 4FPhM and 4BrPhM molecules as a function of the tip-sample distance. Small values of the maximum energies of 0.2 to 0.83 kcal/mol revealed a noncovalent bonding mechanism. In general, the complexes with an Xe-tip are more stable than the complexes with a CO tip, which may be rationalized by a larger dispersion interaction caused by an Xe tip. We observed that the Xe-4BrPhM complex was less stable than the Xe-4FPhM complex (by 0.67 and 0.83 kcal/mol, respectively) despite the larger polarizability of Br that determines the magnitude of the polarization interaction. This effect was caused by the presence of the repulsive electrostatic interaction between the positive σ-hole on a Br atom and the positively charged Xe tip, which partially cancelled the attractive dispersive interaction in the Xe-4BrPhM complex. On the other hand, the dispersive and electrostatic forces are both attractive in the case of the Xe-4FPhM complex, resulting in a larger total interaction energy. This observation not only supported the presence of the positive σ-hole on the Br atom, it also explained the origin of a peculiar intermolecular orientation of halogen-bonded molecular systems (*12*–*15*).

Recently, a vigorous effort has been devoted to the development of computational methods based on DFT with dispersion correction that are able to reliably describe intermolecular interactions in noncovalent complexes (*37*). But their transferability is still limited owing to adopted approximations, and thus, careful benchmarking is desired. From this perspective, the above-described complexes represent interesting noncovalent systems for benchmarks with a complex interplay between the dispersion and the electrostatic interaction. The maximum interaction energies measured were below 1 kcal/mol, which used to be considered as the limit of chemical accuracy, further strengthening the benchmark.

Accurate interaction energies for different types of noncovalent complexes could be obtained from a nonempirical coupled-cluster method covering triple-excitations [CCSD(T)]. Unfortunately, its large computational demands made it impossible to apply this method to a system of the size of the molecules we investigated in the present work.

To circumvent this problem, we performed the CCSD(T) calculations on smaller reference model systems consisting of F- and Br-benzene, exhibiting similar characteristics as 4BrPhM and 4FPhM molecules (supplementary materials). We compared the calculated CCSD(T) interaction energies to interaction energies obtained with several popular DFT functionals (table S3). We found that the range-separated ωB97X-V functional (*38*) that implicitly covers dispersion energy provided good agreement with the benchmarked dataset (table S3). Because this functional was also shown to provide the best results among other popular DFT functionals for various types of systems with noncovalent interactions (*38*), we selected this functional for further use.

To check its transferability to our larger molecular systems, we calculated the interaction energies between 4FPhM and 4BrPhM

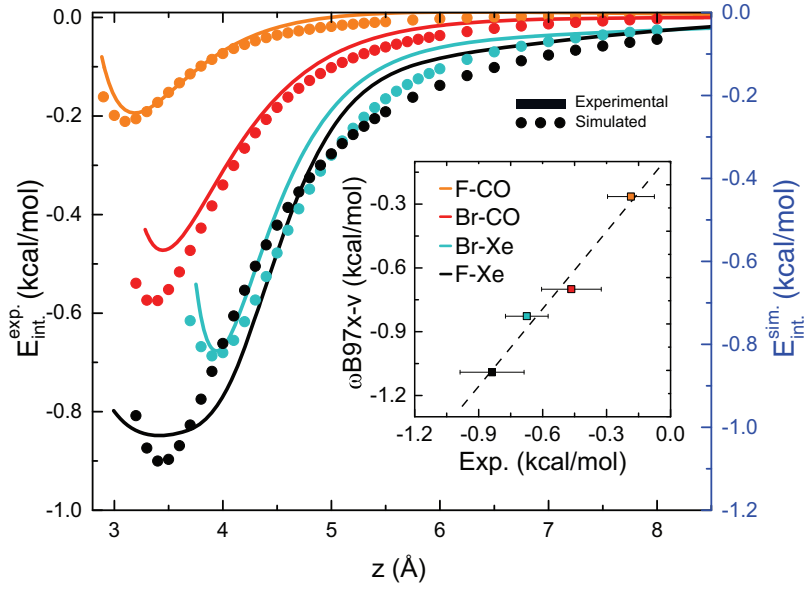


Fig. 4. Comparison of experimental and theoretical interaction energies of four complexes. Experimental (solid curves) and calculated (dots, obtained with DFT/ωB97X-V) energy curves versus tip-sample distance between 4FPhM and 4BrPhM molecules and Xe and CO tips. (Inset) The correlation between experimental and theoretical values [coefficient of determination (R^2) = 0.98] of the energy minima for all complexes. Bars indicate an estimated experimental error of the energy minima calculated as the difference between a polynomial fit and the experimental energy (fig. S12).

molecules and Xe- and CO-tip models. Excellent agreement between the ωB97X-V interaction energies and the experimental data results is shown in Fig. 4. The calculated energy minima for all complexes fit the measured values perfectly within the experimental error (Fig. 4, inset). The PBE0 functional (*39*) with the D3 correction (*40*) reproduced the CCSD(T) results on small-model systems as well (table S3 and fig. S10). However, its transferability on the large systems was no longer as good as the range-separated ωB97X-V functional (fig. S11).

The ωB97X-V functional describes well the interaction trend for all considered systems (Fig. 4, inset), with the caveat that it systematically slightly overestimates the interaction energy by ~0.1 kcal/mol. The perfect agreement between theoretical and experimental values could not be expected because calculations were limited to free-standing 4FPhM and 4BrPhM molecules interacting with Xe- and CO-tip model, and in the experiment, 4FPhM and 4BrPhM molecules were adsorbed at Ag(111) surface. The results confirmed good transferability of the ωB97X-V functional toward larger systems. Moreover, the good agreement between calculated and experimental datasets obtained for all four complexes also gave confidence in the multiscale benchmark technique that uses small-model complexes with the Xe-tip model. Therefore, this approach makes it possible to accurately describe systems whose size does not allow for the direct application of the accurate coupled-cluster technique (or a similar technique), or when other direct experimental measurements are currently not feasible.

Conclusions

We report the possibility of achieving the spatial resolution of anisotropic atomic charge with the KPFM technique, which not only provided direct evidence of the existence of σ-holes but is expected to substantially extend the possibility to characterize charge distribution in complex molecular systems and on surfaces. We anticipate that this technique could be further extended to provide invaluable information about the local inhomogeneous polarizability of individual atoms on surfaces or within molecules with unprecedented spatial resolution in chemical and biologically relevant systems.

REFERENCES AND NOTES

1. N. Ramasubbu, R. Parthasarathy, P. Murray-Rust, *J. Am. Chem. Soc.* **108**, 4308–4314 (1986).
2. O. Hassel, J. Hvoslef, E. H. Vihovde, N. A. Sörensen, *Acta Chem. Scand.* **8**, 873–873 (1954).
3. O. Hassel *et al.*, *Acta Chem. Scand.* **13**, 275–280 (1959).
4. O. Hassel *et al.*, *Acta Chem. Scand.* **12**, 1146–1146 (1958).
5. P. Auffinger, F. A. Hays, E. Westhof, P. S. Ho, *Proc. Natl. Acad. Sci. U.S.A.* **101**, 16789–16794 (2004).
6. T. Clark, M. Hennemann, J. S. Murray, P. Politzer, *J. Mol. Model.* **13**, 291–296 (2007).
7. T. Brinck, J. S. Murray, P. Politzer, *Int. J. Quantum Chem.* **44** (S19), 57–64 (1992).
8. P. Politzer, P. Lane, M. C. Concha, Y. Ma, J. S. Murray, *J. Mol. Model.* **13**, 305–311 (2007).
9. G. R. Desiraju *et al.*, *Pure Appl. Chem.* **85**, 1711–1713 (2013).
10. K. E. Riley, P. Hobza, *Phys. Chem. Chem. Phys.* **15**, 17742–17751 (2013).
11. L. C. Gilday *et al.*, *Chem. Rev.* **115**, 7118–7195 (2015).
12. Z. Han *et al.*, *Science* **358**, 206–210 (2017).
13. J. Tschakert *et al.*, *Nat. Commun.* **11**, 5630 (2020).
14. S. Kawai *et al.*, *ACS Nano* **9**, 2574–2583 (2015).
15. H. Huang *et al.*, *ACS Nano* **10**, 3198–3205 (2016).
16. M. Nonnenmacher, M. P. O'Boyle, H. K. Wickramasinghe, *Appl. Phys. Lett.* **58**, 2921–2923 (1991).
17. T. Glatzel, S. Sadewasser, Eds., *Kelvin Probe Force Microscopy* (Springer, 2018), vol. 65.
18. W. Melitz, J. Shen, A. C. Kummel, S. Lee, *Surf. Sci. Rep.* **66**, 1–27 (2011).
19. L. Nony, A. S. Foster, F. Bocquet, C. Loppacher, *Phys. Rev. Lett.* **103**, 036802 (2009).
20. S. Sadewasser *et al.*, *Phys. Rev. Lett.* **103**, 266103 (2009).
21. F. Mohn, L. Gross, N. Moll, G. Meyer, *Nat. Nanotechnol.* **7**, 227–231 (2012).
22. L. Gross *et al.*, *Science* **324**, 1428–1431 (2009).
23. F. Albrecht *et al.*, *Phys. Rev. Lett.* **115**, 076101 (2015).
24. B. Mallada *et al.*, *ACS Sustain. Chem. Eng.* **8**, 3437–3444 (2020).
25. P. Hapala *et al.*, *Phys. Rev. B Condens. Matter Mater. Phys.* **90**, 085421 (2014).
26. T. R. Albrecht, P. Grütter, D. Horne, D. Rugar, *J. Appl. Phys.* **69**, 668–673 (1991).
27. P. Jelínek, *J. Phys. Condens. Matter* **29**, 343002 (2017).
28. F. Huber *et al.*, *Science* **366**, 235–238 (2019).
29. M. Emmrich *et al.*, *Science* **348**, 308–311 (2015).
30. L. Gross, F. Mohn, N. Moll, P. Liljeroth, G. Meyer, *Science* **325**, 1110–1114 (2009).
31. P. Hapala *et al.*, *Nat. Commun.* **7**, 11560 (2016).
32. M. A. Lantz *et al.*, *Science* **291**, 2580–2583 (2001).
33. Y. Sugimoto *et al.*, *Nature* **446**, 64–67 (2007).
34. S. Kawai *et al.*, *Nat. Commun.* **7**, 11559 (2016).
35. Z. Sun, M. P. Boneschanscher, I. Swart, D. Vanmaekelbergh, P. Liljeroth, *Phys. Rev. Lett.* **106**, 046104 (2011).
36. C. Wagner *et al.*, *Nat. Commun.* **5**, 5568 (2014).
37. S. Grimme, A. Hansen, J. G. Brandenburg, C. Bannwarth, *Chem. Rev.* **116**, 5105–5154 (2016).
38. N. Mardirossian, M. Head-Gordon, *Phys. Chem. Chem. Phys.* **16**, 9904–9924 (2014).
39. C. Adamo, V. Barone, *J. Chem. Phys.* **110**, 6158–6170 (1999).
40. S. Grimme, J. Antony, S. Ehrlich, H. Krieg, *J. Chem. Phys.* **132**, 154104 (2010).
41. B. Mallada *et al.*, Data for "Real-space imaging of anisotropic charge of σ-hole by means of Kelvin probe force microscopy". *Zenodo* (2020); doi:10.5281/zenodo.5172233.

ACKNOWLEDGMENTS

We acknowledge fruitful discussions with A. Růžička and P. Hapala. M.L. acknowledges inspirational advice from his previous supervisor, J. Kuchár. P.J. and B.d.l.T. dedicate this manuscript to the memory of J. M. Gómez-Rodríguez. **Funding:** This work was supported by the Czech Science Foundation GACR 20-13692X (A.G., B.M., and P.J.) and 19-27454X (P.H.); Praemium Academie of the Academy of Science of the Czech Republic (A.G.); Palacký University Internal Grant Association IGA_PrF_2021_031 (M.L.); Palacký University Internal Grant Association IGA_PrF_2021_034 (B.M.); and CzechNanoLab Research Infrastructure, supported by MEYS CR (LM2018110). **Author contributions:** Conceptualization: P.J. Methodology: B.M., A.G., B.d.l.T., and P.J. Theoretical calculations: A.G., M.L., V.Š., P.J., and P.H. Experimental: B.M. and B.d.l.T. Funding acquisition: P.H. and P.J. Supervision: B.d.l.T., P.H., and P.J. Writing, original draft: B.M., A.G., B.d.l.T., P.H., and P.J. **Competing interests:** The authors declare that they have no competing interests. **Data and materials availability:** All data needed to evaluate the conclusions in the paper are present in the paper or the supplementary materials. Data can be found at Zenodo (*41*).

SUPPLEMENTARY MATERIALS

science.org/doi/10.1126/science.abk1479
Materials and Methods
Supplementary Text
Figs. S1 to S20
Tables S1 to S3
References (*42*–*55*)

24 June 2021; resubmitted 28 July 2021
Accepted 20 September 2021
10.1126/science.abk1479

NEURODEGENERATION

CD4$^+$ T cells contribute to neurodegeneration in Lewy body dementia

David Gate[1,2,3]*, Emma Tapp[2,3], Olivia Leventhal[2,3]†, Marian Shahid[2], Tim J. Nonninger[2,3], Andrew C. Yang[4,5], Katharina Strempfl[6,7,8], Michael S. Unger[6,7], Tobias Fehlmann[9], Hamilton Oh[2,3], Divya Channappa[2], Victor W. Henderson[2], Andreas Keller[2,9], Ludwig Aigner[6,7], Douglas R. Galasko[10], Mark M. Davis[11,12], Kathleen L. Poston[2], Tony Wyss-Coray[2,3,5]*

Recent studies indicate that the adaptive immune system plays a role in Lewy body dementia (LBD). However, the mechanism regulating T cell brain homing in LBD is unknown. Here, we observed T cells adjacent to Lewy bodies and dopaminergic neurons in postmortem LBD brains. Single-cell RNA sequencing of cerebrospinal fluid (CSF) identified up-regulated expression of *C-X-C motif chemokine receptor 4* (*CXCR4*) in CD4$^+$ T cells in LBD. CSF protein levels of the CXCR4 ligand, C-X-C motif chemokine ligand 12 (CXCL12), were associated with neuroaxonal damage in LBD. Furthermore, we observed clonal expansion and up-regulated *interleukin 17A* expression by CD4$^+$ T cells stimulated with a phosphorylated α-synuclein epitope. Thus, CXCR4-CXCL12 signaling may represent a mechanistic target for inhibiting pathological interleukin-17–producing T cell trafficking in LBD.

Lewy body dementia (LBD) encompasses two disorders characterized by abnormal deposits of α-synuclein in the brain: dementia with Lewy bodies (DLB) and Parkinson's disease dementia (PDD). PDD is defined by changes in memory and behavior and afflicts patients in late-stage Parkinson's disease (PD) (*1*). The symptoms and cognitive profiles of DLB and PDD are highly similar (*2*). Several lines of evidence suggest involvement of the adaptive immune system in DLB (*3*) and PDD (*4*–*6*). Immune alterations have been reported in the peripheral blood of PD patients, including changes to lymphocyte activation (*7*–*9*). The involvement of CD4$^+$ T cells in PD is supported by studies in mouse models (*10*–*13*) and in vitro culture systems (*6*). Moreover, recent studies have found that a defined set of peptides derived from α-synuclein act as antigenic epitopes and promote T cell responses in nondemented PD patients ex vivo (*4*, *5*, *14*). However, demonstration of a role for T cells in the neurodegenerative process of LBD in vivo is lacking. Furthermore, the mechanism regulating T cell brain homing in LBD remains unknown.

[1]Department of Neurology, Northwestern University, Chicago, IL, USA. [2]Department of Neurology and Neurological Sciences, Stanford University School of Medicine, Stanford, CA, USA. [3]Wu Tsai Neurosciences Institute, Stanford University, Stanford, CA, USA. [4]Department of Bioengineering, Stanford University, Stanford, CA, USA. [5]Chemistry, Engineering, and Medicine for Human Health (ChEM-H), Stanford University, Stanford, CA, USA. [6]Institute of Molecular Regenerative Medicine, Paracelsus Medical University, Salzburg, Austria. [7]Spinal Cord Injury and Tissue Regeneration Center Salzburg, Paracelsus Medical University, Salzburg, Austria. [8]QPS Austria GmbH, Parkring 12, 8074 Grambach, Austria. [9]Chair for Clinical Bioinformatics, Saarland University, Saarbrucken, Germany. [10]Department of Neurosciences, University of California, San Diego, La Jolla, CA, USA. [11]Department of Microbiology and Immunology, School of Medicine, Stanford University, Stanford, CA, USA. [12]Howard Hughes Medical Institute, Stanford University School of Medicine, Stanford, CA, USA.
***Corresponding author. Email: dgate@northwestern.edu (D.G.); twc@stanford.edu (T.W.-C.)**
†Present address: University of California San Francisco School of Medicine, University of California San Francisco, San Francisco, CA, USA.

Results

Neurodegeneration in LBD study subjects

To assess adaptive immunity in LBD, we integrated analyses of multiple cohorts consisting of healthy aged controls (n = 162) and patients with clinical DLB and PD (collectively referred to as PD-DLB; n = 148) (fig. S1A, table S1, and data S1). Montreal Cognitive Assessment scores indicated reduced cognition in PD-DLB subjects ($P = 8.6 \times 10^{-5}$; fig. S1B). Furthermore, proteomic analysis of cerebrospinal fluid (CSF) indicated increased levels of neurofilament light chain (NEFL; P = 0.0031; fig. S1C). NEFL reflects neuronal damage in a variety of neurological disorders (*12*–*14*). Because PD has a long prodromal phase before dementia onset, we stratified patients into PD-not cognitively impaired (PD-NCI) or PDD (those with cognitive impairments and dementia) groups. Compared to healthy subjects, patients diagnosed as PDD ($P = 6.33 \times 10^{-13}$) and DLB ($P = 4.02 \times 10^{-13}$) presented with lower cognitive scores than PD-NCI patients (P = 0.83; fig. S1D). These data suggest increased neurodegeneration in our PDD and DLB subjects.

T cells home to the LBD brain and reside in close proximity to α-synuclein deposits

We next examined postmortem substantia nigra to localize and quantify T cells in LBD. Immunohistochemical analysis showed CD3$^+$ T cells in close proximity to neuronal processes labeled by the dopamine enzyme tyrosine hydroxylase (TH) in the substantia nigra of PDD and DLB brains (Fig. 1A and fig. S2A). Quantification of control (non-neurologic disease) and LBD substantia nigra indicated higher numbers of CD3$^+$ T cells in LBD (Welch's t test, P = 0.006; Fig. 1B). We then probed LBD brains for α-synuclein to determine whether T cells localize to these protein deposits. Indeed, we found CD3$^+$ T cells adjacent to α-synuclein deposits in LBD brains (fig. S2, B and C). Quantification of these cells revealed a higher percentage of CD3$^+$ T cells localized to α-synuclein deposits in LBD substantia nigra (Welch's t test, P = 0.002; Fig. 1C). We also detected CD3$^+$ T cells adjacent to Lewy neurites surrounding TH$^+$ neurons in PDD (Fig. 1D and fig. S3, A and B) and DLB substantia nigra (fig. S3C). CD3$^+$ T cells were also found near α-synuclein$^+$ Lewy bodies adjacent to vesicular glutamate transporter 1 (vGLUT1)$^+$ glutamatergic neurons in the hippocampal CA2 region (fig. S3D). Notably, CD3$^+$ T cells were also bound to Iba1$^+$ innate immune cells, which extended processes toward phosphorylated α-synuclein$^+$ Lewy bodies in PDD (Fig. 1E) and DLB (fig. S3, E and F). In mice expressing human α-synuclein (Thy1-αSyn), CD3$^+$ T cells were found adjacent to α-synuclein deposits in the midbrain (fig. S4). Thus, T cells home to the LBD brain and reside in close proximity to α-synuclein deposits.

CXCR4 is up-regulated in CD4$^+$ T cells in LBD CSF

To uncover potential mechanisms of brain entry in LBD, we performed single-cell RNA sequencing (scRNAseq) (*15*, *16*) of CSF cells isolated from age- and sex-matched healthy (n = 11) and PD-DLB (n = 11) subjects (fig. S5A). Multidimensional reduction of scRNAseq data by t-distributed stochastic neighbor embedding (tSNE) revealed clusters of immune cells (Fig. 2A). Clusters expressed marker genes corresponding to each immune cell subtype (Fig. 2B) and were not specific to group or sex (fig. S5B). Cell-type–specific differential expression of PD-DLB versus healthy CSF cell clusters revealed CD4$^+$ T cells as the most transcriptionally altered immune cell subtype (Fig. 2C and data S2). Highly differentially expressed PD-DLB CD4$^+$ T cell genes included *Janus kinase 1* (*JAK1*), a kinase essential for cytokine signaling, and the T cell activation gene *cluster of differentiation 69* (*CD69*) (Fig. 2D). The chemokine receptor gene *C-X-C motif chemokine receptor 4* (*CXCR4*) was also highly up-regulated in PD-DLB CD4$^+$ T cells (Fig. 2D). Moreover, *CXCR4* and *CD69* were highly expressed by the majority of CD4$^+$ T cells (fig. S5C). Quantification of individual subjects' CD4$^+$ T cell *CXCR4* and *CD69* expression revealed higher levels in PD-DLB versus healthy CSF (Welch's t test, P = 0.03 and P = 0.025, respectively; fig. S5D). Analysis of pathways containing *CXCR4* indicated altered metabolic and catalytic activity and response to cytokine stimulus in CD4$^+$ T cells in PD-DLB (fig. S5E). Thus, enhanced CD4$^+$ T cell cytokine signaling and activation can be observed in PD-DLB CSF.

The increase in activation of CSF CD4$^+$ T cells in PD-DLB prompted us to determine whether

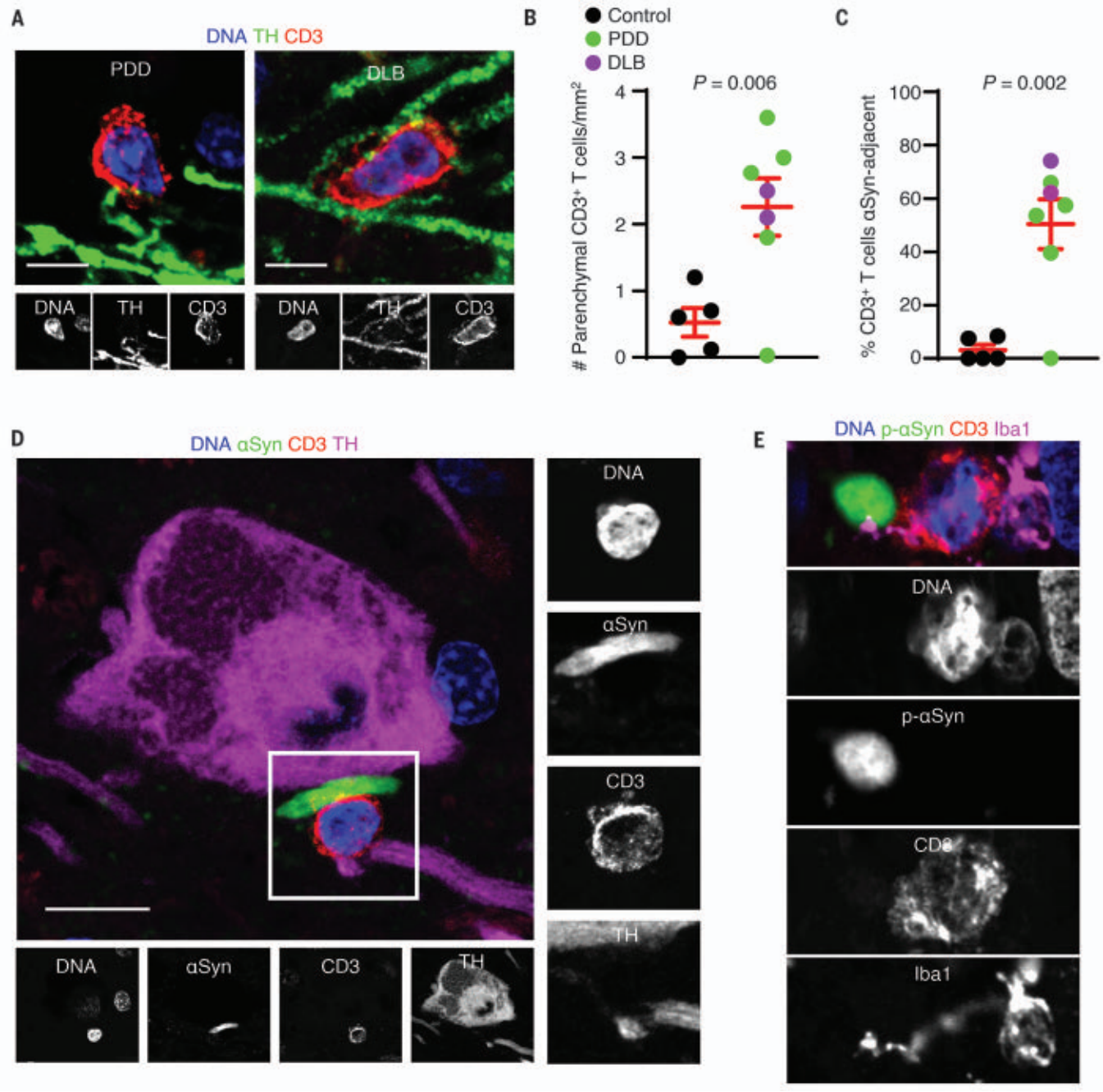


Fig. 1. T cells localize to dopaminergic neurons and α-synuclein deposits in the LBD brain. (**A**) Confocal images of parenchymal $CD3^+$ T cells adjacent to TH^+ neuronal processes in PDD and DLB substantia nigra. Scale bars, 10 μm. $CD3^+$ T cells were detected in six out of seven LBD brains analyzed. (**B**) Quantification of parenchymal $CD3^+$ T cells reveals higher numbers of T cells in LBD versus healthy substantia nigra. Data are mean ± SEM. (**C**) Quantification of percent parenchymal $CD3^+$ T cells adjacent to α-synuclein deposits in LBD brains. Cells determined to be adjacent to α-synuclein deposits were within 5-μm distance. Data are mean ± SEM. (**D**) Confocal image of PDD substantia nigra showing a $CD3^+$ T cell in close proximity to an α-synuclein$^+$ Lewy neurite. Scale bar, 10 μm. Similar results were observed in six out of seven LBD brains. (**E**) An $Iba1^+$ innate immune cell in the PDD substantia nigra. The $Iba1^+$ process appears to contact the $CD3^+$ T cell and α-synuclein$^+$ Lewy body in PDD. Scale bar, 5 μm. Similar results were observed in six out of seven LBD brains.

clonally expanded (i.e., antigen-specific) cells were distinct in PD-DLB. To assess clonal expansion, we performed single-cell T cell receptor sequencing (scTCRseq) on the same CSF cells as above (Fig. 2E). Comparing RNA transcriptomes of clonal $CD4^+$ T cells from healthy and PD-DLB CSF by differential expression again showed increased expression of *CD69* and *CXCR4* in PD-DLB (Fig. 2, F and G, and data S3). Clonal T cells were not specific to disease group or sex (fig. S6A). Pathway analysis of differentially expressed clonal $CD4^+$ PD-DLB T cell genes revealed regulation of cytokine-mediated signaling and intracellular signal transduction as the most altered pathways containing *CXCR4* (fig. S6B). We also detected higher expression of *killer cell lectin-like receptor subfamily B, member 1* (*KLRB1*),

a marker of proinflammatory interleukin-17 (IL-17)–producing [T helper 17 (T_H17)] memory $CD4^+$ T cells (*17*, *18*) (Fig. 2F and data S3). We also localized $CD3^+KLRB1^+$ T cells to phosphorylated α-synuclein deposits in the parenchyma of PDD brains (fig. S6C). Thus, LBD may involve enhanced activation of proinflammatory $CD4^+$ T_H17 cells.

The CXCR4 ligand CXCL12 is associated with neurodegeneration in LBD

To determine if T cells express CXCR4 in the brain, we performed immunohistochemistry

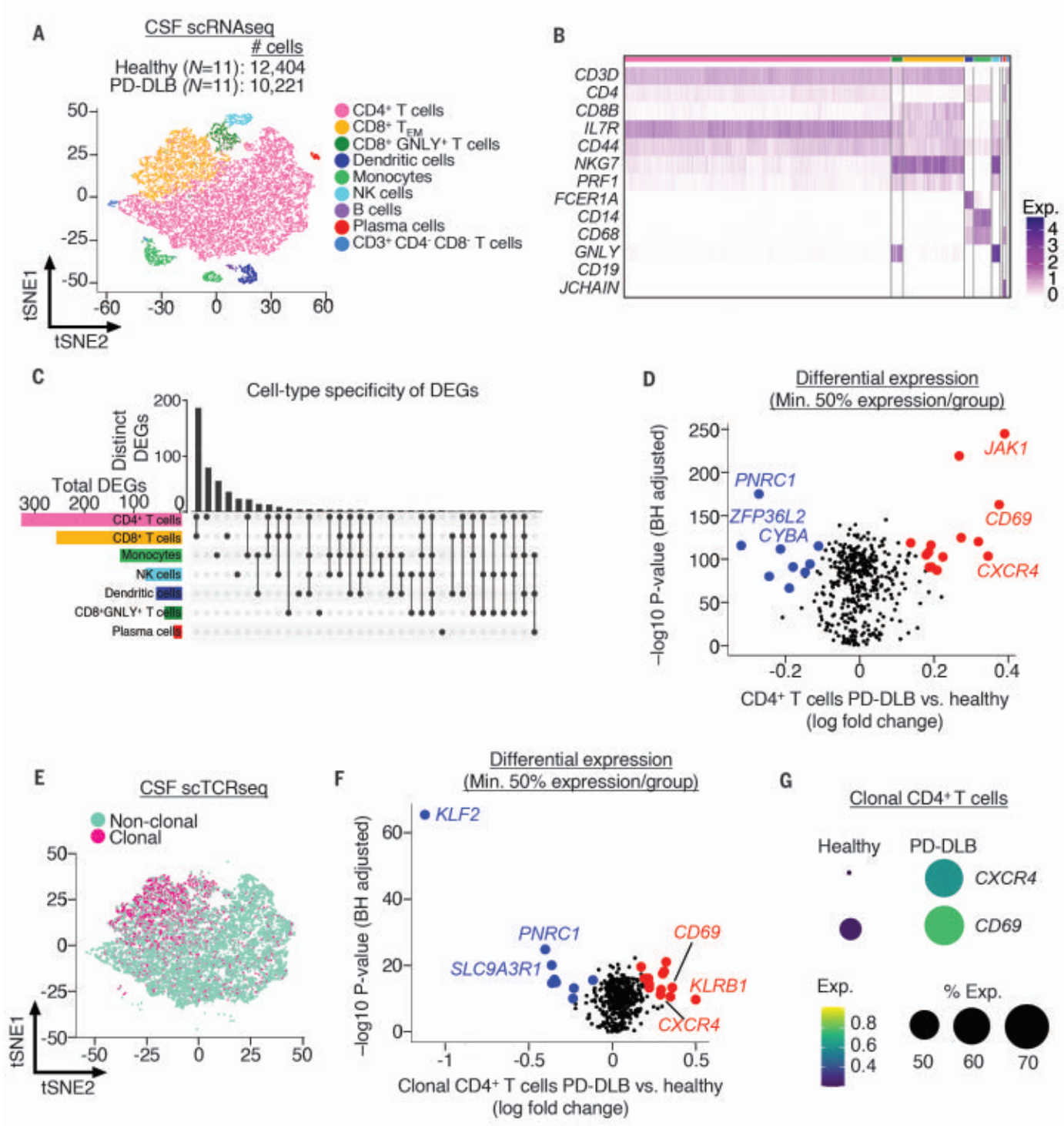


Fig. 2. Up-regulated *CXCR4* demarks $CD4^+$ T cells in PD-DLB. (**A**) scRNAseq of CSF cells shows clusters of various types of immune cells by tSNE. (**B**) Marker expression of CSF immune cells used to classify clusters. (**C**) UpSet plot showing cell-type–specific analysis of differentially expressed genes of PD-DLB versus healthy CSF immune cells indicating that the highest number of differentially expressed genes are in $CD4^+$ T cells. (**D**) Volcano plot showing differentially expressed genes of $CD4^+$ T cells from LBD versus healthy CSF. The increased expression of *CXCR4* in LBD is apparent. (**E**) scTCRseq of CSF immune cells showing clonal versus nonclonal T cells plotted by tSNE. (**F**) Volcano plot of differential expression analysis of clonal $CD4^+$ T cells showing increased expression of *CD69*, *KLRB1*, and *CXCR4* in PD-DLB versus healthy CSF. (**G**) Dot plot showing higher levels of *CXCR4* and *CD69* in PD-DLB versus healthy CSF clonal $CD4^+$ T cells.

on PDD meninges, which revealed meningeal $CD3^+CXCR4^+$ cells (fig. S7A). We noted localization of the CXCR4 ligand, C-X-C motif chemokine ligand 12 (CXCL12) to $CD3^+CXCR4^+$ cells in the meninges (fig. S7A). In mice, CXCL12 is expressed by cerebrovascular endothelial cells and promotes recruitment of $CD4^+$ T cells (*19*). Within the PDD brain, CXCL12 localized to the cerebrovasculature (Fig. 3A), which we confirmed by costaining PDD brains with the vascular marker cluster of differentiation 31 (CD31; fig. S7B). $CD3^+$ T cells resided in the perivascular space adjacent to $CXCL12^+$ vessels (Fig. 3A and fig. S7C).

We next sought to determine whether levels of CSF CXCL12 were associated with cognitive impairment in PD. We measured CXCL12 in a cohort of age- and sex-matched healthy (n = 84) and PD (n = 79) subjects (fig. S8A). This revealed higher amounts of CSF CXCL12 in PD (Welch's t test, P = 0.036; Fig. 3B). We separated this PD cohort by clinical diagnoses as PD-NCI or PDD, which revealed lower cognitive scores in PDD subjects compared to healthy ($P = 3.12 \times 10^{-11}$) and PD-NCI ($P = 7.67 \times 10^{-10}$) subjects {one-way analysis of variance (ANOVA), [F (2,135) = 31.697, $P = 5.18 \times 10^{-12}$]; fig. S8B}. NEFL levels also distinguished PDD from healthy ($P = 1.00 \times 10^{-4}$) and PD-NCI ($P = 8.30 \times 10^{-3}$) subjects {one-way ANOVA, [F (2,117) = 9.161, P = 0.0002]; fig. S8C}. Age did not significantly affect CXCL12 levels in this cohort {analysis of covariance (ANCOVA) [F (2,150) = 2.867, P = 0.071]; fig. S8D}. We then correlated CXCL12 levels with neurodegenerative disease biomarkers, including ubiquitin carboxyl-terminal esterase L1, total tau, phosphorylated tau 181, amyloid-β, α-synuclein, and NEFL (fig. S8E). CXCL12 levels correlated most positively with NEFL in PDD [Spearman's rank correlation coefficient (r_s) = 0.40; P = 0.023), and these correlations were lesser in healthy (r_s = 0.12; P = 0.394) and PD-NCI ($_s$ = 0.17; P = 0.326) subjects {ANCOVA, [F (2,114) = 3.484, P = 0.031]; Fig. 3C}. Thus, dysregulated CXCR4-CXCL12 signaling is associated with neurodegeneration in LBD.

CXCR4 demarks $CD4^+$ T cells that are specific to the CSF

Because peripheral T cells have been shown to be dysregulated in PD (*4*, *5*, *14*), we compared $CD4^+$ T cells of the peripheral immune system and CSF. We performed scRNAseq on peripheral blood mononuclear cells (PBMCs) of the same subjects that we analyzed by CSF scRNAseq and focused our analysis on $CD4^+$ T cells (Fig. 4A). We uncovered $CD4^+$ T cell populations that were specific to the CSF (referred to as CSF unique; Fig. 4B). We also identified up-regulated *CXCR4*, *CD69*, and *TSC22 domain family member 3* (*TSC22D3*) as the primary genes defining CSF unique T cells (Fig. 4D). Quantification of individual subjects' CSF unique $CD4^+$ T cell *CXCR4* and *CD69* expression revealed higher levels in PD-DLB versus healthy CSF (Welch's t test, P = 0.0218 and P = 0.0217, respectively; Fig. 4E). Thus, *CXCR4* may regulate homing of $CD4^+$ T cells to the LBD brain.

α-synuclein stimulation drives T cell clonal expansion and activation

Our immunohistochemistry results indicated close proximity of T cells with α-synuclein in LBD brains. This led us to investigate whether α-synuclein could drive T cell clonal expansion and activation. Several peptides derived from α-synuclein act as antigenic epitopes and promote T cell responses in PD PBMCs (*4*, *5*). We incubated PBMCs from healthy (n = 32) and PD (n = 53) subjects with a pool of eight antigenic α-synuclein peptides and measured activation of $CD3^+$ T cells by flow cytometry using coexpression of HLA-DR and CD38 (fig. S9A). Unexpectedly, control PD patient T cells in the absence of stimulation exhibited higher percentages of $HLA\text{-}DR^+CD38^+$ T cells than healthy subjects (Welch's t test, P = 0.006; fig. S9, B and C), suggesting that higher baseline levels of peripheral T cell activation exists in PD patients in vivo. We also detected higher levels of T cell activation after stimulation with the α-synuclein peptide pool (Welch's t test, P = 0.002; fig. S10C). We confirmed increased activation of PD T cells after α-synuclein stimulation by measuring CD69 by flow cytometry (Welch's t test, P = 0.027; fig. S9D).

To identify patient-specific antigenic α-synuclein peptides, we selected two PD patients who exhibited appreciable increases in T cell activation by the α-synuclein peptide pool (fig. S9E). We then measured T cell activation in these subjects using individual α-synuclein peptides. This strategy revealed activation of T cells by the peptide DNEAYEMPSEEGYQD, which contains a phosphorylated serine residue at amino acid position 129 (Fig. 5, A and B). $HLA\text{-}DR^+CD38^+CD4^+$ T cells up-regulated CXCR4 in response to peptide stimulation (Fig. 5C). To determine transcriptional changes induced by this peptide, we sorted activated T cells from unstimulated and stimulated PBMCs (fig. S10A). We then performed scRNAseq on $HLA\text{-}DR^+CD38^+$ T cells to interpret transcriptomic alterations (data S4). Stimulated T cells had increased expression of *actin gamma*

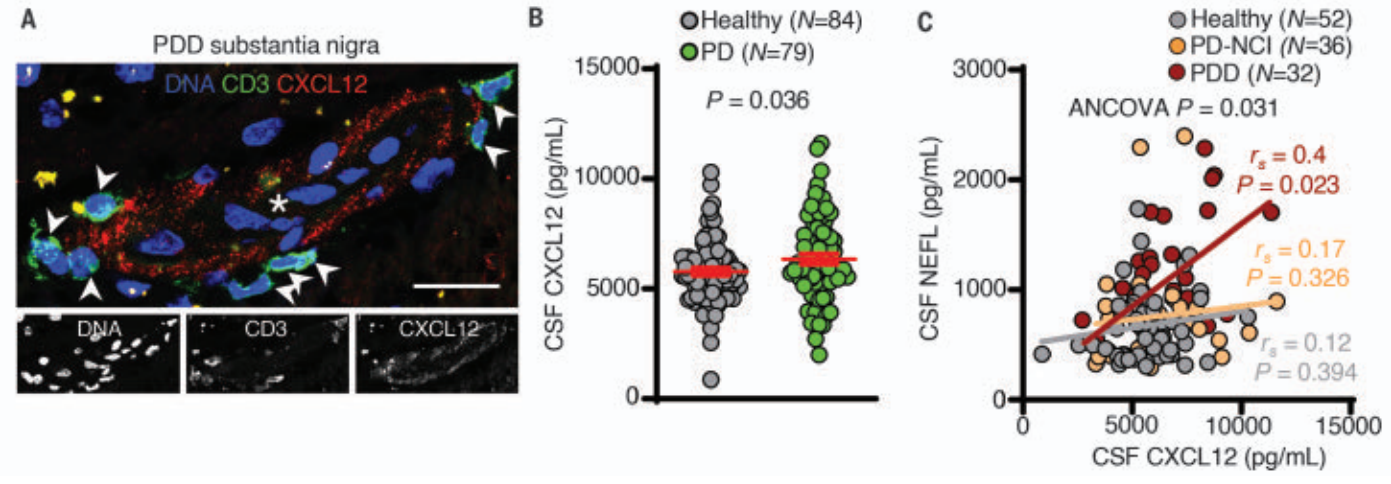


Fig. 3. CXCL12 is associated with neurodegeneration in LBD. (**A**) A PDD substantia nigra brain blood vessel showing localization of CXCL12 to the cerebral vasculature. Arrowheads indicate $CD3^+$ T cells in the perivascular space. Asterisk indicates blood vessel lumen. Scale bar, 50 μm. Similar results were observed in seven out of seven LBD brains. (**B**) Single-molecule array measurement of CXCL12 indicating higher levels in PD versus healthy CSF. Data are mean ± SEM. (**C**) Regression analysis correlating CSF CXCL12 and NEFL levels in healthy, PD-NCI, and PDD. There is a significant correlation of CXCL12 and NEFL in PDD but not PD-NCI or healthy CSF.

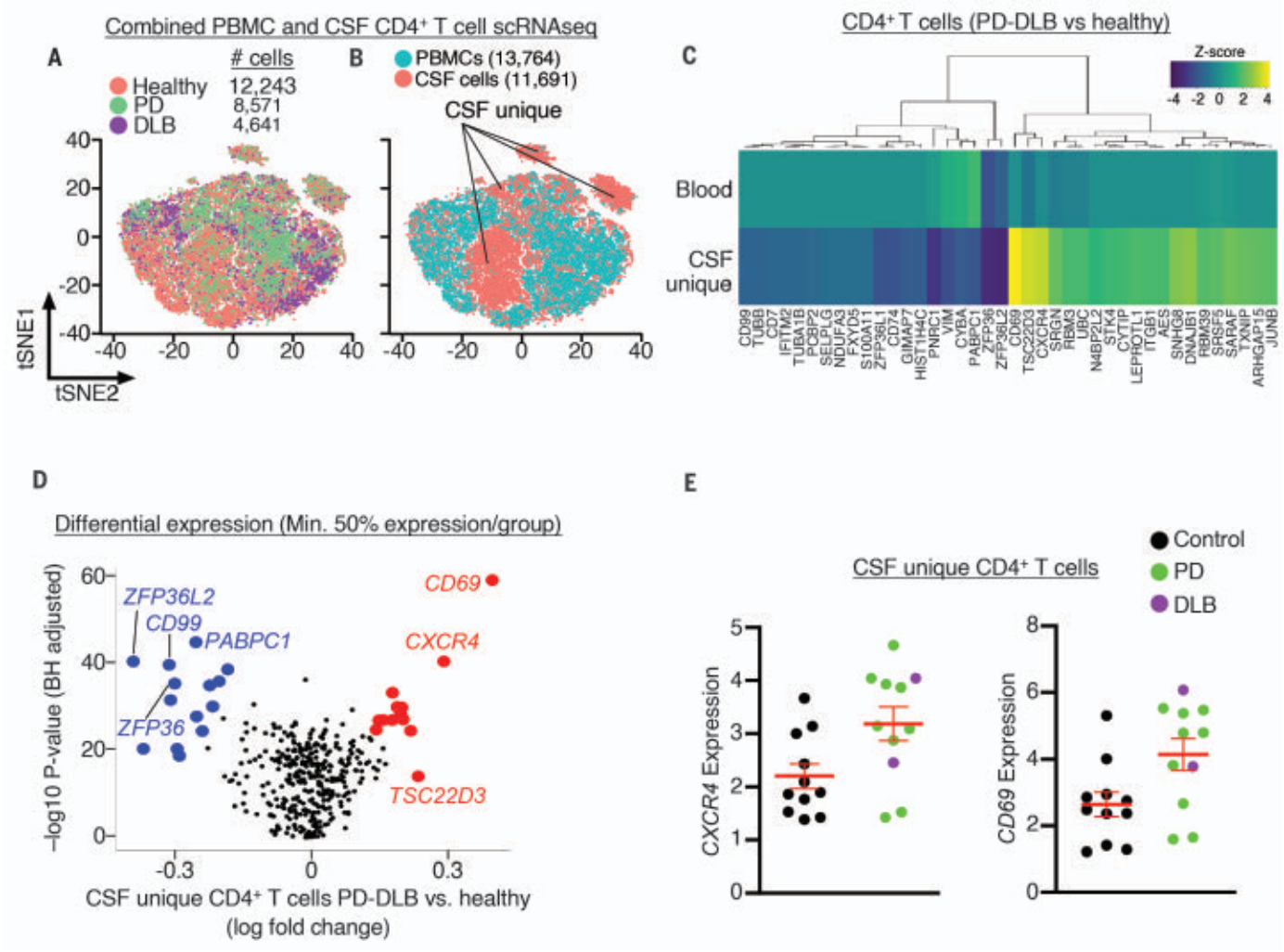


Fig. 4. CXCR4 demarks CD4$^+$ T cells that are specific to the CSF in LBD. (**A**) tSNE plot showing overlayed distribution of peripheral versus CSF CD4$^+$ T cells from healthy, PD, and DLB subjects. (**B**) tSNE plot showing clusters of CD4$^+$ T cells that are specific to the CSF. (**C**) Hierarchical clustering of standardized z-scores comparing PD-DLB to healthy CD4$^+$ T cells from PBMCs and CSF. The clustering of genes *CXCR4*, *CD69*, and *TSC22D3* demarks CSF unique CD4$^+$ T cells. (**D**) Volcano plot showing differential expression analysis comparing PD-DLB to healthy CSF unique CD4$^+$ T cells. (**E**) Quantification of individual subjects' *CXCR4* and *CD69* expression of PD-DLB versus healthy CSF unique CD4$^+$ T cells showing higher expression of each gene in PD-DLB. Data are mean ± SEM.

1 (*ACTG1*) and *actin beta* (*ACTB*) (Fig. 5D), which regulate cytoskeletal control of antigen-dependent T cell activation (*20*). We also noted increased expression of *marker of proliferation Ki-67* (*MKI67*), suggesting increased proliferation of stimulated T cells (Fig. 5D).

T_H17 cell involvement in the degeneration of neurons in LBD

Notably, we also detected higher expression of *interleukin 17A* (*IL17A*) in cells stimulated with α-synuclein (Fig. 5D). *IL17A* encodes the proinflammatory cytokine IL-17, which is secreted by T_H17 cells (*21*). To determine whether *IL17A*-expressing cells were clonally expanded, we performed scTCRseq on stimulated and unstimulated cells. This revealed clonal populations from stimulated cells of both patients (fig. S10B). We then plotted *IL17A* expression by tSNE and identified clonally expanded TCRs (clonotypes) from each subject (Fig. 5E). *IL17A*-expressing cells coexpressed *CD4*, and some clonotypes also expressed the T_H17-associated cytokine gene *interleukin 22* (*IL22*; fig. S10C). We confirmed the presence of CD4$^+$IL-17A$^+$ T cells in the PDD substantia nigra, which were adjacent to TH$^+$IL-17A$^+$ neurons (Fig. 5F). We also detected higher levels of IL-17A immunoreactivity in LBD brains (Welch's *t* test, $P = 0.007$; Fig. 5G). Public datasets revealed lack of *IL17A* RNA expression in the brain, yet the gene encoding the IL17A receptor, *IL17RA*, was highly expressed in the midbrain (fig. S11A), suggesting an external source of IL17A protein in neurons. Public histology data indicated an age-dependent accumulation of IL17A in neurons (fig. S11B). Finally, to confirm IL17A antibody specificity, we preincubated antibodies with recombinant IL-17A, which ablated IL-17A immunoreactivity (fig. S11C).

Discussion

In conclusion, these results implicate T_H17 cell involvement in the degeneration of neurons in LBD. Notably, CXCR4 regulates cell migration (*22*), and antagonism of CXCR4 modulates the pathogenicity of T_H17 cells (*23*). Thus, our investigation of intrathecal immunity uncovered the CXCR4-CXCL12 signaling axis as a potential therapeutic target for LBD. Several CXCR4 antagonists are currently approved for clinical use to treat a wide variety of diseases (*24*–*30*). Given the safety, bioavailability, and tolerability of CXCR4 antagonists (*26*), these drugs could be utilized to inhibit trafficking of pathological T_H17 cells into the LBD brain. Finally, we identified an antigenic α-synuclein epitope

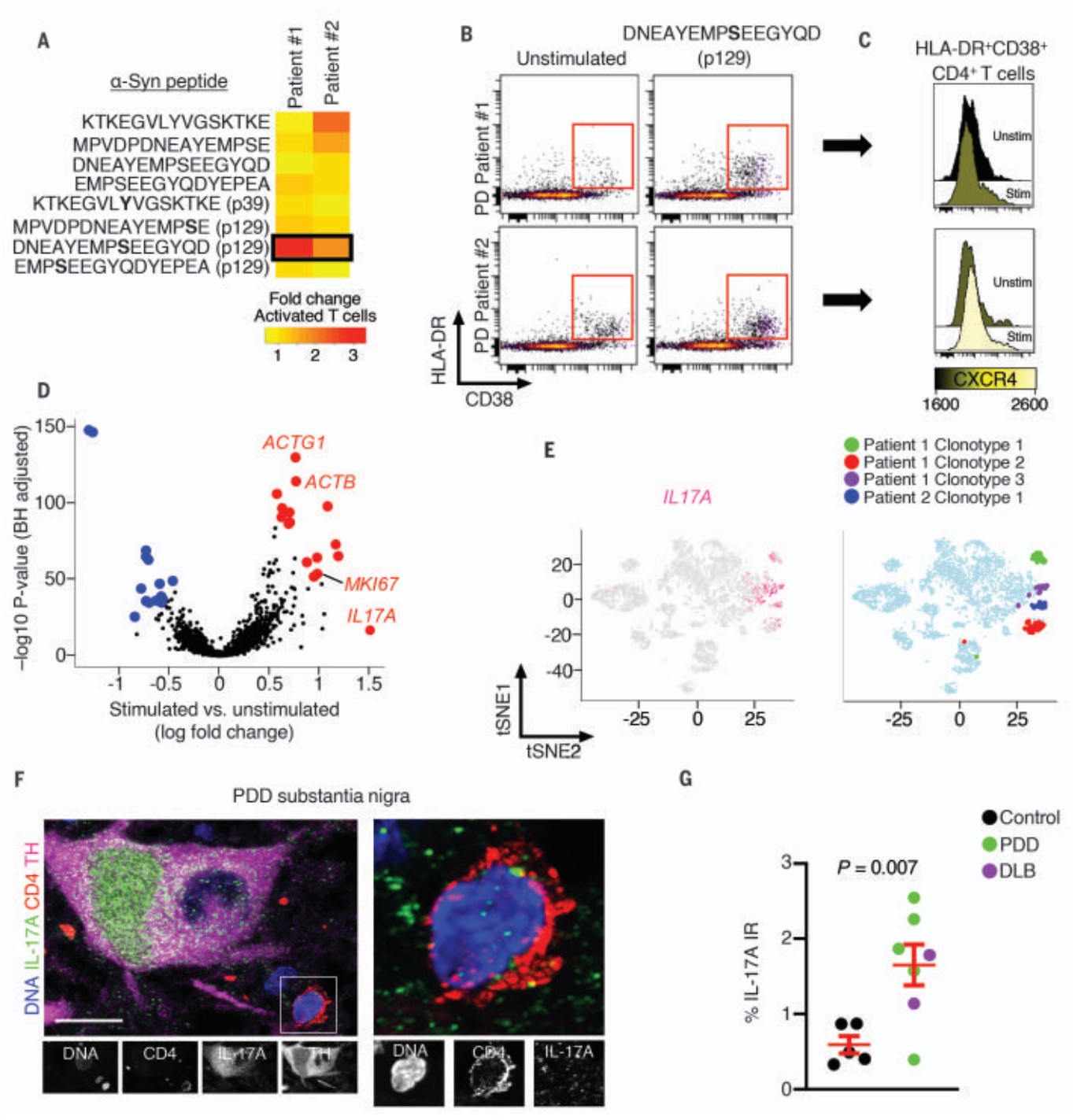


Fig. 5. Stimulation of LBD T cells with α-synuclein promotes *IL-17A* expression. (**A**) Heatmap showing fold change of T cell activation (percent HLA-DR$^+$CD38$^+$ CD3$^+$ T cells) between unstimulated and stimulated PBMCs. Cells were incubated with α-synuclein peptides known to be antigenic. Peptide DNEAYEMPSEEGYQD (p129) increased T cell activation in patients #1 and #2. (**B**) Flow cytometry plots of unstimulated and DNEAYEMPSEEGYQD (p129)–stimulated cells showing increased T cell activation (percent HLA-DR$^+$CD38$^+$ CD3$^+$ T cells) by the α-synuclein peptide. Abbreviations for the amino acid residues are as follows: A, Ala; C, Cys; D, Asp; E, Glu; F, Phe; G, Gly; H, His; I, Ile; K, Lys; L, Leu; M, Met; N, Asn; P, Pro; Q, Gln; R, Arg; S, Ser; T, Thr; V, Val; W, Trp; and Y, Tyr. (**C**) Histograms showing increased expression of CXCR4 in DNEAYEMPSEEGYQD (p129)–stimulated HLA-DR$^+$CD38$^+$CD4$^+$ T cells in both patients by flow cytometry. (**D**) Differential expression analysis of stimulated versus unstimulated HLA-DR$^+$CD38$^+$CD3$^+$ T cells shows increased expression of antigen-dependent T cell activation genes *ACTG1* and *ACTB*, the proliferative gene *MKI67*, and the proinflammatory cytokine *IL17A*. (**E**) tSNE plots indicating overlap of cells expressing *IL17A* and clonally expanded T cells (clonotypes) from both patients. (**F**) Confocal images of control (non-neurologic disease) and PDD postmortem brains showing CD4$^+$IL-17A$^+$ T cells adjacent to an IL-17A$^+$TH$^+$ neuron in the PDD substantia nigra. Scale bar, 10 μm. (**G**) Quantification of IL-17A immunoreactivity (IR) in the substantia nigra of control and LBD brains showing increased IL-17A in LBD. Similar results were observed in six out of seven LBD brains. Data are mean ± SEM.

that promoted expression of *IL17A*, a pro-inflammatory cytokine involved in autoimmune diseases (*21*). In animal models of neurodegenerative disease, T_H17 cells play a direct role in neuronal loss (*31*, *32*). Moreover, human T_H17 cells have been shown to promote blood-brain barrier disruption and central nervous system inflammation via IL-17A (*33*). Thus, our study provides a mechanism for T_H17 cell–mediated dopaminergic cell death through secretion of inflammatory IL-17A, thereby implicating autoimmunity in LBD (fig. S12).

REFERENCES AND NOTES

1. M. J. Armstrong, M. S. Okun, *JAMA* **323**, 548–560 (2020).
2. Z. Walker, K. L. Possin, B. F. Boeve, D. Aarsland, *Lancet* **386**, 1683–1697 (2015).
3. M. Iba *et al*., *J. Neuroinflammation* **17**, 214 (2020).
4. C. S. Lindestam Arlehamn *et al*., *Nat. Commun.* **11**, 1875 (2020).
5. D. Sulzer *et al*., *Nature* **546**, 656–661 (2017).
6. A. Sommer *et al*., *Cell Stem Cell* **23**, 123–131.e6 (2018).
7. G. T. Kannarkat, J. M. Boss, M. G. Tansey, *J. Parkinsons Dis.* **3**, 493–514 (2013).
8. J. A. Saunders *et al*., *J. Neuroimmune Pharmacol.* **7**, 927–938 (2012).
9. C. H. Stevens *et al*., *J. Neuroimmunol.* **252**, 95–99 (2012).
10. V. Brochard *et al*., *J. Clin. Invest.* **119**, 182–192 (2009).
11. C. Cebrián *et al*., *Nat. Commun.* **5**, 3633 (2014).
12. A. S. Harms *et al*., *J. Neurosci.* **33**, 9592–9600 (2013).
13. Z. Liu, Y. Huang, B. B. Cao, Y. H. Qiu, Y. P. Peng, *Mol. Neurobiol.* **54**, 7762–7776 (2017).
14. A. Singhania *et al*., *Sci. Rep.* **11**, 302 (2021).
15. D. Gate *et al*., *Nature* **577**, 399–404 (2020).
16. H. Oh *et al*., *Mol. Neurodegener.* **16**, 3 (2021).
17. L. Maggi *et al*., *Eur. J. Immunol.* **40**, 2174–2181 (2010).
18. K. L. Truong *et al*., *Nat. Commun.* **10**, 2263 (2019).
19. E. E. McCandless, Q. Wang, B. M. Woerner, J. M. Harper, R. S. Klein, *J. Immunol.* **177**, 8053–8064 (2006).
20. H. Colin-York *et al*., *Cell Rep.* **26**, 3369–3379.e5 (2019).
21. L. Steinman, *Nat. Med.* **13**, 139–145 (2007).
22. D. J. Campbell, C. H. Kim, E. C. Butcher, *Immunol. Rev.* **195**, 58–71 (2003).
23. D. Tischner *et al*., *JCI Insight* **2**, e95063 (2017).
24. Y. Iwasaki *et al*., *Cancer Sci.* **100**, 778–781 (2009).
25. T. Murakami *et al*., *Antimicrob. Agents Chemother.* **53**, 2940–2948 (2009).
26. N. D. Stone *et al*., *Antimicrob. Agents Chemother.* **51**, 2351–2358 (2007).
27. G. A. Donzella *et al*., *Nat. Med.* **4**, 72–77 (1998).
28. B. Nervi *et al*., *Blood* **113**, 6206–6214 (2009).
29. U. M. Domanska *et al*., *Neoplasia* **14**, 709–718 (2012).
30. H. Tamamura *et al*., *FEBS Lett.* **550**, 79–83 (2003).
31. A. Reboldi *et al*., *Nat. Immunol.* **10**, 514–523 (2009).
32. J. Zhang, K. F. Ke, Z. Liu, Y. H. Qiu, Y. P. Peng, *PLOS ONE* **8**, e75786 (2013).
33. H. Kebir *et al*., *Nat. Med.* **13**, 1173–1175 (2007).

ACKNOWLEDGMENTS

We thank the clinical staffs of the Stanford and University of California San Diego Alzheimer's Disease Research Centers for their assistance acquiring patient samples. **Funding:** This work was supported by a National Institute of Neurologic Disease and Stroke K99/R00 Pathway to Independence Award (NS112458-01A1) (D.G.); an Irene Diamond Fund/AFAR Postdoctoral Transition Award in Aging (D.G.); a National Institutes of Health National Institute on Aging (NIA) F32 Fellowship (AG055255-01A1) (D.G.); the FFG Momentia Project 867741 (L.A.); Austrian Science Fund (FWF) Project P 31362- B34 (L.A.); FFG Project 867741 PMU FFF E-20/32/169-UNG (L.A.); the Howard Hughes Medical Institute (M.M.D.); NIH U19 AG065156, R01 NS115114, P30 AG066515, and P50 NS062684 (K.L.P.); Michael J. Fox Foundation for Parkinson's Research Grants 020756, 16921, and 18411 (K.L.P.); the Lewy Body Dementia Association (K.L.P.); Alzheimer's Drug Discovery Foundation (K.L.P); Sanofi US Services, Inc. (K.L.P.); the Cure Alzheimer's Fund (T.W-C.); the NOMIS Foundation (T.W.-C.); NIA R01 AG045034 05 (T.W-C.); and the NIA-funded Stanford Alzheimer's Disease Research Center P50AG047366 (V.W.H.).
Author contributions: D.G. designed experiments and prepared the manuscript. D.G. conducted confocal microscopy, flow cytometry, and scRNAseq and scTCRseq. E.T., O.L., A.Y., T.F., A.K., and H.O. assisted with sequencing analysis. T.N. performed ex vivo α-synuclein stimulation experiments. M.S. assisted with clinical data analysis. D.C. performed sample processing of CSF and blood cells. K.S., M.S.U., and L.A. performed histology and analysis of Thy1-αSyn mice. V.W.H., D.R.G., M.M.D., and K.L.P. provided patient samples and assisted with study design. D.G. and T.W.-C. wrote and edited the manuscript. All authors read and approved the final manuscript. **Competing interests:** K.L.P. has stock options and has received paid consulting fees from CuraSen Therapeutics, Inc. **Data and materials availability**: The scRNAseq datasets analyzed during the current study are available in the Gene Expression Omnibus repository under accession numbers GSE141578 and GSE161192.

SUPPLEMENTARY MATERIALS

science.org/doi/10.1126/science.abf7266
Materials and Methods
Figs. S1 to S12
Table S1
References (*34*–*39*)
MDAR Reproducibility Checklist
Data S1 to S4

16 November 2020; resubmitted 1 July 2021
Accepted 20 September 2021
Published online 14 October 2021
10.1126/science.abf7266

REPORTS

DEVELOPMENTAL BIOLOGY

Symmetry breaking in the female germline cyst

D. Nashchekin[1]*, L. Busby[1], M. Jakobs[2], I. Squires[1]†, D. St. Johnston[1]*

In mammals and flies, only one cell in a multicellular female germline cyst becomes an oocyte, but how symmetry is broken to select the oocyte is unknown. Here, we show that the microtubule (MT) minus end-stabilizing protein Patronin/CAMSAP marks the future *Drosophila* oocyte and is required for oocyte specification. The spectraplakin Shot recruits Patronin to the fusome, a branched structure extending into all cyst cells. Patronin stabilizes more MTs in the cell with the most fusome material. Our data suggest that this weak asymmetry is amplified by Dynein-dependent transport of Patronin-stabilized MTs. This forms a polarized MT network, along which Dynein transports oocyte determinants into the presumptive oocyte. Thus, Patronin amplifies a weak fusome anisotropy to break symmetry and select one cell to become the oocyte.

In many organisms, not all female germ cells develop into oocytes. Some cells become accessory cells that contribute material to the oocyte (*1*). Mouse female germ cells form cysts of up to 30 cells, but most cells undergo apoptosis after transferring cytoplasm and centrosomes to the small number of cells that become oocytes (*2*, *3*). In *Drosophila*, germline cyst formation starts in the germarium, which has three regions. A stem cell produces a cystoblast, which then divides four times with incomplete cytokinesis to generate a cyst of 16 germ cells connected by intercellular bridges, or "ring canals" (*4*, *5*). As the cyst moves through regions 2a and 2b of the germarium, it is surrounded by epithelial follicle cells and then rounds up in region 3 to form a follicle. By this stage, one cell has been selected as the oocyte and the others become nurse cells (Fig. 1A). Oocyte selection depends on the formation of a noncentrosomal microtubule organizing center (ncMTOC) in the future oocyte that organizes a polarized microtubule (MT) network that directs the dynein-dependent transport of cell fate determinants and centrosomes into the pro-oocyte (*6*–*8*) (Fig. 1A). How symmetry is broken to specify which cell contains the ncMTOC and becomes the oocyte is unclear.

Patronin and its vertebrate orthologs (CAMSAPs) are MT minus end-binding proteins that have been recently found to be essential components of ncMTOCs (*9*–*13*). To investigate the role of Patronin in oocyte determination, we examined the distribution of oocyte markers in *patronin*$^{c9\text{-}c5}$ mutant (MUT) cysts (Fig. 1, B and C, and fig. S1). In wild-type (WT) cysts, Orb and centrosomes accumulate in future oocytes in regions 2b to 3 (*14*–*16*) but are rarely localized in *patronin* mutants (24 and 3% of MUT cysts, respectively) (Fig. 1, B and C). Several germ cells enter meiosis in region 2a and accumulate the synaptonemal complex protein C(3)G, which becomes restricted to two cells in region 2b and to the oocyte in region 3 (*17*) (fig. S1). C(3)G is not localized in region 3 of *patronin* cysts, and 44% of the cysts in region 2b have three cells in meiosis (fig. S1). Thus, Patronin is required for oocyte determination.

To determine whether Patronin is asymmetrically distributed in the cyst, we imaged germaria expressing endogenously tagged Patronin-Kate. Patronin starts to accumulate in a single cell in each cyst in region 2a, earlier than other markers for the presumptive oocyte,

[1]The Gurdon Institute and the Department of Genetics, University of Cambridge, Cambridge CB2 1QN, UK. [2]The Department of Physiology, Development and Neuroscience, University of Cambridge, Cambridge CB2 3DY, UK.
***Corresponding author. Email: d.stjohnston@gurdon.cam.ac.uk (D.S.J.); d.nashchekin@gurdon.cam.ac.uk (D.N.)**
†Present address: Institute for Cell and Molecular Biosciences, Newcastle University, Newcastle upon Tyne NE2 4HH, UK.

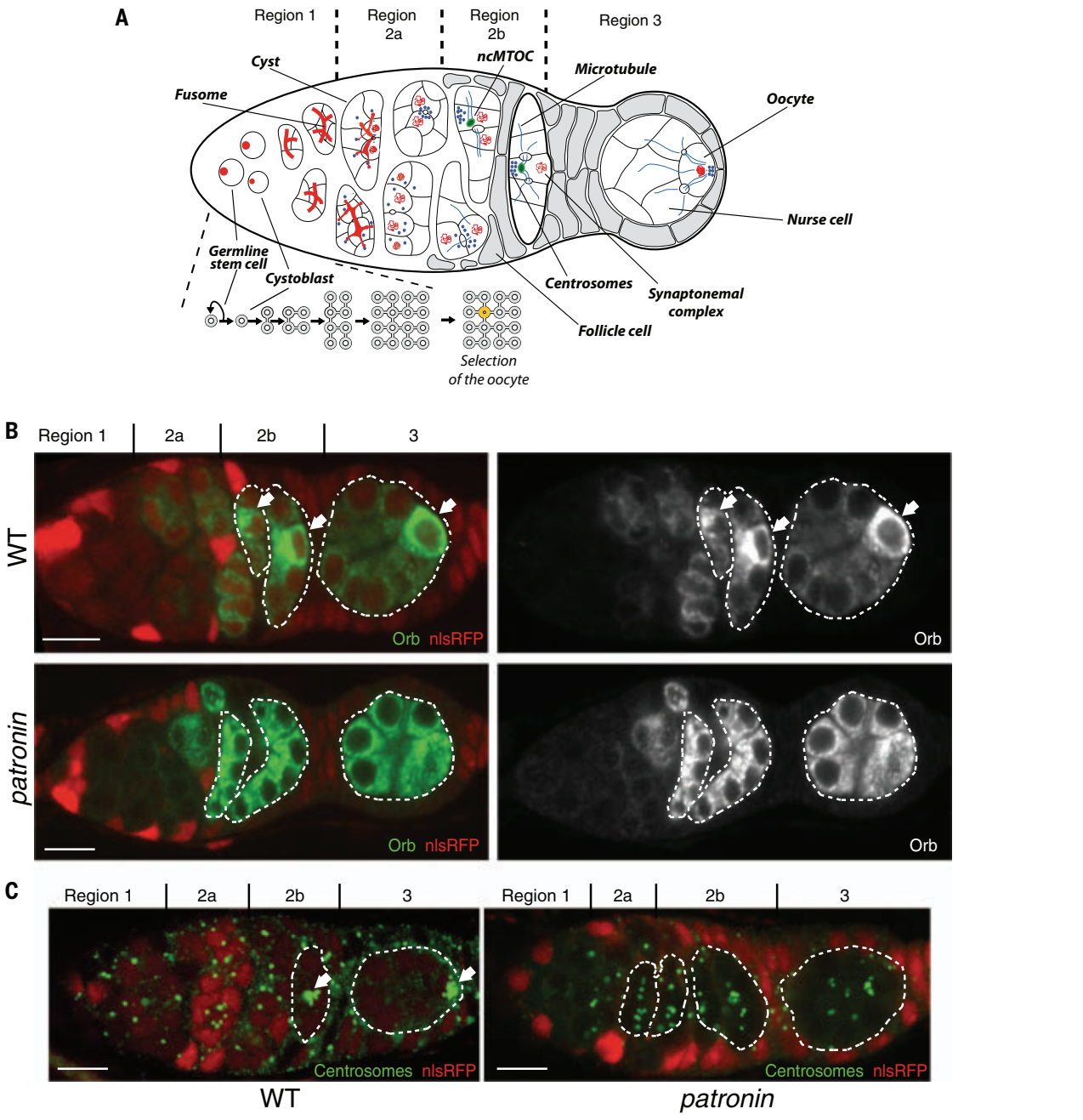


Fig. 1. Patronin is required for oocyte specification. (**A**) Schematic diagram of a *Drosophila* germarium showing germline cyst formation and oocyte selection. (**B** and **C**) Distribution of the oocyte specification markers Orb (B) and centrosomes (C) in WT [top or left in (C)] and *patronin* MUT [bottom or right in (C)] cysts. For all figures, arrows point to the future oocyte, cysts are marked by dashed lines, MUT cysts are labeled by the absence of nuclear localization signal RFP (nlsRFP), and regions of the germarium are indicated on the top. Scale bars, 10 μm.

and remains in one cell in regions 2b to 3, where it forms distinct foci in the cytoplasm (Fig. 2, A and A′). This cell will become the oocyte, because it is also labeled by Orb (Fig. 2B) and C(3)G (Fig. 2C). *patronin* mRNA is not localized within the cyst, and Patronin expressed from a cDNA with heterologous untranslated regions and promoter shows a similar distribution to the endogenous protein, indicating that Patronin is localized as a protein and not by transcription in this cell or by mRNA localization (Fig. 2, B and C, and fig. S2).

Dynein does not localize to the presumptive oocyte in *patronin* MUT cysts (Fig. 3A). This suggests that the loss of Patronin disrupts the formation of the MTOC in the pro-oocyte, leading to the loss of the polarized MT network along which Dynein transports cargoes into one cell. Because most MT plus ends accumulate at the site of MT nucleation, we used the MT plus end-tracking protein EB1-GFP to visualize the putative MTOC in the cyst. Most EB1-GFP comets localize to one cell in regions 2b to 3 (Fig. 3, B and C, and movies S1 and S2). Moreover, the densest EB1-GFP signal colocalizes with the Patronin foci in the same cell, suggesting that the latter are the MTOCs formed in the pro-oocyte (Fig. 3D). This asymmetric distribution of EB1-GFP is lost in *patronin* cysts, where EB1-GFP comets are

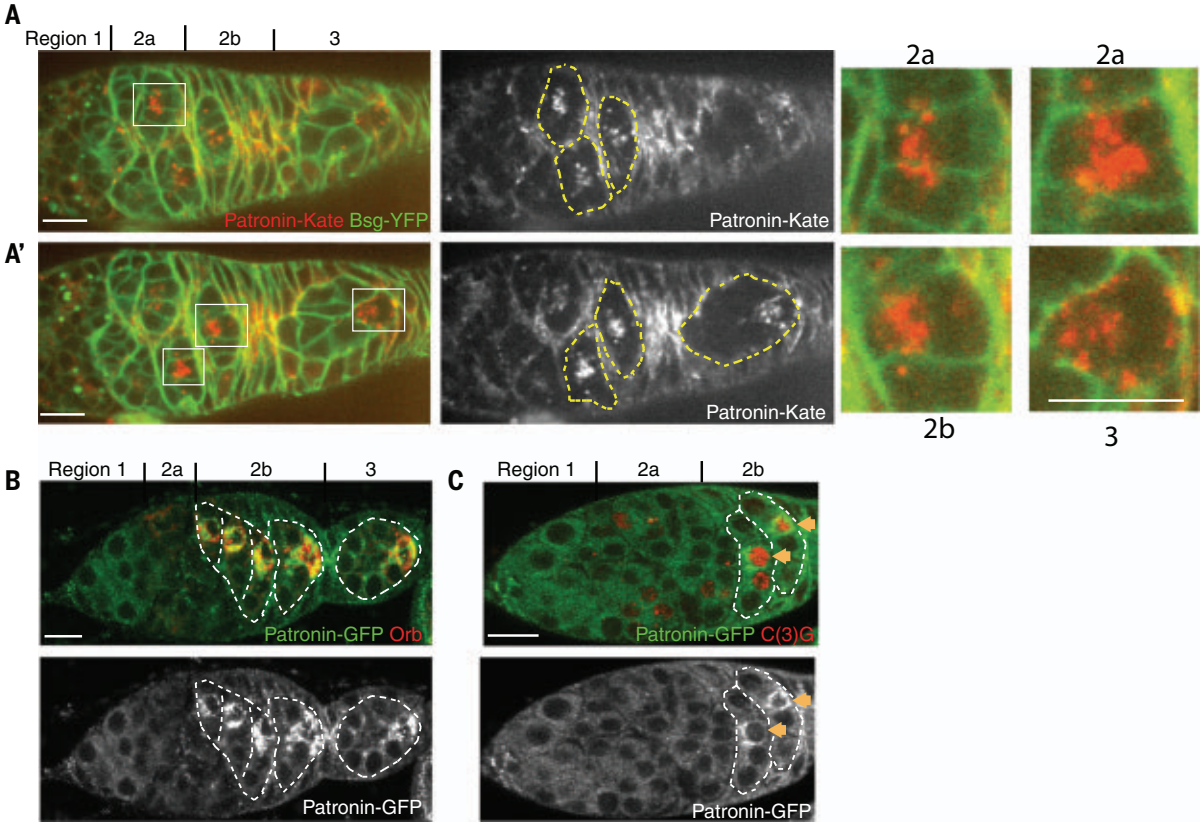


Fig. 2. Patronin accumulates in the future oocyte. (**A** and **A′**) Two different focal planes of a live germarium showing accumulation of endogenously tagged Patronin-Kate in one cell of the cyst. Regions 2a and 2b are shown as close-ups. Cell membranes are labeled by Basigin-YFP (Bsg-YFP). (**B** and **C**) Ectopically expressed ubq>Patronin-GFP accumulates in future oocytes labeled by Orb (B) or C(3)G (C).

distributed more homogeneously (Fig. 3, B and C, and movies S3 and S4). Patronin is therefore required for MTOC formation in the presumptive oocyte and for the organization of a polarized MT network.

WT cysts contain a population of stable, acetylated MTs that form along the fusome, an endoplasmic reticulum-, spectrin-, and actin-rich structure that connects all cells of the cyst (*16*–*19*) (fig. S3). In *patronin* MUT cysts, there is a 2.5-fold reduction in stable MTs (Fig. 3E and fig. S3). Thus, in the absence of Patronin, the whole organization of MTs in the cyst is disrupted. Patronin binds MT minus ends and stabilizes MTs by protecting their minus ends against kinesin-13–induced depolymerization (*11*, *13*). Our results suggest that early accumulation of Patronin in only one cell of the cyst stabilizes MT minus ends there, leading to dynein-dependent transport into this cell, the formation of MTOCs, and the subsequent specification of the oocyte.

To determine whether centrosomes contribute to the formation of Patronin MTOCs, we imaged cysts expressing endogenously tagged Patronin-YFP and the centrosomal protein Asterless-Cherry. Although centrosomal clusters localize near Patronin foci, the Asterless and Patronin signals only partially overlap, and most Patronin foci lie outside of the centrosomal cluster, indicating that Patronin MTOCs are noncentrosomal (fig. S4A). Centrosomes have been proposed to be inactive during their migration into the oocyte and they lack crucial components of the pericentriolar material (*8*). To test whether centrosomes contribute to MT organization, we imaged cysts expressing EB1-GFP and Asterless-Cherry. The centrosomes showed strong MT nucleating activity in region 1, where they organize the mitotic spindles (fig. S4B and movie S5). However, only some Asterless-Cherry labeled centrosomes in the presumptive oocyte produce EB1-GFP comets in region 2b (fig. S4C and movie S6). Thus, Patronin-dependent ncMTOCs create the initial asymmetry in MT organization that leads to the accumulation of centrosomes in the pro-oocyte, which may then be amplified by activation of some centrosomes in this cell. The close proximity of the active centrosomes to the ncMTOCs raises the possibility that new MTs produced by these centrosomes are released and then captured and stabilized by Patronin in ncMTOCs, a mechanism described for CAMSAP proteins (*20*).

The observation that Patronin is the earliest known marker for the future oocyte raises the question of how symmetry is broken in the cyst to enrich Patronin in one cell. One proposed mechanism for symmetry breaking is that the cell that inherits the most fusome becomes the presumptive oocyte (*21*). The fusome is asymmetrically partitioned during mitoses in region 1, so that mother cells inherit more material than their daughters, and one of the two cells with four ring canals has more fusome material than the rest (*19*). To determine whether Patronin associates with the fusome, we imaged germaria expressing endogenously tagged Patronin-YFP and the fusome marker Hts-Cherry. Patronin localizes on the fusome in early region 2a but becomes concentrated in one cell as the cyst progresses toward region 3 (Fig. 4A and fig. S5A). When the MTs are depolymerized with colcemid, however, Patronin remains on the fusome in regions 2b and 3 (Fig. 4B). Thus, the fusome determines the initial localization of Patronin in early region 2a, including its slight enrichment in the pro-oocyte, which is then amplified by an MT-dependent process.

The spectraplakin Shot localizes to the fusome, is required for the oocyte specification, and recruits Patronin to ncMTOCs in the oocyte later in oogenesis, making it a good candidate for a factor that links Patronin to the fusome (*13*, *17*). In *shot*$^{-}$ cysts, Patronin

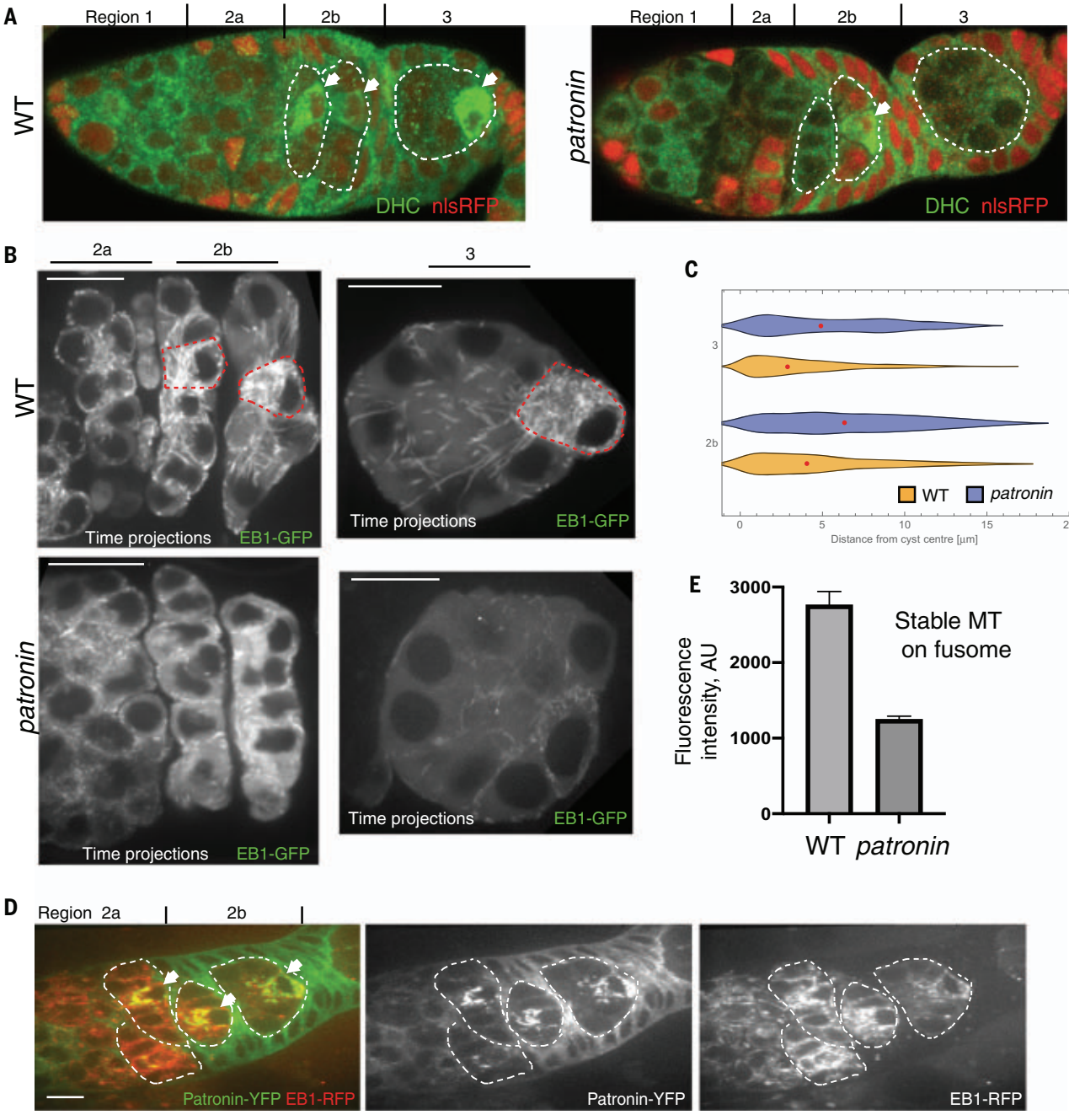


Fig. 3. Patronin is required for MT organization in the cyst. (**A**) Distribution of Dynein heavy chain (DHC) in WT and *patronin* MUT cysts. (**B** to **D**) Patronin is required for MTOC formation in the presumptive oocyte. (B) EB-1 comet tracks in WT (top) and *patronin* MUT (bottom) cysts. The images are projections of several time points from movie S1 (WT; region 2), movie S2 (WT; region 3), movie S3 (*patronin*; region 2), and movie S4 (*patronin*; region 3). The red dashed line marks cells with MTOCs. (C) Quantification of EB-1 comet distribution in WT and *patronin* MUT cysts in region 3 and 2b of the germarium. Red dots indicate median values. (D) Live germarium showing colocalization of Patronin-YFP foci with the MTs plus end marker EB1-GFP in the presumptive oocyte. (**E**) Quantification of the mean fluorescence intensities of fusome-associated acetylated MTs in *patronin* MUT and WT cysts. Errors bars indicate the SEM.

does not accumulate in one cell and fails to form foci (Fig. 4C). Furthermore, loss of Shot prevents Patronin from associating with the fusome (Fig. 4C and fig. S5, B and C). Thus, Shot is required to recruit Patronin to the fusome, thereby transmitting fusome asymmetry to Patronin localization.

The MT-dependent enrichment of Patronin in one cell as the cyst moves through the germarium suggests that its initial, weakly asymmetric distribution on the fusome is then amplified by Dynein-dependent transport toward the minus ends of the MT that have been stabilized by Patronin. We tested Dynein function by examining components of the Dynein-dynactin complex that are required for oocyte specification: *egl*, *BicD*, and *Arp1* (*22–24*), (Fig. 4D and fig. S6, A and B). Like MT depolymerization, mutations in any of these genes disrupt the enrichment of Patronin foci in one cell. Deletion of the MT minus end-binding

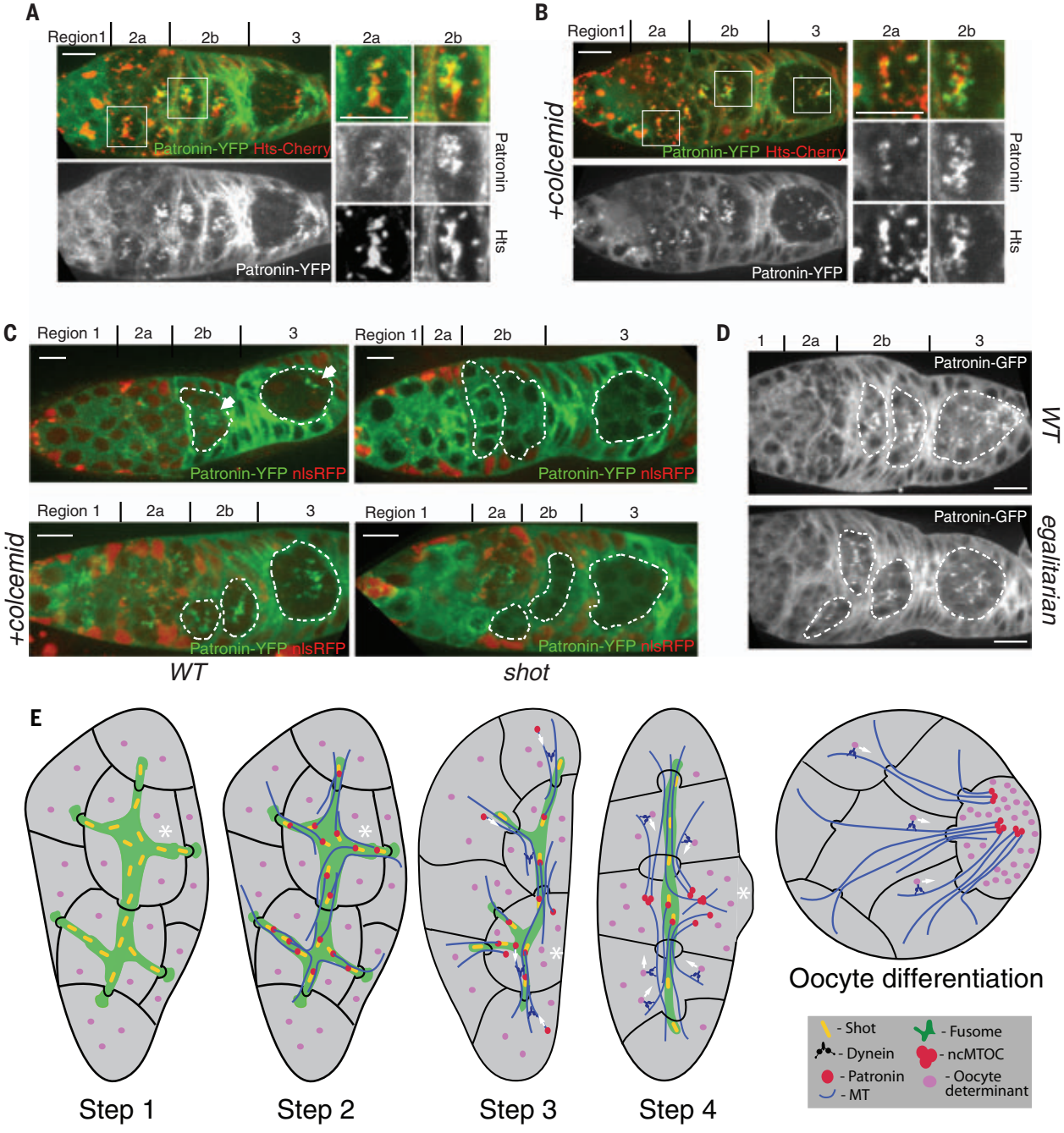


Fig. 4. Patronin localization is defined by the fusome and by a positive feedback loop of Dynein-mediated transport. (**A** and **B**) Patronin associates with the fusome in an MT-dependent manner. Shown are untreated (A) or colcemid-treated (B) live germaria expressing Patronin-YFP and Hts-Cherry. Regions 2a and 2b are shown as close-ups. (**C**) Shot links Patronin to the fusome. Shown are live germaria containing WT (left) and *shot* MUT (right) cysts expressing Patronin-YFP either untreated (top) or treated with colcemid (bottom). (**D**) Patronin localization depends on Dynein activity. Shown are WT (top) and *egalitarian* MUT (bottom) live germaria expressing transgenic Patronin-GFP. (**E**) Diagram showing the four steps in cyst polarization that lead to the specification of the oocyte and its subsequent positioning at the posterior of the cyst in region 3 (see text for details). Asterisk indicates the presumptive oocyte.

domain of Patronin, but not the CKK domain (*25*), also prevents Patronin accumulation in the pro-oocyte (fig. S6, C and D). Thus, Patronin localization depends on its binding to MT minus ends and on Dynein activity, suggesting that Dynein transports Patronin bound to MT minus ends toward the pro-oocyte.

Our observations led us to propose a four-step model of cyst polarization and oocyte selection (Fig. 4E). First, during cyst formation, the asymmetric segregation of the fusome leads to the one cell with more fusome material than the rest. Second, in region 2a, Patronin is recruited to the fusome by Shot. The cell with the most fusome material therefore contains more Patronin, leading to the stabilization of more MT minus ends in this cell and a weakly polarized MT network. Third, Patronin-bound MTs in other cells of the cyst are then transported by Dynein along these MTs toward their minus ends in the pro-oocyte. Fourth,

this creates a positive feedback loop: As Dynein transports more Patronin and MTs into the cell with the most stabilized MT minus ends, more minus ends become stabilized in this cell, amplifying the MT polarity and leading to enhanced Dynein transport of oocyte determinants into this cell. In this way, the small original asymmetry in the fusome is converted into the highly polarized MT network that concentrates the oocyte determinants in one cell.

Patronin is a member of the conserved CAMSAP family, raising the possibility that the molecular mechanisms of oocyte selection in *Drosophila* could be conserved during the formation of mammalian oocytes. Although fusomes have not been observed in mammalian cysts (*26*), MT-dependent transport of organelles through intercellular bridges has been shown to play an important role in oocyte differentiation in mice (*3*).

REFERENCES AND NOTES

1. K. Lu, L. Jensen, L. Lei, Y. M. Yamashita, *Trends Genet.* **33**, 971–978 (2017).
2. L. Lei, A. C. Spradling, *Development* **140**, 2075–2081 (2013).
3. L. Lei, A. C. Spradling, *Science* **352**, 95–99 (2016).
4. M. de Cuevas, M. A. Lilly, A. C. Spradling, *Annu. Rev. Genet.* **31**, 405–428 (1997).
5. J. R. Huynh, D. St Johnston, *Curr. Biol.* **14**, R438–R449 (2004).
6. W. E. Theurkauf, B. M. Alberts, Y.-N. Jan, T. A. Jongens, *Development* **118**, 1169–1180 (1993).
7. M. McGrail, T. S. Hays, *Development* **124**, 2409–2419 (1997).
8. J. Bolívar *et al.*, *Development* **128**, 1889–1897 (2001).
9. W. Meng, Y. Mushika, T. Ichii, M. Takeichi, *Cell* **135**, 948–959 (2008).
10. A. J. Baines *et al.*, *Mol. Biol. Evol.* **26**, 2005–2014 (2009).
11. S. S. Goodwin, R. D. Vale, *Cell* **143**, 263–274 (2010).
12. N. Tanaka, W. Meng, S. Nagae, M. Takeichi, *Proc. Natl. Acad. Sci. U.S.A.* **109**, 20029–20034 (2012).
13. D. Nashchekin, A. R. Fernandes, D. St Johnston, *Dev. Cell* **38**, 61–72 (2016).
14. V. Lantz, J. S. Chang, J. I. Horabin, D. Bopp, P. Schedl, *Genes Dev.* **8**, 598–613 (1994).
15. A. P. Mahowald, J. M. Strassheim, *J. Cell Biol.* **45**, 306–320 (1970).
16. N. C. Grieder, M. de Cuevas, A. C. Spradling, *Development* **127**, 4253–4264 (2000).
17. K. Röper, N. H. Brown, *Curr. Biol.* **14**, 99–110 (2004).
18. H. Lin, L. Yue, A. C. Spradling, *Development* **120**, 947–956 (1994).
19. M. de Cuevas, A. C. Spradling, *Development* **125**, 2781–2789 (1998).
20. K. Jiang *et al.*, *Dev. Cell* **28**, 295–309 (2014).
21. H. Lin, A. C. Spradling, *Dev. Genet.* **16**, 6–12 (1995).
22. C. Navarro, H. Puthalakath, J. M. Adams, A. Strasser, R. Lehmann, *Nat. Cell Biol.* **6**, 427–435 (2004).
23. B. Suter, R. Steward, *Cell* **67**, 917–926 (1991).
24. R. Nieuwburg *et al.*, *eLife* **6**, e27237 (2017).
25. M. C. Hendershott, R. D. Vale, *Proc. Natl. Acad. Sci. U.S.A.* **111**, 5860–5865 (2014).
26. M. E. Pepling, A. C. Spradling, *Development* **125**, 3323–3328 (1998).
27. K. Röper, N. H. Brown, *J. Cell Biol.* **162**, 1305–1315 (2003).
28. B. Ran, R. Bopp, B. Suter, *Development* **120**, 1233–1242 (1994).
29. S. T. Thibault *et al.*, *Nat. Genet.* **36**, 283–287 (2004).
30. T. Schüpbach, E. Wieschaus, *Genetics* **129**, 1119–1136 (1991).
31. F. Port, H.-M. Chen, T. Lee, S. L. Bullock, *Proc. Natl. Acad. Sci. U.S.A.* **111**, E2967–E2976 (2014).
32. N. Lowe *et al.*, *Development* **141**, 3994–4005 (2014).
33. G. B. Gloor, N. A. Nassif, D. M. Johnson-Schlitz, C. R. Preston, W. R. Engels, *Science* **253**, 1110–1117 (1991).
34. P. T. Conduit, A. Wainman, Z. A. Novak, T. T. Weil, J. W. Raff, *eLife* **4**, e08483 (2015).
35. T. Zhao, O. S. Graham, A. Raposo, D. St Johnston, *Science* **336**, 999–1003 (2012).
36. H. Wang, I. Brust-Mascher, G. Civelekoglu-Scholey, J. M. Scholey, *J. Cell Biol.* **203**, 35–46 (2013).
37. T. B. Chou, N. Perrimon, *Genetics* **131**, 643–653 (1992).

ACKNOWLEDGMENTS

We thank R. Hawley, J. Raff, J. Scholey, and the Bloomington Stock Center (NIH P40OD018537) for flies and reagents; the Gurdon Institute Imaging Facility for assistance with microscopy; and N. Lowe and J. Overton for technical assistance. **Funding:** This work was supported by Wellcome principal research fellowships 080007 and 207496 (to D.St.J.), Wellcome core support grants 092096 and 203144 (to D.St.J.), Wellcome doctoral studentship 109145 (to M.J.), Cancer Research UK core support grants A14492 and A24823 (to D.St.J.), and BBSRC grant BB/R001618/1 (to D.St.J., D.N., and I.S.). **Author contributions:** Conceptualization: D.N., D.St.J.; Funding acquisition: D.N., D.St.J.; Investigation: D.N., L.B., M.J., I.S., D.St.J.; Methodology: D.N., M.J.; Project administration: D.N., D.St.J. Supervision: D.N., D.St.J.; Visualization: D.N., M.J., D.St.J.; Writing – original draft: D.N., D.St.J.; Writing – review and editing: D.N., L.B., M.J., I.S., D.St.J. **Competing interests:** The authors declare no competing interests. **Data and materials availability:** All data are available in the main text or the supplementary materials.

SUPPLEMENTARY MATERIALS

science.org/doi/10.1126/science.abj3125
Materials and Methods
Supplementary Text
Figs. S1 to S6
References (*27*–*37*)
Movies S1 to S6
MDAR Reproducibility Checklist

4 May 2021; accepted 20 September 2021
10.1126/science.abj3125

CORONAVIRUS

Monetary incentives increase COVID-19 vaccinations

Pol Campos-Mercade[1]*†, Armando N. Meier[2,3]*†, Florian H. Schneider[4]*†, Stephan Meier[5]*, Devin Pope[6,7]*, Erik Wengström[8,9,10]*

The stalling of COVID-19 vaccination rates threatens public health. To increase vaccination rates, governments across the world are considering the use of monetary incentives. Here we present evidence about the effect of guaranteed payments on COVID-19 vaccination uptake. We ran a large preregistered randomized controlled trial (with 8286 participants) in Sweden and linked the data to population-wide administrative vaccination records. We found that modest monetary payments of 24 US dollars (200 Swedish kronor) increased vaccination rates by 4.2 percentage points (P = 0.005), from a baseline rate of 71.6%. By contrast, behavioral nudges increased stated intentions to become vaccinated but had only small and not statistically significant impacts on vaccination rates. The results highlight the potential of modest monetary incentives to raise vaccination rates.

Severe acute respiratory syndrome coronavirus 2 (SARS-CoV-2) and the emergence of new variants are a grave threat to public health. Effective vaccination deployment is essential to mitigate that risk (*1*–*3*). Yet despite widespread awareness and availability of COVID-19 vaccines, many high-income countries struggle to push vaccination rates beyond 70%. At the core of an effective disease containment strategy lie policies that further increase vaccination rates among the hesitant and among people who intend to get vaccinated but do not follow through (*4*–*6*).

Governments and organizations across the world have started using incentives to encourage vaccination, ranging from payments of US$4 (CA$5) in Vancouver and lotteries in Ohio to payments of US$175 (€150) in Greece (*7*, *8*). Many others are now also considering whether to introduce payments for vaccinations. Notably, US President Biden recently urged "…state, territorial, and local governments to provide US$100 payments for every newly vaccinated American, as an extra incentive to boost vaccination rates, protect communities, and save lives" (*9*). Yet, governments and organizations are limited in their ability to properly assess the impact of monetary incentives because they lack control groups that are not exposed to incentives (*10*). Causal evidence examining the effectiveness of introducing payments for COVID-19 vaccinations is lacking.

Here we report findings from a randomized controlled trial (RCT) to study the impact of guaranteed monetary incentives on COVID-19 vaccination. We paid participants, drawn from a general sample of the Swedish population,

[1]Department of Economics, Center for Economic Behavior and Inequality (CEBI), University of Copenhagen, Copenhagen, Denmark. [2]Unisanté, University of Lausanne, Lausanne, Switzerland. [3]Faculty of Business and Economics, University of Basel, Basel, Switzerland. [4]Department of Economics, University of Zurich, Zurich, Switzerland. [5]Columbia Business School, Columbia University, New York, NY, USA. [6]Booth School of Business, University of Chicago, Chicago, IL, USA. [7]National Bureau of Economic Research, Boston, MA, USA. [8]Department of Economics, Lund University, Lund, Sweden. [9]Department of Finance and Economics, Hanken School of Economics, Helsinki, Finland. [10]Knut Wicksell Centre for Financial Studies, Lund University, Lund, Sweden.
***Corresponding author. Email: pcm@econ.ku.dk (P.C.-M.); armando.meier@unil.ch (A.N.M.); florian.schneider2@uzh.ch (F.H.S.); sm3087@gsb.columbia.edu (S.M.); devin.pope@chicagobooth.edu (D.P.); erik.wengstrom@nek.lu.se (E.W.)**
†These authors contributed equally to this work.

200 Swedish kronor (SEK; about US$24) conditional on getting vaccinated. The Swedish setting allows us to link individual-level survey data from the RCT to exhaustive population-wide Swedish administrative records for actual vaccinations collected by public health authorities. We find that the monetary incentives increased vaccination rates by 4.2 percentage points. This is an increase from a 71.6% baseline rate—a rate that is similar to those of other countries in the European Union (EU)—indicating that incentives can increase vaccine uptake even in countries with high vaccination rates.

Our findings are also notable because it is controversial whether monetary incentives to encourage healthier behavior in general, and for COVID-19 vaccination specifically, lead to the desired result. Although monetary incentives have been shown to sometimes encourage healthier behavior (*11*–*15*), incentives can often be ineffective or even counterproductive (*16*–*20*). On the basis of this evidence, many argue that paying people for COVID-19 vaccinations may signal that vaccination is undesirable or even dangerous (*21*, *22*), or that it could crowd out people's motivation to get vaccinated for the purpose of protecting others (*7*), leading to a decrease in vaccination uptake. By contrast, our results emphasize that modest monetary incentives can increase vaccination rates. However, our findings do not imply that people ought to be paid for getting vaccinated—our paper does not speak to the normative question of whether paying for vaccination is ethically permissible (*23*, *24*).

We also studied the effect of three behavioral nudges on vaccination uptake. Nudges are subtle interventions that do not deny any options or change economic incentives (*25*). They have been used with varying success to alter behaviors (*4*, *26*–*28*). In the context of COVID-19 vaccinations, one study found that in the initial phase of the vaccination rollout, when vaccination rates were around 13%, reminders to book an appointment increased COVID-19 vaccination rates (*29*). However, at the high vaccination rates achieved in many high-income countries, some have argued that nudges may have reached the limit of their potential (*30*). In our trial, we found no statistically significant impact of any of the nudges on vaccination rates.

We conducted the preregistered RCT from May to July 2021, with 8286 participants from 18 to 49 years of age. Participants were recruited from a broadly representative online panel created by Norstat, a large survey company. We sent the survey to each participant as soon as the first Swedish regions opened vaccination for the participant's age group. In the online survey, we randomized participants into five different treatment conditions and one

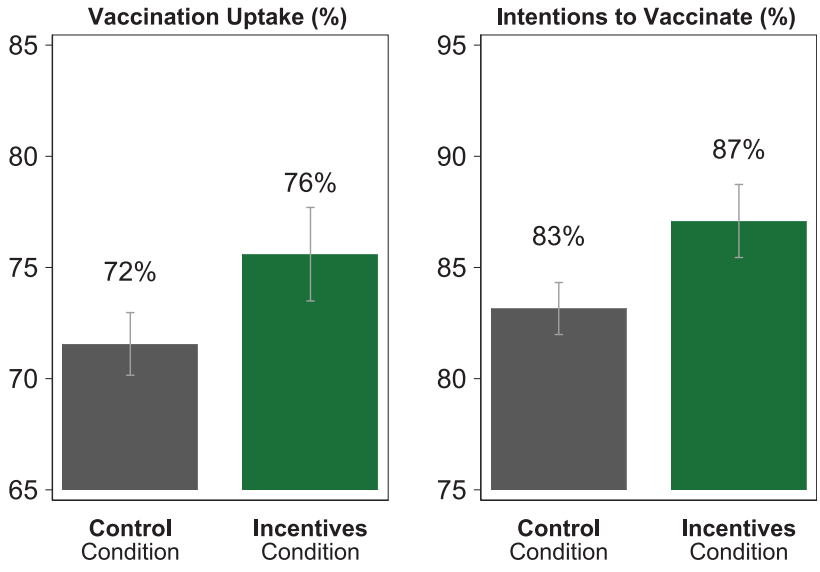


Fig. 1. Vaccination uptake and intentions to get vaccinated, among those in the incentives condition and the control condition. The graphs show the proportion of participants in the incentives and control conditions who got vaccinated or intended to get vaccinated, on the basis of survey data from the trial linked to Swedish administrative records on vaccination. "Vaccination Uptake" indicates the proportion of participants who got vaccinated within 30 days of the trial, according to vaccination records. "Intentions to Vaccinate" indicates the proportion of participants who intended to get vaccinated within 30 days of the trial, according to experimental data. Error bars represent normal-based 90% confidence intervals (CIs; mean ± 1.64 SE) from OLS regressions with heteroscedasticity-robust standard errors. *N* = 1131 participants in the incentives condition; *N* = 2778 participants in the control condition.

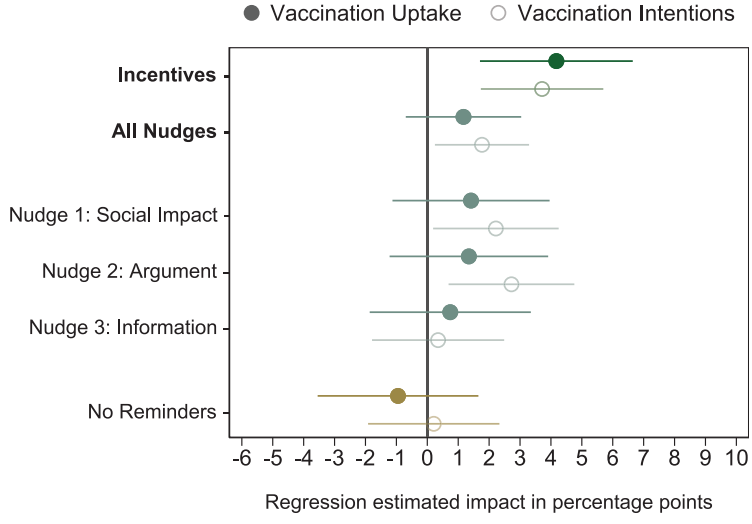


Fig. 2. Regression-estimated effects of experimental conditions on vaccination uptake and vaccination intentions versus the control condition. The graph shows regression-estimated effects (OLS regression) of the experimental conditions relative to the control condition, as preregistered. In addition, "All Nudges" denotes the estimate when the social impact, argument, and information conditions are pooled. Filled circles indicate the estimated impact on vaccination uptake within 30 days after participation in the survey (100 if the participant got vaccinated, 0 otherwise). Open circles indicate the estimated impact on intended vaccination uptake (100 if the participant intended to get vaccinated, 0 otherwise) within 30 days. Error bars represent 90% normal-based CIs (coefficient ± 1.64 SE) from OLS regressions with heteroscedasticity-robust standard errors. *N* = 8286 participants.

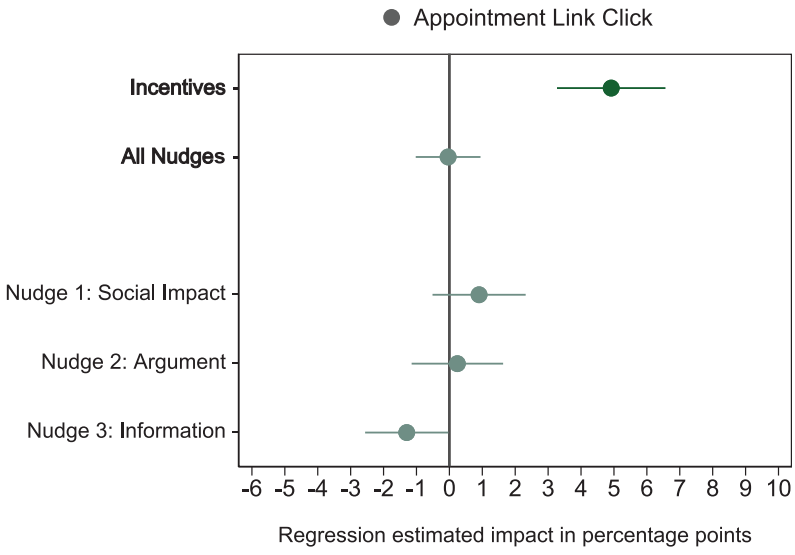


Fig. 3. Regression-estimated effects of experimental conditions on whether participants clicked a link to a website with information for scheduling a vaccine appointment. The graph shows regression-estimated effects (OLS regression) of the experimental conditions relative to the control condition, as preregistered. In addition, "All Nudges" denotes the estimate when the social impact, argument, and information conditions are pooled. Circles indicate the estimated impact of each experimental condition on the probability of clicking the appointment link (100 if the participant clicked the link, 0 otherwise). The no-reminders condition is not included because this condition did not include the link. Error bars represent 90% normal-based CIs (coefficient ± 1.64 SE) from OLS regressions with heteroscedasticity-robust standard errors. N = 7288 participants.

control condition. Immediately after the treatment, we measured participants' intentions to get vaccinated against COVID-19. Except for the participants assigned to the no-reminders condition, all participants (even those in the control group) received two reminders to get vaccinated, sent 2 and 4 weeks after taking the survey. In August 2021, the Public Health Agency of Sweden linked the trial data of each participant to the COVID-19 vaccination records collected for all Swedish residents.

Our preregistered main outcome variables are (i) participants' self-reported intention to get a first dose of a COVID-19 vaccine within 30 days after vaccines become available to them and (ii) whether participants became vaccinated within 30 days, according to the administrative records. All reported results in the text and figures come from ordinary least squares (OLS) regressions with heteroscedasticity-robust standard errors [see supplementary materials (SM) section 1.2.2 for details; all P values come from two-sided t tests].

In the incentives condition, participants were offered a monetary incentive of SEK 200 (about US$24) if they got vaccinated within 30 days of the vaccine becoming available to them. We used the administrative vaccination records to check uptake.

The incentives condition increased both vaccination intention and actual uptake compared with the control condition (Fig. 1). The proportion of participants who intended to get vaccinated within 30 days was 83.2% in the control condition and 87.1% in the incentives condition, a difference of 3.9 percentage points (P = 0.001). The proportion of participants who were vaccinated within 30 days was 71.6% in the control condition and 75.6% in the incentives condition, a difference of 4 percentage points (P = 0.009).

The effect sizes from our preregistered main specification are shown in Fig. 2. We estimated that receiving monetary incentives for getting vaccinated increased participants' intentions to become vaccinated by 3.7 percentage points (P = 0.002) relative to the control condition. Consistent with these elevated intentions, actual vaccination rates increased by 4.2 percentage points (P = 0.005). These results are robust to a battery of robustness checks, such as considering secondary outcome variables, including different sets of control variables, using logistic regressions, correcting for multiple hypothesis testing, and including all participants who went through the experimental intervention but did not finish the survey (SM sections 2.3 and 2.4). We observed similar effects for incentives for vaccination uptake within 10, 20, 30, 40, and 50 days after survey completion (table S7). These results show that monetary incentives not only accelerated immediate vaccination uptake but also increased uptake for at least 50 days.

We collected detailed information on individual characteristics of the participants. We found large baseline differences in vaccination uptake across sociodemographic groups: People with a higher socioeconomic status (college degree, higher income, employed) had higher vaccination rates (SM section 2.6). Notably, and despite the different baseline vaccination rates, we found that monetary incentives boosted vaccination rates similarly across all subgroups (SM section 2.5). This result indicates that monetary incentives have the potential to raise vaccination rates irrespective of people's background.

We also employed different types of behavioral nudges to persuade participants to become vaccinated (*26*, *31*, *32*): We asked participants (i) to make a list of four people who would benefit from the participant getting vaccinated (social impact condition) (*33*, *34*), (ii) to write down arguments that could best convince another person to get vaccinated (arguments condition) (*27*), and (iii) to participate in a quiz with information on the safety and effectiveness of COVID-19 vaccines (information condition) (*29*). In contrast to the other conditions, a final condition (the no-reminders condition) did not include any nudges or reminders, enabling us to study the impact of reminders on vaccination uptake (*29*).

Some behavioral nudges did statistically significantly increase participants' intentions to become vaccinated, but none increased actual vaccination uptake (Fig. 2). When we pooled the data from the three nudge conditions (social impact, argument, and information conditions), we found that nudging may elevate vaccination intentions by 1.8 percentage points (P = 0.056). However, the increase in intentions translates to only a 1.2 percentage point (P = 0.302) rise in vaccination uptake, which is not statistically significantly different from zero. Of the nudges, the social impact and argument conditions had the greatest effect on intentions (social impact: 2.2 percentage points, P = 0.072; argument: 2.7 percentage points, P = 0.028), but neither of them increased actual vaccination uptake in a statistically significant manner (social impact: 1.4 percentage points, P = 0.360; argument: 1.3 percentage points, P = 0.388). The comparison of the no-reminders condition with the control condition indicated that reminders did not substantially affect vaccination rates (P = 0.594). Moreover, there is no statistically significant difference between the no-reminders condition and the three nudge conditions (P = 0.243). We did not find any statistically significant or economically meaningful differences across sociodemographic groups, such as those categorized by immigration status, income, or gender (table S21).

Hence, we found that monetary incentives had greater effects on vaccination uptake than

did behavioral nudges. Although the preregistered main analysis focused on the comparison between each of the experimental conditions and the control condition, we were also able to study the impact of the incentives condition relative to the three nudges. We found that the incentives condition had a larger impact on vaccination uptake than the three nudges pooled (difference of 3.1 percentage points, $P = 0.038$).

We also found a difference between monetary incentives and behavioral nudges in terms of whether, at the end of the survey, participants clicked a link to a website with information to schedule a vaccine appointment (Fig. 3). In the incentives condition, participants were more likely (by 4.9 percentage points, $P < 0.001$) to click on the link, whereas participants in the nudge conditions did not click on the link more often than those in the control condition (−0.08 percentage points, $P = 0.889$). Thus, participants were more likely to click the appointments link in the incentives condition than in the three behavioral nudge conditions (4.8 percentage points, $P < 0.001$).

In sum, our study reveals that even modest monetary incentives can boost COVID-19 vaccination rates. We found that payments of SEK 200 (≈US$24) raised COVID-19 vaccination rates by 4 percentage points. Our trial shows that incentives can increase vaccination uptake even when baseline vaccination rates are high. By contrast, behavioral nudges had small and not statistically significant effects on vaccination rates.

A natural question is whether paying people to get vaccinated is cost-effective for governments. In addition to the direct benefits of saving lives, boosting vaccination rates leads to indirect benefits such as enhanced population immunity, lower hospitalization rates and medical costs, and economic growth. It is beyond the scope of this report to provide a comprehensive analysis of cost-effectiveness, but SM section 2.9 offers some perspectives on why the intervention likely is cost-effective. A key consideration is that paying for vaccination carries much lower costs for society than the sum of all payments—because money is transferred from the government to the citizens, the money paid is not lost.

Our study has several limitations. First, we tested only one size of monetary incentive. Companies and governments around the world have proposed incentives that range from less than US$1 in Philadelphia and US$29 (€25) in Serbia to US$100 in New York. Our trial cannot shed light on whether smaller or larger incentives would be more effective. We also cannot assess the effectiveness of other ways of incentivizing people, such as raising health insurance premiums for the unvaccinated. Second, during summer 2021 Sweden had a vaccination rate in line with the EU average, but countries differ greatly in the proportion of vaccinated population, and the effect of incentives may vary depending on vaccination rates. Relatedly, we offered incentives when the vaccine rollout was starting; results may differ if monetary incentives are offered later—for example, because the reluctance of unvaccinated people may grow over time. Third, the existence of monetary incentives could potentially crowd out people's willingness to get vaccinated in the future (e.g., booster shots) without getting paid. Finally, people might react differently depending on who provides monetary incentives and the corresponding level of trust in receiving the promised payments. In our case, researchers provided incentives, but the effects may differ if incentives are offered by governments or companies.

Despite these limitations, our preregistered trial yields a clear result: Guaranteed incentives can increase COVID-19 vaccination rates. As the COVID-19 pandemic continues, incentives could be an effective tool to reduce COVID-19 spread and fatalities.

REFERENCES AND NOTES

1. B. S. Graham, *Science* **368**, 945–946 (2020).
2. D. Skegg *et al*., *Lancet* **397**, 777–778 (2021).
3. E. Callaway, *Nature* **595**, 17–18 (2021).
4. K. L. Milkman, J. Beshears, J. J. Choi, D. Laibson, B. C. Madrian, *Proc. Natl. Acad. Sci. U.S.A.* **108**, 10415–10420 (2011).
5. T. Rogers, K. L. Milkman, L. K. John, M. I. Norton, *Behav. Sci. Policy* **1**, 33–41 (2015).
6. K. M. Harris, J. Maurer, A. L. Kellermann, *N. Engl. J. Med.* **363**, 2183–2185 (2010).
7. A. Oza, *Science* **373**, 611 (2021).
8. K. Terrell, "These Companies Are Paying Employees to Get Vaccinated" (2021); www.aarp.org/work/working-at-50-plus/info-2021/companies-paying-employees-covid-vaccine.html.
9. Reuters, "Biden wants state, local govts to pay $100 to newly vaccinated Americans" (2021); www.reuters.com/world/us/biden-wants-state-local-govts-give-100-newly-vaccinated-americans-treasury-2021-07-29/.
10. J. Haushofer, C. J. E. Metcalf, *Science* **368**, 1063–1065 (2020).
11. G. Charness, U. Gneezy, *Econometrica* **77**, 909–931 (2009).
12. K. G. Volpp *et al*., *JAMA* **300**, 2631–2637 (2008).
13. K. G. Volpp *et al*., *N. Engl. J. Med.* **360**, 699–709 (2009).
14. A. V. Banerjee, E. Duflo, R. Glennerster, D. Kothari, *BMJ* **340**, c2220 (2010).
15. N. Lacetera, M. Macis, R. Slonim, *Science* **340**, 927–928 (2013).
16. E. L. Deci, *J. Pers. Soc. Psychol.* **18**, 105–115 (1971).
17. U. Gneezy, A. Rustichini, *Q. J. Econ.* **115**, 791–810 (2000).
18. S. Bowles, *Science* **320**, 1605–1609 (2008).
19. C. Mellström, M. Johannesson, *J. Eur. Econ. Assoc.* **6**, 845–863 (2008).
20. U. Gneezy, S. Meier, P. Rey-Biel, *J. Econ. Perspect.* **25**, 191–210 (2011).
21. E. A. Largent, F. G. Miller, *JAMA* **325**, 534–535 (2021).
22. K. G. Volpp, G. Loewenstein, A. M. Buttenheim, *JAMA* **325**, 125–126 (2021).
23. J. Savulescu, *J. Med. Ethics* **47**, 78–85 (2021).
24. N. S. Jecker, *J. Med. Ethics* 10.1136/medethics-2021-107235 (2021).
25. R. Thaler, C. Sunstein, *Nudge: Improving Decisions About Health, Wealth, and Happiness* (Penguin Books, 2008).
26. M. S. Patel, K. G. Volpp, D. A. Asch, *N. Engl. J. Med.* **378**, 214–216 (2018).
27. K. L. Milkman *et al*., *Proc. Natl. Acad. Sci. U.S.A.* **118**, e2101165118 (2021).
28. S. DellaVigna, E. Linos, "RCTs to scale: Comprehensive evidence from two nudge units" (Working Paper no. 27594, National Bureau of Economic Research, 2021); www.nber.org/papers/w27594.
29. H. Dai *et al*., *Nature* **597**, 404–409 (2021).
30. R. Thaler, "More than nudges are needed to end the pandemic," *New York Times* (2021); www.nytimes.com/2021/08/05/business/vaccine-pandemic-nudge-passport.html.
31. C. Jarrett *et al*., *Vaccine* **33**, 4180–4190 (2015).
32. G. B. Chapman, M. Li, H. Colby, H. Yoon, *JAMA* **304**, 43–44 (2010).
33. L. Korn, R. Böhm, N. W. Meier, C. Betsch, *Proc. Natl. Acad. Sci. U.S.A.* **117**, 14890–14899 (2020).
34. P. Campos-Mercade, A. N. Meier, F. H. Schneider, E. Wengström, *J. Public Econ.* **195**, 104367 (2021).
35. P. Campos-Mercade *et al*., Data and code for "Monetary incentives increase COVID-19 vaccinations," Version 1, Zenodo (2021); https://doi.org/10.5281/zenodo.5529625.
36. P. Campos-Mercade *et al*., "Behavioral interventions, economic preferences and vaccination uptake," RCT ID AEARCTR-0007652, AEA RCT Registry (2021); https://doi.org/10.1257/rct.7652-2.0.

ACKNOWLEDGMENTS

We are very grateful for the support of the Public Health Agency of Sweden regarding linkage of the trial data with administrative vaccination records. We thank N. Arnberg for confirming the accuracy of the information condition of the trial. **Funding:** The work was supported by Danish National Research Foundation grant DNRF134 (P.C.-M.), Swiss National Science Foundation grant PZ00P1_201956 (A.N.M.), Swiss National Science Foundation grant 100018_185176 (F.H.S.), the Chazen Institute for Global Business at Columbia Business School (S.M.), Columbia Business School (S.M.), the Booth School of Business at the University of Chicago (D.P.), and Riksbankens Jubileumsfond (E.W.). **Author contributions:** Conceptualization: P.C.-M., A.N.M., F.H.S., S.M., D.P., and E.W. Methodology: P.C.-M., A.N.M., F.H.S., S.M., D.P., and E.W. Investigation: P.C.-M., A.N.M., F.H.S., S.M., D.P., and E.W. Visualization: P.C.-M., A.N.M., F.H.S., S.M., D.P., and E.W. Funding acquisition: P.C.-M., A.N.M., F.H.S., S.M., D.P., and E.W. Project administration: P.C.-M., A.N.M., F.H.S., S.M., D.P., and E.W. Supervision: P.C.-M., A.N.M., F.H.S., S.M., D.P., and E.W. Writing – original draft: P.C.-M., A.N.M., F.H.S., S.M., D.P., and E.W. Writing – review & editing: P.C.-M., A.N.M., F.H.S., S.M., D.P., and E.W. **Competing interests:** The authors do not have any paid or unpaid positions as officers, directors, or board members of an organization whose policy positions, goals, or financial interests relate to this article. Neither does any partner or any close relative have such a position. This research was independent from funders: The funders had no role in study design; collection, analysis, and interpretation of data; writing of the report; or the decision to submit the article for publication. The authors declare that they have no conflicts of interest related to the research described in this study. They confirm that they have followed the regulations of their institutions concerning intellectual property. **Data and materials availability:** All data and code used in the analysis can be freely downloaded from Zenodo (*35*) for the purpose of reproducing the analysis. We preregistered the data collection and analysis at the AEA RCT Registry (*36*). The Swedish Ethical Review Authority approved the protocols of our randomized controlled trial (reference number 2021-01658). This work is licensed under a Creative Commons Attribution 4.0 International (CC BY 4.0) license, which permits unrestricted use, distribution, and reproduction in any medium, provided the original work is properly cited. To view a copy of this license, visit https://creativecommons.org/licenses/by/4.0/. This license does not apply to figures/photos/artwork or other content included in the article that is credited to a third party; obtain authorization from the rights holder before using such material.

SUPPLEMENTARY MATERIALS

science.org/doi/10.1126/science.abm0475
Materials and Methods
Supplementary Text
Figs. S1 to S12
Tables S1 to S28
References (*37*–*44*)
MDAR Reproducibility Checklist

22 August 2021; accepted 1 October 2021
Published online 7 October 2021
10.1126/science.abm0475

TRANSCRIPTION

Structural basis of Integrator-mediated transcription regulation

Isaac Fianu[1], Ying Chen[1], Christian Dienemann[1], Olexandr Dybkov[2], Andreas Linden[3,4], Henning Urlaub[3,4], Patrick Cramer[1]*

Integrator and protein phosphatase 2A (PP2A) form a complex that dephosphorylates paused RNA polymerase II (Pol II), cleaves the nascent RNA, and terminates transcription. We report the structure of the pretermination complex containing the human Integrator-PP2A complex bound to paused Pol II. Integrator binds Pol II and the pausing factors DSIF and NELF to exclude binding of the elongation factors SPT6 and PAF1 complex. Integrator also binds the C-terminal domain of Pol II and positions PP2A to counteract Pol II phosphorylation and elongation. The Integrator endonuclease docks to the RNA exit site and opens to cleave nascent RNA about 20 nucleotides from the Pol II active site. Integrator does not bind the DNA clamps formed by Pol II and DSIF, enabling release of DNA and transcription termination.

Integrator is a cofactor of RNA polymerase II (Pol II)–dependent processing of small nuclear RNAs (snRNAs) (*1*) and other noncoding RNAs (*2*–*4*). It enables 3′ processing of snRNAs and transcription termination by interacting with the Pol II–associating factors DSIF and NELF (*5*). Integrator also functions together with DSIF and NELF in the promoter-proximal region of protein-coding genes (*6*, *7*), where it facilitates premature termination in a process called transcription attenuation (*8*–*13*). Integrator catalyzes endonucleolytic cleavage of nascent RNA for termination (*9*, *10*). In addition, Integrator counteracts the transition of paused Pol II to active elongation by recruiting protein phosphatase 2A (PP2A), which dephosphorylates Pol II and DSIF (*14*–*16*), and attenuates transcription genome-wide (*12*) and also in enhancer regions (*11*, *12*).

Integrator has a molecular weight of ~1.5 MDa and contains 14 subunits called INTS1 to INTS14 (*17*). INTS11 is the RNA endonuclease and associates with INTS9 and INTS4 to form the catalytic cleavage module of Integrator (*18*). The structure of the cleavage module (*19*) confirmed that INTS11 and INTS9 are closely related to CPSF73 and CPSF100, respectively, which are subunits of the cleavage and polyadenylation specificity factor that functions in pre-mRNA 3′ processing and Pol II termination at polyadenylation sites at the 3′ end of protein-coding genes (*20*). The structure of Integrator was recently reported and revealed nine of its subunits and the associated PP2A phosphatase but not the N-terminal region of INTS1 or subunits INTS3, INTS10, INTS12, INTS13, and INTS14 (*15*). INTS10, INTS13, and INTS14 form the INTS10-13-14 subcomplex that has also been analyzed structurally (*21*).

To study Integrator-mediated Pol II regulation, we reconstituted the 14-subunit human Integrator from three recombinant subcomplexes, an eight-subunit Integrator core, the cleavage module, and the INTS10-13-14 module (Fig. 1A; fig. S1, A to C and H, and materials and methods). We also prepared recombinant human PP2A containing subunits PP2A-A and PP2A-C (fig. S1D). Integrator and PP2A formed a stable complex with a paused Pol II-DSIF-NELF elongation complex (PEC), which we prepared as described previously (*22*) (fig. S1, I and J). The resulting 34-subunit PEC-Integrator-PP2A complex was subjected to cryo–electron microscopy (cryo-EM) analysis (fig. S2 and table S1). We obtained a high-confidence structure of the complex at 3.6-Å resolution and used focused refinement to resolve the PEC at 2.7-Å resolution and regions of Integrator and PP2A at 2.9- to 3.2-Å resolution (figs. S2 to S4, tables S1 and S2, and movies S1 and S2). We further used BS3 crosslinking and mass spectrometry to confirm the structure and to localize flexible regions (figs. S5 and S6 and data S1).

The structure shows that Integrator embraces the PEC (Fig. 1 and movie S1). Pol II adopts a paused conformation and contains a tilted DNA-RNA hybrid (fig. S4B) that impairs loading of the next nucleoside triphosphate substrate into the active center (*22*). NELF binds to Pol II as in the known PEC structure (*22*) and shows only minor alterations in conformation (fig. S7A). With respect to DSIF, we observed the SPT5 domains KOW2-3, KOWx-4, and KOW5, whereas other SPT5 domains and SPT4 are disordered (*23*). Comparison of our structure with the structure of the unbound Integrator-PP2A complex (*15*) shows that several Integrator elements move upon PEC binding (fig. S7B and movie S3). As in the reported structure (*15*), Integrator subunits INTS3, INTS10, INTS12, INTS13, and INTS14 are mobile and therefore not present in our structure. Superposition of our structure onto recently reported structures of Pol II preinitiation complexes shows that Integrator is sterically excluded by bound initiation factors and Mediator (fig. S7D).

Integrator approaches Pol II from the side opposite the active center cleft and forms four contact areas that we refer to as interfaces A to D (Fig. 2 and movie S4). Integrator contacts the Pol II subunit RPB2 (interface A), the Pol II subunit dimer RPB3-RPB11 (interface B), the DSIF subunit SPT5 (interface C), and the NELF subunit NELF-B (interface D). These contacts with Pol II, DSIF, and NELF explain how Integrator recognizes the PEC, which is thought to form mainly in the 5′ region of protein-coding genes and at the 3′ end of noncoding genes.

Interface A is formed by contacts between a helical part in the N-terminal region of INTS1 (residues 357 to 1316) and RPB2. The INTS1 N-terminal region contacts the RPB2 external domains 1 and 2, particularly helices α15, α16, and α17 (*24*) (Fig. 2A). The N-terminal region of INTS1 was largely absent in the unbound Integrator structure (*15*) but is observed in our structure and adopts a defined location upon PEC binding. Whereas residues ~357 to 948 of the INTS1 N-terminal region form a helical domain that approaches RPB2, residues 949 to 1316 bind INTS2 and correspond to a protein region that could not be assigned previously (*15*). The INTS1 N-terminal region is connected to the INTS1 C-terminal region by an ~40-residue mobile linker that runs along INTS7 (Fig. 1B and fig. S6A). The N-terminal residues 1 to 300 of INTS1 remain mobile, crosslink to the Pol II clamp and protrusion (*24*), and form a complex with INTS12 that crosslinks to the NELF and Pol II regions close to downstream DNA (fig. S6C). An interaction of INTS1 with INTS12 occurs in *Drosophila* Integrator and is essential for snRNA 3′ processing (*25*).

Interface B is formed by Integrator subunits INTS2 and INTS7, which contact RPB11 and RPB3, respectively (Fig. 2A). Whereas INTS2 makes a minor contact with helix α3 of RPB11 (*24*), a more intimate contact is formed by the INTS7 C-terminal helix α40 that is disordered in the unbound Integrator-PP2A structure (*15*). Helix α40 of INTS7 binds to domain 2 of RPB3 (*24*) and contacts INTS9 in the Integrator cleavage module.

Interface C is formed between the Integrator cleavage module and the PEC region around the RNA exit site of Pol II (Fig. 2B and fig. S4H). INTS9 is located close to the KOW5 domain of SPT5. The MBL and β-CASP domains of INTS11

[1]Department of Molecular Biology, Max Planck Institute for Biophysical Chemistry, 37077 Göttingen, Germany. [2]Department of Cellular Biochemistry, Max Planck Institute for Biophysical Chemistry, 37077 Göttingen, Germany. [3]Bioanalytical Mass Spectrometry, Max Planck Institute for Biophysical Chemistry, 37077 Göttingen, Germany. [4]Institute of Clinical Chemistry, Bioanalytics Group, University Medical Center Göttingen, 37075 Göttingen, Germany.
*Corresponding author. Email: patrick.cramer@mpibpc.mpg.de

contact the SPT5 domain KOWx-4, which forms a clamp on exiting RNA (Fig. 2B and figs. S4H, S5C, and S6D). The active center groove of the INTS11 endonuclease is located between its MBL and β-CASP domains and is closed in the unbound structures of the Integrator-PP2A complex (*15*) and the cleavage module (*19*). However, the β-CASP domain has rotated away from the MBL domain by ~17° in our structure, opening the active center groove such that the endonuclease may accommodate RNA (Fig. 3A and movie S3). Superposition of the closed INTS11 (*19*) onto our structure shows that the β-CASP domain would clash with the KOWx-4 domain (fig. S7C). Thus, binding of Integrator to the PEC apparently leads to opening of the endonuclease active center groove, allowing accommodation of the RNA substrate for cleavage.

The observed open conformation of INTS11 resembles the active conformation of the related CPSF73 endonuclease when bound to an RNA substrate (*26*). Superposition of the CPSF73-RNA complex structure (*26*) onto our structure showed that RNA that exits from Pol II can continue straight into the active center groove of INTS11, and that a minimum of ~20 nucleotides of RNA are required to reach from the Pol II active site to the INTS11 active site (Fig. 3B). This agrees very well with the observation that Integrator-mediated RNA cleavage occurs 35 and 21 nt downstream of the transcription start site in vivo, when the active site of paused Pol II resides at 55 and 41 nt downstream, respectively (*9*, *11*). The cleavage module also cross-links to the flexible INTS10-13-14 module (figs. S5A and S6E), which is known to bind RNA (*21*) and may transiently participate in RNA recognition and cleavage. In summary, interface C may serve to guide nascent RNA to the Integrator endonuclease for RNA cleavage.

To test these predictions, we performed RNA cleavage assays with two different RNA substrates, the hairpin RNA used in our structure and a single-stranded RNA (Fig. 3C and fig. S10). We found that Integrator cleaves RNA in the presence of the PEC but not in its absence, which is consistent with endonuclease activation upon PEC binding (Fig. 3C). RNA cleavage can occur as close as ~20 nt from the RNA 3′ end, consistent with our structure and with in vivo observations (*9*, *11*). Cleavage is more efficient for single-stranded RNA (fig. S10), suggesting that hairpin structures in nascent RNA interfere with Integrator-mediated RNA cleavage. This model is consistent with our previous finding that hairpins in pre-mRNA transcripts correlate with Pol II accumulation in the promoter-proximal region (*27*) and with the observation that 3′ processing of snRNAs occurs in the single-stranded region downstream of an RNA hairpin (*28*–*30*).

Interface D is formed between INTS6 and NELF-B. A loop in INTS6 (residues 403 to 411) binds to helix α9 of NELF-B and the surrounding residues (Fig. 2B and figs. S4F and S5D). Whereas Integrator regions that form interfaces A to C are generally conserved over species (fig. S9), the INTS6 loop is poorly conserved in invertebrates such as *C. elegans*, which lack NELF (fig. S9D), suggesting the absence of interface D in invertebrates. The C-terminal region of INTS6 is mobile and is known to bind to

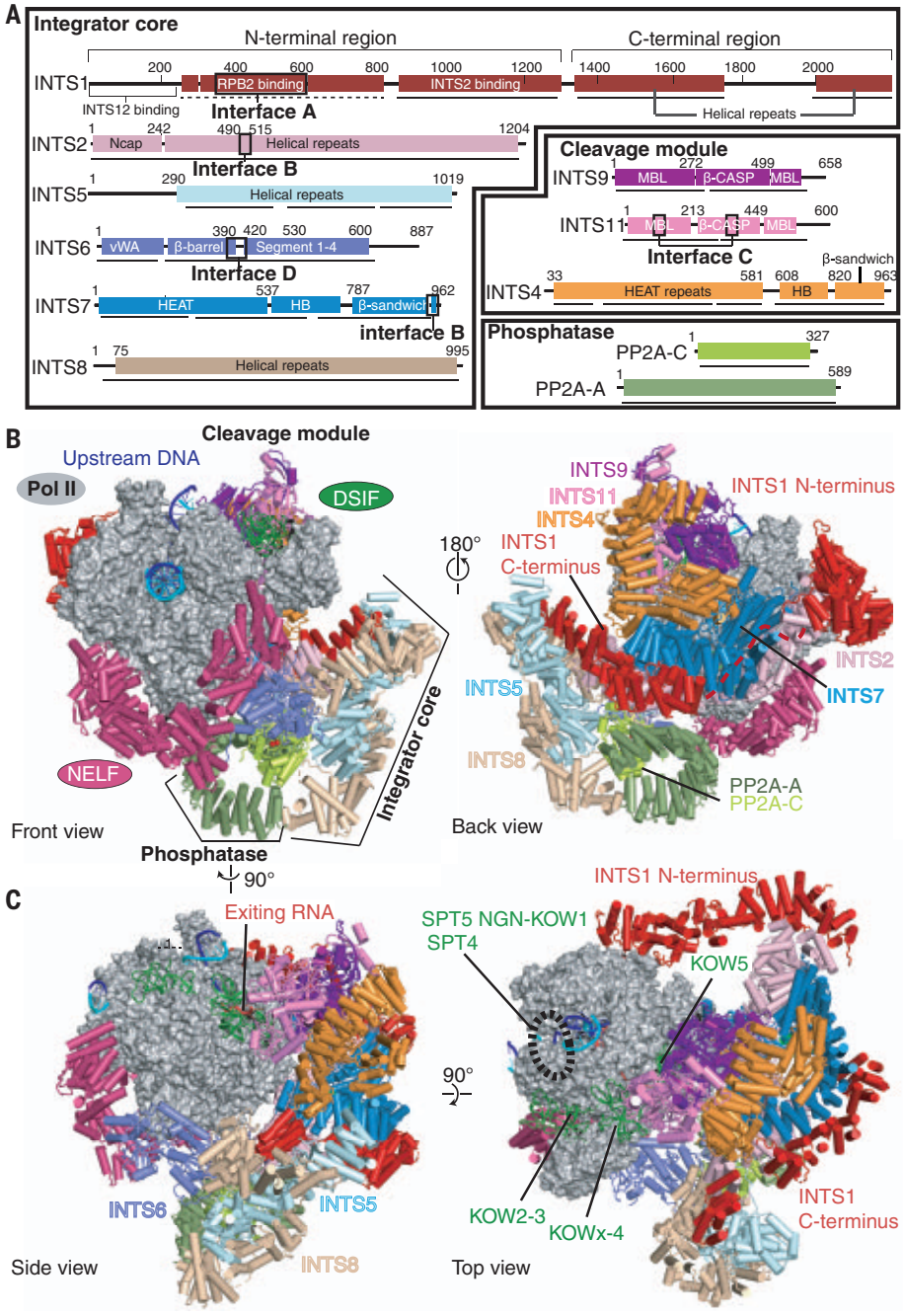


Fig. 1. Structure of PEC-Integrator-PP2A complex. (**A**) Domain organization of Integrator and PP2A subunits. Regions that form interfaces with the PEC are indicated. Black solid and dashed lines indicate regions that are modeled fully or as backbone traces, respectively. Color code is used throughout. HB, helical bundle. (**B** and **C**) Four views of the structure. Pol II is shown as a gray surface, DSIF in green, and NELF in pink. Nucleic acids are in blue, cyan, and red for DNA template, DNA non-template, and RNA, respectively. The canonical location of the DNA clamp formed by the SPT4 and SPT5 NGN domain and the SPT5 KOW1 domain is indicated with a dashed black circle. The active site Mn atoms of PP2A-C are depicted with red spheres.

subunit INTS3 (*31*, *32*), which is also mobile but located nearby according to our cross-linking data (figs. S5A and S6E).

Close to interface D, PP2A adopts a defined position with respect to the PEC (Fig. 1B). INTS6 forms a bridge between NELF and PP2A (fig. S4F), consistent with the observation that INTS6 mediates PP2A recruitment to transcriptional pause sites (*16*). PP2A dephosphorylates the C-terminal domain (CTD) of Pol II (*14*, *16*). Our structure shows that the phosphatase active site in subunit PP2A-C is located ~75 Å from the last ordered residue in RPB1 (M1484), which marks the beginning of the flexible linker that connects to the CTD (Fig. 4, A and B). Therefore, most residues in the linker and any CTD residue can in principle reach PP2A for dephosphorylation.

Integrator also binds to the CTD (*1*) and this can be facilitated by CTD phosphorylation (*7*, *33*–*35*). In our cryo-EM density, we observed two heptad repeats of the unphosphorylated CTD that could be modeled using the two Y1 residues as anchors (Fig. 4, C and D). The CTD repeats bind between Pol II and Integrator within an open space that is lined by residues that form cross-links with the distal part of the CTD (Fig. 4, A and B). The two CTD repeats form extensive hydrophobic contacts with INTS2, INTS4, and INTS7 (Fig. 4, C and D). Our cryo-EM data show that Integrator can bind the two CTD heptad repeats without stably binding to the PEC surface (fig. S11, A to C). This observation is consistent with Integrator being recruited to transcribing Pol II through the CTD and may explain the reported occupancy of gene bodies with Integrator (*2*, *6*, *9*, *11*).

The observed Integrator-bound CTD conformation suggests that phosphorylation of the two Y1 residues could be accommodated and that the negatively charged phosphate groups could bind the conserved positively charged INTS7 residues R73 and K105/R106 (Fig. 4D). Such an interaction of Integrator with the Y1-phosphorylated CTD may explain why Y1 phosphorylation occurs in Pol II that pauses in the promoter-proximal region and how it regulates Integrator recruitment and termination of mammalian Pol II (*35*). It was also reported that CTD phosphorylation at S7 residues has a role in Integrator recruitment (*33*, *34*). Although binding of an S7-phosphorylated CTD is inconsistent with our structure, it is possible that a S7-phosphorylated CTD binds differently to recruit Integrator to specific genes (*36*).

Productive transcription involves the conversion of the PEC to an active elongation complex (EC*) containing DSIF, the PAF1 complex (PAF), and SPT6 (*37*). Comparison of our structure with the EC* structure (*37*) shows

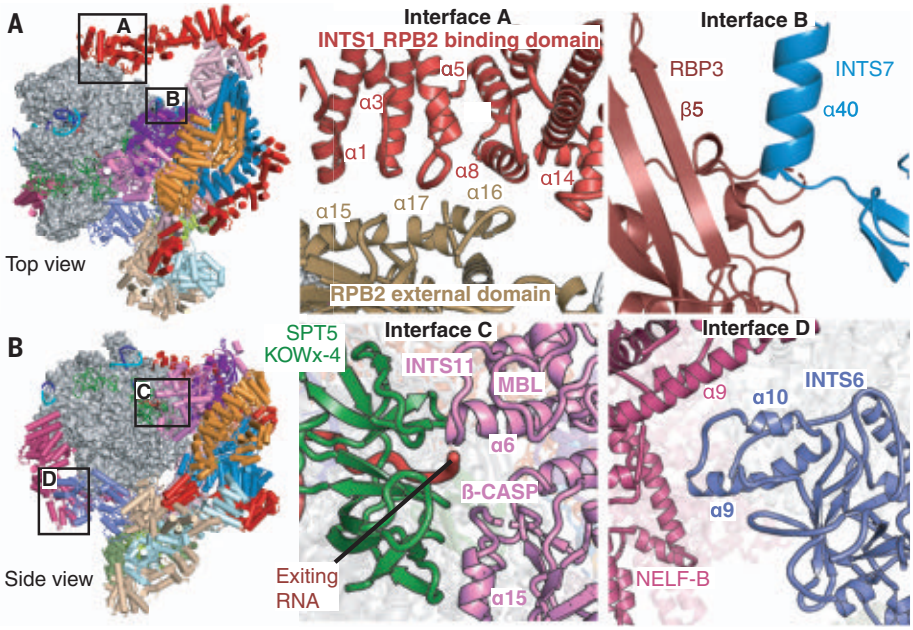


Fig. 2. Integrator-PEC interfaces. (**A**) Location and magnified views of interfaces A and B using the top and side views of the structure, respectively. (**B**) Location and magnified views of interfaces C and D using the side view of the structure.

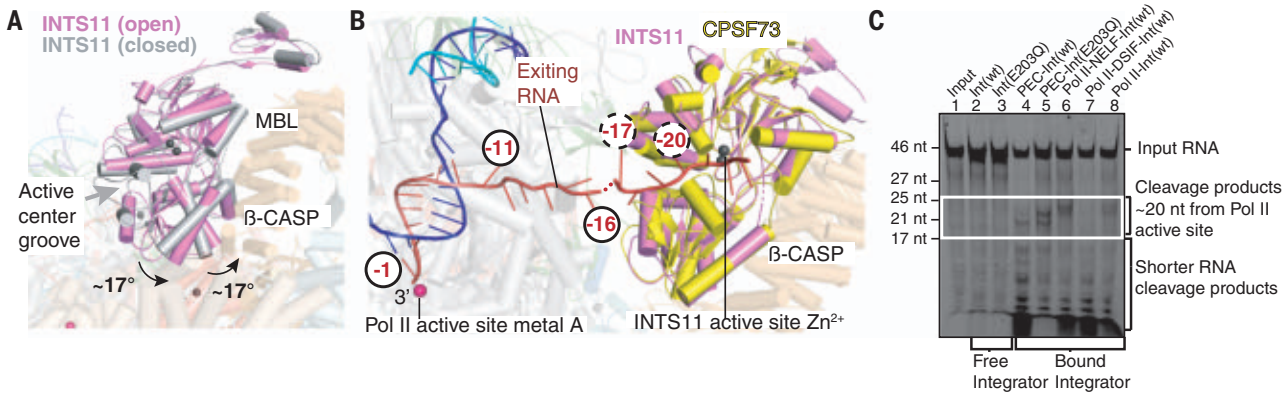


Fig. 3. Integrator-mediated RNA cleavage. (**A**) Comparison of our structure of INTS11 with that of the unbound Integrator-PP2A complex (PDB 7CUN) (*15*) indicating a rotation of the β-CASP domain that results in opening of the active center groove. The view is the same as in Fig. 2B. (**B**) Path of nascent RNA from the Pol II active site to the Integrator endonuclease active site. The register of the RNA nucleotides from the RNA 3′ end in the Pol II active site (register −1) is indicated. RNA nucleotides −17 to −23 are modeled by superposition of RNA bound to CPSF73 (PDB 6V4X) (*26*). The Pol II active site metal A and the INTS11 active site Zn atoms are shown as magenta and dark gray spheres, respectively. (**C**) Integrator is active in RNA cleavage in vitro. Int(wt), wild-type Integrator-PP2A; Int(E203Q), Integrator-PP2A complex with INTS11-E203Q mutation. See fig. S10 for the cleavage assay performed with the hairpin RNA used for structural analysis and replicates.

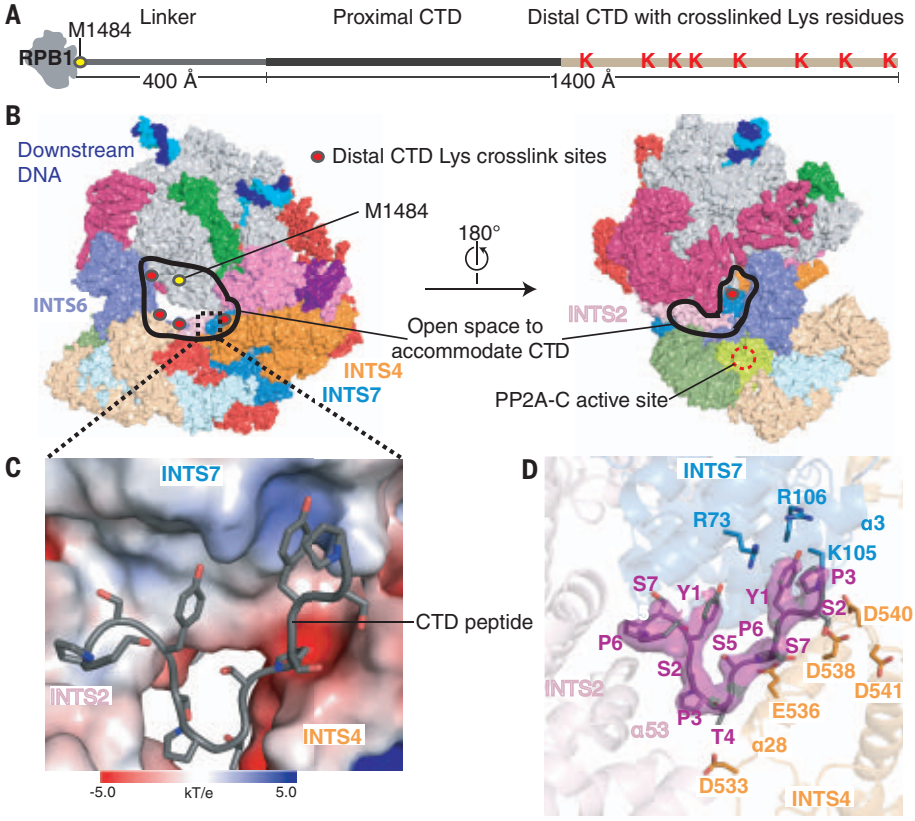


Fig. 4. Integrator-CTD interaction and Pol II dephosphorylation. (**A**) Schematic showing organization of the Pol II subunit RPB1. A linker connects the structured region of RPB1 to the CTD, which consists of a proximal part and a distal part that contains lysine residues (red). The length of a fully extended linker and CTD are indicated. (**B**) Location of lysine residues that cross-linked to the distal CTD within an open space formed between Pol II and Integrator (black outline). (**C**) Two CTD repeats are bound to the open space in (B), interacting with the Integrator surface that is colored according to electrostatic surface potential (*40*). Blue and red showing positively and negatively charged areas, respectively. (**D**) Interactions of the two CTD repeats with INTS2, INTS4, and INTS7. The observed cryo-EM density is shown as a purple semitransparent surface. Charged residues in the vicinity of the CTD are shown as sticks.

that Integrator binding is inconsistent with EC* formation (fig. S8). Integrator excludes PAF binding because the N-terminal region of INTS1 clashes with PAF subunits PAF1 and LEO1 (fig. S8A) and INTS2 clashes with the PAF subunit CTR9 (fig. S8B). Integrator also excludes SPT6 because INTS11 and INTS6 clash with the SPT6 core and tandem SH2 (tSH2) domain, respectively (fig. S8C). Thus, Integrator interferes with EC* formation not only by counteracting phosphorylation but also by steric hinderance.

Finally, our structure provides clues as to how Integrator may facilitate Pol II termination. Termination requires the release of nucleic acids from the Pol II active center cleft, particularly release of the DNA-RNA hybrid that is encircled within Pol II by the closed clamp (*38*) and by the DNA clamp of DSIF that consists of the SPT5 NGN domain and SPT4 (*23*). Our structure shows that the Pol II clamp is still closed but not restricted by Integrator and that the DSIF DNA clamp is open because the NGN domain and SPT4 are mobile (Fig. 1C). DSIF also forms a clamp on exiting RNA with its SPT5 KOWx-4 domain (*23*), which is bound by the INTS11 endonuclease. We speculate that RNA cleavage facilitates opening of the RNA clamp of DSIF and exposes an uncapped RNA 5′ end that is a substrate for the XRN2 nuclease that can cause termination (*39*).

In conclusion, our PEC-Integrator-PP2A structure represents a pretermination complex and provides insights into the mechanisms of Integrator-mediated transcription regulation (fig. S11D). Integrator recognizes the PEC by forming contacts with Pol II, DSIF, and NELF; positions the PP2A phosphatase to counteract PEC phosphorylation; sterically interferes with the association of the positive elongation factors SPT6 and PAF; and positions its cleavage module to cleave nascent RNA ~20 nt from the Pol II active site. Finally, Integrator induces a PEC conformation that is consistent with the release of nucleic acids and transcription termination. These mechanisms likely underlie not only transcription attenuation in the 5′ region of protein-coding genes but also termination at the 3′ end of noncoding transcription units, including enhancers.

REFERENCES AND NOTES

1. D. Baillat *et al.*, *Cell* **123**, 265–276 (2005).
2. F. Lai, A. Gardini, A. Zhang, R. Shiekhattar, *Nature* **525**, 399–403 (2015).
3. M. P. Rubtsova *et al.*, *Sci. Rep.* **9**, 1701 (2019).
4. J. Barra *et al.*, *Sci. Adv.* **6**, eaaz9072 (2020).
5. J. Yamamoto *et al.*, *Nat. Commun.* **5**, 4263 (2014).
6. A. Gardini *et al.*, *Mol. Cell* **56**, 128–139 (2014).
7. B. Stadelmayer *et al.*, *Nat. Commun.* **5**, 5531 (2014).
8. J. R. Skaar *et al.*, *Cell Res.* **25**, 288–305 (2015).
9. N. D. Elrod *et al.*, *Mol. Cell* **76**, 738–752.e7 (2019).
10. D. C. Tatomer *et al.*, *Genes Dev.* **33**, 1525–1538 (2019).
11. F. Beckedorff *et al.*, *Cell Rep.* **32**, 107917 (2020).
12. S. Lykke-Andersen *et al.*, *Mol. Cell* **81**, 514–529.e6 (2021).
13. K. Kamieniarz-Gdula, N. J. Proudfoot, *Trends Genet.* **35**, 553–564 (2019).
14. K. L. Huang *et al.*, *Mol. Cell* **80**, 345–358.e9 (2020).
15. H. Zheng *et al.*, *Science* **370**, eabb5872 (2020).
16. S. J. Vervoort *et al.*, *Cell* **184**, 3143–3162.e32 (2021).
17. J. Chen *et al.*, *RNA* **18**, 2148–2156 (2012).
18. T. R. Albrecht *et al.*, *Nucleic Acids Res.* **46**, 4241–4255 (2018).
19. M. M. Pfleiderer, W. P. Galej, *Mol. Cell* **81**, 1246–1259.e8 (2021).
20. Z. Dominski, X. C. Yang, W. F. Marzluff, *Cell* **123**, 37–48 (2005).
21. K. Sabath *et al.*, *Nat. Commun.* **11**, 3422 (2020).
22. S. M. Vos, L. Farnung, H. Urlaub, P. Cramer, *Nature* **560**, 601–606 (2018).
23. C. Bernecky, J. M. Plitzko, P. Cramer, *Nat. Struct. Mol. Biol.* **24**, 809–815 (2017).
24. P. Cramer, D. A. Bushnell, R. D. Kornberg, *Science* **292**, 1863–1876 (2001).
25. J. Chen, B. Waltenspiel, W. D. Warren, E. J. Wagner, *J. Biol. Chem.* **288**, 4867–4877 (2013).
26. Y. Sun *et al.*, *Science* **367**, 700–703 (2020).
27. S. Gressel *et al.*, *eLife* **6**, e29736 (2017).
28. P. Uguen, S. Murphy, *EMBO J.* **22**, 4544–4554 (2003).
29. J. Chen, E. J. Wagner, *Biochem. Soc. Trans.* **38**, 1082–1087 (2010).
30. N. Hernandez, *EMBO J.* **4**, 1827–1837 (1985).
31. J. Li *et al.*, *J. Biol. Chem.* **296**, 100112 (2021).
32. Y. Jia *et al.*, *Cell Discov.* **7**, 66 (2021).
33. S. Egloff *et al.*, *Science* **318**, 1777–1779 (2007).
34. S. Egloff *et al.*, *J. Biol. Chem.* **285**, 20564–20569 (2010).
35. N. Shah *et al.*, *Mol. Cell* **69**, 48–61.e6 (2018).
36. S. Egloff, J. Zaborowska, C. Laitem, T. Kiss, S. Murphy, *Mol. Cell* **45**, 111–122 (2012).
37. S. M. Vos *et al.*, *Nature* **560**, 607–612 (2018).
38. A. L. Gnatt, P. Cramer, J. Fu, D. A. Bushnell, R. D. Kornberg, *Science* **292**, 1876–1882 (2001).
39. N. J. Proudfoot, *Science* **352**, aad9926 (2016).
40. E. Jurrus *et al.*, *Protein Sci.* **27**, 112–128 (2018).

ACKNOWLEDGMENTS

We thank U. Steuerwald for support at the microscope and for maintaining the EM facility, T. Schulz for maintaining cells and thymus, P. Rus and U. Neef for running the insect cell facility, and F. Wagner for providing the continuous carbon used in cryo-grid preparation. **Funding:** P.C. was supported by the Deutsche Forschungsgemeinschaft (EXC 2067/1-390729940) and the European Research Council (Advanced Investigator Grant CHROMATRANS 882357). H.U. was supported by the Deutsche Forschungsgemeinschaft (SFB860). **Author contributions:** I.F. designed and performed all experiments and data evaluation except as follows. Y.C. prepared PP2A and assisted with structural modeling. C.D. assisted with cryo-EM

data collection, processing, and structural modeling. O.D., A.L., and H.U. performed mass spectrometric analysis. P.C. designed and supervised the research. I.F. and P.C. wrote the manuscript with input from all authors. **Competing interests:** The authors declare no competing interests. **Data and materials availability:** The cryo-EM maps and atomic coordinates were deposited in the Electron Microscopy Data Bank under accession code EMD-13479 and in the Protein Data Bank under accession code 7PKS. Materials are available from P.C. upon request under a materials transfer agreement with the Max Planck Society.

SUPPLEMENTARY MATERIALS

science.org/doi/10.1126/science.abk0154
Materials and Methods
Figs. S1 to S11
Tables S1 and S3
References (*41*–*73*)
Movies S1 to S4
Data S1
MDAR Reproducibility Checklist

16 June 2021; accepted 29 September 2021
10.1126/science.abk0154

LUNAR GEOLOGY

Age and composition of young basalts on the Moon, measured from samples returned by Chang'e-5

Xiaochao Che[1], Alexander Nemchin[1,2]*, Dunyi Liu[1,3]*, Tao Long[1], Chen Wang[1], Marc D. Norman[4], Katherine H. Joy[5], Romain Tartese[5], James Head[6], Bradley Jolliff[7], Joshua F. Snape[5], Clive R. Neal[8], Martin J. Whitehouse[9], Carolyn Crow[10], Gretchen Benedix[2,11], Fred Jourdan[2], Zhiqing Yang[1], Chun Yang[1], Jianhui Liu[1], Shiwen Xie[1], Zemin Bao[1], Runlong Fan[1], Dapeng Li[3], Zengsheng Li[3], Stuart G. Webb[8]

Orbital data indicate that the youngest volcanic units on the Moon are basalt lavas in Oceanus Procellarum, a region with high levels of the heat-producing elements potassium, thorium, and uranium. The Chang'e-5 mission collected samples of these young lunar basalts and returned them to Earth for laboratory analysis. We measure an age of 1963 ± 57 million years for these lavas and determine their chemical and mineralogical compositions. This age constrains the lunar impact chronology of the inner Solar System and the thermal evolution of the Moon. There is no evidence for high concentrations of heat-producing elements in the deep mantle of the Moon that generated these lavas, so alternate explanations are required for the longevity of lunar magmatism.

The Oceanus Procellarum region of the Moon is characterized by high concentrations of potassium, thorium, and uranium, elements that generate heat through long-lived radioactive decay and may have sustained prolonged magmatic activity on the near side of the Moon. The Chang'e-5 spacecraft landed in this region at 43.06°N, 51.92°W, about 170 km east-northeast of Mons Rümker, a location selected because it was expected to host the youngest basalt lavas on the Moon. Orbital data have shown that the geologic unit (designated Em4/P58) exposed around the landing site has high levels of Th [5 to 8.5 parts per million (ppm)], intermediate to high Ti abundances (5 to 8% TiO_2), and high concentrations of the minerals clinopyroxene and olivine (about 31 and 13%, respectively) (*1*–*3*). The mission goal was to return samples of young lunar basalts, identified by the spatial density of impact craters (*1*, *4*).

The number of impact craters on a surface reflects its relative age, with older surfaces having more craters. The Moon is the only planetary body where impact crater ages have been calibrated with radiometric dating, so the lunar chronology is used to infer the ages of other planetary surfaces throughout the Solar System. For example, the climatic evolution of Mars is related directly to the lunar cratering chronology. However, the lunar chronology is highly uncertain for ages younger than ~3 billion years (Ga) (*5*).

Young volcanism on a small body such as the Moon is challenging to explain in its thermal evolution. Although the young basaltic eruptions on the Moon occurred in regions containing increased amounts of heat-producing elements such as K, Th, and U, it is unclear whether this association is responsible for melting the source of magma deep within the Moon (*6*, *7*).

We present mineralogical, chemical, and U-Th-Pb isotopic characteristics of two basalt fragments collected by the Chang'e-5 mission. Our goal was to constrain the age of the Em4/P58 basaltic unit at the landing site, which has a wide range of predicted ages based on impact craters, varying from 1.2 to 3.2 Ga (*1*, *3*, *8*–*14*). We also measured the compositions of these basalts to assess their magmatic source and petrogenesis and to provide calibration for estimates of lunar surface compositions based on remote observations (*15*).

We analyzed two fragments from the Chang'e-5 samples, which we refer to as CE5-B1 and CE5-B2 (*16*). Both are equidimensional, are about 3 to 4 mm in size, and consist of minerals common in lunar basalts, such as chemically zoned clinopyroxene, plagioclase, olivine, and ilmenite, with small amounts of quartz and cristobalite (Fig. 1, data S1, and supplementary text). Both contain multiple interstitial pockets of K-rich glass, barian K-feldspar, troilite, Ca-phosphates (apatite and merrillite), and the Zr-rich minerals baddeleyite and zirconolite. Metallic iron is absent. Both fragments have igneous textures that differ slightly in grain size and crystal habits: CE5-B1 is finer-grained (≤1 mm long) with radiating elongated crystals of plagioclase and ilmenite, whereas CE5-B2 is coarser-grained (<2 mm long) (Fig. 1 and supplementary text). These textures indicate crystallization from a molten magma (melt) and that CE5-B1 cooled more rapidly than CE5-B2. Most mineral phases in CE5-B2 are highly fractured, and shock-melt pockets and veins (a few tens of microns wide) are present along one edge of the sample (Fig. 1D). By contrast, CE5-B1 has no obvious shock-melt pockets or veins and displays fewer fractures ~1 to 10 μm in width. Raman analysis of major, and some accessory, minerals in both fragments (supplementary text) indicates that shock-induced maskelynite is present only in the shock melt zone of fragment CE5-B2. All other minerals (including plagioclase) outside of this zone have not been modified by shocks and preserve their primary magmatic crystallinity (supplementary text).

The pyroxenes and olivines in the two fragments vary widely in their Mg/Fe ratio and include highly Fe-rich compositions for lunar basalts (data S1). The mineral chemistries of these two fragments differ slightly and appear to correspond to their textures (data S1). For example, the olivine in CE5-B2 is more Fe-rich, whereas CE5-B1 has a wider range of TiO_2, Al_2O_3, and Cr_2O_3 in pyroxene (data S1). The mineralogy of these fragments is similar to that of other known lunar basalts. The K-rich glass and the presence of Zr-bearing minerals raise the possibility of a mantle component enriched

[1]The Beijing SHRIMP Center, Institute of Geology, Chinese Academy of Geological Sciences, Beijing 100037, China. [2]School of Earth and Planetary Sciences, Curtin University, Perth, WA 6845, Australia. [3]Shandong Institute of Geological Sciences, Jinan, Shandong 250013, China. [4]Research School of Earth Sciences, The Australian National University, Canberra, ACT 2601, Australia. [5]Department of Earth and Environmental Sciences, The University of Manchester, Manchester M13 9PL, UK. [6]Department of Earth, Environmental, and Planetary Sciences, Brown University, Providence, RI 02912, USA. [7]Department of Earth and Planetary Sciences and The McDonnell Center for the Space Sciences, Washington University in St. Louis, St. Louis, MO 63130, USA. [8]Department of Civil and Environmental Engineering and Earth Sciences, University of Notre Dame, Notre Dame, IN 46556, USA. [9]Department of Geosciences, Swedish Museum of Natural History, SE-104 05 Stockholm, Sweden. [10]Department of Geological Sciences, University of Colorado Boulder, Boulder, CO 80309, USA. [11]Planetary Science Institute, Tucson, AZ 85719, USA.
***Corresponding author. Email: liudunyi@bjshrimp.cn (D.L.); a.nemchin@curtin.edu.au (A.N.)**

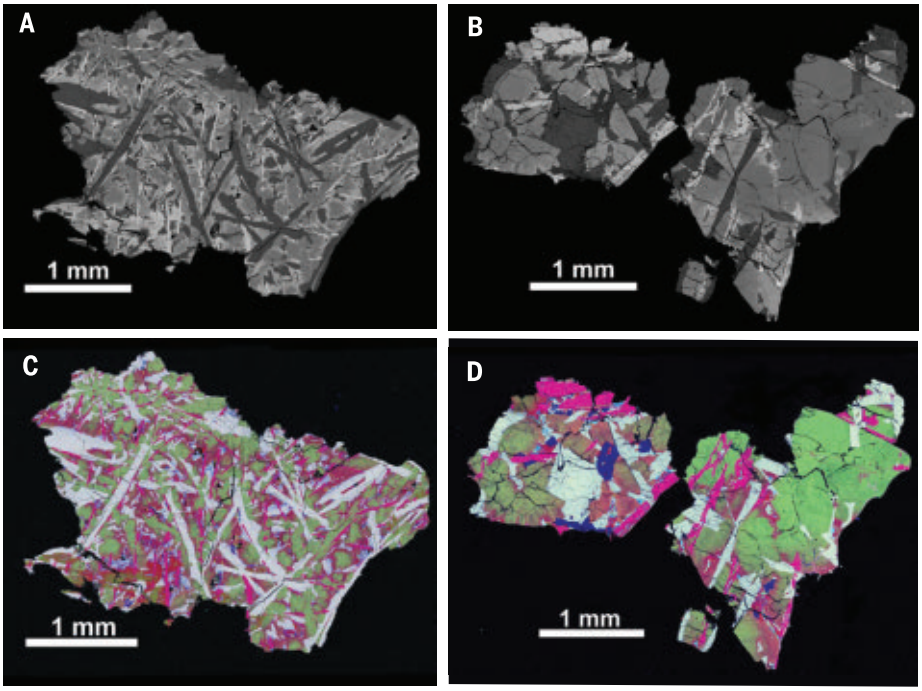


Fig. 1. Back-scattered electron images and false-color energy-dispersive x-ray spectroscopy element maps of the two fragments from the Chang'e 5 sample. (**A** and **B**) Back-scattered electron images of CE-5-B1 and CE-5-B2, respectively. (**C** and **D**) False-color energy-dispersive x-ray spectroscopy images of CE-5-B1 and CE-5-B2. Qualitative concentration and distribution of different elements in both samples are represented by different colors: blue, silica; green, Mg; red, Fe; white, Al; yellow, Ca; pink, Ti; and cyan, K.

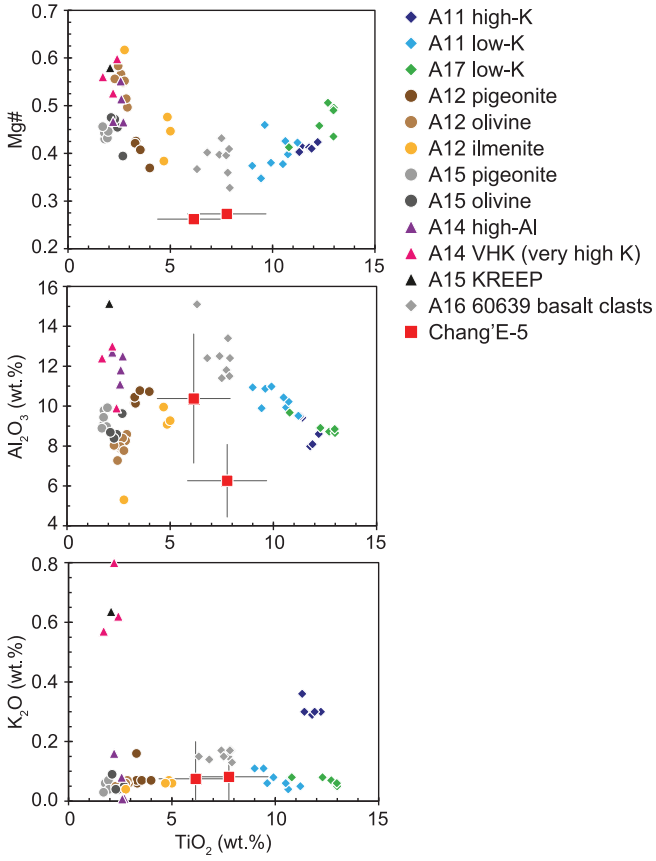


Fig. 2. Bulk chemical composition of basalt fragments. Mg# [defined as Mg/(Mg + Fe)], Al_2O_3, and K_2O versus TiO_2 measurements for the two analyzed Chang'e-5 fragments (red squares with 1σ error bars). These measurements are compared with data from different basalts from Apollo landing sites as indicated in the legend (A11 stands for Apollo 11, and so on; A16 60639 refers to Apollo 16 sample 60639).

in heat-producing elements, but these basalts appear to be compositionally fractionated, so the presence of these evolved minerals may instead reflect a small degree of partial melting and/or extensive fractional crystallization.

The bulk compositions of both fragments calculated from their modal mineralogy indicate increased FeO (~22 to 25 wt %) and low MgO (~5 wt %). Their TiO_2 contents (~6 to 8 wt %), Al_2O_3, (<11 wt %), and K concentrations (<2000 ppm) are consistent with high-Ti, low-Al, low-K mare basalts in standard classifications (*17*) (Fig. 2 and table S1). The mineralogy and bulk compositions of these samples are consistent with remote-sensing observations of this region, implying that they are representative samples of the Em4 unit, despite the differences in grain size and inferred cooling history of CE5-B1 and CE5-B2. However, given the small size of these fragments, it is possible that these calculated bulk compositions are not fully representative of the melts from which they formed, especially for the coarser-grained fragment CE5-B2.

The Pb isotope ratios of the two fragments were analyzed in 50 selected locations (spots with diameters of about 7 μm) within phosphate grains, barian K-feldspar grains, K-rich glass pockets, and areas containing Zr-rich minerals (Fig. 3 and data S4). Determining U-Th-Pb ages of lunar basalts requires knowledge of their initial Pb composition. We adopt an isochron approach, in which the data are presented in $^{207}Pb/^{206}Pb$ versus $^{204}Pb/^{206}Pb$ coordinates. This method allows both the age and the initial Pb isotopic composition to be obtained and has previously been demonstrated through the Pb-Pb study of multiple Apollo basalts (*16*, *18*). The ubiquitous presence of terrestrial contamination in all lunar samples complicates interpretation of the data but is also accounted for in the isochron approach. The individual isochron ages obtained for fragments CE5-B1 and CE5-B2 are 1893 ± 280 million years (Ma) and 1966 ± 59 Ma, respectively. Combining all data for the two fragments, which are consistent within uncertainties, gives an age of 1963 ± 57 Ma (Fig. 3A). Our estimate of the initial lunar Pb isotopic composition ($^{204}Pb/^{206}Pb$ = 0.00226 ± 0.00006, $^{207}Pb/^{206}Pb$ = 0.815 ± 0.009, and $^{208}Pb/^{206}Pb$ = 0.926 ± 0.013) is provided by the intercept of the isochron and a linear model fitted to four K-feldspar analyses (Fig. 3A).

Although these basalt fragments could be susceptible to partial resetting of the U-Pb system, during impacts that transported the fragments to the Chang'e-5 landing site or through subsequent Pb contamination from the host soil, we see no compelling evidence of this in the sample. Shock effects are apparent in one part of CE5-B2, but no isotopic analyses were conducted in this part of the fragment (fig. S6). Any secondary processes

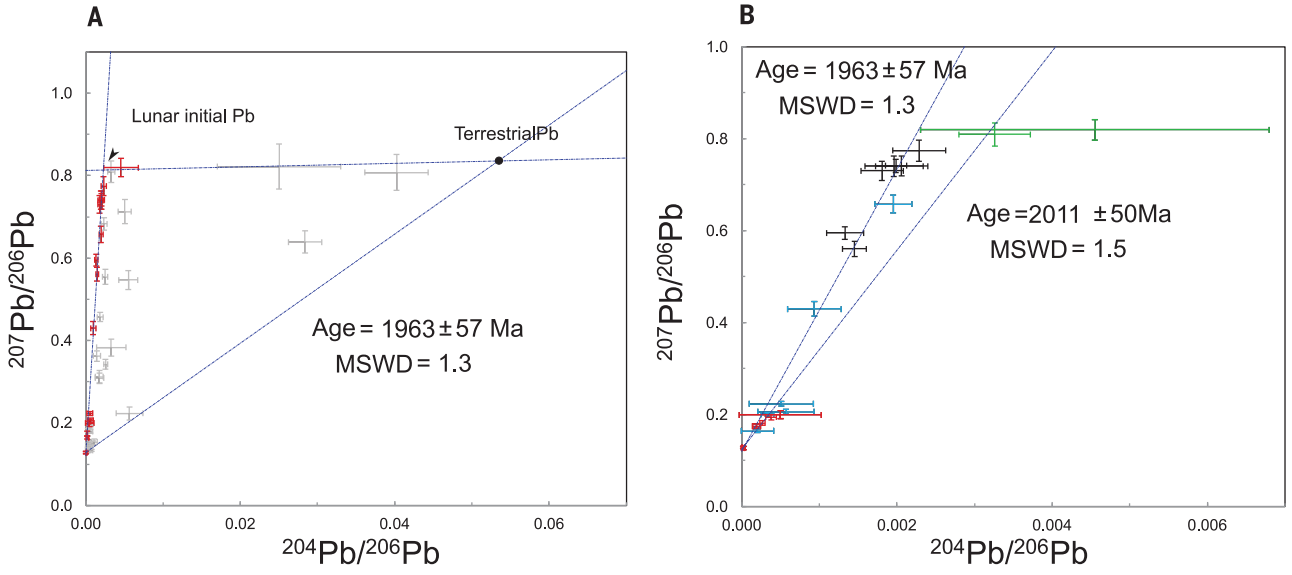


Fig. 3. Pb-Pb isotope data and isochrons for CE-5-B1 and CE-5-B2. (**A**) Data for all measured points in the sample. Red points indicate analyses used to define the isochron, whereas gray points are analyses affected by terrestrial contamination. The black dot shows the terrestrial Pb composition representing contamination. Blue dashed lines define the mixing triangle (*16*), where the steep line at the left is the isochron that defines the age of the sample, the line at the top is the best fit of four K-feldspar analyses used to determine the initial Pb composition, and the line at the bottom is the mixing line with terrestrial Pb. MSWD, mean squared weighted deviation. (**B**) Analyses used to define the isochron. Red data points are Zr minerals, light blue are phosphates, green are K-feldspar, and black are K-glass. The blue lines show isochron constrained from all minerals [as in (A)] and the best-fit line defined by analyses of Zr-rich minerals. All error crosses are at 2σ.

that mobilized Pb would also cause excess scatter in the isochron (i.e., specific minerals offset from the isochron by more than what would be expected from the analytical uncertainties). Glass is most prone to Pb exchange, whereas Zr-rich minerals are likely to better preserve their original Pb-isotope compositions even if shocked (*19*). Shock-induced scatter would also be indicated by a large decrease of $^{207}Pb/^{206}Pb$ in less resistant phases; instead, we find the opposite trend in the $^{207}Pb/^{206}Pb$ versus $^{204}Pb/^{206}Pb$ relationships (Fig. 3). The best-fitting isochron constrained using only Zr-rich minerals indicates an age of 2011 ± 50 Ma, consistent with the full dataset (Fig. 3B). The spatially limited distribution of shock effects and intensity in different parts of the fragments, combined with the internal Pb isotope systematics of the samples, indicate that our measurements closely reflect the primary magmatic compositions of these samples.

Mineral and chemical characteristics of the two basalt fragments are consistent with those inferred for the Em4 unit that was identified at the landing site using remote-sensing data (*1*, *2*). Our isochron age is, therefore, representative of the emplacement age of the Em4/P58 unit and has implications for lunar cratering chronology. Current model ages of the Em4 unit based on crater density measurements range widely from 1.21 (*10*) to 3.3 Ga (*1*), with the results of 1.91 Ga [(*3*), their model A] and 2.07 Ga (*13*) being closest to our measured Pb-Pb crystallization age of 1.96 to 2.01 Ga. If this age is representative of the Em4 unit, it implies that nearly 2000 km^3 of basaltic magma (*1*) erupted near the landing site almost 1 Ga later than the emplacement of any previously measured lunar basalts in the Apollo, Luna, and lunar meteorite sample collections (*18*).

Chemical compositions of the two fragments are distinct from those of lunar basalts from other landing sites (Fig. 2). The Chang'e-5 basaltic fragments are more enriched in Fe and depleted in Mg than other sampled lunar basalts, which implies either an Fe-rich mantle source or unusual conditions of emplacement that allowed a greater extent of fractional crystallization of the magmas sampled by Chang'e-5. Extreme fractionation of the basaltic magmas may have contributed to the high Th concentrations measured remotely at the landing site (5 to 9 ppm). Alternatively, the high Th concentrations inferred from the remote-sensing data may reflect either impact ejecta from the surrounding Oceanus Procellarum region or a primary magmatic component in the source of the Em4 basalts that links their petrogenesis to their spatial association with the high-Th region of the Oceanus Procellarum. The contribution of K-U-Th in the magmatic source or as a contaminant introduced during ascent and evolution of the magma can be assessed by the initial Pb isotopic composition, as determined from the Pb-Pb isochrons. Assuming that the Pb-Pb system remained closed after the formation of these basalts and applying a single-stage Pb isotopic evolution model (*16*), the source of the melt that formed the Chang'e-5 basalt fragments could have attained a Pb composition similar to that measured in the two fragments if the $^{238}U/^{204}Pb$ ratio of this source (referred to as the μ-value) was 665 ± 3. This model does not consider possible fractionation of U and Pb during the earlier Lunar Magma Ocean (LMO) phase. For example, Apollo mare (formed within lunar maria) and KREEP (high potassium, rare earth elements, and phosphorous) basalts have been used to constrain a multistage model of lunar Pb isotopic evolution that indicates a major differentiation event at 4.376 Ga ago (*20*), possibly reflecting the final stages of LMO crystallization and formation of the source reservoir for KREEP, which is enriched in all heat-producing elements (*20*). Applying this multiple-stage Pb isotope model to the Em4 basalts yields a slightly higher μ-value of 677 ± 3.

These μ-values for the Em4 basalts imply only a modest (<2%) KREEP component either in their mantle sources or introduced by assimilation during magma ascent. This estimate shows that the Em4 basalts differ from the trend in source evolution previously suggested for Apollo samples, which show a progressive enrichment of their source regions in heat-producing elements as the basalts become younger (*18*). If this enrichment trend extended to the Em4 basalts, it would predict μ-values >1000, which are not observed. Instead, the data suggest only a small amount of KREEP, at most, in these young basalts.

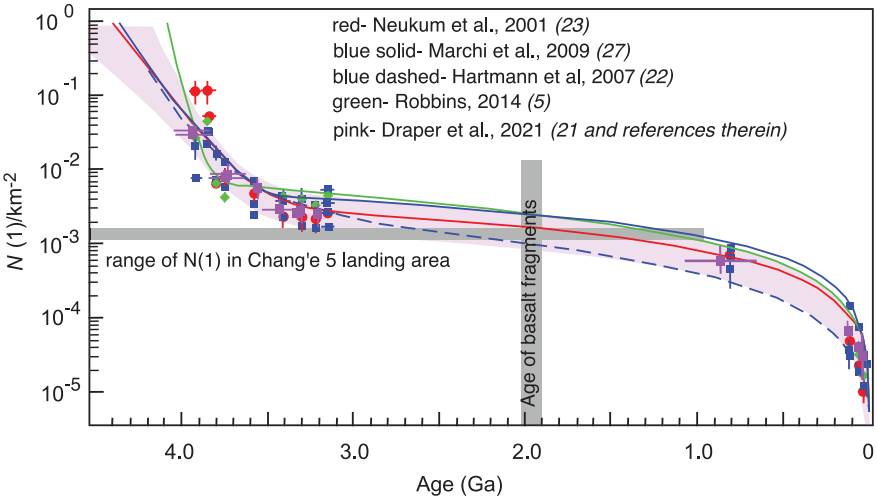


Fig. 4. Lunar cratering chronology models compared with our measurement of the Chang'e-5 sample. Each model relates the radiometric and exposure ages of lunar samples to the frequency of 1-km impact craters $N(1)$ on each sampled unit. The gray-shaded areas indicate the age of Chang'e-5 basalt fragments (this study) and the range of $N(1)$ estimates for the site (*1*, *3*, *12*, *13*). Data used to constrain the curves are from (*5*, *21*–*23*, *27*).

The emplacement age of 1963 ± 57 Ma that we infer for the Em4 unit provides a calibration point for the lunar crater size-frequency distribution chronology curve, which was previously unconstrained between ~1 and 3 Ga (Fig. 4) (*5*, *21*). This age for Em4 falls below many existing crater chronology curves, indicating that the impact flux may have been lower than previously estimated at ages between the youngest Apollo-Luna basalts (~3.1 Ga) and that inferred for the Copernicus crater (~0.8 Ga), consistent with some chronology models (*22*, *23*). $N(1)$, the number density of 1-km craters, on the Em4 unit (1.24×10^{-3} to 1.74×10^{-3} km^{-2}) is similar to the upper limit measured for the Copernicus crater [(*23*, *24*); Fig. 4], so Copernicus might be older than the ~0.8 Ga radiometric age inferred from the glasses sampled by Apollo 12 (*25*).

Orbital data indicates that the youngest basalts on the Moon are expected within the Oceanus Procellarum, a region of the northwest near-side characterized by thin crust and high concentrations of heat-producing elements such as K, Th, and U (*7*). There is a strong spatial correlation between the occurrence of young lunar basalts and the concentrations of heat-producing elements (*26*), but the geophysical and geochemical basis for this correlation remains unclear. One possibility is that increased radioactivity within the lunar mantle produced long-lived thermal anomalies that enhance melting and generate young lunar basalts (*7*). This hypothesis predicts that the young basalts carry increased levels of heat-producing elements compared with the basalts that occur outside of the region enriched in these elements. Our Pb isotope results suggest that the Em4 unit and the source of its magma had U and Th contents that were similar to those of Apollo and Luna mare basalts, suggesting that the mantle source regions of the Em4 basalts did not have increased contents of radioactive elements and that rising magmas were not mixed with KREEP during passage through the crust. Alternative explanations are required for the longevity of lunar magmatism, such as tidal heating or a distinct source mineralogy supporting a lower melting temperature of the mantle. This implies that the increased Th content of the Em4 regolith recorded in remote-sensing data could be due to contamination by secondary ejecta from the Th-rich region of Oceanus Procellarum, which occurs beneath and around the young basalt units (*1*).

REFERENCES AND NOTES

1. Y. Qian *et al.*, *Earth Planet. Sci. Lett.* **561**, 116855 (2021).
2. M. Lemelin *et al.*, *Planet. Space Sci.* **165**, 230–243 (2019).
3. T. Morota *et al.*, *Earth Planet. Sci. Lett.* **302**, 255–266 (2011).
4. H. Hiesinger, J. W. Head III, U. Wolf, R. Jaumann, G. Neukum, *J. Geophys. Res.* **108**, 5065 (2003).
5. S. J. Robbins, *Earth Planet. Sci. Lett.* **403**, 188–198 (2014).
6. G. A. Snyder, L. E. Borg, L. E. Nyquist, L. A. Taylor, in *Origin of the Earth and Moon*, R. M. Canup, K. Righter K, Dds. (Univ. Arizona Press, 2000), pp. 361–395.
7. M. Laneuville, J. Taylor, M. A. Wieczorek, *J. Geophys. Res.* **123**, 3144–3166 (2018).
8. J. M. Boyce, in *Proceedings of the Seventh Lunar Science Conference* (Pergamon Press, 1976), pp. 2717–2728.
9. H. Hiesinger, J. W. Head III, U. Wolf, R. Jaumann, G. Neukum, in *Recent Advances and Current Research Issues in Lunar Stratigraphy*, W. A. Ambrose, D. A. Williams, Eds. (Special Paper 477, Geological Society of America, 2011), pp. 1–51.
10. Y. Q. Qian *et al.*, *J. Geophys. Res.* **123**, 1407–1430 (2018).
11. Y. Qian *et al.*, *Icarus* **337**, 113508 (2020).
12. B. Wu, J. Huang, Y. Li, Y. Wang, J. Peng, *J. Geophys. Res.* **123**, 3256–3272 (2018).
13. M. Jia *et al.*, *Earth Planet. Sci. Lett.* **541**, 116272 (2020).
14. Y. Qian *et al.*, *Earth Planet. Sci. Lett.* **555**, 116702 (2021).
15. D. T. Blewett, P. G. Lucey, B. R. Hawke, B. L. Jolliff, *J. Geophys. Res.* **102**, 16319–16325 (1997).
16. Materials and methods are available as supplementary materials.
17. C. R. Neal, L. A. Taylor, *Geochim. Cosmochim. Acta* **56**, 2177–2211 (1992).
18. J. F. Snape *et al.*, *Geochim. Cosmochim. Acta* **266**, 29–53 (2019).
19. D. E. Moser *et al.*, *Nature* **499**, 454–457 (2013).
20. L. E. Borg, A. M. Gaffney, C. K. Shearer, *Meteoritics* **50**, 715–732 (2015).
21. D. S. Draper *et al.*, *Planet. Sci. J.* **2**, 79 (2021).
22. W. K. Hartmann, C. Quantin, N. Mangold, *Icarus* **186**, 11–23 (2007).
23. G. Neukum, B. A. Ivanov, W. K. Hartmann, *Space Sci. Rev.* **96**, 55–86 (2001).
24. H. Hiesinger *et al.*, *J. Geophys. Res.* **117**, E00H10 (2012).
25. D. Stöffler *et al.*, *Rev. Mineral. Geochem.* **60**, 519–596 (2006).
26. B. L. Jolliff, J. J. Gillis, L. A. Haskin, R. L. Korotev, M. A. Wieczorek, *J. Geophys. Res.* **105**, 4197–4216 (2000).
27. S. Marchi, S. Mottola, G. Cremonese, M. Massironi, E. Martellato, *Astron. J.* **137**, 4936–4948 (2009).
28. China National Space Administration, Notice of China National Space Administration on the distribution of procedures for requesting lunar samples (in Chinese and English), 17 December 2020; www.cnsa.gov.cn/n6758823/n6758839/c6811124/content.html.

ACKNOWLEDGMENTS

We thank the China National Space Administration (CNSA) for providing access to the lunar sample CE5C0000YJYX03501GP. We also thank J. Taylor, D. Moser, and an anonymous reviewer for their thoughtful reviews that helped to improve our manuscript. **Funding:** This work was funded by CNSA grant nos. D020204, D020206, and D020203 (Du.L., X.C., T.L., and C.W.); the National Key R&D Program of China from Ministry of Science and Technology of the People's Republic of China grant no. 2020YFE0202100 (Du.L., X.C., T.L., and C.W.); Science and Technology Facilities Council ST/R000751/1 and ST/P005225/1 (K.H.J. and R.T.); the Royal Society URF\R\201009 (K.H.J.); and the Leverhulme Trust RPG-2019-222 (K.H.J.). **Author contributions:** X.C., A.N., Du.L., M.D.N., B.J., K.H.J., R.T., J.F.S., J.H., and C.R.N. designed the project. All authors contributed to the lunar sample request application to CNSA. X.C., A.N., Du.L., T.L., C.W., M.D.N., B.J., K.H.J., R.T., J.F.S., M.J.W., Z.Y., C.Y., J.L., S.X., Z.B., R.F., Da.L., and Z.L. collected analytical data. X.C., A.N., Du.L., B.J., K.H.J., R.T., J.F.S., C.R.N., and S.G.W. produced tables and figures and performed calculations. A.N., M.D.N., K.H.J., R.T., J.H., J.F.S., B.J., and C.R.N. wrote the draft manuscript. All authors reviewed and edited the manuscript. **Competing interests:** We declare no competing interests. **Data and materials availability:** The lunar sample, designation CE5C0000YJYX03501GP, was provided by the CNSA under a materials transfer agreement (*28*). The two basalt fragments CE5-B1 and CE5-B2 are currently held at the Beijing Sensitive High Resolution Ion Micro Probe Center on a 1-year loan (with a possible extension for another year), after which they will be returned to CNSA. Readers may request Chang'e-5 samples from CNSA through a standard procedure (*28*). Further details are provided in the supplementary materials. Our electron microprobe (EMP) data are provided in data S1 to S3, the Pb isotope results in data S4, and the Raman measurements in data S5 and S6. Calculated bulk compositions of two fragments are given in table S1.

SUPPLEMENTARY MATERIALS

science.org/doi/10.1126/science.abl7957
Materials and Methods
Supplementary Text
Figs. S1 to S13
Table S1
References (*29*–*44*)
Data S1 to S6

5 August 2021; accepted 23 September 2021
Published online 7 October 2021
10.1126/science.abl7957

MINERALOGY

Discovery of davemaoite, $CaSiO_3$-perovskite, as a mineral from the lower mantle

Oliver Tschauner[1]*, Shichun Huang[1], Shuying Yang[2], Munir Humayun[2], Wenjun Liu[3], Stephanie N. Gilbert Corder[4], Hans A. Bechtel[4], Jon Tischler[3], George R. Rossman[5]

Calcium silicate perovskite, $CaSiO_3$, is arguably the most geochemically important phase in the lower mantle, because it concentrates elements that are incompatible in the upper mantle, including the heat-generating elements thorium and uranium, which have half-lives longer than the geologic history of Earth. We report $CaSiO_3$-perovskite as an approved mineral (IMA2020-012a) with the name davemaoite. The natural specimen of davemaoite proves the existence of compositional heterogeneity within the lower mantle. Our observations indicate that davemaoite also hosts potassium in addition to uranium and thorium in its structure. Hence, the regional and global abundances of davemaoite influence the heat budget of the deep mantle, where the mineral is thermodynamically stable.

Calcium silicate, $CaSiO_3$, occurs in a variety of natural and synthetic polymorphs. The low-pressure polymorph wollastonite is a common metamorphic mineral. Breyite (*1*), an intermediate-pressure polymorph (*2*), has been found as inclusions in diamond. At the pressures and depth range of Earth's transition zone (420 to 660 km) and lower mantle (LM; 660 to ~2700 km), $CaSiO_3$ assumes a perovskite structure. Perovskite-type $CaSiO_3$, first synthesized by Liu and Ringwood (*3*), is a liquidus phase for basaltic and peridotic bulk rock compositions at LM pressures and temperatures and has been experimentally shown to host many elements that are incompatible in upper-mantle minerals (*4*–*7*). These include rare-earth elements (REEs), large ion lithophile elements (LILEs; K, Sr, and Ba), Ti, U, and Th. In other words, these elements are compatible rather than incompatible in a LM mineral assemblage that contains a few vol % of $CaSiO_3$-perovskite. The composition and abundance of this phase in the LM are therefore key in constraining the budget and distribution of REEs and LILEs and the elements with abundant radioactive isotopes (K, U, and Th) that make an important contribution to the heat of Earth's mantle (*8*). Through these parameters, $CaSiO_3$ perovskite provides essential constraints on the fate of recycled crust in deep Earth, thermochemical anomalies, and the existence of a magma ocean at the base of Earth's mantle. The synthetic perovskite phase of pure $CaSiO_3$ has been found to assume either cubic or tetragonal symmetry (*9*) and belongs to the tausonite ($SrTiO_3$)–type perovskites that adhere to fundamentally different structural distortion mechanisms (*10*) and crystal-chemical constraints than the $GdFeO_3$-type perovskites such as bridgmanite [$MgSiO_3$-perovskite (*11*)] and the $CaTiO_3$ mineral, actually named perovskite.

The difficulty of finding $CaSiO_3$-perovskite in nature stems from its stability at pressures only above 20 GPa (*3*, *4*) along with a low kinetic barrier for back-conversion into low-pressure polymorphs (*2*). This barrier is lower than for bridgmanite, which has been found as a rare occurrence in highly shocked meteorites despite its stability only above 23 GPa (*11*, *12*). Nestola *et al.* (*13*) reported the presence of $CaSiO_3$-perovskite as an inclusion in a diamond from the Cullinan mine, South Africa. The reported phase deviates from synthetic $CaSiO_3$-perovskite in several ways: (i) its volume at ambient conditions is >20% larger (*9*); (ii) it sustains the beam of an electron microscope, whereas any synthetic $CaSiO_3$-perovskite vitrifies rapidly at ambient conditions; (iii) its cell axis ratios and Raman spectrum are nearly equal to those of $CaTiO_3$; and (iv) its space group indicates a structural distortion mechanism different from that of synthetic $CaSiO_3$-perovskite but much closer to that of $CaTiO_3$ (*7*, *8*). Nestola *et al.* (*13*) proposed that this distinctive phase of $CaSiO_3$ is the result of partial decomposition of a Ti-bearing $CaSiO_3$-perovskite. The coexistence of $CaTiO_3$ + $CaSiO_3$ polymorphs in diamond inclusions may also point to retrograde transformation of stoichiometric Ca-Si-Ti-perovskites (*1*) that form in the deep upper mantle (5 to 10 GPa).

The findings by Nestola *et al.* (*13*) are notable by themselves but differ from the expected high-pressure $CaSiO_3$-perovskite and have not resulted in the approval of $CaSiO_3$-perovskite as a mineral. We report the discovery of $CaSiO_3$-perovskite as a mineral approved by the Commission of New Minerals, Nomenclature and Classification (CNMNC) of the International Mineralogical Association (IMA). The new mineral [IMA2020-012a (*14*)] is named "davemaoite" in honor of Dave (Hokwang) Mao for his eminent contributions to the field of deep-mantle geophysics and petrology. The type material—inclusions in a diamond from Orapa, Botswana—is deposited in the Natural History Museum Los Angeles (catalog number NHMLA 74541, formerly GRR1507 of the Caltech mineral collection) (*15*). Davemaoite coexists with orthorhombic carbonaceous α-iron and wüstite $(Fe_{0.8}Mg_{0.2})O$ at 8 to 9 GPa remnant pressure (Fig. 1). Separate inclusions of ilmenite, iron, and ice-VII in the same diamond (*16*) have remnant pressures of 7 GPa and 8 to 9 GPa, respectively. The x-ray diffraction (XRD) pattern of davemaoite is that of a cubic perovskite (Fig. 1) (*15*), with, at most, contributions of <5 vol % of material with ±2.5% smaller or larger volume, whereas an overall distortion of the lattice can be excluded on the basis of the reflection intensities (Fig. 1). Cubic ABO_3 perovskites have no internal structural degrees of freedom and comprise only one chemical formula unit. Thus, the identification of this phase is unambiguous even in diffraction patterns with contributions from more than one phase (Fig. 1).

Davemaoite was identified through the XRD pattern of cubic perovskite at a location in the hosting diamond with a CaKα x-ray fluorescence (XRF) signal far above background. Both, XRF and XRD data were obtained at beamline 34-ID-E at the Advanced Photon Source (*15*). We superimposed the CaKα XRF map (Fig. 2) on a visible light image of the holotype material at the beamline where we subsequently collected the XRF and XRD data. We also made corresponding maps of Fe and Ti (fig. S1). Areas with XRF signal at noise level in Fig. 2 show no x-ray diffraction besides that of diamond. Right after acquisition of the XRF map, we examined by XRD the inclusions that were found by XRF. XRD and XRF were collected on the inclusions when they were fully entrapped in the doubly polished platelet of the hosting diamond. We focused the x-ray beam to an area of 0.5 μm by 0.5 μm in order to identify inclusions with high spatial resolution. The inclusions of 4 μm by 6 μm and 4 μm by 16 μm areas within the red circle of the Ca XRF map corresponded to the XRD patterns of the cubic perovskite (Fig. 1). We added frames with perovskite patterns to obtain better signal and powder statistics.

We confirmed the identification of davemaoite by infrared spectroscopy. Cubic ABO_3 perovskites have no Raman-active modes and three infrared (IR)–active modes (*15*). We observed two of the three IR-active modes (Fig. 1, inset), while the third one was below the diffraction limit for objects as small as these inclusions. As expected, we observed no Raman peaks (fig. S2). We calculated mode energies by fitting force constants to match ab initio calculated zone-center phonon energies of the

[1]Department of Geoscience, University of Nevada, Las Vegas, NV 89154, USA. [2]National High Magnetic Field Laboratory and Department of Earth, Ocean, and Atmospheric Science, Florida State University, Tallahassee, FL 32310, USA. [3]Advanced Photon Source, Argonne National Laboratory, Lemont, IL 60439, USA. [4]Advanced Light Source, Lawrence Berkeley National Laboratory, Berkeley, CA 94720, USA. [5]Division of Geological and Planetary Sciences, California Institute of Technology, Pasadena, CA 91105, USA.
*Corresponding author. Email: oliver.tschauner@unlv.edu

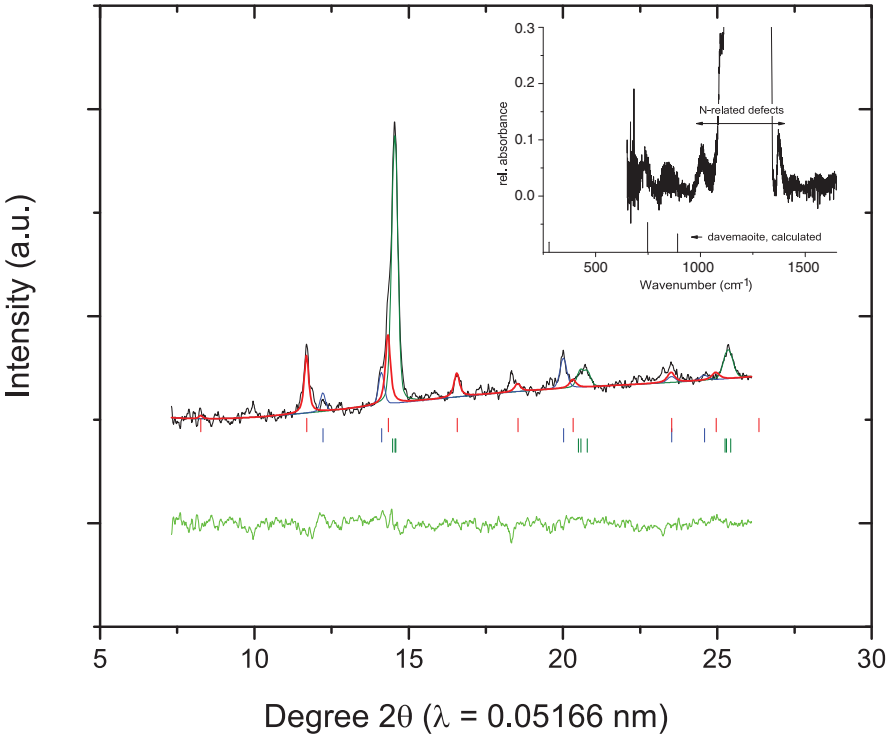


Fig. 1. X-ray diffraction pattern and Rietveld refinement of davemaoite. Davemaoite (dvm), red; (Fe,C), olive; wüstite (wüs), blue; residual of fit, green. Tick marks indicate allowed reflections (same color-coding). The weighted refinement factor, R_{wp}, was 0.046, and the structure-factor moduli-based refinement factor, R_F, for dvm was 0.10. Phase proportions were 35(5), 45(5), and 15(5)% for dvm, (Fe,C), and wüs, respectively. In dvm, the intensity of reflections 100 and 201 indicates sublattice disorder with A-cations shifted from site 1b to the 1/8-occupied site 8g. This is consistent with accommodation of K and Na along with Al and Fe. The paragenesis was found in two inclusions. Volumes of analyzed davemaoite inclusions ranged from 45.1 to 46.3 Å^3 [equal to 0 to 6 GPa (*7*) in pure $CaSiO_3$], but the actual composition of davemaoite markedly changes the pressure inferred from the volume (*9*). Coexisting wüstite $Fe_{0.8(1)}Mg_{0.2(1)}O$ has a volume of 74.34(1) Å^3, corresponding to 8 to 9 GPa (*22*). Indications of weak diffraction around dvm peaks near noise level are assigned to minor contributions of material of slightly larger and smaller volume (probably reflecting chemical variation; fit not shown here) but are inconsistent with a tetragonal distortion. a.u., arbitrary units. (Inset) IR spectrum of davemaoite after subtraction of a diamond spectrum collected close to the inclusion. The unprocessed IR spectrum is shown in fig. S3. Bars indicate all calculated IR bands.

tetragonal structure (*17*) and mapped the tetragonal Brillouin zone onto that of the cubic structure. Intensities are based on the calculated phonon density of state.

Subsequently, we used laser-ablation inductively coupled mass spectrometry (LA-ICP-MS) to excavate and analyze the chemical compositions of two of the inclusions with a 100-μm-diameter laser beam. We indicate the ablation area with a red circle (Fig. 2). We monitored all mass peaks under medium mass resolution ($m/\Delta m$ = 4000), which allowed us to resolve numerous carbon-related molecular interferences on low-mass isotopes. We hit two inclusions of davemaoite at 5 to 8 μm and 80 to 100 μm depth below the polished surface (Fig. 2, inset). The time-resolved ^{44}Ca signal of the LA-ICP-MS measurement (Fig. 2, inset) shows signal clearly above background level. We also collected equivalent profiles for ^{56}Fe, ^{39}K, and ^{52}Cr (fig. S1). In all cases, the signals rose above background at the same depth, consistent with their origin in the same two inclusions. We obtained an average davemaoite composition of $(Ca_{0.43(1)}K_{0.20(1)}Na_{0.06}Fe_{0.11(1)}Al_{0.08}Mg_{0.06}Cr_{0.04(2)})(Si_{1.0(2)}Al_{0.00(1)})O_3$ (*15*). We performed a Rietveld refinement (Fig. 1) and provide a crystallographic information file (*15*).

Next, we describe the hosting diamond and then discuss the pressure-temperature (P-T) conditions of formation of the type davemaoite and its composition. The hosting diamond is different from diamonds that contain potential retrograde products of high-pressure minerals at 0 to 1 GPa remnant pressures (*13*, *18*). The diamond is of type IaAB with frosted octahedral faces and trigon features (*15*). We found davemaoite, iron, wüstite, ilmenite, and ice-VII in the center of the diamond. Our analysis of the N-defect IR bands (fig. S3) (*12*) indicates a low average residence temperature (~1500 K) or a short residence time in the mantle, similar to the holo- and cotype diamonds of ice-VII (*18*). Short residence time and low average residence temperature are common features of lithospheric diamonds, but in sublithospheric diamonds both parameters act in favor of conserving high remnant pressures and high-pressure minerals by reducing viscoelastic relaxation of the hosting diamond and by preventing retrograde transformations. The bulk modulus of davemaoite depends on its composition (*7*, *8*) and is unknown for the given composition. However, coexisting wüstite is at a remnant pressure of 8 to 9 GPa (*16*). For a single inclusion of wüstite, this remnant pressure would correspond to an entrapment pressure of ~40 GPa if pressure were to evolve along a purely elastic path (*15*). However, diamond becomes viscoelastic between 1100 and 1200 K, even at laboratory time scales (*19*). To account for this nonelastic behavior of the hosting diamond, we use the method of Wang *et al.* (*20*), which does not rely on initial assumptions about the entrapment temperature and uses the P-T paths of separate inclusions in the same diamond: wüstite, iron, ice-VII, and ilmenite. Using this approach, we assessed entrapment conditions of 29 ± 5 GPa at 1400 to 1600 K (*15*). Because viscoelastic processes are path- and time-dependent, we cannot exclude a higher entrapment pressure or temperature.

We cannot entirely rule out that our chemical analysis is affected by minor contaminants, although we did not observe an XRD signal or a marked XRF signal of any phase other than davemaoite, wüstite, and iron in the excavated region. Furthermore, we note that (i) the low Ti is a result unaffected by potential contamination and (ii) the ^{39}K signal occurs at the same depth as the ^{44}Ca signal of davemaoite. We did not observe by XRD alternative hosts of K and Ca such as liebermannite and harmunite-type $(Ca,K,Na)(Al,Si)_2O_4$ anywhere in this diamond. Both of these phases, and any phase dominated by K and Ca, give diffraction patterns that are very different from the perovskite-type pattern we observed. Hence, we believe the presence of K and Al in davemaoite is not likely the result of a contaminated analysis but rather indicates coupled substitution of a large and a small cation K,Na + Al,Fe for Ca. Generally, a substitution of K for Ca and Al for Si shifts the material into the stability field of ABO_3 perovskites with a trend toward high crystal symmetry (*21*).

Our result indicates that the postspinel phase $(Ca,Na,K)(Al,Si)_2O_4$ is not required as a host of Ca, alkalis, and Al in at least the upper region of the lower mantle. It is possible that type davemaoite formed retrograde out of postspinel through a reaction $(Ca,Na,K)(Al,Fe^{3+},Si)_2O_4 + Fe^0 \rightarrow (Ca,Na,K)(Al,Si)O_3 + FeO$, but for this process one expects the presence of remnant

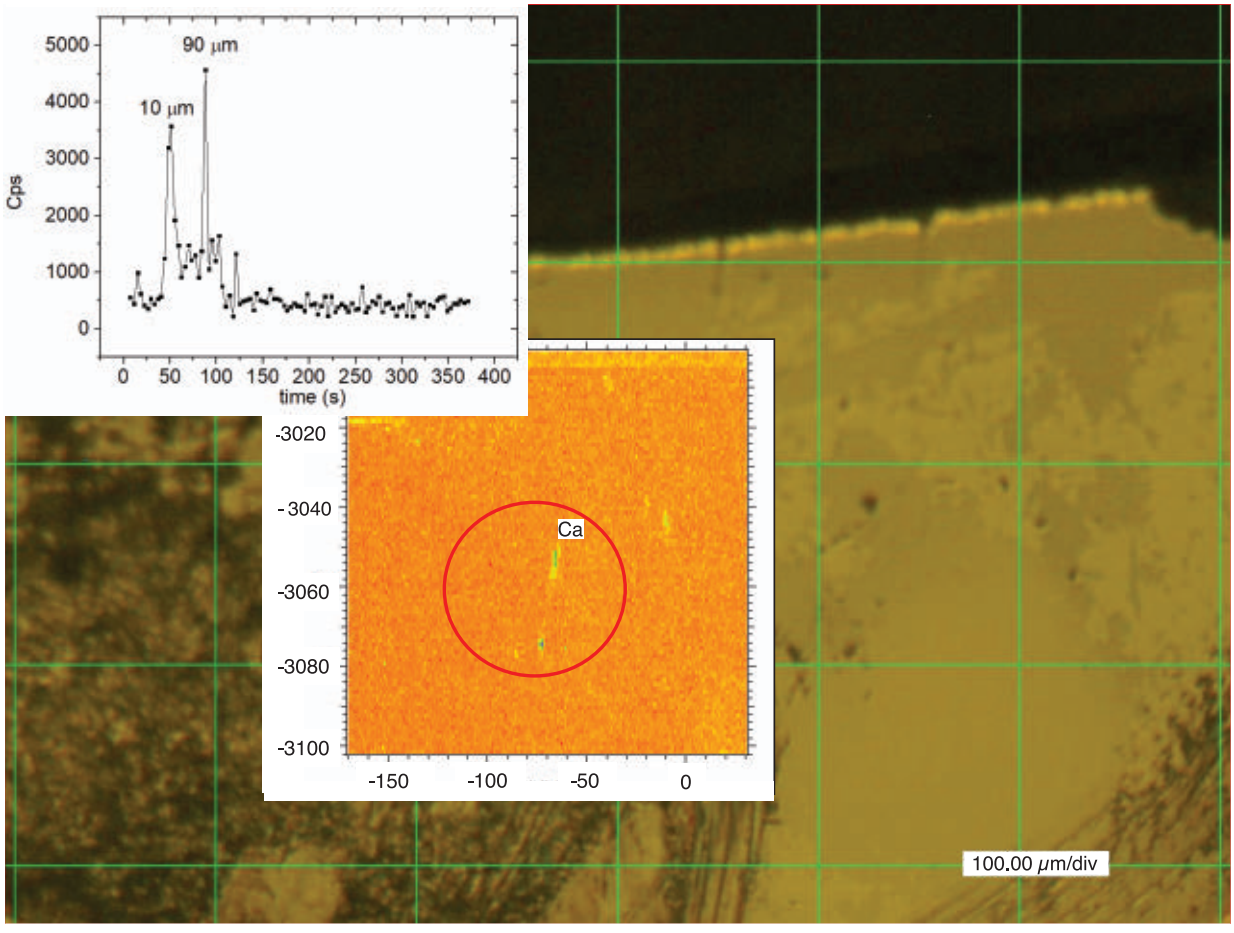


Fig. 2. Reflected light image of the diamond at the beamline. The XRF map of CaKα is superimposed. The *x* and *y* axes give the sample coordinates in micrometers. The red circle indicates the area ablated during LA-ICP-MS analysis. The two Ca-rich areas in the circle correspond to diffraction patterns of davemaoite. The more intense signal around *x*,*y* = 72,−3074 corresponds to the shallow inclusion at 8 to 10 μm depth. Depth was assessed from the attenuation of the XRF signal of Ca and Fe and from the depth of the pit after ablation. (Inset) Time-resolved ^{44}Ca signal of LA-ICP-MS measurement. Ablation started at time (*t*) = 48 s and finished at 108 s. Cps, counts per second; div, divisions of the grid.

postspinel in the paragenesis, which is not observed. In the deep mantle, davemaoite takes on a role similar to that of garnet in the upper mantle. Both minerals have a "garbage can" crystal chemistry that allows them to host many elements that are incompatible in upper-mantle minerals (*6*, *7*). Our observations are fully consistent with the experimental results that this mineral dissolves LILEs, specifically K (*6*, *7*). Experimental studies that were based on peridotite and MORB (mid-ocean ridge basalt)–like bulk compositions formed davemaoite with lower K content and higher Ti content than the type material, which is expected for these starting compositions. We argue that the low Ti and high K content of type davemaoite reflects a different, K-rich source composition, possibly resulting from deep-mantle metasomatism, which is also indicated by the presence of ice-VII and by the hosting diamond itself (*16*). This point emphasizes the importance of studying natural specimens of high-pressure minerals, because they record a petrologic complexity of deep Earth that may not be assessed in experiments. Depletion of Ti in type davemaoite is a possible result of the presence of phases that strongly partition Ti, such as liuite, $FeTiO_3$-perovskite. Ilmenite has been observed in the same diamond at similar remnant pressure as the davemaoite-wüstite-iron inclusion, and its P-T path intersects the phase boundary of liuite (*15*). Hence, our findings indicate that the source rock composition of type davemaoite deviated from peridotite and, thus, that chemical segregation occurs in the lower mantle, possibly down to 900 km according to our estimate (fig. S4). This variation in rock composition affects heat generation through radioactive decay in the lower mantle where davemaoite scavenges K, as shown here, and U and Th, as experimentally shown (*7*).

REFERENCES AND NOTES

1. F. E. Brenker, F. Nestola, L. Brenker, L. Peruzzo, J. W. Harris, *Am. Mineral.* **106**, 38–43 (2020).
2. O. Tschauner, *Am. Mineral.* **104**, 1701–1731 (2019).
3. L. Liu, A. E. Ringwood, *Earth Planet. Sci. Lett.* **28**, 209–211 (1975).
4. K. Hirose, R. Sinmyo, J. Hernlund, *Science* **358**, 734–738 (2017).
5. S. Gréaux *et al.*, *Nature* **565**, 218–221 (2019).
6. K. Hirose, N. Shimizu, W. van Westrenen, Y. W. Fei, *Phys. Earth Planet. Inter.* **146**, 249–260 (2004).
7. S. Gréaux *et al.*, *Phys. Earth Planet. Inter.* **174**, 254–263 (2009).
8. J. Korenaga, *Rev. Geophys.* **46**, RG2007 (2008).
9. H. W. Chen *et al.*, *Am. Mineral.* **103**, 462–468 (2018).
10. A. M. Glazer, *Acta Crystallogr. A* **31**, 756–762 (1975).
11. O. Tschauner *et al.*, *Science* **346**, 1100–1102 (2014).
12. N. Tomioka, K. Fujino, *Science* **277**, 1084–1086 (1997).
13. F. Nestola *et al.*, *Nature* **555**, 237–241 (2018).
14. R. Miyawaki, F. Hatert, M. Pasero, S. J. Mills, *Eur. J. Mineral.* **32**, 645–651 (2020).
15. Materials and methods are available as supplementary materials.
16. O. Tschauner *et al.*, *Science* **359**, 1136–1139 (2018).
17. R. Caracas, R. Wentzcovitch, G. D. Price, J. Brodholt, *Geophys. Res. Lett.* **32**, L06306 (2005).
18. T. Stachel, G. P. Brey, J. W. Harris, *Elements* **1**, 73–78 (2005).
19. D. J. Weidner, Y. Wang, M. T. Vaughan, *Science* **266**, 419–422 (1994).
20. W. Wang *et al.*, *Innovation* **2**, 100117 (2021).

21. V. M. Goldschmidt, *Naturwissenschaften* **14**, 477–485 (1926).
22. S. D. Jacobsen *et al*., *J. Synchrotron Radiat.* **12**, 577–583 (2005).
23. O. Tschauner, S. Huang, S. Yang, M. Humayun, W. Liu, S. N. Gilbert Corder, H. A. Bechtel, J. Tischler, G. R. Rossman, Raw data for davemaoite Dryad (2021); https://doi.org/10.5061/dryad.jq2bvq89m.

ACKNOWLEDGMENTS

We thank N. Tomioka and an anonymous reviewer for their helpful comments. **Funding:** This work was supported by awards NSF-EAR-1838330, -EAR-1942042, and -EAR-1322082; the NSF Cooperative Agreement No. DMR-1644779; and the State of Florida. Use of the Advanced Photon Source and the Advanced Light Source were supported by the US Department of Energy, Basic Energy Sciences, contracts DE-AC02-06CH11357 and DE-AC02-05CH11231, respectively. **Author contributions:** O.T., S.H., S.Y., and M.H. participated in design, interpretation, data collection, and analysis of the reported results and in drafting and revising the manuscript. W.L., S.N.G.C., H.A.B., J.T., and G.R.R. participated in data collection and revising the manuscript. **Competing interests:** The authors have no competing interests. **Data and materials availability:** Additional chemical and crystallographic information about davemaoite is provided in the supplementary materials. Raw data are deposited at Dryad (*23*). Crystallographic and chemical information on type davemaoite is deposited in the Inorganic Crystal Structure Database. The type material is deposited with the NHMLA under accession number 74541.

SUPPLEMENTARY MATERIALS

science.org/doi/10.1126/science.abl8568
Materials and Methods
Figs. S1 to S4
Tables S1 and S2
References (*24*–*40*)
Data S1

9 August 2021; accepted 21 September 2021
10.1126/science.abl8568

FOSSIL CARBON

Methoxyl stable isotopic constraints on the origins and limits of coal-bed methane

M. K. Lloyd[1,2]*, E. Trembath-Reichert[1,3], K. S. Dawson[1,4], S. J. Feakins[5], M. Mastalerz[6], V. J. Orphan[1], A. L. Sessions[1], J. M. Eiler[1]

Microbial coal-bed methane is an important economic resource and source of a potent greenhouse gas, but controls on its formation are poorly understood. To test whether the microbial degradability of coal limits microbial methane, we monitored methoxyl group demethylation—a reaction that feeds methanogenesis—in a global sample suite ranging in maturity from wood to bituminous coal. Carbon isotopic compositions of residual methoxyl groups were inconsistent with a thermal reaction, instead implying a substrate-limited biologic process. This suggests that deep biosphere communities participated in transforming plant matter to coal on geologic time scales and that methoxyl abundance influences coal-bed methane yield. Carbon isotopic enrichments resulting from microbial methylotrophy also explain an enigmatic offset in the carbon-13 content of microbial methane from coals and conventional hydrocarbon deposits.

Coal is currently the world's dominant electricity source, but its combustion carries great environmental costs (*1*). Coal-bed methane (CBM) produces less CO_2 per unit of electricity and far less particulate pollution, but its viability as a transition fuel is debated: CBM production wells often have limited life spans, and efforts to enhance microbial methanogenesis in coal beds have seen inconsistent success (*2*). CBM emissions also account for ~10% of global atmospheric inputs of this potent greenhouse gas (*3*), but substantial uncertainties regarding present and future emissions remain (*4*). The outcomes of these efforts depend on understanding what factors limit CBM generation. Most of the world's coal resources are of low rank (e.g., lignite or subbituminous), where CBM is formed by subsurface microbial communities metabolizing degraded components of the coal structure (*5*, *6*). One substrate of particular interest is the methoxyl group (R–O–CH_3). Methoxyl groups initially make up about one in eight carbon atoms in lignin, and their loss (termed O-demethylation) is a key reaction in the chemical transformation of woody plant tissue to coal (coalification) that is inferred to source the first peak of methane production in humic coals (*7*–*9*). Despite its importance, little is known of the organisms that catalyze coal O-demethylation in the environment or whether this initial step is biogenic at all (*6*). Some have suggested that direct microbial modification of plant matter in nature ends during peat formation (*5*), and therefore abiotic mechanisms [e.g., temperature, acid hydrolysis (*10*)] catalyze subsequent O-demethylations. However, laboratory enrichment cultures of coal-hosted anaerobes directly O-demethylate humic materials beyond the peat stage (*11*, *12*), and scientific drilling continues to extend the depths and temperatures at which hydrocarbon-degrading life can persist (*13*, *14*). Therefore, the extent to which deep-biosphere microbes catalyze early coalification reactions such as O-demethylation (*6*)—or merely consume the by-products (*10*)—is an open question central to understanding the viability of CBM as a transition fuel and its contribution to atmospheric methane. If the ambient temperature, activity, or composition of indigenous microbial assemblages limits methanogenesis in low-rank coals, strategic amendments of microbes or nutrients could enhance CBM generation or emission. Alternatively, if coal's microbial degradability (hereafter, bioavailability) limits CBM formation, only thermal maturation on geologic time scales would measurably increase the abundance of this methane source.

Stable isotopes can distinguish between reaction mechanisms that impart different isotopic fractionations (*15*). However, bulk isotopic analyses are insufficient for macromolecular organics like lignin because the carbon sites that participate in coalification reactions are diluted by those that do not. To constrain how coals are O-demethylated, we analyzed the site-specific concentration and carbon isotopic composition of methoxyl groups in a global suite of natural humic materials representing the major coalification stages from pristine wood to bituminous coal (materials and methods, section S1). Methoxyl abundances (reported as the fraction of all lignin carbon that is methoxyl carbon) and $\delta^{13}C$ values [reported in per mil versus Vienna Pee Dee belemnite (VPDB): $\delta^{13}C_{methoxyl} = ({}^{13}R_{methoxyl} / {}^{13}R_{VPDB}) - 1$] in wood range from 0.13 to 0.19 and −23 to −32 per mil (‰), respectively (Fig. 1). Lignites from Belchatow, Poland (vitrinite reflectance of 0.27 to 0.28% R_o), have 25 to 40% of the initial methoxyl groups remaining and $\delta^{13}C_{methoxyl}$ values of −19 to −13‰. Lignites and subbituminous coals retrieved offshore of the Shimokita peninsula (0.37 to 0.43% R_o) have 0.1 to 2% of the methoxyl groups in lignin and $\delta^{13}C_{methoxyl}$ values of +6 to +27‰. Subbituminous coals from the Powder River Basin are marginally more mature (0.45 to 0.47% R_o), have lower methoxyl contents (0.05 to 0.08% remaining), and $\delta^{13}C_{methoxyl}$ values of +4 to +13‰. Bituminous coals from the San Juan and Michigan Basins (0.5 to 0.8% R_o) contain no methoxyl groups above detection limits. Bulk organic carbon $\delta^{13}C$ are all between −27 and −22‰ (table S1).

A reduction in methoxyl concentration and a marked rise in $\delta^{13}C_{methoxyl}$ values accompany coalification. Our normalization scheme

[1]Division of Geological and Planetary Sciences, California Institute of Technology, Pasadena, CA 91125, USA. [2]Department of Geosciences, The Pennsylvania State University, University Park, PA 16802, USA. [3]School of Earth and Space Exploration, Arizona State University, Tempe, AZ 85287, USA. [4]Department of Environmental Sciences, Rutgers, The State University of New Jersey, New Brunswick, NJ 08901, USA. [5]Department of Earth Sciences, University of Southern California, Los Angeles, CA 90089, USA. [6]Indiana Geological and Water Survey, Indiana University, Bloomington, IN 47405, USA.
*Corresponding author. Email: mlloyd@psu.edu

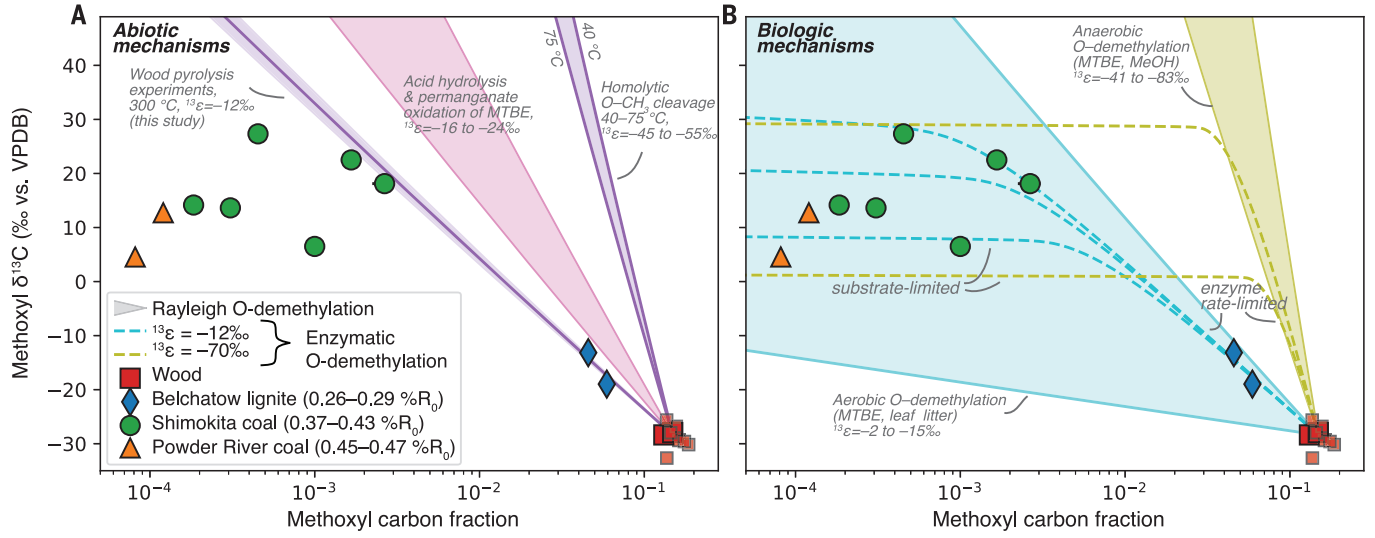


Fig. 1. Evolution of methoxyl concentration and carbon isotopic composition during maturation from lignin to subbituminous coal. (**A** and **B**) Methoxyl data are compared with two types of degradation models: abiotic O-demethylation mechanisms (A), which all follow Rayleigh fractionation, and biologic mechanisms (B), which can conform to Rayleigh models (solid lines and semitransparent regions) or to enzymatic O-demethylation with a potential mass transport limitation (dashed lines) (*21*). Fractionation factors for each mechanism are maximum ranges previously documented (table S5). Existing wood methoxyl data are shown as semitransparent squares (table S6). R$_0$, vitrinite reflectance.

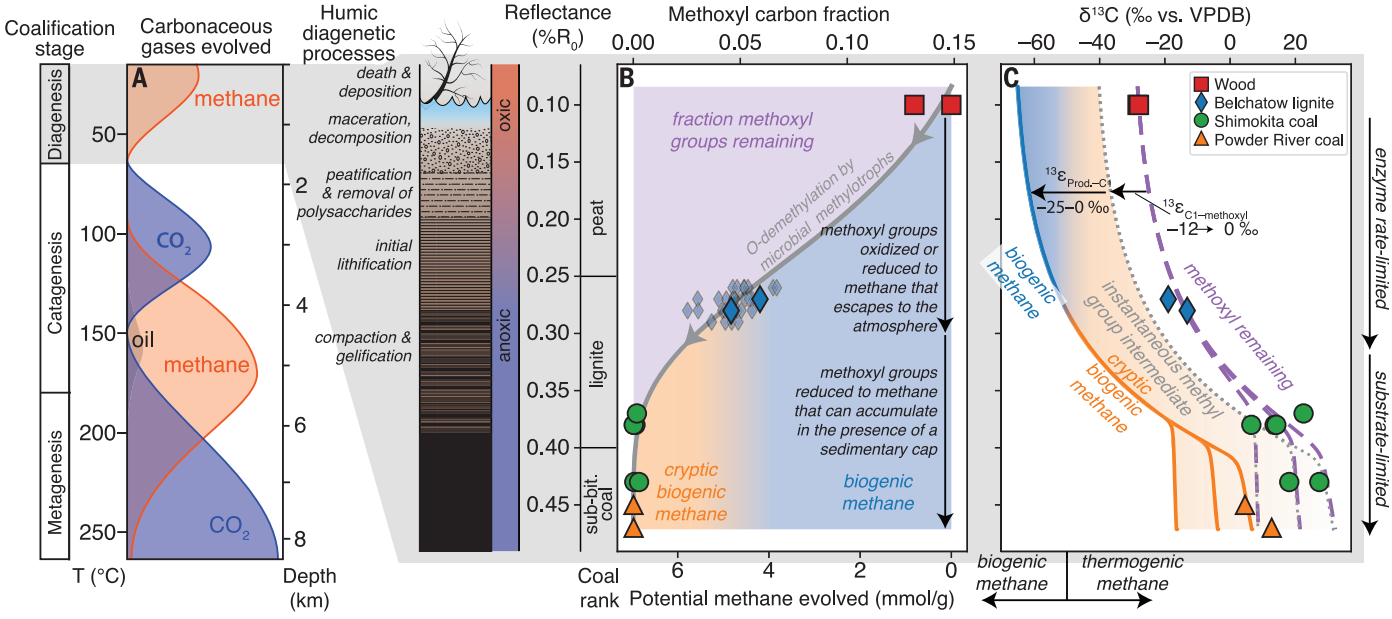


Fig. 2. Conceptual model of O-demethylation in relation to major coalification processes in humic materials. (**A**) Schematic generation of carbonaceous gases as a function of maturity [(*29*); all values approximate]. (**B** and **C**) Concentration (B) and carbon isotopic composition (C) of methoxyl groups and O-demethylation reaction products during the diagenesis of humic materials. Additional Belchatow lignite data (semishaded diamonds) are from (*32*). Relationship between methoxyl carbon fraction and reflectance used to project O-demethylation model to these axes given in fig. S13. sub-bit., subbituminous.

rules out degradation mechanisms in which methoxyl groups are indiscriminately removed in concert with neighboring carbons (materials and methods, section S4) and instead suggests targeted O-demethylation. Four known catalysts could be responsible—heat, acids, oxidants, or enzymes. To distinguish between them, we consider the isotopic consequences of each.

Isotopic fractionations during thermal maturation in coal are often well described by Rayleigh distillation (*16*). To test whether this model applies specifically to thermally activated O-demethylation, we pyrolyzed poplar wood in a dry, open system at 300°C and analyzed the remaining wood sample (table S4; fig. S5; and materials and methods, section S1.1). Methoxyl concentration and $\delta^{13}C_{methoxyl}$ conformed to a Rayleigh process with an isotope effect of $^{13}\varepsilon$ = –12.2 ± 0.4‰ [2σ; $^{13}\varepsilon$ = ($^{13}R_{prod}/^{13}R_{react}$) – 1] (fig. S6). This $^{13}\varepsilon$ is similar to theoretical predictions for O-demethylation through homolytic O–C cleavage at this temperature [–16 to –17‰ (*17*)]. At temperatures of the environmental samples studied here

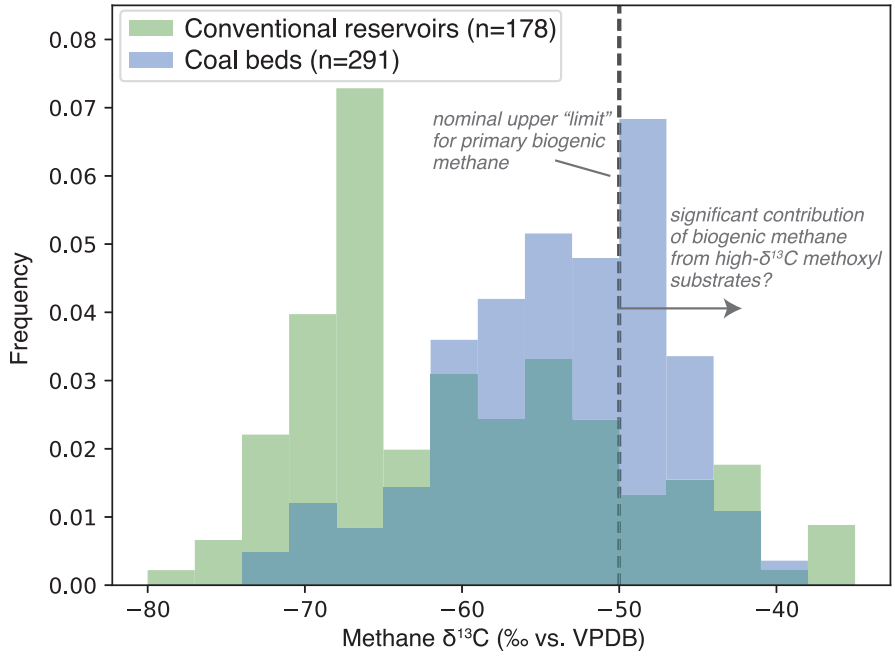


Fig. 3. Histograms of biogenic methane $\delta^{13}C$ values from conventional hydrocarbon reservoirs and coal beds. Conventional hydrocarbon reservoirs are shown in green, and coal beds are shown in blue. Data are compiled in Sherwood *et al*. (*33*). To isolate biogenic methane, only gases with methane/ethane abundance ratios >10^3 from depths <3 km (*15*) are shown. The gray dashed line is the nominal upper $\delta^{13}C$ limit for primary microbial methane [−50‰ (*15*)]. Of biogenic CBM samples, 37% exceed this limit.

(~40° to 75°C), the same theory predicts $^{13}\varepsilon$ values of −55 to −45‰ (*17*) (table S5). No coal methoxyl data fit this prediction (Fig. 1A). Although some data lie on the Rayleigh distillation trend for 300°C pyrolysis, most do not, and we consider this coincidental. We conclude that O-demethylation during coalification is not a thermally activated reaction.

Other abiotic mechanisms impart smaller (less negative) isotope effects. Acid hydrolysis and permanganate oxidation of methyl *tert*-butyl ether (MTBE) fractionate methoxyl groups by $^{13}\varepsilon$ = −16 to −24‰ (table S5). However, the acidic or oxidizing conditions required for these O-demethylations are incompatible with the alkaline and reducing conditions in the Shimokita and Powder River coals (materials and methods, section S1). Even if these reactants were dissolved in coal pore fluids, we would still expect O-demethylation to conform to a Rayleigh model. Because $\delta^{13}C_{methoxyl}$ values in these coals are variable yet uncorrelated with methoxyl concentration, no Rayleigh process with a single $^{13}\varepsilon$ can explain these data, and measured $^{13}\varepsilon$ for these mechanisms are still too large (Fig. 1A). Although each datum could be fit by a Rayleigh-type model with a distinctive $^{13}\varepsilon$—all between −4 and −13‰ (Figs. 1B and fig. S10)—there is no obvious reason why the $^{13}\varepsilon$ of a yet-undiscovered, abiotic process should systematically vary among similar samples.

Our results are better described by an O-demethylation mechanism that is isotopically fractionating at low degrees of reaction progress and then ceases to discriminate between ^{13}C and ^{12}C once methoxyl abundance falls below a certain threshold (~5% of initial; Fig. 1B). This is consistent with a biologic process in a transport-limited environment. We first develop this argument qualitatively and then with a simple model. Although the specific organisms and enzymes responsible for coal methoxyl degradation are unknown, some distinctions can be made. Aerobic O-demethylation has a modest intrinsic isotope effect: −2 to −12‰ in MTBE (an S_N1 reaction; table S5) and no greater than −15‰ during leaf-litter decomposition (fig. S11). Rayleigh models with this $^{13}\varepsilon$ range fit our data (Fig. 1B), but aerobic metabolisms were not viable beyond the least mature samples. Rather, Shimokita and Powder River coals hosted anaerobic communities (materials and methods, section S1). Anaerobes capable of O-demethylation (e.g., some acetogens, sulfate reducers, fermenters, and methanogens) employ S_N2-type methyltransferases with large intrinsic isotope effects (−40 to −80‰; table S5). These would appear incompatible with our data, but intrinsic isotope effects are masked when enzymatic reactions are substrate limited [e.g., (*18*)]. Considering that biologic O-demethylation in coal would require extracellular enzymes to encounter and activate parts of the coal matrix, it is conceivable and perhaps expected that microbial O-demethylation would discriminate less strongly as this moiety is consumed.

We model this process with the Best equation (*19*), which couples the diffusion of substrate to an enzyme site (or vice versa; so-called mass transfer) to the Michaelis-Menten equation for enzymatic rate. Whether a biologic process operates under a mass transfer or enzymatic limitation depends on the substrate delivery rate constant, the specific affinity of the enzyme, and the concentration of substrate (*20*). In a closed system, a biologic process can transition from enzyme limited to mass transfer limited as the substrate pool is depleted. The isotopic fractionation of the reaction observed at any instant (α_{obs}, where $\alpha_{obs} = R_{prod}/R_{react}$) is represented as (*21*)

$$\alpha_{obs} = \alpha_0 \times \frac{1+A}{1+\alpha_0 \times A} \quad (1)$$

where α_0 is the intrinsic enzyme fractionation factor ($\alpha_0 = \varepsilon_0 + 1$) and A is

$$A = \frac{1}{2} \times \left(\frac{1}{B_n} - \frac{c}{K_m} - 1\right) + \sqrt{\frac{1}{B_n} + \frac{1}{4} \times \left(\frac{1}{B_n} - \frac{c}{K_m} - 1\right)^2} \quad (2)$$

Here, c is the methoxyl substrate concentration, K_m is the Michaelis-Menten constant for the O-demethylation reaction, and B_n is the bioavailability number (the ratio of the mass transport rate constant to the specific affinity of the enzyme). Under conditions of high bioavailability (large B_n), $A \to 0$ and the enzymatic fractionation factor is expressed independent of c. Under low bioavailability, $A \to \infty$, and $\alpha_{obs} \to 1$. As the methoxyl pool is depleted, α_{obs} transitions from ~α_0 to 1.

We apply Eq. 1 to predict $\delta^{13}C_{methoxyl}$ during lignin biodegradation in a closed system (Fig. 1B). The model is underconstrained but consistent with our data (within 2‰) when reasonable parameters are chosen. Acceptable (but nonunique) fits have initial $c/K_m = 5 \times 10^3$, $^{13}\varepsilon_0$ = −12‰, and B_n from 0.01 to 0.05. Assuming 1 wt % ≈ 0.01 M methoxyl concentration, this suggests K_m = 0.02 mM, consistent with 0.015 to 0.06 mM for an O_2-dependent lignin monomer *O*-demethylase (*22*) and similar to K_m for an anoxic *O*-demethylase [0.08 mM (*23*)]. A more-complex and descriptive model would transition from a smaller $^{13}\varepsilon_0$ (−12‰) to a larger $^{13}\varepsilon_0$ (~−70‰) as the substrate is depleted, but this model is nearly indistinguishable from the simpler one shown. Alternative models with a fixed $^{13}\varepsilon_0$ of −70‰ and B_n of 0.0005 to 0.001 fit the more-mature coals but not the Belchatow lignites (Fig. 1B).

Our findings suggest that in these samples, lignin O-demethylation was a microbial reaction. Specifically, the data are best explained by a model where initial, perhaps aerobic, enzyme rate–limited O-demethylation was succeeded

by anaerobic O-demethylation under substrate-limited conditions (Fig. 1B and Fig. 2). This model is consistent with the geologic context of these materials. The least-mature Belchatow lignites underwent early coalification in a shallow setting unfavorable for establishing strongly reducing conditions (<250 m of clastic overburden in a tectonic graben; materials and methods, section S1), which would have inhibited anaerobic metabolisms. The onset of microbial CBM production tends to coincide with a thermal maturity of 0.3% R_o—just beyond that of these lignites [0.26 to 0.29% R_o (*24*)] (Fig. 2). Thus, Belchatow lignites likely record only initial O-demethylation, which probably occurred during peat formation within a few meters of the surface and approximately tens of thousands of years after deposition, consistent with previous findings (*7*). In more-mature, deeply buried coals of approximately the same age (early Miocene), methoxyl abundances drop by another 10 to 100×, which suggests a later proliferation of anaerobic O-demethylation. This extends the conditions over which microorganisms directly modify humic materials to depths of 2 km, temperatures of 50°C in subbituminous coals, and therefore on time scales of tens of millions of years.

At low methoxyl concentrations (0.05 to 2% remaining), $\delta^{13}C_{methoxyl}$ vary by 25‰. It is unlikely that this scatter is primarily the result of source variability. Wood $\delta^{13}C_{methoxyl}$ vary by at most 10‰ (table S6). Leaf $\delta^{13}C_{methoxyl}$ are up to 45‰ lower than wood; however, most leaf methoxyl groups are in labile compounds unlikely to survive peatification, wood contains approximately five times more methoxyl groups by dry mass, and woody tissues are the main feedstock for these coals (*7*, *25*) (materials and methods, section S1, and fig. S11). Instead, we speculate that methoxyl isotopic variability results from differences in the physical encapsulation of lignin within the coal matrix (e.g., armored in intact macerals versus disseminated in groundmass), which variably restricted the ability of extracellular enzymes to access the substrate, and is captured in our simple model as a 5× range in B_n.

Combined with evidence for methyl fermentation and methanogenesis in the same Shimokita coals (*13*, *26*), our findings suggest a complete microbial reaction pathway from coal methoxyl groups to methane. Temperature is a key variable for deep biosphere life, influencing community size, activity, and composition (*13*, *14*). However, the observation of pervasive biodegradation with minimal isotopic fractionation in situ in subbituminous coals suggests that substrate availability ultimately limited O-demethylation in these units. Models of the Shimokita coal community also suggest a carbon-starved, substrate-limited existence (*27*). Considering that initial activation of coal moieties may be the rate-limiting step of microbial methanogenesis (*28*), our results indicate that, here, coal bioavailability limited microbial CBM production. If these results are generalizable, the abundance of methoxyl groups that persist until gas can accumulate may be an important control on CBM yield (Fig. 2 and materials and methods, section S5).

The existence of a widespread, labile carbon pool that is anomalously ^{13}C-enriched bears on the interpretation of methane origins in coals. Stable isotopic fingerprinting principles developed in conventional hydrocarbon reservoirs (*15*, *29*) are routinely violated in unconventional coal-bed systems: Coal gases of probable microbial origin (based on thermal maturity and methane/ethane abundance ratio) often have methane $\delta^{13}C$ values above −50‰, which is the nominal upper limit for primary microbial methane (*30*, *31*) (Fig. 3). Existing explanations include the following: Bulk organic carbon is more ^{13}C enriched in coals versus conventional sources (*30*); a greater fraction of microbial CBM is formed through acetoclastic versus CO_2 reductive pathways (*30*, *31*); and methanogenic substrates from coal are partly diverted to other fates, leaving residues ^{13}C enriched (*31*). We suggest an alternative explanation: Near-quantitative coal methylotrophy generates methane with a ^{13}C content similar to this ^{13}C-enriched substrate (Fig. 2). Specifically, initial O-demethylation, probably occurring during peatification, isotopically fractionates lignin methoxyl groups. Remaining ^{13}C-enriched methoxyl groups are anaerobically biodegraded to C1 intermediates (*11*) that can feed methanogenesis (materials and methods, section S5). Because this anaerobic O-demethylation is near quantitative, the cumulative $\delta^{13}C$ of the C1 intermediate matches the initial coal methoxyl pool. If methanogenesis is also quantitative or substrate limited, the $\delta^{13}C$ of accumulated methane will match the initial as well. Taking the methoxyl abundance and ^{13}C content of the Belchatow lignites as representative of the pool delivered to the deep subsurface, this scheme suggests that the biodegradation of humic coals should generate up to 2 to 3 mmol/g of cryptic microbial methane with unusually high $\delta^{13}C$ values (−20 to −10‰; Fig. 2). Considering that total CBM potentials are ~8 mmol/g (materials and methods, section S5), contributions from methoxyl-derived methane could appreciably raise the bulk $\delta^{13}C$ value of microbial CBM (Fig. 3). Given the paucity of methoxyl groups in conventional hydrocarbon deposits, this likely explains the enigmatic $\delta^{13}C$ offset between microbial methane from coal and conventional sources.

REFERENCES AND NOTES

1. World Energy Resources 2016 (World Energy Council, 2016); www.worldenergy.org/publications/entry/world-energy-resources-2016.
2. D. Ritter *et al*., *Int. J. Coal Geol.* **146**, 28–41 (2015).
3. M. Saunois *et al*., *Earth Syst. Sci. Data* **12**, 1561–1623 (2020).
4. A. J. Turner, C. Frankenberg, E. A. Kort, *Proc. Natl. Acad. Sci. U.S.A.* **116**, 2805–2813 (2019).
5. D. Rice, *AAPG Stud. Geol.* **38**, 159–184 (1993).
6. D. Strąpoć *et al*., *Annu. Rev. Earth Planet. Sci.* **39**, 617–656 (2011).
7. P. G. Hatcher, D. J. Clifford, *Org. Geochem.* **27**, 251–274 (1997).
8. C. Durand-Souron, R. Boulet, B. Durand, *Geochim. Cosmochim. Acta* **46**, 1193–1202 (1982).
9. I. Blom, L. Edelhausen, D. W. van Krevelen, *Fuel* **36**, 135–153 (1957).
10. D. F. Payne, P. J. Ortoleva, *Org. Geochem.* **32**, 1073–1085 (2001).
11. J. Heider, G. Fuchs, *Eur. J. Biochem.* **243**, 577–596 (1997).
12. D. Mayumi *et al*., *Science* **354**, 222–225 (2016).
13. F. Inagaki *et al*., *Science* **349**, 420–424 (2015).
14. V. B. Heuer *et al*., *Science* **370**, 1230–1234 (2020).
15. M. J. Whiticar, *Chem. Geol.* **161**, 291–314 (1999).
16. C. Clayton, *Mar. Pet. Geol.* **8**, 232–240 (1991).
17. Y. Tang, J. K. Perry, P. D. Jenden, M. Schoell, *Geochim. Cosmochim. Acta* **64**, 2673–2687 (2000).
18. K. L. Londry, K. G. Dawson, H. D. Grover, R. E. Summons, A. S. Bradley, *Org. Geochem.* **39**, 608–621 (2008).
19. J. B. Best, *J. Cell. Comp. Physiol.* **46**, 1–27 (1955).
20. T. N. P. Bosma, P. J. M. Middeldorp, G. Schraa, A. J. B. Zehnder, *Environ. Sci. Technol.* **31**, 248–252 (1996).
21. M. Thullner, M. Kampara, H. H. Richnow, H. Harms, L. Y. Wick, *Environ. Sci. Technol.* **42**, 6544–6551 (2008).
22. S. J. B. Mallinson *et al*., *Nat. Commun.* **9**, 2487 (2018).
23. D. Naidu, S. W. Ragsdale, *J. Bacteriol.* **183**, 3276–3281 (2001).
24. L. Gao, M. Mastalerz, A. Schimmelmann, in *Coal Bed Methane: From Prospect to Pipeline*, P. Thakur, S. Schatzel, K. Aminian, Eds. (Elsevier, 2014), pp. 7–29.
25. F. Keppler, R. M. Kalin, D. B. Harper, W. C. Mcroberts, J. T. G. Hamilton, *Biogeosciences* **1**, 123–131 (2004).
26. E. Trembath-Reichert *et al*., *Proc. Natl. Acad. Sci. U.S.A.* **114**, E9206–E9215 (2017).
27. S. A. Bowden *et al*., *Basin Res.* **32**, 804–829 (2020).
28. B. Wawrik *et al*., *FEMS Microbiol. Ecol.* **81**, 26–42 (2012).
29. M. Schoell, *AAPG Bull.* **67**, 2225–2238 (1983).
30. M. J. Whiticar, *Int. J. Coal Geol.* **32**, 191–215 (1996).
31. D. S. Vinson *et al*., *Chem. Geol.* **453**, 128–145 (2017).
32. H. Lee, X. Feng, M. Mastalerz, S. J. Feakins, *Org. Geochem.* **136**, 103894 (2019).
33. O. A. Sherwood, S. Schwietzke, V. A. Arling, G. Etiope, *Earth Syst. Sci. Data* **9**, 639–656 (2017).

ACKNOWLEDGMENTS

We thank K. Snell for use of analytical facilities and M. Formolo and S. Petsch for sharing materials. Shimokita samples were provided by the International Ocean Discovery program. H. L. O. McClelland, D. Stolper, A. Schimmelmann, C. Ponton, and H. Lee provided helpful suggestions at various stages of the project. **Funding:** This work was supported by NSF EAR 1322058 to J.M.E.; a NASA postdoctoral fellowship with the NASA Astrobiology Institute to E.T.-R.; the L'Oréal USA For Women in Science fellowship to E.T.-R.; the L'Oréal-UNESCO FWIS International Rising Talent Endowment to E.T.-R.; and the ACS award PRF-53747-ND2 to S.J.F., which initiated their work on this project. **Author contributions:** Conceptualization: M.K.L. and E.T.-R.; Methodology: M.K.L., E.T.-R., S.J.F., A.L.S., and J.M.E.; Investigation: M.K.L., E.T.-R., and K.S.D.; Resources: E.T.-R., S.J.F., M.M., V.J.O., A.L.S., and J.M.E.; Writing – original draft: M.K.L.; Writing – review and editing: M.K.L., E.T.-R., S.J.F., M.M., V.J.O., A.L.S., and J.M.E.; Supervision and funding acquisition: J.M.E. **Competing interests:** The authors have no competing interests on this project. **Data and materials availability:** All data are available in the main text or the supplementary materials.

SUPPLEMENTARY MATERIALS

science.org/doi/10.1126/science.abg0241
Materials and Methods
Figs. S1 to S14
Tables S1 to S6
References (*34*–*88*)
MDAR Reproducibility Checklist

8 December 2020; accepted 13 September 2021
10.1126/science.abg0241



High Shear Homogenizers

By reducing particle size uniformly, Analytik Microfluidizers are helping a growing number of pharmaceutical companies and contact development and manufacturing organizations (CDMOs) improve the efficacy, bioavailability, stability, and process efficiency of their drugs. Today, Microfluidizer technology from Analytik is widely viewed as the gold standard for scalable uniform particle-size reduction for vaccine adjuvants, dispersions, liposomes, and cell disruption manufacturing processes. Microfluidizer technology seamlessly scales up from batch volume to lab, pilot, and even production volumes. Whether you are producing nanoemulsions, pursuing delicate cell disruptions, creating suspensions, or generating cutting-edge liposomes, Microfluidizer Processor High Shear Homogenizers are the right equipment for the job.

Analytik
For info: +44-(0)-1954-232776
analytik.co.uk/microfluidizer-processor-high-shear-homogenisers

Automated Western Blot Processor

The Invitrogen Bandmate Automated Western Blot Processor is a programmable blot rocking system that saves time by automating the tedious hands-on blocking, washing, and antibody incubation steps of Western blot processing. With so many steps, it's challenging to focus on other work or experiments while processing a Western blot, especially if processing several blots simultaneously. Often, a specific protocol and reagents are optimized for a protein of interest. The Bandmate processor requires no special reagents and is programmable to match your current Western blotting protocols. Minimal effort is required to setup the Bandmate, which can process up to four blots using your current reagents and protocols, but with much less hands-on time.

Thermo Fisher Scientific
For info: +1-800-955-6288
www.thermofisher.com

Lysis Buffer for Enzymatic Shearing

The Chromatrap lysis buffer for enzymatic shearing provides users with a complete lysis buffer for the disruption of nuclear cell membranes with a milder detergent than that required for mechanical fragmentation. Lysis is crucial for enabling researchers to better explore and understand the underlying processes and mechanisms that drive biological organisms. Correct shearing is critical to the success of a chromatin immunoprecipitation (ChIP) assay. The buffer is compatible with all Porvair ChIP kits for enzymatic shearing from fixed cells or tissue. Chromatrap lysis buffers are formulated to ensure that the nuclear membrane in your samples is disrupted, releasing a high yield of nuclear material for your research.

Porvair Sciences
For info: +44-(0)-1978-661144
www.chromatrap.com/lysis-buffer-for-enzymatic-shearing

Cryogenic Storage of Biological Specimens

Ziath offers a range of CryzoTraq tubes designed for high-integrity cryogenic storage of biological specimens at temperatures down to −196°C. Each batch is beta-radiation sterilized by an electron beam, eliminating potential biological contaminants from the product preparation workflow and ensuring that the cryotubes are free from RNase, DNase, and other unwanted substances. Ziath's 2D-barcoded tubes are guaranteed leak-free and feature a proprietary two-stage injection-moulded cap that avoids using traditional sealing solutions such as O-rings. CryzoTraq 2D-barcoded tubes are suitable for use with most cryoracking systems, as they are available in 2-mL and 5-mL standard-size formats. These advanced storage tubes are supplied with both internal and external threaded caps, so they are compatible with almost any capping/decapping system. All CryzoTraq tubes have a 2D Datamatrix barcode inserted in the base of the tube. During the manufacturing process, the linear barcode is printed onto the side of the tube first, and the 2D code is automatically generated from the linear barcode, which means the two barcodes will always be the same with no errors.

Ziath
For info: +1-858-880-6920
ziath.com/products/tubes/cryzotraq-tubes-and-racks

FFPE/Fresh Frozen BRCA 1/2-Characterized Breast Tissue

BioChain is expanding its product line of NGS-characterized biosamples by offering ready-to-use *BRCA*-characterized FFPE/frozen sections/blocks for preclinical drug development and as reference samples for Clinical Laboratory Improvement Amendment (CLIA)-certified labs. Mutations within *BRCA* genes result in the loss of DNA repair and are therefore linked to susceptibility of certain cancers. Currently, our *BRCA*-characterized samples derive from breast cancer donors, as the *BRCA* genes are strongly linked to oncogenesis in this tissue type. However, we will continue to characterize additional tissue types where cancer development is linked to *BRCA* mutations. These *BRCA*-characterized samples are excellent reference tissues for scientists in the oncology field who are studying pathways related to *BRCA1* and *BRCA2*. In several cases, samples may be available as matched sets, which include the adjacent normal/primary tumor tissue along with plasma from the same donor.

BioChain Institute, Inc.
For information: +1-888-762-2568
www.biochain.com

Reflective Beam Expanders

Optical Surfaces Ltd. announces a new series of reflective beam expanders with an output clear aperture of 75 mm and a selection of magnifications. Benefiting from a high-throughput, off-axis design and new assembly technique, the A1-Series of reflective beam expanders offers high performance at a market-competitive price and is available on short delivery times. Available in 3.5x, 5x, 7.5x, and 10x fixed-magnification configurations, the A1-Series is easy to use and provides accurate, unobstructed expansion of any collimated-input light source. These new expanders are portable and can be used without the need for internal realignment.

Optical Surfaces
For info: +44-(0)-208-668-6126
www.optisurf.com

Electronically submit your new product description or product literature information! Go to www.science.org/about/new-products-section for more information.

Newly offered instrumentation, apparatus, and laboratory materials of interest to researchers in all disciplines in academic, industrial, and governmental organizations are featured in this space. Emphasis is given to purpose, chief characteristics, and availability of products and materials. Endorsement by *Science* or AAAS of any products or materials mentioned is not implied. Additional information may be obtained from the manufacturer or supplier.

ScienceCareers online @sciencecareers.org

THE UNIVERSITY OF TENNESSEE KNOXVILLE

CLUSTER HIRE

QUANTUM MATERIALS, QUANTUM INFORMATION, AND QUANTUM COMPUTING

THE UNIVERSITY OF TENNESSEE, KNOXVILLE

The Departments of Physics and Astronomy, Materials Science and Engineering (MSE), and Electrical Engineering and Computer Science (EECS) at the University of Tennessee, Knoxville, invite applications for **three tenure-track faculty positions at the assistant professor level**. These positions are part of a cluster hire between the three departments in the area of Quantum Materials for Future Technologies. The appointments are expected to begin **August 1, 2022**. The successful applicants may have joint appointments between the relevant departments. These positions come with highly attractive startup packages to enable innovative research.

The three positions are:

A **computer scientist** or **physicist** with interest and expertise in one or more of the following areas: quantum information, quantum computation, quantum materials, artificial intelligence and/or machine learning. Preference will be given to candidates who can interface between these areas; see **https://apply.interfolio.com/95968.**

A **condensed matter experimentalist** with interest and expertise in scanning tunneling microscopy and spectroscopy. Preference will be given to researchers who can interface with quantum materials researchers and other members of the clusters; see **https://apply.interfolio.com/95969**.

A **researcher** with interest and expertise in experimental quantum materials research with a focus on device fabrication and nanoscale transport phenomena. Preference will be given to candidates who can interface with the other members of the cluster; see **https://apply.interfolio.com/95952**.

These strategic hires will work at the boundaries between physics and engineering. The successful candidate will join a thriving and growing research community working in the broader area of quantum materials and quantum information, which includes three recently appointed cluster faculty. The goal of the cluster is to accelerate the development of quantum science, artificial intelligence, and their technological applications; and to develop new interdisciplinary courses in this area, both at the graduate and undergraduate levels.

Candidates should have a Ph.D. in physics, materials science, electrical engineering, computer science or closely related field. The successful candidate will have established an exemplary record of research that includes significant contributions to the candidate's field of study and that is indicative of future promise and scientific leadership, as demonstrated through publications in peer-reviewed journals, the number and significance of invited talks, evidence of leadership roles the candidate may have assumed, and the candidate's Statement of Research. The successful candidate will be expected to establish an externally funded research program in their home department(s) and provide training for graduate students and postdoctoral researchers.

The successful candidate will also be expected to contribute to the teaching mission of the participating departments. We are looking for candidates committed to effective undergraduate and graduate teaching, as well as, to innovation in the development of curricula and teaching methods, as demonstrated by the candidate's Statement of Teaching. Evidence of prior formal, or informal but notable, teaching, and outreach will be an advantage.

The University respects and values people of all races, genders, creeds, cultures, and sexual orientations, and holds a deep commitment toward developing and promoting an inclusive community. We strongly encourage applications from members of groups that are underrepresented in STEM fields, as well as, candidates who will contribute in meaningful ways to the equity and inclusion goals of the three departments. The latter should be demonstrated in the candidate's Statement on Diversity, Equity, and Inclusion.

The University of Tennessee, Knoxville, is Tennessee's flagship State research institution, a campus of choice for outstanding undergraduates and a premier graduate institution with nationally and internationally ranked programs. Many faculty members are recognized as leaders in their fields. The successful candidate will benefit from the available resources and proximity to unique research facilities at Oak Ridge National Laboratory.

The University's campus is in one of the most beautiful areas of the country, with easy access to miles of inland waterways, pristine state and national parks, diverse cultural opportunities, and a blend of convenient urban and rural living settings. Downtown Knoxville, adjacent to campus, is a thriving neighborhood filled with restaurants, shops, and indoor and outdoor entertainment venues, and is home to the Knoxville Symphony Orchestra, the Knoxville Opera Company, annual international festivals, such as the Big Ears Music Festival, and seasonal and weekly events such as Jazz on the Square, Shakespeare on the Square, and the Farmers Market.

Applicants should send a **1)** Curriculum Vitae including a list of publications and invited talks, **2)** Statement of Research with proposed research program, **3)** Statement of Teaching, **4)** Statement of Diversity, Equity, and Inclusion, and should also arrange for at least three letters of reference to be submitted separately. All application materials, including the letters, should be submitted via the Interfolio links provided above. Only electronic applications will be considered, and acceptable file formats are .pdf or .docx. We will start reviewing applications by **January 10, 2022**.

Equal Employment Opportunity Statement

The University of Tennessee is an EEO/AA/Title VI/Title IX/Section 504/ADA/ADEA institution in the provision of its education and employment programs and services. All qualified applicants will receive equal consideration for employment and admission without regard to race, color, national origin, religion, sex, pregnancy, marital status, sexual orientation, gender identity, age, physical or mental disability, genetic information, veteran status, and parental status.

Mays Cancer Center
UT Health San Antonio MD Anderson Cancer Center

Postdoctoral Fellow – Cancer Research
UT Health San Antonio (UT Health SA)

The Mays Cancer Center, an NCI-designated cancer center located at UT Health SA, is recruiting **postdoctoral fellows** for ongoing translational cancer research. Research at Mays Cancer Center combines the expertise of renowned cancer researchers, state-of-the-art laboratory technologies and a team approach. These capabilities fuel discovery at an accelerated pace. Our goal is to lessen cancer's impact on our community and beyond.

UT Health SA is a research-intensive institution located in San Antonio and it sits in the gateway to the picturesque Texas Hill Country. San Antonio is a vibrant, multicultural city with year-round recreational activities, affordable housing, and a high standard of living.

Individual job postings for Mays Cancer Center faculty are available through the Office of Postdoctoral Affairs: **https://opa.uthscsa.edu/position-listings/postdoctoral-position?category=Cancer#Cancer.**

All postdoctoral appointments are designated as security sensitive positions.

UT Health SA is an Equal Opportunity/Affirmative Action Employer. All qualified applicants will receive consideration for employment without regard to sex, gender identity, sexual orientation, race, color, religion, national origin, disability, protected Veteran status, age, or any other characteristic protected by law or policy.



Science Careers helps you advance your career. Learn how!

- Register for a free online account on **ScienceCareers.org**.
- Search hundreds of job postings and find your perfect job.
- Sign up to receive e-mail alerts about job postings that match your criteria.
- Upload your resume into our database and connect with employers.
- Watch one of our many webinars on different career topics such as job searching, networking, and more.

Visit **ScienceCareers.org** today — all resources are free

ScienceCareers
FROM THE JOURNAL SCIENCE AAAS



SCIENCECAREERS.ORG

Who's the top employer for 2021?

Science Careers' annual survey reveals the top companies in biotech & pharma voted on by *Science* readers.

Read the article and employer profiles at sciencecareers.org/topemployers

Science 2021 TOP EMPLOYER



Massachusetts Institute of Technology

Faculty Position
Department of Biological Engineering

The MIT Department of Biological Engineering in Cambridge, MA invites applications for tenure-track faculty positions at the assistant professor level, to begin July 1, 2022 or on a mutually agreeable date thereafter. Applicants should hold a Ph.D. in a science or engineering discipline related to biological engineering by the beginning of employment. A more senior faculty appointment may be considered in special cases commensurate on experience. Candidates should aspire to lead a research program that fuses molecular/cellular bioscience with quantitative engineering analysis/synthesis approaches. Areas of high priority include non-medical biotechnology, including applications in materials, chemicals, agriculture, sustainability, energy and the environment. Faculty duties include teaching at the graduate and undergraduate levels as well as oversight of research, and candidates should be capable of instructing in our core biological engineering educational curricula.

Candidates must register with the BE search website at http://be-fac-search.mit.edu, and must submit application materials electronically to this website. Candidate applications should include a description of professional interests and goals in both teaching and research. Each application should include a curriculum vita and the names and addresses of three or more references who will provide recommendation letters. References should submit their letters directly at the http://be-fac-search.mit.edu website.

Applications received by February 28, 2022 will be given priority.

Questions may be directed to: Prof. Angela Belcher, Head, Department of Biological Engineering MIT16-343, Cambridge, MA 02139, bedh@mit.edu.

With MIT's strong commitment to diversity in engineering and science education and research, we especially encourage those who will contribute to our diversity and outreach efforts to apply.

MIT is an equal employment opportunity employer. All qualified applicants will receive consideration for employment and will not be discriminated against on the basis of race, skin color, gender identity, sexual orientation, religion, disability, age, genetic information, veteran status, ancestry, or national or ethnic origin. MIT's full policy on Nondiscrimination can be found at: https://policies.mit.edu/policies-procedures/90-relations-and-responsibilities-within-mit-community/92-nondiscrimination

http://web.mit.

The National Academies of SCIENCES · ENGINEERING · MEDICINE

Postdoctoral Research Associates - NRC Research Associateship Programs

The National Academies of Sciences, Engineering, and Medicine administers **postdoctoral** and **senior** research awards at participating federal laboratories and affiliated institutions at locations throughout the U.S and abroad.

We are seeking highly qualified candidates who hold, or anticipate earning, a doctorate in a variety of fields of science or engineering. Degrees from foreign universities should be equivalent in training and research experience to a doctoral degree from a U.S. institution. Citizenship eligibility varies among the sponsoring laboratories.

Application deadline dates (four annual review cycles):
- February 1
- May 1
- August 1
- November 1

Awardees have the opportunity to:
- Conduct independent research in an area compatible with the interests of the sponsoring laboratory
- Devote full-time effort to research and publication
- Access the excellent and often unique facilities of the federal research enterprise
- Collaborate with leading scientists and engineers at the sponsoring laboratories

Awardee benefits include:
- Stipends ranging from $45,000 to $87,000; may be higher based on experience
- Health insurance (including dental and vision), relocation benefits, and a professional travel allowance

For detailed program information, to search Research Opportunities, and to contact prospective Research Adviser(s) visit **www.nas.edu/rap**.

The National Academies of SCIENCES · ENGINEERING · MEDICINE

Postdoctoral Research Fellows - Air Force Science & Technology Fellowship Program

The National Academies of Sciences, Engineering, and Medicine administers **postdoctoral** and **senior** fellowship awards at the U.S. Air Force Research Laboratory (AFRL), the U.S. Air Force Institute of Technology (AFIT), and the U.S. Air Force Academy (USAFA) under the Air Force Science & Technology Fellowship Program (AF STFP).

We are seeking highly qualified candidates who are U.S. citizens and hold, or anticipate earning, a doctorate in a variety of fields of science or engineering.

Application deadline dates (four annual review cycles):
- February 1
- May 1
- August 1
- November 1

Awardees have the opportunity to:
- Conduct independent research in an area compatible with the interests of the Air Force laboratories
- Devote full-time effort to research and publication
- Access the excellent and often unique Air Force research facilities
- Collaborate with leading scientists and engineers

Awardee benefits include:
- Base stipend starting at $76,542; may be higher based on experience
- Health insurance (including dental and vision), relocation benefits, and a professional travel allowance

For detailed program information, to search for AFRL, AFIT, and USAFA Research Opportunities, and to contact prospective Research Adviser(s), visit **www.nas.edu/afstfp**.

By **E.A.D.**

Out of the fog

The tile floor was cold and hard against my knees, but I couldn't move from my spot in front of the toilet. It was the third morning that week I had spent violently throwing up because of anxiety at the prospect of going into the lab. So far, I had been able to stay home without consequence. But that day I was scheduled to meet other lab members to work on an experiment essential for my Ph.D. project. At 5:45 a.m. I let them know I wouldn't be coming in, feeling a wave of guilt. "How did I get here?" I wondered.

I entered grad school in July 2019. The first semester went smoothly—I did well in my classes, met interesting people, and found an adviser after a series of lab rotations. But everything changed during my second semester, as COVID-19 spread.

With our lab shut down and bench work impossible, I tried to focus on my classes, which had gone virtual. Eventually, though, I experienced Zoom burnout and began to pay less attention. As in-person interactions waned, so did my mental health.

When the semester finished, I moved to doing research full time, and my days had even less structure and social connection. My university lifted restrictions on lab work in July 2020, but I couldn't find the will to go in. The only person I saw for the next few months was my husband. Friends and family reached out, but as I sank deeper into depression, I stopped responding.



"It took a major downturn in my mental health to find the courage to open up."

Throughout my life I had dealt with more minor mental health issues, but what I experienced during the pandemic was unlike anything before. My depression was so bad I was essentially bed-bound. I barely managed to shower once a week, could not sleep, and had zero motivation to work—a problem I never imagined I would have. Yet there I was, doing nothing day after day. The inertia was insurmountable.

I noticed that many of my peers were publishing papers and winning awards. I felt certain I didn't belong in my program and would be asked to leave as soon as my lack of progress was brought to light. I canceled meetings with my adviser for 2 months straight, hoping she wouldn't notice.

But by April, I felt I couldn't keep it up much longer. My qualifying exam was coming up and I feared I would fail. I was also scheduled to meet with my adviser to complete a progress report. I decided to use the report as a chance to disclose why I wasn't productive—depression. This was my first time revealing a personal issue to a mentor. The other labs I had worked in all seemed to treat personal life as completely private, so I had as well. It took a major downturn in my mental health to find the courage to open up.

I expected disappointment, but instead my adviser expressed sympathy and support. I wished I'd spoken to her sooner. She told me she was concerned about my lack of progress, and her feedback motivated me to get back to the lab and prepare for my exam, which I passed. But my mouse colonies could only reproduce at a certain pace, so I still felt stymied and unproductive. Slowly, I slipped back into depression.

Through it all, my husband had been urging me to see a psychiatrist, and in July, I finally went. I was put on medication to try and get my life back on track. Shortly before taking that step, I also got involved in my program's graduate organization. I volunteered to serve as chair of the social committee, hoping to give my social side a stimulus.

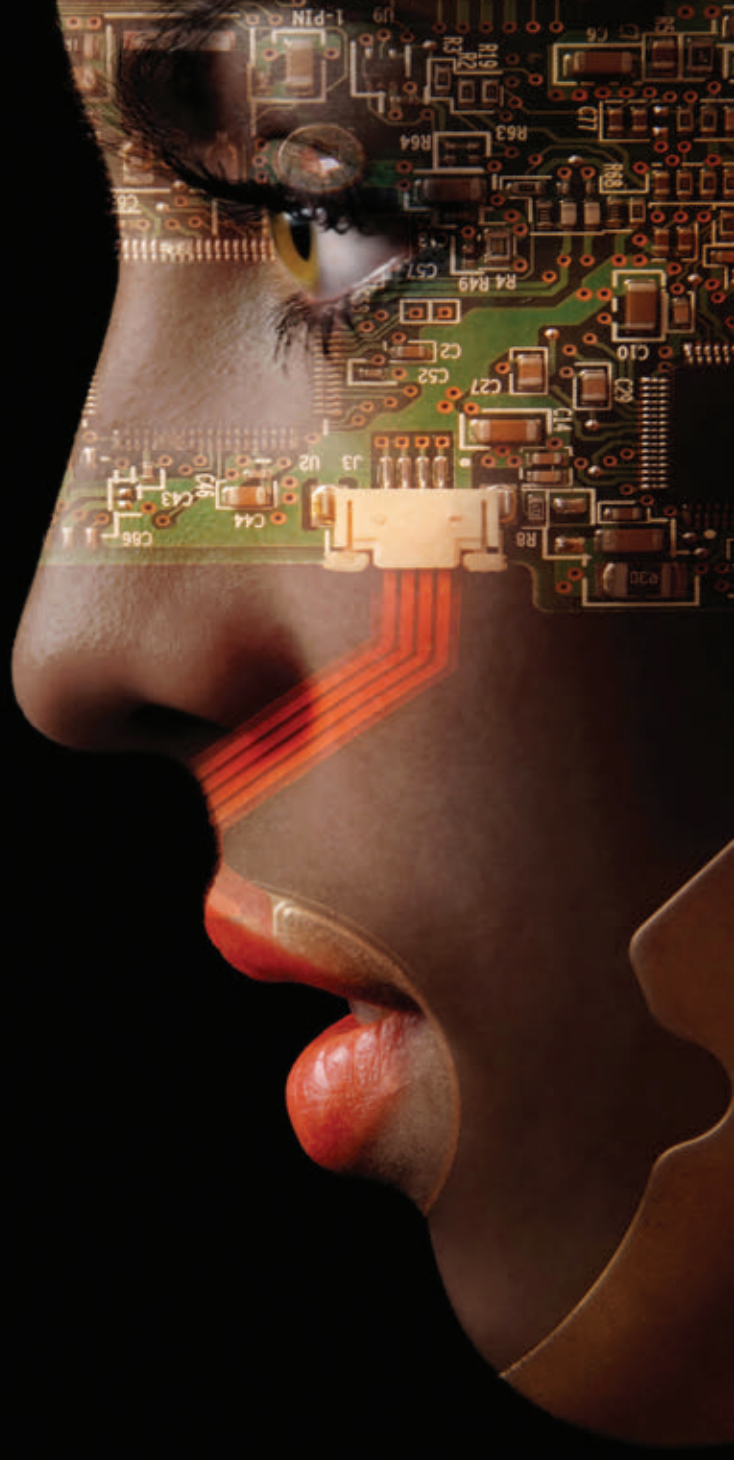
My role on the committee was key, helping me more than the meds. It forced me to get out of bed, shower, and socialize, even when I didn't want to. At first, my body rebelled. I'd become so accustomed to inactivity that simply leaving the apartment left me sore. But I liked coordinating events, interacting with peers, and having structure and purpose to my days. I began to come out of the fog that had enveloped me.

Gradually, I started to go into the lab more often. I still go through periods where I struggle. But I have experiments lined up and data to analyze, and I'm eager to move my projects forward again. I'm thankful for the understanding my husband and my adviser showed me during one of the darkest chapters of my life. If you're going through something similar, I'd recommend reaching out for support. It's not easy finding your way out of a mental health crisis, but it's less daunting when you have an empathetic shoulder to lean on. ■

The author, whose initials are E.A.D., is a Ph.D. student at the University of Virginia. Send your career story to SciCareerEditor@aaas.org.

ILLUSTRATION: ROBERT NEUBECKER

Share **Your Robotics Research** with the **World**.



Shaping the future of robotics with high impact research!

As a multidisciplinary online-only journal, *Science Robotics* publishes original, peer-reviewed, research articles that advance the field of robotics. The journal provides a central forum for communication of new ideas, general principles, and original developments in research and applications of robotics for all environments.

Submit your research today. Learn more at: **ScienceRobotics.org**

Twitter: @SciRobotics
Facebook: @ScienceRobotics

Science Robotics
AAAS

Prix Liliane Bettencourt *pour les sciences du vivant*



LAURÉATE 2021

Valérie Gabelica

European Institute of Chemistry and Biology
Bordeaux, France

For the project: New mass spectrometry approaches to study the stability of nucleic acids

© Alexandre Darmon / Art in Research

Fondation Bettencourt Schueller

Reconnue d'utilité publique depuis 1987